NANO-HETERO-STRUCTURES FOR CHEMICAL SENSING: OPPORTUNITIES AND CHALLENGES

EDITED BY: Sheikh A. Akbar, Xiaogan Li and Qasem Ahmed Drmosh
PUBLISHED IN: Frontiers in Materials

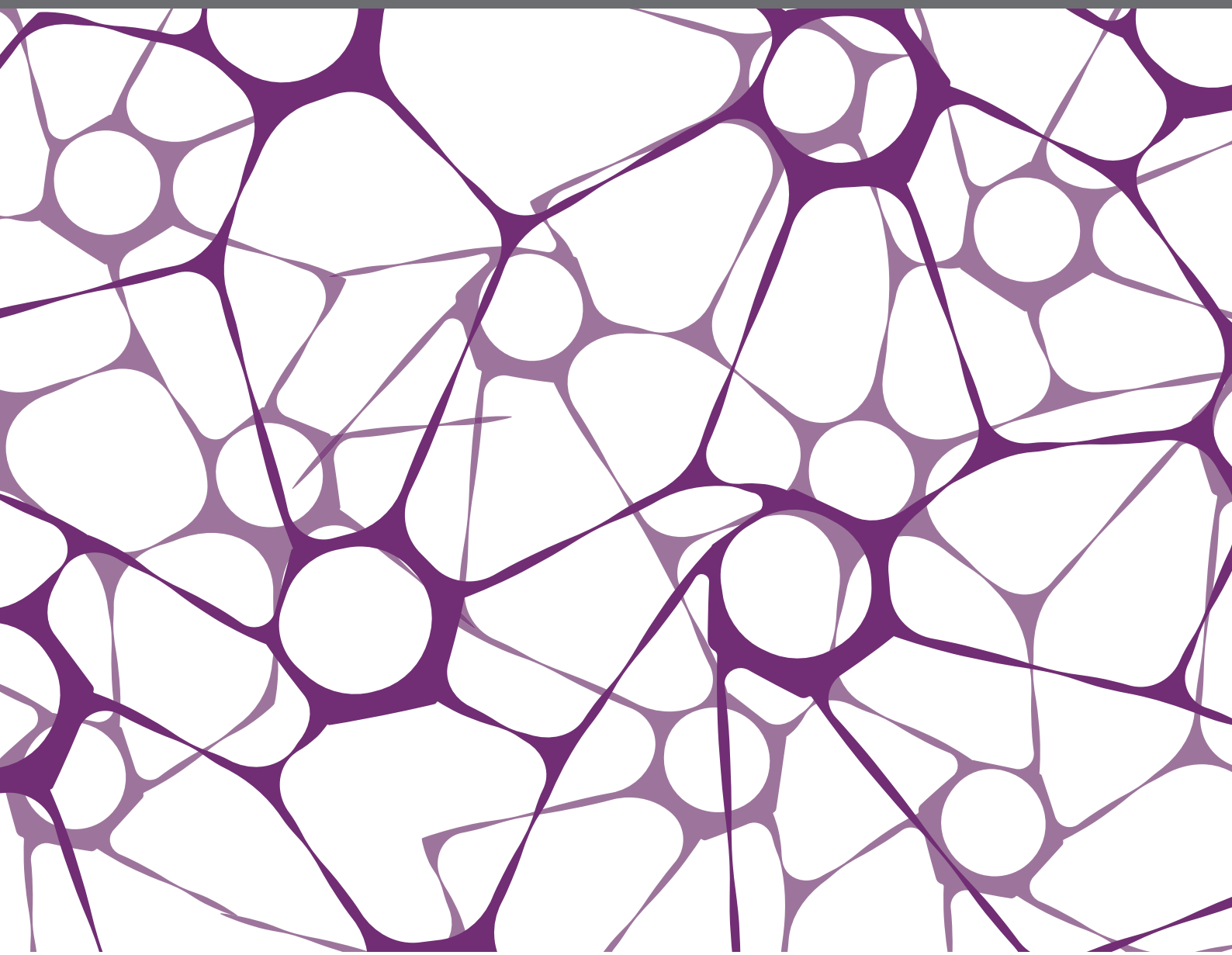

frontiers Research Topics

frontiers

ISSN 1664-8714
ISBN 978-2-88963-447-7
DOI 10.3389/978-2-88963-447-7

About Frontiers

Frontiers is more than just an open-access publisher of scholarly articles: it is a pioneering approach to the world of academia, radically improving the way scholarly research is managed. The grand vision of Frontiers is a world where all people have an equal opportunity to seek, share and generate knowledge. Frontiers provides immediate and permanent online open access to all its publications, but this alone is not enough to realize our grand goals.

Frontiers Journal Series

The Frontiers Journal Series is a multi-tier and interdisciplinary set of open-access, online journals, promising a paradigm shift from the current review, selection and dissemination processes in academic publishing. All Frontiers journals are driven by researchers for researchers; therefore, they constitute a service to the scholarly community. At the same time, the Frontiers Journal Series operates on a revolutionary invention, the tiered publishing system, initially addressing specific communities of scholars, and gradually climbing up to broader public understanding, thus serving the interests of the lay society, too.

Dedication to Quality

Each Frontiers article is a landmark of the highest quality, thanks to genuinely collaborative interactions between authors and review editors, who include some of the world's best academicians. Research must be certified by peers before entering a stream of knowledge that may eventually reach the public - and shape society; therefore, Frontiers only applies the most rigorous and unbiased reviews.
Frontiers revolutionizes research publishing by freely delivering the most outstanding research, evaluated with no bias from both the academic and social point of view. By applying the most advanced information technologies, Frontiers is catapulting scholarly publishing into a new generation.

What are Frontiers Research Topics?

Frontiers Research Topics are very popular trademarks of the Frontiers Journals Series: they are collections of at least ten articles, all centered on a particular subject. With their unique mix of varied contributions from Original Research to Review Articles, Frontiers Research Topics unify the most influential researchers, the latest key findings and historical advances in a hot research area! Find out more on how to host your own Frontiers Research Topic or contribute to one as an author by contacting the Frontiers Editorial Office: researchtopics@frontiersin.org

NANO-HETERO-STRUCTURES FOR CHEMICAL SENSING: OPPORTUNITIES AND CHALLENGES

Topic Editors:
Sheikh A. Akbar, The Ohio State University, United States
Xiaogan Li, Dalian University of Technology (DUT), China
Qasem Ahmed Drmosh, King Fahd University of Petroleum and Minerals, Saudi Arabia

Citation: Akbar, S. A., Li, X., Drmosh, Q. A., eds. (2020). Nano-Hetero-Structures for Chemical Sensing: Opportunities and Challenges. Lausanne: Frontiers Media SA. doi: 10.3389/978-2-88963-447-7

Table of Contents

frontiers in Materials

EDITORIAL
published: 17 December 2019
doi: 10.3389/fmats.2019.00332

Editorial: Nano-Hetero-Structures for Chemical Sensing: Opportunities and Challenges

Sheikh A. Akbar[1]*, *Qasem A. Drmosh*[2] *and Xiaogan Li*[3]

[1] *The Ohio State University, Columbus, OH, United States,* [2] *King Fahd University of Petroleum and Minerals, Dhahran, Saudi Arabia,* [3] *Dalian University of Technology, Dalian, China*

Keywords: gas sensors, hydrogen sensors, volatile gas sensors, nitrogen dioxide sensors, nano-hetero-structure

Editorial on the Research Topic

Nano-Hetero-Structures for Chemical Sensing: Opportunities and Challenges

Developing novel materials with desired microstructure and active surfaces can bring about significant advances in the field of gas sensors. Nanostructured materials such as metal oxides, graphene and its derivatives, and metal sulfides have been established to have great potentials for use in gas sensing due to their high specific surface area, abundant surface active sites, large surface-to-volume ratio, and availability of crystal facets with high surface reactivity. Lately, there is a clear and steady tendency to explore the opportunities available from 1D, 2D, and 3D nanostructured materials for fabrication of high-performance gas sensors for a wide variety of applications. Chemical gas sensors based on nano-hetero-structures provide novel opportunities to design sensors with improved performance in different applications such as agriculture, safety and security, environmental monitoring, and in medical applications to predict, monitor, and diagnose a wide range of diseases. However, there are still many challenges in the field of chemi-resistive gas sensors such as relatively poor sensitivity and selectivity to the low concentration especially at low operating temperature limiting their commercial viability.

This Frontiers in Materials Research Topic aims to present recent advances in the development of nano-hetero-structure-based chemical gas sensors which integrate experimental and theoretical resources and cutting-edge expertise in the fields of thin films, chemistry, physics, materials science, nanotechnology, and biotechnology.

This Research Topic contains a collection of 21 contributions: 1 review article and 20 original articles. Note that the web-page number count is 22, because one article appears twice: one is referred to as "original article" and the other "correction article." The title of the review article is "*Gas Sensing by Microwave Transduction: Review of Progress and Challenges*" by Li et al. The original articles include "*Improved Gas Selectivity Based on Carbon Modified SnO_2 Nanowires*" by Tonezzer et al., "*Synthesis, Characterization and Ethanol Sensing Properties of Nanocrystalline α-MoO_3*" by Sau et al., "*A Simple Flow Injection Sensing System for the Real-Time On-Line Determination of Chemical Oxygen Demand Based on 3D Au-NPs/TiO_2 Nanotube Arrays*" by Si et al., "*Detection of Semi-volatile Plasticizers as a Signature of Early Electrical Fire*" by Han et al., "*Flame Spray Synthesis of $VOPO_4$ Polymorphs*" by Jodhani et al., "*Light-Activated Sub-ppm NO_2 Detection by Hybrid ZnO/QD Nanomaterials vs. Charge Localization in Core-Shell QD*" by Chizhov et al., "*Metal Decoration and Magnetic Field Effect on the Electrical Breakdown Voltage for ZnO Nanorods Gas Ionization Sensor*" by Liu et al., "*Three-Dimensional Fe_3O_4@Reduced Graphene Oxide Heterojunctions for High-Performance Room-Temperature NO_2 Sensors*" by Zou et al., "*Improvement of NO_2 Sensing Properties in Pd Functionalized Reduced Graphene Oxides by Electron-Beam Irradiation*" by Choi et al., "*Silver Nanoparticle-Decorated Tin Oxide Thin Films: Synthesis, Characterization, and Hydrogen Gas Sensing*"

Edited by:
Vardan Galstyan, University of Brescia, Italy

Reviewed by:
Yuliya Silina, Saarland University, Germany
Matteo Valt, University of Ferrara, Italy

***Correspondence:**
Sheikh A. Akbar
akbar.1@osu.edu

Specialty section:
This article was submitted to Functional Ceramics, a section of the journal Frontiers in Materials

Received: *15 November 2019*
Accepted: *03 December 2019*
Published: *17 December 2019*

Citation:
Akbar SA, Drmosh QA and Li X (2019) Editorial: Nano-Hetero-Structures for Chemical Sensing: Opportunities and Challenges. Front. Mater. 6:332. doi: 10.3389/fmats.2019.00332

by Mohamedkhair et al., "*UV Light Activated SnO_2/ZnO Nanofibers for Gas Sensing at Room Temperature*" by Li et al., "*Heating Method Effect on SnO Micro-Disks as NO_2 Gas Sensor*" by Masteghin et al., "*Highly Sensitive and Selective Ethanol Sensor Based on ZnO Nanorod on SnO_2 Thin Film Fabricated by Spray Pyrolysis*" by Tharsika et al., "*Sol-gel Synthesis of TiO_2 With p-Type Response to Hydrogen Gas at Elevated Temperature*" by Xie et al., "*Improving Hydrogen Sensing Performance of TiO_2 Nanotube Arrays by ZnO Modification*" by Yu et al., "*Improvement in NO_2 Sensing Properties of Semiconductor-Type Gas Sensors by Loading of Au Into Porous In_2O_3 Powders*" by Ueda et al., "*Effect of Zinc Oxide Modification by Indium Oxide on Microstructure, Adsorbed Surface Species, and Sensitivity to CO*" by Marikutsa et al., "*Kinetic Insight on Improved Chemi-Resistive Response of Hydrothermal Synthesized Pt Loaded TiO_2 Nano-rods Toward Vapor Phase Isopropanol*" by Das et al., "*High-Performance Non-enzymatic Glucose Sensors Based on CoNiCu Alloy Nanotubes Arrays Prepared by Electrodeposition*" by Gong et al., and "*Enhanced Acetone-Sensing Properties of PEI Thin Film by GO-NH_2 Functional Groups Modification at Room Temperature*" by Zhao et al.

The review of Li et al. summarizes the recent progress of microwave gas sensors including the characteristic of the various nanostructured materials, and propagative structures (non-resonator and resonator). Original articles in this Research Topic can be classified according to the target gas into four groups: nitrogen dioxide gas sensors (5 articles), hydrogen gas sensors (3 articles), volatile gas sensors (ethanol, isopropanol, and acetone) (4 articles), and other gas sensors (8 articles).

Multiple types of chemical gas sensors to detect NO_2 gas have been demonstrated in this special issue. The paper by Choi et al. reports the effect of electron-beam irradiation on the NO_2 gas-sensing properties of Pd-functionalized rGO. The so-fabricated sensors are subjected to different irradiation doses (0, 100, and 500 kGy) and their NO_2 gas-sensing performance are measured and compared. Their results show that the response of the fabricated sample increases with increasing the irradiation doses which is attributed by the authors to the formation of high energy defects. Zou et al. report the fabrication of a core-shell 3D Fe_3O_4@rGO p-n heterojunctions using self-assembly method for NO_2 gas sensor. The contribution from Chizhov et al. demonstrates that the illumination of ZnO/CdSe, ZnO/CdS@CdSe, and ZnO/ZnSe@CdS nanocomposites fabricated by the immobilization of nanocrystals colloidal quantum dots by a green light ($\lambda_{max} = 535$ nm) changes the population of surface states, which strongly affects the response of the fabricated materials toward NO_2. Masteghin et al. compare the response of SnO micro-disks toward NO_2 using two different heating methods: (1) self-heating in which the heater circuit deposited on the back side of the interdigitated electrode, and (2) external heating such as a tube furnace. According to their results, the external heating method shows higher sensor response and lower recovery time, which is ascribed by the authors to the lack of a temperature gradient between the SnO micro-disks and the sensor chamber atmosphere. In the study of Ueda et al., porous In_2O_3 powders loaded with noble metals (Pd, Au, or Pt) fabricated using ultrasonic spray pyrolysis and their NO_2 sensing properties are examined. The Au nanoparticles loading on the In_2O_3 show higher response toward NO_2 than that of Pd or Pt loaded In_2O_3.

Furthermore, there are four papers focused on H_2 sensing applications. Mohamedkhair et al. report the formation of well-dispersed Ag nanoparticles over the surface of SnO_2 thin films via DC reactive sputtering and a subsequent heat treatment process for detecting low concentration of H_2 at low operating temperature. The so-fabricated sensor shows butter response compared to that of pristine and heated SnO_2 films. They propose that the depletion layer caused by Ag, Ag_2O, and SnO_2 played a vital role in the improvement of H_2 sensing properties. In another paper, Xie et al. discuss H_2 sensing properties of Cr doped TiO_2 nanoparticles fabricated by sol-gel method and investigates the effect of doping concentration (1–10 at.%) on the gas sensing performance. Yu et al. investigate the hydrogen gas sensing behavior based on ZnO decorated onto the surface of TiO_2 nanotubes, where anodization and facile impregnation synthesis methods are employed to fabricate TiO_2 nanotubes and ZnO decorated TiO_2.

The contribution from Sau et al. reports the fabrication of α-MoO_3 nanoparticles fabricated via facile sol-gel technique and their gas sensing properties for breath diagnostics applications. Although, the sensor is highly sensitive toward ethanol, it is insensitive toward the main interfering agent of exhaling human breath. The paper by Tharsika et al. reports the preparation of mixed structure of ZnO nanorod on SnO_2 thin film via spray pyrolysis followed by thermal annealing and their gas sensing properties toward ethanol. In the study of Ueda et al., flower like architecture consisting of innumerable numbers of TiO_2 nanorods are fabricated hydrothermally and subsequently modified chemically with platinum nanoparticles. The isopropanol gas sensing properties of the fabricated materials are examined at different temperatures and concentrations of isopropanol. In another paper, Zhao et al. focuses on fabrication of PEI/GO-NH_2 composite film on quartz crystal microbalance using a spraying and drop coating method. Furthermore, the acetone-sensing performance is explored at room temperature. PEI/GO-NH_2 composite film sensor shows an enhancement in acetone sensitivity compared with the pristine PEI film.

Tonezzer et al. demonstrate that carbon modified SnO_2 nanowires fabricated by chemical vapor deposition can be used as a sensing material to detect different gases (carbon monoxide, ammonia, acetone, ethanol, toluene, and hydrogen). Furthermore, machine learning algorithms are employed in their work to distinguish various gases based on the obtained data. Si et al. propose a real-time on-line sensing system combining with 3D Au nanoparticles/TiO_2 nanotube sensing electrode and photoelectrochemical reactor for the determination of chemical oxygen demand. The proposed sensing system displays a linear range from about 2 to more than 3,000 mg/L with low detection limit of 0.18 mg/L. The paper by Han et al. reports the detection of semi-volatile Dioctyl phthalate and 2-Ethylhexanol released from over-heated PVC cables for early warning of electrical fire using SnO_2 nanofibers synthesized via electrospinning followed by calcination at 600°C for 3 h. The contribution from Jodhani et al. introduces a novel method

to fabricate different $VOPO_4$ polymorphs using two different organic compounds as precursors via flame spray pyrolysis. The article by Liu et al. focuses on the fabrication of ZnO nanorod arrays with sharp tips via chemical vapor deposition and use them as the anode for gas ionization sensor. The authors also explore the effects of metal (Ni81Fe19, Mn, and Au) decoration and magnetic field on the electrical breakdown voltage. The synthesis of SnO_2/ZnO nanocomposites composed of SnO_2 nanofiber and ZnO nanorods is reported by Li et al. The so-prepared sensor shows a good response to various concentrations of formaldehyde gas and a good selectivity against many possible interferents such as methanol, ethanol, acetone, toluene, and benzene at room temperature under UV irradiation. Marikutsa et al. focus on nanostructured ZnO modified by 1–7 at.% of indium synthesized via coprecipitation and annealing at 450°C and their CO gas sensing properties are tested at temperatures ranging from room temperature to 450°C. Finally, the article by Gong et al. reports the preparation of CoNiCu alloy nanotube arrays using a template-assisted electrodeposition method. The glucose sensing performance of CoNiCu alloy nanotube arrays exhibits wider linear range, higher sensitivity, high selectivity to glucose, and low operation potential compared to that of single or binary alloy electrodes reported in literature.

While rapid progress in new synthesis routes has made it possible to engineer and optimize specific types of nano-hetero-structures for a given application, the largely trial-and-error approach has failed to effectively understand and model the response behavior of these nano-hetero-structures in a way that could otherwise advance the field toward bottom-up design for specific applications. It is hoped that this Research Topic on nanostructured chemical gas sensors will be of great interest to the Frontiers in Materials readers and will inspire considerable future R&D activities and progress in the field.

The Editors are grateful to the authors and the reviewers for their contributions and cooperation in adhering to the timetable. Special thanks go to the Frontiers staff and editorial team for their outstanding support and collaboration during the entire process.

AUTHOR CONTRIBUTIONS

These authors were co-editors of the Research Topic and contributed equally to reviewing process. Each author contributed in the writing and editing of this editorial as well.

FUNDING

SA's time on this article was partly funded by the National Science Foundation grant 160914.

Conflict of Interest: The authors declare that the research was conducted in the absence of any commercial or financial relationships that could be construed as a potential conflict of interest.

frontiers in Materials

PERSPECTIVE
published: 15 January 2019
doi: 10.3389/fmats.2018.00082

Enhanced Acetone-Sensing Properties of PEI Thin Film by GO-NH_2 Functional Groups Modification at Room Temperature

*Qiuni Zhao[1], Zaizhou He[1], Yadong Jiang[1], Zhen Yuan[1], Hongru Wu[2], Chenliang Su[2] and Huiling Tai[1]**

[1] State Key Laboratory of Electronic Thin Films and Integrated Devices, School of Optoelectronic Science and Engineering, University of Electronic Science and Technology of China, Chengdu, China, [2] International Collaborative Laboratory of 2D Materials for Optoelectronic Science and Technology, Engineering Technology Research Center for 2D Material Information Function Devices and Systems of Guangdong Province, College of Optoelectronic Engineering, Shenzhen University, Shenzhen, China*

The functional groups of organic gas-sensing materials play a crucial role in adsorbing specific gas molecules, which is significant to the sensing performances of gas sensor. In this work, amido-graphene oxide (GO-NH_2) loaded poly(ethyleneimine) (PEI) composite thin film (PEI/GO-NH_2) with abundant amino functional groups -NH_2 was successfully prepared on quartz crystal microbalance (QCM) by a combined spraying and drop coating method for acetone detection at room temperature (25°C). The morphological, spectrographic and acetone-sensing properties of composite film were investigated. The results demonstrated that a wrinkled surface morphology was formed and the ratio of nucleophilic -NH_2 was increased for PEI/GO-NH_2 composite film. Meanwhile, the composite film sensor possessed excellent acetone-sensing performances, and its sensitivity was about 4.2 times higher than that of pure PEI one owing to the increased -NH_2 groups. This study reveals the important role of absorbing favorable functional groups and provides a novel method for the rational design and construction of acetone-sensing materials.

Keywords: amino functional groups, composite materials, poly(ethyleneimine), amido-graphene oxide, acetone sensing performances

OPEN ACCESS

Edited by:
Xiaogan Li,
Dalian University of Technology (DUT), China

Reviewed by:
Yangong Zheng,
Ningbo University, China
Shiwei Lin,
Hainan University, China

****Correspondence:***
Huiling Tai
taitai1980@uestc.edu.cn

Specialty section:
This article was submitted to Functional Ceramics, a section of the journal Frontiers in Materials

Received: *17 November 2018*
Accepted: *20 December 2018*
Published: *15 January 2019*

Citation:
Zhao Q, He Z, Jiang Y, Yuan Z, Wu H, Su C and Tai H (2019) Enhanced Acetone-Sensing Properties of PEI Thin Film by GO-NH_2 Functional Groups Modification at Room Temperature. Front. Mater. 5:82. doi: 10.3389/fmats.2018.00082

INTRODUCTION

Acetone is a volatile, flammable and deleterious industrial product that widely used in our daily life (Jia et al., 2014). In addition, acetone detection can be applied to painless diabetes diagnosis because the concentration of acetone exhaled by diabetics is much higher than that by healthy people (Righettoni and Tricoli, 2011; Shin et al., 2013; Zhang et al., 2017). Therefore, it is urgent to develop acetone gas sensors with excellent performances through optimizing the sensing materials (Wang et al., 2017). So far, many types of acetone gas sensors have been developed (Xu et al., 2009; Epifani et al., 2015; Kim et al., 2016; Wang et al., 2016), in which most of them were chemiresistive sensor operated at high temperature with metal-oxide sensing-materials. On the other hand, quartz crystal microbalance (QCM, for short) is an excellent and reliable mass gas sensing device that can detect mass change at sub-nanogram level and has attracted attention for its room working

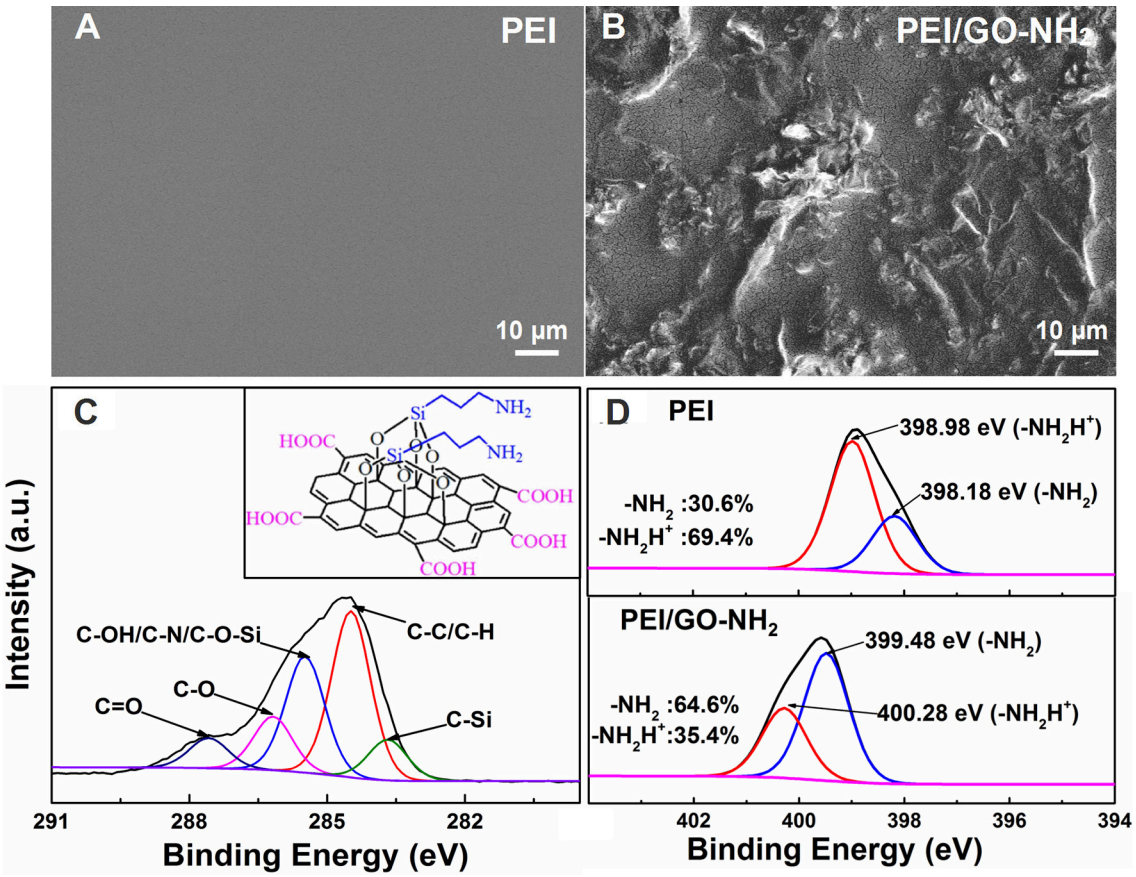

FIGURE 1 | SEM images of **(A)** PEI and **(B)** PEI/GO-NH_2 film. High-resolution XPS of **(C)** C1s spectra of PEI/GO-NH_2 and **(D)** N1s spectra of pure PEI and PEI/GO-NH_2, the inset of **(C)** is GO-NH_2 material structure.

temperature, high sensitivity, good stability, and small physical size (Matsuguchi and Uno, 2006; Lal and Tiwari, 2018). The gas sensing properties of QCM gas sensor are mainly determined by the coated sensing material to the gas molecules (Wang et al., 2017). Conductive polymer materials were widely used as sensing films in QCM gas sensors because they possess specific functional groups for adsorbing target gas molecules. In order to develop high performance gas sensor based on QCM, one of important strategies is to construct gas sensing materials with special functional groups. As a typical organic polymer, poly(ethyleneimine) (PEI) can be used in QCM-based acetone sensors due to the amino functional groups (-NH_2, for short) that can adsorb acetone molecules through nucleophilic addition reaction (Smith and March, 2007). However, the acetone-sensing properties of pure PEI based QCM gas sensors are restricted and still need to be further improved. Inspired by the large specific surface area of graphene oxide (GO, for short) and the importance of functional groups in gas sensing materials, compositing with GO to improve the acetone performance of PEI is a good strategy. In view of the amide reaction between—NH_2 of PEI and hydroxyl groups (-OH, for short) of GO (Tai et al., 2016), the amido-graphene oxide (GO-NH_2, for short) could be chose to prepare composite film, and the acetone-sensing properties would be enhanced by loading more -NH_2 onto the PEI film. In this work, PEI film loaded GO-NH_2 (PEI/GO-NH_2, for short) with abundant -NH_2 was prepared by a combined spraying and drop coating method, and characterized by scanning electron microscopy (SEM), X-ray photoelectron spectroscopy (XPS), ultraviolet-visible spectroscopy (UV-vis). The QCM acetone sensors based on PEI and PEI/GO-NH_2 films were fabricated and their acetone gas sensing properties including dynamic response, repeatability, selectivity and stability were investigated. Moreover, the mechanisms for the enhanced acetone sensing properties of the PEI/GO-NH_2 gas sensors were discussed.

EXPERIMENTAL

All the chemicals used in the experiment were analytical reagents. PEI aqueous solution [50% (w/v)] was obtained from Sigma-Aldrich and diluted to 1% (w/v) by deionized water. GO-NH_2 aqueous solution (0.5 mg/ml) was prepared by Shenzhen University (-NH_2 was carried by 3-aminopropyltriethoxysilane (APTES), which was modified on GO by a one-pot hydrothermal method described in Liu et al. (2013). QCM devices (Wuhan Hitrusty Electronics Co., Ltd., China) consist of AT-cut quartz

crystal with a fundamental resonance frequency of 10 MHz and the 5 mm diameter sliver electrodes were used on both sides of devices.

PEI/GO-NH_2 composite thin film was deposited on QCM devices by spraying 0.9 ml PEI solution and dropping 20 μl GO-NH_2 solution in sequence. After the deposition, the composite thin film sensors were dried in vacuum drying oven at 80°C for 48 h. For comparison, pure PEI film QCM gas sensor was also fabricated by the same spray method. The SEM, XPS and UV-vis of PEI and PEI/GO-NH_2 composite films were characterized by S4800 (HITACHI, Japan), UV-1700 (Shimadzu, Japan), and ESCALAB 250Xi (Thermo Fisher, American), respectively.

The details for measurement of QCM gas sensors can refer to our previous work (Yuan et al., 2016). The acetone gas was generated by MF-3C (Beijing Ruiyisi Technology Co., Ltd.). QCM-5 Oscillator (ShenyangVacuum Technology Institute, China) drived the QCM gas sensors, and an SS7200 intelligent frequency counter (The Fourth Radio Factory, China) was used to measure the resonance-frequency of QCM gas sensors. All the sensing measurements were executed at room temperature 25°C. The response (Δf) of the sensor is calculated as following equation: $\Delta f = f_{air}\text{-}f_{gas}$, where f_{air} and f_{gas} is the frequency measured in air and target gases, respectively. The slope coefficient of response vs. gas concentrations curve is defined as sensitivity of the gas sensor:

$$\mathbf{S = \Delta f/(\Delta Conc.)}$$

where ΔConc. is the gas range of linear concentration. The response/recovery times (τ_{res}/τ_{rec}) are defined as the time spans to the sensor achieved 90% of total frequency change exposure to gas and air.

RESULTS AND DISCUSSION

The SEM and XPS of pure PEI and PEI/GO-NH_2 composite films are shown in **Figure 1**. As can be seen, the SEM image in **Figure 1A** indicates a smooth and uniform deposition of PEI film. However, **Figure 1B** displays a rough and wrinkled surface morphology caused by GO-NH_2, which should be beneficial to enlarging the specific surface area of sensing film and improving the adsorption capacity of gas molecules (Kuila et al., 2011). As shown in **Figure 1C**, the binding energy of GO-NH_2 at O1s can be assigned to individual peaks at 283.7, 284.5, 285.5, 286.2, and 287.6 eV, corresponding to C-Si,C-C/C-H,C-OH/ C-N/C-O-Si, C-O, and C=O, respectively, which are conformed to the structure diagram (inset of **Figure 1C**) of GO-NH_2 (Liu et al., 2013). N1s spectra of pure PEI and PEI/GO-NH_2 are curve fitted and shown in **Figure 1D**. The N1s peaks are assigned to -NH_2 and protonated amine groups (-NH_2H^+), respectively. The N1s peaks of PEI/GO-NH_2 shifted about 1.3 eV compared with that of pure PEI, implying the existence of hydrogen bonds between PEI and GO-NH_2 (Finšgar et al., 2009). On the other hand, -NH_2 are nucleophilic while -NH_2H^+ are not nucleophilic, so the

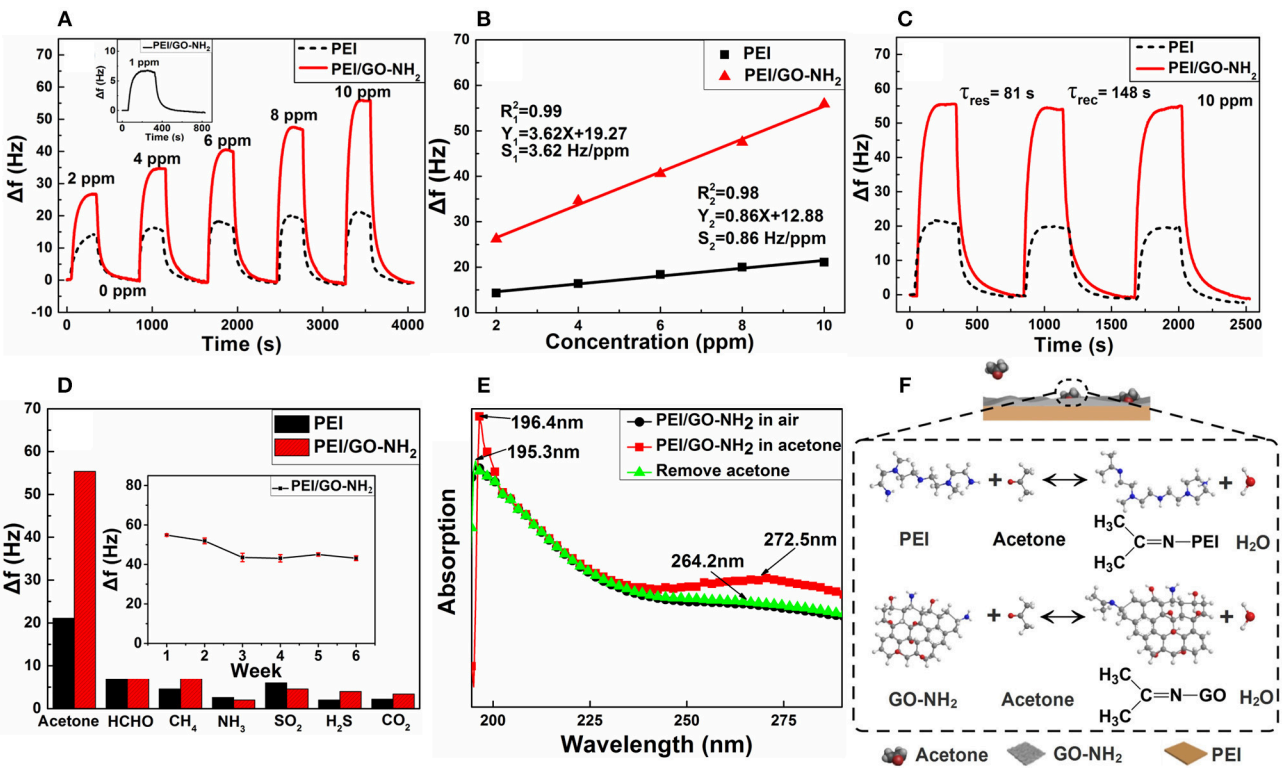

FIGURE 2 | (A) Dynamic response curves. **(B)** Linear fitting curves. **(C)** Repeatability curves and **(D)** selectivity of PEI and PEI/GO-NH_2 QCM sensors to acetone, the inset of **(A)** is the response curve of PEI/GO-NH_2 sensor for 1 ppm acetone, the inset of **(D)** is long-term stability curve. **(E)** UV-Vis spectrum of PEI/GO-NH_2 films. **(F)** Schematic of acetone-sensing mechanism.

increased ratio of nucleophilic -NH_2 in PEI/GO-NH_2 (from 30.6 to 64.6%) can increase the acetone gas molecules adsorption and enhance the acetone-sensing properties of composite thin film (Smith and March, 2007).

Typical dynamic responses of pure PEI and PEI/GO-NH_2 film sensors vs. acetone concentration (2–10 ppm) were measured at room temperature (25°C), as shown in **Figure 2A**. It can be observed that the responses of two gas sensors increase gradually with the increasing acetone concentrations and reach saturation, and the frequency come back to the initial state with insignificant baseline drift after the acetone is replaced by dry air. The response of pure PEI and PEI/GO-NH_2 sensors to 10 ppm acetone is about 21.1 and 55.4 Hz, respectively. **Figure 2B** demonstrates the linear fitting curves of two gas sensors, indicating both pure PEI and PEI/GO-NH_2 film sensors are of good linearity to 2–10 ppm acetone. The sensitivity of pure PEI and PEI/GO-NH_2 QCM gas sensor is 0.86 and 3.62 Hz/ppm, respectively, indicating that the sensitivity of PEI/GO-NH_2 composite thin film sensor shows about 4.2 times higher than that of pure PEI one. It is worth noting that the PEI/GO-NH_2 film sensor could detect 1 ppm acetone with 6.4 Hz response as shown in the inset of **Figure 2A**, whereas PEI film sensor shows no obvious response. **Figure 2C** shows good repeatability for two film sensors on successive exposure to 10 ppm acetone. It can be observed that the responses of two sensors exhibit very little fluctuation in adsorption and desorption process, indicating excellent repeatability and baseline stability. The response and recovery times of the PEI/GO-NH_2 film sensor are 81 s and 148 s. As shown in **Figure 2D**, the selectivity of PEI/GO-NH_2 acetone sensor was investigated in comparison to different kinds of interference gases (10 ppm HCHO, CH_4, NH_3, SO_2, H_2S, and 1,000 ppm CO_2), which demonstrate that the composite film has higher response to acetone gas than other gases. Except for formaldehyde and acetone, other gases have no carbon-heteroatom double bond (C=O) which plays an important role in nucleophilic addition reaction with –NH_2. In addition, the molecular mass of formaldehyde is less than that of acetone at the same concentration. Therefore, PEI/GO-NH_2 composite film shows a comparatively good selectivity to acetone. The insert in **Figure 2D** shows the long-term stability of PEI/GO-NH_2 acetone sensor during a period of 6 weeks. The result shows the response of composite sensor to 10 ppm acetone decreases about 18% in the first 14 days and tends to be stable afterwards.

UV-Vis spectra were carried out to further confirm the recoverability of PEI/GO-NH_2 film. As shown in **Figure 2E**, when exposed to acetone atmosphere, enhancement and redshift of absorption peaks appeared in PEI/GO-NH_2 film, representing the adsorption of acetone molecules. When above films were replaced back to the air atmosphere, the absorption peaks also restored to their positions, indicating the good recovery characteristic of the films. The acetone-sensing mechanism is further proposed. **Figure 2F** indicates the chemical reaction during adsorption/desorption process. Carbon atom of polar carbon-heteroatom double bond (C=O) on acetone molecule carries a partial positive charge, making the carbon atom as electrophilic center. When exposed to acetone gas, negatively charged nucleophilic -NH_2 on PEI/GO-NH_2 film will attack and bond with the electrophilic carbon atom to form an imine and produce a molecule of water. The above adsorption will lead to mass increase of PEI/GO-NH_2 film and the frequency shift of QCM sensor based on Sauerbrey's equation (Sauerbrey, 1959). According to the pattern followed by analogous nucleophiles, the produced compounds are generally unstable. In the process of acetone molecular desorption, carbon atom of polar carbon-nitrogen double bond (C=N) for produced compounds carries a partial positive charge, produced water molecule will bond with the electrophilic carbon atom to form reversible reaction, thus the PEI/GO-NH_2 film coated QCM acetone sensors possess good response and recoverability (Madura and Jorgensen, 1986; Smith and March, 2007).

CONCLUSION

In summary, PEI/GO-NH_2 composite film was fabricated on QCM via a combined spraying and drop coating method. Moreover, the acetone-sensing properties were investigated at room temperature (25°C). Compared with the pure PEI film based QCM acetone sensor, PEI/GO-NH_2 composite film sensor exhibited an improved acetone-sensing performance, and its sensitivity was about 4.2 times higher than that of pure PEI film. The gas sensor based on PEI/GO-NH_2 composite film showed nearly linear response at acetone gas concentrations ranges of 2–10 ppm, and its sensitivity was about 3.62 Hz/ppm. In addition, the PEI/GO-NH_2 composite film sensor possessed good repeatability and selectivity. The enhanced acetone-sensing performances could be attributed to the rich -NH_2 and enlarged surface area introduced by GO-NH_2. This work demonstrated a promising PEI/GO-NH_2 composite film for high-performance acetone-sensing materials construction.

AUTHOR CONTRIBUTIONS

QZ and ZH co-wrote the submitted perspective and performed the experiments. HW and CS prepared GO-NH_2 aqueous solution. YJ, ZY, and HT designed and guided the entire experimental process.

ACKNOWLEDGMENTS

This work is supported by the National Science Funds for Excellent Young Scholars of China (Grant No. 61822106), National Science Funds for Creative Research Groups of China (Grant No. 61421002), and Natural Science Foundation of China (Grant No. 61671115).

REFERENCES

Epifani, M., Comini, E., Siciliano, P., Faglia, G., and Morante, J. R. (2015). Evidence of catalytic activation of anatase nanocrystals by vanadium oxide surface layer: acetone and ethanol sensing properties. *Sensors Actuat. B Chem.* 217, 193–197. doi: 10.1016/j.snb.2014.07.118

Finšgar, M., Fassbender, S., Hirth, S., and Milošev, I. (2009). Electrochemical and XPS study of polyethyleneimines of different molecular sizes as corrosion

inhibitors for AISI 430 stainless steel in near-neutral chloride media. *Mater. Chem. Phys*. 116, 198–206. doi: 10.1016/j.matchemphys.2009.03.010

Jia, Q., Ji, H., Zhang, Y., Chen, Y., Sun, X., and Jin, Z. (2014). Rapid and selective detection of acetone using hierarchical ZnO gas sensor for hazardous odor markers application. *J. Hazard. Mater*. 276, 262–270. doi: 10.1016/j.jhazmat.2014.05.044

Kim, N. H., Choi, S. J., Kim, S. J., Cho, H. J., Jang, J. S., Koo, W. T., et al. (2016). Highly sensitive and selective acetone sensing performance of WO_3 nanofibers functionalized by Rh_2O_3 nanoparticles. *Sensors Actuators B Chem*. 224, 185–192. doi: 10.1016/j.snb.2015.10.021

Kuila, T., Bose, S., Khanra, P., Mishra, A. K., Kim, N. H., and Lee, J. H. (2011). Recent advances in graphene-based biosensors. *Biosens. Bioelectron*. 26, 4637–4648. doi: 10.1016/j.bios.2011.05.039

Lal, G., and Tiwari, D. C. (2018). Investigation of nanoclay doped polymeric composites on piezoelectric Quartz Crystal Microbalance (QCM) sensor. *Sensors Actuat. B Chem*. 262, 64–69. doi: 10.1016/j.snb.2018.01.200

Liu, Z., Duan, X., Qian, G., Zhou, X., and Yuan, W. (2013). Eco-friendly one-pot synthesis of highly dispersible functionalized graphene nanosheets with free amino groups. *Nanotechnology* 24:045609. doi: 10.1088/0957-4484/24/4/045609

Madura, J. D., and Jorgensen, W. L. (1986). *Ab initio* and Monte Carlo calculations for a nucleophilic addition reaction in the gas phase and in aqueous solution. *J. Am. Chem. Soc*. 108, 2517–2527. doi: 10.1021/ja00270a005

Matsuguchi, M., and Uno, T. (2006). Molecular imprinting strategy for solvent molecules and its application for QCM-based VOC vapor sensing. *Sensors Actuat. B Chem*. 113, 94–99. doi: 10.1016/j.snb.2005.02.028

Righettoni, M., and Tricoli, A. (2011). Toward portable breath acetone analysis for diabetes detection. *J. Breath Res*. 5:037109. doi: 10.1088/1752-7155/5/3/037109

Sauerbrey, G. (1959). Verwendung von schwingquarzen zur wägung dünner schichten und zur mikrowägung. *Zeitschrift Für Phys*. 155, 206–222. doi: 10.1007/BF01337937

Shin, J., Choi, S. J., Lee, I., Youn, D. Y., Park, C. O., Lee, J. H., et al. (2013). Thin-wall assembled SnO_2 fibers functionalized by catalytic Pt nanoparticles and their superior exhaled-breath-sensing properties for the diagnosis of diabetes. *Adv. Funct. Mater*. 23, 2357–2367. doi: 10.1002/adfm.201202729

Smith, M. B., and March, J. (2007). *March's Advanced Organic Chemistry: Reactions, Mechanisms, and Structure, Sixth Edition.* Hoboken, NJ: John Wiley and Sons.

Tai, H., Yuan, Z., Liu, C., Ye, Z., Xie, G., Du, X., et al. (2016). Facile development of high performance QCM humidity sensor based on protonated polyethylenimine-graphene oxide nanocomposite thin film. *Sensors Actuat. B Chem*. 230, 501–509. doi: 10.1016/j.snb.2016.01.105

Wang, L., Wang, Z., Xiang, Q., Chen, Y., Duan, Z., and Xu, J. (2017). High performance formaldehyde detection based on a novel copper (II) complex functionalized QCM gas sensor. *Sensors Actuat. B Chem*. 248, 820–828. doi: 10.1016/j.snb.2016.12.015

Wang, P., Wang, D., Zhang, M., Zhu, Y., Xu, Y., Ma, X., et al. (2016). ZnO nanosheets/graphene oxide nanocomposites for highly effective acetone vapor detection. *Sensors Actuat. B Chem*. 230, 477–484. doi: 10.1016/j.snb.2016.02.056

Xu, X., Cang, H., Li, C., Zhao, Z. K., and Li, H. (2009). Quartz crystal microbalance sensor array for the detection of volatile organic compounds. *Talanta* 78, 711–716. doi: 10.1016/j.talanta.2008.12.031

Yuan, Z., Tai, H., Ye, Z., Liu, C., Xie, G., Du, X., et al. (2016). Novel highly sensitive QCM humidity sensor with low hysteresis based on graphene oxide (GO)/poly (ethyleneimine) layered film. *Sensors Actuat. B Chem*. 234, 145–154. doi: 10.1016/j.snb.2016.04.070

Zhang, Z., Zhu, L., Wen, Z., and Ye, Z. (2017). Controllable synthesis of Co_3O_4 crossed nano sheet arrays toward an acetone gas sensor. *Sensors Actuat. B Chem*. 238, 1052–1059. doi: 10.1016/j.snb.2016.07.154

Conflict of Interest Statement: The authors declare that the research was conducted in the absence of any commercial or financial relationships that could be construed as a potential conflict of interest.

frontiers in Materials

ORIGINAL RESEARCH
published: 25 January 2019
doi: 10.3389/fmats.2019.00003

High-Performance Non-enzymatic Glucose Sensors Based on CoNiCu Alloy Nanotubes Arrays Prepared by Electrodeposition

Xuewen Gong[1,2], Yan Gu[1], Faqiang Zhang[1], Zhifu Liu[1]*, Yongxiang Li[1,3], Guanyu Chen[1,2] and Bo Wang[1]*

[1] CAS Key Laboratory of Inorganic Functional Materials and Devices, Shanghai Institute of Ceramics, Chinese Academy of Sciences, Shanghai, China, [2] Center of Materials Science and Optoelectronics Engineering, University of Chinese Academy of Sciences, Beijing, China, [3] School of Engineering, RMIT University, Melbourne, VIC, Australia

Transition metal alloys are good candidate electrodes for non-enzymatic glucose sensors due to their low cost and high performance. In this work, we reported the controllable electrodeposition of CoNiCu alloy nanotubes electrodes using anodic aluminum oxide (AAO) as template. Uniform CoNiCu alloy arrays of nanotubes about 2 μm in length and 280 nm in diameter were obtained by optimizing the electrodeposition parameters. Scanning electron microscopy (SEM) and energy dispersive X-ray spectroscopy (EDS) measurements indicated that the as-prepared alloy nanotubes arrays are composed of 64.7 wt% Co-19.4 wt% Ni-15.9 wt% Cu. Non-enzymatic glucose sensing measurements indicated that the CoNiCu nanotubes arrays possessed a low detection limit of 0.5 μM, a high sensitivity of 791 μA mM^{-1} cm^{-2} from 50 to 1,551 μM and 322 μA mM^{-1} cm^{-2} from 1,551 to 4,050 μM. Besides, they showed high reliability with the capacity of anti-jamming. Tafel plots showed that alloying brought higher exchange current density and faster reaction speed. The high performance should be due to the synergistic effect of Co, Ni, and Cu metal elements and high surface area of nanotubes arrays.

Keywords: CoNiCu alloy, nanotubes arrays, electrodeposition, non-enzymatic glucose sensors, synergistic effect

OPEN ACCESS

Edited by:
Xiaogan Li,
Dalian University of Technology (DUT), China

Reviewed by:
Yanbai Shen,
Northeastern University, China
Yangong Zheng,
Ningbo University, China

***Correspondence:**
Yan Gu
guyan@mail.sic.ac.cn
Zhifu Liu
liuzf@mail.sic.ac.cn

Specialty section:
This article was submitted to Functional Ceramics, a section of the journal Frontiers in Materials

Received: *03 December 2018*
Accepted: *09 January 2019*
Published: *25 January 2019*

Citation:
Gong X, Gu Y, Zhang F, Liu Z, Li Y, Chen G and Wang B (2019) High-Performance Non-enzymatic Glucose Sensors Based on CoNiCu Alloy Nanotubes Arrays Prepared by Electrodeposition. Front. Mater. 6:3. doi: 10.3389/fmats.2019.00003

INTRODUCTION

With the increasing demand in medical, food, and pharmaceutical industry, more attention has been paid to develop glucose sensors with high sensitivity, high stability, and low price (Yoo and Lee, 2010; Tian et al., 2014; Galant et al., 2015). Although traditional enzymatic glucose sensors have undergone three generations of development and possess high sensitivity and selectivity, they always suffer from the performance variation with environment and the degradation of enzyme activity (Katakis and Dominguez, 1995; Toghill and Compton, 2010). In recent years, non-enzymatic electrochemical glucose sensors based on the oxidation of glucose to gluconolactone on electrode surface arise as a promising candidate for glucose concentrations detection (Lu et al., 2009; Wang et al., 2012). Many non-enzymatic electrode materials have been developed including noble metal nanomaterials (Jena and Raj, 2006) and their alloy (Sun et al., 2015; Wang et al., 2018), transition metals and their alloys (Jafarian et al., 2008; Mu et al., 2011; Liu et al., 2017). Although noble metals exhibit fascinating properties, there are two main drawbacks: (i) The overall kinetics of glucose electrooxidation is too slow to produce a significant Faraday current;

(ii) The activity of the noble electrode is strongly damaged by chloride ions and intermediates adsorbed on electrode surfaces (Tee et al., 2017). Also, noble metals are too expensive for mass production. The oxidation of glucose by transition metal electrode involves the electrontransfer mediation of the multivalentmetal redox couple which leads to better current response and has no fouling by adsorbed interference species. Hence, transition metal electrodes attract much attention for fabrication more active and cheaper non-enzymatic glucose sensors in recent years.

At present, more and more alloy research in glucose detection has replaced pure metal to improve the stability by forming bimetallic structure (Mahshid et al., 2013; Miao et al., 2013; Sheng et al., 2014; Vilana et al., 2015). Wang et al. (2008) synthesized three-dimensional PtPb alloy networks on Ti substrates to overcome the shortcomings of pure metal and significantly improved the performance. Gao et al. (2011) reported a PtNi alloy nanoparticle-Graphene electrode which had a high nanoparticle loading and effective reduction of graphene oxide. Li et al. (2015) studied a series of MCo (M = Cu, Fe, Ni, and Mn) alloy nanoparticles doped carbon nanofibers electrodes and explored the distinction of different alloy sensors. These alloys had higher electrocatalytic activities and stabilities compared with those of pure metals due to the synergistic effect (Luo and Kuwana, 1994; Li et al., 2015; Vilana et al., 2015). Transition metal-based alloy is a prospective direction and worthy of further study for low-cost and high-performance non-enzymatic glucose sensors. In different alloy systems, more attention was paid to cobalt material due to its excellent catalytic ability and chemical stability (Ding et al., 2010; Kung et al., 2011; Madhu et al., 2015; Shu et al., 2018). Unlike the transition metals such as nickel and copper, cobalt could form various oxidation states in alkaline conditions(Hwang et al., 2018).

On the other hand, since the non-enzymatic glucose sensing is based on the electrode surface, the morphology of electrode material will have a large effect on the performance of sensors. Therefore, nanoparticles, nanosheets, nanowires, and other nanomaterials were widely used in glucose sensors research to solve the problem of electrode surface saturated (Liu et al., 2014; Jiang et al., 2017; Zhang et al., 2017). However, some nanomaterials like particles need to be loaded onto other materials which cause interference current and complex production process (Jena and Raj, 2006). Attributed to large surface-to-volume ratio and ordered arrangement, more interest was focused on one-dimensional nanowires and nanotubes structures which was considered as the beneficial dimensionality for electrontransfer (Hu et al., 1999). In order to compare the difference in glucose detection, Li et al. (2014) used Pt-Pd as the electrodes material and demonstrated that nanotubes had a higher activity for glucose electro-oxidation. To the best of our knowledge, no studies concerning ternary transition alloy nanotubes have been reported for glucose sensor yet.

In this work, we fabricated well-aligned cobalt-based ternary alloy nanotubes by using the template-assisted potentiostatic electrodeposition method. The non-enzymatic glucose sensing performance of the alloy nanotubes was investigated. The cobalt-based ternary alloy nanotubes showed excellent performance with low detection limit, wide detection range, and high sensitivity.

EXPERIMENTAL SECTION

The anodic aluminum oxide (AAO) template with diameter of 280 nm was obtained from Top Membranes Technology Ltd. The source materials nickel sulfate hexahydrate, cobalt sulfate, copper sulfate pentahydrate, boric acid, sodium chloride, L-tyrosine, ascorbic acid, and dopamine hydrochloride were purchased from Shanghai Aladdin Biochemical Polytron Technologies Inc. Sodium citrate and ethanol were purchased from China National Pharmaceutical Group Corporation. All chemicals involved were of analytical grade and were used directly. Before the electrodeposition, a thin conductive layer of Au was sputtered onto one side of the AAO template as a working electrode in a three-electrode cell. A platinum sheet was used as the counter electrode and a saturated calomel electrode as the reference electrode. The deposition was carried out at room temperature with different DC voltages and time on a CHI 660C electrochemical working station (Shanghai Chenhua, China). For the ternary alloy deposition, water solution with 0.1 M $CoSO_4{\cdot}7H_2O$, 0.2 M $NiSO_4{\cdot}6H_2O$, 0.01 M $CuSO_4{\cdot}5H_2O$, 0.4 M H_3BO_3, and 0.5 M $Na_3C_6H_5O_7{\cdot}2H_2O$ were used as electrolyte. For comparison, the Co nanotubes arrays were deposited at −1.5 V voltage for 5 min using 0.1 M $CoSO_4{\cdot}7H_2O$, 0.4 M H_3BO_3 water solution as electrolyte. After deposition, the AAO template containing the nanotubes was immersed in a 1 M NaOH solution to remove the template.

The phase composition of the prepared nanotubes was determined by X-ray Diffraction (XRD, D8 DISCOVER DAVINCI). The morphology and microstructure were characterized using field-emission scanning electron microscopy (SEM, SU8220) equipped with an energy dispersive X-ray spectroscopy (EDS). For glucose sensing performance measurement, the nanotubes arrays were transferred to an indium tin oxide (ITO) substrate with a nail polish covered the edge between the ITO and the nanotubes arrays. All of the electrodes were activated by 60 cyclic voltammetry (CV) cycles at a scanning rate of 30 mV s^{-1} in a 0.1 M NaOH solution, respectively, before the performance test. Subsequently, the nanotubes arrays were used for glucose test in the 0.1 M NaOH solution with a different concentration of glucose and 0.4 V was chosen as the working potential for the amperometric performance test. A platinum sheet was used as the counter electrode and an Ag/AgCl electrode as the reference electrode.

RESULTS AND DISCUSSIONS

Fabrication of Nanotubes Arrays

Although template-based electrochemical deposition is a well-accepted process to synthesize nanostructures, the morphology and component of the products could be largely affected by the deposition parameters like applied voltage and deposition time because of the diversity of electrochemical properties of different elements. In this work, we tuned the electrodeposition voltage and time to obtain high-quality alloy nanotubes arrays. The SEM

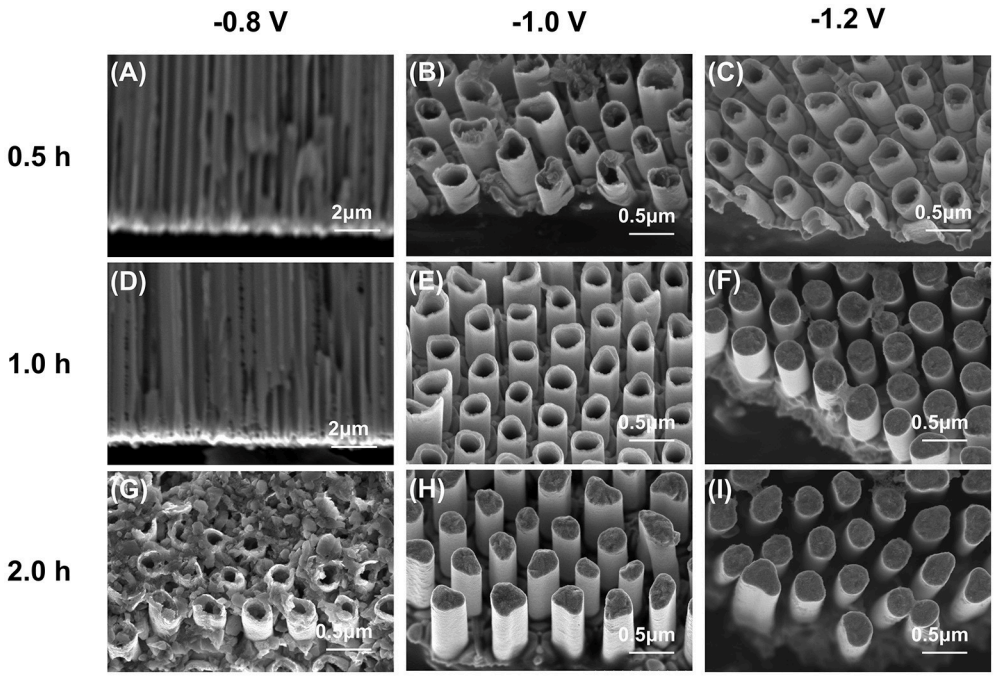

FIGURE 1 | SEM images of the products deposited at different potential and time. **(A,B)** cross-section image with AAO template. **(C–I)** products after removing the AAO template.

images of products synthesized at −0.8, −1.0, and −1.2 V within different deposition time are shown in **Figure 1**. As shown in **Figures 1A,B**, the deposition rate is too slow to observe the product from the cross-section at the low deposition voltage −0.8 V within 1 h. Fortunately, extending the deposition time to 2 h, the short nanotubes arrays are obtained (**Figure 1C**). When the deposition voltage was increased to −1.0 V (**Figures 1D–F**), nanotubes are grown easily in a relatively short time. The wall of nanotubes become thicker with time prolonging (**Figures 1D,E**) and eventually, the nanotubes are filled and nanorods arrays are obtained (**Figure 1F**). When the deposition voltage increases to −1.2 V, nanotubes arrays can also be obtained in half hour (**Figure 1G**). But the wall of the nanotubes is even thicker than these deposited at −1.0 V for 1 h. So, extending the deposition time, only nanorods arrays can be obtained at a deposition voltage of −1.2 V (**Figures 1H,I**).

The possible growth process of alloy nanotubes is illustrated in **Figure 2**. **Figure 2A** is the cross-section of the AAO template. After spraying the gold as the working electrode, some gold particles are sprayed on the bottom wall of the AAO (**Figure 2B**). When deposition voltage applied, high charge density would form near the bottom wall of AAO around gold particles. Such a stronger electrochemical activity makes the alloy conducive to growth along the wall of AAO template (**Figure 2C**). As time goes on, the nanotubes become longer while the thickness increases (**Figures 2D,E**), and finally turn into nanorods (**Figure 2F**). Throughout the process, the influence of the electric field and adsorption energy on the growth of alloy exists which cause different growth priorities and results in the product morphology variation from nanotubes to nanorods (Li et al., 2009). At the initial stage of growth, the alloy grows along the wall of the AAO template, which may be because of the increased metal ion concentration around the wall of AAO template induced by surface absorption and the existence of conductive particles in tubes. Considering the narrow channel between electrolyte and cathode surface, the metal ion concentration around the AAO has a dominating effect in the initial electrodeposition process. These reasons make the growth of nanotubes more favorable in the early stage of deposition. But with the extension of time, the wall of nanotubes gets thicker gradually. The adsorption effect becomes weaker and the electric field effect is more prominent. The nanoparticles begin to stack inside the tubes until the product are completely filled. Besides, the increase of voltage is helpful to deposit. But the growth rate is too fast to control when the voltage is too high.

Thus, it is clear that the voltage and time play a critical role during the formation of nanotubes. We choose the deposition voltage of −1.0 V and deposition time for 1 h to do more detailed study after taking into account all the above-mentioned experimental condition. The morphology and composition of the nanotubes are shown in **Figure 3**. The high magnification of SEM observation (**Figure 3A**) reveals that well-aligned CoNiCu nanotubes are formed on the substrate face. The diameter of nanotubes is about 280 nm, indicating that the nanotubes grow along the wall. The average length of the nanotubes is about 2 μm from the cross-section image (**Figure 3B**). The result of EDS shown in **Figure 3C** confirms that the nanotubes are composed of 64.7 wt% Co-19.4 wt% Ni-15.9 wt% Cu. The Al, O, and Au peaks

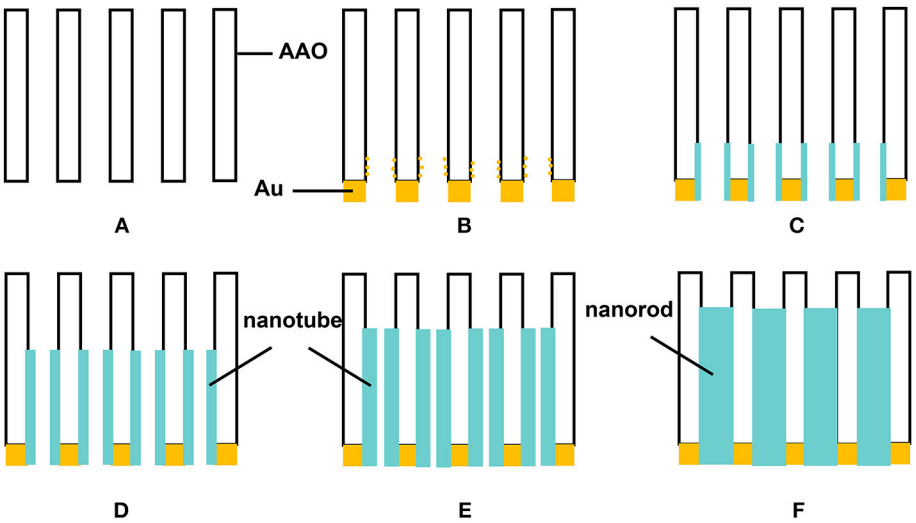

FIGURE 2 | Schematic diagram of the growth of alloy nanotubes. **(A)** section of AAO template, **(B)** section after spraying gold, **(C–F)** deposition process in template.

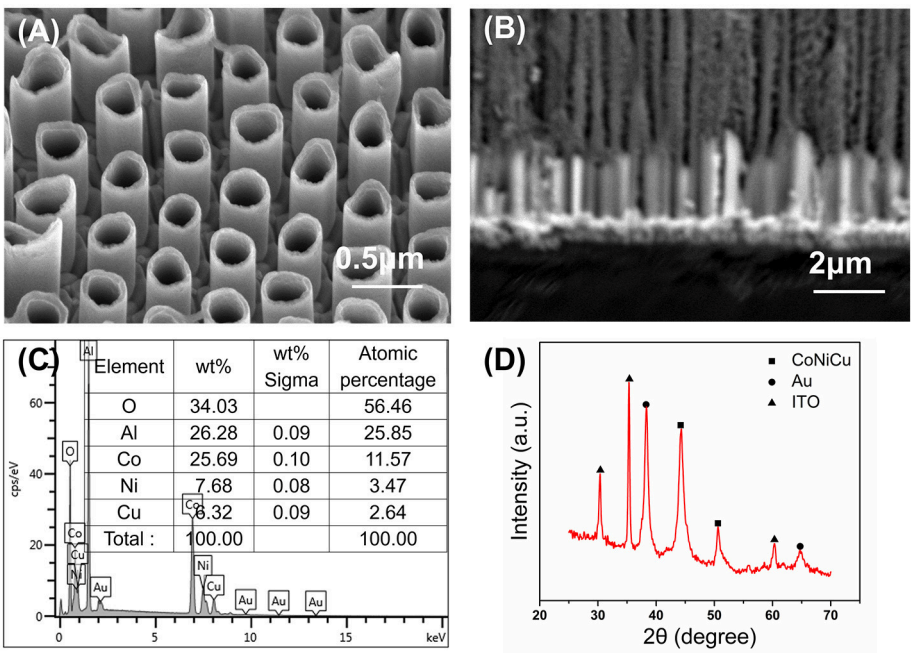

FIGURE 3 | CoNiCu nanotubes arrays with applied potential −1.0 V **(A)** dissolving the AAO template; **(B)** cross-section image embedded in AAO channels; **(C)** energy dispersive spectra of CoNiCu embedded in AAO channels; **(D)** XRD patterns of prepared nanotubes arrays transferred on ITO.

originate from the AAO temple. The crystal phase of CoNiCu nanotubes was further confirmed by XRD. The XRD patterns (**Figure 3D**) indicate that the nanotubes are of high crystallinity. The background interfering peaks are due to residual alumina, ITO, and Au. Furthermore, no peaks assigned to the pure metals are observed which reveals a ternary alloy was formed.

It is worth noting that the difference in deposition potential will be a problem to handle the composition. The standard electrode potentials for Co, Ni, Cu deposition are −0.277, −0.257, and 0.159 V, respectively. The more positive the potential is, the easier the metal ions are to reduce. It is clear that the reduction of copper is most likely to occur. If not controlled, copper will grow more rapid and desired cobalt-based alloy cannot form. And what's worse is, anomalous phenomena occur when it is a co-precipitation of a mixed metal ions system and the growth rate of cobalt is much faster than nickel at low current

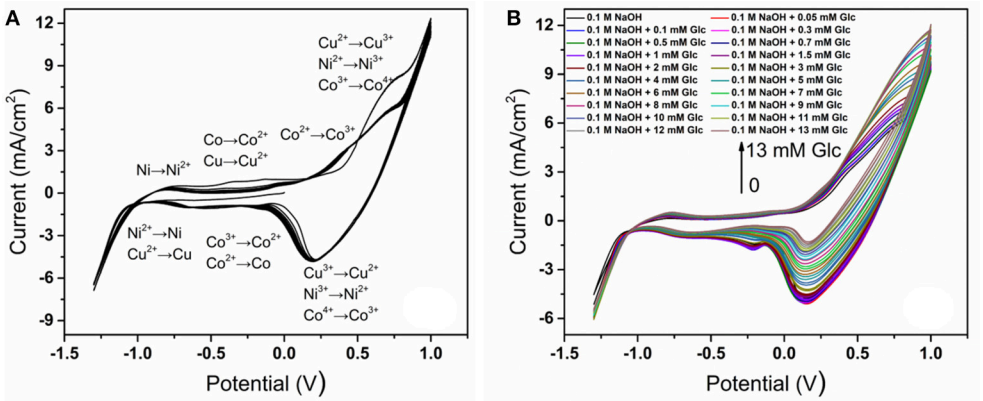

FIGURE 4 | (A) Activated CoNiCu electrode in 0.1 M NaOH by CV for multiple cycles; **(B)** CVs of activated CoNiCu electrode in 0.1 M NaOH + different glucose concentrations.

density typically (Fan and Piron, 1996). So we set the mole concentration of the solution to Co: Ni: Cu = 10: 20: 1. Besides, sodium citrate, as the complex metal ion, is used to guarantee the similar precipitation potential of Co^{2+}, Ni^{2+}, and Cu^{2+} to get controllable components. As a result, uniform CoNiCu alloy nanotubes arrays were obtained at a deposition voltage of −1.0 V for 1 h and were used as electrodes for glucose sensing characterization.

Glucose Sensing Performance Characterization

Cyclic voltammetry is used to activate the electrode and test the reaction response between the electrode and glucose solution. After carried the cyclic voltammetry reaction at a scanning rate of 30 mV s^{-1} in a 0.1 M NaOH solution, the alloy electrode surface is activated. The reaction corresponding to the peak value of cyclic voltammetric curve is deduced in **Figure 4A**. During oxidation, metals are first oxidized to divalent and oxidized to trivalent follow. Ni^{3+} and Cu^{3+} show good chemical stability but Co^{3+} is further oxidized into CoO_2 at higher potential (Liang et al., 2006; Hu et al., 2009).

The possible electrochemical reaction is as follows (Wang et al., 2013; Zhang et al., 2017):

$$Co + 2OH^- \rightarrow Co(OH)_2 + 2e^-$$
$$Co(OH)_2 + OH^- \rightarrow CoOOH + H_2O + e^-$$
$$CoOOH + OH^- \rightarrow CoO_2 + H_2O + e^-$$
$$Ni + 2OH^- \rightarrow Ni(OH)_2 + 2e^-$$
$$Ni(OH)_2 + OH^- \rightarrow NiOOH + H_2O + e^-$$
$$Cu + 2OH^- \rightarrow CuO + H_2O + 2e^-$$
$$CuO + H_2O \rightarrow Cu(OH)_2$$
$$Cu(OH)_2 + OH^- \rightarrow CuOOH + H_2O + e^-$$

A comparative study of electrochemical response on the CoNiCu electrocatalytic performance of different glucose concentrations was conducted in 0.1 M NaOH solution from −1.3 to +1.0 V (**Figure 4B**). With the increase of glucose concentration, the peak current of the alloy electrode varied strongly accompanied by the increase of oxidation current and the decrease of reduction current, demonstrating that the electrode could achieve efficient electrooxidation of glucose. Comparing with the cyclic voltammetric curve of the CoNiCu alloy electrode, the changed electrocatalytic current of alloy electrode indicates that the following reactions occurred:

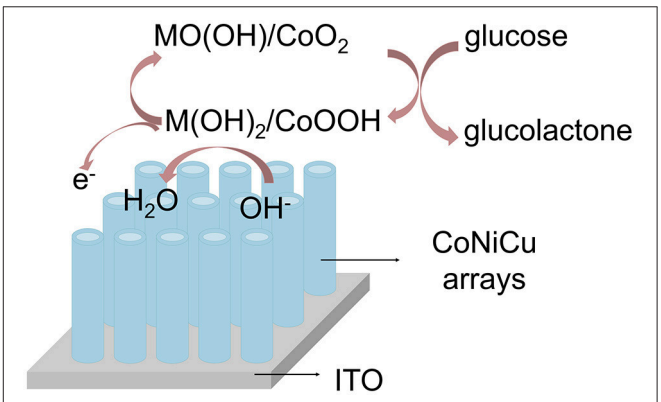

FIGURE 5 | Schematic representation of the glucose electrocatalytic reaction on CoNiCu nanotubes array.

$$2CoO_2 + \text{glucose} \rightarrow 2CoOOH + \text{gluconolactone}$$
$$NiOOH + \text{glucose} \rightarrow Ni(OH)_2 + \text{gluconolactone}$$
$$CuOOH + \text{glucose} \rightarrow Cu(OH)_2 + \text{gluconolactone}$$

Figure 5 shows the schematic illustration of glucose reaction on the CoNiCu nanotubes array under electrochemical condition. According to the "Incipient Hydrous Oxide Adatom Mediator" model Burke proposed (Burke, 1994; Rahman et al., 2010), the metal could be oxidized to $M^{II}(OH)_2$ and following $M^{III}OOH$ or $M^{IV}O_2$ in an alkaline solution. When glucose is added, it is oxidized to gluconolactone by $M^{III}OOH$ or $M^{IV}O_2$. As a result, CV oxidation peak current increases and reduction current

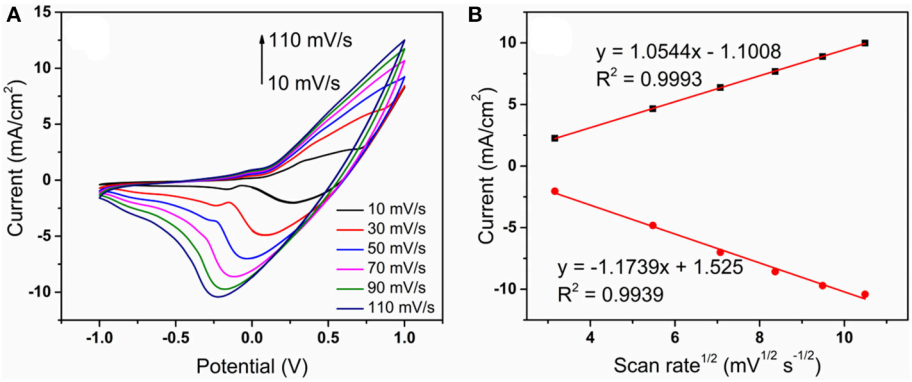

FIGURE 6 | (A) CVs of the CoNiCu electrodes in 0.1 M NaOH + 0.3 mM glucose at different scanning rates (10–110 mV s^{-1}); **(B)** redox peak currents as a function of the square root of the scan rate.

decreases. Different response currents result from different metal elements electrodes and solution environment. The high surface-to-volume ratio and good electron transfer channel of the nanotubes array largely enhanced the electrocatalytic reaction. So, the CoNiCu alloy nanotubes array could be an excellent glucose sensor electrode.

Kinetic study of reaction process is based on the effect of the potential scanning rate in a 0.1 M NaOH solution containing 0.3 mM glucose (**Figure 6**). The result shown in **Figure 6A** displays that the reduction potential shifts negatively and the oxidation potential shifts positively with the increase of scanning speed. Besides, both the anodic and cathodic peak current increase with the scanning rate from 10 to 110 mV s^{-1}. There are good relationships between the peak currents and the square root of the scanning rate (**Figure 6B**). This indicates that it is a diffusion-controlled process on the electrode. The rate of the whole reaction depends on the diffusion process of the ions from the solution to the surface of the electrode. To further investigate the difference after alloying, Co nanotubes electrode was prepared for a comparison. The oxidation peak of Co electrode is at about 0.3 V which is similar to CoNiCu electrode. However, according to existing reports, the anodic peak of the anodic peak of Ni electrode is at about 0.45 V, while that of Cu at about 0.4 V (Lu et al., 2009; Luo et al., 2012). Alloying did not increase the peak position of oxidation. Besides, since Co reacts more preferentially at 0.3 V, electrons could transfer from Ni/Cu to supplement and promote the oxidation of glucose.

To further understand the enhanced performance of CoNiCu nanotubes array, the Tafel plots of the Co nanotubes array, and CoNiCu nanotubes array were obtained in a 0.1 M NaOH with 0.3 M glucose (**Figure 7**). We draw tangents of the two curves at open circuit potential +60∼120 mV to get the Tafel slope and exchange current density (i_0). The Tafel slope of the CoNiCu nanotubes array is close to that of Co nanotubes array, which means they have similar overpotential and reaction activity. But a higher exchange current density i_0 indicates a faster reaction speed of CoNiCu nanotubes array electrode. This might be because the alloying expands the lattice which causes the d-band state changing and increases the adsorption of the

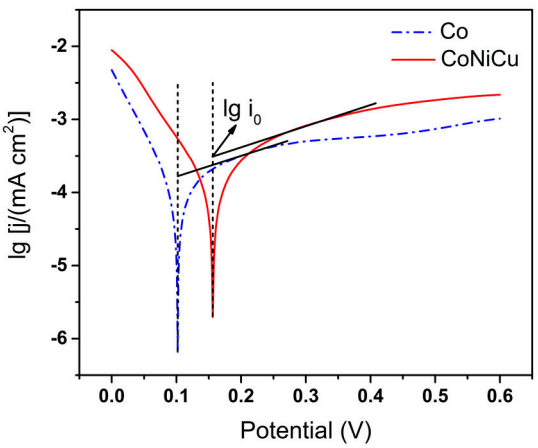

FIGURE 7 | Tafel plots of Co and CoNiCu electrodes in 0.1 M NaOH + 0.3 mM glucose.

reactants. As a result, the reaction is promoted (Groß, 2006). This kind of synergistic effect of three different metals should large contribution to the excellent performance of the ternary alloy nanotubes.

In order to quantitatively analyze the variation of sensor response current with the concentration glucose, the current is measured by continuously dropping glucose solution under a constant voltage. As can be seen from **Figure 6A**, there is a current peak near 0.3–0.6 V at the low scan rate. So we choose the potential of 0.4 V to do the amperometric test. **Figure 8** shows the amperometric response of CoNiCu electrode with a successive addition of glucose to a 0.1 M NaOH solution. A low stirring rate (150 rpm) was used to accelerate mixing during the experiment. Inset of **Figure 8A** is the glucose response current curve at extremely low concentration. Although the noise current is very large, we could see an obvious trend of current rising at about 0.5 μM. In order to get a more accurate linear curve of current varying with glucose concentration, the linear experiment was started from 50 μM. As shown in **Figure 8A**, once injected the

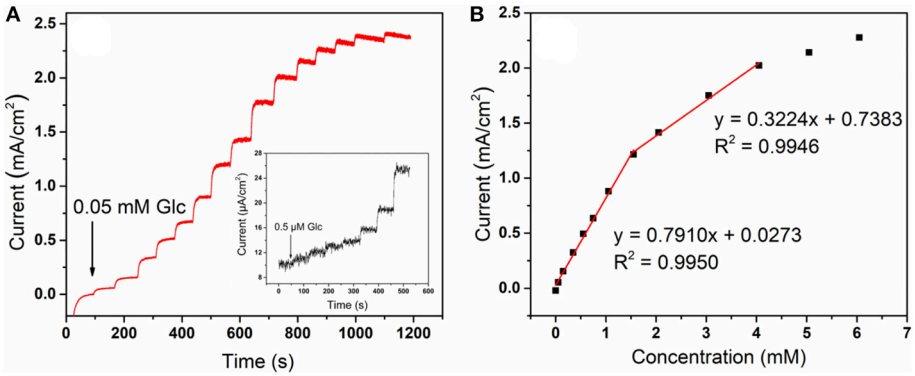

FIGURE 8 | (A) Amperometric response of CoNiCu electrode with a successive addition of glucose from 0.05 to 6 mM at 0.4 V. Inset: a successive addition of glucose from 0.5 to 11 μM; **(B)** the linear correlation between the concentration and response current of CoNiCu electrode.

TABLE 1 | Comparison of Co-based ternary alloy non-enzymatic glucose sensors.

Electrode materials	Sensitivity ($\mu A\ mM^{-1}\ cm^{-2}$)	Linear range (μM)	LOD (μM)	Operation potential (V)	Medium	References
CuCo-carbon nanofibers	507	20–1100	1.0	+0.6	0.1 M NaOH	Li et al., 2015
NiCu/GC	–	1000–9000	0.8	+0.54 vs. Ag/AgCl	1 M NaOH	Jafarian et al., 2008
$Co_{0.7}Ni_{0.3}$ nanorods	544	100–1000	–	0.5–0.65	0.1 M NaOH	Vilana et al., 2015
$Co_{0.6}Ni_{0.4}$ nanorods	383	100–1000	–	0.5–0.65	0.1 M NaOH	
CoNiCu nanotubes arrays	791	50–1551	0.5	+0.4 vs. Ag/AgCl	0.1 M NaOH	our work
	322	1551–4050				

glucose to the solution, the current responded immediately and it was stable in <5 s. We also noticed that the noise current increases with the increase of concentration, which may have an impact on the current acquisition. But, throughout the testing process, the signal-to-noise(S/N) ratio of the collected current is still more than three times. By collecting the current in each stable state, relation of the current intensity on the different glucose concentrations is displayed in **Figure 8B**. The electrode has a low detection limit (0.5 μM) and two-segment linear regions with a high sensitivity of 791 $\mu A\ mM^{-1}\ cm^{-2}$ from 50 to 1,551 μM and 322 $\mu A\ mM^{-1}\ cm^{-2}$ from 1,551 to 4,050 μM. Such a good performance may be attributed to the large surface area of the well-aligned nanotubes structure which provides more sites for the redox reaction. Transition metals with excellent electrical conductivity could also offer good charge transmission channels. The performance of CoNiCu nanotubes array was compared with other Co-based alloys glucose sensors reported previously. As listed in **Table 1**, CoNiCu nanotubes arrays exhibit ultrahigh sensitivity, low limit of detection (LOD), and wide linear range. In addition, the operating potential of CoNiCu nanotubes arrays is lower than others. Low voltage will reduce the response current, but it is more energy efficient in actual use and avoids the influence of possible intermediates which is also a development trend for non-enzymatic glucose sensors (Sun et al., 2015).

Biosensors are eventually used in complex organisms which contain complicated electroactive species such as ascorbic acid (AA), dopamine (DA), L-tyrosine, and sodium chloride

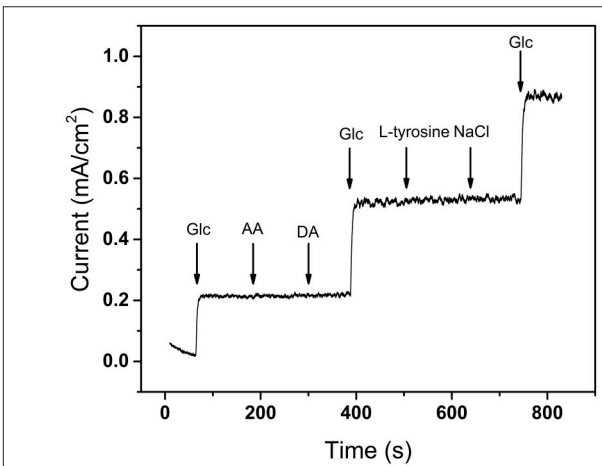

FIGURE 9 | Amperometric response of CoNiCu electrode to a successive addition of glucose and interferences.

(NaCl). Normally, a transition metal-based electrode could also oxidize part of small organic molecules after the formation of $M^{III}OOH$, making the interferential response hard to be avoided (Fleischmann et al., 1972). The selectivity is one of the important criteria for judging whether a sensor is qualified. According to the normal physiological level, the selectivity

of CoNiCu nanotubes array electrode was investigated by a successive addition of glucose, 0.017 mM AA, 0.017 mM DA, 0.017 mM L-tyrosine, and 0.05 mM NaCl, separately. As shown in **Figure 9**, the negligible interferential signal occurs which prove that the CoNiCu nanotubes array has good glucose selectivity. The high sensitivity, LOD, wide linear range, high selectivity, and the relative low price of the CoNiCu alloy nanotubes arrays indicate that it could be a promising electrode material for high performance non-enzymatic glucose sensors.

CONCLUSION

Uniform CoNiCu alloy nanotubes arrays were prepared using a template-assisted electrodeposition method. Deposition voltage and time are the key factors to control the morphology of the ternary alloy. The glucose sensing properties of CoNiCu alloy nanotubes arrays were systematically investigated. The non-enzymatic glucose sensors based on CoNiCu electrodes exhibit higher sensitivity, wider linear range, low operation potential, and high selectivity to glucose compared to those of reported single or binary alloy electrodes. Co is the active element of the CoNiCu alloy nanotubes array. The synergistic effect of the three metals leads to the high performance, which makes the CoNiCu alloy nanotubes array a promising electrode for non-enzymatic glucose sensors.

AUTHOR CONTRIBUTIONS

GX, GY, and LZ contributed conception and design of the study. GX is responsible for experiments and performed the statistical analysis with the help of ZF, CG, and WB. GX and LZ wrote the manuscript. All authors listed have made a substantial, direct and intellectual contribution to the work, and approved it for publication.

ACKNOWLEDGMENTS

We acknowledge the financial support from the National Natural Science Foundation of China (61601444, 61501438) and Youth Innovation Promotion Association of CAS.

REFERENCES

Burke, L. D. (1994). Premonolayer oxidation and its role in electrocatalysis. *Electrochim. Acta* 39, 1841–1848. doi: 10.1016/0013-4686(94)85173-5

Ding, Y., Wang, Y., Su, L., Bellagamba, M., Zhang, H., and Lei, Y. (2010). Electrospun Co3O4 nanofibers for sensitive and selective glucose detection. *Biosens. Bioelectron*. 26, 542–548. doi: 10.1016/j.bios.2010.07.050

Fan, C., and Piron, D. L. (1996). Study of anomalous nickel-cobalt electrodeposition with different electrolytes and current densities. *Electrochim. Acta* 41, 1713–1719. doi: 10.1016/0013-4686(95)00488-2

Fleischmann, M., Korinek, K., and Pletcher, D. (1972). The oxidation of hydrazine at a nickel anode in alkaline solution. *J Electroanal. Chem. Interfacial Electrochem*. 31, 39–49. doi: 10.1016/S0022-0728(72)80425-X

Galant, A. L., Kaufman, R. C., and Wilson, J. D. (2015). Glucose: detection and analysis. *Food Chem*. 188, 149–160. doi: 10.1016/j.foodchem.2015.04.071

Gao, H., Xiao, F., Ching, C. B., and Duan, H. (2011). One-step electrochemical synthesis of PtNi nanoparticle-graphene nanocomposites for nonenzymatic amperometric glucose detection. *ACS Appl. Mater. Interfaces* 3, 3049–3057. doi: 10.1021/am200563f

Groß, A. (2006). Reactivity of bimetallic systems studied from first principles. *Top. Catal*. 37, 29–39. doi: 10.1007/s11244-006-0005-x

Hu, J., Odom, T. W., and Lieber, C. M. (1999). ChemInform abstract: chemistry and physics in one dimension: synthesis and properties of nanowires and nanotubes. *Acc.Chem.Res*. 32, 435–445 doi: 10.1021/ar9700365

Hu, Z.-A., Xie, Y.-L., Wang, Y.-X., Wu, H.-Y., Yang, Y.-Y., and Zhang, Z.-Y. (2009). Synthesis and electrochemical characterization of mesoporous CoxNi1–x layered double hydroxides as electrode materials for supercapacitors. *Electrochim Acta* 54, 2737–2741. doi: 10.1016/j.electacta.2008.11.035

Hwang, D. W., Lee, S., Seo, M., and Chung, T. D. (2018). Recent advances in electrochemical non-enzymatic glucose sensors - a review. *Anal. Chim. Acta* 1033, 1–34. doi: 10.1016/j.aca.2018.05.051

Jafarian, M., Forouzandeh, F., Danaee, I., Gobal, F., and Mahjani, M. G. (2008). Electrocatalytic oxidation of glucose on Ni and NiCu alloy modified glassy carbon electrode. *J Solid State Electrochem*. 13, 1171–1179. doi: 10.1007/s10008-008-0632-1

Jena, B. K., and Raj, C. R. (2006). Enzyme-free amperometric sensing of glucose by using gold nanoparticles. *Chemistry* 12, 2702–2708. doi: 10.1002/chem.200501051

Jiang, J., Zhang, P., Liu, Y., and Luo, H. (2017). A novel non-enzymatic glucose sensor based on a Cu-nanoparticle-modified graphene edge nanoelectrode. *Anal. Methods* 9, 2205–2210. doi: 10.1039/c7ay00084g

Katakis, I., and Dominguez, E. (1995). Characterization and stabilization of enzymebiosensors. *Trac Trends Anal. Chem*. 14, 310–319.

Kung, C. W., Lin, C. Y., Lai, Y. H., Vittal, R., and Ho, K. C. (2011). Cobalt oxide acicular nanorods with high sensitivity for the non-enzymatic detection of glucose. *Biosens. Bioelectron*. 27, 125–131. doi: 10.1016/j.bios.2011.06.033

Li, M., Liu, L., Xiong, Y., Liu, X., Nsabimana, A., Bo, X., et al. (2015). Bimetallic MCo (M=Cu, Fe, Ni, and Mn) nanoparticles doped-carbon nanofibers synthetized by electrospinning for nonenzymatic glucose detection. *Sens. Actuat. B Chem*. 207, 614–622. doi: 10.1016/j.snb.2014.10.092

Li, X., Wang, Y., Song, G., Peng, Z., Yu, Y., She, X., et al. (2009). Synthesis and growth mechanism of Ni nanotubes and nanowires. *Nanoscale Res. Lett*. 4, 1015–1020. doi: 10.1007/s11671-009-9348-0

Li, Y., Niu, X., Tang, J., Lan, M., and Zhao, H. (2014). A Comparative study of nonenzymatic electrochemical glucose sensors based on Pt-Pd nanotube and nanowire arrays. *Electrochim. Acta* 130, 1–8. doi: 10.1016/j.electacta.2014.02.123

Liang, Y.-Y., Bao, S.-J., and Li, H.-L. (2006). Nanocrystalline nickel cobalt hydroxides/ultrastable Y zeolite composite for electrochemical capacitors. *J. Solid State Electrochem*. 11, 571–576. doi: 10.1007/s10008-006-0197-9

Liu, X., Yang, W., Chen, L., and Jia, J. (2017). Three-dimensional copper foam supported CuO nanowire arrays: an efficient non-enzymatic glucose sensor. *Electrochim. Acta* 235, 519–526. doi: 10.1016/j.electacta.2017.03.150

Liu, Y., Zhang, Y., Wang, T., Qin, P., Guo, Q., and Pang, H. (2014). Mesoporous Ni0.3Co2.7O4 hierarchical structures for effective non-enzymatic glucose detection. *RSC Adv*. 4, 33514–33519. doi: 10.1039/c4ra02665a

Lu, L. M., Zhang, L., Qu, F. L., Lu, H. X., Zhang, X. B., Wu, Z. S., et al. (2009). A nano-Ni based ultrasensitive nonenzymatic electrochemical sensor for glucose: enhancing sensitivity through a nanowire array strategy. *Biosens. Bioelectron*. 25, 218–223. doi: 10.1016/j.bios.2009.06.041

Luo, J., Jiang, S., Zhang, H., Jiang, J., and Liu, X. (2012). A novel non-enzymatic glucose sensor based on Cu nanoparticle modified graphene sheets electrode. *Anal. Chim. Acta* 709, 47–53. doi: 10.1016/j.aca.2011.10.025

Luo, P. F., and Kuwana, T. (1994). Nickel-titanium alloy electrode as a sensitive and stable LCEC detector for carbohydrates. *Anal. Chem*. 66, 2775–2782. doi: 10.1021/ac00089a028

Madhu, R., Veeramani, V., Chen, S. M., Manikandan, A., Lo, A. Y., and Chueh, Y. L. (2015). Honeycomb-like porous carbon-cobalt oxide nanocomposite for high-performance enzymeless glucose sensor and supercapacitor applications. *ACS Appl. Mater. Interfaces* 7, 15812–15820. doi: 10.1021/acsami.5b04132

Mahshid, S. S., Mahshid, S., Dolati, A., Ghorbani, M., Yang, L., Luo, S., et al. (2013). Electrodeposition and electrocatalytic properties of Pt/Ni–Co

nanowires for non-enzymatic glucose detection. *J. Alloys Comp*. 554, 169–176. doi: 10.1016/j.jallcom.2012.10.186

Miao, Y., Wu, J., Zhou, S., Yang, Z., and Ouyang, R. (2013). Synergistic effect of bimetallic Ag and Ni alloys on each other's electrocatalysis to glucose oxidation. *J. Electrochem. Soc*. 160, B47–B53. doi: 10.1149/2.059304jes

Mu, Y., Jia, D., He, Y., Miao, Y., and Wu, H. L. (2011). Nano nickel oxide modified non-enzymatic glucose sensors with enhanced sensitivity through an electrochemical process strategy at high potential. *Biosens. Bioelectron*. 26, 2948–2952. doi: 10.1016/j.bios.2010.11.042

Rahman, M. M., Ahammad, A. J., Jin, J. H., Ahn, S. J., and Lee, J. J. (2010). A comprehensive review of glucose biosensors based on nanostructured metal-oxides. *Sensors* 10, 4855–4886. doi: 10.3390/s100504855

Sheng, Q., Mei, H., Wu, H., Zhang, X., and Wang, S. (2014). PtxNi/C nanostructured composites fabricated by chemical reduction and their application in non-enzymatic glucose sensors. *Sens. Actuat. B Chem*. 203, 588–595. doi: 10.1016/j.snb.2014.06.090

Shu, Y., Li, B., Chen, J., Xu, Q., Pang, H., and Hu, X. (2018). Facile synthesis of ultrathin nickel-cobalt phosphate 2D nanosheets with enhanced electrocatalytic activity for glucose oxidation. *ACS Appl. Mater. Interfaces* 10, 2360–2367. doi: 10.1021/acsami.7b17005

Sun, Y., Yang, H., Yu, X., Meng, H., and Xu, X. (2015). A novel non-enzymatic amperometric glucose sensor based on a hollow Pt–Ni alloy nanotube array electrode with enhanced sensitivity. *RSC Adv*. 5, 70387–70394. doi: 10.1039/c5ra13383a

Tee, S. Y., Teng, C. P., and Ye, E. (2017). Metal nanostructures for non-enzymatic glucose sensing. *Mater. Sci. Eng. C Mater. Biol. Appl*. 70, 1018–1030. doi: 10.1016/j.msec.2016.04.009

Tian, K., Prestgard, M., and Tiwari, A. (2014). A review of recent advances in nonenzymatic glucose sensors. *Mater. Sci. Eng. C Mater. Biol. Appl*. 41, 100–118. doi: 10.1016/j.msec.2014.04.013

Toghill, K. E., and Compton, R. G. (2010). Electrochemical non-enzymatic glucose sensors: a perspective and an evaluation. *Int. J. Electrochem. Sci*. 5, 1246–1301. Available online at: http://www.electrochemsci.org/papers/vol5/5091246.pdf

Vilana, J., Lorenzo, M., Gómez, E., and Vallés, E. (2015). Electrochemical deposition of CoNi micro/nanostructures as new materials for electrochemical sensing of glucose. *Mater. Lett*. 159, 154–158. doi: 10.1016/j.matlet.2015.06.116

Wang, G., Lu, X., Zhai, T., Ling, Y., Wang, H., Tong, Y., et al. (2012). Free-standing nickel oxide nanoflake arrays: synthesis and application for highly sensitive non-enzymatic glucose sensors. *Nanoscale* 4, 3123–3127. doi: 10.1039/c2nr30302g

Wang, J., Thomas, D. F., and Chen, A. (2008). Nonenzymatic electrochemical glucose sensor based on nanoporous PtPb networks. *Anal. Chem*. 80, 997–1004. doi: 10.1021/ac701790z

Wang, L., Lu, X., Ye, Y., Sun, L., and Song, Y. (2013). Nickel-cobalt nanostructures coated reduced graphene oxide nanocomposite electrode for nonenzymatic glucose biosensing. *Electrochim. Acta* 114, 484–493. doi: 10.1016/j.electacta.2013.10.125

Wang, L., Zhu, W., Lu, W., Qin, X., and Xu, X. (2018). Surface plasmon aided high sensitive non-enzymatic glucose sensor using Au/NiAu multilayered nanowire arrays. *Biosens. Bioelectron*. 111, 41–46. doi: 10.1016/j.bios.2018.03.067

Yoo, E.-H., and Lee, S.-Y. (2010). Glucose biosensors: an overview of use in clinical practice. *Sensors* 10, 4558–4576. doi: 10.3390/s100504558

Zhang, L., Ye, C., Li, X., Ding, Y., Liang, H., Zhao, G., and Wang, Y. (2017). A CuNi/C nanosheet array based on a metal–organic framework derivate as a supersensitive non-enzymatic glucose sensor. *Nano Micro Lett*. 10:28. doi: 10.1007/s40820-017-0178-9

Conflict of Interest Statement: The authors declare that the research was conducted in the absence of any commercial or financial relationships that could be construed as a potential conflict of interest.

frontiers in Materials

ORIGINAL RESEARCH
published: 08 March 2019
doi: 10.3389/fmats.2019.00031

Kinetic Insight on Improved Chemi-Resistive Response of Hydrothermal Synthesized Pt Loaded TiO_2 Nano-rods Toward Vapor Phase Isopropanol

Priyanka Das[1,2], *Biswanath Mondal*[1,2] *and Kalisadhan Mukherjee*[1,3]*

[1] Centre for Advanced Materials Processing, CSIR-Central Mechanical Engineering Research Institute, Durgapur, India, [2] Academy of Scientific and Innovative Research (AcSIR), CSIR-Central Mechanical Engineering Research Institute, Durgapur, India, [3] Department of Electrical and Computer Engineering, Science and Engineering Hall, Washington, DC, United States

Flower like microstructure composed of eccentrically grown vertically aligned titania nano-rods is prepared through spherical carbon template mediated hydrothermal route. Mechanistic pathways for the growth of said esthetic architecture is proposed by studying their phase formation behavior and morphological features. Chemi-resistive type sensing properties of prepared titania flowers for the detection of isopropanol are studied by varying the sensor operating temperature (225–300°C) and vapor concentration (10–200 ppm). Distinguishable sensitivity of titania flowers is identified for the detection of even 10 ppm isopropanol. Catalytic amount of Pt nano-particles (synthesized through chemical method) are introduced over prepared flower like titania to improve further their sensitivity. The plausible isopropanol sensing mechanism over TiO_2 flowers as well as influence of operating temperature and role of Pt nanoparticles as chemical sensitizer in enhancing the response is explained. The current response transients of both the TiO_2 flowers and their Pt modified counterpart for detecting low concentration (10–50 ppm) of isopropanol are modeled in accordance to Langmuir-Hinshelwood reaction mechanism and the rate constants for the respective surface reactions are estimated. The higher rate constant for the interaction of isopropanol over titania flowers than Pt modified counterparts is explained using the concept of decaying depleted layer during sensing.

Keywords: titania, morphology, nano-rod, gas sensor, noble metal, spill-over technique

OPEN ACCESS

Edited by:
Sheikh A. Akbar,
The Ohio State University,
United States

Reviewed by:
Priyanka Karnati,
The Ohio State University,
United States
Rodrigo Moreno,
Instituto de Cerámica y Vidrio (ICV),
Spain

***Correspondence:**
Kalisadhan Mukherjee
kalisadhanm@yahoo.com

Specialty section:
This article was submitted to Functional Ceramics, a section of the journal Frontiers in Materials

Received: *09 January 2019*
Accepted: *14 February 2019*
Published: *08 March 2019*

Citation:
Das P, Mondal B and Mukherjee K (2019) Kinetic Insight on Improved Chemi-Resistive Response of Hydrothermal Synthesized Pt Loaded TiO_2 Nano-rods Toward Vapor Phase Isopropanol. Front. Mater. 6:31. doi: 10.3389/fmats.2019.00031

INTRODUCTION

Titania (TiO_2) is an important semiconducting metal oxide (SMO) which remains attractive to the researchers for its high physicochemical stability, low toxicity and widespread applications in catalysis, gas sensors, Li-ion batteries, photo-splitting of water, photovoltaic devices etc. (O'Regan and Grätzel, 1991; Bai and Zhou, 2014; Schneider et al., 2014; Li et al., 2017; Zhou et al., 2017). In most of these applications, the performance of TiO_2 often significantly varies with its phase formation behavior and morphological features (Park et al., 2000; Yurdakal et al., 2008). Researchers have prepared various simple as well as complex architectures of TiO_2 for different applications (Wang et al., 2010; Damodaran et al., 2015). As evident from the literatures, syntheses

of these morphologies are generally carried out either using physical or chemical methods. Physical methods e.g., chemical vapor deposition (CVD), physical vapor deposition (PVD), molecular beam epitaxial (MBE) growth etc. are very popular for preparing fascinating homogeneous morphologies of SMOs including titania (Lao et al., 2002; Tian et al., 2003; Shi and Wang, 2011). However, the high investment and operational cost of these sophisticated instruments often limit their use in industries as well as R&D sectors. On contrary, chemical methods are cost effective and capable yet to prepare the SMOs in different nano/micron size architectures. Chemical methods (e.g., co-precipitation, auto-combustion etc.) are usually influenced by the precursor type as well as pH, temperature, pressure of the reaction media which as a whole changes the reaction kinetics and restricts obtaining desired morphology repetitively. On contrary, template mediated synthesis of hydrothermal/sol-gel methods are considered effective techniques to reproduce desired esthetically impressive architectures of SMOs in different batch reactions. For instance, anodized alumina template assisted wet chemical methods for the preparation of 1D SMO nano-structures are reported elsewhere (Lakshmi et al., 1997; Mao and Wong, 2004; Lee et al., 2011; Mukherjee and Majumder, 2013). Polysaccharide templates are used to fabricate SnO_2, Al_2O_3, TiO_2, CeO_2, ZrO_2 etc. metal oxide by Sun et al. (Sun et al., 2006). Titirici et al. has described the synthesis of Fe_2O_3, Co_3O_4, NiO hollow spheres using spherical carbon templates (Titirici et al., 2006). In the present work, flower like distinctive architecture composed of innumerable numbers of TiO_2 nano-rods is prepared through spherical carbon template mediated hydrothermal process. Phase, morphology, lattice fringe pattern and selected area electron diffraction patterns of the prepared TiO_2 are studied and a mechanistic pathway for the growth of said esthetic architecture is proposed. Chemi-resistive changes of TiO_2 flowers for the detection of isopropanol are studied using a static flow gas sensing measurement set-up developed in the laboratory. The sensitive detection of isopropanol using low cost sensors is demanding since this widely used solvent/reagent causes eye, nose, dermal irritation and critical central nervous system damage for animals (Jammalamadaka and Raissi, 2010). Prepared TiO_2 flowers can detect even 10 ppm isopropanol and the catalytic modification of these using Pt nano-particles can improve its sensitivity further. The nano-structured SMOs while are promising for the detection of toxic gases, catalytic modification using noble metals are attractive to make them more sensitive (Hotovy et al., 2004; Epifani et al., 2008; Hu et al., 2010; Wang et al., 2012; Bhowmik and Bhattacharyya, 2015). For instances, Wang et al. has reported ethanol sensing characteristics of Pd nanoparticle decorated TiO_2 nanobelts with improved sensitivity (Wang et al., 2012). Hotovy et al. shows the enhanced H_2 sensing characteristics of Pt modified NiO thin films as compared to its unmodified counterpart (Hotovy et al., 2004). Epifani et al. (2008) reports the effect of Pt on the H_2 sensitivity of anatase phase TiO_2 thin films. The sensing of isopropanol by primitive SMOs or their noble metal modified counterparts however nurtured by very few researchers (Dong et al., 2014). In this context, the cost effective synthesis of novel TiO_2 esthetic architecture, their catalytic modification using wet chemically synthesized Pt nano-particles, detail study on their phase and morphological features as well as operating temperature dependent isopropanol sensing characteristics could provide comprehensive insight to the researchers. The explanation on the role of Pt nanoparticles as chemical sensitizer in improving the sensitivity of TiO_2 is also important. Further, the current response transients of primitive and Pt modified TiO_2 are correlated with the sequential surface reactions operative for detection of isopropanol and modeled in accordance to Langmuir Hinshelwood reaction mechanism. The values of characteristic time constants (τ), rate constants (k_a) are estimated from the model and the underlying reasons for their differed values for primitive and Pt modified TiO_2 sensing elements are discussed.

EXPERIMENTAL

Synthesis of Materials

Synthesis of TiO_2 Flower Like Architecture (Ti-Nr)

The flow diagram for the synthesis of flower like architecture of TiO_2 nano-rods (Ti-Nr) is described in **Figure 1**. For typical synthesis of TiO_2 flowers, 5 ml Ti (IV) tetra isopropoxide (TTIP) is poured into 20 ml of water in ice-cold condition to form white precipitate of titanium hydroxide. Hydrochloric acid is then added drop wise in the solution under stirring condition until the precipitate is dissolved completely to form a transparent solution. Cetyl trimethyl-ammonium bromide (CTAB) is added to the clear solution and stirred for another 30 min. Spherical carbon templates (diameter in the range 2–2.5 μm) are then added into the mixture. The spherical carbon templates are derived from sucrose through hydrothermal synthesis route described elsewhere (Mukherjee and Majumder, 2012). The whole mixture is kept under ultra-sonication for 15 min and then transferred in a teflon-lined stainless steel autoclave. The autoclave is heated at 180°C for 8 h and cooled thereafter in air at ambient temperature. Resulting product is centrifuged and washed repeatedly with water and ethanol to achieve white mass. The product is dried at 80°C for 24 h and then calcined at 450°C for 2 h to achieve flower like architecture composed of TiO_2 nano-rods.

Synthesis of Pt Nano-Particles and Pt Modified TiO_2 Flower Like Structure (Ti-Nr-Pt)

Pt nano-particles are synthesized separately by the chemical reduction of hexachloroplatinic acid ($H_2PtCl_6.2H_2O$) using sodium borohydride ($NaBH_4$). First 50 mg of $H_2PtCl_6.2H_2O$ is dissolved in 100 ml of water within a round bottom flask. $NaBH_4$ and CTAB are added as reducing agent and surfactant, respectively to the aqueous solution of $H_2PtCl_6.2H_2O$. The mixture is refluxed at 110°C for 2h in N_2 atmosphere to achieve dark brown residue which resulted black mass after centrifugation. The black mass is repeatedly washed with distilled water and finally using ethanol to remove the dissolved inorganics and surfactants. The synthesized Pt nano-particles are finally dispersed with the synthesized TiO_2 flowers ultrasonically for 1 h to obtain the Pt modified flower like TiO_2 architecture (Ti-Nr-Pt).

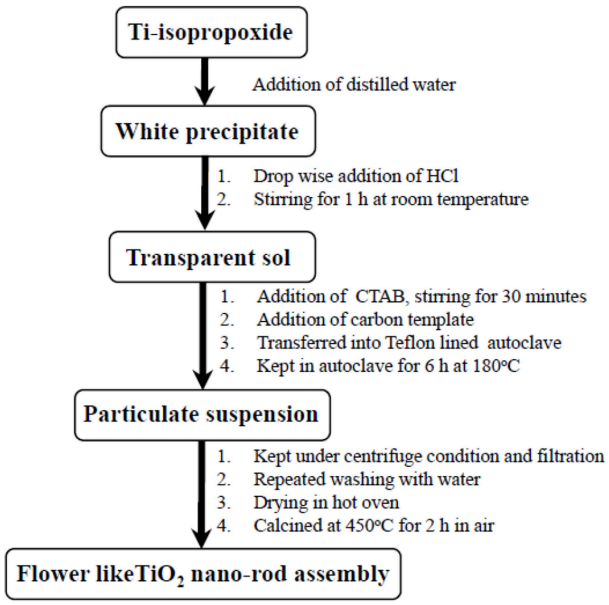

FIGURE 1 | Flow diagram for synthesis of flower like TiO_2 nano-rod assembly.

Phase and Morphological Characterizations of the Synthesized Materials

The crystalline nature of the synthesized Ti-Nr samples is studied using X-ray diffractometer (XRD) (PW 3040/60, Panalytical, Netherland). The morphologies of Ti-Nr and Ti-Nr-Pt samples are studied using field emission scanning electron microscope (FESEM) (Σigma HD, Zeiss, Germany) and transmission electron microscope (TEM) (JEM 2100, Jeol Ltd., Japan). The energy dispersive X-ray spectra (EDS), lattice fringe pattern and selected area electron diffraction patterns of Ti-Nr and Ti-Nr-Pt samples are acquired from transmission electron microscope.

Preparation of Sensing Elements and Protocols for Sensing Measurements

Thick films of Ti-Nr and Ti-Nr-Pt samples are coated on alumina substrate using a mixture of ethyl cellulose and terpineol to prepare the sensing element. The alumina substrate having thickness ∼2 mm was procured from ANTS Ceramic Pvt. Ltd. To prepare the thick film of Ti-Nr and Ti-Nr-Pt nano particles, a binder was prepared by mixing ethyl cellulose and terpineol (weight ratio 1:10) at 60°C to make a viscous liquid. Next, the prepared samples were ultrasonicated with ethanol for ∼30 min and then the binder was mixed with this ultrasonicated mixture of TiO_2 samples to make a smooth paste. Finally the paste of the TiO_2 samples were spread over the alumina substrate by doctor blade technique to prepare the thick films. Here, the role of ethyl cellulose and terpineol is to be used as a binder which helps to create the inter particle contact of the prepared materials and also it makes the good adhesion of the samples over the alumina substrate. The coated alumina substrates are heat treated at 400°C for 1 h to remove the organics. Silver paste based strip electrodes (separated by ∼2 mm) are prepared on their surface to measure the current response of prepared sensing elements. Sensing characteristics are measured using a static flow gas sensing measurement set-up developed in the laboratory. The details of the set-up have already been described elsewhere (Das et al., 2017a). The sensing characteristics are measured by varying the operating temperature (225–300°C) of the sensor and concentration (10–200 ppm) of isopropanol. Sensing elements are kept at the respective operating temperature for ∼30 min to achieve a constant current response in air (I_0) prior to perform the experiments. During the sensing measurements, the surface current of the sensor is measured by applying a fixed voltage (∼20 V) on one of the electrode. The sensitivity (S) of the sensor is estimated by measuring the change of current (ΔI) during sensing with respect to its initial value of current (I_0) using following relationship (Equation 1).

$$S = \Delta I / I_0 \quad (1)$$

RESULTS AND DISCUSSIONS

Phase and Morphological Features of Synthesized Materials

The FESEM image of the prepared carbon sphere templates is shown in the **Figure 2a**. As indicated from the figure, the sizes of the spheres are homogenous having diameter in the range of 2–2.5 μm. Surface of these carbon spheres possess hydrophilic C=O and –OH groups which act as nucleation center for the growth of metal oxide nano-structures (Das et al., 2016). **Figures 2b–d** shows the typical FESEM images of Ti-Nr samples at different magnifications. The acentric growth of nano-rods to form flower like structure is reflected in FESEM images. It is predicted here that spherical morphology of the carbon template facilitates the growth of TiO_2 flower like architecture. The plausible mechanism for the formation of the said flower like architecture is represented in **Figure 2e**. In presence of HCl, initially TTIP hydrolyses in the reaction medium and forms ($Ti(OC_4H_9)_{4-m-n}(OH)_mCl_n$) complex where m and n are the stoichiometry of the associated hydroxyl group (OH^-) and chloride (Cl^-) ion. During hydrothermal condition the said complex dissociates and forms TiO_2 nucleation center. The HCl medium here controls the hydrolysis of TTIP and rate for the nucleation of TiO_2 nano-rods. Pottier et al. reported that the formation of rutile phase titania is promoted in HCl environment (Pottier et al., 2001). CTAB plays the important role for the growth of nucleation centers by preventing their agglomeration.

Typical TEM micrographs of Ti-Nr samples are shown in **Figures 3a,b** where flower like architecture composed of TiO_2 nano-rods is distinguished clearly. The polycrystalline nature of the samples is confirmed in the SAED pattern shown in inset of **Figure 3b**. The patterns are indexed as rutile TiO_2 by matching the calculated "d" spacing with standard JCPDS (Card No. 86-0147). The arrangement of each TiO_2 nano-rod with nib like end is identified in the TEM image shown in **Figure 3c**. The length and width of individual nano-rods are found in the range of 60–65 and 25–27 nm respectively. The lattice fringes shown in the

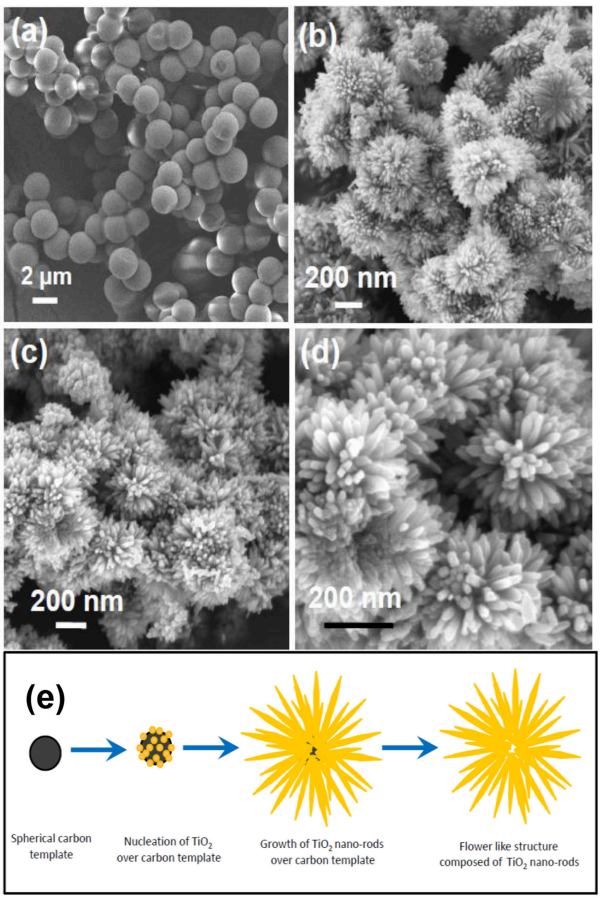

FIGURE 2 | **(a)** Surface morphology of synthesized carbon sphere templates. **(b–d)** FESEM images of flower like TiO_2 nano-rod assembly (Ti-Nr) at different magnification. **(e)** Plausible mechanism for the formation of Ti-Nr structure.

TEM image of the nano-rods are representing the (101) plane of rutile phase TiO_2. The rutile crystal structure of synthesized Ti-Nr samples is further confirmed from the X-ray diffraction (XRD) pattern represented in **Figure 3d**. The diffraction peaks match well with the standard rutile phase TiO_2.

Figures 4a,b represent the TEM images of Ti-Nr-Pt samples where Pt nano-particles are distributed over TiO_2 nano-rods. **Figure 4c** shows enlarged view of the Pt particles within the size range of 5–8 nm. The presence of Pt, Ti, O elements in the composition of Ti-Nr-Pt is confirmed in the EDS presented in **Figure 4d**. The peaks for Cu arise from copper grid which has been used as substrate for TEM study. The low magnification tilted view of SEM micrograph of the TiO_2 thick film is shown in the **Figure 5**. The thickness of TiO_2 thick film is in the range of 50–55 μm and it is uniformly coated on the alumina substrate.

Chemi-Resistive Sensing Characteristics

In chemi-resistive gas/vapor sensors, the resistance/conductance of a sensing element changes in exposure of reducing/oxidizing vapors. The principle of sensing mechanism is illustrated well by researchers (Franke et al., 2006). However, for the ease of understanding to the readers, the schematic sensing mechanism for nano-rod like structure is presented briefly in **Figure 6A**. The SMO based chemi-resistive sensors operate generally at elevated temperature at which atmospheric O_2 is first chemi-adsorbed on the surface of the sensing element. Here,

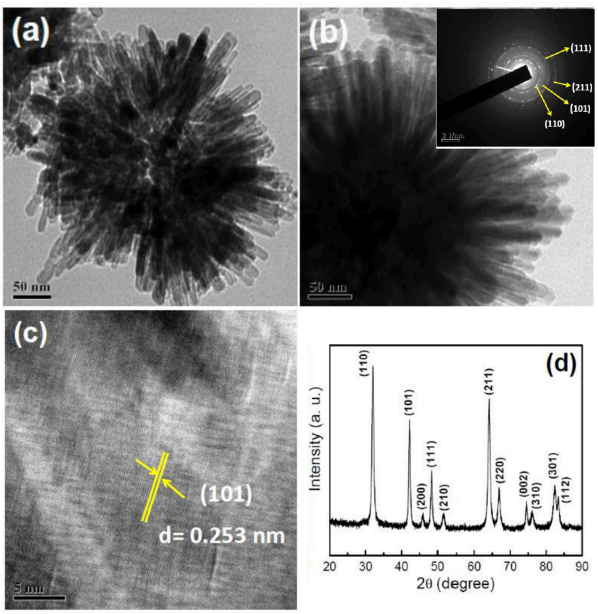

FIGURE 3 | TEM images of Ti-Nr structure at **(a)** low and **(b)** high magnification. Inset of Figure **(b)** SAED pattern of Ti-Nr sample. **(c)** Lattice fringe and **(d)** X-ray diffraction pattern of rutile Ti-Nr particles.

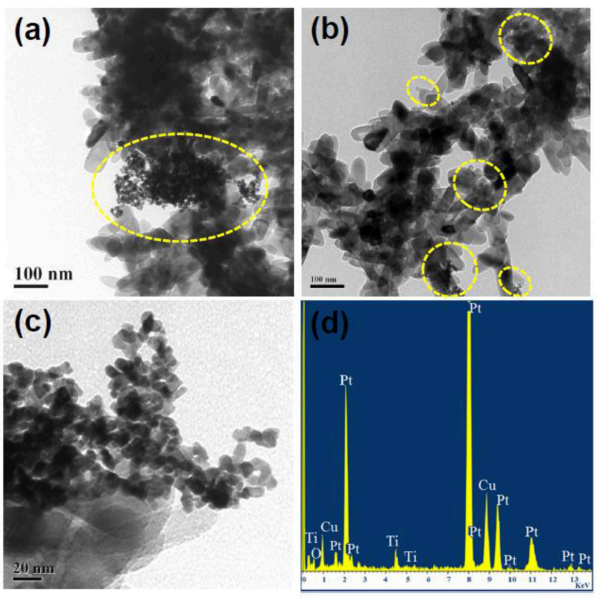

FIGURE 4 | **(a,b)** TEM images of Pt modified flower like TiO_2 (Ti-Nr-Pt) samples. **(c)** Enlarged view of Pt nano-particles within Ti-Nr-Pt sample. **(d)** EDS of Ti-Nr-Pt sample.

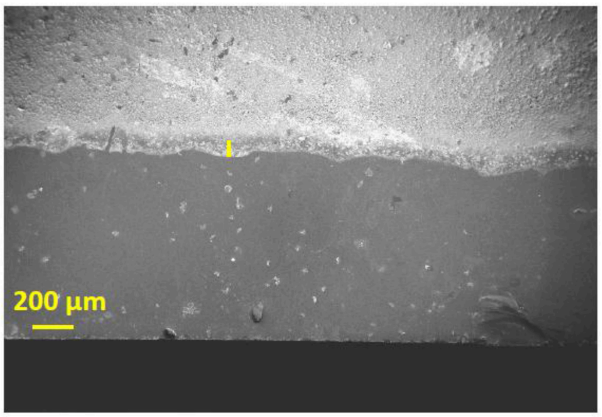

FIGURE 5 | SEM micrograph of TiO_2 thick film of thickness 50-55 µm.

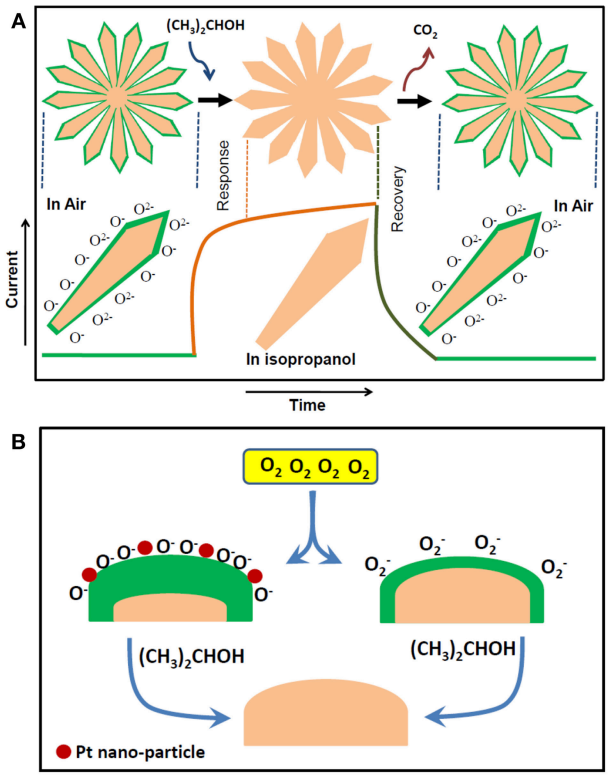

FIGURE 6 | Schematic representation of **(A)** isopropanol sensing phenomenon over flower like architecture comprised of TiO_2 nano-rods (Ti-Nr). **(B)** Sensitization of sensing surface by Pt nano-particles for chemi-adsorption of atomic oxygen.

the chemi-adsorption represents the phenomenon of electron trapping from the conduction band of SMOs by atmospheric oxygen. Depending on the temperature of the sensing element, oxygen may chemi-adsorbed in the atomic/molecular form which is described in Equation (2). Such chemi-adsorbed oxygen develop electronically depleted layer on sensor surface and forms Schottky potential barrier for electron conduction leading to decrease in sensor's electrical conductance. Chemi-adsorbed oxygens then oxidize the exposed reducing vapor (e.g., isopropanol) and release the trapped electrons back to the conduction band of the sensor. As a consequence, the value of surface current for "n" type SMO sensor increases. The reaction of chemi-adsorbed oxygen with isopropanol vapor on sensor surface is presented in Equations (3, 4) (Kulkarni and Wachs, 2002). Sequential change in the surface current of flower like TiO_2 architecture due to the formation and decay of electron depleted layer when it is switching back and forth between oxygen and isopropanol at elevated temperature is illustrated in the figure.

$$O_2(\text{atmospheric}) + e^- \rightarrow O_2^-/2O^-(\text{chemi}-\text{adsorbed}) \quad (2)$$

$$(CH_3)_2CHOH_{ad} + O_2^-/O^- \rightarrow (CH_3)_2CO_{ad} + H_2O_{ad} + e^- \quad (3)$$

$$(CH_3)_2CO_{ad} + H_2O_{ad} \rightarrow CO_2(g) + H_2O(g) \quad (4)$$

Noble metal nano-particles (e.g., Pt nano-particles) on SMO surface expedite the transformation of molecular oxygen to atomic oxygen (**Figure 6B**) which is known as "spillover effect" (Cao et al., 2008). As a consequence, larger amount of electrons is trapped by atomic oxygen than molecular oxygen leading to the higher depletion width for Ti-Nr-Pt than its unmodified counterpart. Likewise, the reaction of reducing vapor (e.g., isopropanol) with chemi-adsorbed atomic oxygen (O^-) will release more electrons than chemi-adsorbed molecular oxygen resulting higher change of electrical conductance of Ti-Nr-Pt than Ti-Nr.

In the forthcoming discussion, operating temperature and gas concentration dependent sensing performances of Ti-Nr and Ti-Nr-Pt based sensing elements are described. The current response transients of both Ti-Nr and Ti-Nr-Pt sensor for the detection of 200 ppm isopropanol at 250 and 275°C are shown in **Figures 7A–D**, respectively. As reflected from the figures, the current response of both Ti-Nr and Ti-Nr-Pt sensors gradually increases with time due to interaction with isopropanol and ultimately saturates. The sensitivity (S) of the sensors Ti-Nr and Ti-Nr-Pt is found 3.0 and 7.0, respectively for the detection of 200 ppm isopropanol at 275°C. The promising isopropanol sensing of both Ti-Nr and Ti-Nr-Pt samples are confirmed in **Figures 7A–D**. However, comparing the figures it is stated that the sensitivity of Ti-Nr-Pt sample toward isopropanol is higher than Ti-Nr.

The operating temperature dependent sensitivity of Ti-Nr and Ti-Nr-Pt samples for the detection of 200 ppm isopropanol is presented in **Figure 7E**. Higher sensitivity of Ti-Nr-Pt than Ti-Nr is observed in the entire operating temperature range (225–300°C). It is notable here that for both the samples, sensitivity first increases with operating temperature, attains maximum and then decreases leading to maximum sensitivity at an optimum temperature. The optimum operating temperature of both Ti-Nr and Ti-Nr-Pt samples for the detection of isopropanol is observed at ~ 275°C. Similar change of sensitivity with operating temperature is generic for other SMO based chemi-resistive sensors (Barsan and Tomescu, 1995; Das et al., 2017b). The

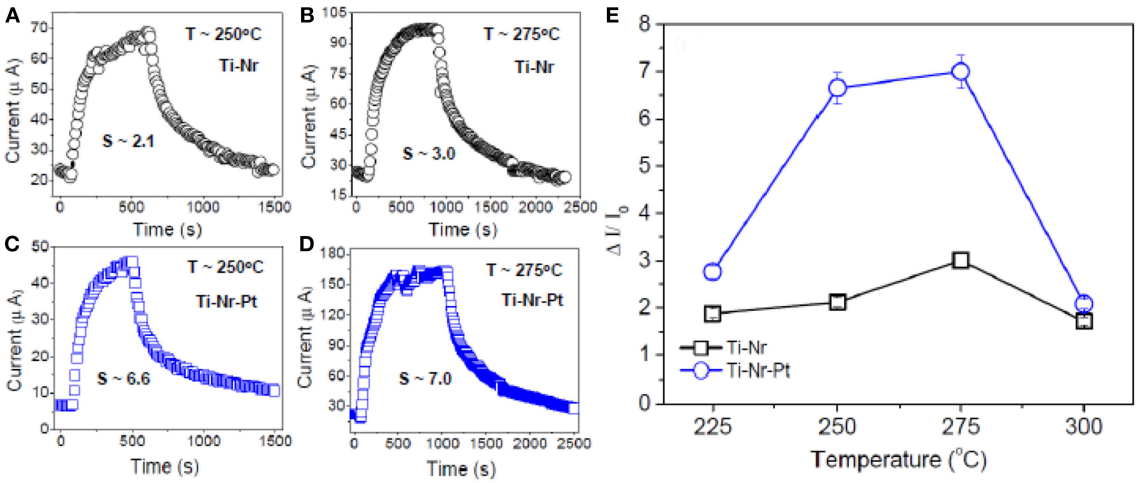

FIGURE 7 | Typical current transients for **(A,B)** Ti-Nr and **(C,D)** Ti-Nr-Pt sensor for the detection of 200 ppm isopropanol at 250° and 275°C, respectively. The sensitivity values are mentioned in the figure. **(E)** Operating temperature (range 225–300°C) dependent sensitivity of both the sensors toward 200 ppm isopropanol.

maximum sensitivity for SMO sensors at an optimum operating temperature can be explained using the concept of depleted layer width and the larger desorption of vapors at high temperature. The initial rise of sensitivity (S) with operating temperature can be explained using the following relationship of sensitivity (S) with depletion layer width (L_D) and charge carrier concentration (Equations 5, 6).

$$L_D = (\varepsilon_o KT/n_o e^2)^{1/2} \quad (5)$$

$$S = \Delta G/G_o = (\Delta n/n_o)L_D \quad (6)$$

where ε_o is the static dielectric constant, n_o is the total carrier concentration, e is the carrier charge, K is the Boltzmann constant, T is the absolute temperature, Δn is the change in the carrier concentration.

The electrical conductance as well as charge carrier concentration of SMO sensors increases with the rise in operating temperature and thus from the aforementioned relationships, it can be stated that the maximum response of the sensor will be obtained at an optimum operating temperature. The enhanced desorption of vapors at sufficiently high temperature results poor gas-solid interaction which predominates over the increase of charge career concentration leading to decreased sensitivity. The higher sensitivity of Ti-Nr-Pt than Ti-Nr due to the formation of wider depleted layer and larger change of charge carrier concentration can also be described by Equation (5). The current response transients of Ti-Nr and Ti-Nr-Pt samples for the detection of 10–100 ppm isopropanol (at optimum operating temperature ~275°C) are presented in **Figures 8A,B** respectively. Comparing the figures, it is observed that Ti-Nr-Pt samples shows better sensitivity than Ti-Nr within the studied concentration range. In order to compare the kinetics for the change of sensitivity of Ti-Nr-Pt and Ti-Nr sensors for the detection of isopropanol, the current response transients of both the sample are modeled in accordance to Langmuir Hinshelwood reaction mechanism. The reaction of isopropanol with chemi-adsorbed molecular or atomic oxygen over Ti-Nr and Ti-Nr-Pt (described in Equation 3) sensors is reflected through the current response transients. As the reaction of isopropanol with chemi-adsorbed oxygen progresses, the current response of sensor also increases with time. On the way to model the current response transient of the sensor in accordance to the reaction presented in Equation (3), it is assumed that the site fraction θ is covered by reaction product ($(CH_3)_2CO_{ad}$) and the rest available unoccupied sites (F- θ) are occupied by chemi-adsorbed oxygen (O^- or O_2^-) on the sensor surface. Here, full surface coverage site is considered as F and rate constant of this reaction is defined as k_a. The rate of formation of the product considering the reaction mentioned in Equation (3) is thus can be described by the following relation:

$$d[(CH_3)_2CO_{ad}]/dt = k_a[O_{ad}^-/O_{2ad}^-][(CH_3)_2CHOH_{ad}] \quad (7)$$

Rewriting Equation (7) in terms of respective site occupancies

$$d\theta/dt = k_a[F - \theta]C_g \quad (8)$$

Assuming full adsorption of low concentration (C_g) of $(CH_3)_2CHOH$, thus $[(CH_3)_2CHOH_{ad}] \sim C_g$, Solving Equation (8) one can write

$$d[(CH_3)_2CO_{ad}]/dt = F(1 - \exp^{-(kaCgt)}) \quad (9)$$

The maximum sensitivity of the sensor corresponds to the situation when all its active sites (F) are occupied by the reaction product $[(CH_3)_2CO_{ad}]$. Therefore the transient sensitivity (S(t)) can be expressed by the following relation.

$$S(t) = S_{max}(1 - \exp^{-(k_a c_g t)}) \quad (10)$$

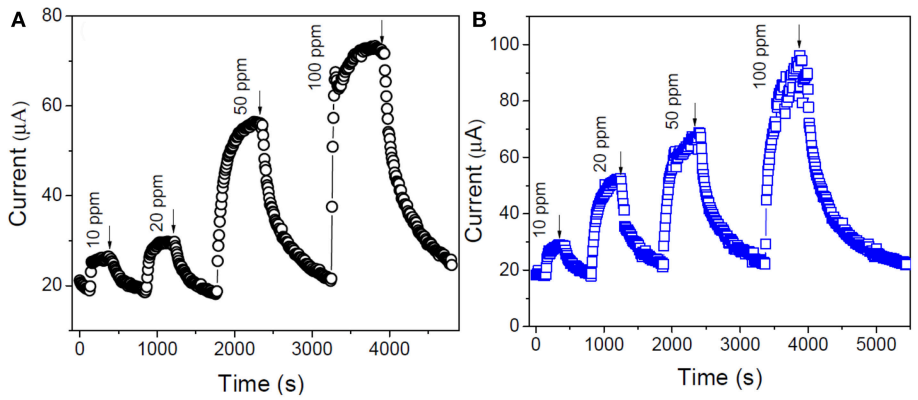

FIGURE 8 | Typical current response transients for **(A)** Ti-Nr and **(B)** Ti-Nr-Pt sensor for the detection of 10-100 ppm isopropanol at 275°C.

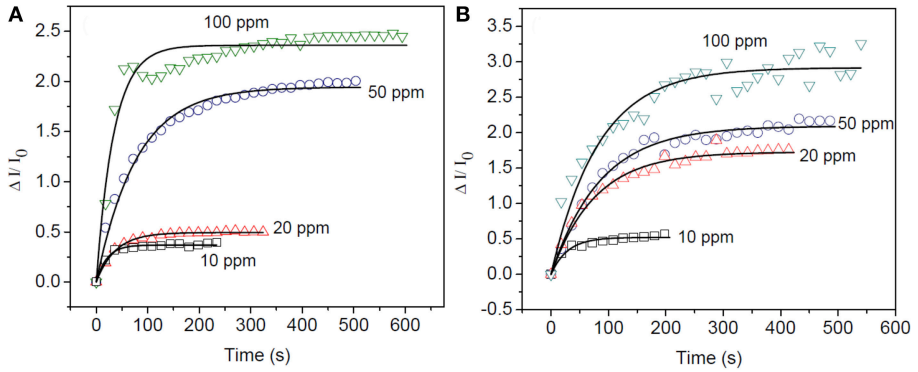

FIGURE 9 | Modeling of transient sensitivity of **(A)** Ti-Nr and **(B)** Ti-Nr-Pt samples for the detection of 10-100 ppm of isopropanol in accordance to Langmuir Hinshelwood mechanism.

Figures 9A,B represents the time dependent sensitivity plot of Ti-Nr and Ti-Nr-Pt for the detection of 10–100 ppm of isopropanol as well as their modeling in accordance to Equation (10). It is notable from the figure that at lower concentration ($\leq$ 50 ppm), the model fits well with the experimental results. However, the model is observed deviated at higher vapor concentration ($\sim$100 ppm). The values of sensitivity, time constants and rate constants for the sensing of isopropanol are estimated from the fitting (summarized in **Table 1**). As estimated, the time constant increases and the rate of the reaction lowers with the rise in isopropanol concentration. The rate for the sensing of isopropanol over Ti-Nr-Pt is also found slower as compared to the sensing over Ti-Nr sample. The decay of wider depletion layer by the released electron due to the oxidation of isopropanol over Ti-Nr-Pt samples takes longer time as compared over Ti-Nr which is reflected in the values of time constant and rate constant in **Table 1**. The improvement of the value of sensitivity or response on the noble metal modified SMO surface is reported in literature (Kolmakov et al., 2005; Dolbec et al., 2007; Xiang et al., 2010; Jang et al., 2013). However, comparative study regarding the kinetics for the sensing of vapors over primitive and noble metal modified SMO surface can hardly found in open literature.

TABLE 1 | Kinetic parameters estimated from the fitting of transient sensitivity of Ti-Nr and Ti-Nr-Pt samples for the detection of 10–50 ppm isopropanol.

Sample	Conc^n (ppm)	S_{max}	τ (s)	k_a (s^{-1})
(Ti-Nr)	10	0.37	20	0.05
	20	0.49	37	0.027
	50	1.94	78	0.128
(Ti-Nr-Pt)	10	0.52	28	0.035
	20	1.72	76	0.0131
	50	2.09	85	0.0117

CONCLUSION

In the present study, flower like architecture comprised of innumerable numbers of TiO_2 nano-rods (Ti-Nr samples) are synthesized hydrothermally and thereafter modified chemically with Pt nano-particles (Ti-Nr-Pt samples). The plausible mechanism for the spherical carbon template mediated hydrothermal growth of Ti-Nr samples is described. The synthesized materials are characterized in terms of their phase formation behavior and morphological features. The Ti-Nr

samples are identified as rutile phase by analyzing the X-ray diffraction patterns. The scanning/transmission electron microscope images along with the associated energy dispersive X-ray spectrum and selected area electron diffraction patterns are used to evaluate the morphology and crystalline nature of the samples. As observed, micron size flowers are composed of eccentrically grown vertically aligned TiO_2 nano-rods which provide larger surface area for the chemi-adsorption of oxygen and facilitate better interaction with isopropanol. The chemi-resistive type sensing toward isopropanol for both Ti-Nr and Ti-Nr-Pt sensors are investigated in a static flow reactor unit developed in the laboratory. The operating temperature (225–300°C) of sensing materials and concentration (10–200 ppm) of isopropanol are varied to measure the sensitivity of the prepared materials. It is found that both the Ti-Nr and Ti-Nr-Pt sensors show promising response toward isopropanol. The optimum sensing performances for both the samples are observed at ∼275°C. The Pt modified Ti-Nr-Pt samples however show better sensitivity than the unmodified Ti-Nr samples within the range of studied operating temperature. The sensitivity at optimum operating temperature ∼275°C for Ti-Nr and Ti-Nr-Pt sensors toward the detection of 10 ppm isopropanol is found 0.37 and 0.52, respectively. The formation of wider depleted layer by chemi-adsorbed oxygen, generation of more electrons during the interaction of isopropanol on Ti-Nr-Pt sensor leads to the better sensitivity as compared to Ti-Nr sensor. The current response transients of Ti-Nr and Ti-Nr-Pt sensors are modeled in accordance to Langmuir-Hinshelwood mechanism in order to understand their kinetics for sensing low concentration (10–50 ppm) of isopropanol. The characteristic time constants for both the samples for sensing isopropanol increase with the rise in isopropanol concentration. The rate constant for the decay of depletion layer due to the interaction of isopropanol with atomic oxygen over Ti-Nr surface is found larger than the same interaction with molecular oxygen over Ti-Nr-Pt surface.

DATA AVAILABILITY

All datasets generated for this study are included in the manuscript.

AUTHOR CONTRIBUTIONS

PD: conceptualization, data acquisition, methodology, analysis, and writing-original draft; BM: conceptualization, supervision, and writing-review and editing; KM: conceptualization, analysis, supervision, writing-review and editing, and funding acquisition.

ACKNOWLEDGMENTS

The author KM is thankful to DST, Govt. of India for providing him Inspire Faculty fellowship (Ref. DST/IFA12-CH-43) and associated research grant for this work. PD is thankful to DST, Govt. of India for supporting her fellowship. KM has partly spent time in analyzing the data, preparing and communicating the manuscript as Fulbright Nehru Postdoc Fellow from his present affiliation George Washington University, USA.

REFERENCES

Bai, J., and Zhou, B. (2014). Titanium dioxide nanomaterials for sensor applications. *Chem. Rev.* 114, 10131–10176. doi: 10.1021/cr400625j

Barsan, N., and Tomescu, A. (1995). The temperature dependence of the response of SnO_2-based Gas Sensing Layers to O_2, $CH_4$and CO. *Sens. Actuator B-Chem.* 26, 45–48. doi: 10.1016/0925-4005(94)01553-T

Bhowmik, B., and Bhattacharyya, P. (2015). Highly stable low temperature alcohol sensor based on hydrothermally grown tetragonal titania nanorods. *RSC Adv.* 5, 82159–82168. doi: 10.1039/C5RA14518J

Cao, M., Wang, Y., Chen, T., Antonietti, M., and Niederberger, M. (2008). A highly sensitive and fast-responding ethanol sensor based on $CdIn_2O_4$ nanocrystals synthesized by a nonaqueous Sol-Gel Route. *Chem. Mater.* 20:5781–5786. doi: 10.1021/cm800794y

Damodaran, V. B., Bhatnagar, D., Leszczak, V., and Popat, K. C. (2015). Titania nanostructures: a biomedical perspective. *RSC Adv.* 5:37149. doi: 10.1039/C5RA04271B

Das, P., Mondal, B., and Mukherjee, K. (2016). Hierarchical Zinc Oxide nano-tips and micro-rods: hydrothermal synthesis and improved chemiresistive response towards ethanol. *RSC Adv.* 6:1408. doi: 10.1039/C5RA23203A

Das, P., Mondal, B., and Mukherjee, K. (2017a). Simultaneous adsorption-desorption processes in the conductance transient of anatase titania for sensing ethanol: a distinctive feature with kinetic perception. *J. Phys. Chem. C.* 121, 1146–1152. doi: 10.1021/acs.jpcc.6b10041

Das, P., Mondal, B., and Mukherjee, K. (2017b). Chemi-resistive response of rutile titania nano-particles towards isopropanol and formaldehyde: a correlation with the volatility and chemical reactivity of vapors. *Mater. Res. Exp.* 4:015503. doi: 10.1088/2053-1591/4/1/015503

Dolbec, R., and E. I., Khakani, M. A. (2007). Sub-ppm sensitivity towards carbon monoxide by means of pulsed laser deposited SnO_2:Pt Based Sensors. *Appl. Phys. Lett.* 90:173114. doi: 10.1063/1.2731710

Dong, C., Liu, X., Xiao, X., Chen, G., Wang, Y., and Djerdj, I. (2014). Combustion synthesis of porous pt-functionalized SnO_2 sheets for isopropanol gas detection with a significant enhancement in response. *J. Mater. Chem. A.* 2:20089. doi: 10.1039/C4TA04251D

Epifani, M., Helwig, A., Arbiol, J., Díaz, R., Francioso, L., Siciliano, P., et al. (2008). TiO_2 Thin Films from titanium butoxide: synthesis, pt addition, structural stability, microelectronic processing and gas-sensing properties. *Sens. Actuator B Chem.* 130, 599–608. doi: 10.1016/j.snb.2007.10.016

Franke, M. E., Koplin, T. J., and Simon, U. (2006). Metal and metal oxide nanoparticles in chemiresistors: does the nanoscale matter? *Small.* 2:36. doi: 10.1002/smll.200500261

Hotovy, I., Huran, J., Siciliano, P., Capone, S., Spiessd, L., and Rehacek, V. (2004). Enhancement of H_2 sensing properties of NiO-based thin films with a pt surface modification. *Sens. Actuator B Chem.* 103, 300–311. doi: 10.1016/j.snb.2004.04.109

Hu, P., Du, G., Zhou, W., Cui, J., Lin, J., Liu, H., et al. (2010). Enhancement of ethanol vapor sensing of TiO_2 nanobelts by surface engineering. *ACS Appl. Mater. Interfaces* 2:3263. doi: 10.1021/am100707h

Jammalamadaka, D., and Raissi, S. (2010). Ethylene glycol, methanol and isopropyl alcohol intoxication. *Am. J. Med. Sci.* 339, 276–281. doi: 10.1097/MAJ.0b013e3181c94601

Jang, B. H., Landau, O., Choi, S. J., Shin, J., Rothschild, A., and Kim, I. D. (2013). Selectivity Enhancement of SnO_2 nanofiber gas sensors by functionalization with pt nanocatalysts and manipulation of the operation temperature. *Sens. Actuator B Chem.* 188, 156–168. doi: 10.1016/j.snb.2013.07.011

Kolmakov, A., Klenov, D. O., Lilach, Y., Stemmer, S., and Moskovits, M. (2005). Enhanced gas sensing by individual SnO_2 nanowires and nanobelts functionalized with Pd catalyst particles. *Nano Lett.* 5, 667–673. doi: 10.1021/nl050082v

Kulkarni, D., and Wachs, I. E. (2002). Isopropanol oxidation by pure metal oxide catalysts: number of active surface sites and turnover frequencies. *Appl. Catal. A.* 237, 121–137. doi: 10.1016/S0926-860X(02)00325-3

Lakshmi, B. B., Dorhout, P. K., and Martin, C. R. (1997). Sol-Gel template synthesis of semiconductor nanostructures. *Chem. Mater.* 9, 857–862.

Lao, J. Y., Wen, J. G., and Ren, Z. F. (2002). Hierarchical ZnO nanostructures. *Nano Lett.* 2, 1287–1291. doi: 10.1021/nl025753t

Lee, J., Kim, D. H., Hong, S. H., and Jho, J. Y. (2011). A hydrogen gas sensor employing vertically aligned TiO_2 nanotube arrays prepared by template-assisted method. *Sens. Actuator B Chem.* 160, 1494–1498. doi: 10.1016/j.snb.2011.08.001

Li, K., Li, B., Wu, J., Kang, F., Kim, J. K., and Zhang, T. Y. (2017). Ultrafast-charging and long-life li-ion battery anodes of TiO_2-B and anatase dual-phase nanowires. *ACS Appl. Mater. Interfaces* 9, 35917–35926. doi: 10.1021/acsami.7b11652

Mao, Y., and Wong, S. S. (2004). General room-temperature method for the synthesis of isolated as well as arrays of single-crystalline ABO_4-type nanorods. *J. Am. Chem. Soc.* 126, 15245–15252. doi: 10.1021/ja046331j

Mukherjee, K., and Majumder, S. B. (2012). Promising methane sensing characteristics of hydrothermal synthesized magnesium zinc ferrite hollow sphere. *Scr. Mater.* 67, 617–620. doi: 10.1016/j.scriptamat.2012.06.025

Mukherjee, K., and Majumder, S. B. (2013). Synthesis of embedded and isolated $Mg_{0.5}Zn_{0.5}Fe_2O_4$ nano-tubes and investigation on their anomalous gas sensing characteristics. *Sens. Actuator B Chem.* 177, 55–63. doi: 10.1016/j.snb.2012.10.108

O'Regan, B., and Grätzel, M. (1991). A low-cost, high-efficiency solar cell based on dye-sensitized colloidal TiO_2 Films, *Nature.* 353, 737–740.

Park, N. G., J., and van de Lagemaat, Frank, A. J. (2000). Comparison of dye-sensitized rutile- and anatase-based TiO_2 Solar Cells. *J. Phys. Chem. B.* 104, 8989–8994. doi: 10.1021/jp994365l

Pottier, A., Chanéac, C., Tronc, E., Mazerolles, L., and Jolivet, J. P. (2001). Synthesis of brookite TiO_2 nanoparticles by thermolysis of $TiCl_4$ in strongly acidic aqueous media. *J. Mater. Chem.* 11, 1116–1121. doi: 10.1039/b100435m

Schneider, J., Matsuoka, M., Takeuchi, M., Zhang, J., Horiuchi, Y., Anpo, M., et al. (2014). Understanding TiO_2 photocatalysis: mechanisms and materials. *Chem. Rev.* 114, 9919–9986. doi: 10.1021/cr5001892

Shi, J., and Wang, X. (2011). Growth of rutile titanium dioxide nanowires by pulsed chemical vapor deposition. *Cryst. Growth Des.* 11, 949–954. doi: 10.1021/cg200140k

Sun, X., Liu, J., and Li, Y. (2006). Use of carbonaceous polysaccharide microspheres as templates for fabricating metal oxide hollow spheres. *Chem. Eur. J.* 12:2039. doi: 10.1002/chem.200500660

Tian, Z. R., Voigt, J. A., Liu, J., Mckenzie, B., and Xu, H. (2003). Large oriented arrays and continuous films of TiO_2-based nanotubes. *J. Am. Chem. Soc.* 125, 12384–12385. doi: 10.1021/ja0369461

Titirici, M. M., Antonietti, M., and Thomas, A. (2006). A generalized synthesis of metal oxide hollow spheres using a hydrothermal approach. *Chem. Mater.* 18, 3808–3812. doi: 10.1021/cm052768u

Wang, C., Yin, L., Zhang, L., Qi, Y., Lun, N., and Liu, N. (2010). Large scale synthesis and gas-sensing properties of anatase tio_2 three-dimensional hierarchical nanostructures. *Langmuir* 26, 12841–12848. doi: 10.1021/la100910u

Wang, D., Zhou, W., Hu, P., Guan, Y., Chen, L., Li, J., et al. (2012). High ethanol sensitivity of Palladium/TiO_2 nanobelt surface heterostructures dominated by enlarged surface area and nano-schottky junctions. *J. Colloid Interface Sci.* 388, 144–150. doi: 10.1016/j.jcis.2012.08.034

Xiang, Q., Meng, G. F., Zhao, H. B., Zhang, Y., Li, H., Ma, W. J., et al. (2010). Au Nanoparticle Modified WO_3 nanorods with their enhanced properties for photocatalysis and gas sensing. *J. Phys. Chem. C.* 114, 2049–2055. doi: 10.1021/jp909742d

Yurdakal, S., Palmisano, G., Loddo, V., Augugliaro, V., and Palmisano, L. (2008). Nanostructured rutile TiO_2 for selective photocatalytic oxidation of aromatic alcohols to aldehydes in water. *J. Am. Chem. Soc.* 130, 1568–1569. doi: 10.1021/ja709989e

Zhou, X., Liu, N., and Schmuki, P. (2017). Photocatalysis with TiO_2 Nanotubes: "Colorful" reactivity and designing site-specific photocatalytic centers into TiO_2 Nanotubes. *ACS Catal.* 7, 3210–3235. doi: 10.1021/acscatal.6b03709

Conflict of Interest Statement: The authors declare that the research was conducted in the absence of any commercial or financial relationships that could be construed as a potential conflict of interest.

frontiers in Materials

ORIGINAL RESEARCH
published: 15 March 2019
doi: 10.3389/fmats.2019.00043

Effect of Zinc Oxide Modification by Indium Oxide on Microstructure, Adsorbed Surface Species, and Sensitivity to CO

Artem Marikutsa[1], Marina Rumyantseva[1], Alexander Gaskov[1], Maria Batuk[2], Joke Hadermann[2], Nasrin Sarmadian[3], Rolando Saniz[3], Bart Partoens[3] and Dirk Lamoen[3]*

[1] Department of Chemistry, Moscow State University, Moscow, Russia, [2] EMAT, Departement of Physics, University of Antwerp, Antwerp, Belgium, [3] CMT, Departement of Physics, University of Antwerp, Antwerp, Belgium

Additives in semiconductor metal oxides are commonly used to improve sensing behavior of gas sensors. Due to complicated effects of additives on the materials microstructure, adsorption sites and reactivity to target gases the sensing mechanism with modified metal oxides is a matter of thorough research. Herein, we establish the promoting effect of nanocrystalline zinc oxide modification by 1–7 at.% of indium on the sensitivity to CO gas due to improved nanostructure dispersion and concentration of active sites. The sensing materials were synthesized via an aqueous coprecipitation route. Materials composition, particle size and BET area were evaluated using X-ray diffraction, nitrogen adsorption isotherms, high-resolution electron microscopy techniques and EDX-mapping. Surface species of chemisorbed oxygen, OH-groups, and acid sites were characterized by probe molecule techniques and infrared spectroscopy. It was found that particle size of zinc oxide decreased and the BET area increased with the amount of indium oxide. The additive was observed as amorphous indium oxide segregated on agglomerated ZnO nanocrystals. The measured concentration of surface species was higher on In_2O_3-modified zinc oxide. With the increase of indium oxide content, the sensor response of ZnO/In_2O_3 to CO was improved. Using *in situ* infrared spectroscopy, it was shown that oxidation of CO molecules was enhanced on the modified zinc oxide surface. The effect of modifier was attributed to promotion of surface OH-groups and enhancement of CO oxidation on the segregated indium ions, as suggested by DFT in previous work.

Keywords: zinc oxide, indium oxide, semiconductor gas sensor, carbon monoxide, surface modification, active sites

OPEN ACCESS

Edited by:
Qasem Ahmed Drmosh, King Fahd University of Petroleum and Minerals, Saudi Arabia

Reviewed by:
Yong Zhou, Chongqing University, China
Yingming Xu, Heilongjiang University, China

****Correspondence:***
Artem Marikutsa
artem.marikutsa@gmail.com

Specialty section:
This article was submitted to Functional Ceramics, a section of the journal Frontiers in Materials

Received: *06 December 2018*
Accepted: *22 February 2019*
Published: *15 March 2019*

Citation:
Marikutsa A, Rumyantseva M, Gaskov A, Batuk M, Hadermann J, Sarmadian N, Saniz R, Partoens B and Lamoen D (2019) Effect of Zinc Oxide Modification by Indium Oxide on Microstructure, Adsorbed Surface Species, and Sensitivity to CO. Front. Mater. 6:43. doi: 10.3389/fmats.2019.00043

INTRODUCTION

Zinc oxide is an *n*-type semiconductor with band gap 3.2 eV that is of interest for resistive gas sensors (Kołodziejczak-Radzimska and Jesionowski, 2014). Doping by M(III) cations (Al, Ga, In) soluble in bulk Zno is commonly used to improve electronic conduction in nanocrystalline zinc oxide (Pearton et al., 2005; Ellmer, 2010; Kołodziejczak-Radzimska and Jesionowski, 2014). It has also been observed that dopants influence the sensitivity of zinc oxide to various target gases

(Han et al., 2009; Kim et al., 2009; Phan and Chung, 2013; Hou and Jayatissa, 2014; Hjiri et al., 2015; Nulhakim et al., 2017; Vorobyeva et al., 2017). Understanding the effect of dopants on gas sensing requires a description of the chemical processes in gas-solid interactions, i.e., target molecule adsorption and redox reaction of the adsorbate with the surface. Such descriptions are usually lacking in literature, since most studies are focused on the electronic properties of doped zinc oxide (Han et al., 2009; Hou and Jayatissa, 2014; Vorobyeva et al., 2017). Among the chemical aspects to be taken into account, there is information on active sites on the surface of the sensing material, adsorption sites for particular gas molecules and reactivity of the surface in redox interaction with the target gas. For example, the sensitivity of Ga-doped ZnO to acceptor NO_2 molecules was correlated to the concentration of paramagnetic donor sites in the materials, while a detrimental effect on the response to H_2S was established because of increased surface acidity (Vorobyeva et al., 2013).

Besides bulk doped materials, heterostructures of ZnO with M(III) oxides are often obtained. The nanocomposites ZnO/In_2O_3 have been synthesized with different morphologies and in a wide composition range for the use as gas sensors (Rambu et al., 2011; Singh et al., 2011; Lee et al., 2013, 2017; Trakhtenberga et al., 2013; Ma et al., 2016; Espid and Taghipour, 2017; Ilin et al., 2017; Wang et al., 2017; Wei et al., 2017; Zou et al., 2017; Choo et al., 2018; Guo et al., 2018; Liu et al., 2018), humidity sensors (Liang et al., 2012), photocatalysts (Wei et al., 2017; Markova et al., 2018), UV-light detectors (Wang et al., 2009). The studies of gas sensor behavior suggested the increased gas sensitivity of composites, in comparison to pure oxides. The increased sensitivity was revealed either to reducing analyte gases like hydrogen (Trakhtenberga et al., 2013; Ilin et al., 2017; Choo et al., 2018), ammonia (Rambu et al., 2011) and $(CH_3)_3N$ (Lee et al., 2013), volatile organic compounds (Singh et al., 2011; Ma et al., 2016; Lee et al., 2017; Wang et al., 2017; Wei et al., 2017; Guo et al., 2018; Liu et al., 2018), or when the oxidizing gases were detected (Espid and Taghipour, 2017; Zou et al., 2017). The data on optimal Zn:In ratios in the gas sensors are contradictory and likely dependent on the synthesis procedure, materials morphology and microstructure and the properties of gas molecules to be detected. For example, improved sensitivity to butanol and chlorine was found for nanorods and nanoparticles of ZnO modified by In_2O_3 (3–4 at % indium) (Zou et al., 2017; Liu et al., 2018), while ZnO/In_2O_3 heterostructures with comparable molar fractions were established for sensing H_2 (Trakhtenberga et al., 2013; Ilin et al., 2017), trimethylamine (Lee et al., 2013) and NO_2 (Espid and Taghipour, 2017). The mechanism of sensitization due to the ZnO/In_2O_3 heterojunctions is most often speculated based on the electron band energy model at the interface between two oxides proposed in Markova et al. (2018). The increase of surface sensitivity to gases is rationalized in terms of potential barrier modification and charged double layer formation within the contact of ZnO/In_2O_3 phases (Singh et al., 2011; Ma et al., 2016; Wei et al., 2017; Guo et al., 2018). Nonetheless important is the influence of oxides adsorption, catalytic and acid-base properties (Lee et al., 2013, 2017; Trakhtenberga et al., 2013). Increment of active sites number at the composites surface due to oxygen adsorption promoted by electronic effects in the ZnO/In_2O_3 junctions is often speculated as the reason for high sensitivity (Wang et al., 2017; Zou et al., 2017; Liu et al., 2018). However, no experimental evidences for the effect of materials composition on the surface active sites have yet been reported.

Carbon monoxide is a toxic gas to be obligatorily monitored in indoors and outdoors. Since the CO molecule has neither pronounced donor-acceptor nor acid-base properties, establishing the factors controlling sensitivity to carbon oxide is a challenge. Computational DFT-based methods are useful for estimating the possible surface sites, geometry and energetics of gas molecules adsorption, as demonstrated for pristine and Ga-doped ZnO models (Derakhshandeh and Anaraki-Ardakani, 2016). The task for the experimental investigation is to establish the relations between CO sensitivity and the effect of ZnO doping on the microstructure, active surface sites and the reactivity to the target gas.

This work is focused on the effect of zinc oxide modification by indium oxide on sensitivity and surface reactivity to CO. Saniz et al. (2018) reported on the DFT-modeling of impurity atoms formation in 4 wt.% In-doped Zno slabs, showing that the localization of In at the surface of zinc oxide is energetically favorable. It was found that the adsorption of CO and OH-species would be enhanced in the presence of In atoms on the surface. Moreover, interatomic bond elongation and charge transfer from the adsorbed CO molecule to the In-doped surface was predicted, suggesting that the electronic state of Zno would have improved sensitivity to CO (Saniz et al., 2018). Here we report on the experimental investigation of nanocrystalline In_2O_3-modified zinc oxide: materials microstructure, distribution of the additive, concentration of surface OH-species and chemisorbed oxygen, sensor response to CO and reactivity to the target gas in relation to the indium oxide amount in ZnO/In_2O_3. The sensitivity to CO correlated to the concentration of surface oxidizing species, OH-groups and to the reactivity of the surface to CO in presence of segregated In_2O_3 species, in agreement with the theoretical results in Saniz et al. (2018).

MATERIALS AND METHODS

Nanocrystalline zinc oxide modified by different amounts of In_2O_3 was synthesized via an aqueous coprecipitation route (Vorobyeva et al., 2013, 2017). The concentrations of In were 1, 3, 5, and 7 at %. Pristine ZnO was obtained as a reference sample. Solution of 1.23 M $Zn(NO_3)_2$ mixed with a calculated volume of 0.25 M $In(NO_3)_3$ solution was added to a 2-fold excess of 1.9 M NH_4HCO_3 solution and stirred at 50°C for 30 min, then left for 1 h at room temperature. The white precipitates of mixed zinc-indium basic carbonates were washed by deionized water and centrifuged, dried at 50°C overnight and annealed at 450°C in air for 24 h to obtain ZnO/In_2O_3 samples.

Phase composition and crystal structure were studied by X-ray diffraction using a DRON-4 instrument. The crystallite size (d_{XRD}) of ZnO was calculated from the broadening of the (100) peak using the Scherrer equation, wave length $\lambda = 1.5406$ Å (Cu $K_{\alpha 1}$ radiation). Microstructure and indium oxide distribution

were studied by transmission electron microscopy (TEM). The materials were ultrasonically dispersed in ethanol and drop-deposited onto a Cu-grid covered with carbon. The TEM images and electron diffraction (ED) patterns were acquired on a FEI Osiris microscope operated at 200 kV. High angle annular dark field scanning transmission electron microscopy (HAADF-STEM) images and energy dispersive X-ray (EDX) maps were acquired using a FEI Titan 80–300 "cubed" microscope equipped with a Super-X detector and operated at 300 kV. The probe current was 200 pA. Zn-K, In-L, and O-K lines were used for the chemical maps.

The specific surface area was measured by low-temperature nitrogen adsorption (Brunauer-Emmett-Teller, BET method) on a Chemisorb 2,750 (Micromeritics) instrument. Cationic composition was determined with micro X-ray fluorescent (XRF) analysis on a Mistral M1 (Bruker) device, acceleration voltage 50 kV, scanning area 1.5 × 1.5 mm and accumulation 30 s. Surface hydroxyl species were analyzed using FTIR transmission spectra of samples pressed in KBr pellets. Spectra were registered in the 4,000–400 cm^{-1} range with a Frontier (Perkin Elmer) spectrometer. Temperature-programmed reduction by hydrogen was performed without pretreatment of the samples. The powders (∼30 mg) were placed in a flow reactor through which H_2(10%):Ar was purged. Hydrogen consumption from gas flow was measured with a thermo-conductivity detector under heating to 900°C with a rate of 5°C/min.

Sensor measurements were performed using a laboratory setup consisting of an automatized electrometer with a flow chamber and gas-regulation system. The source of carrier gas was a generator of purified air, model "1,2–3,5" (Himelectronica, Russia), contamination levels within the limits of 10 ppm H_2O, 2 ppm CO_2, 0.1 ppm hydrocarbons. Certified gas mixtures of CO (1,050 ± 50 ppm):N_2, H_2 (1 ± 0.05%):N_2, CO_2 (10 ± 0.4%):air, NH_3 (1,600 ± 50 ppm):N_2, NO (100 ± 5 ppm):N_2, C_6H_6 (44 ± 4 ppm):N_2, SO_2 (98 ± 5 ppm):N_2, NO_2 (100 ± 7 ppm):N_2 (MGPZ, Russia) were used as the sources of test gases. Relative humidity of carrier gas was varied by mixing dry air and 100% RH humid air flows at room temperature and measured by humidity meter IVTM-7 (NTC-IGD, Russia). Gas concentrations and flows were controlled by EL-FLOW mass-flow controllers (Bronkhorst). Powders were ground with terpineol into a paste which was drop-deposited onto alumina microhotplates provided with vapor-deposited Pt-contacts and heater, forming a sensing layer sized 1 × 0.5 mm and 5–7 μm thick (**Supplementary Data**). Prior to measurements, the sensors were annealed at 350°C in air for 20 h to remove the binder. The sensor resistance was measured at DC-voltage 1.3 V under *in situ* controlled composition of gas flow (100 ml/min) at temperatures fixed in the range 25–450°C. The sensor signal was defined as the ratio of resistance in air (R_a) relative to that in test gas (R_g):

$$S = (R_a - R_g)/R_g. \quad (1)$$

Diffuse-reflectance infrared Fourier-transformed (DRIFT) spectra were collected using a Frontier (Perkin Elmer) spectrometer equipped with DiffusIR annex and a flow test chamber HC900 (Pike Technologies) with a heater and ZnSe window. Spectra were registered in the 4,000–1,000 cm^{-1} region, accumulating 30 scans at ambient conditions with automatic H_2O/CO_2 compensation. Powders (30 mg) were compressed in an alumina crucible (5 mm diameter). The surface acidity of the samples was compared under adsorption of NH_3 probe molecules (200 ppm in air, flow 100 ml/min) at room temperature. Before exposure to ammonia, the samples were heated in air at 150°C for 1 h to remove adsorbed water and then held at room temperature for 1 h. Interaction with test gases was studied under *in situ* exposure to CO (200 ppm), H_2 (200 ppm), and CO_2 (0.1 %) at 150° and 450°C after heating in air for 3 h at the same temperatures. DRIFT spectra in test gases were collected each 15 min for 1.5 h, relative to the background spectrum which was registered after the pretreatment.

RESULTS AND DISCUSSION

Materials Composition, Microstructure and Indium Oxide Distribution

The element composition of ZnO/In_2O_3 estimated by XRF agreed with the loaded indium amounts (1–7 at.%) within the measurement errors. According to X-ray diffraction, the samples of pure ZnO and modified ZnO/In_2O_3 contain a single crystalline phase, i.e., wurtzite-like zinc oxide (**Figure 1**). Because of peak broadening, any changes in unit cell parameters were within the refinement error interval. With the increase of indium oxide content, the mean crystallite size (d_{XRD}) of ZnO decreased and the BET surface area increased (**Figure 2**). This is due to inhibited crystallite growth during the thermal treatment of the co-precipitated metal hydroxocarbonates. Previously it was attributed to the formation of defects (interstitial cations $M_{Zn}^{\cdot}$, oxygen vacancies $V_O^{\cdot\cdot}$) and/or lattice distortions upon incorporation of In(III) into ZnO, because of the difference of ionic radii of Zn(II) (0.60 Å) and In(III) (0.62 Å) in tetrahedral coordination (Shannon, 1976). This assumption is in line with the change of Zn-O bond length following the introduction of In, as shown by DFT (Saniz et al., 2018). Previously, the solubility of In in similarly prepared nanocrystalline ZnO(In) was estimated to be 1 at.% In Vorobyeva et al. (2017). However, in the current study, TEM and EDX detected indium only in segregated form on the surface of ZnO. Hence, most likely the segregated additive blocked the diffusion of zinc and oxygen ions, hampering the crystallization of zinc oxide nanoparticles.

In HAADF-STEM images (**Figure 3a** and **Figure S2**) one can distinguish two types of material: agglomerated nanoparticles and porous spheres. The nanoparticles have a size of 8–30 nm and correspond to wurtzite-like ZnO phase, as confirmed by electron diffraction (inset in **Figure 3a**). The porous spheres range in size from 60 to 100 nm and correspond to In_2O_3. High resolution TEM images (**Figure 3b**) and EDX elemental mapping (**Figure 4**) allowed distinguishing the crystalline ZnO nanoparticles with ordered atomic planes from amorphous In_2O_3. No indium signal was detected on the EDX spectra of the ZnO/In_2O_3 (1 at % In) sample taken from the individual ZnO nanoparticles (areas 1, 2 in **Figure 4b**, spectra are in **Figure S3**). Yet, 1 at.% is below the detection limit of the

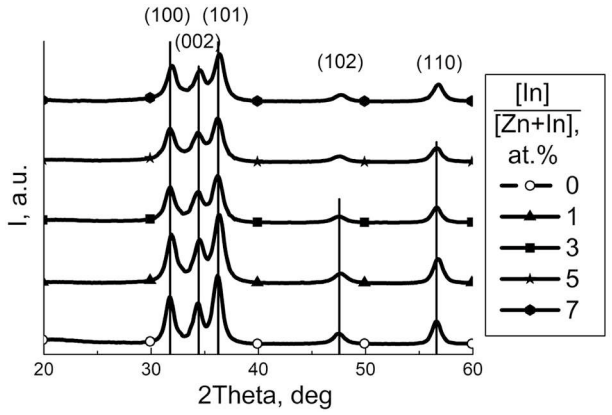

FIGURE 1 | XRD patterns of zinc oxide modified by different amount of In_2O_3. Peaks are indexed for wurtzite ZnO phase (JCPDS 36-1451).

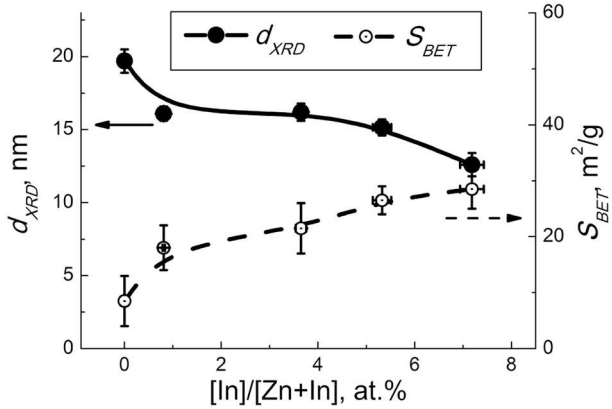

FIGURE 2 | Mean particle size of ZnO (d_{XRD}, solid lines) and BET area (S_{BET}, dashed lines) in relation to the concentration of indium oxide.

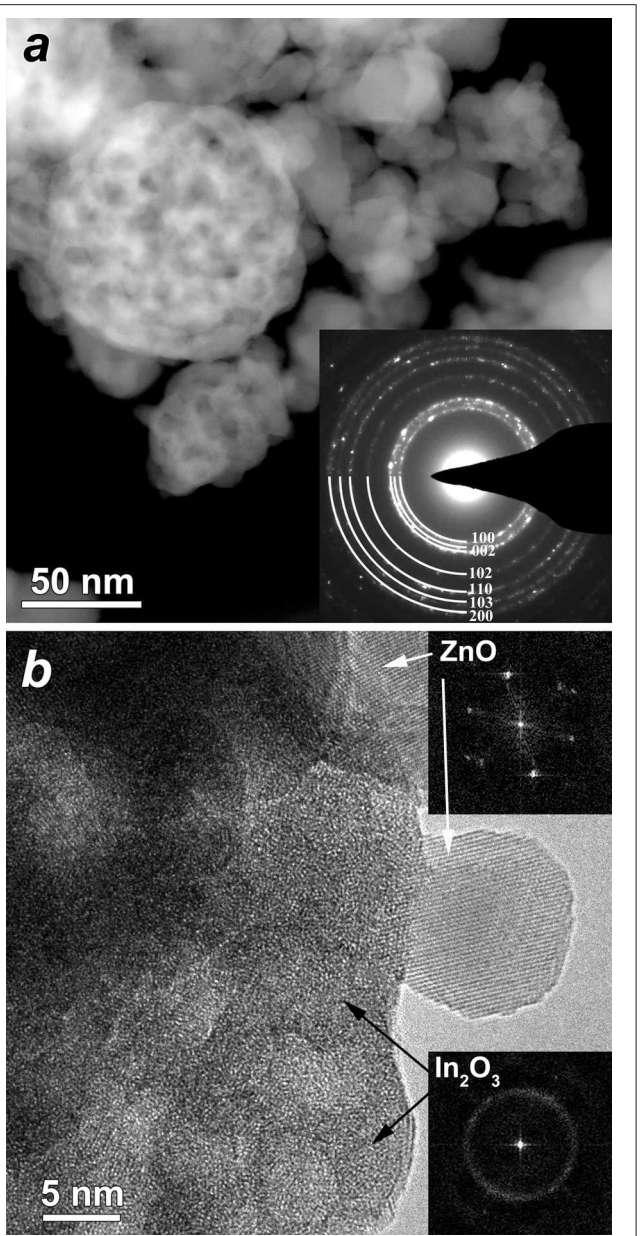

FIGURE 3 | (a) HAADF-STEM image of the ZnO(In, 5 at.%) sample; inset–ring electron diffraction pattern acquired from the large area. The rings are completely indexed using wurtzite structure, (i.e., from center to periphery) 010; 002; 011; 012; −120; 013; −122. **(b)** HRTEM image of the ZnO(In, 5 at.%) sample showing individual crystalline ZnO particle and amorphous In_2O_3 (corresponding FFT's are inserted).

technique and cannot be seen on the spectra. Since indium oxide is abundantly present as an amorphous segregation in all the studied ZnO/In_2O_3 materials, it is possible that there is effectively no indium in the ZnO nanoparticles. A failure to incorporate In(III) in the ZnO lattice could be explained by the preference of In(III) for an octahedral oxygen coordination (Shannon, 1976). Furthermore, the annealing temperature of 450°C might be not enough for the elimination of amorphous phase and crystallization of ZnO(In) as a solid solution. Noteworthy, the preferred segregation of In atoms on a model ZnO surface, rather than incorporation into the bulk, was suggested by first-principles calculations (Saniz et al., 2018).

Effect of Additive on Surface Species of ZnO/In_2O_3

Hydroxyl species on the surface of materials were examined by FTIR spectroscopy. The spectra (**Figure 5A**) consist of peaks relevant to lattice ZnO (420–460 cm^{-1}) and surface Zn-O (800–1,200 cm^{-1}) vibrations (Davydov, 2003) and/or phonon mode vibrations of ZnO (700–1,100 cm^{-1}) (Boccuzzi et al., 1981). The multicomponent bands at 1,300–1,700 cm^{-1} can be contributed by bending vibrations of adsorbed H_2O (1650 cm^{-1}) and surface Zn-O-H groups (1,320, 1,395, 1,410, 1,560, 1,605, and 1,640 cm^{-1}; Keyes et al., 2005) as well as carbonate (1,350 and 1,530 cm^{-1}; Boccuzzi et al., 1979), hydrocarbonate (1,635 cm^{-1}; Saussey et al., 1982) or adsorbed CO_2 (1,370 cm^{-1}; Saussey et al., 1982; 1,360–1,450 cm^{-1}, 1,540–1,650

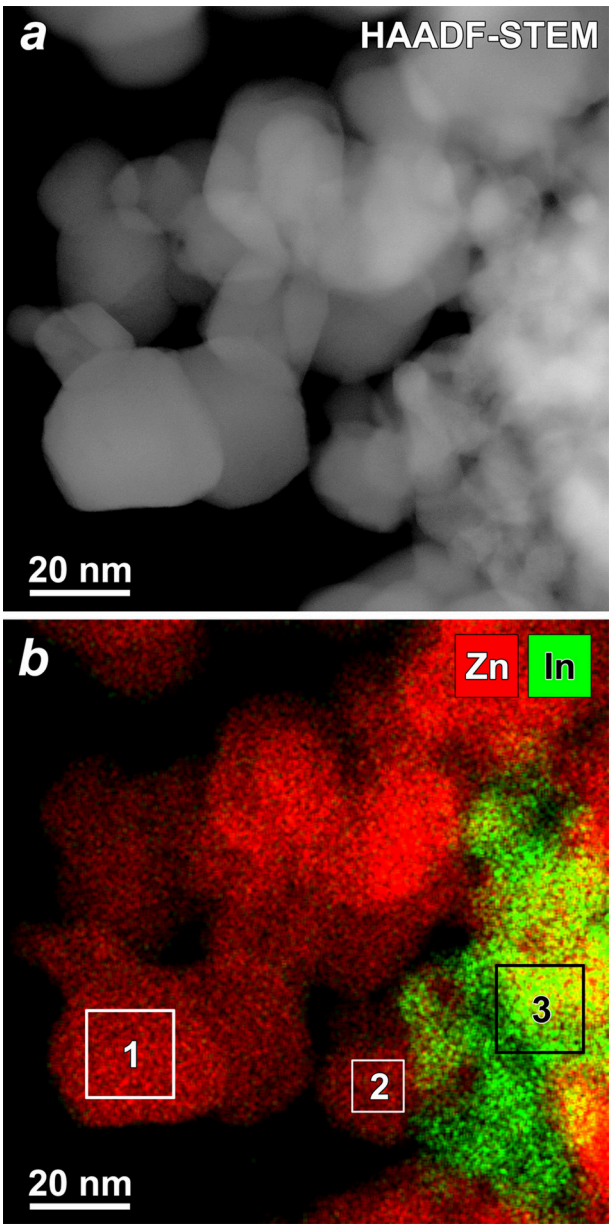

FIGURE 4 | (a) HAADF-STEM image of the ZnO(In, 1 at.%) sample and **(b)** complementary EDX map (red–Zn, green–In). EDX spectra from selected areas showed no In in areas 1 and 2, and presence of In in area 3 (**Figure S3**).

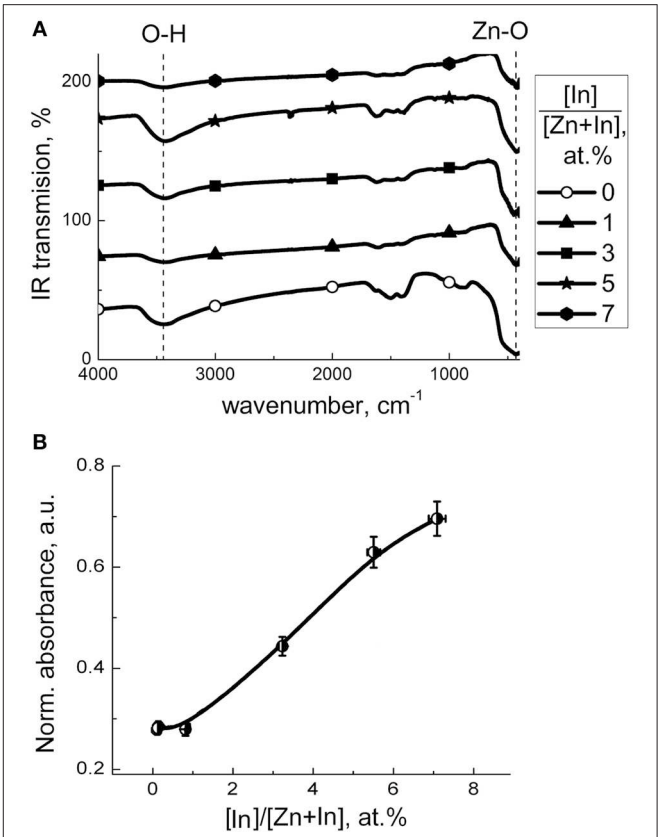

FIGURE 5 | (A) FTIR transmission spectra of zinc oxide modified by different amount of In_2O_3. **(B)** IR absorbance at OH-stretching vibrational peak (3,400 cm^{-1}) normalized to that at lattice Zn-O peak (460 cm^{-1}) in relation to the content of indium oxide in ZnO/In_2O_3.

cm^{-1}; Keyes et al., 2005). The wide band of stretching O–H vibrations at 2,400–3,700 cm^{-1} is indicative of a wide range of hydrated surface species including separate OH-groups (3,500–3,700 cm^{-1}; Atherton et al., 1971; Keyes et al., 2005), hydrogen-bound groups OH…OH at 3,400 cm^{-1} (Atherton et al., 1971), and OH-groups associated with zinc vacancies (3,220–3,230 cm^{-1}; Keyes et al., 2005). The main difference in the spectra of the modified samples was in the relative intensities of hydroxyl-related bands at 3,700–2,400 cm^{-1} and 1,700–1,300 cm^{-1}. In **Figure 5B** the intensity of the most prominent O-H band (3,400 cm^{-1}) normalized by that of lattice ZnO vibrations (420–460 cm^{-1}) is plotted in relation to sample composition. It suggests that the concentration of surface OH-species increased with the content of indium oxide. The hydration could be due to an increasing number of In(III)-ions segregated on the surface, which is in agreement with the higher OH adsorption energy on doped ZnO(In) surface, as theoretically suggested (Saniz et al., 2018). From the chemical point of view, it originates from increased chemisorption of donor H_2O molecules on triple-charged positive In(III) cations at the surface of ZnO. By DRIFT spectroscopy of probe NH_3 molecules adsorption, it was shown that the acidity of modified zinc oxide increased with the content of indium oxide (**Figure 6**). The intensities of the bands corresponding to stretching N-H vibrations (3,260–3,380 cm^{-1}; Morimoto et al., 1976; Belokopytov et al., 1979) and bending NH_3 vibrations (symmetric 1,610 cm^{-1}, asymmetric 1,255 cm^{-1}; Belokopytov et al., 1979) of cation-bound NH_3 and those of OH-bound NH_4^+ species (stretching 3,200 cm^{-1}, symmetric bending 1,455 cm^{-1}; Morimoto et al., 1976) increased with the amount of indium oxide.

Temperature profiles of hydrogen consumption during temperature-programmed reduction (TPR) of the materials are shown in **Figure 7A**. Prominent hydrogen consumption was detected at temperature 150–600°C, but bulk reduction of ZnO

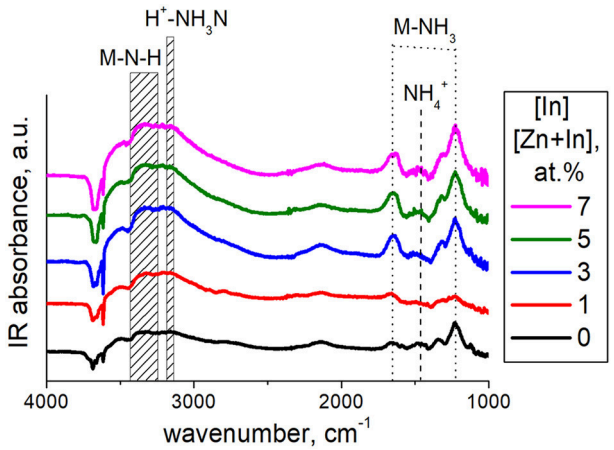

FIGURE 6 | DRIFT spectra of ZnO and ZnO/In_2O_3 samples exposed to NH_3 (200 ppm) at room temperature.

was not achieved on heating to 900°C. In the lower-temperature range 150–450°C the consumption of H_2 is attributable to the reduction of chemisorbed oxygen species (Marikutsa et al., 2013):

$$mH_{2,g} + O^{n-}_{m\ surf} = mH_2O_g + ne^-. \quad (2)$$

where m and n designates the kind of oxygen surface species, which depends on temperature: O_2^- at temperature below 200°C, O^- – at temperature 200–400°C and O^{2-} – at temperature higher than 400°C (Chon and Pajares, 1969). Reduction of hydroxyl surface species can also take place in the lower-temperature range:

$$½H_{2,g} + OH^-_{surf} = H_2O_g + e^-. \quad (3)$$

The consumption of hydrogen at temperature higher than 450°C must be due to a partial reduction of ZnO and of segregated In_2O_3 phase on the surface of ZnO/In_2O_3:

$$3H_{2,g} + In_2O_{3,s} = 3H_2O_g + 2In_l. \quad (4)$$

The profile of ZnO/In_2O_3 (1 at.% In) was similar to that of the pristine ZnO. With the increase of indium content to 3–7 at % In, the peaks of H_2 consumption at 150–600°C increased (**Figure 7A**). It can be due to the increase of indium oxide content and the increase of surface coverage by chemisorbed oxygen species. To distinguish the effect of reducible surface species we subtracted the amount of H_2 needed for reduction of present amounts of In_2O_3 in the samples from the total hydrogen consumption in this temperature range. The results (**Figure 7B**) show that hydrogen consumption by the samples still increased with the In_2O_3 content in ZnO/In_2O_3, although the uptake by the In_2O_3 was excluded. Thus, the concentration of reducible chemisorbed species on the surface of zinc oxide was likely increased due to the modification by indium oxide. The promotion of oxygen chemisorption should be due to the influence of segregated In_2O_3. Indium oxide is an n-type semiconductor with the intrinsic defects being oxygen

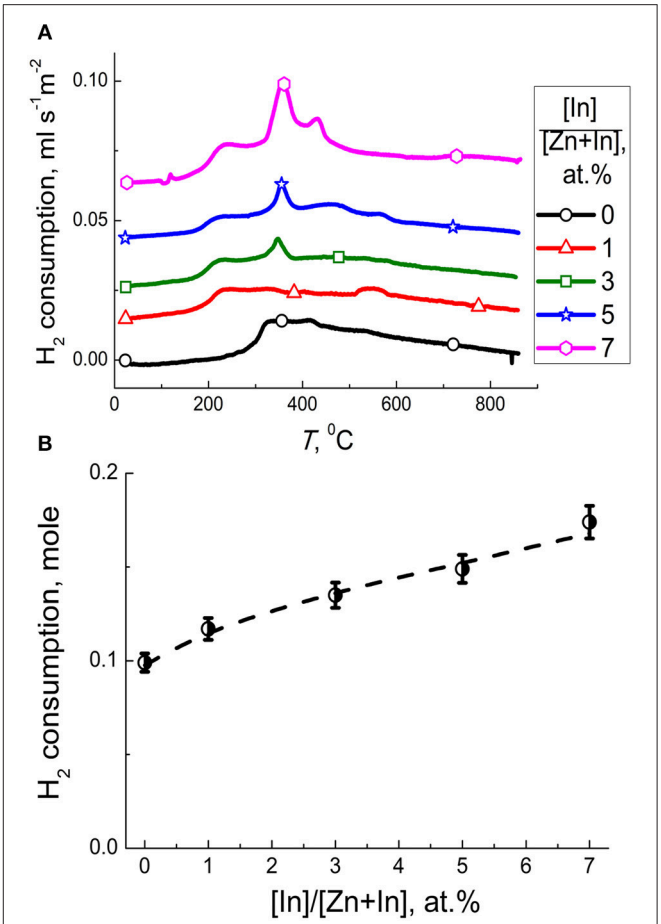

FIGURE 7 | (A) Temperature profiles of H_2 consumption by zinc oxide modified by different amounts of In_2O_3. **(B)** Amount of hydrogen consumed per one mole of ZnO/In_2O_3 with different indium oxide content at temperature 150–600°C excluding the hydrogen uptake by the In_2O_3 additive.

vacancies (Korotcenkov et al., 2016). The junction model between crystalline ZnO and In_2O_3 oxides predicts that electron-enriched layer is formed in ZnO that favors chemisorption of acceptor O_2 molecules, as had been expected in other works (Wang et al., 2017; Zou et al., 2017; Liu et al., 2018). An alternative reason for higher oxygen coverage can be the larger surface area of the modified samples (**Figure 2**).

Sensing Behavior to CO

Figure 8 shows dynamic response of the sensors to different concentrations of CO. At all temperatures tested, the baseline resistance in air was highest for pristine ZnO and decreased non-monotonously with increasing In_2O_3 content. Sensors responses were stable and reproducible, as shown by continuous tests at fixed temperature and CO concentration (dynamic response plot is shown in **Supplementary data**) and repeated tests with the same sensors after several weeks of delay. For the modified sensors, the temperature dependence of the sensor signal to a fixed CO concentration (5 ppm) increased with temperature to 450°C (**Figure 9A**), showing a local maximum at ∼150°C.

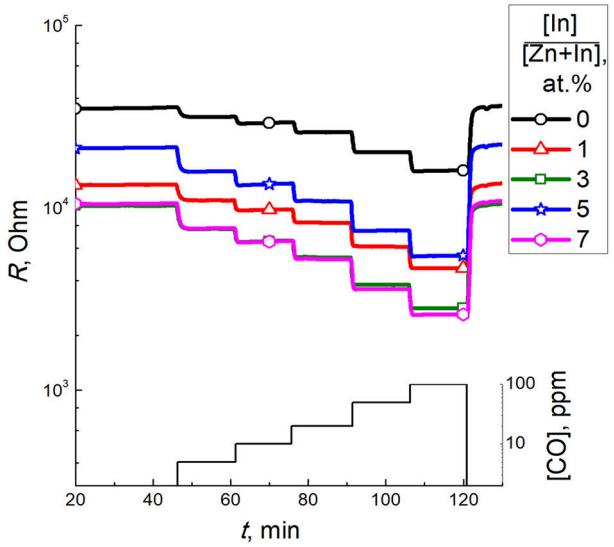

FIGURE 8 | Dynamic response of zinc oxide modified by different amounts of In_2O_3 to 5–100 ppm CO at 450°C.

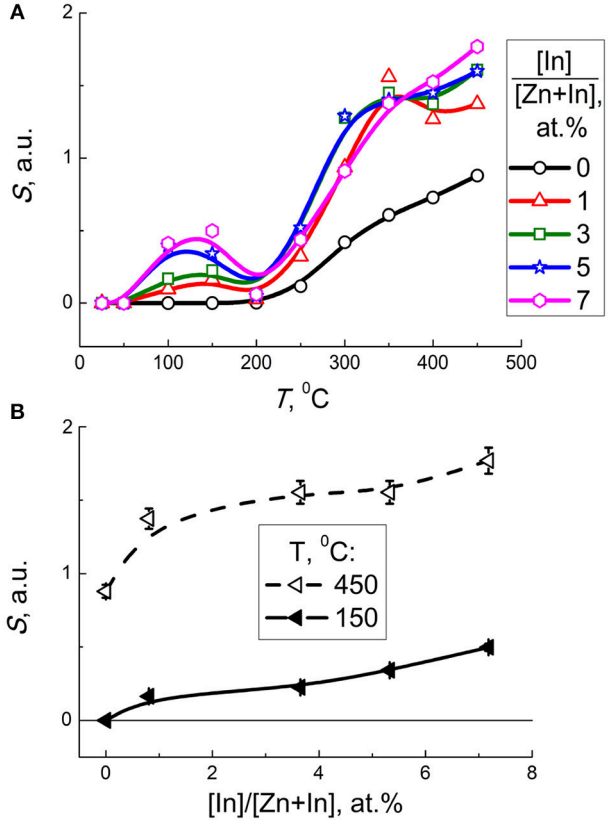

FIGURE 9 | (A) Sensor signal of zinc oxide modified by different amounts of In_2O_3 to 5 ppm CO as a function of temperature. **(B)** Sensor signal of modified zinc oxide to 5 ppm CO at 150°C (solid lines) and 450°C (dashed lines) as a function of In content.

Similar to previous research, the increase of CO sensitivity upon heating to high temperature could be assigned to thermal activation of the reaction of CO with chemisorbed oxygen (Kim et al., 2009; Hjiri et al., 2015; Lim et al., 2015). However, heating to 150°C would be insufficient for thermal activation. In this case the redox reaction at the surface of modified zinc oxide could be facilitated via CO adsorption. As theoretically shown, the In atoms localized at the surface of ZnO should favor CO adsorption and loosen the interatomic C-O bond in the adsorbate (Saniz et al., 2018). This should lower the activation energy for oxidation of adsorbed CO:

$$2CO + O^-_{2\ surf} = 2CO_{2,g} + e^-. \quad (5)$$

Taking into account the entropy factor, inhibition of CO adsorption at raised temperature may account for the decline of the sensor signal on heating to ~200°C (**Figure 9A**). Further increase of sensor response at 200–450°C can be either due to thermal activation of the redox reaction, or due to transformation of predominant surface oxygen species into more reactive atomic forms (Chon and Pajares, 1969).

As follows from the plot of sensor signal vs. indium oxide content in zinc oxide, the sensitivity to CO increased with the concentration of additive (**Figure 9B**). The factor of microstructure (lower particle size, larger BET area) could not be excluded from the effect of the additive on the sensitivity of nanocomposites. Considering the role of surface chemistry in the reception of target molecules, the promotion of sensitivity to CO on increasing In_2O_3 content in ZnO/In_2O_3 agrees both with the increased concentration of chemisorbed oxygen, and with the In-cations being favorable adsorption sites for CO molecules as inferred from DFT (Saniz et al., 2018). The role of surface acidity of ZnO/In_2O_3 inferred from DRIFT and FTIR data discussed above might also contribute to CO sensitivity, e.g., via the interaction of target gas with active surface OH-groups.

Sensor response to CO decreased with the increase of relative humidity (**Figure 10**). Dynamic response to 5 ppm CO at different humidity is provided in **Supplementary Data**. It can be explained by competing water molecules adsorption and blocking the active sites of CO adsorption and oxidation. The drop of sensitivity was larger for the sensors with higher In_2O_3 content (5–7 at.% In), in accordance with the higher surface acidity and water adsorption capacity of these ZnO/In_2O_3 samples inferred from FTIR data.

Selectivity of the sensor response to CO was compared to different interfering gases. For this purpose, the sensor signals to 5 ppm or a higher concentration of a test gas were divided by the signal to 5 ppm CO measured at 450°C for each sensor (**Figure 11**). The dynamic sensor responses are in **Supplementary Data**. As follows from the data in **Figure 11**, the least selectivity was demonstrated by pure ZnO: the cross-sensitivity to benzene was 3 times higher than to CO and the signals to other gases tested were not < 50% of the signal to CO. However, for the samples ZnO/In_2O_3 with 3–7 at % indium content the sensor signals to most of tested

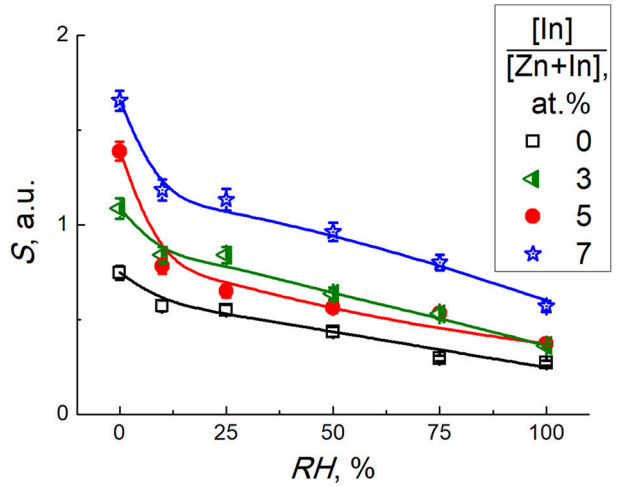

FIGURE 10 | Sensor signal of zinc oxide modified by different amounts of In_2O_3 to 5 ppm CO at temperature 450°C and different relative humidity.

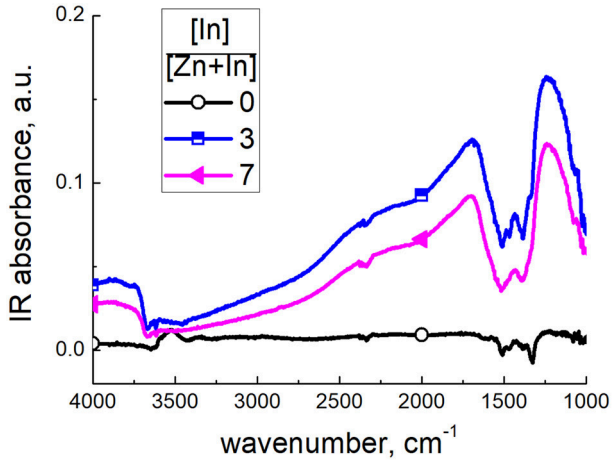

FIGURE 12 | DRIFT spectra of zinc oxide modified by different amounts of In_2O_3, exposed to 200 ppm CO at 150°C.

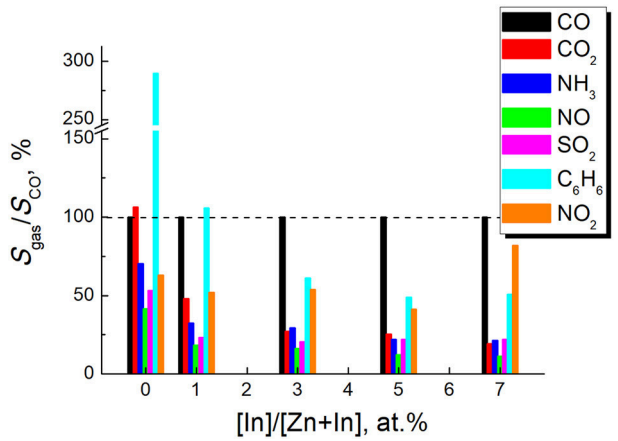

FIGURE 11 | Sensor signals to different tested gases divided by the sensor signal to 5 ppm CO for the samples of zinc oxide modified by different amounts of In_2O_3. Sensor signals were measured at temperature 450°C. The test gases and concentrations were: CO_2-1%, NH_3-5 ppm, SO_2-5 ppm, NO–5 ppm, C_6H_6-5 ppm, NO_2-5 ppm.

interfering gases were below 25% of the sensor signals to CO, except the interference from benzene and nitrogen dioxide. The persistent cross-sensitivity to NO_2 is unproblematic, since it is an oxidizing gas in contrast to the other reducing gases tested. These types of analytes can be discriminated by the direction of resistance response (increase or decrease) of the *n*-type ZnO/In_2O_3 samples.

DRIFT Study of Interaction With CO

The interaction with CO was probed by DRIFT spectroscopy at a temperature corresponding to higher sensitivity. The spectra of zinc oxide exposed to CO at 150°C displayed negative IR absorption peaks at 1,510 and 1,330 cm^{-1} and increased baseline absorption in case of modified samples (**Figure 12**). The intensity of spectral changes corresponded to the CO concentration (100–200 ppm) and recovered the initial state in 1 h after the end of exposure to CO. Modulation of the baseline can be due to increasing charge density in the semiconductor oxide following the adsorption and redox interaction with CO (Equation 5), both resulting in charge transfer from adsorbate to the surface. Moreover, its variation is consistent with higher conductivity of modified zinc oxide (**Figure 8**). The origin of the negative band at 1,690–1,280 cm^{-1} is unclear. It matches the range of bending Zn-O-H vibrations, adsorbed carbonate, CO_2 and water molecules, as discussed above. However, were it due to carbonate, there should have been positive IR absorbance in the presence of CO. Furthermore, the dynamic behavior of this spectral feature was simultaneous with the baseline variation. Thus, this band could be related to the change of electronic state of the materials exposed to CO.

Interaction with CO at 450°C resulted in the same DRIFT spectral features, as at lower temperature, except for the appearance of sharp peaks at 1,510 and 1,320 cm^{-1} (**Figure 13A**). These positive peaks overlapped with the negative absorption band in the presence of CO, more for modified zinc oxide. However, these bands had different dynamic behavior. As demonstrated in **Figure 13B**, the baseline shift and negative band almost disappeared within 15 min after the end of the exposure to CO. However, the pair of sharp peaks at 1,510 and 1,320 cm^{-1} remained for this period, and disappeared only in 60–90 min after the end of CO exposure. These peaks are relevant to stretching vibrations of bidentate carbonate groups (Nakamoto, 1986). This attribution was confirmed by the comparison of DRIFT spectra of materials interacting with CO_2 gas (**Figure 13C**). The peak intensities were higher for modified ZnO/In_2O_3 in agreement with the higher CO sensitivity, as opposed to pristine ZnO. However, comparing the spectra of the sample with higher In_2O_3 content (7 at % In) it is seen that carbonate peaks formed in presence of CO (**Figure 13A**) disappeared within 15 min after CO flow was stopped (**Figure 13B**). That carbonate species

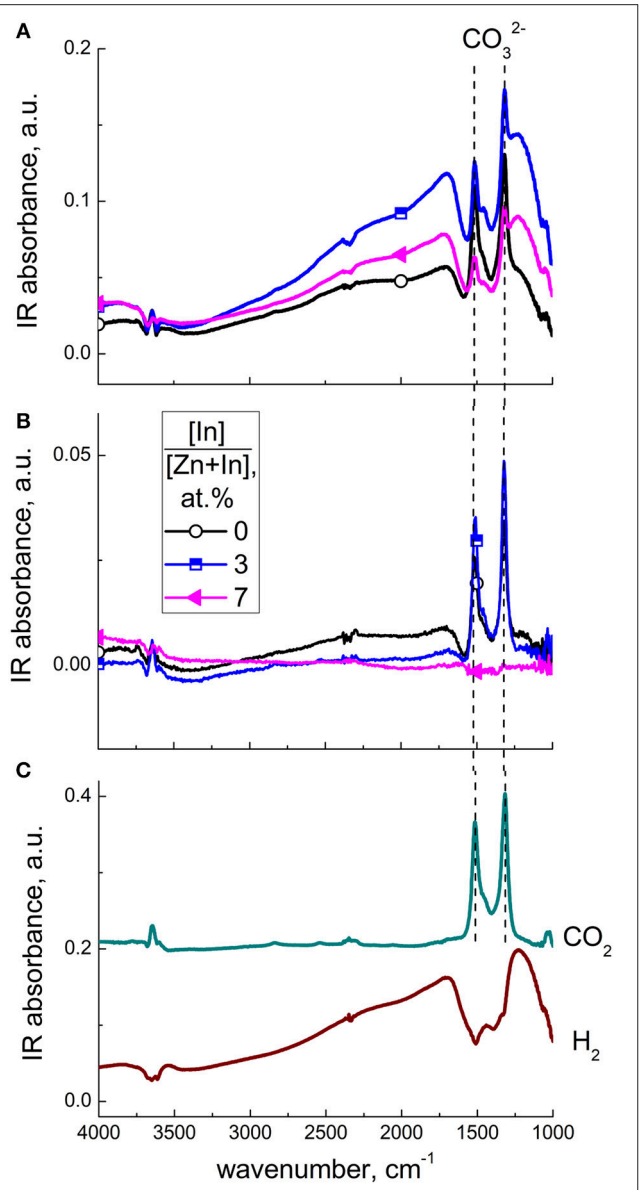

FIGURE 13 | DRIFT spectra of zinc oxide modified by different amounts of In_2O_3, exposed to 200 ppm CO at 450°C **(A)** and to air, 15 min after the end of CO exposure **(B)**. DRIFT spectra of ZnO(In, 3 at.%) exposed to 200 ppm H_2 and 0.1 % CO_2 at 450°C **(C)**.

disappeared from this sample readily while retained for this period on pure ZnO and ZnO/In_2O_3 with 3 at.% In content can be attributed to the increasing surface acidity of the samples with increasing indium oxide content, as discussed in section Effect of additive on surface species of ZnO/In2O3. The higher metal oxide acidity is favorable for carbonate decomposition and evolution of acidic CO_2. Thus, the interaction of pristine and In_2O_3-modified zinc oxide with CO at higher temperature could be formulated taking into account the predominant surface oxygen type as:

$$CO + 2O^-_{surf} = CO_{3,surf} + 2e^-. \quad (6)$$

From the comparison of DRIFT spectra of modified zinc oxide exposed to CO (**Figure 13A**) and H_2 (**Figure 13C**) at 450°C the same observations were made, i.e., fast and reversible (within 15 min) increase of baseline IR absorption accompanied by a negative band at 1,690–1,280 cm^{-1}. Since the interaction with H_2 could not produce any carbonate species and the reversible behavior of Zn-OH groups at such high temperature is unlikely, these spectral features seem to be characteristic of solid-state behavior of modified zinc oxide in the presence of reducing gas molecules.

CONCLUSIONS

Nanocrystalline zinc oxide modified by In_2O_3 (0–7 at % In) was obtained via coprecipitation and annealing at 450°C. By XRD, BET, and TEM analyses it was shown that the modified samples had lower particle size of wurtzite-like ZnO and larger surface area. The additive was observed as amorphous In_2O_3 segregated on the agglomerations of ZnO nanoparticles. No solubility in bulk zinc oxide being detected. This coincides with the DFT-predicted preference of In adatoms to be located at the surface, rather than in the bulk of a model ZnO structure. It was demonstrated, that on raising the indium oxide content, the concentration of chemisorbed oxygen and surface OH-species increased on the surface of nanocrystalline ZnO/In_2O_3. The sensor response to 5–100 ppm CO in air improved due to ZnO modification by In_2O_3. Promotion of CO adsorption on segregated indium oxide species was assumed as the reason for the improved sensitivity at 150°C, in agreement with the effect inferred from DFT modeling of target molecules adsorption. Equally important, the improved sensitivity was in line with the influence of the additive on the materials microstructure and on the concentration of active oxygen and OH-species on the surface of ZnO/In_2O_3. The interaction with CO at temperature 450°C yielded surface carbonate species due to oxidation of the target molecules. The redox reaction was more prominent with the modified ZnO/In_2O_3 materials, thus accounting for the higher CO sensitivity.

DATA AVAILABILITY

All datasets generated for this study are included in the manuscript and/or the supplementary files.

AUTHOR CONTRIBUTIONS

AM, MR, and AG contributed to experimental work by materials synthesis, surface sites investigation, sensing tests, infrared measurements, and dissemination of the experimental data. MB and JH performed electron microscopy studies of materials and contributed to the manuscript preparation. NS, RS, BP, and DL contributed to the justification of the objectives of the study, discussion of experimental results and manuscript preparation.

FUNDING

Research was supported by the grant from Russian Science Foundation (project No. 18-73-00071).

SUPPLEMENTARY MATERIAL

The Supplementary Material for this article can be found online at: https://www.frontiersin.org/articles/10.3389/fmats.2019.00043/full#supplementary-material

REFERENCES

Atherton, K., Newbold, G., and Hockey, J. A. (1971). Infra-red spectroscopic studies of zinc oxide surfaces. *Discuss. Faraday Soc.* 52, 33–43. doi: 10.1039/df9715200033

Belokopytov, Y. U. V., Kholyavenko, K. M., and Gerei, S. V. (1979). An infrared study of the surface properties of metal oxides 2. the interaction of ammonia with the surface of Fe_2O_3, ZnO, MoO_3, and V_2O_5. *J. Catal.* 60, 1–7. doi: 10.1016/0021-9517(79)90061-7

Boccuzzi, F., Borello, E., Chiorino, A., and Zecchina, A. (1979). IR detection of surface microscopic modes of microcrystalline ZnO. *Chem. Phys. Lett.* 61, 617–619. doi: 10.1016/0009-2614(79)87186-9

Boccuzzi, F., Morterra, C., Scala, R., and Zecchina, A. (1981). Infrared spectrum of microcrystalline Zinc Oxide. electronic and vibrational contributions under different temperature and environmental conditions. *J. Chem. Soc. Faraday Trans.* 2, 2059–2066. doi: 10.1039/f29817702059

Chon, H., and Pajares, J. (1969). Hall effect studies of oxygen chemisorption on zinc oxide. *J. Catal.* 14, 257–260. doi: 10.1016/0021-9517(69)90433-3

Choo, T. F., Saidin, N. U., and Kok, K. Y. (2018). A novel self-heating zinc oxide/indium tin oxide based hydrogen gas sensor: dual sensing mode of hydrogen gas detection. *Chem. Phys. Lett.* 713, 180–184. doi: 10.1016/j.cplett.2018.10.043

Davydov, A. (2003). *Molecular Spectroscopy of Oxide Catalyst Surfaces*. Chichester: Wiley. doi: 10.1002/0470867981

Derakhshandeh, M., and Anaraki-Ardakani, H. (2016). A computational study on the experimentally observed sensitivity of Ga-doped ZnO nanocluster toward CO gas. *Physica E.* 84, 298–302. doi: 10.1016/j.physe.2016.06.026

Ellmer, K. (2010). "Transparent conductive zinc oxide and its derivatives," in *Handbook of Transparent Conductors*, ed D. S. Ginley (New York, NY: Springer), 193–265.

Espid, E., and Taghipour, F. (2017). Development of highly sensitive ZnO/In_2O_3 composite gas sensor activated by UV-LED. *Sens. Actuators B.* 241, 828–839. doi: 10.1016/j.snb.2016.10.129

Guo, L., Chen, F., Xie, N., Kou, X., Wang, C., Sun, Y., et al. (2018). Ultra-sensitive sensing platform based on Pt-ZnO-In_2O_3 nanofibers for detection of acetone. *Sens. Actuators B* 272, 185–194. doi: 10.1016/j.snb.2018.05.161

Han, N., Tian, Y., Wu, X., and Chen, Y. (2009). Improving humidity selectivity in formaldehyde gas sensing by a two-sensor array made of Ga-doped ZnO. *Sens. Actuators B* 138, 228–235. doi: 10.1016/j.snb.2009.01.054

Hjiri, M., Dhahri, R., El Mira, L., Bonavita, A., and Donato, N., Leonardi, S. G., et al. (2015). CO sensing properties of Ga-doped ZnO prepared by sol–gel route. *J. Alloys Comps.* 634, 187–192. doi: 10.1016/j.jallcom.2015.02.083

Hou, Y., and Jayatissa, A. H. (2014). Low resistive gallium doped nanocrystalline zinc oxide for gas sensor application via sol–gel process. *Sens. Actuators B* 204, 310–318. doi: 10.1016/j.snb.2014.07.082

Ilin, A. S., Ikim, M. I., Forsh, P. A., Belysheva, T. V., Martyshov, M. N., Kashkarov, P. K., et al. (2017). Green light activated hydrogen sensing of nanocrystalline composite ZnO-In_2O_3 films at room temperature. *Sci. Rep.* 7:12204. doi: 10.1038/s41598-017-12547-5

Keyes, B. M., Gedvilas, L. M., Li, X., and Coutts, T. J. (2005). Infrared spectroscopy of polycrystalline ZnO and ZnO:N thin films. *J. Cryst. Growth* 281, 297–302. doi: 10.1016/j.jcrysgro.2005.04.053

Kim, K., Song, Y.-W., Chang, S., Kim, I.-H., Kim, S., and Lee, S. Y. (2009). Fabrication and characterization of Ga-doped ZnO nanowire gas sensor for the detection of CO. *Thin Solid Films* 518, 1190–1193. doi: 10.1016/j.tsf.2009.03.229

Kołodziejczak-Radzimska, A., and Jesionowski, T. (2014). Zinc Oxide–from synthesis to application: a review. *Materials* 7, 2833–2881. doi: 10.3390/ma7042833

Korotcenkov, G., Brinzari, V., and Cho, B. K. (2016). In_2O_3- and SnO_2-Based Thin Film Ozone sensors: fundamentals. *J. Sens.* 2016:3816094. doi: 10.1155/2016/3816094

Lee, C.-S., Kim, I.-D., and Lee, J.-H. (2013). Selective and sensitive detection of trimethylamine using ZnO–In_2O_3 composite nanofibers. *Sens. Actuators B.* 181, 463–470. doi: 10.1016/j.snb.2013.02.008

Lee, S., Sun, G.-J., Lee, J. K., Hyun, S. K., and Lee, C. (2017). Enhanced ethanol gas sensing performance of the networked pd, In_2O_3-Codecorated ZnO Nanorod Sensor. *J. Korean Phys. Soc.* 71, 494–499. doi: 10.3938/jkps.71.494

Liang, Q., Xu, H., Zhao, J., and Gao, S. (2012). Micro humidity sensors based on ZnO–In_2O_3 thin films with high performances. *Sens. Actuators B.* 165, 76–81. doi: 10.1016/j.snb.2012.02.019

Lim, S. K., Hong, S. H., Hwang, S.-H., Choi, W. M., Kim, S., Park, H., et al. (2015). Synthesis of Al-doped ZnO nanorods via microemulsion method and their application as a CO gas sensor. *J. Mater. Sci. Technol.* 31, 639–644. doi: 10.1016/j.jmst.2014.12.004

Liu, F., Huang, G., Wang, X., Xie, X., Xu, G., Lu, G., et al. (2018). High response and selectivity of single crystalline ZnO nanorods modified by In_2O_3 nanoparticles for n-butanol gas sensing. *Sens. Actuators B.* 277, 144–151. doi: 10.1016/j.snb.2018.08.144

Ma, L., Fana, H., Tian, H., Fang, J., and Qian, X. (2016). The n-ZnO/n-In_2O_3 heterojunction formed by a surface-modification and their potential barrier-control in methanal gas sensing. *Sens. Actuators B.* 222, 508–516. doi: 10.1016/j.snb.2015.08.085

Marikutsa, A., Rumyantseva, M., Frolov, D., Morozov, I., Boltalin, A., Fedorova, A., et al. (2013). Role of PdO_x and RuO_y clusters in oxygen exchange between nanocrystalline tin dioxide and the gas phase. *J. Phys. Chem. C* 117, 23858–23867. doi: 10.1021/jp408646k

Markova, N., Berezina, O., Avdeev, N., and Pergament, A. (2018). UV sensitivity of indium-Zinc Oxide nanofibers. *Adv. Mater. Sci. Eng.* 2018:6351620. doi: 10.1155/2018/6351620

Morimoto, T., Yanal, H., and Nagao, M. (1976). Infrared spectra of ammonia adsorbed on Zinc Oxide. *J. Phys. Chem.* 80, 471–475. doi: 10.1021/j100546a010

Nakamoto, K. (1986). *Infrared and Raman Spectra of Inorganic and Coordination Compounds: Part A: Theory and Applications in Inorganic Chemistry, 6th Edn.* Hoboken, New Jersey: Wiley.

Nulhakim, L., Makinoa, H., Kishimoto, S., Nomoto, J., and Yamamoto, T. (2017). Enhancement of the hydrogen gas sensitivity by large distribution of c-axis preferred orientation in highly Ga-doped ZnO polycrystalline thin films. *Mater. Sci. Semicondu. Process.* 68, 322–326. doi: 10.1016/j.mssp.2017.06.045

Pearton, S. J., Norton, D. P., Ip, K., Heo, Y. W., and Steiner, T. (2005). Recent progress in processing and properties of ZnO. *Progress Mater. Sci.* 50, 293–340. doi: 10.1016/j.pmatsci.2004.04.001

Phan, D.-T., and Chung, G.-S. (2013). Effects of defects in Ga-doped ZnO nanorods formed by a hydrothermal method on CO sensing properties. *Sens. Actuators B.* 187, 191–197. doi: 10.1016/j.snb.2012.10.080

Rambu, A. P., Sirbu, D., Iftimie, N., and Rusu, G. I. (2011). Polycrystalline ZnO–In_2O_3 thin films as gas sensors. *Thin Solid Films* 520, 1303–1307. doi: 10.1016/j.tsf.2011.04.158

Saniz, R., Sarmadian, N., Partoens, B., Batuk, M., Hadermann, J., Marikutsa, A., et al. (2018). First-principles study of CO and OH adsorption on In-doped ZnO surfaces. *arXiv:1806.01338*.

Saussey, J., Lavalley, J.-C., and Bovet, C. (1982). Infrared study of CO_2 adsorption on ZnO. Adsorption sites. *J. Chem. Soc. Faraday Trans.* 1, 1457–1463. doi: 10.1039/f19827801457

Shannon, R. D. (1976). Revised effective ionic radii and systematic studies of interatomic distances in halides and chalcogenides. *Acta Cryst. A* 32, 751–767. doi: 10.1107/S0567739476001551

Singh, N., Ponzoni, A., Gupta, R. K., Lee, P. S., and Comini, E. (2011). Synthesis of In_2O_3-ZnO core–shell nanowires and their application in gas sensing. *Sens. Actuators B* 160, 1346–1351. doi: 10.1016/j.snb.2011.09.073

Trakhtenberga, L. I., Gerasimov, G. N., Gromov, V. F., Belysheva, T. V., and Ilegbusi, O. J. (2013). Conductivity and sensing properties of In_2O_3 + ZnO mixed nanostructured films: Effect of composition and temperature. *Sens. Actuators B*. 187, 514–521. doi: 10.1016/j.snb.2013.03.017

Vorobyeva, N., Rumyantseva, M., Filatova, D., Konstantinova, E., Grishina, D., Abakumov, A., et al. (2013). Nanocrystalline ZnO(Ga): Paramagnetic centers, surface acidity and gas sensor properties. *Sens. Actuators B* 182, 555–564. doi: 10.1016/j.snb.2013.03.068

Vorobyeva, N., Rumyantseva, M., Filatova, D., Spiridonov, F., Zaytsev, V., Zaytseva, A., et al. (2017). Highly Sensitive ZnO(Ga, In) for Sub-ppm level NO_2 detection: effect of indium content. *Chemosensors* 5:18. doi: 10.3390/chemosensors5020018

Wang, B., Jin, H. T., Zheng, Z. Q., Zhou, Y. H., and Gao, C. (2017). Low-temperature and highly sensitive C_2H_2 sensor based on Au decorated ZnO/In_2O_3 belt-tooth shape nano-heterostructures. *Sens. Actuators B* 244, 344–356. doi: 10.1016/j.snb.2016.12.044

Wang, Z., Huang, B., Dai, Y., Qin, X., Zhang, X., Wang, P., et al. (2009). Highly photocatalytic ZnO/In2O3 heteronanostructures synthesized by a coprecipitation method. *J. Phys. Chem. C* 113, 4612–4617. doi: 10.1021/jp8107683

Wei, N., Cui, H., Wang, X., Xie, X., Wang, M., Zhang, L., et al. (2017). Hierarchical assembly of In_2O_3 nanoparticles on ZnO hollow nanotubes using carbon fibers as templates: Enhanced photocatalytic and gas sensing properties. *J. Colloid Interface Sci.* 498, 263–270. doi: 10.1016/j.jcis.2017.03.072

Zou, X., Yan, X., Li, G., Tian, Y., Zhang, M., and Liang, L. (2017). Solution combustion synthesis and enhanced gas sensing properties of porous In_2O_3/ZnO heterostructures. *RSC Adv*. 7:34482. doi: 10.1039/C7RA04852A

Conflict of Interest Statement: The authors declare that the research was conducted in the absence of any commercial or financial relationships that could be construed as a potential conflict of interest.

frontiers in Materials

ORIGINAL RESEARCH
published: 24 April 2019
doi: 10.3389/fmats.2019.00081

Improvement in NO_2 Sensing Properties of Semiconductor-Type Gas Sensors by Loading of Au Into Porous In_2O_3 Powders

Taro Ueda, Keijiro Ishida, Kai Kamada, Takeo Hyodo and Yasuhiro Shimizu*

Graduate School of Engineering, Nagasaki University, Nagasaki, Japan

Porous (pr-) In_2O_3 powders loaded with and without noble metals (Au, Pd, or Pt) were prepared by ultrasonic spray pyrolysis employing the PMMA microspheres as a template (typical particle size (ps): 28 or 70 nm with a diameter), and their NO_2 sensing properties were examined. The Au loading on the pr-In_2O_3 was effective to increase the NO_2 response at lower operating temperature (≤200°C), while the metal loading of Pd or Pt were hardly effective. In addition, a decrease in the PMMA microspheres (from 70 to 28 nm in ps) largely increased the NO_2 response, and an optimized amount of Au loaded on the pr-In_2O_3 sensor was 1.0 wt%. The decrease in the thickness of the sensing layer improved the NO_2 response and response speed. It was suggested that the Au loading enhanced the amount of the negatively adsorbed NO_2 on the bottom part of the sensing layer, leading to the increase in the NO_2 response. Furthermore, the introduction of additional macropores (ps: 150 nm) to the 1.0 wt% Au loaded pr-In_2O_3 sensor increased the response to a low concentration of NO_2 (0.025 ppm) at 30°C. Therefore, it was found that easy gas diffusion from the surface to the bottom part of the sensing layer increased the effective concentration of NO_2, and thus the NO_2 response was increased.

Keywords: NO_2 sensor, porous In_2O_3 powder, loading of Au, ultrasonic spray pyrolysis, polymethylmethacrylate microsphere, ultrasonic-assisted emulsion polymerization

OPEN ACCESS

Edited by:
Qasem Ahmed Drmosh, King Fahd University of Petroleum and Minerals, Saudi Arabia

Reviewed by:
Nittaya Tamaekong, Maejo University, Thailand
Subhasis Roy, University of Calcutta, India

****Correspondence:***
Taro Ueda
taroueda@nagasaki-u.ac.jp

Specialty section:
This article was submitted to Functional Ceramics, a section of the journal Frontiers in Materials

Received: *23 January 2019*
Accepted: *05 April 2019*
Published: *24 April 2019*

Citation:
Ueda T, Ishida K, Kamada K, Hyodo T and Shimizu Y (2019) Improvement in NO_2 Sensing Properties of Semiconductor-Type Gas Sensors by Loading of Au Into Porous In_2O_3 Powders. Front. Mater. 6:81. doi: 10.3389/fmats.2019.00081

INTRODUCTION

Sensing performances of semiconductor-type gas sensors are largely improved by the morphological control of the sensing layer, probably due to the promotion of the gas reactivity on their oxide surfaces by an increase in the surface area per unit volume and the gas diffusivity in the sensing layer (Chen et al., 2014; Sun et al., 2014). Therefore, many researchers have reported the enhanced sensing performances by the structural modification of the sensing layer with rod-like (Wei et al., 2014; Takacs et al., 2015), plate-like (Chen et al., 2014; Guo, 2016), flower-like (Wang et al., 2014, 2015), or urchin-like structured oxide (Tang et al., 2013). Our group has also studied the introduction of ordered porous structures into metal-oxide layers of semiconductor-type gas sensors to enhance their gas diffusivity and surface area during the last 20 years (Hyodo et al., 2001, 2002, 2003, 2005, 2010, 2013, 2017; Hashimoto et al., 2008; Hieda et al., 2008; Firooz et al., 2010). For example, we synthesized mesoporous SnO_2 powders by utilizing the self-assembly of surfactants with a size of several nanometers, and their sensors showed the quite large H_2 response due to an increase in the specific surface area (Hyodo et al., 2001, 2002, 2003). We also reported macroporous SnO_2 layers fabricated by a sol-gel technique employing polymethylmethacrylate

(PMMA) microspheres (Soken Chem. & Eng. Co., Ltd., typical particle size (ps): 150, 400, 800, and 1,500 nm in diameter) as a template, and the one fabricated by using the smallest PMMA microspheres (ps: 150 nm) showed the largest H_2 response among them (Hyodo et al., 2005). In addition, we also attempted the fabrication of the macroporous In_2O_3 powders by ultrasonic spray pyrolysis employing a precursor solution containing PMMA microspheres (ps: 150 nm), and their sensors showed much larger NO_2 response and quicker NO_2 response/recovery speeds than those of the conventional In_2O_3 sensor prepared by the similar preparation technique employing a PMMA-free $In(NO_3)_3$ aqueous solution (Hashimoto et al., 2008; Hyodo et al., 2010). Recently, we focused on the preparation of smaller-sized PMMA microspheres by an ultrasonic-assisted emulsion polymerization technique, and demonstrated an increase in the amount of sodium lauryl sulfate as a surfactant in the polymerization process of methyl methacrylate monomers decreased the size of the synthesized PMMA microspheres (Hyodo et al., 2013). In addition, the fabricated porous (pr-) In_2O_3 sensor employing smaller-sized PMMA microspheres (ps: 26 nm) as a template in a precursor solution of ultrasonic spray pyrolysis was effective in improving the magnitude of NO_2 response to a low concentration of NO_2 (e.g., 1 ppm) at relatively low temperature (150°C) (Hyodo et al., 2017).

Another important technique to realize a large sensor response of semiconductor-type gas sensors is loading of a noble metal such as Au, Pd, Pt, etc., to metal oxides. The effects are known as the chemical and/or electronic sensitization phenomena (Yamazoe et al., 2003). Kim et al. reported the Au decoration on hematite nanotubes improved the magnitude of acetone response as well as acetone selectivity against ethanol (Kim et al., 2018b). Degler et al. clarified that the Au loading on the surface of SnO_2 accelerated negative adsorption of O_2 on the surface by the spillover effects, leading to the enhancement of the CO sensing performances (Degler et al., 2016a). They also demonstrated that the Pt loading on SnO_2 increased the CO response in humidified air, and nano-sized PtO_2 clusters on SnO_2 surface accelerated the CO oxidation reaction (Degler et al., 2016b). Ogel et al. synthesized Pd-loaded hollow-structured SnO_2 powders by a water-in-oil (w/o) microemulsion-based method, and found that the Pd loading on the outside of the SnO_2 shell was effective in achieving large CO response at lower operating temperatures (≤150°C) (Ogel et al., 2017). Kim et al. reported that the sensor of nitrogen-doped WO_3-nanofiber functionalized with Pt nanoparticles by physical mixing showed the enhanced NO_2 response (Kim et al., 2018a). We also confirmed that the loading of Sb (Hieda et al., 2008) increased H_2 responses of pr-SnO_2 powders synthesized by ultrasonic spray pyrolysis employing the PMMA microspheres as a template.

In this study, we synthesized pr-In_2O_3 powders loaded with and without a noble metal such as Au, Pd, or Pt by ultrasonic spray pyrolysis employing home-made PMMA microspheres (ps: 28, 70, 150 nm) as a template, and their NO_2 sensing properties were examined. On the basis of the results obtained, the effects of the introduction of well-developed porous structure into the spherical In_2O_3 powders and the loading of the noble metal to the In_2O_3 surface on their NO_2 sensing properties were discussed.

EXPERIMENTAL

Synthesis of PMMA Microspheres

PMMA microspheres were synthesized by ultrasonic-assisted emulsion polymerization. Methyl methacrylate monomer (MMA; Wako Pure Chem. Ind., Ltd., 150 cm^3) was washed with 0.05 M NaOH aqueous solution (1 dm^3) for three times, to remove a polymerization inhibitor from the MMA monomer. The pure MMA monomer obtained (8 g), sodium lauryl sulfate (SLS; Nacalai Tesque, Inc., 0.1 or 0.5 g) as a surfactant and ammonium persulfate (Wako Pure Chem. Ind., 0.3 g) as an initiator were added to deionized water (100 cm^3), and then the resultant oil/water (o/w) emulsion was ultrasonically treated by an ultrasonic homogenizer (Nissei Corp., US-150T, 19.5 ± 1 kHz). The polymerization of MMA to PMMA was initiated in the micelles, just upon the irradiation of strong ultra-sonic wave to the o/w emulsion at RT, and the temperature of the o/w emulsion increased from RT to ca. 65°C within 15 min. After the ultrasonic irradiation for 30 min, the aqueous dispersion containing PMMA microspheres was obtained (Hyodo et al., 2017). The particle-size distribution of the synthesized PMMA microspheres in the aqueous dispersion was measured at 25°C by dynamic light scattering (DLS; Malvern Instrument Ltd., HPPS), and the average particle size of PMMA microspheres in the aqueous dispersion was confirmed as ca. 70 or 28 nm for the additive amount of SLS of 1.0 g or 5.0 g, respectively.

Preparation of pr-In_2O_3 Powders by Ultrasonic Spray Pyrolysis

The aqueous dispersion containing PMMA microspheres (37.5 cm^3) was mixed with 0.05 mol dm^{-3} $In(NO_3)_3$ aqueous solution (62.5 cm^3) and the mixture was served as an aqueous precursor solution. In some cases, an appropriate amount of $HAuCl_4$, $Pd(NO_3)_2$, or $PtCl_4$ aqueous solution (0.1 mol dm^{-3}) was added to the precursor solution for the loading of Au, Pd, or Pt, respectively. Precursor mists were obtained by ultrasonication of the aqueous precursor solution in a plastic container equipped with a polyethylene thin film at one end, which was perpendicularly set over an ultrasonic vibrator (Honda Electric Co., Ltd., HM-303 N, 2.4 MHz) at a distance of 0.5–1.0 cm in water. A specially designed mist-supplier for the ultrasonic-spray pyrolysis was used to get uniform mists of the precursor solution (Hyodo et al., 2017). Only small droplets separated in a glass vessel were fed into an electric furnace heated at 1,000°C under flowing air (1,500 cm^3 min^{-1}). As the mists were momentarily heated at the electric furnace, the evaporation of water and the thermal decomposition of $In(NO_3)_3$ and PMMA microspheres simultaneously happened and spherical indium oxide powders are produced in the electric furnace under the air flow. The detail of the ultrasonic spray pyrolysis was already reported in our previous paper (Hyodo et al., 2017). The obtained porous powders loaded with and without noble metal were denoted as M(m)/pr-In_2O_3(n) and pr-In_2O_3(n) [M: the kind of noble metal, m: the loading amount of M (wt%), n: the diameter of PMMA microspheres (nm)], respectively. The microstructure of these powders was observed by scanning electron microscopy (SEM; JEOL Ltd., JSM-7500F) and transmission electron microscopy

(TEM; JEOL Ltd., JEM2010). The pore-size distribution and specific surface area (SSA) of these powders were measured by Barrett–Joyner–Halenda (BJH) and Brunauer–Emmett–Teller (BET) methods using N_2 adsorption-desorption isotherms (Micromeritics Instrument Corp., Tristar3000), respectively. Crystal phase of these powders was characterized by X-ray diffraction analysis (XRD; Rigaku Corp., RINT2200) using Cu Kα radiation (40 kV, 40 mA), and their crystallite size (CS) was calculated from the (222) diffraction peak using Scherrer equation. Chemical state of the surface of these powders was characterized by X-ray photoelectron spectroscopy using Al Kα radiation (XPS, Kratos Analytical Ltd., Axis Ultra DLD), and the binding energy was calibrated by using the C1s level (285.0 eV) from usual contamination.

Fabrication of Thick Film Sensors and Measurement of Their Gas Sensing Properties

The fabricated In_2O_3-based powder was mixed with an appropriate amount of α-terpineol (generally, powder: α-terpineol = 1: 2, in weight), and the obtained paste was screen-printed onto an alumina substrate equipped with a pair of interdigitated Pt electrodes (gap size: ca. 200 μm), followed by drying at 100°C. In some cases, this paste was laminated three times to increase the thickness of the sensing layer, while the paste containing the larger amount of α-terpineol (weight ratio: 1:5 or 1:10) was also prepared to decrease the thickness of the sensing layer. Then, they are calcined at 550°C for 5 h in ambient air. Gas responses of these sensors were measured to 0.025, 0.25, 1.0, and 5.0 ppm NO_2 balanced with dry air at a flow rate of 100 cm^3 min^{-1} at 25–500°C. The magnitude of response to NO_2 was defined as the ratio (R_g/R_a) of resistance in NO_2 balanced with air (R_g) to that in air (R_a). The obtained sensors were denoted as pr-In_2O_3(*n*)-*t* or M(*m*)/pr-In_2O_3(*n*)-*t* [*t*: thickness of the sensing layer (μm)].

RESULTS AND DISCUSSION

Characterizations of pr-In_2O_3(*n*) and M(*m*)/pr-In_2O_3(*n*) Powders and Their NO_2 Sensing Properties

Figure 1 shows SEM photographs of representative pr-In_2O_3(*n*) and M(*m*)/pr-In_2O_3(*n*) powders. All the In_2O_3-based particles were spherical with well-developed homogenous porous structures on the surface, due to the thermal decomposition of the PMMA microspheres. The pore size of the pr-In_2O_3(*70*) powder was larger than that of the pr-In_2O_3(*28*) powder, and the observed pore structure was unchanged by the loading of Au. **Supplementary Figures 1, 2** show their XRD patterns and pore-size distributions, respectively. **Table 1** summarizes crystallite sizes (CSs) calculated from their XRD spectra, most frequent values of diameter (mode diameters) of pores in pore-size distributions calculated from N_2 adsorption and desorption isotherms, and specific surface areas (SSAs) of pr-In_2O_3(*n*) and Au(*0.5*)/pr-In_2O_3(*n*) powders. All the powders were assigned to cubic In_2O_3 and the CS of the pr-In_2O_3(*70*) powder was larger than that of the pr-In_2O_3(*28*) powder. In addition, the pore diameter of the pr-In_2O_3(*70*) powder was also larger than that of the pr-In_2O_3(*28*) powder. For details, the pore diameter calculated from N_2 adsorption isotherm of the pr-In_2O_3(*70*) powder (ca. 80 nm) was much larger than that of the pr-In_2O_3(*28*) powder (ca. 30 nm), while the pore diameter calculated from N_2 desorption isotherm of the pr-In_2O_3(*70*) powder (ca. 30 nm) was slightly larger than the that of the pr-In_2O_3(*28*) powder (ca. 22 nm). Generally, the difference between pore diameters calculated from N_2 adsorption and desorption isotherms arises from the ink-bottle porous morphology of both the pr-In_2O_3(*n*) powders. Therefore, the pore diameter calculated from N_2 desorption isotherm reflects the width of the necks formed between the spherical pores, and the one calculated from N_2 adsorption isotherm reflects the diameter of spherical pores, which originates from the morphology of PMMA microspheres as a template. Actually, the size of pores on the surface of both the pr-In_2O_3(*n*) powders was quite similar to the pore diameter calculated from N_2 adsorption isotherm. Furthermore, the loading of Au hardly affected the values of their SSA and CS as well as their pore-size distributions, and the XRD peaks derived from Au were not confirmed in XRD spectra of the Au(*0.5*)/pr-In_2O_3(*n*) powders. The porous morphology on the surface of both the Au(*0.5*)/pr-In_2O_3(*n*) powders was also comparable to that of both the pr-In_2O_3(*n*) powders. These results indicate that Au could be highly dispersed in the Au(0.5)/pr-In_2O_3(*n*) powders.

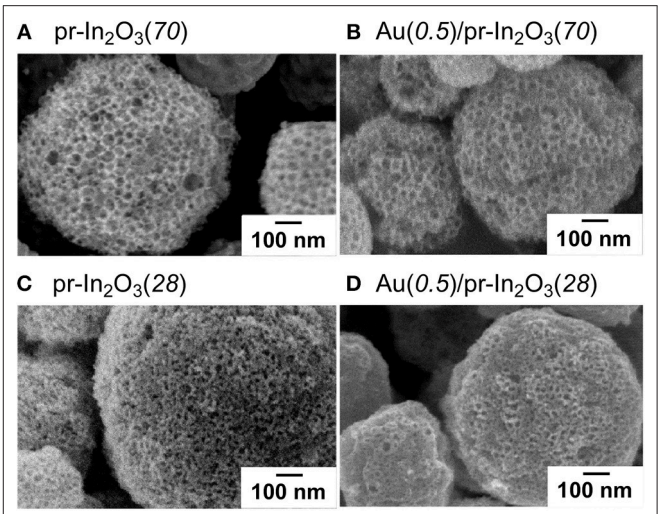

FIGURE 1 | SEM photographs of **(A,C)** pr-In_2O_3(*n*) and **(B,D)** Au(*0.5*)/pr-In_2O_3(*n*) powders [*n*: 28 and 70 (nm)].

Figure 2 shows variations in response of the pr-In_2O_3(*70*)-*20* and the M(*0.5*)/pr-In_2O_3(*70*)-*20* sensors (M: Au, Pd, Pt) to 1 and 5 ppm NO_2 in dry air with operating temperature. **Supplementary Figure 3** shows their typical response transients. The magnitude of response of these sensors increased with a decrease in the operating temperatures, regardless of NO_2 concentration. The loading of Pd to pr-In_2O_3(*70*) was hardly effective in improving the NO_2 response and the loading of Pt

TABLE 1 | Comparison of crystallite size (CS), pore diameter, and specific surface area (SSA) of the pr-In_2O_3(*n*), and Au(*0.5*)/pr-In_2O_3(*n*) powders.

Sensor	CS/nm	Pore diameter*/nm		SSA/m^2 g^{-1}
		Adsorption	Desorption	
pr-In_2O_3(*70*)	14.5	80	30	26.6
Au(*0.5*)/pr-In_2O_3(*70*)	14.2	70	30	23.7
pr-In_2O_3(*28*)	12.9	30	22	37.8
Au(*0.5*)/pr-In_2O_3(*28*)	12.9	30	22	34.3

**Mode diameter obtained from N_2 adsorption and desorption isotherms.*

to pr-In_2O_3(*70*) had negative effect on the NO_2 response in the whole operating temperature range examined. On the other hand, the loading of Au increased the NO_2 response especially at lower temperatures (≤200°C), even though the NO_2 response of the Au(*0.5*)/pr-In_2O_3(*70*)-*20* sensor was much smaller than that of the pr-In_2O_3(*70*)-*20* sensor at higher temperatures of more than 300°C. In addition, the Au(*0.5*)/pr-In_2O_3(*70*)-*20* sensor showed faster recovery speed at lower temperatures (≤300°C) than that of the pr-In_2O_3(*70*)-*20* sensor. The loading of Au to pr-In_2O_3(*70*) is found to be effective to improve response properties at lower operating temperatures. Therefore, sensing properties of Au(*0.5*)/pr-In_2O_3(*n*)-*20* sensors to further low concentration of NO_2 were evaluated at the lower operating temperatures. **Figure 3** shows variations in response of the pr-In_2O_3(*n*)-*20* and the Au(*0.5*)/pr-In_2O_3(*n*)-*20* sensors (*n*: 28, 70) to 0.25 ppm NO_2 with operating temperature in dry air. **Figure 4** shows response transients of the pr-In_2O_3(*n*)-*20* and the Au(*0.5*)/pr-In_2O_3(*n*)-*20* sensors (*n*: 28, 70) to 0.25 ppm NO_2 in dry air at 30 and 200°C. Both the pr-In_2O_3(*n*)-*20* sensors showed quite a small response to 0.25 ppm NO_2 at 350°C, but their NO_2 response increased with a decrease in the operating temperature at 200–350°C. However, the NO_2 response of the pr-In_2O_3(*n*)-*20* sensors decreased with a decrease in operating temperature at <200°C. In addition, the NO_2 response of the pr-In_2O_3(*28*)-*20* sensor was comparable to that of the pr-In_2O_3(*70*)-*20* sensor in the entire examined temperature range. On the other hand, the NO_2 responses of the Au(*0.5*)/pr-In_2O_3(*n*)-*20* sensors increased with a decrease in operating temperatures, and especially they were much larger than those of the pr-In_2O_3(*n*)-*20* sensors at <150°C. These results indicate that the loading of *0.5* wt% Au was effective in improving the NO_2 response, only at lower temperatures. In addition, the NO_2 response of the Au(*0.5*)/pr-In_2O_3(*28*)-*20* sensor was much larger than that of the Au(*0.5*)/pr-In_2O_3(*70*)-*20* sensor at the lower temperatures, and the Au(*0.5*)/pr-In_2O_3(*28*) sensor showed the largest NO_2 response (ca, 1×10^5) at 30°C among the sensors. On the other hand, the response speed of these sensors at 30°C was much slower than that at 200°C, and their resistance did not recover to their original values.

Figure 5 shows variations in response of the Au(*m*)/pr-In_2O_3(*28*)-*20* sensors (*m*: 1.0, 1.5, 2.0, 5.0) to 0.25 ppm NO_2 in dry air with operating temperature in order to examine the effects of the loading amount of Au. **Figure 6** shows response transients of the Au(*m*)/pr-In_2O_3(*28*)-*20* sensors (*m*: 1.0, 1.5, 2.0, 5.0) to

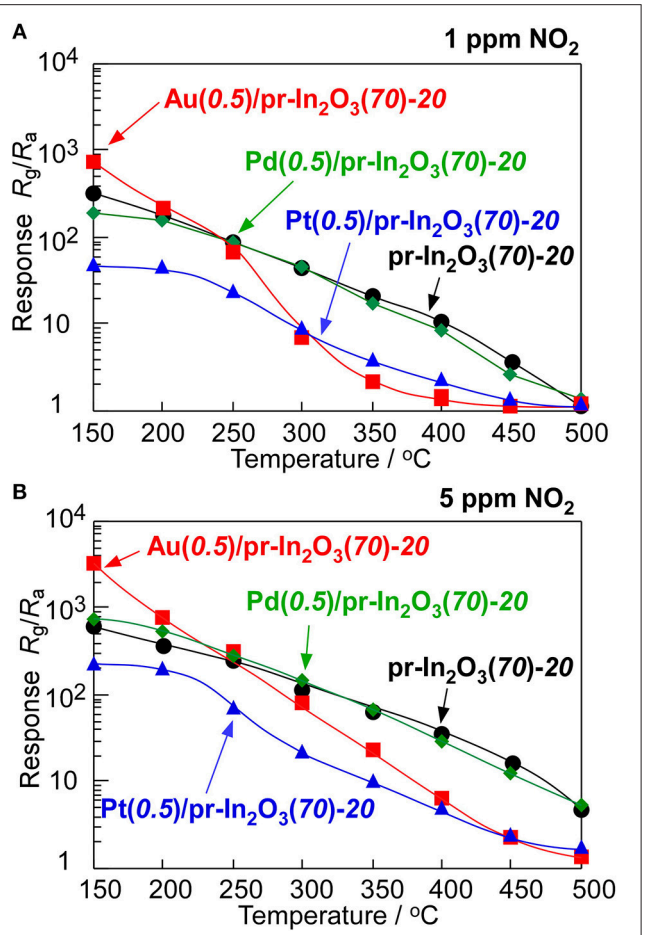

FIGURE 2 | Variations in response of the pr-In_2O_3(*70*)-*20* and M(*0.5*)/pr-In_2O_3(*70*)-*20* sensors to **(A)** 1 and **(B)** 5 ppm NO_2 in dry air with operating temperature.

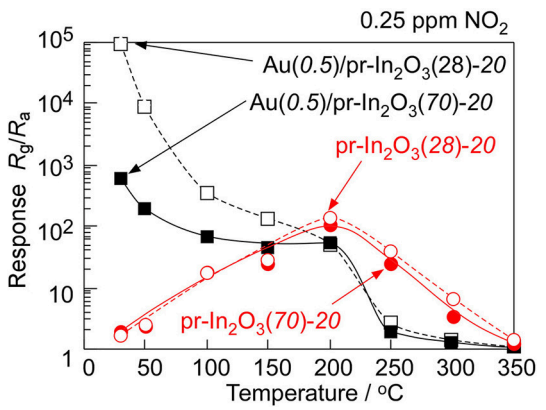

FIGURE 3 | Variations in response of the pr-In_2O_3(*n*)-*20* and Au(*0.5*)/pr-In_2O_3(*n*)-*20* sensors to 0.25 ppm NO_2 in dry air with operating temperature.

0.25 ppm NO_2 in dry air at 50°C. These Au(*m*)/pr-In_2O_3(*28*)-*20* sensors also showed extremely large NO_2 responses at 30°C, as is the case with the Au(*0.5*)/pr-In_2O_3(*28*)-*20* sensor, but the

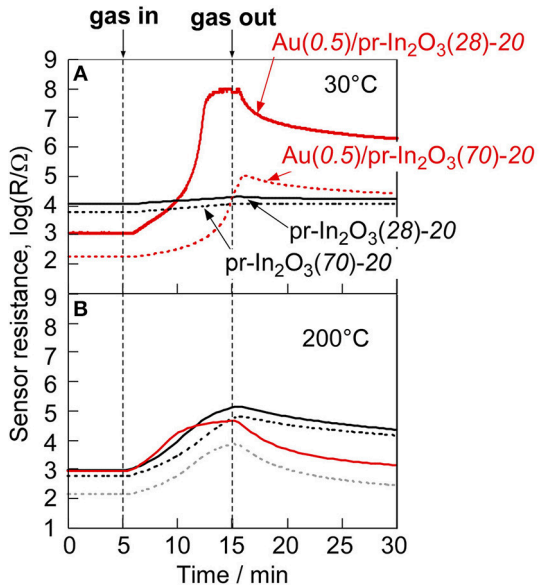

FIGURE 4 | Response transients of the pr-In_2O_3(*n*)-*20* and Au(*0.5*)/pr-In_2O_3(*n*)-*20* sensors to 0.25 ppm NO_2 at **(A)** 50 and **(B)** 200°C in dry air.

resistance values of these sensors in 0.25 ppm NO_2 were as large as 10^9 Ω, which is beyond the limitation of our measurement setup. Thus, we did not obtain correct response values at 30°C. The NO_2 response of all the Au(*m*)/pr-In_2O_3(*28*)-*20* sensors increased with a decrease in the operating temperature, and the Au(*1.0*)/pr-In_2O_3(*28*)-*20* sensor showed the largest NO_2 response among them. All the Au(*m*)/pr-In_2O_3(*28*)-*20* sensors showed quite slow response behavior. The resistance of the Au(*1.0*)/pr-In_2O_3(*28*)-*20* sensor most swiftly increased upon exposure to NO_2 and it reached a constant value, just like that of the Au(*0.5*)/pr-In_2O_3(*28*)-*20* sensor. However, the resistance of other Au(*m*)/pr-In_2O_3(*28*)-*20* sensors (*m*: 1.5, 2.0, 5.0) did not reach a constant value during the exposure period of NO_2 (10 min), which indicates that too large loading of Au (*m*: 1.5, 2.0, 5.0) slowed down the response speed to 0.25 ppm NO_2 in air.

Effects of the Au Loading to pr-In_2O_3(*n*) Powders on the NO_2 Sensing Properties

The In_2O_3-based sensors generally respond to NO_2 since NO_2 molecules are negatively adsorbed on the oxide surface (Roso et al., 2017). The magnitude of NO_2 response of the pr-In_2O_3(*n*)-*20* sensors was increased by the loading of a small amount of Au as shown in the previous section, which indicates that the highly dispersed Au nanoparticles loaded enhanced the amount of negatively charged NO_2 adsorbed on the oxide surface. Several researchers also reported an increase in the NO_2 response of the semiconductor-type gas sensors by Au loading onto the metal oxides, and they suggested an increase in the adsorption amount of NO_2 as a result of spillover effects (Choi et al., 2011; Mun et al., 2013; Shim et al., 2013). In addition, the Au(*m*)/pr-In_2O_3(*28*)-*20* (*m*: 0.5, 1.0) sensors showed rather larger NO_2 response than the Au(*m*)/pr-In_2O_3(*28*)-*20* (*m*: 1.5, 2.0, 5.0) sensors.

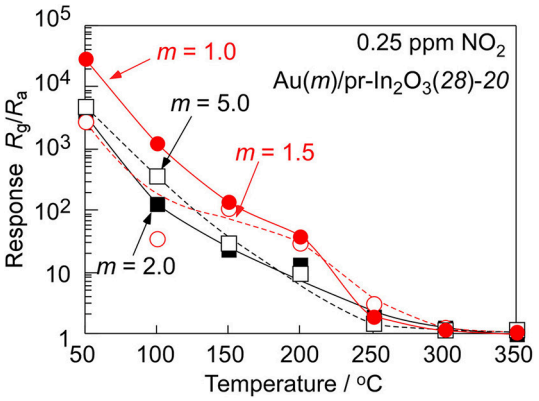

FIGURE 5 | Variations in response of the Au(*m*)/pr-In_2O_3(*28*)-*20* sensors to 0.25 ppm NO_2 in dry air with operating temperature.

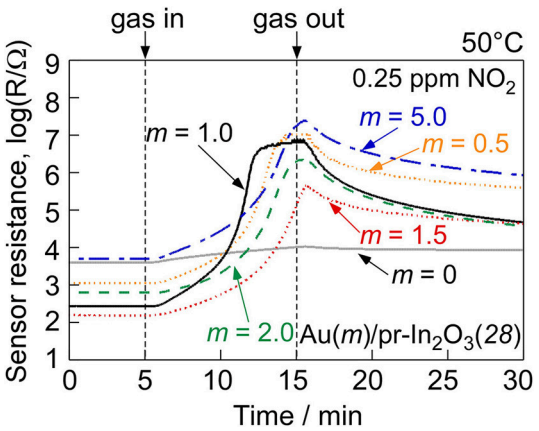

FIGURE 6 | Response transients of the Au(*m*)/pr-In_2O_3(*28*)-*20* sensors to 0.25 ppm NO_2 at 50°C in dry air.

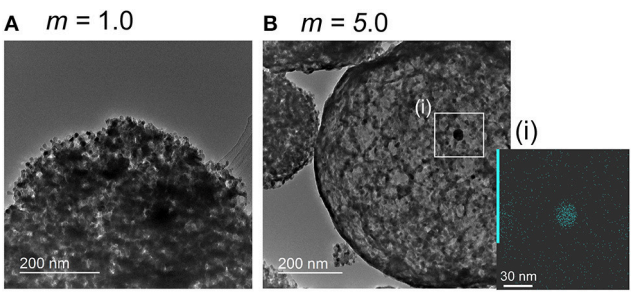

FIGURE 7 | TEM photographs of **(A)** the Au(*1.0*)/pr-In_2O_3(*28*) powder and **(B)** the Au(*5.0*)/pr-In_2O_3(*28*) powder, and [inset in B(i)] an EDX photograph of the Au(*5.0*)/pr-In_2O_3(*28*) powder.

Supplementary Figure 4 shows XRD patterns of the Au(*m*)/pr-In_2O_3(*28*) powders (*m*: 1.0, 5.0). The both powders were assigned to cubic In_2O_3, and a small amount of Au was detected in the Au(*5.0*)/pr-In_2O_3(*28*) powder. **Supplementary Figure 5** shows XPS spectra of In3d and Au4f of the pr-In_2O_3(*28*) and the Au(*m*)/pr-In_2O_3(*28*) powders (*m*: 1.0, 5.0). Two peaks

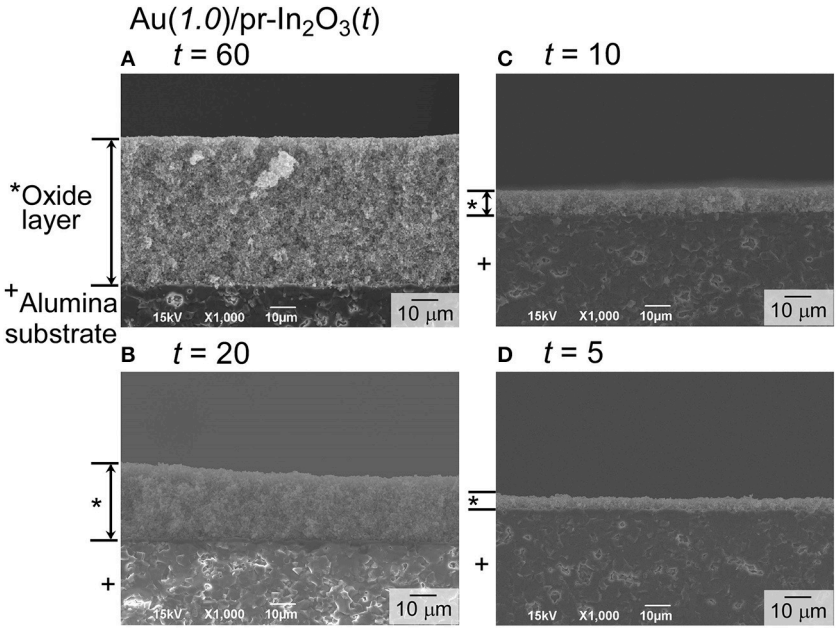

FIGURE 8 | Cross-sectional views of the sensing layers of the Au(*1.0*)/pr-In_2O_3(*70*)-*t* sensors [*t*: **(A)** 60, **(B)** 20, **(C)** 10, and **(D)** 5 (μm)]. The weight ratio between the Au(*1.0*)/pr-In_2O_3(*28*) powder and α-terpineol was 1:2 (*t*: 20 and 60), 1:5 (*t*: 10), 1:10 (*t*: 5). The paste for the Au(*1.0*)/pr-In_2O_3(*70*)-*60* sensor was laminated three times to obtain the thickest sensing layer.

corresponding to $In3d_{5/2}$ (e.g., ca. 444.7, 444.7, and 444.8 eV for the pr-In_2O_3(*28*), the Au(*1.0*)/pr-In_2O_3(*28*), and the Au(*5.0*)/pr-In_2O_3(*28*), respectively) and $In3d_{3/2}$ (e.g., ca. 452.2, 452.2, and 452.3 eV for the pr-In_2O_3(*28*), the Au(*1.0*)/pr-In_2O_3(*28*), and the Au(*5.0*)/pr-In_2O_3(*28*), respectively) were observed, and all the In3d peaks indicate the chemical state of In^{3+} (Atashbar et al., 1999; Wu et al., 2003). In addition, two peaks corresponding to $Au4f_{7/2}$ [e.g., ca. 83.9 eV for the Au(*1.0*)/pr-In_2O_3(*28*) and the Au(*5.0*)/pr-In_2O_3(*28*)] and $Au4f_{5/2}$ [e.g., ca. 87.6 eV for the Au(*1.0*)/pr-In_2O_3(*28*), and the Au(*5.0*)/pr-In_2O_3(*28*)] showed the chemical state of Au loaded on the pr-In_2O_3 was metal (Seah et al., 1998; Liu et al., 2012). **Supplementary figure 6** shows SEM photographs and pore-size distributions of the Au(*m*)/pr-In_2O_3(*28*) powders (*m*: 1.0, 5.0). Well-developed spherical pores were observed on the surface of the both powders. The mode diameter in pore-size distribution calculated from the N_2 desorption isotherm of the Au(*5.0*)/pr-In_2O_3(*28*) powders was ca. 18 nm, which was smaller than those of the Au(*1.0*)/pr-In_2O_3(*28*) powders (ca. 22 nm) and the Au(*0.5*)/p-In_2O_3(*28*) powders (ca. 22 nm, **Table 1**). In addition, the SSA of the Au(*5.0*)/p-In_2O_3(*28*) powders (33.1 m^2/g) was smaller than that of the Au(*1.0*)/p-In_2O_3(*28*) powders (36.9 m^2/g). Considering the SSA values of all the Au(*m*)/p-In_2O_3(*28*) powders and the magnitude of NO_2 responses of all the Au(*m*)/p-In_2O_3(*28*) sensors, the increase in the SSA was obviously effective in enhancing the NO_2 responses. **Figure 7** shows TEM images of the Au(*m*)/pr-In_2O_3(*28*) powders (*m*: 1.0, 5.0), together with an EDX image of Au in the Au(*5.0*)/pr-In_2O_3(*28*) powders. The TEM photographs showed that the Au loaded was highly dispersed in both the Au(*m*)/pr-In_2O_3(*28*) particles, while a quite large Au agglomerate with a diameter of ca. 22 nm was also observed in a Au(*5.0*)/pr-In_2O_3(*28*) particle(particle **(Figure 7Bi)**). This result suggests the 5 wt% loading of Au exceeds the limit for the well-dispersion of Au on the pr-In_2O_3 surface. In addition, the resistance of the Au(*1.0*)/pr-In_2O_3(*28*)-*20* sensor in air was much smaller than that of the pr-In_2O_3(*28*)-*20* sensor, while the resistance of the Au(*5.0*)/pr-In_2O_3(*28*)-*20* sensor in air was comparable with that of the pr-In_2O_3(*28*)-*20* sensor (**Figure 6**). Subramanian et al., revealed the size of Au nanoparticles largely affects the flat band potential of Au/TiO_2. They reported that the loading of 3-nm-diameter Au nanoparticles on TiO_2 induced a greater negative shift in flat band potential than that of 8-nm-diameter Au nanoparticles. Therefore, the size of the Au nanoparticles possibly affects the number of free electrons and thus decrease the resistance of the Au(*m*)/pr-In_2O_3(*28*)-*20* sensors in air. The lower resistance of the Au(*1.0*)/pr-In_2O_3(*28*) sensor in air is one of advantages to detect the oxidizing gases such as NO_2, because the resistance increases by the negatively adsorption of NO_2. Furthermore, the response of semiconductor-type gas sensors arises from the resistance change at the bottom part of the sensing layer between interdigitated Pt electrodes. Therefore, the NO_2 adsorption on the oxide surface at the upper part of the sensing layer decreases the effective concentration of NO_2 at the bottom part of the sensing layer at the initial process of the NO_2 response, and thus it brings a large delay to reach the maximum concentration (e.g., ca. 0.25 ppm in **Figure 6**) of NO_2. Especially, the Au(*5.0*)/pr-In_2O_3(*28*)-*20* sensor didn't reach to the steady-state value during the NO_2 exposure in this study, while the Au(*1.0*)/pr-In_2O_3(*28*)-*20* sensor reached to the almost constant value. This results showed the larger adsorption amount

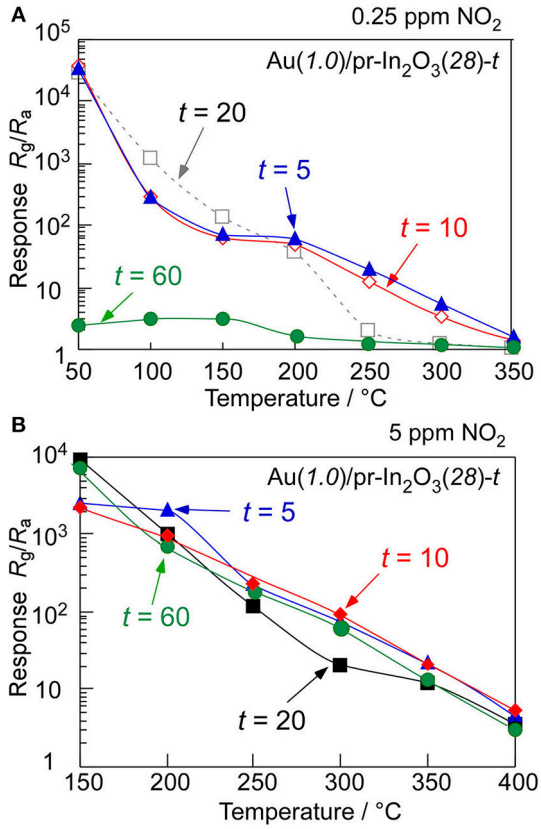

FIGURE 9 | Variations in response of the Au(*1.0*)/pr-In_2O_3(*28*)-*t* sensors to **(A)** 0.25 and **(B)** 5 ppm NO_2 in dry air with operating temperature.

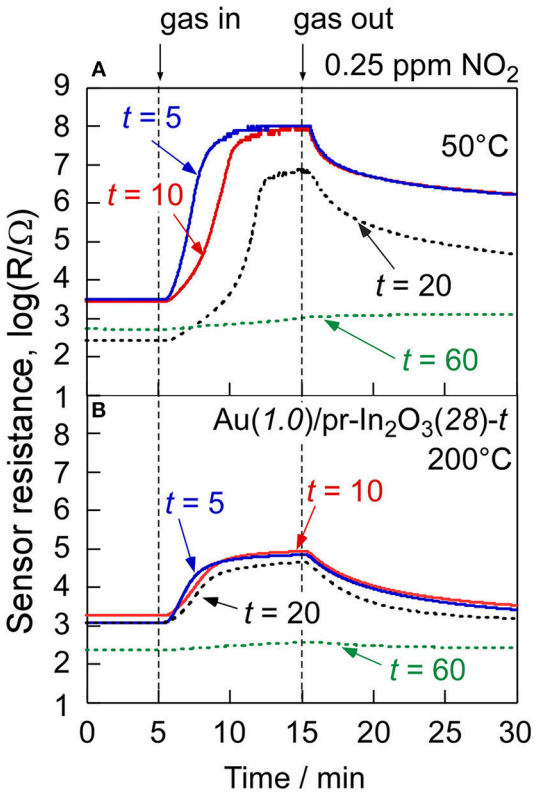

FIGURE 10 | Response transients of the Au(*1.0*)/pr-In_2O_3(*28*)-*t* sensors to 0.25 ppm NO_2 at **(A)** 50 and **(B)** 200°C in dry air.

of NO_2 on the surface of the sensing layer of the Au(*5.0*)/pr-In_2O_3(*28*)-*20* sensor than that of the Au(*1.0*)/pr-In_2O_3(*28*)-*20* sensor, leading to a decrease in the NO_2 response. As a result, these facts suggest that the *1.0* wt% of Au loading on the pr-In_2O_3 was the most effective in increasing the amount of NO_2 adsorbed on the bottom part of the sensing layer among the sensors. In addition, the response speed of the Au(*0.5*)/pr-In_2O_3(*70*)-*20* sensor was much slower than that of the Au(*0.5*)/pr-In_2O_3(*28*)-*20* sensor at 30°C, probably due to facile gas diffusion of the Au(*0.5*)/pr-In_2O_3(*28*)-*20* sensor. Introducing the pores using the PMMA microspheres as a template improves gas diffusion from the surface part to the bottom part of the sensing layer. In addition, the sensing layer of the Au(*0.5*)/pr-In_2O_3(*28*)-*20* sensor contains larger number of pores than that of the Au(*0.5*)/pr-In_2O_3(*70*)-*20* sensor. This is because the PMMA microspheres were polymerized by using the same weight of MMA, and thus the concentration of PMMA microspheres (ps: 28 nm) in the precursor solution of ultrasonic spray pyrolysis was higher than that of the ones (ps: 70 nm). Therefore, the gases rapidly diffused to the whole sensing layer of the Au(*0.5*)/pr-In_2O_3(*28*)-*20* sensor, leading to the faster response speed.

On the other hand, the NO_2 response of the pr-In_2O_3(*70*)-*20* sensor was largely decreased by the small loading amount of Au at the higher temperatures (≥300°C) (**Figure 2**). Generally, the given amount of NO_2 partially converts to NO, especially at more than 200°C, and the ratio of conversion increased with an increase in the temperature (Miura et al., 2007; Kim et al., 2010). Therefore, the loading of Au onto the In_2O_3 surface increased the decomposition efficiency from NO_2 to NO, leading to a reduction of the effective concentration of NO_2 at the bottom part of the sensing layer and a decrease in the NO_2 response of the sensor.

NO_2 Sensing Properties of Au(*1.0*)/pr-In_2O_3(*28*)-*t* Sensors

In order to understand effects of the Au loading, the NO_2-sensing properties of the Au(*1.0*)/pr-In_2O_3(*28*)-*t* sensors (*t*: 5, 10, 60) were also examined. **Figure 8** shows cross-sectional SEM photographs of the sensing layers of the Au(*1.0*)/pr-In_2O_3(*28*)-*t* (*t*: 5, 10, 20, 60) sensors, together with their thickness. **Figure 9** shows variations in response of these sensors to 0.25 and 5 ppm NO_2 in dry air with operating temperature, together with that of the Au(*1.0*)/pr-In_2O_3(*28*)-*20* sensor. **Figure 10** shows response transients of all these sensors to 0.25 ppm NO_2 in dry air at 50 and 200°C. The response of all the sensors to NO_2 increased with a decrease in the operating temperature, whereas only the Au(*1.0*)/pr-In_2O_3(*28*)-*60* sensor showed much smaller response only to 0.25 ppm NO_2 than others. The response speed of these sensors to NO_2 increased with a decrease in the thickness of the Au(*1.0*)/pr-In_2O_3(*28*)-*t* sensors, especially at 50°C. Among them, note that the response speed of the Au(*1.0*)/pr-In_2O_3(*28*)-*5* sensor was faster than that of the Au(*1.0*)/pr-In_2O_3(*28*)-*10*

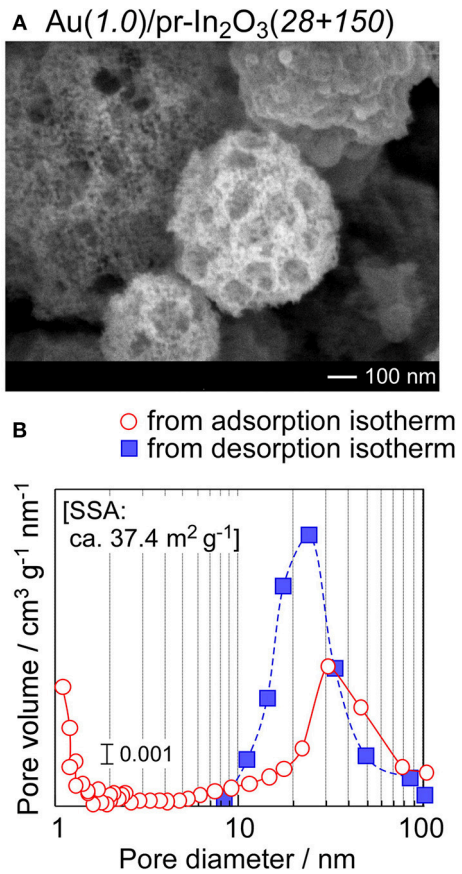

FIGURE 11 | (A) SEM photograph and **(B)** pore-size distribution of the Au(*1.0*)/pr-In_2O_3(*28 + 150*) powder with its specific surface area (SSA).

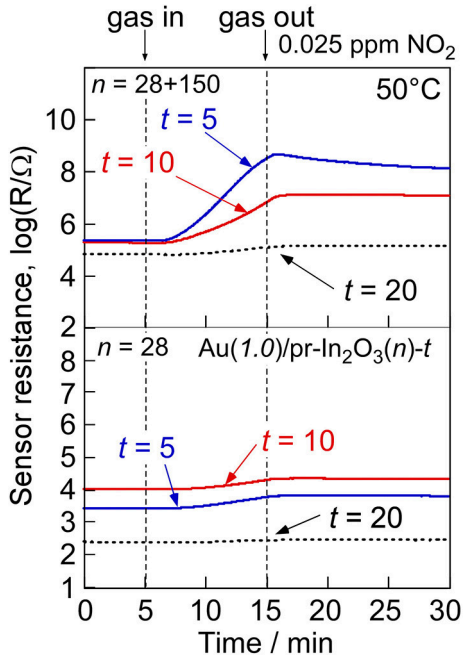

FIGURE 12 | Response transients of the Au(*1.0*)/pr-In_2O_3(*28+150*)-*20* and Au(*1.0*)/pr-In_2O_3(*28*)-*20* sensors to 0.025 ppm NO_2 at 50°C in dry air.

sensor, even though the magnitude of NO_2 response and the recovery speed of the both sensors were quite comparable to each other. This trend is understandable by a decrease in the NO_2 diffusion time from the surface part to the bottom part of the sensing layer between interdigitated Pt electrodes. In addition, the smaller NO_2 diffusion may bring the smaller NO_2 response, especially for the detection of lower concentration of NO_2, because the effective concentration of NO_2 at the bottom part of the sensing layer won't change for a long time by the adsorption of NO_2 on the surface of the Au(*1.0*)/pr-In_2O_3(*28*) during gas diffusion. The sensing properties to lower concentration of NO_2 at 50°C were examined in the next section.

In addition, the Au(*1.0*)/pr-In_2O_3(28)-*t* (*t*: 5, 10) sensors showed larger response to 0.25 ppm NO_2 than that of the Au(*1.0*)/pr-In_2O_3(*28*)-*20* sensor at high temperatures more than 200°C. Furthermore, the response and recovery speeds as well as the magnitude of NO_2 response of the Au(*1.0*)/pr-In_2O_3(*28*)-*5* sensor were also comparable to those of the Au(*1.0*)/pr-In_2O_3(*28*)-*10* sensor at 200°C, because the gas-diffusion rate at 200°C was much higher than that at 50°C and thus the effects of thickness of the sensing layers on the NO_2-sensing properties were decreased. On the other hand, the decrease in the response to a low concentration of NO_2 (0.25 ppm) with an increase in the thickness of the sensing layers at more than 200°C is probably due to the decomposition of NO_2 in the sensing layer and thus the decrease in the effective concentration of NO_2 at the bottom part of the sensing layer. Since the increase in the thickness of the sensing layer increased the decomposition efficiency from NO_2 to NO to reduce the effective concentration of NO_2 at the bottom part of the sensing layer at more than 200°C, the NO_2 response of the Au(*1.0*)/pr-In_2O_3(*28*)-*t* sensors decreased with an increase in the thickness of the sensing layer in the temperature range. However, the catalytic activity of the decomposition of NO_2 to NO over the oxide surface in air is not so high. Therefore, a decrease in the effective concentration of NO_2 at higher concentration (5 ppm) on the basis of the catalytic decomposition of NO_2 to NO is not significant to a decrease in the NO_2 response, compared to that at lower concentration (0.25 ppm) as shown in **Figure 9**.

NO_2 Sensing Properties of Au(*1.0*)/pr-In_2O_3(*28+150*)-*t* Sensors

Easy gas diffusion of NO_2 from the oxide surface to the bottom part of the sensing layer enhances the NO_2 response and the response speed at low operating temperatures. Thus, the introduction of much larger pores has been attempted into the Au(*1.0*)/pr-In_2O_3(*28*) powder. Commercial PMMA microspheres with a diameter of ca. 150 nm (Soken Chem. & Eng. Co. Ltd., MP-1451) were mixed into the precursor solution containing homemade PMMA microspheres with a diameter of ca. 28 nm, and then *1.0* wt% Au-loaded pr-In_2O_3 powder with two kinds of spherical pores (Au(*1.0*)/pr-In_2O_3(*28+150*) powders) were prepared by ultrasonic spray

pyrolysis. **Figure 11** shows an SEM photograph and pore-size distribution of the Au(*1.0*)/pr-In_2O_3(*28+150*) powder with its SSA. The SEM photograph shows that both macropores (80–100 nm in diameter) and mesopores (20–30 nm in diameter) are well developed in the Au(*1.0*)/pr-In_2O_3(*28+150*) powder. The existence of the macropores was also confirmed in the pore-size distribution calculated from N_2 adsorption isotherm in a diameter range of 80–100 nm. These results strongly support that the macropores were based on the commercial large PMMA microspheres. On the other hand, the introduction of macropores has little effect on SSA. **Figure 12** shows response transients of the Au(*1.0*)/pr-In_2O_3(*28*)-*t* and Au(*1.0*)/pr-In_2O_3(*28+150*)-*t* sensors (*t*: 5, 10, 20) to 0.025 ppm NO_2 in dry air at 50°C. The resistance of all the sensors gradually increased upon exposure to the very low concentration of NO_2, and the Au(*1.0*)/pr-In_2O_3(*28+150*)-*t* sensors showed larger NO_2 response than those of the Au(*1.0*)/pr-In_2O_3(*28*)-*t* sensors. In addition, a decrease in the thickness of the Au(*1.0*)/pr-In_2O_3(*28+150*)-*t* sensors increased the NO_2 response. Among them, the Au(*1.0*)/pr-In_2O_3(*28+150*)-*5* sensor showed the largest NO_2 response. This is because the introduction of the well-developed macropores improves the gas diffusion from the surface to the bottom part of the sensing layer and increases the effective concentration of NO_2 at the bottom part of the sensing layer. Therefore, it was confirmed that the smaller NO_2 diffusion brings the smaller NO_2 response due to the adsorption of NO_2 during gas diffusion, especially for the detection of the lower concentration of NO_2.

CONCLUSION

The NO_2 sensing properties of the pr-In_2O_3 sensors loaded with and without noble metal (Au, Pd, or Pt) were examined, and factors for enhancing the NO_2 sensing properties were discussed. The Au(*0.5*)/pr-In_2O_3(*70*)-*20* sensor showed larger NO_2 response at lower temperatures ($\leq$200°C) than the pr-In_2O_3(*70*)-*20* sensor, while the Pd or Pt loading were hardly effective for improving the NO_2 response. The NO_2 response of the pr-In_2O_3(*n*)-*20* sensors increased with a decrease in the operating temperature at 200–350°C, but their NO_2 response decreased with a decrease in operating temperature at <200°C. However, the NO_2 response of the Au(*0.5*)/pr-In_2O_3(*n*)-*20* sensors increased with a decrease in operating temperature, and the Au(*0.5*)/pr-In_2O_3(*28*)-*20* sensor showed the much larger NO_2 response than that of the Au(*0.5*)/pr-In_2O_3(*70*)-*20* sensor at <150°C. Therefore, we concluded the highly dispersed Au nanoparticles enhance the amount of negatively charged NO_2 adsorbed on the oxide surface.

The Au(*1.0*)/pr-In_2O_3(*28*)-*20* sensor showed the highest NO_2 response among the Au(*m*)/pr-In_2O_3(*28*)-*20* sensors. The magnitude of response to 0.25 ppm NO_2 of the Au(*1.0*)/pr-In_2O_3(*28*)-*60* sensor was smallest and the response speed of the Au(*1.0*)/pr-In_2O_3(*28*)-*5* sensor was fastest among the Au(*1.0*)/pr-In_2O_3(*28*)-*t* sensors at 50°C. In addition, the Au(*1.0*)/pr-In_2O_3(*28+150*)-*t* sensors showed larger NO_2 response than those of the Au(*1.0*)/pr-In_2O_3(*28*)-*t* sensors. A decrease in the thickness of the Au(*1.0*)/pr-In_2O_3(*28+150*)-*t* sensors increased the NO_2 response. Among them, the Au(*1.0*)/pr-In_2O_3(*28+150*)-*5* sensor showed the largest NO_2 response. It was suggested that the introduction of the well-developed macropores improves the gas diffusion from the surface to the bottom part of the sensing layer. And thus, the effective concentration of NO_2 at the bottom part of the sensing layer increased, leading to the large NO_2 response.

AUTHOR CONTRIBUTIONS

TU, KK, TH, and YS: manuscript writing and results interpretation; KI: experiments.

SUPPLEMENTARY MATERIAL

The Supplementary Material for this article can be found online at: https://www.frontiersin.org/articles/10.3389/fmats.2019.00081/full#supplementary-material

REFERENCES

Atashbar, M., Gong, B., Sun, H. T., Wlodarski, W., and Lamb, R. (1999). Investigation on ozone-sensitive In_2O_3 thin films. *Thin Solid Films* 354, 222–226. doi: 10.1016/S0040-6090(99)00405-8

Chen, D., Ge, L., Yin, L., Shi, H., Yang, D., Yang, J., et al. (2014). Solvent-regulated solvothermal synthesis and morphology-dependent gas-sensing performance of low-dimensional tungsten oxide nanocrystals. *Sens. Actuators B* 205, 391–400. doi: 10.1016/j.snb.2014.09.007

Choi, S.-W., Jung, S.-H., and Kim, S. S. (2011). Significant enhancement of the NO_2 sensing capability in networked SnO_2 nanowires by Au nanoparticles synthesized via γ-ray radiolysis. *J. Hazard. Mater.* 193, 243–248. doi: 10.1016/j.jhazmat.2011.07.053

Degler, D., Carvalho, H. W. P., Kvashnina, K., Grunwaldt, J.-D., Weimar, U., and Barsan, N. (2016b). Structure and chemistry of surface-doped Pt:SnO_2 gas sensing materials. *RSC Adv.* 6, 28149–28155. doi: 10.1039/C5RA26302F

Degler, D., Rank, S., Müller, S., Carvalho, H. W., Grunwaldt, J.-D., Weimar, U., et al. (2016a). Gold-loaded tin dioxide gas sensing materials: mechanistic insights and the role of gold dispersion. *ACS Sens.* 1, 1322–1329. doi: 10.1021/acssensors.6b00477

Firooz, A. A., Hyodo, T., Mahjoub, A. R., Khodadadi, A. A., and Shimizu, Y. (2010). Synthesis and gas-sensing properties of nano- and meso-porous MoO_3-doped SnO_2. *Sens. Actuators B* 147, 554–560. doi: 10.1016/j.snb.2010.03.021

Guo, W. (2016). Design of gas sensor based on Fe-doped ZnO nanosheet-spheres for low concentration of formaldehyde detection. *J. Electrochem. Soc.* 163, B517–B525. doi: 10.1149/2.1261609jes

Hashimoto, M., Inoue, H., Hyodo, T., Shimizu, Y., and Egashira, M. (2008). Preparation and gas sensor application of ceramic particles with submicron-size spherical macropores. *Sens. Lett.* 6, 887–890. doi: 10.1166/sl.2008.524

Hieda, K., Hyodo, T., Shimizu, Y., and Egashira, M. (2008). Preparation of porous tin dioxide powder by ultrasonic spray pyrolysis and their application to sensor materials. *Sens. Actuators B* 133, 144–150. doi: 10.1016/j.snb.2008.02.002

Hyodo, T., Abe, S., Shimizu, Y., and Egashira, M. (2003). Gas-sensing properties of ordered mesoporous SnO_2 and effects of coatings thereof. *Sens. Actuators B* 93, 590–600. doi: 10.1016/S0925-4005(03)00208-9

Hyodo, T., Fujii, E., Ishida, K., Ueda, T., and Shimizu, Y. (2017). Microstructural control of porous In_2O_3 powders prepared by ultrasonic-spray pyrolysis

employing self-synthesized polymethylmethacrylate microspheres as a template and their NO_2-sensing properties. *Sens. Actuators B* 244, 992–1003. doi: 10.1016/j.snb.2017.01.091

Hyodo, T., Furuno, S., Fujii, E., Matsuo, K., Motokucho, S., Kojio, K., et al. (2013). Porous In_2O_3 powders prepared by ultrasonic-spray pyrolysis as a NO_2-sensing material: Utilization of polymethylmethacrylate microspheres synthesized by ultrasonic-assisted emulsion polymerization as a template. *Sens. Actuators B* 187, 495–502. doi: 10.1016/j.snb.2013.02.090

Hyodo, T., Inoue, H., Motomura, H., Matsuo, K., Hashishin, T., Tamaki, J., et al. (2010). NO_2 sensing properties of macroporous In_2O_3-based powders fabricated by utilizing ultrasonic spray pyrolysis employing polymethylmethacrylate microspheres as a template. *Sens. Actuators B* 151, 265–273. doi: 10.1016/j.snb.2010.09.002

Hyodo, T., Nishida, N., Shimizu, Y., and Egashira, M. (2001). Preparation of thermally stable mesoporous tin dioxide powders with high specific surface area by utilizing self-assembly of surfactants. *J. Ceram. Soc. Jpn*. 109, 481–483. doi: 10.2109/jcersj.109.1270_481

Hyodo, T., Nishida, N., Shimizu, Y., and Egashira, M. (2002). Preparation and gas-sensing properties of thermally stable mesoporous SnO_2. *Sens. Actuators B* 83, 209–215. doi: 10.1016/S0925-4005(01)01042-5

Hyodo, T., Sasahara, K., Shimizu, Y., and Egashira, M. (2005). Preparation of macroporous SnO_2 films using PMMA microspheres and their sensing properties to NOx and H_2. *Sens. Actuators B* 106, 580–590. doi: 10.1016/j.snb.2004.07.024

Kim, C. H., Qi, G., Dahlberg, K., and Li, W. (2010). Strontium-doped perovskites rival platinum catalysts for treating NOx in simulated diesel exhaust. *Science* 327, 1624–1627. doi: 10.1126/science.1184087

Kim, D.-H., Jung, J.-W., Choi, S.-J., Jang, J.-S., Koo, W.-T., and Kim, I.-D. (2018a). Pt nanoparticles functionalized tungsten oxynitride hybrid chemiresistor: low-temperature NO_2 sensing. *Sens. Actuators B* 273, 1269–1277. doi: 10.1016/j.snb.2018.07.002

Kim, D.-H., Kim, T.-H., Sohn, W., Suh, J.-M., Shim, Y.-S., Kwon, K.-C., et al. (2018b). Au decoration of vertical hematite nanotube arrays for further selective detection of acetone in exhaled breath. *Sens. Actuators B* 274, 587–594. doi: 10.1016/j.snb.2018.07.159

Liu, X., Liu, M.-H., Luo, Y.-C., Mou, C.-Y., Lin, S. D., Cheng, H., et al. (2012). Strong metal–support interactions between gold nanoparticles and ZnO nanorods in CO oxidation. *J. Am. Chem. Soc.* 134, 10251–10258. doi: 10.1021/ja3033235

Miura, N., Wang, J., Elumalai, P., Ueda, T., Terada, D., and Hasei, M. (2007). Improving NO_2 sensitivity by adding WO_3 during processing of NiO sensing-electrode of mixed-potential-type zirconia-based sensor. *J. Electrochem. Soc.* 154, J246–J252. doi: 10.1149/1.2747532

Mun, Y., Park, S., An, S., Lee, C., and Kim, H. W. (2013). NO_2 gas sensing properties of Au-functionalized porous ZnO nanosheets enhanced by UV irradiation. *Ceram. Int*. 39, 8615–8622. doi: 10.1016/j.ceramint.2013.04.035

Ogel, E., Meller, S. A., Sackmann, A., Gyger, F., Bockstaller, P., Brose, E., et al. (2017). Comparison ofthe catalytic performance and carbon monoxide sensing behavior of Pd-SnO_2 Core@Shell nanocomposites. *ChemCatChem* 9, 407–413. doi: 10.1002/cctc.201601132

Roso, S., Degler, D., Llobet, E., Barsan, N., and Urakawa, A. (2017). Temperature-dependent NO_2 sensing mechanisms over indium oxide. *ACS Sens*. 2, 1272–1277. doi: 10.1021/acssensors.7b00504

Seah, M. P., Gilmore, I. S., and Beamson, G. (1998). XPS: Binding energy calibration of electron spectrometers 5–Re-evaluation of the reference energies. *Surf. Interface Anal.* 26, 642–649. doi: 10.1002/(SICI)1096-9918(199808)26:9<642::AID-SIA408>3.0.CO;2-3

Shim, Y.-S., Moon, H. G., Kim, D. H., Zhang, L., Yoon, S.-J., Yoon, Y. S., et al. (2013). Au-decorated WO_3 cross-linked nanodomes for ultrahigh sensitive and selective sensing of NO_2 and C_2H_5OH. *RSC Adv.* 3, 10452–10459. doi: 10.1039/c3ra41331d

Sun, P., Zhou, X., Wang, C., Wang, B., Xu, X., and Lu, G. (2014). One-step synthesis and gas sensing properties of hierarchical Cd-doped SnO_2 nanostructures. *Sens. Actuators B* 190, 32–39. doi: 10.1016/j.snb.2013.08.045

Takacs, M., Ducso, C., and Pap, A. E. (2015). Fine-tuning of gas sensitivity by modification of nano-crystalline WO_3 layer morphology. *Sens. Actuators B* 221, 281–289. doi: 10.1016/j.snb.2015.06.081

Tang, L., Tian, Y., Liu, Y., Wang, Z., and Zhou, B. (2013). One-step solution synthesis of urchin-like ZnO superstructures from ZnO rods. *Ceram. Int*. 39, 2303–2308. doi: 10.1016/j.ceramint.2012.08.077

Wang, C., Li, X., Feng, C., Sun, Y., and Lu, G. (2015). Nanosheets assembled hierarchical flower-like WO_3 nanostructures: synthesis, characterization, and their gas sensing properties. *Sens. Actuators B* 210, 75–81. doi: 10.1016/j.snb.2014.12.020

Wang, C., Sun, R., Li, X., Sun, Y., Sun, P., Liu, F., et al. (2014). Hierarchical flower-like WO_3 nanostructures and their gas sensing properties. *Sens. Actuators B* 204, 224–230. doi: 10.1016/j.snb.2014.07.083

Wei, S., Wang, S., Zhang, Y., and Zhou, M. (2014). Different morphologies of ZnO and their ethanol sensing property. *Sens. Actuators B* 192, 480–487. doi: 10.1016/j.snb.2013.11.034

Wu, X. C., Hong, J. M., Han, Z. J., and Tao, Y. R. (2003). Fabrication and photoluminescence characteristics of single crystalline In_2O_3 nanowires. *Chem. Phys. Lett*. 373, 28–32. doi: 10.1016/S0009-2614(03)00582-7

Yamazoe, N., Sakai, G., and Shimanoe, K. (2003). Oxide semiconductor gas sensors. *Catal. Surv. Asia* 7, 63–75. doi: 10.1023/A:1023436725457

Conflict of Interest Statement: The authors declare that the research was conducted in the absence of any commercial or financial relationships that could be construed as a potential conflict of interest.

frontiers in Materials

ORIGINAL RESEARCH
published: 30 April 2019
doi: 10.3389/fmats.2019.00070

Improving Hydrogen Sensing Performance of TiO_2 Nanotube Arrays by ZnO Modification

*Aihua Yu, Haitao Xun and Jianxin Yi**

State Key Laboratory of Fire Science, Department of Safety Science and Engineering, University of Science and Technology of China, Hefei, China

In this work, anodization was utilized to synthesize highly ordered TiO_2 nanotube arrays, and ZnO was successfully decorated onto the surface of as-prepared TiO_2 nanotubes *via* a facile impregnation method. The gas sensing performance of a TiO_2@ZnO composite was systematically studied. At a working temperature of 300°C, the response of TiO_2@ZnO to 100 ppm H_2 was ~340, 2.7 times larger than that of pristine TiO_2. A power–law relationship between the response and H_2 concentration was observed. In addition, the response time was significantly reduced by four times, and improved selectivity to H_2 was achieved. The highly improved sensing performance of TiO_2 nanotubes by ZnO decoration may be attributed to the enhanced oxygen adsorption and formation of n-n heterojunctions.

Keywords: hydrogen sensor, semiconductor, TiO_2 nanotubes, heterojunction, anodic oxidation

OPEN ACCESS

Edited by:
Xiaogan Li,
Dalian University of Technology (DUT), China

Reviewed by:
Han Jin,
Ningbo University, China
Alexander Gaskov,
Lomonosov Moscow State University, Russia

****Correspondence:***
Jianxin Yi
yjx@ustc.edu.cn

Specialty section:
This article was submitted to Functional Ceramics, a section of the journal Frontiers in Materials

Received: *28 January 2019*
Accepted: *01 April 2019*
Published: *30 April 2019*

Citation:
Yu A, Xun H and Yi J (2019) Improving Hydrogen Sensing Performance of TiO_2 Nanotube Arrays by ZnO Modification. Front. Mater. 6:70. doi: 10.3389/fmats.2019.00070

INTRODUCTION

Hydrogen is widely used as an important energy carrier and chemical material. Rapid and accurate detection of hydrogen is highly important due to its risky properties such as low minimum ignition energy (0.017 mJ) and high heat of combustion (142 kJ/g H_2) (Silva et al., 2012). Among the various types of hydrogen sensing technology (Hübert et al., 2011), the resistance-based semiconductor gas sensor has attracted considerable attention due to its high sensitivity, short response time, and long-term stability. On the one hand, using various nanostructures of large surface area, such as nanofibers, nanowires, and nanotubes, has been well demonstrated to favor high gas sensing performance (Li et al., 2015a; Zhang et al., 2016; Chen and Yi, 2018). On the other hand, modification of the materials' surface with noble metals and/or oxides is another simple method to improve the gas sensor performance (Miller et al., 2014).

Among various n-type semiconductors, TiO_2 has been widely studied for gas sensing (Zhao et al., 2015; Wang et al., 2017). A TiO_2 ordered nanotube was proved to have exceptionally high response to hydrogen owing to its unique hierarchical morphology (Varghese et al., 2003). Further improvement of its gas sensing performance was mainly achieved through (1) optimizing the microstructural parameters of the nanotubes such as pore diameter and tube length (Mor et al., 2006) and (2) decorating the surface with noble metals such as Pt and Pd as a catalyst (Joo et al., 2010; Şennik et al., 2010; Xiong et al., 2016). Recently, it was found that by decorating the TiO_2

ordered nanotubes with nanoparticles of non-noble metal, i.e., SnO_2, both the sensitivity and response/recovery speed can be significantly enhanced (Xun et al., 2018), which was ascribed to formation of heterojunctions. Similar heterojunction formation and its promoting effect may also occur when other gas sensing semiconductor oxides are employed as a modifier for TiO_2, which is yet to be studied.

This work synthesized highly aligned TiO_2 nanotubes by anodic oxidation and decorated the nanotubes with ZnO nanoparticles *via* an immersion–calcination method. The sensing performance of the nanotubes was systemically studied, and possible sensing mechanism was discussed.

EXPERIMENTAL SECTION

Synthesis

Chemical reagents were purchased from Sinopharm Chemical Reagent Co., Ltd, China. Ti foils were purchased from Tianjin Ida. Pretreatment of high-purity titanium foils (25-mm thickness, 10 × 20 mm) including cleaning and chemical polishing is similar to that of previous research. The anodization process of the Ti foil was conducted in a two-electrode configuration connected to the DC power supply (Querli, Shanghai) with a voltage of 30 V for 3 h, using electrolyte of ethylene glycol containing 0.3 wt% NF_4F and 5 vol% DI water. The anodized titanium foil was cleaned with ethylene glycol and deionized water in sequence before it was annealed in ambient air at 450°C for 3 h to induce crystallization. For the preparation of TiO_2@ZnO, 0.0652 g of zinc acetate [$Zn(CH_3COO)_2{\cdot}2H_2O$] was dissolved in 20 mL of ethanol as precursor. TiO_2 nanotubes were immersed into the solution for 12 h before they were calcined at 450°C. Two similar samples were prepared for either composition, denoted as TiO_2 and TiO_2-2 for pristine TiO_2 and as TiO_2@ZnO and TiO_2@ZnO-2 for TiO_2@ZnO.

Sensor Test

The typical gas sensor fabrication process and measurement setup parameters can be found in other work (Xun et al., 2018). In brief, the sensor was attached to two electrodes using conductive paste (DAD-87, Shanghai Research Institute of Synthetic Resins) and placed in a testing apparatus with a ceramic heating plate. The temperature and gas-flow rate were controlled by a DC power supply and mass flow controller (CS200, Sevenstar Electronics, Beijing), respectively. Resistance variation was recorded by Keithley 6482. Sensor response was defined as $S = R_a/R_g$ (or R_g/R_a in the case of NO_2 as target gas), where R_a and R_g are the resistance of the sensor in air and test gas, respectively. The response (recovery) time was the time that the resistance variation reached 90% of the total value after introduction (removal) of the target gas.

Characterization

Crystal structure was analyzed by powder X-ray diffraction (XRD, TTR III) using Cu Kα radiation. The morphologies and microstructure of the nanotubes were investigated by scanning electron microscopy (FE-SEM, SU8220) equipped with an energy-dispersive spectrometer (EDS) and transmission electron microscopy (TEM, JEM-2011). X-ray photoelectron spectroscopy (XPS) was performed on an ESCLAB 250 spectrometer using Al Kα as an excitation source and C1s binding energy at 284.8 eV as energy reference.

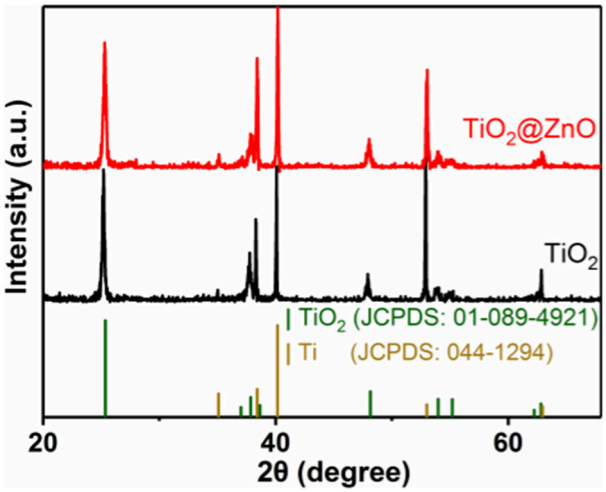

FIGURE 1 | X-ray diffraction (XRD) patterns of pristine TiO_2 and TiO_2@ZnO composites.

RESULTS AND DISCUSSIONS

Material Analysis

Figure 1 shows the XRD patterns of the as-prepared samples. For the pristine TiO_2 sample, all the peaks can be indexed to the anatase structure of titanium dioxide (JCPDS 01-089-4921) and Ti (JCPDS 044-1294). The XRD pattern of the as-synthesized TiO_2@ZnO sample was similar to that of the pristine sample. The diffraction peak of zinc oxide was not observed, which may be due to the low loading amount of zinc oxide.

To illustrate the composition and chemical states of the elements in the samples, XPS studies were carried out, and results were presented in **Figure 2**. Ti and O were present in all the samples, and Zn was detected for the impregnated one (**Figure 2A**). No impurity element other than carbon contamination was observed. As shown in **Figure 2B**, two peaks at a binding energy of ∼458.8 and ∼464.6 eV could be attributed to Ti $2p_{1/2}$ and Ti $2p_{3/2}$, respectively, indicating that the Ti element was present in the form of Ti^{4+}. The binding energy for both Ti $2p_{1/2}$ and Ti $2p_{3/2}$ remained almost invariant after ZnO decoration. **Figure 2C** demonstrates two peaks at a binding energy of ∼1,045.3 and ∼1,022.2 eV, corresponding to Zn $2p_{1/2}$ and Zn $2p_{3/2}$, respectively, implying the +2 oxidation state of Zn in the composite. Besides, the Zn/(Ti + Zn) ratio at the surface of the TiO_2 nanotube was confirmed to be 25.2 at% by XPS analysis. The O 1s peak for both samples can be deconvoluted into two peaks at a binding energy of ∼529.9 and ∼531.4 eV, which corresponded to lattice oxygen (O_{lat}) and absorbed oxygen (O_{abs}), respectively. The $O_{abs}/(O_{abs} + O_{lat})$ ratio of TiO_2@ZnO composites (22.0%) was distinctly larger than that of pristine

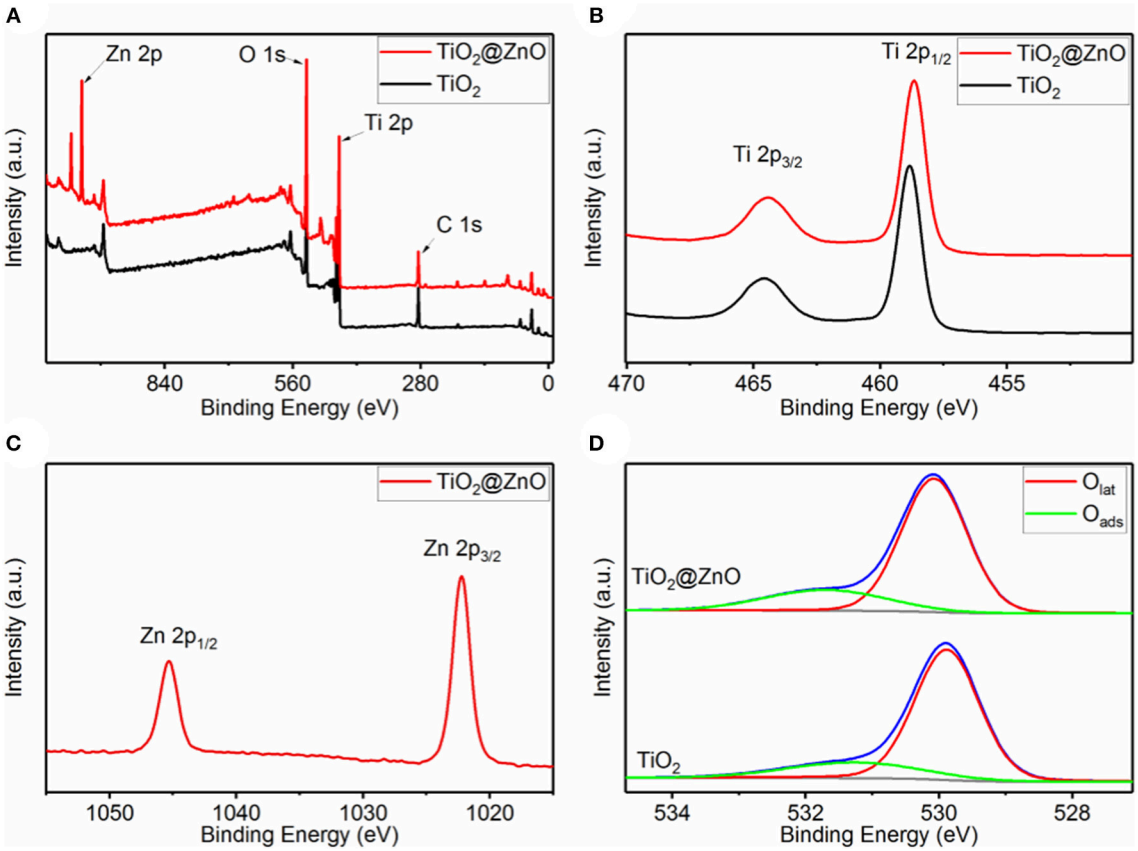

FIGURE 2 | X-ray photoelectron spectroscopy (XPS) spectra of pristine TiO_2 and TiO_2@ZnO nanotubes. **(A)** Survey spectrum, **(B)** Ti 2p, **(C)** Zn 2p, and **(D)** O 1s.

TiO_2 (19.5%), suggesting that ZnO decoration generated more surface adsorption sites.

Figures 3A–D show the SEM micrographs of the as-prepared ordered arrays of pristine TiO_2 and TiO_2@ZnO samples. The pore diameter of the pristine TiO_2 nanotubes is ∼80 nm with a wall thickness of ∼10 nm, and the length is ∼2.4 μm. There was no evident difference between the TiO_2@ZnO sample and the pristine one, indicating that the impregnation treatment did not affect the morphology of the nanotubes. EDS elemental mapping analysis was performed on TiO_2@ZnO as showed in **Figures 3E–G**, which revealed a homogeneous distribution of the Zn elements throughout the surface (**Figure 3G**). It can also be noticed that the Ti signal in the hollow part of the nanotube is more intense than that around the tube wall (**Figure 3F**), which can be ascribed to the unreacted Ti foil at the bottom. EDX analysis confirmed the coexistence of Ti, Zn, and O elements for the composite with a Zn/(Ti + Zn) ratio of 3.5 at%.

More in-depth microstructural analysis was performed on both samples with TEM (**Figure 4**). The pristine TiO_2 nanotubes presented a clear view (**Figure 4A**), while some extra nanoparticles in the size of 5–10 nm were observed with an even distribution throughout the ZnO-decorated nanotubes (**Figure 4B**). Selected area electron diffraction (SAED) revealed some extra diffraction pots in addition to the main diffraction rings of TiO_2 (**Figure 4C**), corresponding to the (100) and (002) planes of ZnO (JCPDS 36-4521). These results indicated that TiO_2 nanotubes modified with ZnO nanoparticles were successfully obtained.

Gas Sensing Properties

ZnO decoration was found to significantly increase the resistance in air of the TiO_2 nanotubes, corresponding to an increase in R_a from ∼40 kΩ to ∼6 MΩ at 300°C. **Figure 5A** compares the response of the sensors to 100 ppm H_2 at different temperatures. The pristine TiO_2 sensor exhibited typical volcano-shape temperature dependence of response. The response at the working temperature of 300°C is 126, which is 3.2 times that of samples with a tube length of 3–4 μm and a diameter of ∼100 nm under the same conditions (Xun et al., 2018). This indicates that the response can be increased by changing the morphology of nanotubes, i.e., reducing the diameter and length. A similar behavior of temperature dependence of response was observed, and the response was improved after the ZnO impregnation. At the optimum temperature of 350°C for both sensors, the response of the TiO_2@ZnO composite to 100 ppm H_2 was ∼520, about 1.8 times higher than that of pristine TiO_2.

Figure 5B shows that response increased with the increase in H_2 concentration for both kinds of sensors. A linear relationship between the response and H_2 concentration on the log–log scale was observed for all samples, which accords with the power–law theory proposed by Yamazoe and Shimanoe (2008). The response of the TiO_2@ZnO composite was higher than that of

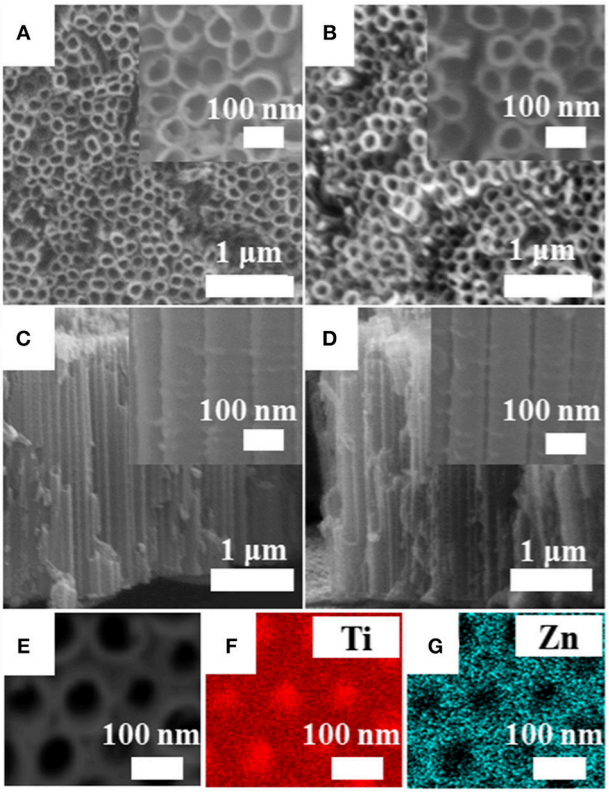

FIGURE 3 | Scanning electron microscopy (SEM) images of **(A,B)** surface and **(C,D)** cross-sectional view of **(A,C)** pristine TiO_2 and **(B,D)** TiO_2@ZnO nanotubes. Energy-dispersive spectrometer (EDS) elemental images of TiO_2@ZnO with **(E)** SEM images, **(F)** Ti, and **(G)** Zn.

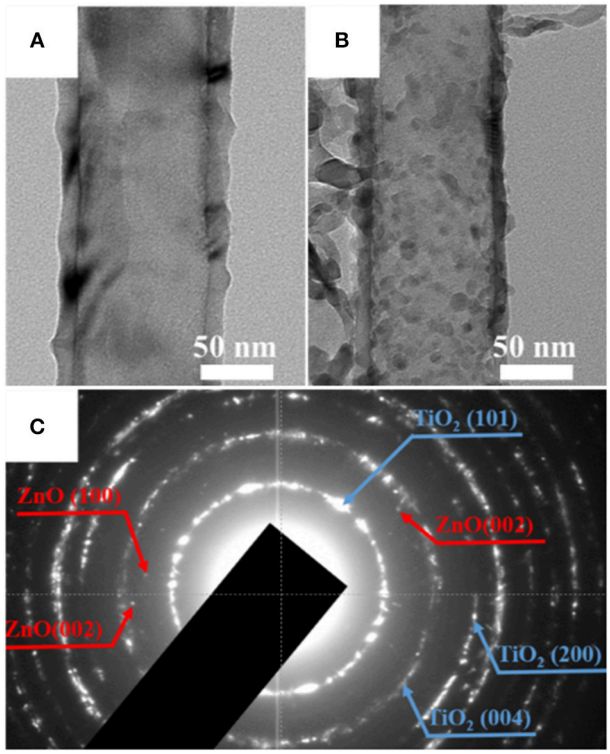

FIGURE 4 | Transmission electron microscopy (TEM) images of **(A)** pristine TiO_2 nanotubes and **(B)** TiO_2@ZnO composites. **(C)** SAED pattern of TiO_2@ZnO.

the pristine one at all tested concentrations, and the enhancement was more pronounced at higher concentrations. Taking $S = 1.2$ as the detection threshold (Liu et al., 2017; Gao et al., 2019), the detection limit calculated for the TiO_2@ZnO composite sensor was 7.5 ppm, which was smaller than that of the pristine TiO_2 sensor (10.3 ppm). It can also be seen that the response of two different TiO_2@ZnO sensors was very close to each other, indicating good consistency of the sensors.

Figure 5C shows that for both pristine TiO_2 and TiO_2@ZnO, the response time decreased as the concentration increased. A much faster response speed was observed for the latter sample. The response time of TiO_2@ZnO is 22 s for 100 ppm H_2 at 300°C, which is 4.2 times faster than that of the pristine sample. A power–law relationship was observed between the response time and the concentration, which may be accounted for by a nonlinear diffusion-reaction model (Xun et al., 2018). In contrast to the fast response speed, the recovery process was sluggish, typically with a recovery time over 2,000 s. Moreover, the recovery became slower while the concentration increased.

To illustrate the selectivity of the sensors, the response to 100-ppm various gases at 300°C was compared (**Figure 5D**). Because hydrogen is highly combustive and explosive, NH_3, C_3H_8, NO_2, CO, and CH_4 were selected to examine the cross-sensitivity, which are very common interfering gases for fire detection. It can be seen that the pristine TiO_2 showed some minor response to NH_3 and insignificant response to the other interfering gases. The response to both H_2 and NH_3 increased while that to other gases remained after ZnO decoration. Nevertheless, the H_2 response increased much more pronouncedly than the NH_3 one. As a result, the selectivity, i.e., the response ratio of H_2 over the most interfering gas, NH_3, increased from 19.6 to 82.3 after ZnO loading. It should be noted that humidity is also a very common interference for semiconductor gas sensors. Although the humidity effect was not tested for the present samples, a significant humidity effect has been observed for other similar gas sensors based on TiO_2 nanotubes in our group's research. Some strategies have been adopted to eliminate the humidity impact, e.g., by using a reference element for compensation (Zhan et al., 2007) or by decorating hydrophobic materials (Yao et al., 2016).

Gas Sensing Mechanism

The relatively high sensitivity of pristine TiO_2 toward H_2 can be attributed to the unique hierarchical morphology of the nanotubes. The small half-tube-wall thickness is comparable to that of the space charge layer, which favors hydrogen adsorption and its reaction with surface oxygen (Paulose et al., 2005; Hazra et al., 2015). The improved H_2 response of TiO_2@ZnO may be a result of the synergistic contribution from two effects. Firstly, the enhanced O_2 adsorption due to ZnO decoration

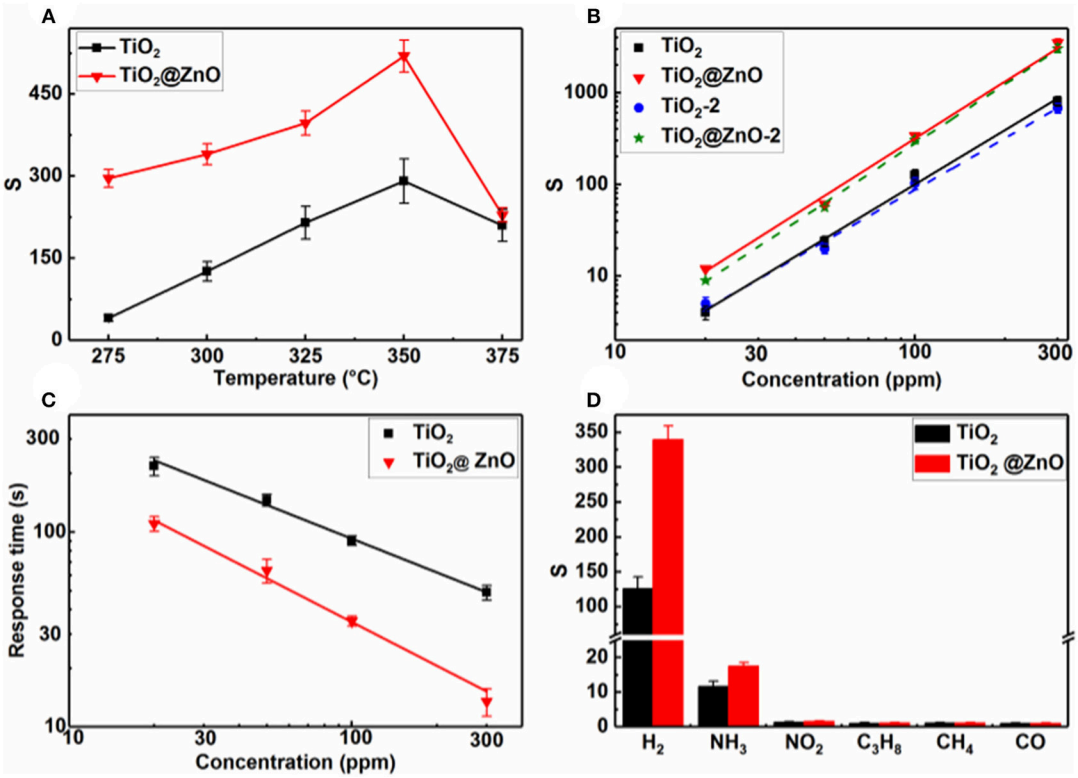

FIGURE 5 | Response of pristine TiO_2 and TiO_2@ZnO composite sensors as a function of **(A)** temperature to 100-ppm H_2 and **(B)** H_2 concentration at 300°C; **(C)** response time of pristine TiO_2 and TiO_2@ZnO composite sensors vs. H_2 concentration at 300°C; **(D)** response of pristine TiO_2 and TiO_2@ZnO composite sensors to 100-ppm various gases at 300°C.

revealed by XPS in **Figure 2** suggested generation of more active sites on the material surface, which is beneficial to the gas surface reactions. Secondly, n-n heterojunctions would be formed between the ZnO nanoparticles and TiO_2 nanotubes. Previous research has reported that ZnO (3.37 eV) has a slightly larger band gap than that of TiO_2 (3.2 eV); (Lin et al., 2013), and both conduction band energy and valance band energy of ZnO are higher than those of TiO_2, leading to transfer of electrons from the conduction band of ZnO to that of TiO_2 (Yang et al., 2009; Sarkar et al., 2014; Ng et al., 2018). Heterojunctions formed on the materials surface have been suggested to benefit the gas sensing performance *via* several routes, such as promoting gas reactions and regulating the conduction channel inside the materials (Lou et al., 2013; Li et al., 2015b; Gu et al., 2017), which can be applied to explain the enhancement of the composite sensor in this work.

CONCLUSIONS

Highly ordered TiO_2 nanotube arrays were synthesized by anodic oxidation. Decoration of ZnO nanoparticles on the nanotubes was achieved by immersion and calcination. Gas sensing test results indicate that significantly larger response and better selectivity to H_2 as well as shorter response time were achieved by ZnO loading. The TiO_2@ZnO sensor exhibited a response as high as 520 toward 100-ppm H_2 at 350°C. The excellent gas sensing performance of the composite may be attributed mainly to the highly ordered nanotube morphology and heterojunction formation at the interface of ZnO and TiO_2.

AUTHOR CONTRIBUTIONS

JY designed the experiments. AY and HX conducted the experiments and analyzed the results. JY and AY wrote the manuscript.

FUNDING

This work was supported by the National Natural Science Foundation of China (grant nos. 61871359 and U1432108).

REFERENCES

Chen, D., and Yi, J. (2018). One-pot electrospinning and gas-sensing properties of $LaMnO_3$ perovskite/SnO_2 heterojunction nanofibers. *J. Nanopart. Res.* 20:65. doi: 10.1007/s11051-018-4158-x

Gao, H., Yu, Q., Chen, K., Sun, P., Liu, F., Yan, X., et al. (2019). Ultrasensitive gas sensor based on hollow tungsten trioxide–nickel oxide (WO_3-NiO) nanoflowers for fast and selective xylene detection. *J. Colloid Interface Sci.* 535, 458–468. doi: 10.1016/j.jcis.2018.10.010

Gu, D., Li, X., Zhao, Y., and Wang, J. (2017). Enhanced NO_2 sensing of SnO_2/SnS_2 heterojunction based sensor. *Sens. Actuators B* 244, 67–76. doi: 10.1016/j.snb.2016.12.125

Hazra, A., Bhowmik, B., Dutta, K., Chattopadhyay, P., and Bhattacharyya, P. (2015). Stoichiometry, length, and wall thickness optimization of TiO_2 nanotube array for efficient alcohol sensing. *ACS Appl. Mater. Interfaces* 7, 9336–9348. doi: 10.1021/acsami.5b01785

Hübert, T., Boon-Brett, L., Black, G., and Banach, U. (2011). Hydrogen sensors—a review. *Sens. Actuators B* 157, 329–352. doi: 10.1016/j.snb.2011.04.070

Joo, S., Muto, I., and Hara, N. (2010). Hydrogen gas sensor using Pt-and Pd-added anodic TiO_2 nanotube films. *J. Electrochem. Soc.* 157, J221–J226. doi: 10.1149/1.3374643

Li, T., Zeng, W., and Wang, Z. (2015a). Quasi-one-dimensional metal-oxide-based heterostructural gas-sensing materials: a review. *Sens. Actuators B* 221, 1570–1585. doi: 10.1016/j.snb.2015.08.003

Li, W., Ma, S., Li, Y., Yang, G., Mao, Y., Luo, J., et al. (2015b). Enhanced ethanol sensing performance of hollow ZnO–SnO_2 core–shell nanofibers. *Sens. Actuators B* 211, 392–402. doi: 10.1016/j.snb.2015.01.090

Lin, L., Yang, Y., Men, L., Wang, X., He, D., Chai, Y., et al. (2013). A highly efficient TiO_2@ ZnO n–p–n heterojunction nanorod photocatalyst. *Nanoscale* 5, 588–593. doi: 10.1039/c2nr33109h

Liu, J., Wang, T., Wang, B., Sun, P., Yang, Q., Liang, X., et al. (2017). Highly sensitive and low detection limit of ethanol gas sensor based on hollow ZnO/SnO_2 spheres composite material. *Sens. Actuators B* 245, 551–559. doi: 10.1016/j.snb.2017.01.148

Lou, Z., Li, F., Deng, J., Wang, L., and Zhang, T. (2013). Branch-like hierarchical heterostructure (α-Fe_2O_3/TiO_2): a novel sensing material for trimethylamine gas sensor. *ACS Appl. Mater. Interfaces* 5, 12310–12316. doi: 10.1021/am402532v

Miller, D. R., Akbar, S. A., and Morris, P. A. (2014). Nanoscale metal oxide-based heterojunctions for gas sensing: a review. *Sens. Actuators B* 204, 250–272. doi: 10.1016/j.snb.2014.07.074

Mor, G. K., Varghese, O. K., Paulose, M., Shankar, K., and Grimes, C. A. (2006). A review on highly ordered, vertically oriented TiO_2 nanotube arrays: Fabrication, material properties, and solar energy applications. *Sol. Energy Mater. Sol. Cells* 90, 2011–2075. doi: 10.1016/j.solmat.2006.04.007

Ng, S., Kuberský, P., Krbal, M., Prikryl, J., Gärtnerová, V., Moravcová, D., et al. (2018). ZnO coated anodic 1D TiO_2 nanotube layers: efficient photo-electrochemical and gas sensing heterojunction. *Adv. Eng. Mater.* 20:1700589. doi: 10.1002/adem.201700589

Paulose, M., Varghese, O. K., Mor, G. K., Grimes, C. A., and Ong, K. G. (2005). Unprecedented ultra-high hydrogen gas sensitivity in undoped titania nanotubes. *Nanotechnology* 17:398. doi: 10.1088/0957-4484/17/2/009

Sarkar, A., Singh, A. K., Khan, G. G., Sarkar, D., and Mandal, K. (2014). TiO_2/ZnO core/shell nano-heterostructure arrays as photo-electrodes with enhanced visible light photoelectrochemical performance. *RSC Adv.* 4, 55629–55634. doi: 10.1039/c4ra09456e

Şennik, E., Colak, Z., Kılınç, N., and Ozturk, Z. Z. (2010). Synthesis of highly-ordered TiO_2 nanotubes for a hydrogen sensor. *Int. J. Hydrogen Energy* 35, 4420–4427. doi: 10.1016/j.ijhydene.2010.01.100

Silva, S. F., Coelho, L., Frazão, O., Santos, J. L., and Malcata, F. X. (2012). A review of palladium-based fiber-optic sensors for molecular hydrogen detection. *IEEE Sens. J.* 12, 93–102. doi: 10.1109/jsen.2011.2138130

Varghese, O. K., Gong, D., Paulose, M., Ong, K. G., and Grimes, C. A. (2003). Hydrogen sensing using titania nanotubes. *Sens. Actuators B* 93, 338–344. doi: 10.1016/s0925-4005(03)00222-3

Wang, Y., Wu, T., Zhou, Y., Meng, C., Zhu, W., and Liu, L. (2017). TiO_2-based nanoheterostructures for promoting gas sensitivity performance: designs, developments, and prospects. *Sensors* 17:1971. doi: 10.3390/s17091971

Xiong, Y., Chen, W., Li, Y., Cui, P., Guo, S., Chen, W., et al. (2016). Contrasting room-temperature hydrogen sensing capabilities of Pt-SnO_2 and Pt-TiO_2 composite nanoceramics. *Nano Res.* 9, 3528–3535. doi: 10.1007/s12274-016-1229-0

Xun, H., Zhang, Z., Yu, A., and Yi, J. (2018). Remarkably enhanced hydrogen sensing of highly-ordered SnO_2-decorated TiO_2 nanotubes. *Sens. Actuators B* 273, 983–990. doi: 10.1016/j.snb.2018.06.120

Yamazoe, N., and Shimanoe, K. (2008). Theory of power laws for semiconductor gas sensors. *Sens. Actuators B* 128, 566–573. doi: 10.1016/j.snb.2007.07.036

Yang, H. Y., Yu, S. F., Lau, S. P., Zhang, X., Sun, D. D., and Jun, G. (2009). Direct growth of ZnO nanocrystals onto the surface of porous TiO_2 nanotube arrays for highly efficient and recyclable photocatalysts. *Small* 5, 2260–2264. doi: 10.1002/smll.200900724

Yao, M. S., Tang, W. X., Wang, G. E., Nath, B., and Xu, G. (2016). MOF thin film-coated metal oxide nanowire array: significantly improved chemiresistor sensor performance. *Adv. Mater.* 28, 5229–5234. doi: 10.1002/adma.201506457

Zhan, Z., Lu, J., Song, W., Jiang, D., and Xu, J. (2007). Highly selective ethanol In_2O_3-based gas sensor. *Mater. Res. Bull.* 42, 228–235. doi: 10.1016/j.materresbull.2006.06.006

Zhang, J., Liu, X., Neri, G., and Pinna, N. (2016). Nanostructured materials for room-temperature gas sensors. *Adv. Mater.* 28, 795–831. doi: 10.1002/adma.201503825

Zhao, Z., Tian, J., Sang, Y., Cabot, A., and Liu, H. (2015). Structure, synthesis, and applications of TiO_2 nanobelts. *Adv. Mater.* 27, 2557–2582. doi: 10.1002/adma.201405589

Conflict of Interest Statement: The authors declare that the research was conducted in the absence of any commercial or financial relationships that could be construed as a potential conflict of interest.

frontiers in Materials

ORIGINAL RESEARCH
published: 30 April 2019
doi: 10.3389/fmats.2019.00096

Sol-gel Synthesis of TiO_2 With p-Type Response to Hydrogen Gas at Elevated Temperature

Lijuan Xie[1,2], *Zhong Li*[1,2*], *Linchao Sun*[1,2], *Baoxia Dong*[3], *Qawareer Fatima*[1,2], *Zhe Wang*[1,2], *Zhengjun Yao*[1,2] *and Azhar Ali Haidry*[1,2*]

[1] College of Materials Science and Technology, Nanjing University of Aeronautics and Astronautics, Nanjing, China, [2] Key Laboratory of Materials Preparation and Protection for Harsh Environment, Ministry of Industry and Information Technology, Nanjing, China, [3] College of Chemistry and Chemical Engineering, Yangzhou University, Yangzhou, China

Titanium dioxide is considered as one of the potential candidates for high-temperature gas sensing applications due to its excellent sensitivity and stability. However, its practical use as a gas sensor under elevated conditions is limited on account of its selectivity and insufficient understanding of response conversion from n- to p-type. To this context, the present work is intended to prepare and understand the p-type response of anatase TiO_2 toward H_2 gas (20–1,000 ppm) at elevated temperature (500°C). Sol-gel route is adopted to facilely synthesize powders containing pure and chromium (1–10 at.%) doped TiO_2 nanoparticles, which are then brushed onto substrates with already patterned inter-digitated platinum electrodes. In this work, even, the undoped TiO_2 samples showed p-type gas sensing response, which then decreased with Cr doping. However, in comparison to previously reported work, the sensing characteristics of all sensors is improved. For instance, 5 at.% Cr-TiO_2 showed high response (147), fast response and recovery (142/123s) time, and good selectivity to hydrogen against monoxide and methane. Despite better response values, the TiO_2 based samples show instability and drift in baseline resistance; such issues were not observed for Cr-doped TiO_2 samples (≥3 at.%). The powders were further analyzed by XRD, SEM, TEM, and XPS to understand the basic characteristics, p-type response and stability. Further, a plausible sensing mechanism is discussed on basis of results obtained from aforementioned techniques.

Keywords: sol-gel method, Cr doped TiO_2, nanoparticles, hydrogen sensitivity, high temperature

OPEN ACCESS

Edited by:
Kalisadhan Mukherjee, Pandit Deendayal Petroleum University, India

Reviewed by:
Tarapada Sarkar, University of Maryland, College Park, United States
Shyambo Chatterjee, University of Nebraska-Lincoln, United States

***Correspondence:**
Zhong Li
nuaalizhong@163.com
Azhar Ali Haidry
aa.haidry@nuaa.edu.cn

Specialty section:
This article was submitted to Functional Ceramics, a section of the journal Frontiers in Materials

Received: *25 February 2019*
Accepted: *15 April 2019*
Published: *30 April 2019*

Citation:
Xie L, Li Z, Sun L, Dong B, Fatima Q, Wang Z, Yao Z and Haidry AA (2019) Sol-gel Synthesis of TiO_2 With p-Type Response to Hydrogen Gas at Elevated Temperature. Front. Mater. 6:96. doi: 10.3389/fmats.2019.00096

INTRODUCTION

Expected to be widely used energy source in the near future, hydrogen has gained increasing attention as one of the cleanest energy sources. However, its use in practical applications is limited because, during production, storage, transportation and use, H_2 can effortlessly leak out as the atomic distance between the centers of two hydrogen atoms in H_2 molecules is very small (~1.06 Å). Refer to the lower and upper explosive limit (LEL-UEL~4.0–75.0), H_2 gas possesses flammable and explosive nature when leaked and, subsequently, mixed with oxygen from the surrounding air. As a consequence, explosion caused by hydrogen leakage presents a major threat to not only human but also the environment (Haidry et al., 2012; Hermawan et al., 2018; Li et al., 2018). From this perspective,

it is utmost important to monitor hydrogen in production plants, pipelines, storage tanks, refilling stations and automotive vehicles, specifically at high temperature. Thus, it is urgent and worthwhile to develop low-cost sensors to monitor the concentrations of H_2. One of the main challenges in hydrogen sensor working at high temperature is to aim higher sensitivity, selectivity, faster response time with excellent stability.

With the capacity to operate in harsh environment, gas sensors based on metal oxides (MOXs) are one of the potent candidates for hydrogen sensing applications (Bai and Zhou, 2014; Li et al., 2017). Among them, n-type semiconductor titanium dioxide (TiO_2) based gas sensor has attracted the enormous interest of researchers due to its outstanding physical and chemical properties: low cost facile fabrication, non-toxic nature, wide energy gap (E_g = 3.0–3.4 eV), and high sensitivity. Furthermore, the chemical stability of TiO_2 at high temperature make it exquisite contender for high temperature sensing applications (Li et al., 2009; Liu et al., 2014). TiO_2 in nature has three crystal structures, known as brookite, anatase, and rutile; rutile, and anatase are most widely used as a gas sensor. Rutile is more stable at high temperature while anatase has better gas sensitivity due its eminent gas reaction capability (Comini et al., 2005; Li et al., 2009; Jing et al., 2015). Currently, the TiO_2-coatings based on physical vapor deposition (e.g., sputtering) are mainly for high temperature gas sensing, which is carried out under high vacuum, thus increasing the cost of the final device. On the other, the sol-gel method has several advantages, such as facile, low cost, uncomplicated environmental requirements, and mass production.

Although TiO_2 is promising high-temperature gas sensitive material, it still has several inadequacies, such as low selectivity and surface contamination, reduction and aging in high temperature and harsh environments. Up to now, an accepted strategy to improve metal oxides gas sensor properties is to dope with metals or surface modification with catalytic metals. Metal ions of different valence states act as donors or acceptors in TiO_2, respectively, which can change the electrical conductivity of TiO_2, thereby having effects on the response time and sensitivity (Sennik et al., 2016; Luo et al., 2017; Pan et al., 2018). Chromium, one of the non-noble metals, is suggested to be suited as a dopant for improved TiO_2 sensing applications (Lyson-Sypien et al., 2012; Haidry et al., 2016; Sun et al., 2018; Monamary et al., 2019). The ionic radii of Ti^{4+}(0.60 Å) and Cr^{3+}(0.61 Å) is circa similar, thus Cr^{3+} can replace Ti^{4+} in TiO_2 lattice to form additional defects (as oxygen vacancies and interstitial Ti atoms), which can change the electronic structure of TiO_2 and transform TiO_2 into p-type. Based on its p-type conductivity, Cr^{3+} doped TiO_2 exhibits better sensitivity to H_2.

The ultimate aim of this work is to fabricate hydrogen sensors with high sensitivity that can work stably at high temperatures by simple and cost-effective sol-gel method. The motivation for this study is to improve the stability of TiO_2 based gas sensors at high temperature for hydrogen detection as well as to investigate the sensing mechanism of pure and Cr doped TiO_2 sensing materials. The effect of chromium dopant on the crystallite structure and topography of titanium dioxide was analyzed. The dynamic responses of synthesized sensor at high temperature to hydrogen are also discussed.

MATERIALS AND METHODS

Preparation of Cr-Doped TiO_2

In this work, the nanomaterials based on Cr_XTiO_2 (X = 0, 1, 3, 5, 10 at.%) prepared by sol-gel method. All chemicals used were of analytical grade reagents purchased from commercial channels and were used without any further purification unless mentioned elsewhere. The analytical grade Tetrabutyl titanate ($C_{16}H_{36}O_4Ti$, purity ≥98.0% from Aladdin, abbreviated as TBOT) precursor was used served as the source of titanium. The chromium acetate ($C_6H_9O_6Cr$, purity ≥99.9% from Aladdin) was used as a source of chromium, nitric acid as a chelating agent, acetic acid (CH_3COOH) as a catalysts, and ethanol as a solvent. Firstly, 12 ml TBOT and 1 ml acetic acid were dissolved in 25 ml ethanol in a beaker (named solution A), under continuous stirring at room temperature and ambient pressure for 1 h. The chromium acetate with different atomic contents (1, 3, 5, 10 at.%) and 3 ml DI water were dissolved in 25 ml ethanol in another flask (named solution B). Then, to adjust the pH value of solution B to 1, the nitric acid was added drop-wise under continuous stirring for 30 min. Following, the solution B was added drop-wise into stirred solution A. After stirring for 2 h under ambient condition, homogenous light yellow sol was formed. After aging for 12 h, the gel was dried in an oven for 12 h at 70°C. Afterwards, the obtained powder was grinded and subsequently annealed at 600°C for 1 h in a muffle furnace (HeFei Kejing Materials Teccnology Company) under static air condition. The synthesized TiO_2 and Cr_XTiO_2 (X = 0, 1, 3, 5, 10 at.%) powder were named as TO, TOC1, TOC3, TOC5, TOC10, respectively.

Characterization

The crystal structure analysis of the obtained TiO_2 powder was performed using X-ray diffraction (XRD, Rigaku Ultimate IV from Japan) with Cu Ka (λ = 1.5406 Å) and the diffraction angle range 20–80° at a scanning rate 5° min^{-1} The surface morphology of the nanoparticles was investigated using scanning electron microscopy (Hitachi S-4800) from Japan, and the compositions of the materials were determined by energy dispersive spectroscopy (EDS) attached to the SEM. The transmission electron microscopy (TEM) images were obtained by using JEM-2100F transmission electron microscope (JEOL Ltd. Japan). Thermo ESCALAB 250XI X-ray photoelectron spectroscopy (XPS) was performed on the prepared powder to analyze elemental chemical.

Fabrication and Measurement of the Sensors

After annealing at 600°C, the powder was grinded for several hours and then mixed in deionized water to form thick paste. Using a brush, the pastes were coated on alumina substrates having Pt interdigital electrodes. Then, the substrates adhered gas sensing paste was dried in hot plate for 30 min at 80°C.

The gas sensing characteristics were carried out by independent design gas sensing measurement device (Functional

Materials and Chemical Sensor Lab, FuMS). The detailed of the sensing apparatus is already reported elsewhere (Haidry et al., 2018). To measure the resistance change of the sensor, different voltages (0.1, 1, 2 V were applied on the sensors in high operating temperatures (300–500°C) toward different gases (CO, H_2, CH_4). Here, the sensor response (S_R) is defined as the ratio

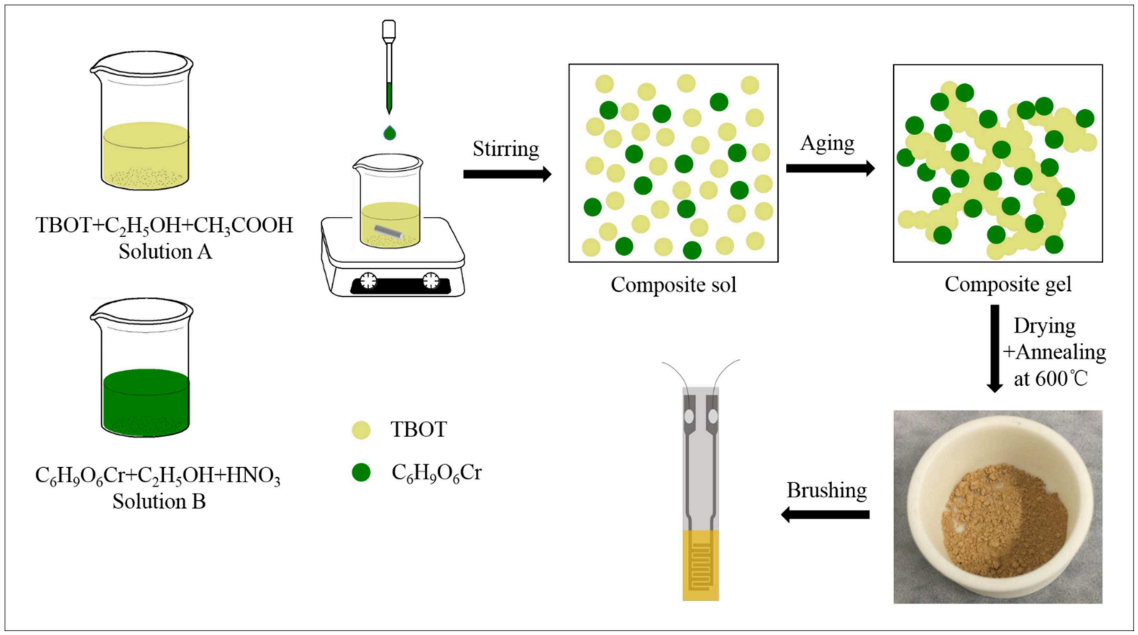

FIGURE 1 | The schematic illustrating the fabrication process of undoped and Cr-doped TiO_2 nanopowders and gas sensors is shown.

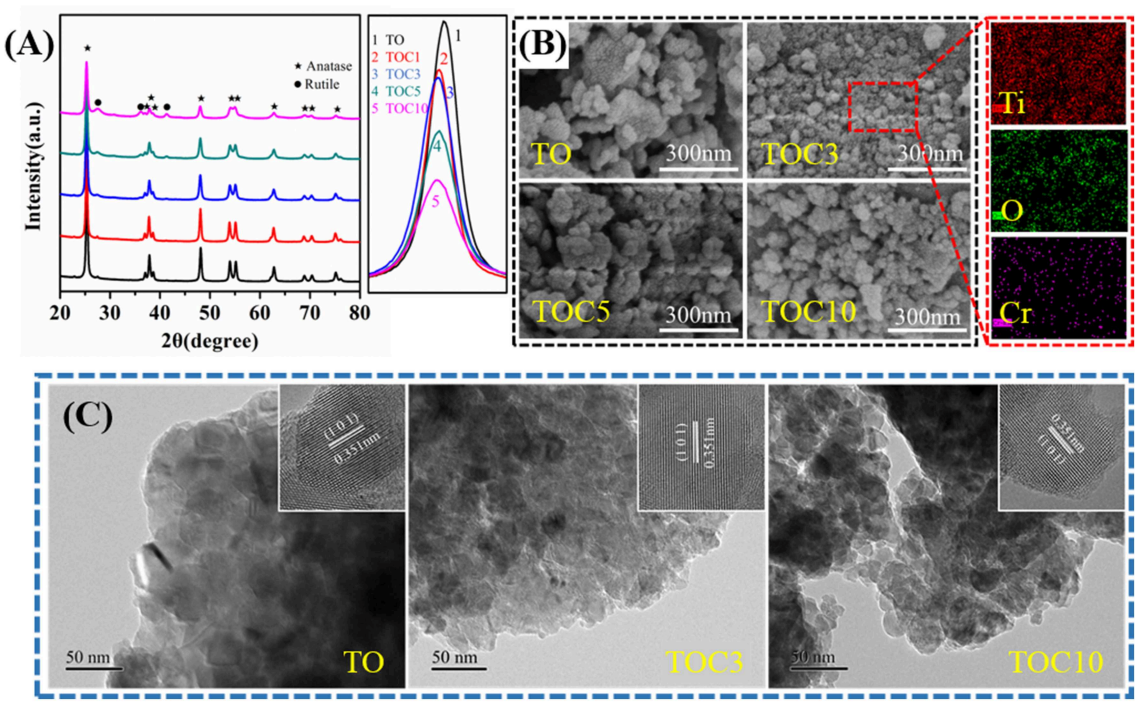

FIGURE 2 | XRD diffractograms **(A)** of TOC, TOC1, TOC3, TOC5, TOC10, and the comparison of anatase (101) peak, SEM micrographs **(B)** of TOC, TOC3, TOC5, TOC10, and elemental mapping of TOC3, TEM, and HRTEM images **(C)** of TO, TOC3, TOC10.

of R_{gas}/R_{air} where R_{air} and R_{gas} are the resistance in dry air and gas, respectively. The response and recovery times are defined as 90% change in the baseline stable resistance, respectively. The selectivity factor (S_F) was estimated as the response ratio of hydrogen against other gases. The typical schematics of the process of Cr doped TiO_2 nanopowders and gas sensors fabrication procedure is shown in **Figure 1**.

RESULTS AND DISCUSSION

Structural and Morphological Characteristics

The structural change of TiO_2 before and after doping Cr was characterized by XRD diffractograms. **Figure 2A** shows the XRD diffractograms of pure and Cr-doped TiO_2 nanoparticles annealed at 600°C. Comparing with the standard XRD patterns of TiO_2 (JCPDS Card 21-1272 and 21-1276), the prepared nanopowders are mainly anatase with a minor amount of rutile phase. The diffraction peaks at 2θ [°] = 25.35, 36.88, 37.78, 38.51, 48.07, 53.92, 55.11, 62.07, 68.59, 70.36, 75.09 are indexed to anatase TiO_2 phases (101), (103), (004), (112), (200), (105), (211), (213), (116), (200), (215), and the peak at 2θ [°] = 27.51, 36.04, 41.19 are indexed to rutile TiO_2 phases (110), (101), and (111). With the increasing Cr contents, the diffraction peaks of rutile become obvious. Thus, it can be concluded that Cr ions can promote the transformation of anatase to rutile when annealed at 600°C. On the basis of the reports (Gonullu et al., 2015), it can be explained by the formation electric stress produced as a result of Cr replacing Ti^{4+} in TiO_2 lattice. Having similar ionic radii with Ti^{4+} (0.60 Å), Cr^{3+} (0.61 Å) can substitute Ti^{4+} without any visible deformation. However, Cr doping forms oxygen vacancies with positive charges and generates electrical stress which facilitates the transformation from anatase to rutile even at 600°C. In this work, no diffraction

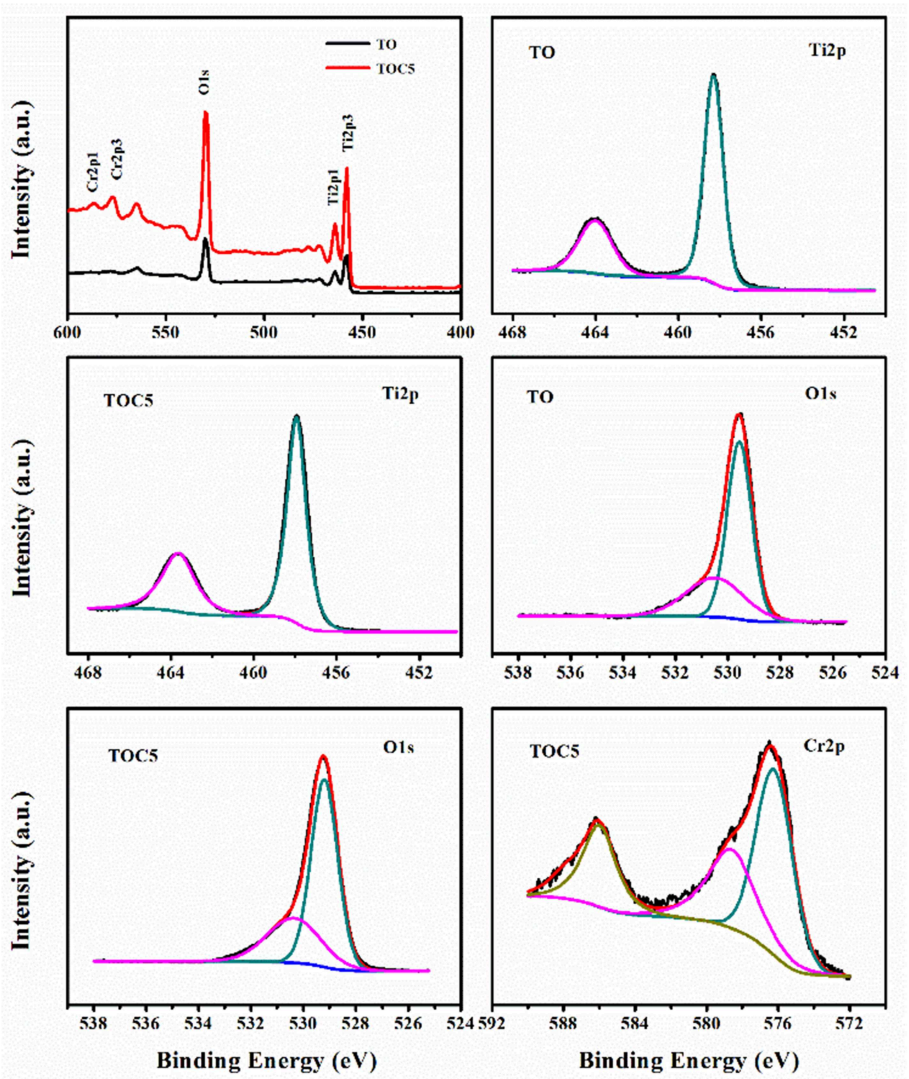

FIGURE 3 | XPS spectra of TO and TOC5, Ti 2p of TO and TOC5, O 1s of TO and TOC5, and Cr 2p of TOC5.

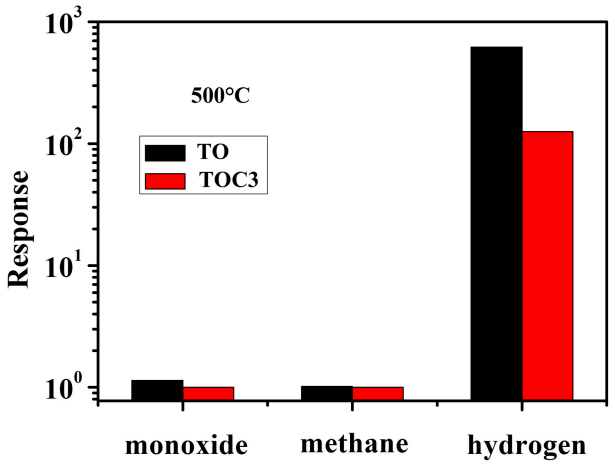

FIGURE 4 | H_2-selectivity of the sensors against monoxide and methane (1,000 ppm).

peaks associated with Cr appear even for the powder having is up to 10 at.% Cr concentration. Thus, it can be speculated that Cr is successfully incorporated into the TiO_2 lattice. According to Scherrer's equation ($D_{XRD} = 0.9\frac{\lambda}{dcos\theta}$), the average crystallite sizes of nanoparticles are 25.1, 24, 23.2, 21.4, 21.3 nm for TO, TOC1, TOC3, TOC5, TOC10, respectively. The results indicate that the crystallite size decreases slightly with the increasing of Cr concentration, which strongly agrees with previous publication (Asemil et al., 2017).

SEM analysis in **Figure 2B** reveal similar microstructure of pure and Cr doped TiO_2. All samples are composed of irregular nanoparticles ranging from 20 to 200 nm, and the nanoparticles are piled up to form loose structure. There is contrasting difference between the XRD and SEM grain sizes since values of TiO_2 grains from XRD means the volume where the crystalline structure is intact. It can be clearly seen from **Figure 2B** that the size of pure TiO_2 particles is bigger than Cr doped TiO_2. The elemental mapping of TOC3 indicates the presence and distribution of Ti, O, Cr elements.

The TEM and HRTEM images of the pure and Cr-doped TiO_2 calcined at 600°C are presented in **Figure 2C**. The aggregation of the nanoparticles is more obviously observed in TEM images. As shown in the images, with the increase of chromium concentration, the aggregation becomes weak and, therefore, it is speculated that Cr dopant can prevent TiO_2 nanoparticles aggregating. The main interplanar crystal spacing value measured from lattice fringes is 0.35 nm, which corresponds to the A (101) plane of the TiO_2. No evidence on spacing on metallic Cr or oxidized Cr was found.

The x-ray photoelectron spectroscopy (XPS) measurements were carried out to investigate the changes in the chemical and electronic states of the elements. The XPS survey and high-resolution spectra of Ti 2p, O 1s, Cr 2p are presented in **Figure 3**. The XPS spectrum of TOC5 reveals Cr, Ti, and O element. The peaks in Ti spectra of TO around 458.3 and 464 eV describe Ti^{4+} 2p3/2 and Ti^{4+} 2p1/2, respectively (Peng et al., 2012), which shift slightly to lower binding energy (∼0.4 eV) in TOC5. The O 1s spectra of TO display overlapping peaks at 529.6 and 530.5 eV, which are attributed to lattice oxygen (Ti-O-Ti) in TiO_2 and surface absorbed oxygen, respectively (Alvarez et al., 2019). These peaks also shift slightly to lower band energy of 529.2 eV and 530.4 eV displayed in TOC5. The Cr 2p3/2 spin-orbital splitting photoelectrons for TOC5 located at binding energies of 576.3 and 586.2 eV, could be assigned to Cr^{3+}, binding energy at 578.6 and 587.9 eV that assigned to Cr^{6+} was also detected (Lacz et al., 2018; Alvarez et al., 2019). The above results prove Cr incorporation into the TiO_2 lattice, which are in good agreement with previous reports (Low et al., 2013; Alvarez et al., 2019).

Gas Sensing Properties

Generally, TiO_2 is n-type but in our case it shows p-type H_2 response. In this work, with the purpose of developing TiO_2 based gas sensors for high temperature application, the sensing measurements were performed at 500°C toward reducing gases monoxide (CO), methane (CH_4), and hydrogen (H_2) firstly. **Figure 4** demonstrates the response S_R of TO and TOC3 sensors to 1,000 ppm of CO, CH_4, and H_2. The selectivity factor S_F of pure TiO_2 for H_2 is ∼543.6 and ∼607.5 against interfering gases CO and CH_4, respectively, indicating the gas sensor exhibits high selectivity to H_2.

For the sensors based on TO, the relationship between the response and operating temperature was studied see **Figure 5A**. Using low applied voltage 0.1 V, the sensor showed much higher response to hydrogen at 500°C. For 1,000 ppm hydrogen, the response ($S_R \sim 619.7$) at 500°C is about 200 times higher than at 300°C ($S_R \sim 3.28$). It is well-known that the sensitivity of metal oxides depends on the temperature and there exist an optimal operating temperature. In a typical case, the sensing response increases with the temperature and after a maximum value it falls. At lower temperature, the energy is not strong enough to overcome the reaction activation energy barrier, leading to a poor sensitivity. However, over the optimal temperature, the accumulation of a large number of heat energy on the surface makes exothermic gas chemisorption difficult and the gas desorption dominate, resulting in reducing response value (Yamazoe and Shimanoe, 2008; Diao et al., 2016). In this work, the optimal temperature was not found. Thus, 500°C is selected as operating temperature and all the following measurements were performed at this temperature except to understand the influence of applied voltage. The influence of applied voltage on the sensitivity was also studied. **Figure 5B** shows the response value of TiO_2 sensor to 50–1,000 ppm hydrogen at 300°C with 0.1, 1, and 2 V. As can be seen in **Figure 5B**, when the applied voltage increases, the sensitivity of the TiO_2 sensor promotes obviously. For instance, the response values are ∼3.28 with ∼82.91 and ∼ 465.18 with 0.1, 1, and 2 V, respectively, toward 1,000 ppm hydrogen.

The real time changes in the electrical resistance R of undoped TiO_2 sensor materials upon interaction with H_2 as a function of time in **Figure 5C** (known as dynamic response) exhibit that the pure TiO_2 sensor yields p-type semiconductor behaviors at all operating temperatures. At 500°C, when the target gas released,

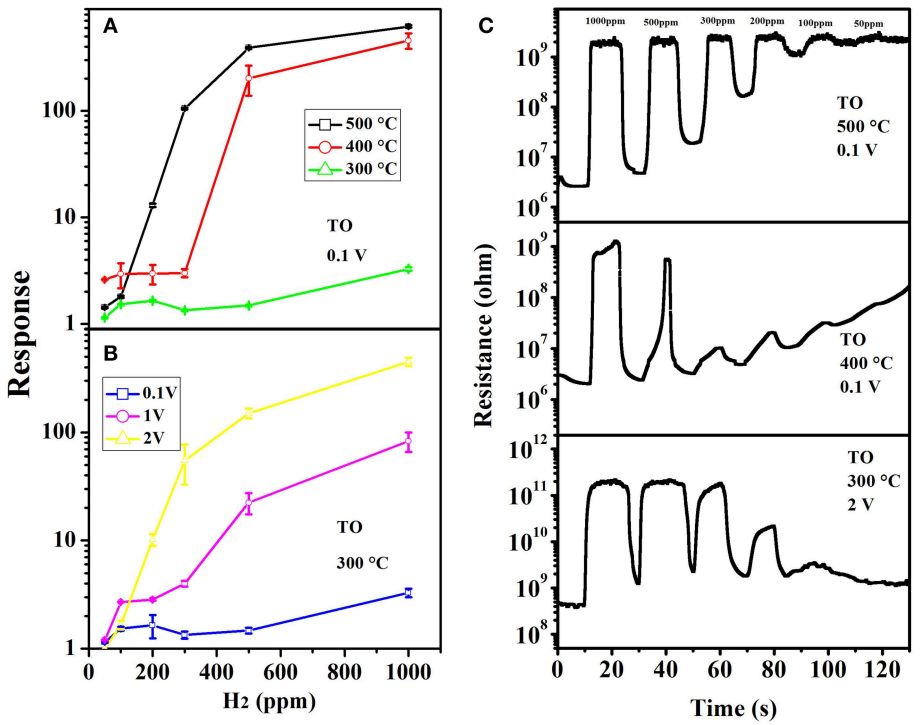

FIGURE 5 | Response values of sensors **(A)** based on TO to 50–1,000 ppm hydrogen at different operating temperatures (300–500°C) with 0.1 V. Comparative response values of sensors **(B)** based on TO to 50–1,000 ppm hydrogen at 300°C with 0.1, 1, and 2 V. The dynamic response curves of sensors **(C)** based on TO vs. 50–1,000 ppm hydrogen at different operating temperatures (300–500°C).

the resistance of the sensor cannot return to the initial value. This phenomenon calls the baseline resistance drift, and with the temperature increases, the baseline resistance drift becomes more severe. To sum up, for TiO_2 sensor, the most suitable working condition is at 300°C with 2 V applied voltage.

The dynamic response curves toward various concentrations of hydrogen ranging from 20 to 1,000 ppm at 500°C with 0.1 V applied voltage are presented in **Figures 6A,B**. The resistance of all sensors increases rapidly when exposed to hydrogen and then decrease when exposed to the background air, which presents the p-type semiconducting gas sensing behaviors. It is clearly illustrated that not only the pure TiO_2 but also lower content Cr doped TiO_2 sensors, when hydrogen is exposed, the resistance of these sensors cannot return to the initial value. Furthermore, the baseline resistance drift notably improves with the increase of Cr concentration; with Cr concentration up to 5 at.%, the resistance drift removes completely. However, when Cr concentration reaches up to 10 at.%, the sensor does not show any response to hydrogen. Therefore, we can conclude that Cr dopant can improve the stability of TiO_2 sensors. The response and recovery time are given in **Table 1**. **Figure 6C** shows the sensing performance of pure TiO_2 and different content Cr doped TiO_2 sensors on 20–1,000 ppm at 500°C. It is found that the response is 619.7, 197.8, 125.8, 147 for TO, TOC1, TOC3, TOC5, respectively, at 500°C under similar conditions as shown in **Figure 6C**. Pure TiO_2 sensors show high sensitivity to all hydrogen concentrations. Responses of pure and Cr doped TiO_2 sensors are further observed to 20–100 ppm of hydrogen in **Figure 6D**. Minimum hydrogen concentration that the fabricated sensor is detecting at 500°C is 20 ppm as can be seen in the **Figure 6B**. It is also noticeable in **Figure 6** that Cr dopant reduces the sensing response of TiO_2 sensors toward hydrogen. Both sensitivity and stability are vital for an excellent gas sensor. Thus, we can select 5 at.% Cr doped TiO_2 sensor as the optimum sensor that can work at high temperature considering all factors.

Sensing Mechanism

The gas-sensing characteristics of p-type and n-type semiconductors are notably different in the context of the resistance variation during targeting gas exposure. Taking n-type semiconductors as an example, the oxygen molecules get trapped by taking electrons from conduction band near the surface that leads to the formation of negatively charged chemisorbed oxygen species, such as O_2^-, O^-, and O^{2-} in the flow of air, see Equations (1–3). Upon exposing to the reducing gas, the trapped electrons are subsequently released back to TiO_2-surface due to interaction between the target gas and adsorbed oxygen species. This reaction reduces the thickness of space charge region (depletion layer) resulting an increase of surface conduction electron density [e^-] and thus the increased electronic conductivity, see Equation (4). Usually, titanium dioxide exhibits an n-type response to hydrogen, but some factors lead to a p-type transition, such as impurities,

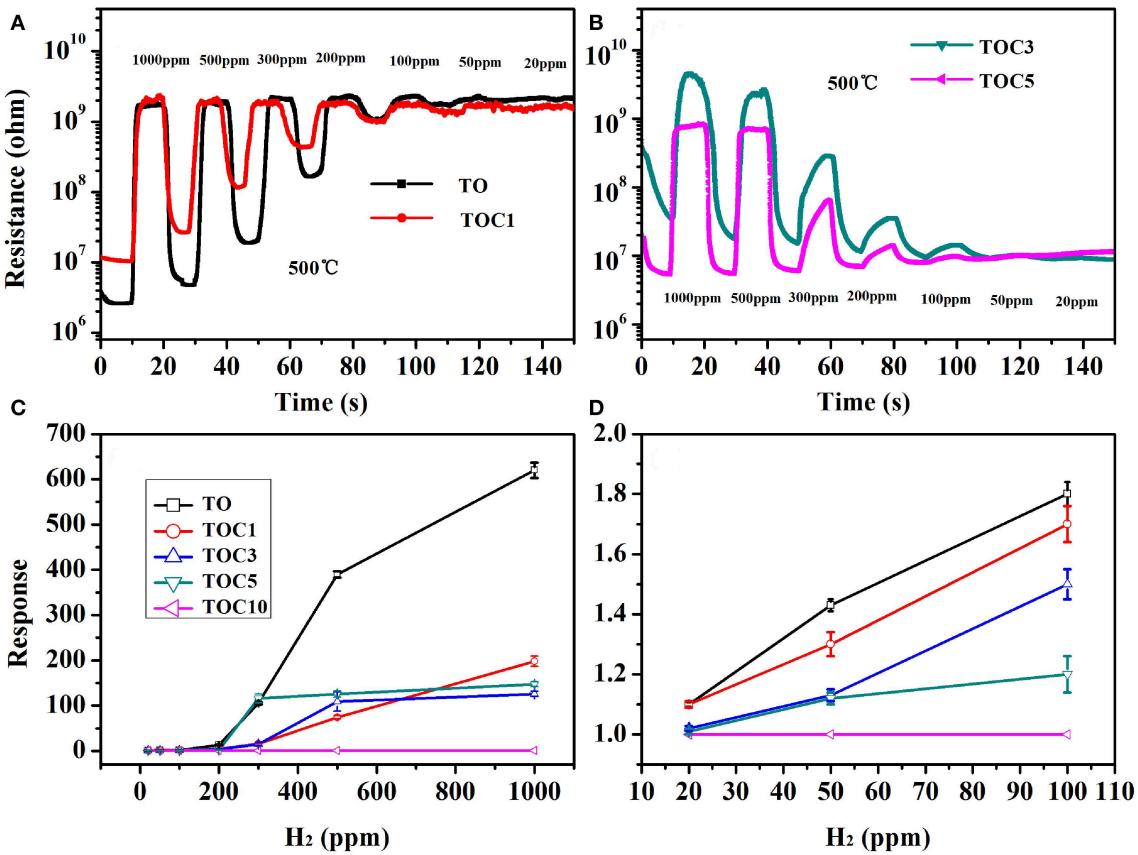

FIGURE 6 | The dynamic response curves of sensors based on TO, TOC1, TOC3, TOC5 vs. 20–1,000 ppm hydrogen at 500°C with 0.1 V applied voltage **(A,B)**. Hydrogen sensing performance (20–1,000 ppm) of TO, TOC1, TOC3, TOC5, TOC10 at 500°C with 0.1 V applied voltage **(C)**. Response values of TO, TOC1, TOC3, TOC5, TOC10 vs. 20–100 ppm hydrogen at 500°C with 0.1 V applied voltage **(D)**.

temperature, applied electric field, and gas concentration (Li et al., 2009; Haidry et al., 2018). However, contradicting with (Haidry et al., 2018), in this work the transition point and the influencing factors leading to transition were not found.

$$T<100°C: O_2\,(gas)+e^-\rightarrow O_2^-\ (ads) \quad (1)$$

$$100°C<T<300°C:\ O_2\,(gas)+2e^-\rightarrow 2O^-\,(ads) \quad (2)$$

$$T>300°C:\ \ O_2\,(gas)+4e^-\rightarrow 2O^{2-}(ads) \quad (3)$$

$$H_2+O^{2-}\rightarrow H_2O+2e^- \quad (4)$$

According to the author's best knowledge, in the temperature range of 300–500°C, pure n-type semiconductors might also show p-type response, which is resulted due to the formation of inversion layer on the surface (Li et al., 2009; Haidry et al., 2018). In detail, at the aforementioned operating temperature, strong oxygen adsorption on TiO_2 surface increases band bending greatly, also raising intergranular surface barrier. Thus, it is hard for electrons to transfer between TiO_2 grains leading to the formation of an inversion layer and holes become the majority surface charge carriers that yield a p-type sensor response. When hydrogen is supplied to the sensor surface, while the concentration of holes decreases since hydrogen reacts with adsorbed oxygen, inversion layer becomes thinner and conductivity decreases causing a p-type response. To date, the phenomenon related to the inversion layer formation and its thickness decrease is still debatable, which requires further in-deeper research.

In terms of Kroger-Vink notation, chromium may incorporate into TiO_2 lattice with 2, 3, and 6 oxide states, following Equations (5–7). Some researchers (Nowotny et al., 2016) attributed the change of the oxidation state of chromium to the increase in oxygen activity.

$$CrO\leftrightarrow Cr_{Ti}^{''}+V_{\ddot{O}}+O_O^x \quad (5)$$

$$Cr_2O_3\leftrightarrow 2Cr_{Ti}^{'}+3O_O^x+V_{\ddot{O}} \quad (6)$$

$$2CrO_3\leftrightarrow 2Cr_{\ddot{T}i}+6O_O^x+V_{Ti}^{''''} \quad (7)$$

TABLE 1 | Response and recovery time TO, TOC1, TOC3, TOC5 at 500°C (1,000 ppm).

Sample	Response time (s)	Recovery time (s)
TO	114	112
TOC1	224	130
TOC3	223	332
TOC5	142	123

With the addition of chromium dopant, the interpretation of p-type behavior is usually associated with the presence of acceptor states. Generally, chromium dopant has an effect on the electronic structure of TiO_2 and forms localized acceptor levels in the forbidden band gap. The Cr dopant in TiO_2 crystals can exist in three possible modes, isolated substitutional doping (Cr at Ti sites), substitutional doping with oxygen vacancy compensation and interstitial doping (Yang et al., 2009). On the basis of the XRD and XPS analysis, we knew that Cr can be incorporated into the lattice, as shown in reaction (8):

$$Cr_2O_3+\frac{1}{2}O_2\rightarrow 2Cr'_{Ti}+4O_O+2h* \quad (8)$$

Thus, electron holes become the dominant charge carriers. When exposed to hydrogen, the reaction between hydrogen molecular and adsorbed oxygen releases electrons making resistance increase.

CONCLUSION

In conclusion, Cr doped TiO_2 nanoparticles were successfully synthesized by sol-gel method and the hydrogen gas sensor based on TiO_2 is investigated at high temperature. Five at.% Cr doped TiO_2 gas sensor showed best gas sensing performance at 500°C. The response value is 152.65 and the response/recovery time is fast (142/123s) when it is exposed to 1,000 ppm hydrogen and it is of good selectivity to hydrogen. The results indicate that Cr doped TiO_2 synthesized by sol-gel method is promising materials for application as hydrogen gas sensor at high temperature. Cr dopant was proved to improve stability of TiO_2 gas sensor at high temperature in this work.

DATA AVAILABILITY

All datasets generated for this study are included in the manuscript and/or the supplementary files.

AUTHOR CONTRIBUTIONS

LX prepared the nanopowders and wrote this article. LS, QF, and ZW analyzed the gas sensing performance. ZL and BD carried out the characterization of the samples. AH and ZY revised, read, and approved the submitted version.

FUNDING

This research was financially supported by the Funding of Natural Science Foundation of Jiangsu Province (BK20170795) and National Natural Science Foundation of China (51850410506). This work was also supported by Opening Project from key Laboratory of Materials Preparation and Protection for Harsh Environment (56XCA17006-3) and Postgraduate Research and Practice Innovation Program of Jiangsu Province (KYCX18_0281).

REFERENCES

Alvarez, S. Y. M., Mar, J. L. G., Palomino, G. T., Alejandro, F. M., Quintero, A. C., Ramirez, A. H., et al. (2019). Synthesis of Cr^{3+}-doped TiO_2 nanoparticles: characterization and evaluation of their visible photocatalytic performance and stability. *Environ. Technol.* 40, 144–153. doi: 10.1080/09593330.2017.1380715

Asemil, M., Malekil, S., and Ghanaatshoar, M. (2017). Cr-doped TiO_2-based dye-sensitized solar cells with Cr-dopedTiO_2 blocking layer. *J. Sol-Gel Sci. Technol.* 81, 645–651. doi: 10.1007/s10971-016-4257-z

Bai, J., and Zhou, B. X. (2014). Titanium dioxide nanomaterials for sensor applications. *Chem. Rev.* 114, 10131–10176. doi: 10.1021/cr400625j

Comini, E., Ferroni, M., Guidi, V., Vomiero, A., Merli, P. G., and Morandi, V. (2005). Effects of Ta/Nb-doping on titania-based thin films for gas-sensing. *Sens. Actuators B.* 108, 18–21. doi: 10.1016/j.snb.2004.10.041

Diao, K., Huang, Y., Zhou, M., Zhang, J., Tang, Y., Wang, S., et al. (2016). Selectively enhanced sensing performance for oxidizing gases based on ZnO nanoparticle-loaded electrospun SnO_2 nano-tube heterostructures. *RSC Adv.* 6, 28419–28427. doi: 10.1039/C6RA03061K

Gonullu, Y., Haidry, A. A., and Saruhan, B. (2015). Nanotubular Cr-doped TiO_2 for use as high-temperature NO_2 gas sensor. *Sen. Actuators B.* 217, 78–87. doi: 10.1016/j.snb.2014.11.065

Haidry, A. A., Cetin, C., Kelm, K., and Saruhan, B. (2016). Sensing mechanism of low temperature NO_2 sensing with top-bottom electrode (TBE) geometry. *Sens. Actuators B.* 236, 874–884. doi: 10.1016/j.snb.2016.03.016

Haidry, A. A., Puskelova, J., Plecenik, T., Durina, P., Gregus, J., Truchly, M., et al. (2012). Characterization and hydrogen gas sensing properties of TiO_2 thin films prepared by sol-gel method. *Appl. Surf. Sci.* 259, 270–275. doi: 10.1016/j.apsusc.2012.07.030

Haidry, A. A., Sun, L. C., Saruhan, B., Plecenik, A., Plecenik, T., Shen, H. L., et al. (2018). Cost-effective fabrication of polycrystalline TiO_2 with tunable n/p response for selective hydrogen monitoring. *Sens. Actuators B.* 274, 10–21. doi: 10.1016/j.snb.2018.07.082

Hermawan, A., Asakura, Y., Kobayashi, M., Kakihana, M., and Yin, S. (2018). High temperature hydrogen gas sensing property of GaN prepared from α-GaOOH. *Sens. Actuators B.* 276, 388–396.doi: 10.1016/j.snb.2018.08.021

Jing, Z. H., Ling, B. P., Yu, Y., Qi, W., and Zhang, S. F. (2015). Preparation and gas sensing activity of La and Y co-doped titania nanoparticles. *J. Sol-Gel Sci. Techn.* 73, 112–117. doi: 10.1007/s10971-014-3501-7

Lacz, A., Lancucki, L., Lach, R., Kamecki, B., and Drozdz, E. (2018). Structural and electrical properties of Cr-doped $SrTiO_3$ porous materials. *Int. J. Hydrogen Energy.* 43, 8999–9005. doi: 10.1016/j.ijhydene.2018.03.180

Li, X. G., Ramasamy, R., and Dutta, P. K. (2009). Study of the resistance behavior of anatase and rutile thick films towards carbon monoxide and oxygen at high temperatures and possibilities for sensing applications. *Sens. Actuators B* 1, 308–315. doi: 10.1016/j.snb.2009.09.021

Li, Z., Haidry, A. A., Wang, T., and Yao, Z. J. (2017). Low-cost fabrication of highly sensitive room temperature hydrogen sensor based on ordered mesoporous Co-doped TiO_2 structure. *Appl. Phys. Lett.* 111:032104. doi: 10.1063/1.4994155

Li, Z., Yao, Z. J., Haidry, A. A., Plecenik, T., Xie, L. J., Sun, L. C., et al. (2018). Resistive-type hydrogen gas sensor based on TiO_2: a review. *Int. J. Hydrogen Energy*. 43, 21114–21132. doi: 10.1016/j.ijhydene.2018.09.051

Liu, Y. X., Parisi, J., Sun, X. C., and Lei, Y. (2014). Solid-state gas sensors for high temperature applications–a review. *J. Mater. Chem. A*. 2, 9919–9943. doi: 10.1039/C3TA15008A

Low, I. M., Albetran, H., Prida, V. M., Vega, V., Manurung, P., and Ionescu, M. (2013). A comparative study on crystallization behavior, phase stability, and binding energy in pure and Cr-doped TiO_2 nanotubes. *J Mater. Res*. 28, 304–312. doi: 10.1557/jmr.2012.275

Luo, Y. F., Zhang, C., Zheng, B. B., Geng, X., and Debliquy, M. (2017). Hydrogen sensors based on noble metal doped metal-oxide semiconductor: a review. *Int. J. Hydrogen Energy* 42, 20386–20397. doi: 10.1016/j.ijhydene.2017.06.066

Lyson-Sypien, B., Czapla, A., Lubecka, M., Gwizdz, P., Schneider, K., Zakrzewska, K., et al. (2012). Nanopowders of chromium doped TiO_2 for gas sensors. *Sens. Actuators B*. 175, 163–172. doi: 10.1016/j.snb.2012.02.051

Monamary, A., Vijayalakshmi, K., DavidJereil, S. (2019). Hybrid Cr/TiO_2/ITO nanoporous film prepared by novel two step deposition for room temperature hydrogen sensing. *Physica B*. 553, 182–189. doi: 10.1016/j.physb.2018.10.049

Nowotny, J., Macyk, W., Wachsman, E., and Rahman,. K. (2016). Effect of oxygen activity on the n-p transition for pure and Cr doped TiO_2. *J. Phys. Chem. C*. 120, 3221–3228. doi: 10.1021/acs.jpcc.5b12101

Pan, F. J., Lin, H., Zhai, H. Z., Miao, Z., Zhang, Y., Xu, K. L., et al. (2018). Pd-doped TiO_2 film sensors prepared by premixed stagnation flames for CO and NH_3 gas sensing. *Sens. Actuators B*. 261, 451–459. doi: 10.1016/j.snb.2018.01.173

Peng, Y. H., Huang, G. F., and Huang, W. Q. (2012). Visible-light absorption and photocatalytic activity of Cr-doped TiO_2 nanocrystal films. *Adv. Powder Technol*. 3, 8–12. doi: 10.1016/j.apt.2010.11.006

Sennik, E., Alev, O., and Ozturk, Z. Z. (2016). The effect of Pd on the H_2 and VOC sensing properties of TiO_2 nanorods. *Sens. Actuators B*. 229, 692–700. doi: 10.1016/j.snb.2016.01.089

Sun, L. C., Yao, Z. J., Haidry, A. A., Li, Z., Fatima, Q., and Xie, L. J. (2018). Facile one-step synthesis of TiO_2 microrods surface modified with Cr_2O_3 nanoparticles for acetone sensor applications. *J. Mater. Sci*. 29, 14546–14556. doi: 10.1007/s10854-018-9589-8

Yamazoe, N., and Shimanoe, K. (2008). Theory of power laws for semiconductor gas sensors. *Sens. Actuators B*. 128, 566–573. doi: 10.1016/j.snb.2007.07.036

Yang, K., Dai, Y., and Huang, B. B. (2009). Density functional characterization of the electronic structure and visible-light absorption of Cr-doped anatase TiO_2. *Chem. Phys. Chem*. 10, 2327–2333. doi: 10.1002/cphc.200900188

Conflict of Interest Statement: The authors declare that the research was conducted in the absence of any commercial or financial relationships that could be construed as a potential conflict of interest.

frontiers in Materials

CORRECTION
published: 02 August 2019
doi: 10.3389/fmats.2019.00184

Corrigendum: Sol-gel Synthesis of TiO_2 With p-Type Response to Hydrogen Gas at Elevated Temperature

Lijuan Xie[1,2], *Zhong Li*[1,2]*, *Linchao Sun*[1,2], *Baoxia Dong*[3], *Qawareer Fatima*[1,2], *Zhe Wang*[1,2], *Zhengjun Yao*[1,2] and *Azhar Ali Haidry*[1,2]*

[1] College of Materials Science and Technology, Nanjing University of Aeronautics and Astronautics, Nanjing, China, [2] Key Laboratory of Materials Preparation and Protection for Harsh Environment, Ministry of Industry and Information Technology, Nanjing, China, [3] College of Chemistry and Chemical Engineering, Yangzhou University, Yangzhou, China

OPEN ACCESS

Approved by:
Frontiers Editorial Office,
Frontiers Media SA, Switzerland

***Correspondence:**
Zhong Li
nuaalizhong@163.com
Azhar Ali Haidry
aa.haidry@nuaa.edu.cn

Specialty section:
This article was submitted to Functional Ceramics, a section of the journal Frontiers in Materials

Received: 16 July 2019
Accepted: 17 July 2019
Published: 02 August 2019

Citation:
Xie L, Li Z, Sun L, Dong B, Fatima Q, Wang Z, Yao Z and Haidry AA (2019) Corrigendum: Sol-gel Synthesis of TiO_2 With p-Type Response to Hydrogen Gas at Elevated Temperature. Front. Mater. 6:184. doi: 10.3389/fmats.2019.00184

Keywords: sol-gel method, Cr doped TiO_2, nanoparticles, hydrogen sensitivity, high temperature

A Corrigendum on

Sol-gel Synthesis of TiO_2 With p-Type Response to Hydrogen Gas at Elevated Temperature
by Xie, L., Li, Z., Sun, L., Dong, B., Fatima, Q., Wang, Z., et al. (2019). Front. Mater. 6:96. doi: 10.3389/fmats.2019.00096

There is an error in the Funding statement. The correct number for "Postgraduate Research and Practice Innovation Program of Jiangsu Province" is "KYCX18_0281".

A correction has therefore been made to the **Funding** statement:

"This research was financially supported by the Funding of Natural Science Foundation of Jiangsu Province (BK20170795) and National Natural Science Foundation of China (51850410506). This work was also supported by Opening Project from key Laboratory of Materials Preparation and Protection for Harsh Environment (56XCA17006-3) and Postgraduate Research and Practice Innovation Program of Jiangsu Province (KYCX18_0281)."

The authors apologize for this error and state that this does not change the scientific conclusions of the article in any way. The original article has been updated.

frontiers in Materials

REVIEW
published: 03 May 2019
doi: 10.3389/fmats.2019.00101

Gas Sensing by Microwave Transduction: Review of Progress and Challenges

Fangxin Li, Yangong Zheng, Changzhou Hua* and Jiawen Jian*

Faculty of Electrical Engineering and Computer Science, Ningbo University, Ningbo, China

Microwave transduction is a novel research field in gas sensing owing to its simplicity, low cost, passive, and non-contact operations that indicate a huge potential in applications for gas sensing. At present, the study of microwave gas sensors is limited to testing the macroscopic performance of materials. Although the permittivity change of materials is the reason for microwave transduction, the knowledge of the fundamental mechanism is an urgent requirement for boosting the development of microwave gas sensors. In this review, we summarized the presented progresses of microwave gas sensors, including the performance of the different materials and propagative structures, as well as their sensitive signal. We have attempted to explain the sensitive mechanism of these materials, discuss the function of the propagative structure, and analyze the sensitive signal extracted from the parameters of electromagnetic waves. Finally, the challenges in the study of sensitive materials and propagative structures used in microwave gas sensors are analyzed. It is clear from the published literatures that microwave transduction provide a new route for gas detection, and it is expected that commercial manifestation will occur. The future research on microwave gas sensors will continue to exploit their sensitive materials and propagative structure for different applications. The understanding of the microscopic polarization interactions with gases will assist in and guide the fabrication of high-performance microwave gas sensors in the future.

Keywords: gas sensor, microwave transduction, polarization, propagative structure, electromagnetic wave

OPEN ACCESS

Edited by:
Xiaogan Li,
Dalian University of Technology (DUT), China

Reviewed by:
Jianxin Yi,
University of Science and Technology of China, China
Ding Wang,
University of Shanghai for Science and Technology, China

****Correspondence:***
Yangong Zheng
zhengyangong@nbu.edu.cn
Changzhou Hua
huachangzhou@nbu.edu.cn

Specialty section:
This article was submitted to Functional Ceramics, a section of the journal Frontiers in Materials

Received: *16 March 2019*
Accepted: *17 April 2019*
Published: *03 May 2019*

Citation:
Li F, Zheng Y, Hua C and Jian J (2019) Gas Sensing by Microwave Transduction: Review of Progress and Challenges. Front. Mater. 6:101. doi: 10.3389/fmats.2019.00101

INTRODUCTION

In the recent decade, increasing interest in detecting gases and their composition have resulted in intensive studies applied to various fields, such as industrial emission control, household security, medical diagnostics, and environmental monitoring (Korotcenkov, 2012). Generally, gas sensing is the process of converting gas sensitive interactions to a measurable signal, which involves two different processes (Yamazoe and Shimanoe, 2009). The first process is to sense gas via physical or chemical interactions with sensitive materials, which is called the sensitive process; the second process is to transduce the interactions to signals, which is called transduction. Various transduction technologies have been employed in the gas sensors, e.g., conductometric transduction converts redox reactions of gas molecules into electrical signals (Xing et al., 2015; Wang et al., 2019); optical transduction utilizes infrared spectral characteristics of gas molecules (Babeva et al., 2017); mass transduction measures weight of gas molecules using a microbalance, and converts it to a vibration frequency signal (Tu et al., 2015; Lv et al., 2018); electrochemical

transduction is based on electron transfer between electrolyte and gas molecules (Zheng et al., 2015).

Although the performance parameters (sensitivity, selectivity, and stability) of gas sensors based on conventional transduction were constantly improved (Moos et al., 2009; Kim et al., 2013), the use of the electromagnetic waves for sensing purposes is an actively researched approach with considerable potential for commercialization (Alshamma'a et al., 2014). In particular, microwave is an important frequency band for communication and remote sensing applications; it is a fast-growing technology and has been successfully applied in industrial and medical applications (Barochi et al., 2011).

The microwave transduction is based on the dielectric response of sensitive materials incorporated with propagative structures in the presence of gas that is subjected to a microwave signal (Fonseca et al., 2015b). Batteryless and wireless operations are suggested to be the major advantages of microwave gas sensors; however, the lack of fundamental understanding of the sensitive mechanism hinders the development of microwave gas sensors. Several challenges were presented in the study of microwave transduction. There is the need of a review to focus on the presented progress and challenges of microwave gas sensors.

Table 1 summaries the reported microwave gas sensor. This review article will start by describing the working principles of the microwave gas sensor. Then, the current progress will be discussed corresponding to the sensitive material, propagative structure, and sensitive signal. Subsequently, the difficulties and challenges will be discussed. Furthermore, an outlook on the future development of microwave gas sensor will be presented.

WORKING PRINCIPLE OF MICROWAVE TRANSDUCTION

The evolving research on microwave transduction at frequencies ranging from 300 MHz to 300 GHz demonstrates that gas sensing is based on the phenomena of propagation and reflection of an incident electromagnetic wave in sensitive material. As the characteristics (modulus and phase) of the reflected and transmitted electromagnetic waves depend on the physical and chemical properties of the materials, the interactions with gas molecules should modify their permittivity and change the velocity of the electromagnetic waves (El Bouazzaoui et al., 2011). By measuring the variations in the transmitted and reflected microwaves at discrete frequency intervals, the frequency change or attenuation of the incident electromagnetic waves can be linked to the gas sensitive interactions (Huang et al., 2018).

The permittivity ε of a material is a complex quantity; it describes the dielectric polarization of the materials to an applied electric field (Xie et al., 2015). Because there is a lag between the changes in polarization of the materials and the alternating electric field, the permittivity depends on the frequency of the field. According to the Maxwell–Garnett equation, the permittivity of materials is described as follow (Auerbach et al., 2003):

$$\varepsilon - \varepsilon_\infty = \varepsilon' - j\varepsilon'' = \frac{\varepsilon_s - \varepsilon_\infty}{1+\omega^2\tau^2} - j\left(\frac{\omega\tau(\varepsilon_s - \varepsilon_\infty)}{1+\omega^2\tau^2} + \frac{\sigma}{\omega\varepsilon_0}\right) \quad (1)$$

ε_s is the static permittivity, ε_∞ is the permittivity at the high frequency limit, ω is the angular frequency, τ is the characteristic relaxation time, and σ is the conductivity of the material. The real part of the permittivity (ε') represents the energy stored in the material. The imaginary part of the permittivity (ε'') is linked to the conductivity of the material.

The evolution of permittivity with the frequency of electric field indicates the change of dominant polarization process, which is shown in the **Figure 1**. If a polarization process follows the oscillation frequency of the field, its permittivity become dominant; otherwise, it decreases. The averaged time for a polarization process is characteristic relaxation time. Thus, according to the relaxation time from slow to fast, the polarization processes are ionic conduction, dipolar polarization, ionic polarization, atomic polarization, and electronic polarization. Further, there is no clear boundary for different polarizations. When the frequency is above the ultraviolet range, the permittivity approaches the constant ε_0, which is the permittivity of free space.

The permittivity is influenced by the dipolar polarization in the low microwave frequency range and ionic polarization in the high microwave frequency range. The dipolar polarization is orientation of permanent dipoles in materials responsed to electric field, and the ionic polarization is the polarization caused by relative displacements between the positive and negative ions (Mitroy et al., 2010). For microwave gas sensing, the adsorption of polar gas molecules is expected to induce dipole-dipole interactions with the permanent dipole of the materials. These dipole interactions will vary the timescale or strength of the orientation of the permanent dipole and the displacement of ions; consequently, a change in the polarization as well as the permittivity of the materials is demonstrated.

Besides the sensitive materials, the microwave gas sensor requires propagative structures to transmit the microwave (Fonseca et al., 2014). The propagative structure can be classified as non-resonator and resonator depend on the propagation of electromagnetic waves; standing wave transmits in resonator and traveling wave transmits in non-resonator. The non-resonator has simple structure and wide bandwidth; the structure of resonator is designed in a narrow bandwidth, its resonant frequency is stable during measurement, so higher resolution can be achieved for the resonator. There are many geometric structures that are used for microwave gas sensing, e.g., microstrip line, coplanar waveguide, coaxial line, and resonant cavity (**Figure 2**). By designing their geometry, the sensors are operated in different microwave ranges.

Sensitive materials are deposited in various forms on the propagative structures. In general, there are two forms, which are surface film and volumic bulk. The surface film is formed by depositing sensitive materials on the propagative structure, and volumic bulk uses sensitive materials to replace the substrate of the propagative structure. Although gas diffusion in the volumic bulk requires a longer time than the surface film, the volumic bulk has a larger cross-sectional area to interact with the microwave. Various procedures using sensors are implemented in accordance with the chosen sensitive materials, propagative structures, and their integrated forms (surface film or volumic bulk).

TABLE 1 | Summary of microwave gas sensors on their materials, targeted gas, propagative structure and signal.

	Materials	Targeted gas	Propagative structure	Signal	References
Metal oxide	TiO_2	Ammonia	Microstrip line	S parameter (S11)	Bailly et al., 2016a
	TiO_2	Ammonia	Microstrip interdigital capacitor	S parameter (S11 and S21)	Bailly et al., 2016b
	Fe_2O_3	Ammonia	Coplanar waveguide	Reflection coefficient	Bailly et al., 2016c
	$SrTiO_3$	Ethanol and toluene	Transmission coaxial line	Reflection coefficient	Rossignol et al., 2010
	SnO_2	Hydrogen	Waveguide phase shifter	S parameter (S21)	Fei et al., 2011
	CuO, SnO_2 and TiO_2	Acetone, ethanol and methanol	a single coupled-line section	Transmission coefficient	Rydosz et al., 2019
Zeolite	Silicalite-1 and NaX	Toluene	Coplanar waveguide	Reflection coefficient	Fonseca et al., 2014
	Zeolite 13X	Carbon dioxide and methane	Microstrip resonator	Resonant frequency shift	Zarifi et al., 2017
	Zeolite Y	Toluene	Coplanar waveguide	Reflection coefficien	Fonseca et al., 2015a
	Zeolite 13X and MOF	Carbon dioxide	Planar active-resonator	Resonant frequency shift	Zarifi et al., 2018
	Fe-zeolite	Ammonia	Planar microstrip ring	S parameter (S11)	Bogner et al., 2017
	ZSM-5	Ammonia	Resonant cavity	S parameter (S11)	Reiß et al., 2011
Organic	CNTs	Ammonia	Microstrip circular disk	Resonant frequency shift	Chopra et al., 2002
	CNTs	Methane	Coplanar waveguide	S parameter (S21)	Cismaru et al., 2016
	PDMS	Acetone	Coplanar strip	Resonant frequency shift	Zarifi et al., 2015b
	Cobalt phthalocyanine	Ammonia and toluene	Microstrip line	Reflection coefficient	Rossignol et al., 2012
	Cobalt phthalocyanine	Ammonia	Coplanar grounded waveguide	Reflected coefficient	Barochi et al., 2011
	Activated carbon and polymer-based bead	Butoxyethanol	Resonant cavity	Resonant frequency shift	Zarifi et al., 2015a
	PEDOT–CNTs	Ethanol	Microstrip line	S parameter (S21)	Bahoumina et al., 2017
	Cobalt phthalocyanine	Ammonia and toluene	Coplanar waveguide	Reflection coefficient	Rossignol et al., 2013
	CNTs	Nitrogen	Coplanar waveguide	S parameter (S21)	Dragoman et al., 2007
	Polymethylsiloxane-graft-phthalocyanine	Acetone	Six-port reflectometer	S parameter (S11)	Staszek et al., 2017
	Pt-decorated reduced graphene oxide	Hydrogen	Antenna	Reflectance properties	Lee et al., 2015
	Carboxyl group functionalized polypyrrole	Ammonia and acetic acid	Antenna	Reflectance properties	Jun et al., 2016
	Graphene	Nitrogen dioxide	Dielectric resonator	Central frequency, linewidth (full width at half maximum)	Black et al., 2018
	Fluoroalcohol polysiloxanes and polyhydroxyethyl-methacrylate	Acetone and isopropanol	Dielectric resonant	S parameter (S11)	Chen and Mansour, 2018
	Beaded activated carbon	VOCs	Open-ended resonator coupled to input/output microstrip transmission lines	Resonant frequency	Fayaz et al., 2019

SENSITIVE MATERIALS

So far, metal oxide, zeolite, and organic, which are the conventional sensing materials, were applied in the microwave gas sensors to detect gaseous compounds such as volatile organic compound, NH_3, CO_2, CO, O_2, or H_2. Although the gas sensitive reactions of these materials under conductometric transduction were extensively studied, the link between the dipole reaction and microwave signals is still unknown.

Metal Oxides

Since the gas sensing of oxides is based on surface interactions with gas molecules, nano-oxides with high surface area present advantage on enhancing sensitivity. TiO_2 and α-Fe_2O_3 nanoparticles in the form of a surface film on the waveguide

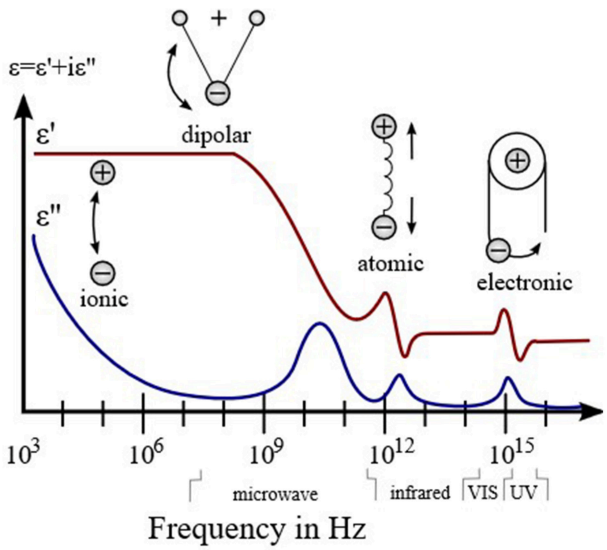

FIGURE 1 | Dielectric permittivity spectrum over a wide range of frequencies. Various processes are labeled in the image.

substrate were applied for NH_3 sensing (Bailly et al., 2016a,b,c); the principle of measurement is shown in **Figure 3A**. The permittivity of oxides changed when exposed to NH_3 at room temperature, which caused the variation of the reflected coefficient (S11) and the transmitted coefficient (S21). Although an increase in the conductivity of TiO_2 and α-Fe_2O_3 with ammonia exposure were reported in Moseley and Williams (1990), the authors assumed that the formation of NH_4^+ species on the surface of the oxides was the source for the permittivity change; however, the relation of NH_4^+ to the decrease in permittivity is unclear. Furthermore, the effect of the shape of oxides involved in microwave transduction was studied. It was observed that different morphologies presented a significant difference in behavior upon ammonia adsorption; the sensitive responses of different morphologies are shown in **Figure 3B**. The crystal planes with high surface energy and abundant unsaturated active sites usually serve as a promising platform to interact with gas molecules (Gao and Zhang, 2018). Controlled morphology with exposed high energy facets are still valid for the metal oxides in microwave transduction (Bailly et al., 2016c).

Other metal oxides such as SnO_2 and $SrTiO_3$ presented decreasing permittivity to hydrogen, ethanol, and toluene in microwave transduction (Rossignol et al., 2010; Fei et al., 2011). In the literatures, SnO_2 and $SrTiO_3$ employed volumic bulk form; a small concentration of hydrogen was detected by filling SnO_2 in the substrate of a waveguide phase shifter. Increasing the cross-sectional area of sensitive material in electromagnetic wave could be a way for enhancing the sensitivity of the microwave sensor.

Zeolites

Bulk adsorption is expected to increase the influence of gas molecule on the overall permittivity of sensitive materials; thus, microporous and mesoporous materials were applied in the microwave gas sensors.

Zeolite is crystalline aluminosilicates with pores and channels of molecular dimensions. Approximately 190 zeolites with distinct framework topologies have been reported (Zheng et al., 2012). Four commonly used zeolites are shown in **Figure 4**. The aluminosilicate framework of zeolites is negative owing the Al^{3+} presented in the network of $[SiO_4]^{4-}$ tetrahedra; thus, a cation is introduced to balance the negative charge around Al^{3+} sites; the extra-framework cations are mobile in the channel of zeolites as the zeolites are ionic conductors (Xu et al., 2006; Sahner et al., 2008).

Because of the large volume of pores in the zeolites, the accessible volume for gas molecules is from 5 to 30%. The overall permittivity of zeolite is contributed by the aluminosilicate framework (ε_{frame}) and pores (ε_{pore}), so the filling of gas molecules into the pores can alter the permittivity of the zeolites. The change of the permittivity of the pores based on bulk gas adsorption is described as follow:

$$\varepsilon_{pore} = \varepsilon_n + 3f\varepsilon_n \frac{\varepsilon_g - \varepsilon_n}{2\varepsilon_n + \varepsilon_g - f(\varepsilon_g - \varepsilon_n)} \quad (2)$$

where ε_n is the initial permittivity of the pores, which usually is 1 (N_2, $\varepsilon_{N_2} = 1$), ε_g is the permittivity of the gas molecules, f is the filling factor ($f = V_g/V_{pore}$),V_g is the volume of adsorbed gas molecules, and V_{pore} is the volume of the pores. Thus, increasing the permittivity of zeolite can be achieved by adsorbed polar gas. Several studies have observed this performance (Zarifi et al., 2017). The evolution of gas adsorption in zeolite and the permittivity change are shown in **Figure 5**.

Besides the physical adsorption, the coordinatively unsaturated metal sites in the zeolite are also sites for gas adsorption by the electrostatic process (Zarifi et al., 2018). Therefore, more unsaturated metal sites in the sensitive material induce higher adsorption capacity, and this demonstrated a larger sensitive response.

The amplitude variations at resonant frequencies were observed for zeolite Y on coplanar waveguides for toluene exposure in the range of 2–10 GHz (Fonseca et al., 2015a). The variable orientations (increasing or decreasing orientations) of the signals differed at different resonant frequencies. Although the amplitude variation of resonant frequency originated from the permittivity change of zeolite, different variable orientations revealed complicated interactions of zeolite with gas molecules.

For the dipole interaction of zeolites with gas molecules, scarce characterizations were presented. Based on the ionic model of zeolite, the mobile cation was localized in the center of a neighboring tetrahedron $[AlO_4]^-$, and their dipole ($\mu 1$) was parallel to the electric field vector. When gas molecules enter into the cavity, they will perturb the original electric field, the cation will jump a distance and orient itself to a new dipole moment ($\mu 2$) (**Figure 6**) (Wei and Hillhouse, 2006; Nicolas et al., 2008). This dipole change could modify the permittivity of zeolite, and the cations at different sites in zeolitic framework are expected to introduce dipole interactions with different strength. Detailed characterizations are needed to verify the dipole interaction.

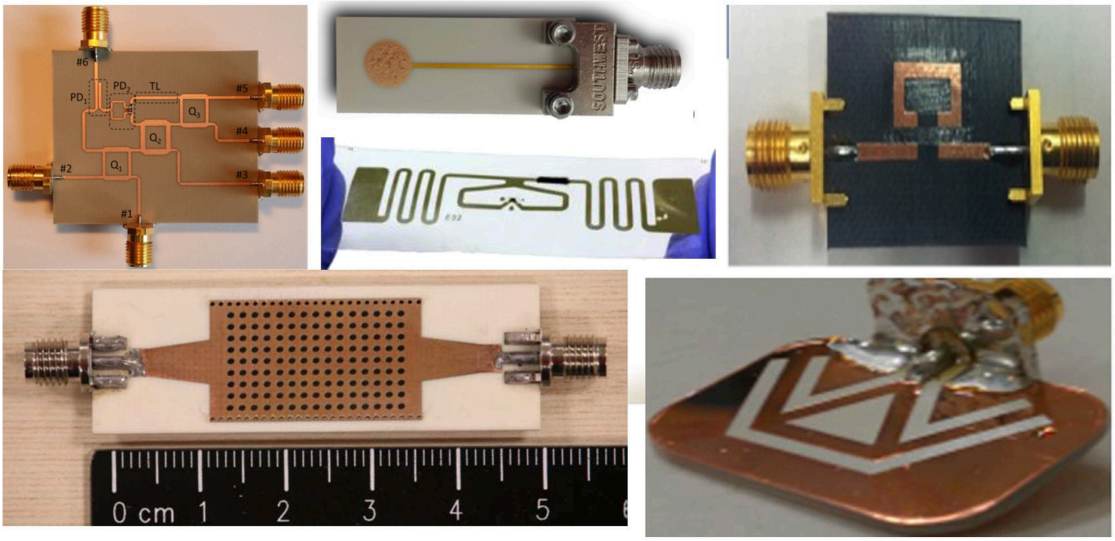

FIGURE 2 | Various propagative structures applied in microwave gas sensors. Reproduced with permissions from Fei et al. (2011), Fonseca et al. (2014), Zarifi et al. (2016), Bogner et al. (2017), and Staszek et al. (2017). Copyright 2014, 2016, 2017 Elsevier; copyright 2016 American Chemical Society; copyright 2016 IEEE.

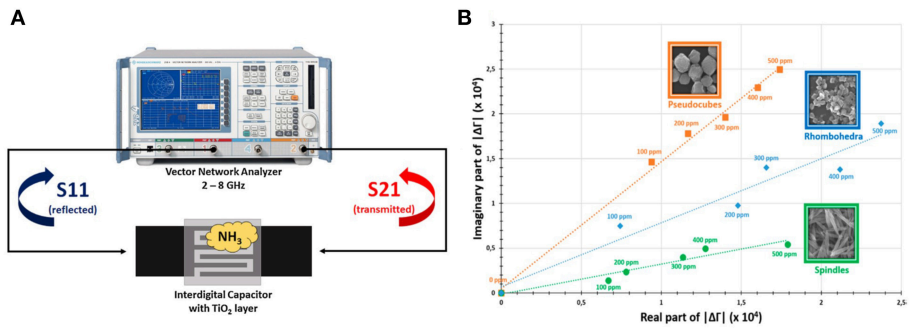

FIGURE 3 | (A) Principle of microwave transduction applied to reflection/transmission measurements, **(B)** response and recovery times for a microwave sensor exposed to ammonia. Reproduced with permissions from Bailly et al. (2016b,c). Copyright 2016 Elsevier; copyright 2016 American Chemical Society.

Organics

Carbon materials and polymers were widely applied as gas sensitive materials. Carbon nanotubes (CNTs) and graphene have high surface areas, and their properties can be modified by simple chemical processes (Kauffman and Star, 2008; Yuan and Shi, 2013).

It is well-known that the conductivity of carbon nanotubes decreases when exposed to NH_3 and CH_4 (Kauffman and Star, 2008). However, frequency shifts were observed for a resonator based on carbon nanotubes under NH_3 or CH_4 environment (Chopra et al., 2002; Occhiuzzi et al., 2011; Cismaru et al., 2016). The conductivity change, which is the imaginary part of permittivity, can vary the amplitude of resonant frequency, but the frequency shift indicates a change of the real part of permittivity. A possible explanation is that gas molecules interact with carbon nanotubes to create bound charges resulting in changes in the real part of permittivity of carbon nanotubes.

Noble metal loading on carbon materials can effectively enhance the sensitivity of a sensor. Pt loaded graphene can detect H_2 in concentrations as minimal as 1 ppm in the frequency range from 880 to 940 MHz (Lee et al., 2015), which is shown in the **Figure 7**. The large surface area of graphene and uniform Pt decoration provide an excellent platform for gas adsorption and dielectric response. However, the mechanism of permittivity change for the nano-composition of Pt/graphene under H_2 is rarely discussed.

Many advantages lead to polymers being a good candidate for gas sensing, such as low cost, high sensitivity at low temperature, good gas permeability, flexibility, simple synthesis, and environmental stability (Kubersky et al., 2015; Wang et al., 2017). In microwave transduction, a physically adsorbed gas molecule can diffuse into polymer and swell its volume, which contribute to permittivity change (Zarifi et al., 2015a,b). With the support of a six-port reflectometer, the limit of detection of copolymer Pc film to acetone was identified to be 0.5 ppm

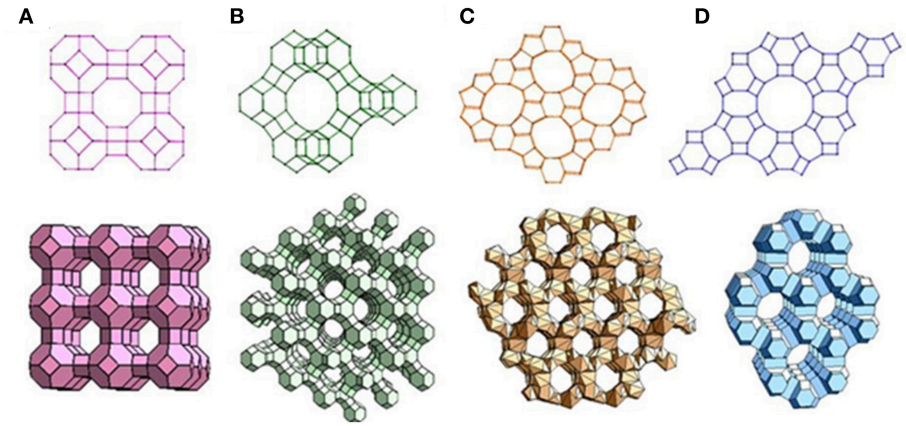

FIGURE 4 | Representative zeolite frameworks (with pore openings). **(A)** Zeolite A (3D, 4.2 Å); **(B)** zeolite Y (3D, 7.4 Å); **(C)** Zeolite L (1D, 7.1 Å); **(D)** ZSM-5 (2D, 5.3 × 5.6 Å, 5.1 × 5.5 Å). D indicates the dimensions of the channel system. Reproduced from Zheng et al. (2012).

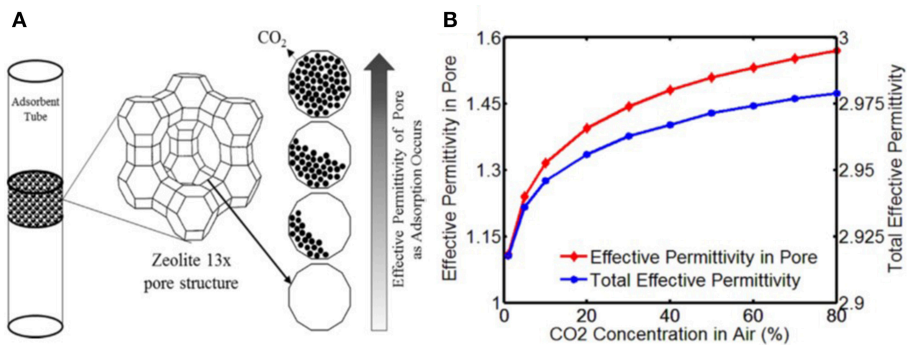

FIGURE 5 | (A) Evolution of CO_2 adsorption in Zeolite X and the corresponding permittivity change, **(B)** simulation results of concentration effect on permittivity of pores and adsorbents. Reproduced with permission from Zarifi et al. (2017). Copyright 2017 Elsevier.

(Staszek et al., 2017). The dynamic change of S11 for different acetone concentrations are shown in the **Figure 8**. Except for the physical adsorption of gas molecules, the conductivity of polymer also results in a permittivity change. The composition of conducting polymer and carbon nanotubes were explored for ethanol detection, and insertion losses and frequency shifts on the resonant frequency were observed (Bahoumina et al., 2017). A conducting polymer with a functional group exhibited high sensitivity to ammonia and acetic acid. The authors observed that the increase in density of carboxylic functional groups enhanced the sensitivity (Jun et al., 2016), which indicate that the dipole of functional groups are involved in the dielectric response.

Metal phthalocyanines are sensitive to various gases owing to their catalyst. The redox with gas molecules can not only modify their density of charge carriers and conductivity, but also the permittivity of material (Bai and Shi, 2007). Cobalt phthalocyanine (CoPc) was applied for toluene and ammonia detection on various substrate (Barochi et al., 2011; Rossignol et al., 2012, 2013). The real and imaginary part of the reflected coefficient changed when exposed to NH_3, except for the conductivity change. The surface dipoles or electronic structure of CoPc is supposed to vary through the interactions with gas molecules; however, this is merely a hypothesis.

In summary, the mechanism of sensitive materials in microwave gas sensor is rather complicated. Only conductivity change is not sufficient to explain the variation of complex permittivity. So far, lack of experimental evidences for dipoles and ionic polarization in microwave range prevents further discussion. However, there are two strategies are suggested for increasing the sensitivity of materials. Increasing adsorption capacity of materials is a valid method to detect polar gas molecules, higher adsorption capacity could leads to larger dielectric response of materials. Thus, microporous and mesoporous materials will be effective materials for microwave gas sensor. The other aspect is the polarized species in materials which can interact with targeted gas molecules. For example, hydroxide radicals could bind NH_3 to form dipoles (NH_4^+), which modify the polarization of material; lewis acids can interact with reducing gases that form intermediate dipoles or annihilate Lewis sites, which change the permittivity of materials. Well-designed polar species in materials devoted for gas sensing are required. At the same time, increasing the density of

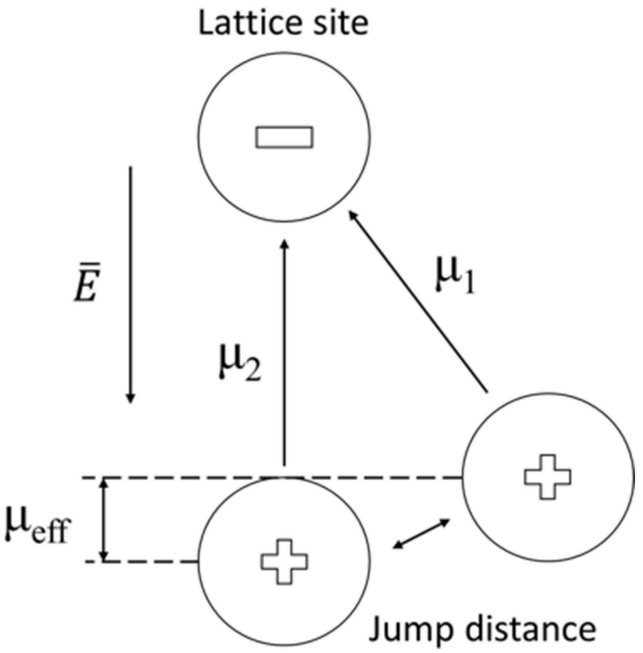

FIGURE 6 | Schematic for dipole moment between cation and lattice site by a change of place of the cation in a zeolite channel.

polarized species can greatly improve the sensitivity. Moreover, the morphology of oxides is observed to have effect on dielectric response, different density of defects and dangle groups are supposed to the reason.

PROPAGATIVE STRUCTURES

A propagative structure is used to transmit electromagnetic waves and supports the sensitive materials for adapting in different environments. Its quality factor determines the resolution of the sensor. The quality factor is a ratio of energy loss related to the stored energy of the propagative structures; a high quality factor indicates a resonance profile with narrow resonator's bandwidth relative to its center frequency (Zarifi et al., 2015c).

The microwave resonant cavity has an significantly high quality factor, which increases the resolution of the sensor, but it only works at a single frequency (Tooski, 2010, 2011). The planar microstrip line, coplanar waveguide, and interdigital capacitor are the common structures employed in the experiments on microwave sensors because of their merits, such as simple structure, compact size, low-cost manufacturing, large operation frequency range, and simplicity in integrating in an antenna for remote sensing. For precise measurement, an active microstrip line and six-port reflectometer were applied to increase the quality factor of the sensors. Their resonance peaks were sharp and a small frequency shift could be easily detected as shown in **Figure 9**.

To cancel the influence of temperature or humidity on the electromagnetic behavior, the differential method was proposed by using a reference resonator (Bahoumina et al., 2017; Huang et al., 2018). The response is the difference between the sensitive resonator and the reference resonator with a blank or with materials with known permittivity. The configuration of differential resonators is shown in **Figure 10**. The differential method ensures a low variance signal with good repeatability.

The microwave cavity waveguide provided a powerful technique for measuring NH_3 loading in the catalyst of a diesel engine (Dietrich et al., 2017). The catalyst itself was the sensitive material, and the catalyst canning was the propagative structure. A planar propagative structure was also applied in non-contact mode for monitoring of the adsorbent; the adsorbent in the gas tube was above the planar microstrip line, which is shown in **Figure 11**. The permittivity change of adsorbent influenced the electromagnetic waves propagated in the microstrip line (Reiß et al., 2011; Zarifi et al., 2015a, 2017). This contactless technique is attractive for dangerous and toxic gas detection as the sensing platform does not need to be in the gas-flowing medium.

SIGNAL ANALYSIS

The gas sensing tests of the microwave sensors were carried out by vector network analyzer (VNA). The sensitive signal was derived from various parameters of the VNA measurement. Despite the lack of permittivity measurements of materials in microwave range, the permittivity of sensitive materials applied in microwave gas sensors were distributed over a wide range, polymers demonstrated measurements between 2 and 5, and the permittivity of oxides and zeolites could be adjusted from 3 to 15. The materials with lower initial permittivity are assumed to possess higher sensitivity for small permittivity changes, because the dielectric response is usually calculated by the ratio of the permittivity change and the initial value. In most microwave gas sensors, the reflection characteristics of electromagnetic waves are extracted as signals, which include the S parameter, reflection coefficient, return loss, and input impedance. All these parameters describe the degree of mismatch in impedance. No comparative study about different parameters on gas sensing has been conducted.

The alteration of parameters can be classified as a frequency shift in the frequency spectra or magnitude variation at a fixed frequency. To analyze the response and recovery time, each parameter was measured at a fixed frequency with the evolution of time. The time taken by a sensor to achieve 90% of the total parameter change is defined as response time in the case of adsorption or the recovery time in the case of desorption as shown in **Figure 12a** (Zheng et al., 2015; Bailly et al., 2016b). Combining both the real and imaginary parts of a parameter is considered as a powerful tool to assess the overall performance of a sensor (Rossignol et al., 2013). **Figures 12b,c** present the real vs. imaginary plot for S11 measurement. Here, each concentration outlines a full ellipsoid, whose radius is correlated to the concentration of ammonia. The obtained ellipsoids could facilitate the optimization of the sensor performance in predicting the concentration. Besides optimizing

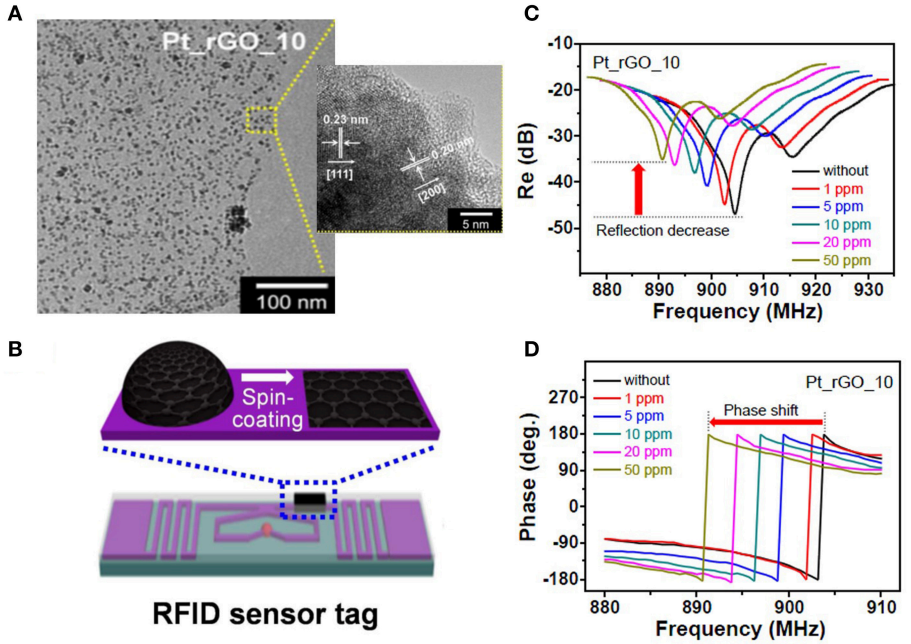

FIGURE 7 | (A) Transmission electron microscopy images of Pt-decorated reduced graphene oxide (Pt_rGO), **(B)** Pt_rGO-immobilized radio-frequency identification sensor tag, **(C,D)** change in the reflectance properties and measured reflection phase of different Pt_rGO-based wireless sensors as a function of the hydrogen gas concentration. Reproduced with permission from Lee et al. (2015). Copyright 2015 American Chemical Society.

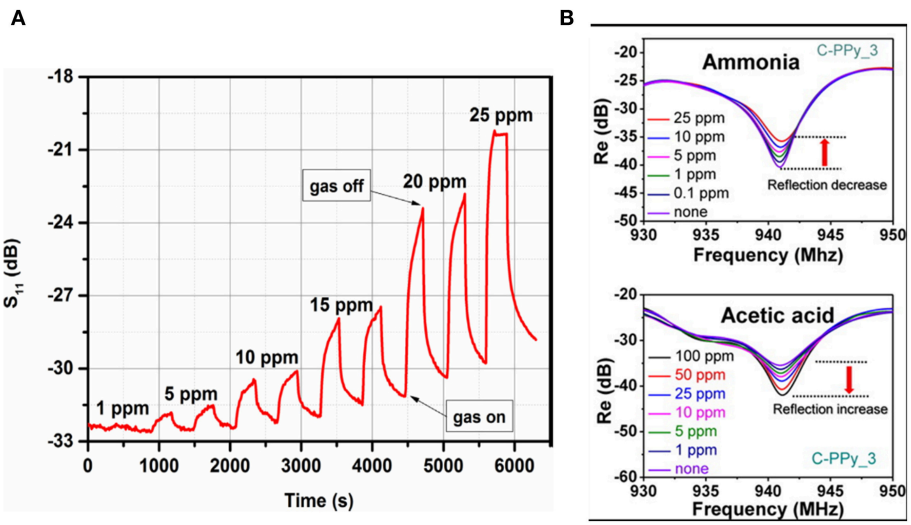

FIGURE 8 | (A) Magnitude of reflection coefficient S11 measured at the resonant frequency under exposure to acetone in the 0–25 ppm concentration range, **(B)** change in the reflectance properties of different concentrations of ammonia and acetic acid. Reproduced with permissions from Jun et al. (2016) and Staszek et al. (2017). Copyright 2017 Elsevier; copyright 2016 American Chemical Society.

the sensor performance, the imaginary part of the parameter as a function of the real part shows a set of aligned points for a concentration at fixed frequency (Barochi et al., 2011). This assists the discriminated power of sensors in concentration prediction through the use of pattern recognition algorithms (Chen et al., 2017).

OUTLOOK

We have demonstrated the presented progress of microwave gas sensors. This is a considerably vigorous and fast evolving field and continuous rapid growth can be expected with advances in materials and device fabrication, characterization, and signal

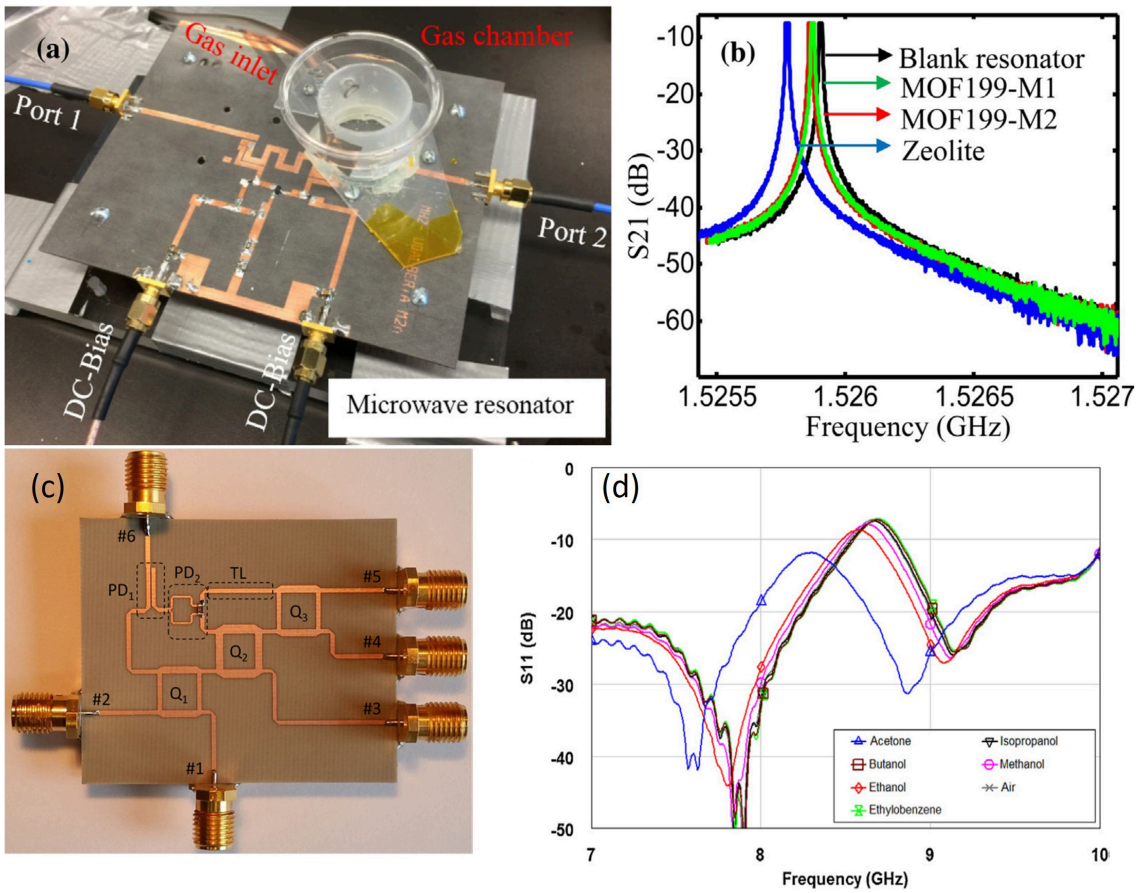

FIGURE 9 | (a) Experimental setup with the microwave active resonator sensor, **(b)** resonant profile (S21) of the sensor based on the active resonator, **(c)** photograph of the fabricated six-port reflectometer, **(d)** resonant profile S11 of the sensor based on the six-port reflectometer. Reproduced with permissions from Staszek et al. (2017) and Zarifi et al. (2018). Copyright 2017, 2018 Elsevier.

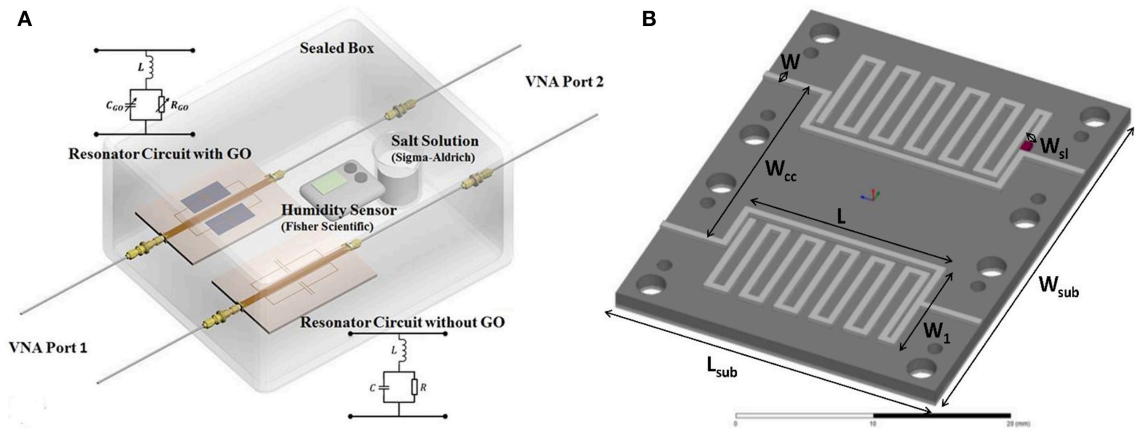

FIGURE 10 | (A) Separated sensitive resonator and reference resonator, **(B)** dimensions and geometry of differential sensor based on two stub resonators. Reproduced with permissions from Bahoumina et al. (2017) and Huang et al. (2018). Copyright 2017 Elsevier.

processing. The use of the novel microwave transduction process in a gas sensor is still in its infancy. Based on the examples discussed in the review, most sensors were developed to serve the environmental industry; however, important parameters for gas sensors, such as selectivity, sensitivity, and long-term stability as well as reproduction were not satisfactorily reported

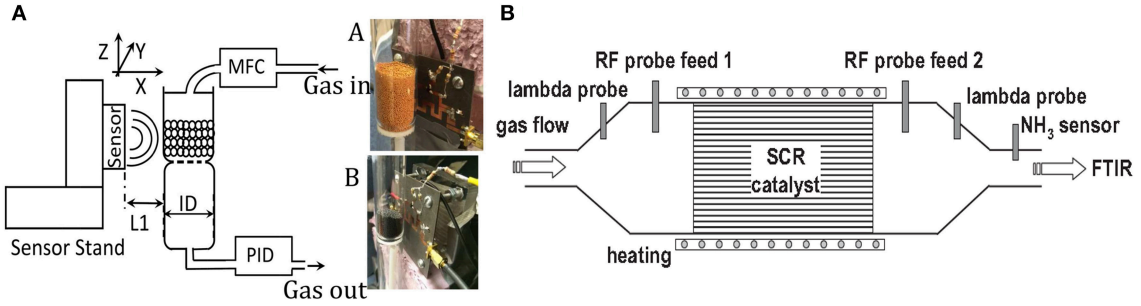

FIGURE 11 | (A) Schematic of the measurement setup of the sensor to perform noncontact gas sensing, **(B)** illustration of the setup for the resonance cavity of catalyst. Reproduced with permissions from Zarifi et al. (2015a) and Dietrich et al. (2017). Copyright 2017 John Wiley and Sons; copyright 2015 AIP Publishing.

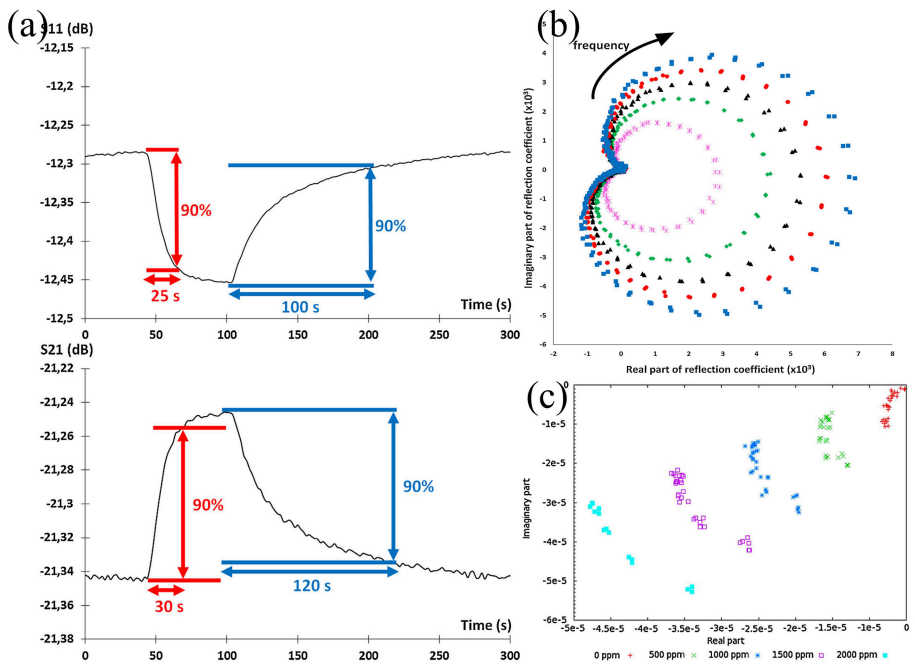

FIGURE 12 | (a) Evolution of S-parameters during the gas sensing, and determination of response and recovery times, **(b)** imaginary part as a function of real part of S11 for different gas concentrations between 2 and 2.5 GHz, frequency evolution follows the clockwise direction, **(c)** imaginary part as a function of real part of signal in linear scale at fixed frequency. Reproduced with permissions from Rossignol et al. (2013) and Bailly et al. (2016b). Copyright 2013, 2016 Elsevier.

in the literatures. Other relevant aspects include operational conditions such as temperature, humidity, and packaging. It is now necessary to improve our fundamental knowledge on microwave gas sensors and consider the future trends. Although we may overlook certain important issues, it is useful to consider which developments and challenges may deserve careful scrutiny.

A key challenge is the gas sensitive mechanism for different materials pertaining to permittivity change. The interactions of materials with gas molecules related to the conductivity change were extensively studied as conductometric gas sensors are the most popular in recent decades. Nevertheless, it is unsuitable for microwave gas sensors. The signal of the microwave gas sensor originates from the permittivity change. However, to the best of our knowledge, no study has reported the permittivity change of materials because of the complicated methods required for measuring permittivity in the microwave range. Therefore, designing a novel experiment is necessary for directly measuring the permittivity changes for gas sensing. The permittivity reflects various polarizations and the gas sensitive process is related to the polarization processes. A fundamental study is urgently required to understand the relation between the polarization changes of materials in gas sensing. Consequently, "permittivity synthesis" can become possible. This introduces the possibility of adapting the desired dielectric interactions with gas molecules by ordering the proper atoms and molecules into specified materials.

The dielectric properties of materials in gas sensing attracted the most attention, but the design of the propagative structure is important for practical applications. Propagative structures

with high sensitivity can be designed, as long as the permittivity of materials is measured. High quality factor is also desired for precise measurement, but the permittivity change in gas sensing will degrade the quality factor. The degrading quality factor narrows the test range of gas concentrations. Simultaneously, the bandwidth impacts the concentration range of sensors. Therefore, the contradiction between high quality factor and wide bandwidth requires balanced optimization. Various functions are demanded for better suitability in different fields. The omnidirectional polarized sensor is desired for the ease of use in wireless measurements. The coupling effects of electromagnetic waves is a critical issue for developing a sensor array. Flexibility and compact size maybe necessary for integrating the sensors into wearable devices. Digestible antenna is required for sensing in human body. Furthermore, the resonant cavity method lends itself well for *in situ* and non-contact measuring gas adsorption of materials in pipe.

In conclusion, there appears to be considerable advantages for microwave transduction in gas sensing. There are several fundamental challenges that need to be addressed before microwave gas sensors can become viable candidates for commercial implementation. The future of microwave gas sensors looks bright, and continued progress in this field will overcome the current challenges and lead to a class of sensors that can be used in a wide range of environments and applications.

AUTHOR CONTRIBUTIONS

YZ and CH conceived the paper. FL and YZ analyzed the references and wrote the paper. JJ reviewed the paper.

FUNDING

This work was supported by the National Natural Science Foundation of China [grant numbers 61871245]; the Natural Science Foundation of Ningbo Municipality [grant number 2018A610021], and K. C. Wong Magna Fund in Ningbo University.

REFERENCES

Alshamma'a, A., Mason, A., and Korostynska, O. J. S. R. (2014). Microwave sensors for the non-invasive monitoring of industrial and medical applications. *Sens. Rev.* 34, 182–191. doi: 10.1108/SR-11-2012-725

Auerbach, S. M., Carrado, K. A., and Dutta, P. K. (2003). *Handbook of Zeolite Science and Technology*. New York, NY: Marcel Dekker Inc. doi: 10.1201/9780203911167

Babeva, T., Andreev, A., Grand, J., Vasileva, M., Karakoleva, E., Zafirova, B. S., et al. (2017). Optical fiber-Ta2O5 waveguide coupler covered with hydrophobic zeolite film for vapor sensing. *Sens. Actuat. B-Chem.* 248, 359–366. doi: 10.1016/j.snb.2017.03.157

Bahoumina, P., Hallil, H., Lachaud, J. L., Abdelghani, A., Frigui, K., Bila, S., et al. (2017). Microwave flexible gas sensor based on polymer multi wall carbon nanotubes sensitive layer. *Sens. Actuat. B Chem.* 249, 708–714. doi: 10.1016/j.snb.2017.04.127

Bai, H., and Shi, G. (2007). Gas sensors based on conducting polymers. *Sensors* 7, 267–307. doi: 10.3390/s7030267

Bailly, G., Harrabi, A., Rossignol, J., Domenichini, B., Bellat, J. P., Bezverkhyy, I., et al. (2016a). Influence of the design in microwave-based gas sensors: ammonia detection with titania nanoparticles. *Proc. Eng.* 168, 264–267. doi: 10.1016/j.proeng.2016.11.185

Bailly, G., Harrabi, A., Rossignol, J., Stuerga, D., and Pribetich, P. (2016b). Microwave gas sensing with a microstrip interDigital capacitor: detection of NH_3 with TiO_2 nanoparticles. *Sens. Actuat. B Chem.* 236, 554–564. doi: 10.1016/j.snb.2016.06.048

Bailly, G., Rossignol, J., Fonseca, B. D., Pribetich, P., and Stuerga, D. (2016c). Microwave gas sensing with hematite: shape effect on ammonia detection using pseudocubic, rhombohedral and spindle-like particles. *ACS Sens.* 1, 656–662. doi: 10.1021/acssensors.6b00297

Barochi, G., Rossignol, J., and Bouvet, M. (2011). Development of microwave gas sensors. *Sens. Actuat. B Chem.* 157, 374–379. doi: 10.1016/j.snb.2011.04.059

Black, N. C. G., Rungger, I., Li, B., Maier, S., Cohen, L. F., Gallop, J. C., et al. (2018). Adsorption dynamics of CVD graphene investigated by a contactless microwave method. *2D Mater.* 5:035024. doi: 10.1088/2053-1583/aac231

Bogner, A., Steiner, C., Walter, S., Kita, J., Hagen, G., and Moos, R. (2017). Planar microstrip ring resonators for microwave-based gas sensing: design aspects and initial transducers for humidity and ammonia sensing. *Sensors* 17:2422. doi: 10.3390/s17102422

Chen, W. T. S., and Mansour, R. R. (2018). Miniature gas sensor and sensor array with single- and dual-mode RF dielectric resonators. *IEEE Trans. Microw. Theory Tech.* 66, 1–8. doi: 10.1109/TMTT.2018.2854551

Chen, Z., Zheng, Y., Chen, K., Li, H., and Jian, J. (2017). Concentration estimator of mixed VOC gases using sensor array with neural networks and decision tree learning. *IEEE Sens. J.* 17, 1884–1892. doi: 10.1109/JSEN.2017.2653400

Chopra, S., Pham, A., Gaillard, J., Parker, A., and Rao, A. M. (2002). Carbon-nanotube-based resonant-circuit sensor for ammonia. *Appl. Phys. Lett.* 80, 4632–4634. doi: 10.1063/1.1486481

Cismaru, A., Aldrigo, M., Radoi, A., and Dragoman, M. (2016). Carbon nanotube-based electromagnetic band gap resonator for CH4 gas detection. *J. Appl. Phys.* 119, 1801–1804. doi: 10.1063/1.4944708

Dietrich, M., Hagen, G., Reitmeier, W., Burger, K., Hien, M., Grass, P., et al. (2017). Radio-frequency-based NH_3-selective catalytic reduction catalyst control: studies on temperature dependency and humidity influences. *Sensors* 17:1615. doi: 10.3390/s17071615

Dragoman, M., Grenier, K., Dubuc, D., Bary, L., Plana, R., Fourn, E., et al. (2007). Millimeter wave carbon nanotube gas sensor. *J. Appl. Phys.* 101:106103. doi: 10.1063/1.2734873

El Bouazzaoui, S., Achour, M. E., and Brosseau, C. (2011). Microwave effective permittivity of carbon black filled polymers: Comparison of mixing law and effective medium equation predictions. *J. Appl. Phys.* 110:074105. doi: 10.1063/1.3644947

Fayaz, M., Jahandar Lashaki, M., Abdolrazzaghi, M., Zarifi, M. H., Hashisho, Z., Daneshmand, M., et al. (2019). Monitoring the residual capacity of activated carbon in an emission abatement system using a non-contact, high resolution microwave resonator sensor. *Sens. Actuat. B Chem.* 282, 218–224. doi: 10.1016/j.snb.2018.11.038

Fei, Y., Yu, H. X., Bo, Z., Ying, Z., and Zhu, Z. X. (2011). "Substrate integrated waveguide phase shifter," in *International Conference on Electronics* (Ningbo: IEEE).

Fonseca, B. D., Rossignol, J., Bezverkhyy, I., Bellat, J. P., Stuerga, D., and Pribetich, P. (2014). VOCs detection by microwave transduction using zeolites as sensitive material. *Proc. Eng.* 87, 1019–1022. doi: 10.1016/j.proeng.2014.11.334

Fonseca, B. D., Rossignol, J., Bezverkhyy, I., Bellat, J. P., Stuerga, D., and Pribetich, P. (2015a). Detection of VOCs by microwave transduction using dealuminated faujasite DAY zeolites as gas sensitive materials. *Sens. Actuat. B Chem.* 213, 558–565. doi: 10.1016/j.snb.2015.02.006

Fonseca, B. D., Rossignol, J., Stuerga, D., and Pribetich, P. J. U. C. (2015b). Microwave signature for gas sensing: 2005 to present. *Urban Clim.* 14, 502–515. doi: 10.1016/j.uclim.2014.10.010

Gao, X., and Zhang, T. (2018). An overview: facet-dependent metal oxide semiconductor gas sensors. *Sens. Actuat. B Chem.* 277, 604–633. doi: 10.1016/j.snb.2018.08.129

Huang, X., Leng, T., Georgiou, T., Abraham, J., Raveendran Nair, R., Novoselov, K. S., et al. (2018). Graphene oxide dielectric permittivity at

ghz and its applications for wireless humidity sensing. *Sci. Rep.* 8:43. doi: 10.1038/s41598-017-16886-1

Jun, J., Oh, J., Shin, D. H., Kim, S. G., Lee, J. S., Kim, W., et al. (2016). Wireless, room temperature volatile organic compound sensor based on polypyrrole nanoparticle immobilized ultrahigh frequency radio frequency identification tag. *ACS Appl. Mater. Interfaces* 8, 33139–33147. doi: 10.1021/acsami.6b08344

Kauffman, D. R., and Star, A. (2008). Carbon nanotube gas and vapor sensors. *Angew. Chem.* 47, 6550–6570. doi: 10.1002/anie.200704488

Kim, I.-D., Rothschild, A., and Tuller, H. L. (2013). Advances and new directions in gas-sensing devices. *Acta Mater.* 61, 974–1000. doi: 10.1016/j.actamat.2012.10.041

Korotcenkov, G. (2012). *Handbook of Gas Sensor Materials Properties, Advantages and Shortcomings for Applications Volume 1: Conventional Approaches.* New York, NY: Springer. doi: 10.1007/978-1-4614-7165-3

Kubersky, P., Syrovy, T., Hamacek, A., Nespurek, S., and Syrova, L. (2015). Towards a fully printed electrochemical NO_2 sensor on a flexible substrate using ionic liquid based polymer electrolyte. *Sens. Actuat. B-Chem.* 209, 1084–1090. doi: 10.1016/j.snb.2014.12.116

Lee, J. S., Oh, J., Jun, J., and Jang, J. (2015). Wireless hydrogen smart sensor based on Pt/graphene-immobilized radio-frequency identification tag. *ACS Nano* 9, 7783–7790. doi: 10.1021/acsnano.5b02024

Lv, Y., Yu, H., Xu, P., Xu, J., and Li, X. (2018). Metal organic framework of MOF-5 with hierarchical nanopores as micro-gravimetric sensing material for aniline detection. *Sens. Actuat. B-Chem.* 256, 639–647. doi: 10.1016/j.snb.2017.09.195

Mitroy, J., Safronova, M. S., and Clark, C. W. (2010). Theory and applications of atomic and ionic polarizabilities. *J. Phys. B Atom. Mol. Opt. Phys.* 43:202001. doi: 10.1088/0953-4075/43/20/202001

Moos, R., Sahner, K., Fleischer, M., Guth, U., Barsan, N., and Weimar, U. (2009). Solid state gas sensor research in Germany - a status report. *Sensors* 9, 4323–4365. doi: 10.3390/s90604323

Moseley, P. T., and Williams, D. E. (1990). A selective ammonia sensor. *Sens. Actuat. B-Chem.* 1, 113–115. doi: 10.1016/0925-4005(90)80183-Z

Nicolas, A., Devautour-Vinot, S., Maurin, G., Giuntini, J. C., and Henn, F. (2008). Location and de-trapping energy of sodium ions in dehydrated X and Y faujasites determined by dielectric relaxation spectroscopy. *Microporous Mesoporous Mater.* 109, 413–419. doi: 10.1016/j.micromeso.2007.05.039

Occhiuzzi, C., Rida, A., Marrocco, G., and Tentzeris, M. (2011). RFID passive gas sensor integrating carbon nanotubes. *IEEE Trans. Microw. Theory Tech.* 59, 2674–2684. doi: 10.1109/TMTT.2011.2163416

Reiß, S., Schönauer, D., Hagen, G., Fischerauer, G., and Moos, R. (2011). Monitoring the ammonia loading of zeolite-based ammonia SCR catalysts by a microwave method. *Chem. Eng. Technol.* 34, 791–796. doi: 10.1002/ceat.201000546

Rossignol, J., Barochi, G., Fonseca, B. D., Brunet, J., Bouvet, M., Pauly, A., et al. (2012). Development of gas sensors by microwave transduction with phthalocyanine film. *Proc. Eng.* 47, 1191–1194. doi: 10.1016/j.proeng.2012.09.365

Rossignol, J., Barochi, G., Fonseca, B. D., Brunet, J., Bouvet, M., Pauly, A., et al. (2013). Microwave-based gas sensor with phthalocyanine film at room temperature. *Sens. Actuat. B-Chem.* 189, 213–216. doi: 10.1016/j.snb.2013.03.092

Rossignol, J., Stuerga, D., and Jouhannaud, J. (2010). Broadband microwave gas sensor: a coaxial design. *Microw. Opt. Technol. Lett.* 52, 1739–1741. doi: 10.1002/mop.25359

Rydosz, A., Brudnik, A., and Staszek, K. (2019). Metal oxide thin films prepared by magnetron sputtering technology for volatile organic compound detection in the microwave frequency range. *Materials* 12:877. doi: 10.3390/ma12060877

Sahner, K., Hagen, G., Schonauer, D., Reiss, S., and Moos, R. (2008). Zeolites–versatile materials for gas sensors. *Solid State Ionics* 179, 2416–2423. doi: 10.1016/j.ssi.2008.08.012

Staszek, K., Rydosz, A., Maciak, E., Wincza, K., and Gruszczynski, S. (2017). Six-port microwave system for volatile organic compounds detection. *Sens. Actuat. B-Chem.* 245, 882–894. doi: 10.1016/j.snb.2017.01.194

Tooski, S. B. (2010). Sense toxins/sewage gases by chemically and biologically functionalized single-walled carbon nanotube sensor based microwave resonator. *J. Appl. Phys.* 107, 14702–14708. doi: 10.1063/1.3277020

Tooski, S. B. (2011). Theoretical study of carbon-nanotube-based gas pressure sensors. *J. Appl. Phys.* 109, 622–236. doi: 10.1063/1.3525059

Tu, M., Wannapaiboon, S., Khaletskaya, K., and Fischer, R. A. (2015). Engineering zeolitic-imidazolate framework (ZIF) thin film devices for selective detection of volatile organic compounds. *Adv. Funct. Mater.* 25, 4470–4479. doi: 10.1002/adfm.201500760

Wang, D., Tian, L., Li, H., Wan, K., Yu, X., Wang, P., et al. (2019). Mesoporous ultrathin SnO_2 nanosheets *in situ* modified by graphene oxide for extraordinary formaldehyde detection at low temperatures. *ACS Appl. Mater. Interfaces* 11, 12808–12818. doi: 10.1021/acsami.9b01465

Wang, Z., Huang, L., Zhu, X., Zhou, X., and Chi, L. (2017). An ultrasensitive organic semiconductor NO_2 sensor based on crystalline TIPS-pentacene films. *Adv. Mater.* 11:1703192. doi: 10.1002/adma.201703192

Wei, T.-C., and Hillhouse, W. H. (2006). Ion transport in the microporous titanosilicate ETS-10. *J. Phys. Chem. B* 110, 13728–13733. doi: 10.1021/jp061037u

Xie, C., Oganov, A. R., Dong, D., Liu, N., Li, D., and Debela, T. T. (2015). Rational design of inorganic dielectric materials with expected permittivity. *Sci. Rep.* 5:16769. doi: 10.1038/srep16769

Xing, R., Xu, L., Song, J., Zhou, C., Li, Q., Liu, D., et al. (2015). Preparation and gas sensing properties of In_2O_3/Au nanorods for detection of volatile organic compounds in exhaled breath. *Sci. Rep.* 5:10717. doi: 10.1038/srep10717

Xu, X. W., Wang, J., and Long, Y. C. (2006). Zeolite-based materials for gas sensors. *Sensors* 6, 1751–1764. doi: 10.3390/s6121751

Yamazoe, N., and Shimanoe, K. (2009). New perspectives of gas sensor technology. *Sens. Actuat. B Chem.* 138, 100–107. doi: 10.1016/j.snb.2009.01.023

Yuan, W. J., and Shi, G. Q. (2013). Graphene-based gas sensors. *J. Mater. Chem. A* 1, 10078–10091. doi: 10.1039/c3ta11774j

Zarifi, M. H., Ayaz, M., Goldthorp, J., Abdolrazzaghi, M., Hashisho, Z., and Daneshmand, M. (2015a). Microbead-assisted high resolution microwave planar ring resonator for organic-vapor sensing. *Appl. Phys. Lett.* 106, 12868–12882. doi: 10.1063/1.4907944

Zarifi, M. H., Gholidoust, A., Abdolrazzaghi, M., Shariaty, P., Hashisho, Z., and Daneshmand, M. (2018). Sensitivity enhancement in planar microwave active-resonator using metal organic framework for CO_2 detection. *Sens. Actuat. B Chem.* 255, 1561–1568. doi: 10.1016/j.snb.2017.08.169

Zarifi, M. H., Rahimi, M., Daneshmand, M., and Thundat, T. (2016). Microwave ring resonator-based non-contact interface sensor for oil sands applications. *Sens. Actuat. B Chem.* 224, 632–639. doi: 10.1016/j.snb.2015.10.061

Zarifi, M. H., Shariaty, P., Hashisho, Z., and Daneshmand, M. (2017). A non-contact microwave sensor for monitoring the interaction of zeolite 13X with CO_2 and CH_4 in gaseous streams. *Sens. Actuat. B Chem.* 238, 1240–1247. doi: 10.1016/j.snb.2016.09.047

Zarifi, M. H., Sohrabi, A., Shaibani, P. M., Daneshmand, M., and Thundat, T. (2015b). Detection of volatile organic compounds using microwave sensors. *Sens. J. IEEE* 15, 248–254. doi: 10.1109/JSEN.2014.2345477

Zarifi, M. H., Thundat, T., and Daneshmand, M. (2015c). High resolution microwave microstrip resonator for sensing applications. *Sens. Actuat. A Phys.* 233, 224–230. doi: 10.1016/j.sna.2015.06.031

Zheng, Y., Li, X., and Dutta, P. K. (2012). Exploitation of unique properties of zeolites in the development of gas sensors. *Sensors (Basel)* 12, 5170–5194. doi: 10.3390/s120405170

Zheng, Y., Qiao, Q., Wang, J., Li, X., and Jian, J. (2015). Gas sensing behavior of palladium oxide for carbon monoxide at low working temperature. *Sens. Actuat. B Chem.* 212, 256–263. doi: 10.1016/j.snb.2015.02.035

Conflict of Interest Statement: The authors declare that the research was conducted in the absence of any commercial or financial relationships that could be construed as a potential conflict of interest.

frontiers in Materials

ORIGINAL RESEARCH
published: 07 June 2019
doi: 10.3389/fmats.2019.00122

Highly Sensitive and Selective Ethanol Sensor Based on ZnO Nanorod on SnO_2 Thin Film Fabricated by Spray Pyrolysis

T. Tharsika[1], M. Thanihaichelvan[2], A. S. M. A. Haseeb[3]* and S. A. Akbar[4]*

[1] Department of Interdisciplinary Studies, Faculty of Engineering, University of Jaffna, Kilinochchi, Sri Lanka, [2] Department of Physics, Faculty of Science, University of Jaffna, Jaffna, Sri Lanka, [3] Department of Mechanical Engineering, Faculty of Engineering, University of Malaya, Kuala Lumpur, Malaysia, [4] Department of Materials Science and Engineering, Center for Industrial Sensors and Measurements, Ohio State University, Columbus, OH, United States

This work reports the fabrication of mixed structure of ZnO nanorod on SnO_2 thin film via spray pyrolysis followed by thermal annealing and their gas sensing properties. ZnO/SnO_2 nanostructures are successfully prepared on a gold interdigitated alumina substrate by spraying varying mixed precursor concentrations of zinc acetate and tin (IV) chloride pentahydrate solutions in ethanol and thermal annealing. The morphology of the nanostructures is controlled by tailoring the Zn:Sn ratio in the precursor solution mixture. Unique ZnO crystals and ZnO nanorods are observed under a field emission scanning electron microscopy (FESEM) when the Zn/Sn ratio in the precursor solution is in between 13:7 and 17:3 after thermal annealing. The fabricated nanostructures are tested for ethanol, methane and hydrogen in air ambient for various gas concentrations ranging from 25 to 400 ppm and the effect of fabrication conditions on the sensitivity and selectivity are studied. Among the nanostructure sensors studied, the film fabricated with molar ratio of Zn/Sn =3:1 shows better sensitivity and selectivity to ethanol due to high sensing surface area of the nanorod. The response to 25 ppm ethanol is found to be as high as 50 at an operating temperature of 400°C.

Keywords: spray pyrolysis, ZnO, nanorod, SnO_2, thin film, gas sensor, ethanol, nanocomposite

OPEN ACCESS

Edited by:
Kalisadhan Mukherjee, Pandit Deendayal Petroleum University, India

Reviewed by:
Dr. Subhasis Roy, University of Calcutta, India
Sudip Mondal, Pukyong National University, South Korea

****Correspondence:***
T. Tharsika
tharsika@eng.jfn.ac.lk
A. S. M. A. Haseeb
haseeb@um.edu.my

Specialty section:
This article was submitted to Functional Ceramics, a section of the journal Frontiers in Materials

Received: *25 January 2019*
Accepted: *13 May 2019*
Published: *07 June 2019*

Citation:
Tharsika T, Thanihaichelvan M, Haseeb ASMA and Akbar SA (2019) Highly Sensitive and Selective Ethanol Sensor Based on ZnO Nanorod on SnO_2 Thin Film Fabricated by Spray Pyrolysis. Front. Mater. 6:122. doi: 10.3389/fmats.2019.00122

INTRODUCTION

Gas sensors based on metal oxide nanostructures have been widely studied and used in applications ranging from health and safety to emission control (Comini et al., 2002; Lin et al., 2015; Yao et al., 2016; Kwak et al., 2018; Liu et al., 2019a). These sensors are attractive because of their high sensitivity, low cost, simplicity and compatibility with modern electronic devices due to direct electrical readouts (Miller et al., 2014). Until now, several metal oxides including TiO_2, In_2O_3, WO_3, ZnO, TeO_2, CuO, SnO_2, and NiO are used in resistive-type metal oxide gas sensors (Dey, 2018). However, these single metal oxide gas sensors generally have the disadvantage of low sensitivity, high operating temperature, and poor selectivity between gases (Arafat et al., 2014).

Ethanol sensors are being used in numerous applications, such as, to monitor chemical reactions, breath analysis, biomedical productions, and quality control of foods (Kolmakov et al., 2003; Timmer et al., 2005). Augmented usage of ethanol increases the issues of explosion hazards

(Powers et al., 2001) and ground-water pollution (Freitas et al., 2010). Lower selectivity is one of the major drawbacks of the metal oxide-based sensors for selective ethanol sensing applications. Several approaches have been used to improve the sensitivity and selectivity of single metal oxide-based ethanol sensor. These include addition of noble metals (Chen et al., 2019; Liu et al., 2019b; ul Haq et al., 2019) doping of metal oxide catalyst (Park et al., 2015; NaderiNasrabadi et al., 2016; Lupan et al., 2017; Tan et al., 2018), developing composite metal oxides consisting of binary or ternary phase metal oxide systems (Li et al., 2019; Wang et al., 2019) and development of nanostructures with different morphologies (Drobek et al., 2016; Wang et al., 2018; Yang et al., 2018). Among the approaches used, tailoring of composite metal oxides with different morphologies presents a good potential for tuning the sensitivity and selectivity during gas sensing. Many recent studies have shown that the selectivity and operating temperature of resistive-type gas sensors can be improved through the use of composite metal oxides (Andre et al., 2019; He et al., 2019; Rong et al., 2019; Sakthivel and Nammalvar, 2019).

The composite nanostructures of ZnO and SnO_2 received special attention due to their unique electronic properties that are keys for selective gas sensing. Stoichiometric nature of each varies significantly and that leads to increase gas sensing potential of the composite material. Generally SnO_2 has non-stoichiometric nature below the substrate temperature of 450°C in spray pyrolysis process (Amma et al., 2005), while ZnO has defects in structure (Demir-Cakan et al., 2008). Due to this behavior, chemisorption of oxygen is high on ZnO than on SnO_2. SnO_2 also enhances the desorption process in ZnO-nanorod/SnO_2-thinfilm gas sensors by transferring electron from SnO_2 to ZnO due to the lower work function of the latter (Lu et al., 2012; Park et al., 2013).

ZnO/SnO_2 based nanostructures have been mostly synthesized by a two-step fabrication process (Cheng et al., 2009; Pan et al., 2012; Park et al., 2013), and extensively used in various applications such as, transparent electrode, photovoltaic, light emitting diodes, field emission transistor and energy harvesting due to their great potential properties (Wang and Rogach, 2014; Rong et al., 2019). In our previous studies (Tharsika et al., 2014a,b), we reported on the fabrication of ZnO-SnO_2 thin films by spray pyrolysis on glass substrate and studied the structural and optical properties of the films. We observed the formation of ZnO nanorods for films sprayed with Zn/Sn = 3:1 followed by thermal annealing at 350°C and reported as short communication (Tharsika et al., 2015).

In this study, we investigate the role of Zn:Sn molar ratio on the morphology of the nanostructures fabricated by the same spray pyrolysis and thermal annealing method. A wide range of precursor mixtures (Zn/Sn = 13:7, 14:6, 15:5, 16:4, and 17:3) are tested and the aspect ratio of ZnO nanorod is investigated in detail. We also fabricate solid state gas sensors using the composite films on gold interdigitated alumina substrate and their gas sensing properties toward number of reducing gases such as, ethanol, methane and hydrogen are studied. The selectivity toward ethanol for the ZnO/SnO_2 composite sensor is studied for various molar ratio of the precursor solution. A possible mechanism for the improved selectivity along with higher sensitivity for 15Z5S nanostructure sensor is suggested.

MATERIALS AND METHODS

Fabrication of ZnO/SnO_2 Nanostructures

ZnO/SnO_2 nanostructures were deposited by spray pyrolysis on gold interdigitated alumina substrates using zinc acetate ($Zn(C_2H_3O_2)_2$) [98% purity, Sigma Aldrich-USA] and tin (IV) chloride pentahydrate ($SnCl_4.5H_2O$) [99.99% trace metals basis, Sigma Aldrich-USA] solutions in absolute ethanol. The detailed procedure was reported elsewhere (Tharsika et al., 2014b). Briefly, the mixed precursor solutions were obtained by adding proportional volumes of equimolar $Zn(C_2H_3O_2)_2$ and $SnCl_4.5H_2O$ solutions in ethanol with the volume ratios of 13:7, 14:6, 15:5, 16:4, and 17:3. The mixed solution was ultrasonicated for a minute and directly sprayed onto the substrate by a spray gun using dry nitrogen as the carrier gas. The substrate temperature was maintained at 350°C throughout the spraying process and the number of spray was kept as constant at 180 for all the samples. Finally, the sprayed films were annealed at 350°C for 1 h. The designation of the deposited films is given in **Table 1**. For comparison of gas sensing characteristics, ZnO and SnO_2 thin films were also fabricated.

Characterizations of Nanostructures

X-ray diffraction patterns of ZnO/SnO_2 nanostructures before and after annealing were determined using X-ray diffractometer (XRD: Siemen D-5000 model) with a monochromatic CuKα radiation (λ = 0.15406 nm) and a Ni filter. The current and voltage were 40 mA and 40 kV, respectively. The data were collected in the range of 20–80° (2θ), with a scanning step of 0.05°/s. The surface morphology of the films was investigated by using a field-emission scanning electron microscopy (FESEM: Auriga Zeiss Ultra-60). Elemental composition was obtained at two different places including on the nanorod and on the surface of the underlying film using FESEM coupled with an energy dispersive X-ray spectroscopy (EDX) with applied beam voltage of 20 keV.

TABLE 1 | Volume of Zn and Sn ion in mixed precursor solution for different thin films.

Film designation	Volume in mixed precursor solution (ml)	
	$Zn(C_2H_3O_2)_2$	$SnCl_4.5H_2O$
13Z7S	13	7
14Z6S	14	6
15Z5S	15	5
16Z4S	16	4
17Z3S	17	3

Gas Sensing Measurements

The fabricated nanostructures on printed Au interdigitated alumina substrates were directly used as a gas sensor for sensing measurements. The distance between the adjacent Au fringes and fringe width were 200 and 100 μm, respectively. A gold wire (99.9% metal basis) with a diameter of 0.2 mm was jointed to Au interdigitated electrode using conducting Au paste to make the electrical connection between electrode and gold wire.

The sensor was placed inside a horizontal tube furnace, and sensing measurements were carried out for various target gases such as ethanol, methane and hydrogen. The concentration of the gases (25, 50, 100, 200, and 400 ppm) was controlled by a digital mass flow controller. A mixture of 80% of nitrogen and 20% of oxygen was used as the ambient to simulate the air atmosphere inside the furnace. Measurements were done by using a computer-controlled data acquisition system. The resistance in air (R_a) and in the presence of the test gases (R_g) were recorded, and the sensitivity of the sensor was calculated as R_a/R_g.

RESULTS AND DISCUSSION

Morphological Studies

Figure 1 shows the FESEM images of ZnO/SnO_2 nanostructures sprayed with different Zn:Sn molar ratio in the precursor solution of 13:7, 14:6, 15:5, 16:4, and 17:3 on alumina substrates before and after thermal annealing. As seen in **Figures 1A–E**, all as-sprayed films show flake like structures on the surface and no evidences for nanorods or other nanostructures are found.

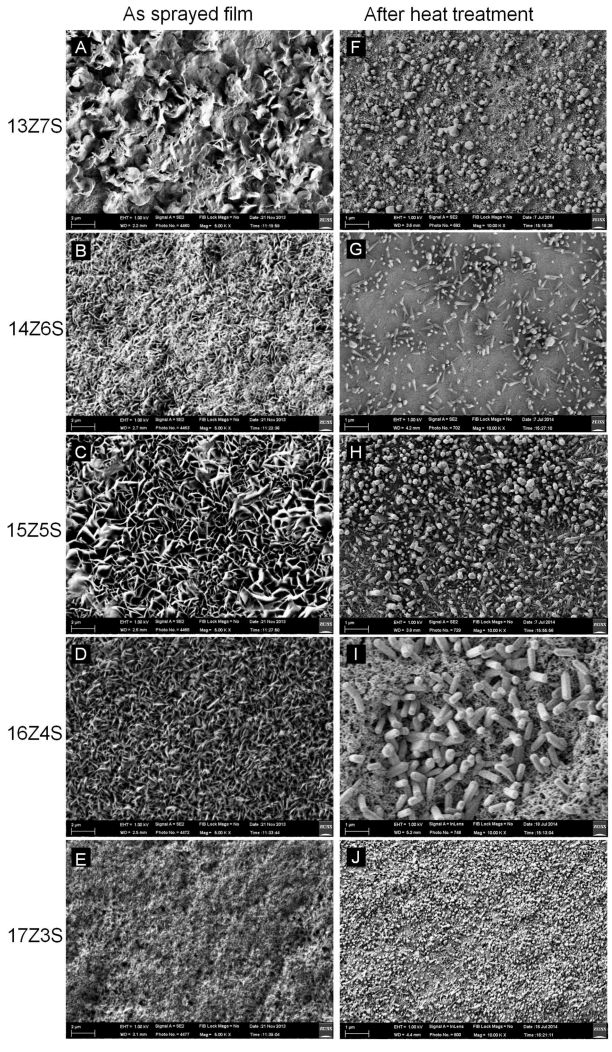

FIGURE 1 | FESEM images of nanostructures fabricated with different molar ratio of Zn and Sn in mixed precursor solution before thermal annealing **(A)** 13Z7S, **(B)** 14Z6S, **(C)** 15Z5S, **(D)** 16Z4S, and **(E)** 17Z3S, and after thermal annealing at 350°C for 1 h **(F)** 13Z7S, **(G)** 14Z6S, **(H)** 15Z5S, **(I)**16Z4S, and **(J)** 17Z3S.

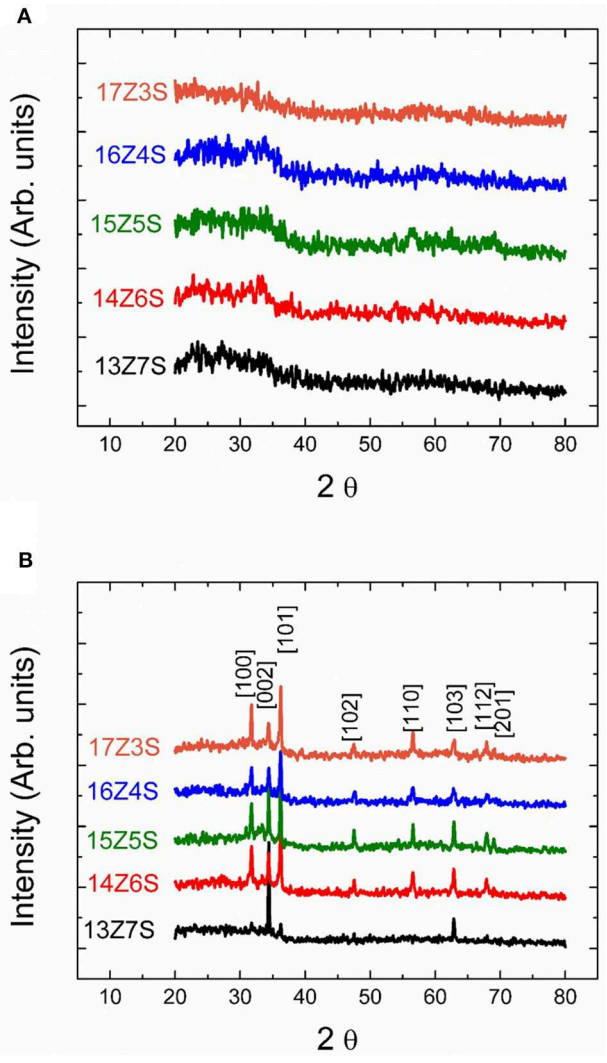

FIGURE 2 | The XRD patterns of ZnO/SnO_2 nanostructures **(A)** before thermal annealing (as-sprayed) and **(B)** after thermal annealing at 350°C.

Similar morphology was reported for film sprayed using $SnCl_4$ precursor solution at spray temperature of 450°C (Korotcenkov et al., 2001; Korotcenkov and Cho, 2009). The films after thermal treatment show different morphology. This morphology tends to contain hexagonal shaped nanostructures. Hexagonal nanocrystals are observed in **Figure 1F** when the molar ratio of Zn:Sn in precursor solution is 13:7, while for values above 13:7, the microstructural feature changes from nanocrystals to nanorods (**Figures 1G–I**).

The size of the hexagonal nanocrystal is measured within the range of 52–210 nm for 13Z7S film and 43–85 nm for 17Z3S composite film, while the aspect ratio of nanorods (length divided by width) is calculated as 4.5 (length $l = 450$ nm and diameter $d = 100$ nm), 5.2 ($l = 650$ nm, $d = 125$ nm), and 3 ($l = 1200$ nm, $d = 400$ nm), for 14Z6S, 15Z5S, and 16Z4S films, respectively. As we reported earlier, high aspect ratio of ZnO nanorods was observed when the mass ratio of Zn:Sn in the precursor solution was 3:1. Here, similar result with dense structure is obtained for 15Z5S film after thermal annealing (**Figure 1H**) when optimize the growth of ZnO by changing various molar ratio of Zn/Sn in the precursor mixture. The nanorod-like nanostructures start to disappear when the Zn:Sn molar ratio is 13:7 and lower. These also seem to disappear when the ratio is 17:3 and higher. The compact film and porous film like structure are obtained when the molar ratio of Zn:Sn in precursor solution is 12:8 and 18:2, respectively (**Supplementary Figure 1**).

XRD Analysis

The crystal structure of sprayed thin films before and after thermal annealing at 350°C is investigated by X-ray diffractometer and the patterns are shown in **Figure 2**. No sharp peaks are observed in the unannealed films regardless of the molar ratio of Zn to Sn in the precursor solution (**Figure 2A**). This indicates that the films are amorphous in nature before thermal annealing. However, sharp diffraction peaks corresponding to ZnO are observed in the sprayed mixed films after thermal annealing at 350°C for 1 h (**Figure 2B**), demonstrating the formation of well-crystalline ZnO nanorod. This indicates that the crystalline structures formed during the thermal annealing process. Formation of crystalline structures during thermal annealing is also supported by FESEM with the presence of nanostructures in the films after thermal treatment. The diffraction peaks in **Figure 2B** at 2θ values of 32, 34, 36, 47.5, 56, 63, 68, and 69 degree can be indexed as (100), (002), (101), (102), (110), (103), (112), and (201) crystal planes of the hexagonal wurtzite structure of ZnO (JCPDS No. 79-0208). The XRD pattern of 13Z7S film shows weak ZnO peaks compared to other XRD patterns observed for various Zn/Sn ratio. This is due to low amount of zinc precursor used in the mixture of Zn:Sn = 13:7 as compared to high amount of zinc used in the mixture of Zn:Sn = 17:3. The intensity of XRD peaks is increasing with increase of Zn precursor in the mixture. Interestingly there are no pronounced peaks corresponding to SnO_2 observed in any of the annealed mixed thin film. However,

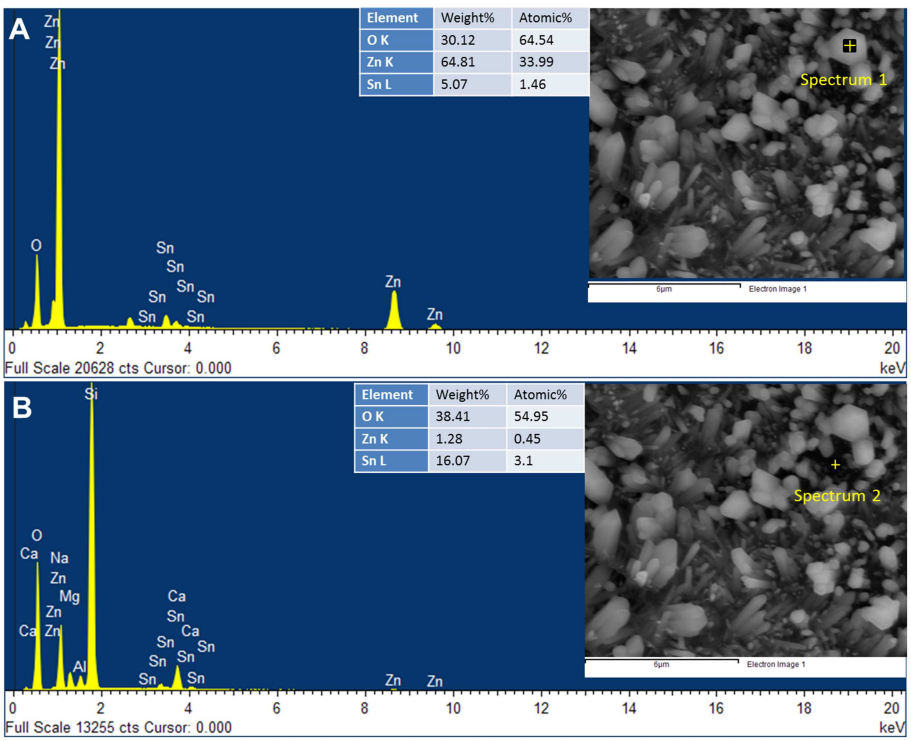

FIGURE 3 | The EDX spectra obtained at two different positions: **(A)** on the ZnO nanorod and **(B)** on the surface of the 15Z5S film.

the EDX measurement shows that nanorods are composed of ZnO, while the underlying film contains significant amount of Sn as shown in **Figure 3B**. This can be attributed to the presence of amorphous SnO_2 in the film. It is reported that the crystallization temperature of spray deposited SnO_2 films are above 500°C. Patil et al. (2011) reported that the sprayed films baked at 550°C shows very small peaks corresponding SnO_2, indicating their predominantly amorphous nature. So, it is suggested that the SnO_2 remains amorphous at 350°C which is considerably lower than the crystallization temperature of SnO_2. On the other hand, researchers reported that the crystallization temperature of ZnO films was 350°C or lower (Cho et al., 1999; Lee et al., 2004). From the FESEM images and XRD spectra, we can conclude that the films contain crystalline ZnO nanostructures and amorphous SnO_2 underlying film.

EDX spectrum obtained on the nanorod of the 15Z5S film shows that nanorods are composed of ZnO (**Figure 3A**), while less amount of Sn is detected. It may arise due to deep penetration of EDX beam and probing the underlying film. However, the EDX spectrum obtained on the surface of the 15Z5S film (**Figure 3B**) reveals the underlying film contains significant amount of Sn, while peaks for Si, Ca, Al, Na, and Mg are detected from the substrate.

Ethanol Sensing Properties

The fabricated ZnO/SnO_2 nanostructures are then tested for ethanol sensing at an optimum operating temperature of 400°C. Pure ZnO and SnO_2 thin films are also studied for comparison with the ZnO/SnO_2 nanostructures sensors toward ethanol. **Figure 4A** illustrates the sensitivity of sensors to ethanol at different concentrations from 25 to 400 ppm. As clearly seen in **Figure 4A**, the gas sensing performances of ZnO/SnO_2 nanostructures are exceptionally high when compared to pure ZnO and SnO_2 thin film sensors. Sensitivity of ethanol first

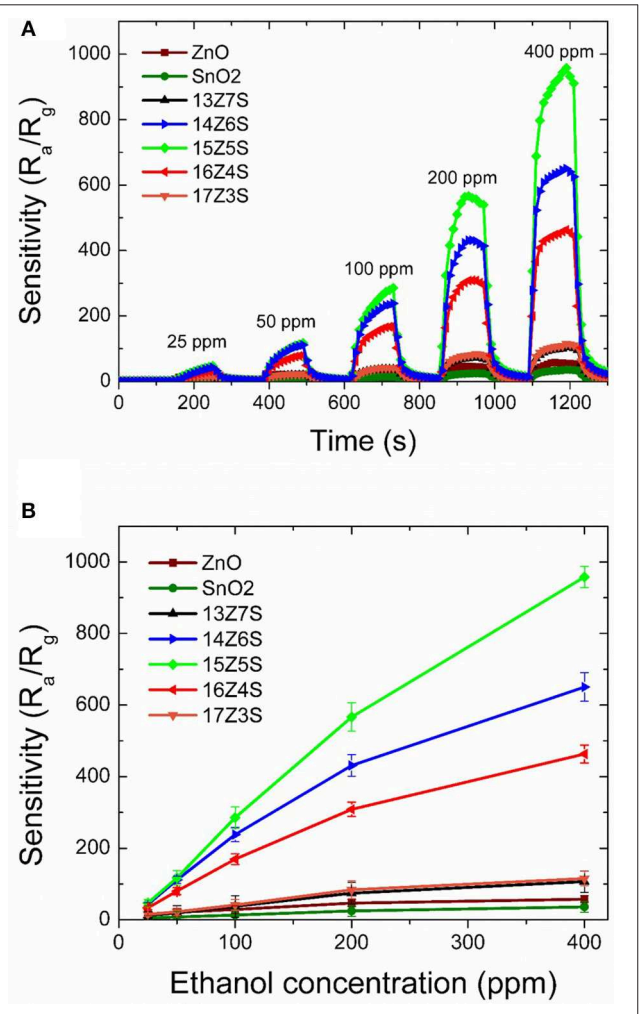

FIGURE 4 | (A) Time-dependent response recovery characteristics of various ZnO/SnO_2 nanostructure sensors with different gas concentrations at an optimum operating temperature of 400°C, **(B)** Sensitivity of various ZnO/SnO_2 nanostructure sensors as a function of ethanol concentrations.

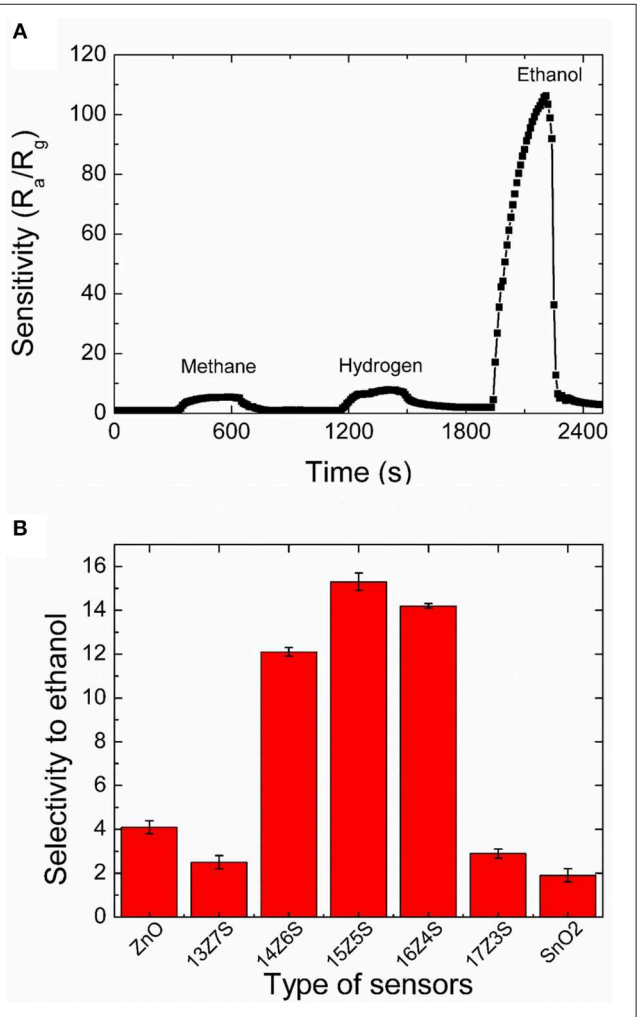

FIGURE 5 | (A) Selectivity of 15Z5S film sensors toward 50 ppm of methane, hydrogen and ethanol at an operating temperature of 400°C and **(B)** the variation of selectivity (ratio between the sensitivity of 50 ppm ethanol and hydrogen at 400°C) of the sensors fabricated with different films.

rises as the molar ratio of Zn/Sn in the film increases from 13:7 to 15:5 which corresponds to the films 13Z7S, 14Z6S, and 15Z5S. Sensitivity then decreases when the molar ratio of Zn/Sn increases beyond the limit of 15:5 (16Z4S and 17Z3S). It can be seen from **Figure 4A** that sensitivities toward an ethanol concentration of 25 ppm are about 4, 5, 12, 42, 50, 33, and 16 for pure SnO_2, pure ZnO, 13Z7S, 14Z6S, 15Z5S, 16Z4S, and 17Z3S nanostructure film sensors, respectively. 15Z5S film sensor exhibits highest sensitivity toward ethanol among other sensors. The enhancement of the ethanol sensing performance of 15Z5S nanostructured film can be attributed to the greater sensing surface area due to the high aspect ratio of nanorod structure. Sensitivity as a function of ethanol concentration is shown in **Figure 4B**. The sensitivity toward ethanol gas increases linearly up to 200 ppm concentration for all film sensors. Beyond 200 ppm concentration, the sensitivity tends to reach saturation gradually after climbing over the point of 400 ppm concentration. But, 15Z5S sensor exhibits linear ethanol sensing property as compared to other sensors. Further, these sensors exhibit the lowest detection limit for ethanol as 25 ppm. As can be seen the sensitivity of 15Z5S nanostructure film sensors for ethanol is almost ten times higher than that of the pure sensors for 25 ppm of ethanol concentration.

Thermodynamic analysis reveals that methane and hydrogen are formed from ethanol at moderate temperatures and high temperatures (400–700°C), respectively (Vasudeva et al., 1996; Fishtik et al., 2000; Galvita et al., 2001). Therefore, selective ethanol sensing is important in presence of hydrogen and methane. Thus, the selectivity of the 15Z5S film sensor toward ethanol is studied. **Figure 5A** represents the continuous response of 15Z5S film to 50 ppm methane, hydrogen and ethanol. The 15Z5S sensor reveals sensitivity of 5 to methane, 7 to hydrogen, and 108 to ethanol. The sensitivity of 108 is obtained for ethanol for the 15Z5S film sensor which is nearly 15-fold higher than that of the response for methane and hydrogen at an operating temperature of 400°C. **Figure 5B** summarizes the selectivity of ethanol in terms of the sensing ratios of ethanol and hydrogen which produced the second largest sensing signal in all sensors regardless of Zn:Sn ratio. Thus, the 15Z5S film shows better selectivity toward ethanol than the other mixed thin films sensor which is higher than that of the pure ZnO and SnO_2 film sensors due to the one-dimensional nanostructure (nanorod) nature with high sensing surface area. Therefore, 15Z5S nanostructure film-based sensor can be used to detect ethanol in practical applications in the environmental field.

Gas Sensing Mechanism

The detailed sensing mechanism of ZnO nanorod on SnO_2 thin film is shown in **Figure 6**. It is commonly accepted that the sensing of a reducing gas in a metal oxide surface at elevated temperature is a two-step process which includes the formation of oxygen ion species on the surface and reducing gases are oxidized on the surface (Barsan and Weimar, 2001; Kolmakov et al., 2003). Due to variation of band gap, work function and electron affinity of ZnO and SnO_2 a Fermi electron transfer is possible at the ZnO/SnO_2 interface (Zheng et al., 2009). Thus, a net electron flow from SnO_2 to ZnO can be expected at the ZnO/SnO_2 interface which is mainly due to the difference in work functions of ZnO (5.2 eV) and SnO_2 (4.9 eV) (Tang et al., 2014; Li et al., 2015). This increases the electron density at the ZnO nanorods and the underlying SnO_2 layer will suffer from an electron deficiency (**Figure 6A**).

When the sensor is exposed to air at elevated temperature, due to the increased electron density at ZnO nanostructures, the amount of oxygen ions (O^{2-}) present in the ZnO surface also increases. At operating temperature of 400°C, the O^{2-} ions are more stable and predominant when compared to other oxygen species such as (O^-, O_2^-) (Barsan and Weimar, 2001; Yao et al., 2014) (**Figure 6B**). When the sensor is exposed to ethanol, the surface oxygen species reacts with the ethanol molecules and the chemisorbed electrons will be left freely to the films (**Figure 6C**).

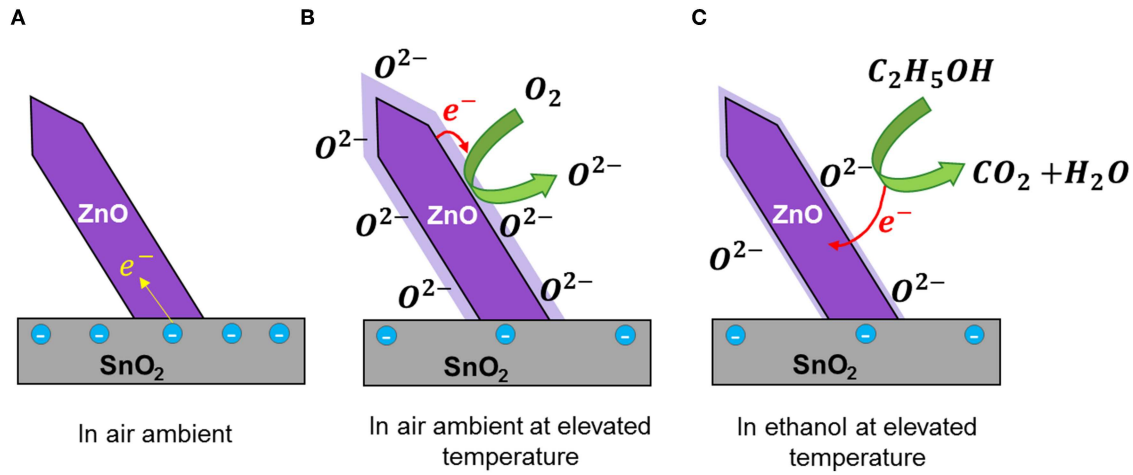

FIGURE 6 | Schematic ethanol sensing mechanism of ZnO nanorod on SnO_2 thin film **(A)** In air ambient, **(B)** In air ambient at elevated temperature, and **(C)** In ethanol at elevated temperature.

TABLE 2 | Brief summary of ZnO/SnO_2 nanostructures gas sensor upon exposure to 100 ppm ethanol.

ZnO/SnO_2 nanostructures	Fabrication method	Detection range (ppm)	Sensitivity**	Working temperature (°C)	References
ZnO/SnO_2 nanostructures	Hydrothermal	10–1,000	30	300	Li et al., 2011
ZnO/SnO_2 hollow nanospheres	Hydrothermal	0.5–100	78.2	225	Liu et al., 2017
SnO_2- core/ZnO-shell nanowires	Thermal evaporation and Spray coating*	25–500	14.05	400	Thanh Le et al., 2013
ZnO/SnO_2 hollow nanospheres	Hydrothermal*	10–500	14.7	150	Ma et al., 2013
SnO_2/ZnO nanofibers	Electrospinning and Hydrothermal*	5–1,000	80	300	Yan et al., 2015a
Hollow ZnO/SnO_2 nanofibers	Electrospinning and Hydrothermal*	5–1,000	392.29	200	Li et al., 2015
ZnO sphere and SnO_2 nanofiber composite	Electrospinning and Hydrothermal*	20 ppm	100 (for 20ppm)	210	Guo and Wang, 2016
SnO_2/ZnO hetero-nanofibers	Electrospinning	5–1,000	54	300	Yan et al., 2015b
Ag-doped ZnO-SnO_2 hollow nanofiber	Electrospinning and Hydrothermal*	1–6,000	128.6	200	Ma et al., 2017
ZnO-nanorod/SnO_2 thin film	Spray pyrolysis	20–400	285	400	This work

The methods are 2-step process for each metal oxide.

***Sensitivity for 100 ppm ethanol at optimum temperature unless mentioned.*

As a result, a rapid drop in net resistance of the film was observed. Therefore, sensitivity is increased toward ethanol.

According to the sensing results, 15Z5S nanostructure film sensor exhibits maximum ethanol sensing properties compared with pure ZnO, pure SnO_2, and other mixed thin films (13Z7S, 14Z6S, 16Z4S, and 17Z3S). The improved sensitivity of 15Z5S film sensor with high aspect ratio nanorods for ethanol than the pure and other mixed thin film sensor can be feasibly explained by highly crystalline ZnO nanorods, which improve the effective sensing surface with improved surface oxygen species density. Ethanol sensing results of our ZnO-nanorod/SnO_2-thinfilm (15Z5S) sensor is compared with the previous reported values. **Table 2** summarizes the ethanol sensing properties of ZnO/SnO_2 composite gas sensors. It clearly shows that the sensitivity of our ZnO-nanorod/SnO_2-thinfilm (15Z5S) sensor is comparable to some of the recent works with relatively simple and low-cost fabrication techniques and exhibits greater sensitivity toward ethanol. Therefore, the present ethanol sensor can be used to detect ethanol in environmental monitoring.

CONCLUSIONS

We report a simple spray pyrolysis and heating route to fabricate ZnO nanorod on SnO_2 thin film with controllable morphologies. The nanostructures are tailored by controlling the Zn:Sn ion ratio in the precursor solution. The resulting nanostructures turns into high aspect ratio nanorods when the Zn:Sn ratio is 15:5. The ethanol sensing studies reveals that the mixed films perform well when compared to pure ZnO and SnO_2 films. The sensitivity of 108 is obtained for 50 ppm ethanol from ZnO-nanorod/SnO_2-thinfilm (15Z5S) sensor which is nearly 15-fold higher than that of the response for methane and hydrogen at an operating temperature of 400°C. Also, the ZnO nanorod on the SnO_2 thin film sensor shows better sensitivity and selectivity toward ethanol due to high aspect ratio of nanorod structure with greater sensing surface area than film.

AUTHOR CONTRIBUTIONS

TT conducted all the experimental work and analyzed the data. MT and TT wrote the manuscript with the guidance of SA and AH. SA guided the sensing part of this work and corrected the manuscript. AH directed the fabrication part of ZnO nanorod on SnO_2 film and supervised the manuscript writing.

ACKNOWLEDGMENTS

Authors acknowledge University of Malaya and Ministry of Higher Education, Malaysia for its financial assistance for this research work under FRGS Grant (FP014-2015A). SA work was supported by the National Science Foundation Grant 1609142.

SUPPLEMENTARY MATERIAL

The Supplementary Material for this article can be found online at: https://www.frontiersin.org/articles/10.3389/fmats.2019.00122/full#supplementary-material

Supplementary Figure S1 | FESEM images of 12Z8S and 18Z2S thinfilms before **(a)**, **(c)** and after **(b)**, **(d)** heating at 350C for 1 hour.

REFERENCES

Amma, D. S. D., Vaidyan, V. K., and Manoj, P. K. (2005). Structural, electrical and optical studies on chemically deposited tin oxide films from inorganic precursors. *Mater. Chem. Phys.* 93, 194–201. doi: 10.1016/j.matchemphys.2005.03.045

Andre, R. S., Mercante, L. A., Facure, M. H. M., Mattoso, L. H. C., and Correa, D. S. (2019). Enhanced and selective ammonia detection using In 2 O 3 /reduced graphene oxide hybrid nanofibers. *Appl. Surf. Sci.* 473, 133–140. doi: 10.1016/j.apsusc.2018.12.101

Arafat, M. M., Haseeb, A. S. M. A., and Akbar, S. A. (2014). "Developments in semiconducting oxide-based gas-sensing materials,"

in *Comprehensive Materials Processing* (Elsevier), 205–219. doi: 10.1016/B978-0-08-096532-1.01307-8

Barsan, N., and Weimar, U. (2001). Conduction model of metal oxide gas sensors. *J. Electroceramics* 7, 143–167. doi: 10.1023/A:1014405811371

Chen, X., Deng, N., Zhang, X., Li, J., Yang, Y., Hong, B., et al. (2019). Cerium-doped indium oxide nanosphere arrays with enhanced ethanol-sensing properties. *J. Nanoparticle Res.* 21:77. doi: 10.1007/s11051-019-4516-3

Cheng, C., Liu, B., Yang, H., Zhou, W., Sun, L., Chen, R., et al. (2009). Hierarchical assembly of ZnO nanostructures on SnO $_2$ backbone nanowires: low-temperature hydrothermal preparation and optical properties. *ACS Nano* 3, 3069–3076. doi: 10.1021/nn900848x

Cho, S., Ma, J., Kim, Y., Sun, Y., Wong, G. K. L., and Ketterson, J. B. (1999). Photoluminescence and ultraviolet lasing of polycrystalline ZnO thin films prepared by the oxidation of the metallic Zn. *Appl. Phys. Lett.* 75, 2761–2763. doi: 10.1063/1.125141

Comini, E., Ferroni, M., Guidi, V., Faglia, G., Martinelli, G., and Sberveglieri, G. (2002). Nanostructured mixed oxides compounds for gas sensing applications. *Sens. Actu. B Chem.* 84, 26–32. doi: 10.1016/S0925-4005(02)00006-0

Demir-Cakan, R., Hu, Y.-S. S., Antonietti, M., Maier, J., and Titirici, M.-M. M. (2008). Facile one-pot synthesis of mesoporous SnO 2 microspheres via nanoparticles assembly and lithium storage properties. *Chem. Mater.* 20, 1227–1229. doi: 10.1021/cm7031288

Dey, A. (2018). Semiconductor metal oxide gas sensors: a review. *Mater. Sci. Eng. B Solid-State Mater. Adv. Technol.* 229, 206–217. doi: 10.1016/j.mseb.2017.12.036

Drobek, M., Kim, J. H., Bechelany, M., Vallicari, C., Julbe, A., and Kim, S. S. (2016). MOF-based membrane encapsulated ZnO nanowires for enhanced gas sensor selectivity. *ACS Appl. Mater. Interfaces* 8, 8323–8328. doi: 10.1021/acsami.5b12062

Fishtik, I., Alexander, A., Datta, R., and Geana, D. (2000). Thermodynamic analysis of hydrogen production by steam reforming of ethanol via response reactions. *Int. J. Hydrogen Energy* 25, 31–45. doi: 10.1016/S0360-3199(99)00004-X

Freitas, J. G., Fletcher, B., Aravena, R., and Barker, J. F. (2010). Methane production and isotopic fingerprinting in ethanol fuel contaminated sites. *Ground Water* 48, 844–857. doi: 10.1111/j.1745-6584.2009.00665.x

Galvita, V. V., Semin, G. L., Belyaev, V. D., Semikolenov, V. A., Tsiakaras, P., and Sobyanin, V. A. (2001). Synthesis gas production by steam reforming of ethanol. *Appl. Catal. A Gen.* 220, 123–127. doi: 10.1016/S0926-860X(01)00708-6

Guo, W., and Wang, Z. (2016). Composite of ZnO spheres and functionalized SnO2nanofibers with an enhanced ethanol gas sensing properties. *Mater. Lett.* 169, 246–249. doi: 10.1016/j.matlet.2016.01.118

He, M., Xie, L., Zhao, X., Hu, X., Li, S., and Zhu, Z. G. (2019). Highly sensitive and selective H 2 S gas sensors based on flower-like WO 3 /CuO composites operating at low/room temperature. *J. Alloys Compd.* 788, 36–43. doi: 10.1016/j.jallcom.2019.01.349

Kolmakov, A., Zhang, Y., Cheng, G., and Moskovits, M. (2003). Detection of CO and O2 using tin oxide nanowire sensors. *Adv. Mater.* 15, 997–1000. doi: 10.1002/adma.200304889

Korotcenkov, G., Brinzari, V., Schwank, J., DiBattista, M., and Vasiliev, A. (2001). Peculiarities of SnO2 thin film deposition by spray pyrolysis for gas sensor application. *Sensors Actuators B Chem.* 77, 244–252. doi: 10.1016/S0925-4005(01)00741-9

Korotcenkov, G., and Cho, B. K. (2009). Thin film SnO2-based gas sensors: film thickness influence. *Sensors Actuators B Chem.* 142, 321–330. doi: 10.1016/j.snb.2009.08.006

Kwak, C. H., Kim, T. H., Jeong, S. Y., Yoon, J. W., Kim, J. S., and Lee, J. H. (2018). Humidity-independent oxide semiconductor chemiresistors using terbium-doped SnO 2 yolk-shell spheres for real-time breath analysis. *ACS Appl. Mater. Interfaces* 10, 18886–18894. doi: 10.1021/acsami.8b04245

Lee, J. H., Yeo, B. W., and Park, B. O. (2004). Effects of the annealing treatment on electrical and optical properties of ZnO transparent conduction films by ultrasonic spraying pyrolysis. *Thin Solid Films* 457, 333–337. doi: 10.1016/j.tsf.2003.09.075

Li, B., Liu, J., Liu, Q., Chen, R., Zhang, H., Yu, J., et al. (2019). Core-shell structure of ZnO/Co 3 O 4 composites derived from bimetallic-organic frameworks with superior sensing performance for ethanol gas. *Appl. Surf. Sci.* 475, 700–709. doi: 10.1016/j.apsusc.2018.12.284

Li, C. C., Yin, X. M., Li, Q. H., and Wang, T. H. (2011). Enhanced gas sensing properties of ZnO/SnO2 hierarchical architectures by glucose-induced attachment. *CrystEngComm* 13, 1557–1563. doi: 10.1039/C0CE00244E

Li, W., Ma, S., Li, Y., Yang, G., Mao, Y., Luo, J., et al. (2015). Enhanced ethanol sensing performance of hollow ZnO-SnO2core-shell nanofibers. *Sensors Actuators B Chem.* 211, 392–402. doi: 10.1016/j.snb.2015.01.090

Lin, Y., Wei, W., Li, Y., Li, F., Zhou, J., Sun, D., et al. (2015). Preparation of Pd nanoparticle-decorated hollow SnO_2 nanofibers and their enhanced formaldehyde sensing properties. *J. Alloys Compd.* 651, 690–698. doi: 10.1016/j.jallcom.2015.08.174

Liu, D., Pan, J., Tang, J., Liu, W., Bai, S., and Luo, R. (2019a). Ag decorated SnO2 nanoparticles to enhance formaldehyde sensing properties. *J. Phys. Chem. Solids* 124, 36–43. doi: 10.1016/j.jpcs.2018.08.028

Liu, J., Wang, T., wang, B., Sun, P., Yang, Q., Liang, X., et al. (2017). Highly sensitive and low detection limit of ethanol gas sensor based on hollow ZnO/SnO_2 spheres composite material. *Sensors Actuators B Chem.* 245, 551–559. doi: 10.1016/j.snb.2017.01.148

Liu, S., Sun, Q., Wang, J., and Hou, H. (2019b). Charge imbalance induced oxygen-adsorption enhances the gas-sensing properties of Al-doped SnO 2 powders. *J. Phys. Chem. Solids* 124, 163–168. doi: 10.1016/j.jpcs.2018.09.017

Lu, G., Xu, J., Sun, J., Yu, Y., Zhang, Y., and Liu, F. (2012). UV-enhanced room temperature NO2sensor using ZnO nanorods modified with SnO2nanoparticles. *Sensors Actuators B Chem.* 162, 82–88. doi: 10.1016/j.snb.2011.12.039

Lupan, O., Postica, V., Gröttrup, J., Mishra, A. K., de Leeuw, N. H., and Adelung, R. (2017). Enhanced UV and ethanol vapour sensing of a single 3-D ZnO tetrapod alloyed with Fe2O3nanoparticles. *Sensors Actuators B Chem.* 245, 448–461. doi: 10.1016/j.snb.2017.01.107

Ma, L., Ma, S.Y., Kang, H., Shen, X. F., Wang, T. T., Jiang X. H., et al. (2017). Preparation of Ag-doped $ZnO\text{-}SnO_2$ hollow nanofibers with an enhanced ethanol sensing performance by electrospinning. *Mater. Lett.* 209, 188–192. doi: 10.1016/j.matlet.2017.08.004

Ma, X., Song, H., and Guan, C. (2013). Enhanced ethanol sensing properties of ZnO-doped porous SnO2 hollow nanospheres. *Sensors Actuators B Chem.* 188, 193–199. doi: 10.1016/j.snb.2013.06.099

Miller, D. R., Akbar, S. A., and Morris, P. A. (2014). Nanoscale metal oxide-based heterojunctions for gas sensing: a review. *Sensors Actuators B Chem.* 204, 250–272. doi: 10.1016/j.snb.2014.07.074

NaderiNasrabadi, M., Mortazavi, Y., and Khodadadi, A. A. (2016). Highly sensitive and selective Gd2O3-doped SnO2 ethanol sensors synthesized by a high temperature and pressure solvothermal method in a microreactor. *Sensors Actuators B Chem.* 230, 130–139. doi: 10.1016/j.snb.2016.02.045

Pan, K. Y., Lin, Y. H., Lee, P. S., Wu, J. M., and Shih, H. C. (2012). Synthesis of SnO 2-ZnO core-shell nanowires and their optoelectronic properties. *J. Nanomater.* 2012, 1–6. doi: 10.1155/2012/279245

Park, S., An, S., Mun, Y., and Lee, C. (2013). UV-Enhanced NO $_2$ gas sensing properties of SnO_2 -core/ZnO-shell nanowires at room temperature. *ACS Appl. Mater. Interfaces* 5, 4285–4292. doi: 10.1021/am400500a

Park, S., Kim, S., Sun, G. J., and Lee, C. (2015). Synthesis, structure, and ethanol gas sensing properties of In_2O_3 nanorods decorated with Bi_2O_3 nanoparticles. *ACS Appl. Mater. Interfaces* 7, 8138–8146. doi: 10.1021/acsami.5b00972

Patil, G. E., Kajale, D. D., Chavan, D. N., Pawar, N. K., Ahire, P. T., Shinde, S. D., et al. (2011). Synthesis, characterization and gas sensing performance of SnO_2 thin films prepared by spray pyrolysis. *Bull. Mater. Sci.* 34, 1–9. doi: 10.1007/s12034-011-0045-0

Powers, S. E., Hunt, C. S., Heermann, S. E., Corseuil, H. X., Rice, D., and Alvarez, P. J. J. (2001). The transport and fate of ethanol and BTEX in groundwater contaminated by gasohol. *Crit. Rev. Environ. Sci. Technol.* 31, 79–123. doi: 10.1080/20016491089181

Rong, P., Ren, S., and Yu, Q. (2019). Fabrications and applications of ZnO nanomaterials in flexible functional devices-a review. *Crit. Rev.Anal. Chem.* 49, 333–349. doi: 10.1080/10408347.2018.1531691

Sakthivel, B., and Nammalvar, G. (2019). Selective ammonia sensor based on copper oxide/reduced graphene oxide nanocomposite. *J. Alloys Compd.* 788, 422–428. doi: 10.1016/j.jallcom.2019.02.245

Tan, W., Tan, J., Fan, L., Yu, Z., Qian, J., and Huang, X. (2018). Fe2O3-loaded NiO nanosheets for fast response/recovery and high response gas sensor. *Sensors Actuators B Chem.* 256, 282–293. doi: 10.1016/j.snb.2017.09.187

Tang, W., Wang, J., Yao, P., and Li, X. (2014). Hollow hierarchical SnO2-ZnO composite nanofibers with heterostructure based on electrospinning method for detecting methanol. *Sensors Actuators B Chem.* 192, 543–549. doi: 10.1016/j.snb.2013.11.003

Thanh Le, D. T., Trung, D. D., Chinh, N. D., Thanh Binh, B. T., Hong, H. S., Van Duy, N., et al. (2013). Facile synthesis of SnO2-ZnO core-shell nanowires for enhanced ethanol-sensing performance. *Curr. Appl. Phys.* 13, 1637–1642. doi: 10.1016/j.cap.2013.06.024

Tharsika, T., Haseeb, A. S. M. A., and Sabri, M. F. M. (2014a). Photoluminescence studies on spray pyrolysis deposited ZnO-SnO2 mixed thin films. *Adv. Mater. Res.* 25, 318–322. doi: 10.4028/www.scientific.net/AMR.925.318

Tharsika, T., Haseeb, A. S. M. A., and Sabri, M. F. M. (2014b). Structural and optical properties of ZnO-SnO2mixed thin films deposited by spray pyrolysis. *Thin Solid Films* 558, 283–288. doi: 10.1016/j.tsf.2014.02.022

Tharsika, T., Haseeb, A. S. M. A. S. M. A., Akbar, S. A. A., and Thanihaichelvan, M. (2015). Tailoring ZnO nanostructures by spray pyrolysis and thermal annealing. *Ceram. Int.* 41, 5205–5211. doi: 10.1016/j.ceramint.2014.12.062

Timmer, B., Olthuis, W., and Van Den Berg, A. (2005). Ammonia sensors and their applications—A review. *Sensors Actuators B Chem.* 107, 666–677. doi: 10.1016/j.snb.2004.11.054

ul Haq, M., Zhang, Z., Wen, Z., Khan, S., ud Din, S., Rahman, N., et al. (2019). Humidity sensor based on mesoporous Al-doped NiO ultralong nanowires with enhanced ethanol sensing performance. *J. Mater. Sci. Mater. Electron.* 30, 1–14. doi: 10.1007/s10854-019-01030-8

Vasudeva, K., Mitra, N., Umasankar, P., and Dhingra, S. C. (1996). Steam reforming of ethanol for hydrogen production: thermodynamic analysis. *Int. J. Hydrogen Energy* 21, 13–18. doi: 10.1016/0360-3199(95)00030-H

Wang, H., and Rogach, A. L. (2014). Hierarchical SnO2 nanostructures: recent advances in design, synthesis, and applications. *Chem. Mater.* 26, 123–133. doi: 10.1021/cm4018248

Wang, Q., Bai, J., Huang, B., Hu, Q., Cheng, X., Li, J., et al. (2019). Design of $NiCo_2O_4$@SnO_2 heterostructure nanofiber and their low temperature ethanol sensing properties. *J. Alloys Compd.* 791, 1025–1032. doi: 10.1016/j.jallcom.2019.03.364

Wang, T., Xu, S., Hu, N., Hu, J., Huang, D., Jiang, W., et al. (2018). Microwave preparation and remarkable ethanol sensing properties of ZnO particles with controlled morphologies in water-ethylene glycol binary solvent system. *Sensors Actuators B Chem.* 255, 1006–1014. doi: 10.1016/j.snb.2017.08.099

Yan, S. H., Ma, S. Y., Li, W. Q., Xu, X. L., Cheng, L., Song, H. S., et al. (2015a). Synthesis of SnO2-ZnO heterostructured nanofibers for enhanced ethanol gas-sensing performance. *Sensors Actuators B Chem.* 221, 88–95. doi: 10.1016/j.snb.2015.06.104

Yan, S. H., Ma, S. Y., Xu, X. L., Li, W. Q., Luo, J., Jin, W. X., et al. (2015b). Preparation of SnO_2–ZnO hetero-nanofibers and their application in acetone sensing performance. *Mater. Lett.* 159, 447–450. doi: 10.1016/j.matlet.2015.07.051

Yang, X., Yu, Q., Zhang, S., Sun, P., Lu, H., Yan, X., et al. (2018). Highly sensitive and selective triethylamine gas sensor based on porous SnO2/Zn2SnO4 composites. *Sensors Actuators B Chem.* 266, 213–220. doi: 10.1016/j.snb.2018.03.044

Yao, M., Ding, F., Cao, Y., Hu, P., Fan, J., Lu, C., et al. (2014). Sn doped ZnO layered porous nanocrystals with hierarchical structures and modified surfaces for gas sensors. *Sensors Actuators B Chem.* 201, 255–265. doi: 10.1016/j.snb.2014.04.078

Yao, M.-S., Tang, W.-X., Wang, G.-E., Nath, B., and Xu, G. (2016). MOF thin film-coated metal oxide nanowire array: significantly improved chemiresistor sensor performance. *Adv. Mater.* 28, 5229–5234. doi: 10.1002/adma.201506457

Zheng, L., Zheng, Y., Chen, C., Zhan, Y., Lin, X., Zheng, Q., et al. (2009). Network structured SnO_2/ZnO heterojunction nanocatalyst with high photocatalytic activity. *Inorg. Chem.* 48, 1819–1825. doi: 10.1021/ic802293p

Conflict of Interest Statement: The authors declare that the research was conducted in the absence of any commercial or financial relationships that could be construed as a potential conflict of interest.

frontiers in Materials

ORIGINAL RESEARCH
published: 16 July 2019
doi: 10.3389/fmats.2019.00171

Heating Method Effect on SnO Micro-Disks as NO_2 Gas Sensor

Mateus G. Masteghin[1,2], *Denis R. M. Godoi*[2] *and Marcelo O. Orlandi*[2]*

[1] *Advanced Technology Institute, University of Surrey, Guildford, United Kingdom,* [2] *Department of Physical-Chemistry, São Paulo State University, Araraquara, Brazil*

There is an increasing concern about NO_x emission, and many studies have been carried out using metal oxide semiconductors (MOS) aiming its detection. Among the MOS, the SnO micro-disks present a high sensor response and a great selectivity toward NO_2. Nevertheless, sensor signal, limit of detection (LOD), and recovery time are related to the experimental setup used to carry on the measurements. Thus, two different heating methods (*self-heating* and *external heating*) have been carried out to understand in what manner they change the sensor properties of the SnO micro-disks onto interdigitated electrodes. The *external heating* method presented higher sensor signal, best LOD, and lower recovery time, mainly due to the lack of a temperature gradient between the SnO disks and the chamber atmosphere. On the other hand, response time was shown to be the same regardless of the method. Briefly, the authors used thermodynamic equations to better understand the temperature effect on the gas-solid interactions occurring between SnO disks and NO_2 species.

Keywords: SnO, gas sensor, heating mode, *self-heating*, *external heating*, NO_2

OPEN ACCESS

Edited by:
Xiaogan Li,
Dalian University of Technology, China

Reviewed by:
Yueli Liu,
Wuhan University of Technology, China
Peng Sun,
Jilin University, China

***Correspondence:**
Marcelo O. Orlandi
marcelo.orlandi@unesp.br

Specialty section:
This article was submitted to Functional Ceramics, a section of the journal Frontiers in Materials

Received: *17 May 2019*
Accepted: *01 July 2019*
Published: *16 July 2019*

Citation:
Masteghin MG, Godoi DRM and Orlandi MO (2019) Heating Method Effect on SnO Micro-Disks as NO_2 Gas Sensor. Front. Mater. 6:171. doi: 10.3389/fmats.2019.00171

INTRODUCTION

Human activities such as the use of mobile sources and electric power plants are major contributors that generate NO_2, which is one of the compounds in the NO_x family (Nagase and Funatsu, 1990; Correa, 1993). In addition to the intrinsic toxicity of the NO_2 (Azoulay-Dupuis et al., 1983) and its eutrophication aptitude (Glibert et al., 2005), the NO_2 reacts with other molecules in the atmosphere giving rise to acid rain and O_3 (likewise toxic in the troposphere) (Rietjens et al., 1986; Chang et al., 1988). Furthermore, among the NO_x species, NO_2 has the longest lifespan making it difficult to control as this causes spreading (Crutzen, 1979). In this context, there is a need to use highly sensitive and selective gas sensor devices for the detection of this pollutant.

Gas sensor devices based on chemo-resistive metal oxide semiconductors (MOSs), (Barsan and Weimar, 2001; Comini et al., 2002; Barsan et al., 2007; Lee, 2009; Wang et al., 2010; Jin et al., 2017) such as SnO_2 (Batzill and Diebold, 2005; Ren et al., 2015; Xu et al., 2015; Cheng et al., 2016; Kida et al., 2016; Li et al., 2016), ZnO (Xu et al., 2000; Wan et al., 2004; Li et al., 2017; Morandi et al., 2017), In_2O_3 (Li et al., 2003; Zhang et al., 2004; Xiao et al., 2017), WO_3 (Li et al., 2004; Yang and Guo, 2017), and CuO (Kim and Lee, 2014), are widely used for the detection of toxic and explosive gases (NO_2, CO, CH_4, H_2S, and H_2) as well as VOCs (C_3H_6O, and C_2H_5OH). The detection mechanism of these MOSs is based on the resistivity change after the interaction of the analyte gas with the surface of the material, either by direct (NO_2) or indirect (H_2, CO, CH_4) mechanisms (Barsan and Weimar, 2001; Batzill and Diebold, 2005). Among the cited MOSs, SnO_2 has been studied the most, due to its great performance and chemical stability (Batzill and Diebold, 2005). However, more attention has recently been given to other Sn_xO_y stoichiometries with less

stable oxidation states, such as SnO (Suman et al., 2013, 2015; Hien and Heo, 2016; Masteghin and Orlandi, 2018) and Sn_3O_4 (Suman et al., 2014, 2015; Li et al., 2015; Liu et al., 2016).

These unusual stoichiometries were reported as gas sensors, nevertheless, many studies with respect to their sensor mechanism must be performed in order to understand the causes of the high sensor signals, especially regarding NO_2. Suman et al. (2013) reported a giant chemo-resistance of SnO disk-like structures when exposed to 100 ppm of NO_2, achieving a sensor signal of 1,000 (with high selectivity toward H_2, CO, and CH_4), which was attributed to the existence of the lone pairs in the (0 0 1) surface planes (Le Bellac et al., 1995; Walsh and Watson, 2004). Considering the performance of the SnO micro-disks as a gas sensor, this study used the same material, aiming to further understand the gas-solid interactions using different experimental setups.

In summary, this work compares the gas sensor signal of the SnO micro-disks when subjected to distinct experimental arrangements, such as different types of heating. For example, when heated through power controlled external resistors in a horizontal tubular furnace or in a specially designed gas sensor chamber, or else when the measurements were performed through the *self-heating* method. The 1,000-fold increase in the SnO disks resistance is observed when the measurement is performed in the horizontal tubular furnace (Suman et al., 2013) and the lowest recorded sensor signal is observed through the *self-heating* method. The main contribution of this work is to correlate the gas sensor properties to the measurement setup.

EXPERIMENTAL

In order to synthesize the SnO disks, SnO_2 powder (Sigma-Aldrich, 99.9% purity), was mechanically mixed with carbon black (Union Carbide, >99% purity) in a molar ratio of 1.5:1 and submitted to the carbothermal reduction route (Suman et al., 2013; Masteghin and Orlandi, 2018). The procedure involved preparing 1 g of the SnO_2:C mixture that was inserted in the central region of a horizontal tubular furnace, and held at 1,135°C for 75 min using heating and cooling rates of 10°C min^{-1}. A nitrogen flow of 150 cm^3 min^{-1} was used throughout the synthesis in order to maintain an inert atmosphere inside the tube. A dark-colored wool-like material was removed from the alumina tube (cold region) containing a mixture of SnO nanobelts and micro-disks. The mixture was submitted to a separation process in order to decant the SnO micro-disks, which were the subject of this study.

The morphological characteristics of materials were studied in a JEOL (model JSM-7500F) field emission scanning electron microscope (FEG-SEM) and a FEI Dual Beam Microscope (model Helios Nanolab 600i).

The phase and the crystallinity of the SnO disks were analyzed by X-ray diffraction (XRD) using Cu *Kα* radiation (λ = 15,406 Å) and a D/teX Ultra two linear detector in a Rigaku (model RINT2000) diffractometer. Raman spectroscopy was performed to study the surface structural variations and the presence of intermediate phases. Micro-Raman scattering spectroscopy was carried out using a 514 nm laser (Melles Griot) coupled to an iHR550 Horiba module with the microscope head adapted by Jobin Yvon (model M.F.O.).

Gas sensor measurements were performed after small drops (0.5 μL each) of a SnO micro-disks suspension were dropped onto the platinum interdigitated electrodes deposited over alumina substrates.

Meant for the *self-heating* measurements, a built-in-electrode consisting of an interdigitated electrode (IDE) and a heater circuit was used (**Figure 1A**). The heater circuit is made of platinum deposited by sputtering on the back of the substrate. Then, the built-in-electrode containing the SnO disks was inserted in the gas sensor chamber to carry out the measurements.

In order to perform the gas sensor measurements using the *external heating* method, an external resistance present in the sensor chamber heats the SnO sample placed on the gray ceramic piece depicted in **Figure 1B**. Therefore, only the IDE part of the substrate (**Figure 1A**) was used during this kind of measurement. Moreover, the heater warms the whole test chamber (including the analyte) by means of both conduction and convection.

Figure 1C shows another experimental setup previously used to carry on gas sensor measurements heated by the *external heating* method. The details of the horizontal tubular furnace arrangement used to study the SnO micro-disks can be seen in the work of Suman et al. (2013), but a schematic draw is presented in **Figure 1C**. Comparing **Figures 1B,C**, it can be observed that the main difference between the two setups is the larger warm area provided by the external heater of the tubular furnace.

The gas sensor measurements were fixed at 200°C for the *external heating* (conventional heating), the temperature at which the SnO micro-disks presented higher sensor response (Suman et al., 2013). The *self-heating* mode measurements were carried out at 150, 200, and 250°C.

The measurements were carried out by monitoring changes in resistance using a stabilized voltage source (Agilent 34972A) during cyclic exposures to different concentrations of NO_2 (1–50 ppm) diluted in synthetic dry air (baseline gas) using mass flow controllers (MKS). The sensor signal was evaluated by considering the $RNO_2/R_{Baseline}$ ratio. The controlled release of the analyte gas (NO_2) at its different concentrations was done after 12 h stabilization of device in dry synthetic air baseline; each NO_2 concentration was released for 20 min at intervals of 1 h between successive releases. The flow remained constant and equal to 200 cm^3 min^{-1} all over the measurements.

RESULTS AND DISCUSSION

A dark brown material was removed from the alumina tube after synthesis. The desired SnO material was sited in a region where the temperature range was between 200 and 350°C.

Figures 2A,B show FEG-SEM images of the SnO micro-disks obtained after the decantation process, showing that the disks and nanobelts were well-separated. It is clearly visible in **Figure 1B** that many of the disks appear to be the

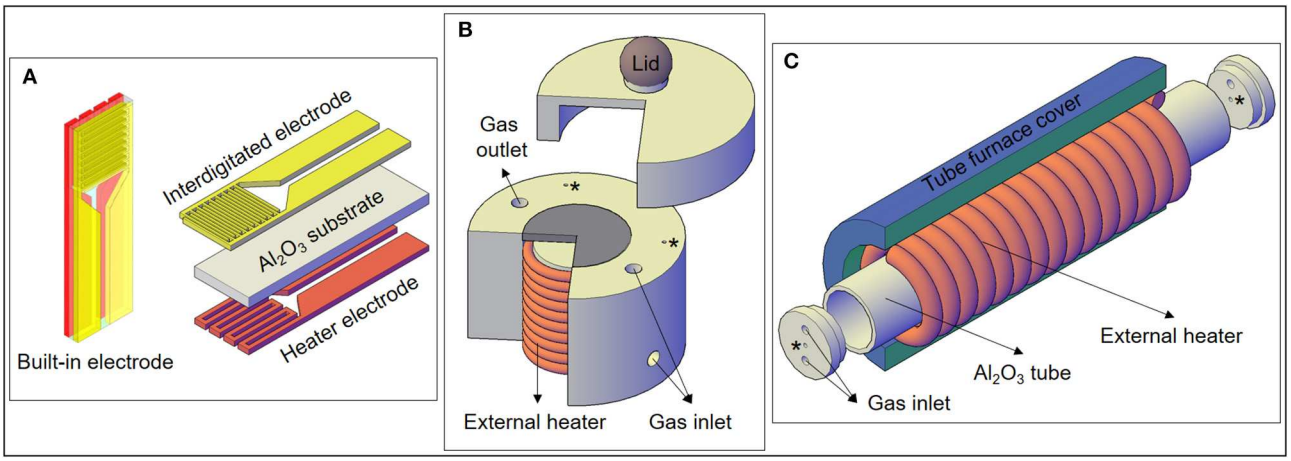

FIGURE 1 | (A) Electrodes used for the experiments, including the heater electrode for the *self-heating* method. **(B)** Specially designed gas sensor chamber used for the *external heating* measurements of this work, with a cross-section showing the external heater. **(C)** Representation of the *external heating* setup used in a previous experiment with SnO micro-disks (Suman et al., 2013). The "*" correspond to wires feedthroughs.

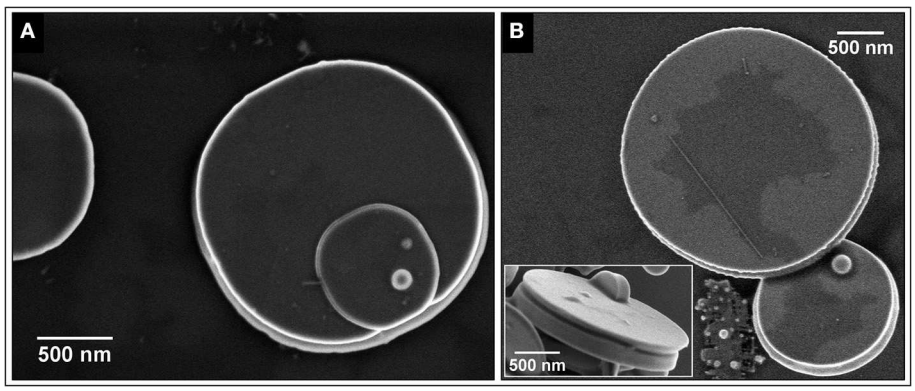

FIGURE 2 | (A) SEM image of a typical SnO micro-disk. **(B)** Micro-disk with conical edge and a big one showing that it can appear flat and slim depending on the angle. The inset shows the side view of a SnO micro-disk displaying the middle-out growth mechanism even in a disk with a smooth surface.

result of two disks stuck together, being this morphological feature related to the vapor-solid (VS) growth mechanism (Dai et al., 2002; Orlandi et al., 2008).

The FEG-SEM images (**Figure 2**) show the existence of at least two phases–disk itself and the bright spheres. Further characterization by XRD (**Figure 3A**) indicates the predominance of the *Romarchite* phase of the SnO (Space group P4/nmm, *Litharge*-type Tetragonal structure, similar to α-PbO), nonetheless secondary phases corresponding to the metallic tin (Sn^0) and *cassiterite* phase of the SnO_2 (*Rutile*-type Tetragonal structure) were also indexed as minor amount. A small amount of Sn_3O_4 phase cannot be discarded from the XRD results. For TEM and XANES characterizations, one can refer to the work of Suman et al. (2013).

Figure 3B shows the Raman spectra of the SnO micro-disks alongside the peaks fitting of each present phase. The blue line shows the peaks fit for the SnO phase. The means (χ_c) of the Lorentz simulations are at 113 and 210 cm^{-1}, corresponding to the E_{1g} and A_{1g} vibrational modes of the SnO phase, respectively. These two χ_c values are somewhat shifted to smaller Raman values compared to the theoretical results (Eifert et al., 2017), as can be seen in **Table 1**.

The existence of the secondary Sn_3O_4 phase (red line) is minor but still present in the Raman measurements, since its A_g vibrational mode appears at 141 cm^{-1}, and the B_g vibrational mode is shown at 170 cm^{-1}. Nevertheless, through Raman measurements, it was also possible to attribute the existence of the Sn_2O_3 phase (green line)–or most probably clusters with this coordination–in the SnO micro-disks (B_g vibrational mode at 189 cm^{-1}). This peak at 189 cm^{-1} and the absence of peaks regarding the SnO_2 phase makes Raman spectroscopy complementary to the XRD, because in the Raman analysis the local bonding and the electronic structure play the main role, in contrast to the XRD, in which only the symmetry, the long-range 3D arrangements, and the atomic factors are taken into account (Sangaletti et al., 1998; Eifert et al., 2017). Besides, theoretical

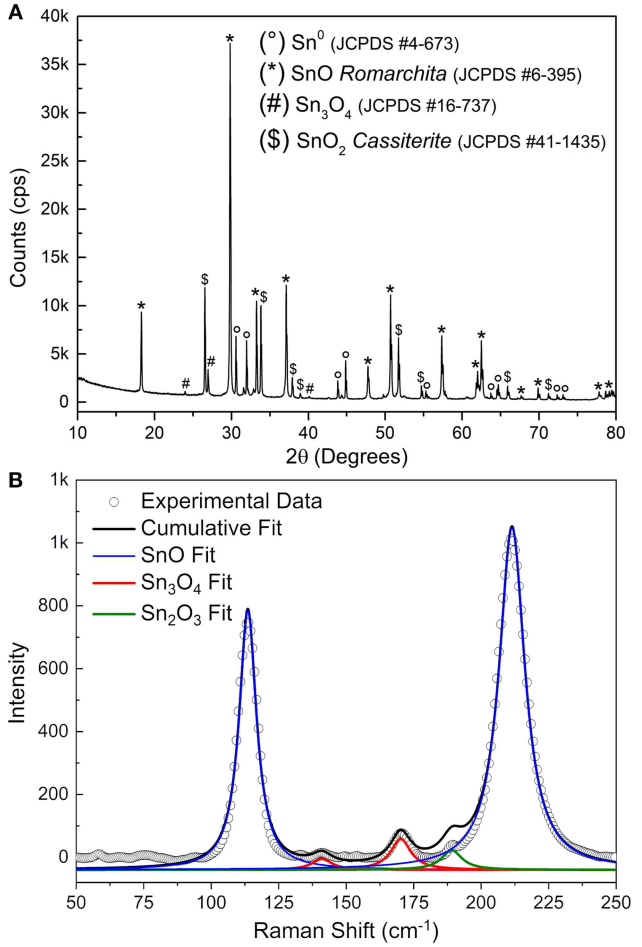

FIGURE 3 | (A) XRD of the SnO micro-disks after synthesis and sedimentation process. **(B)** Raman spectra of the same SnO micro-disks. The continuous lines represent the multiple peaks fit for each phase presented in the disks (different colors).

studies showed that the Sn_2O_3 is the strongest Raman scatterer–and that is the most probable reason it was detected–followed by SnO, Sn_3O_4, and SnO_2 (Eifert et al., 2017).

Comparing the redshift results for the SnO peaks it can be said that the experimental bond lengths are longer than the ones used for the theoretical simulations (Hardcastle and Wachs, 1991). This outcome supports the existence of the lone pairs localized in the Sn^{2+} ions in the tetragonal structure of the SnO (Walsh and Watson, 2004). One noteworthy point is the higher redshift of the A_{1g} mode compared to the E_{1g} mode of the SnO, endorsing the contribution of the lone pairs for increasing the Sn-O binding length, once the A_{1g} mode coincides to the oxygen vibration in the c direction and the E_{1g} corresponds to the atoms vibration perpendicular to the c direction (Geurts et al., 1984). This finding paves the way for a more sophisticated *in-situ* and operando spectroscopy which can detect the interaction of oxidizing molecules (O_2 and NO_2, for example) with the SnO lone pairs, by shifting the peaks at 113 and 210 cm^{-1} to higher wavenumbers values, since an interacting molecular orbital causes less repulsion to the surrounding atoms rather than a lone pair (Atkins et al., 2018).

Figure 4A shows the gas sensor response of the SnO micro-disks under three different temperatures reached via the *self-heating* method. One can see the higher sensor signal obtained at 200°C (except for 1 ppm of NO_2), as expected based on the measurements carried out in an adapted tubular furnace (Suman et al., 2013). This result emphasizes the need for a balance between the adsorption and desorption rate of the gases onto the SnO surface–both exponentially reliant on the temperature. Equation 1 shows an easier way of understanding this temperature effect on the sensor signal only by means of surface coverage (Θ):

$$\Theta = \frac{k_{ads}}{k_{des}} * \exp \frac{\Delta H_{Chem}}{kT}, \quad (1)$$

where k_{ads} and k_{des} are the adsorption and desorption constants, respectively; ΔH_{Chem} is the chemisorption enthalpy; k is the Boltzmann constant; and T is the temperature in Kelvin.

It is well-known that some amount of energy (heat) is necessary to overcome the activation barrier for the chemisorption (ΔH_{Chem}), otherwise, the gas molecules would be in a physisorbed state (Batzill and Diebold, 2005). However, by Equation 1, if the temperature goes too high the coverage decreases and sensor signal drops, in full agreement with previous results involving SnO micro-disks in multi- and single-device configurations (Suman et al., 2013; Masteghin and Orlandi, 2018).

Figure 4B shows the sensor response for the SnO micro-disks at 200°C reached through two different heating modes, *external heating* (red spheres), and *self-heating* (blue triangles). The sensor signal is higher for the device when it is in a hermetically sealed chamber heated by conventional resistances (*external heating*)–equals to 52 at 50 ppm–rather than when *self-heating* method was used–sensor signal equals to nine. Furthermore, the detection limit (LOD) for NO_2 analyte went from 1 ppm using the *self-heating* mode to 600 ppb using the *external heating* method, both below the toxic limits. Despite the different sensor signals obtained for the two samples when exposed to different heating modes, both presented increasing sensor signals as the NO_2 concentration increased. This is a result of the increased values of resistance reached after different concentrations of the analyte gas were released, corresponding to an n-type semiconductor behavior.

Table 2 summarizes the obtained sensor signals for 50 ppm of NO_2, with a constant flow of 200 sccm, at 200°C. Previous results obtained in a horizontal tubular furnace were added in **Table 2** for comparative purposes (Suman et al., 2013).

To understand how the experimental setup influences the gas sensor response is necessary to elucidate the interactions between the surface of the material and the gases (mainly O_x^{y-} species, and NO_2 from the baseline and analyte gas, respectively). The SnO micro-disks deposited onto the IDE will be considered as a porous layer with grain boundaries generated by the contact between the discs. The initial oxygen species that can vary within

TABLE 1 | Obtained peaks mean values (χ_c) for the SnO micro-disks Raman Spectra, and the theoretical results for comparative purposes.

Peak Number	Experimental χ_c	Theoretical (Eifert et al., 2017)
1) E_{1g} SnO	113 cm^{-1}	115 cm^{-1}
2) A_g Sn_3O_4	141 cm^{-1}	140 cm^{-1}
3) B_g Sn_3O_4	170 cm^{-1}	170 cm^{-1}
4) B_g Sn_2O_3	189 cm^{-1}	190 cm^{-1}
5) A_{1g} SnO	210 cm^{-1}	217 cm^{-1}

TABLE 2 | The gas sensor signals for 50 ppm of NO_2 at 200°C.

Heating mode	Sensor signal
External heating	52
Self-heating	9
Horizontal tubular furnace (Suman et al., 2013)	550

The first two methods were the ones used in this study and the last one was included for a comparative purpose (Suman et al., 2013). All of them used a constant flow of 200 sccm consisting of NO_2 and dry synthetic air mixture.

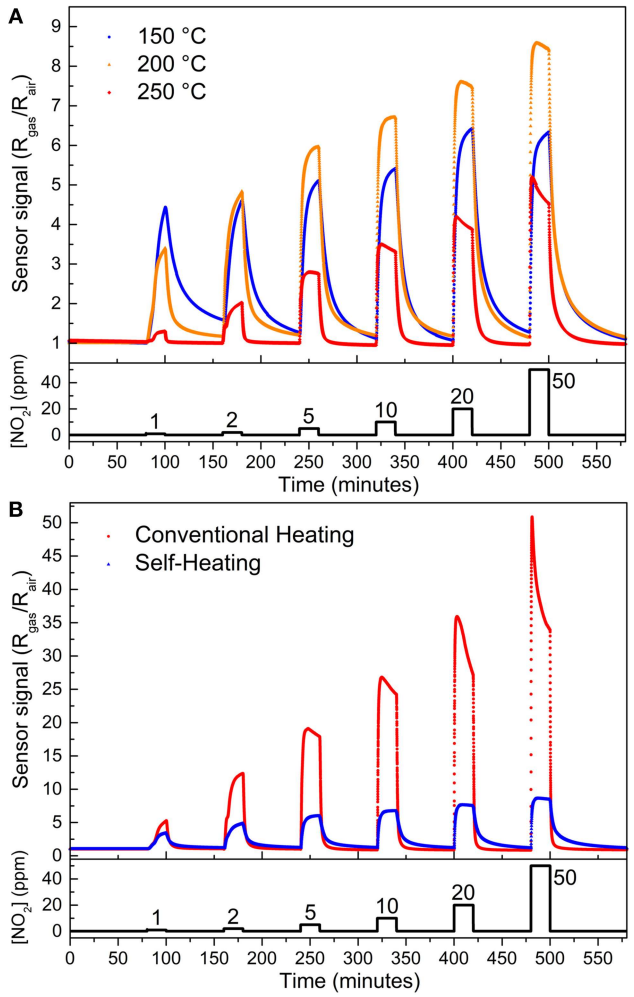

FIGURE 4 | Gas sensor signal as a function of NO_2 concentration obtained **(A)** by *self-heating* method at 150°C (blue sphere), 200°C (orange triangle), and 250°C (red rhomb). **(B)** at 200°C reached by two different methods: *self-heating* (blue triangles) and *external heating* (red spheres). Gas flow fixed at 200 cm^3 min^{-1}.

the operating temperature adsorb onto the material surface generating back-to-back potential barriers at the boundaries. Afterward, the NO_2 interacts with the empty tin sites through the overlap of NO_2 empty π_u molecular orbital with the (Sn 5s–O $2p_z$)* lone pairs, further increasing the resistivity of the material by heightening and enlarging those potential barriers (Barsan and Weimar, 2001; Batzill and Diebold, 2005).

Thus, knowing that NO_2 directly interacts with SnO surface, the higher availability of the analyte will enhance the sensor signal, due to a higher amount of electrons transferred from the semiconductor to the chemisorbed gas. Bearing this in mind, the setup heated by the *external heating* method is the most likely to present a larger sensor signal since it would deliver a greater amount of NO_2 to react with SnO. This occurs because the NO_2 dimerization reaction (Equation 2) is an exothermic reaction which releases (–)57.2 kJ mol^{-1}. Consequently, by the Le Chatelier Principle the heat (temperature) can change the reaction direction to the NO_2 side (Atkins and Jones, 2005).

$$2NO_{2(g)} \rightarrow N_2O_{4(g)} \quad (2)$$

NO_2 dimerization has a relatively high Kp (equilibrium constant) of 6.5 at 25°C, which decreases to Kp equals 1.18 at 49.5°C (and, ∼0.05 at 200°C) (Yu and Gao, 1997), endorsing the temperature effect on the amount of NO_2 delivered to the SnO disks. So, Equation (2) and the Kp values support the *external heating* method presenting a higher sensor signal than the *self-heating* method.

Another factor contributing to the higher sensor signal of the *external heating* mode is the temperature effect (T) on the chemical potential of the NO_2 molecules (μ_{NO2}) in the vapor phase [$\mu_{NO2} = \mu_0 + RT \ln (P_{NO2})$]. It takes place because the difference in the chemical potential of the vapor phase and the adsorbed state drives the equilibrium, and once NO_2 molecules have a higher μ_{NO2} value in the heated chamber, it has a higher probability to form the Sn-NO_2 adsorbed state. Nonetheless, the higher sensor signal obtained in the tubular furnace (**Table 2**), is related to having a larger room for the analyte gas to be heated before reaching the sample.

Figure 5A shows the response times for the *self-heating* measurements at three different temperatures (150, 200, and 250°C), where an exponential behavior (continuous lines) can be seen in each working temperature. The increasing temperature resulted in smaller response times, especially at higher NO_2 concentration, and this effect is most pronounced between response times at 150 and 200°C. These features indicate an Arrhenius kinetics with a given threshold activation energy for the chemisorption process that is supplied to the material as heat (Zaza et al., 2019). Moreover, **Figure 5B** shows that different heating methods do not cause a meaningful variation in the response time at 200°C.

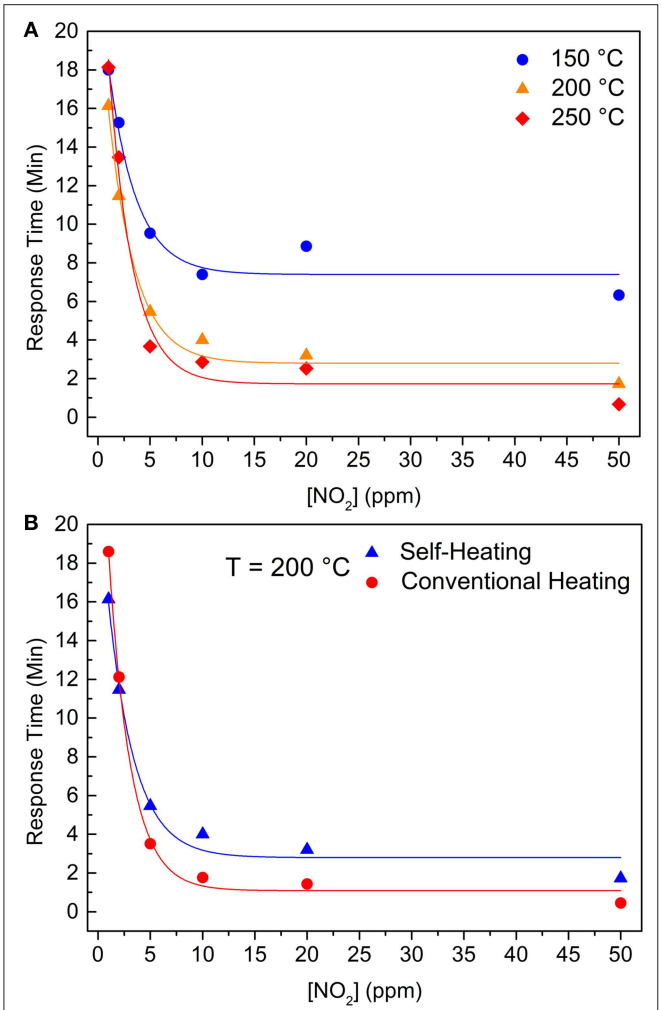

FIGURE 5 | Response times as a function of NO_2 concentration **(A)** for the *self-heating* method at 150°C (blue sphere), 200°C (orange triangle), and 250°C (red rhomb). **(B)** at 200°C reached by two different methods: *self-heating* (blue triangles) and *external heating* (red spheres). Continuous lines are exponential fitting of the data.

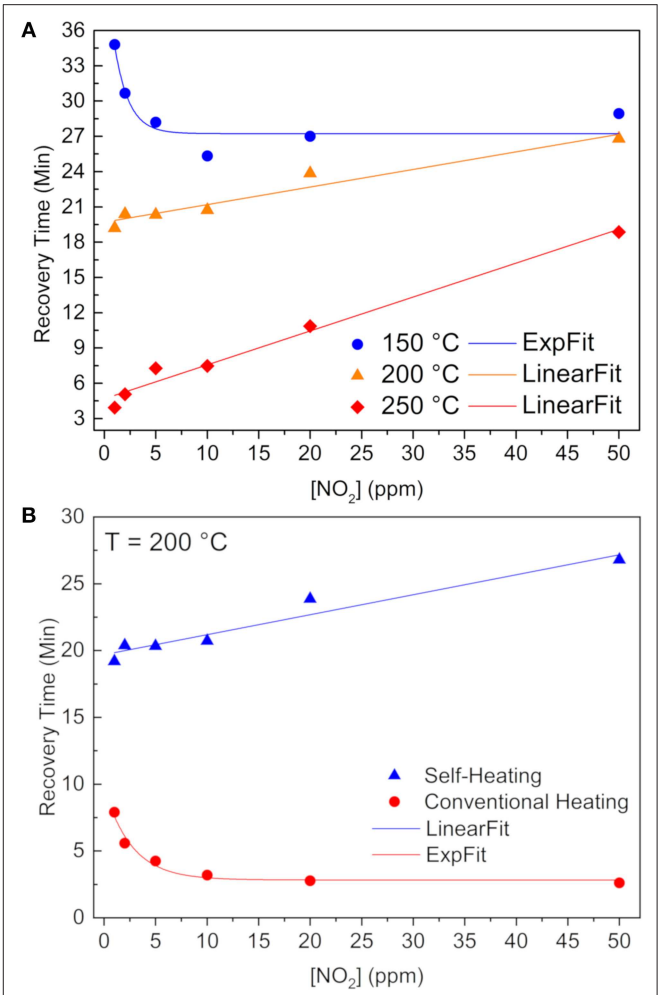

FIGURE 6 | Recovery times as a function of NO_2 concentration **(A)** for *self-heating* method at 150°C (blue sphere), 200°C (orange triangle), and 250°C (red rhomb). **(B)** at 200°C reached by two different methods: *self-heating* (blue triangles) and *external heating* (red spheres). Continuous lines are exponential or linear fitting of the data.

Thus, one can infer that the velocity of resistance change during the gas adsorption/chemisorption is controlled by the energy given to the electrons to cross an electric field of a charged surface (with a dipole momentum), reaching the NO_2 molecule. Once this energy is mainly provided as *heat*, and the temperature close to the IDE is the same for both heating methods, electrons have the same probability of reaching the surface and, consequently, the same response times, regardless being *self-heating* or *external heating*.

From **Figure 6A** one can see a recovery time behavior change whilst increasing the operating temperature throughout the *heater*. In order to have a 90% recovery of the baseline resistance value, chemisorbed NO_2 molecules must be released from the tin atoms. Thus, considering an Arrhenius kinetics for this removal rate constant ($k = A*e^{\frac{-E}{kT}}$), the limiting factor at 200 and 250°C is the pre-exponential factor (A), because at higher IDE temperatures, the NO_2 are loosely overlapped with the SnO lone pairs, so the required energy (ΔE) does not control the kinects any longer, but rather the amount of favorable collisions, which are smaller in the *self-heating* system when compared to *external heating* method (Batzill and Diebold, 2005).

Figure 6B clearly shows a lower recovery time when submitted to the *external heating* method, as a result of both higher pre-exponential factor and more energy available. Besides, we showed that $O_{(ads)}-$ species still remain onto the SnO surface, after stopping the release of the NO_2 (Masteghin and Orlandi, 2018), indicated in Equation (3) (Kaur et al., 2007; Sharma et al., 2013):

$$NO_2(gas) + Sn^{+2} \xrightarrow{Charg\ Transfer} (Sn^{3+} - NO_2(ads)^-) \xrightarrow{Dessorp} (Sn^{3+} - O_{(ads)}-) + NO_{(gas)} \quad (3)$$

Thus, having oxygen atomic species (O^-) is the quickest way to withdrawal these $O_{(ads)}-$ of the SnO surface and restore the baseline as observed for the *external heating* measurements. It is well-known that oxygen species depend on temperature (Barsan and Weimar, 2001), and that atomic oxygen is the majority at 200°C, in contrast with lower temperatures–like the atmosphere inside the chamber when using the *self-heating* method–where O_2^- are present.

In the present investigation, it has been shown how the experimental setup can influence the obtained gas sensor properties, such as sensor signal, limit of detection, and recovery time. This shows that the sensor signal increases and the recovery time decreases when using the *external heating* method (conventional), and no meaningful effect on the response time was observed when using the *self-heating* mode.

CONCLUSION

The present work has used SnO micro-disks in "carpet" mode, previously proven to be an excellent NO_2 sensor, to show how the experimental setup affects the gas sensor properties. XRD showed a majority of SnO phase (*Litharge*-type tetragonal structure), and this result was endorsed by Raman spectroscopy. Raman was also used to experimentally evince the existence of the so-called *lone pairs*, theoretically predicted and used to explain the high sensor response toward NO_2. Gas sensor measurements have shown that the gradient of temperature between the sample and the chamber atmosphere is responsible for the lower sensor signal obtained by the *self-heating* method, as well as the higher recovery time. Although the former properties have changed with the heating method, the response time was not influenced.

This work main contribution is the use of basic thermodynamic equations to explain how temperature affects the dimerization equilibrium of NO_2 molecules, the chemical potential of the analyte gas, the material coverage, and the desorption rate constant. Accordingly, the need to detail the experimental arrangement whilst analyzing the sensor properties.

DATA AVAILABILITY

The datasets generated for this study are available on request to the corresponding author.

AUTHOR CONTRIBUTIONS

MM executed the experimental work, wrote the first version of the manuscript, and was involved in the data analysis. DG analyzed the Raman results and revised the manuscript. MO is the coordinator of the research project, revised the manuscript, and worked on electron microscopy and electrical data analysis.

FUNDING

This research was funded by FAPESP [#2013/07296-2, #2015/21033-0, #2017/12870-0, and #2017/26219-0] and CNPq [#447760/2014-9, #303542/2015-2, and #443138/2016-8].

ACKNOWLEDGMENTS

The authors thank LMA-IQ for providing electron microscopy facilities.

REFERENCES

Atkins, P., De Paula, J., and Keeler, J. (2018). *Atkin's Physical Chemistry*. Oxford, UK: Oxford University Press.

Atkins, P., and Jones, L. (2005). *Chemical Principles. The Quest for Insight*. New York, NY: W. H. Freeman.

Azoulay-Dupuis, E., Torres, M., Soler, P., and Moreau, J. (1983). Pulmonary NO_2 toxicity in neonate and adult guinea pigs and rats. *Environ. Res.* 30, 322–339. doi: 10.1016/0013-9351(83)90218-9

Barsan, N., Koziej, D., and Weimar, U. (2007). Metal oxide-based gas sensor research: how to? *Sens. Actuators B Chem.* 121, 18–35. doi: 10.1016/j.snb.2006.09.047

Barsan, N., and Weimar, U. (2001). Conduction model of metal oxide gas sensors. *J. Electroceram.* 7, 143–167. doi: 10.1023/A:1014405811371

Batzill, M., and Diebold, U. (2005). The surface and materials science of tin oxide. *Prog. Surf. Sci.* 79, 47–154. doi: 10.1016/j.progsurf.2005.09.002

Chang, L.-Y., Mercer, R. R., Stockstill, B. L., Miller, F. J., Graham, J. A., Ospital, J. J., et al. (1988). Effects of low levels of NO_2 on terminal bronchiolar cells and its relative toxicity compared to O3. *Toxicol. Appl. Pharmacol.* 96, 451–464. doi: 10.1016/0041-008X(88)90005-1

Cheng, J. P., Wang, J., Li, Q. Q., Liu, H. G., and Li, Y. (2016). A review of recent developments in tin dioxide composites for gas sensing application. *J. Ind. Eng. Chem.* 44, 1–22. doi: 10.1016/j.jiec.2016.08.008

Comini, E., Faglia, G., Sberveglieri, G., Pan, Z., and Wang, Z. L. (2002). Stable and highly sensitive gas sensors based on semiconducting oxide nanobelts. *Appl. Phys. Lett.* 81, 1869–1871. doi: 10.1063/1.1504867

Correa, S. M. (1993). A review of NOx formation under gas-turbine combustion conditions. *Combust. Sci. Technol.* 87, 329–362. doi: 10.1080/00102209208947221

Crutzen, P. J. (1979). The role of NO and NO_2 in the chemistry of the troposphere and stratosphere. *Annu. Rev. Earth Planet Sci.* 7, 443–472. doi: 10.1146/annurev.ea.07.050179.002303

Dai, Z. R., Pan, Z. W., and Wang, Z. L. (2002). Growth and structure evolution of novel tin oxide diskettes. *J. Am. Chem. Soc.* 124, 8673–8680. doi: 10.1021/ja026262d

Eifert, B., Becker, M., Reindl, C. T., Giar, M., Zheng, L., Polity, A., et al. (2017). Raman studies of the intermediate tin-oxide phase. *Phys. Rev. Mater.* 1:14602. doi: 10.1103/PhysRevMaterials.1.014602

Geurts, J., Rau, S., Richter, W., and Schmitte, F. J. (1984). SnO films and their oxidation to SnO_2: raman scattering, IR reflectivity and X-ray diffraction studies. *Thin Solid Films*. 121, 217–225. doi: 10.1016/0040-6090(84)90303-1

Glibert, P. M., Seitzinger, S., Heil, C. A., Burkholder, J. M., Parrow, M. W., Codispoti, L. A., et al. (2005). The role of eutrophication in the global proliferation of harmful algal blooms. *Oceanography* 18, 198–209. doi: 10.5670/oceanog.2005.54

Hardcastle, F. D., and Wachs, I. E. (1991). Determination of vanadium-oxygen bond distances and bond orders by Raman spectroscopy. *J. Phys. Chem.* 95, 5031–5041. doi: 10.1021/j100166a025

Hien, V. X., and Heo, Y.-W. (2016). Effects of violet-, green-, and red-laser illumination on gas-sensing properties of SnO thin film. *Sens. Actuators B Chem.* 228, 185–191. doi: 10.1016/j.snb.2015.12.105

Jin, H., Abu-Raya, Y. S., and Haick, H. (2017). Advanced materials for health monitoring with skin-based wearable devices. *Adv. Healthc. Mater*. 6:1700024. doi: 10.1002/adhm.201700024

Kaur, J., Kumar, R., and Bhatnagar, M. C. (2007). Effect of indium-doped SnO_2 nanoparticles on NO_2 gas sensing properties. *Sens. Actuators B Chem*. 126, 478–484. doi: 10.1016/j.snb.2007.03.033

Kida, T., Suematsu, K., Hara, K., Kanie, K., and Muramatsu, A. (2016). Ultrasensitive detection of volatile organic compounds by a pore tuning approach using anisotropically shaped SnO_2 nanocrystals. *ACS Appl. Mater. Interfaces*. 8, 35485–35495. doi: 10.1021/acsami.6b13006

Kim, H.-J., and Lee, J.-H. (2014). Highly sensitive and selective gas sensors using p-type oxide semiconductors: overview. *Sens. Actuators B Chem*. 192, 607–627. doi: 10.1016/j.snb.2013.11.005

Le Bellac, D., Kiat, J. M., and Garnier, P. (1995). Electronic lone pair localization and electrostatic energy calculations: application to α-PbO, $SnO,Pb_{1-x}(TiO)_xO$, Pb_3O_4, $Pb_3(V,P)_2O_8$, and a BiSrCaCuO-type superconductor. *J. Solid State Chem*. 114, 459–468. doi: 10.1006/jssc.1995.1069

Lee, J.-H. (2009). Gas sensors using hierarchical and hollow oxide nanostructures: overview. *Sens. Actuators B Chem*. 140, 319–336. doi: 10.1016/j.snb.2009.04.026

Li, C., Zhang, D., Liu, X., Han, S., Tang, T., Han, J., et al. (2003). In_2O_3 nanowires as chemical sensors. *Appl. Phys. Lett*. 82, 1613–1615. doi: 10.1063/1.1559438

Li, S.-H., Chu, Z., Meng, F.-F., Luo, T., Hu, X.-Y., Huang, S.-Z., et al. (2016). Highly sensitive gas sensor based on SnO_2 nanorings for detection of isopropanol. *J. Alloys Compd*. 688, 712–717. doi: 10.1016/j.jallcom.2016.07.248

Li, S.-M., Zhang, L.-X., Zhu, M.-Y., Ji, G.-J., Zhao, L.-X., Yin, J., et al. (2017). Acetone sensing of ZnO nanosheets synthesized using room-temperature precipitation. *Sens. Actuators B Chem*. 249, 611–623. doi: 10.1016/j.snb.2017.04.007

Li, X., Wang, F., Tu, J., Shah, H. U., Hu, J., Li, Y., et al. (2015). Synthesis and ethanol sensing properties of novel hierarchical Sn_3O_4 nanoflowers. *J. Nanomater*. 16:980170. doi: 10.1155/2015/980170

Li, X.-L., Lou, T.-J., Sun, X.-M., and Li, Y.-D. (2004). Highly sensitive WO3 hollow-sphere gas sensors. *Inorg. Chem*. 43, 5442–5449. doi: 10.1021/ic049522w

Liu, J., Wang, C., Yang, Q., Gao, Y., Zhou, X., Liang, X., et al. (2016). Hydrothermal synthesis and gas-sensing properties of flower-like Sn_3O_4. *Sens. Actuators B Chem*. 224, 128–133. doi: 10.1016/j.snb.2015.09.089

Masteghin, M., and Orlandi, M. (2018). A gas sensor based on a single sno micro-disk. *Sensors*. 18:3229. doi: 10.3390/s18103229

Morandi, S., Fioravanti, A., Cerrato, G., Lettieri, S., Sacerdoti, M., and Carotta, M. C. (2017). Facile synthesis of ZnO nano-structures: morphology influence on electronic properties. *Sens. Actuators B Chem*. 249, 581–589. doi: 10.1016/j.snb.2017.03.114

Nagase, K., and Funatsu, K. (1990). "A study of NOx generation mechanism in diesel exhaust gas," in *SAE and Technical Paper* (Warrendale, PA), doi: 10.4271/901615

Orlandi, M. O., José Ramirez, A., Leite, E. R., and Longo, E. (2008). Morphological evolution of tin oxide nanobelts after phase transition. *Cryst. Growth Des*. 8, 1067–1072. doi: 10.1021/cg7009379

Ren, H., Zhao, W., Wang, L., Ryu, S. O., and Gu, C. (2015). Preparation of porous flower-like SnO 2 micro/nano structures and their enhanced gas sensing property. *J. Alloys Compd*. 653, 611–618. doi: 10.1016/j.jallcom.2015.09.065

Rietjens, M.,Poelen, C. M., Hempenius, R. A., Gijbels, M. J., and Alink, G. M. (1986). Toxicity of ozone and nitrogen dioxide to alveolar macrophages: comparative study revealing differences in their mechanism of toxic action. *J. Toxicol. Environ. Heal.* 19, 555–568. doi: 10.1080/15287398609530952

Sangaletti, L., Depero, L. E., Allieri, B., Pioselli, F., Comini, E., Sberveglieri, G., et al. (1998). Oxidation of Sn thin films to SnO_2. Micro-Raman mapping and x-ray diffraction studies. *J. Mater. Res*. 13, 2457–2460. doi: 10.1557/JMR.1998.0343

Sharma, A., Tomar, M., and Gupta, V. (2013). WO3 nanoclusters– SnO_2 film gas sensor heterostructure with enhanced response for NO_2. *Sens. Actuators B Chem*. 176, 675–684. doi: 10.1016/j.snb.2012.09.094

Suman, P. H., Felix, A. A., Tuller, H. L., Varela, J. A., and Orlandi, M. O. (2013). Giant chemo-resistance of SnO disk-like structures. *Sens. Actuators B Chem*. 186, 103–108. doi: 10.1016/j.snb.2013.05.087

Suman, P. H., Felix, A. A., Tuller, H. L., Varela, J. A., and Orlandi, M. O. (2015). Comparative gas sensor response of SnO_2, SnO and Sn_3O_4 nanobelts to NO_2 and potential interferents. *Sens. Actuators B Chem*. 208, 122–127. doi: 10.1016/j.snb.2014.10.119

Suman, P. H., Longo, E., Varela, J. A., and Orlandi, M. O. (2014). Controlled synthesis of layered Sn_3O_4 nanobelts by carbothermal reduction method and their gas sensor properties. *J. Nanosci. Nanotechnol*. 14, 6662–6668. doi: 10.1166/jnn.2014.9356

Walsh, A., and Watson, G. W. (2004). Electronic structures of rocksalt, litharge, and herzenbergite SnO by density functional theory. *Phys. Rev. B Condens. Matter Mater. Phys*. 70:235114. doi: 10.1103/PhysRevB.70.235114

Wan, Q., Li, Q. H., Chen, Y. J., Wang, T.-H., He, X. L., Li, J. P., et al. (2004). Fabrication and ethanol sensing characteristics of ZnO nanowire gas sensors. *Appl. Phys. Lett*. 84, 3654–3656. doi: 10.1063/1.1738932

Wang, C., Yin, L., Zhang, L., Xiang, D., and Gao, R. (2010). Metal oxide gas sensors: sensitivity and influencing factors. *Sensors*. 10, 2088–2106. doi: 10.3390/s100302088

Xiao, B., Wang, D., Song, S., Zhai, C., Wang, F., and Zhang, M. (2017). Fabrication of mesoporous In_2O_3 nanospheres and their ultrasensitive NO 2 sensing properties. *Sens. Actuators B Chem*. 248, 519–526. doi: 10.1016/j.snb.2017.04.022

Xu, G., Zhang, L., He, C., Ma, D., and Lu, Z. (2015). Adsorption and oxidation of NO on various SnO_2(110), surfaces: a density functional theory study. *Sens. Actuators B Chem*. 221, 717–722. doi: 10.1016/j.snb.2015.06.143

Xu, J., Pan, Q., and Tian, Z. (2000). Grain size control and gas sensing properties of ZnO gas sensor. *Sens. Actuators B Chem*. 66, 277–279. doi: 10.1016/S0925-4005(00)00381-6

Yang, F., and Guo, Z. (2017). Different post-treatment processes and different gas sensing behaviors of hierarchical hollow tungsten trioxide shell. *Mater. Lett*. 203, 93–96. doi: 10.1016/j.matlet.2017.05.096

Yu, Q., and Gao, H. (1997). A simple determination of the NO_2 dimerization equilibrium constant. *J. Chem. Educ*. 74:233. doi: 10.1021/ed074p233

Zaza, F., Pallozzi, V., and Serra, E. (2019). Optimization of working conditions for perovskite-based gas sensor devices by multiregression analysis. *J. Nanotechnol.* 2019:4628765. doi: 10.1155/2019/4628765

Zhang, D., Liu, Z., Li, C., Tang, T., Liu, X., Han, S., et al. (2004). Detection of NO_2 down to ppb levels using individual and multiple In2O3 nanowire devices. *Nano Lett.* 4, 1919–1924. doi: 10.1021/nl0489283

Conflict of Interest Statement: The authors declare that the research was conducted in the absence of any commercial or financial relationships that could be construed as a potential conflict of interest.

frontiers in Materials

ORIGINAL RESEARCH
published: 24 July 2019
doi: 10.3389/fmats.2019.00158

UV Light Activated SnO_2/ZnO Nanofibers for Gas Sensing at Room Temperature

Jinze Li[1], *Ding Gu*[1], *Yating Yang*[1], *Haiying Du*[2] *and Xiaogan Li*[1]*

[1] Key Laboratory of Liaoning for Integrated Circuits Technology, School of Microelectronics, Dalian University of Technology, Dalian, China, [2] College of Mechanical and Electronic Engineering, Dalian Minzu University, Dalian, China

Hierarchical SnO_2/ZnO nanofiber heterojunctions composed of SnO_2 nanofiber matrix on top of which ZnO nanorods protruding 30–90 nm long were assembled, were examined for chemiresistive-type gas sensors under UV activation at room temperature. The sensor demonstrated excellent sensitivity to different concentrations of formaldehyde and selectivity to several possible interferents such as alcohols, methanol, benzene, methylbenzene, and acetone with UV LED at a wavelength of 365 nm. The fiber-like heterojunctions can facilitate the electron transfer from ZnO to SnO_2 and this effect would be augmented further under UV light activation. Consequently it enhanced the oxygen adsorptions on the surface of the heterojunctions thus leading to the excellent sensing performance even at room temperature. The influence of the power density and wavelength of UV light used and ambient humidity on the sensor response was systematically investigated. Comparing to the conventional thermal activated one that instead showed preferred response to acetone at 375°C, the enhanced sensitivity and selectivity of the same sensor at room temperature under LED UV light can be attributed to selective photo-catalytic effect induced by the UV light.

Keywords: SnO_2/ZnO nanofiber, heterojunctions, formaldehyde, gas sensor, UV activation

OPEN ACCESS

Edited by:
Rajesh Adhikari,
Institut National de la Recherche Scientifique (INRS), Canada

Reviewed by:
Zhenyu Li,
Southwest Petroleum University, China
Tong Zhang,
Jilin University, China

***Correspondence:**
Xiaogan Li
lixg@dlut.edu.cn

Specialty section:
This article was submitted to Functional Ceramics, a section of the journal Frontiers in Materials

Received: *26 April 2019*
Accepted: *19 June 2019*
Published: *24 July 2019*

Citation:
Li J, Gu D, Yang Y, Du H and Li X (2019) UV Light Activated SnO_2/ZnO Nanofibers for Gas Sensing at Room Temperature. Front. Mater. 6:158. doi: 10.3389/fmats.2019.00158

INTRODUCTION

Semiconductor metal oxides (SMO) based chemical gas sensors have been used for detection of the harmful and toxic gases in many fields because of its fast response, high precision, small size, and low cost since it was introduced in 1962 (Seiyama and Kagawa, 1966; Shimizu and Egashira, 1999; Barsan and Weimar, 2001; Yamazoe, 2005; Tiemann, 2007; Lee, 2009; Miller et al., 2014; Liang et al., 2015; Walker et al., 2019). Formaldehyde is one of the most common indoor air pollutant and many furniture materials are the potential source of formaldehyde, which is the allergen of skins and a typical carcinogen (Wood and Coleman, 1995). Therefore, it is significant to develop a reliable sensor to detect the formaldehyde and it is also meaningful for the Internet of Things (IOTs). Nanostructured semiconducting metal oxides such as SnO_2, ZnO, In_2O_5, and TiO_2 have been studied to detect formaldehyde because the nanostructure enhances the interaction with the targeted gas and improves the selectivity and response speed (Seiyama and Kagawa, 1966; Shimizu and Egashira, 1999; Barsan and Weimar, 2001; Yamazoe, 2005; Tiemann, 2007; Lee, 2009; Miller et al., 2014; Liang et al., 2015; Walker et al., 2019). However, the traditional metal oxide based

chemiresistive-type gas sensors often require to work at high temperatures from 200 to 400°C and thus it demands a high electrical power supply (Seiyama and Kagawa, 1966; Shimizu and Egashira, 1999; Barsan and Weimar, 2001; Yamazoe, 2005; Tiemann, 2007; Lee, 2009; Miller et al., 2014; Liang et al., 2015; Walker et al., 2019). Furthermore, it would also have a safety-issue when it is used for detecting flammable gases. Moreover, at the elevated temperature, Metal oxides grain boundaries have an undesirable long-term drift problems caused by the sintering effects.

Recently, an alternative method utilizing the light energy to activate the sensing process of the SMO based gas sensors have been reported extensively (Camagni et al., 1996; Fan et al., 2009; Prades et al., 2009; Lu et al., 2012; Wu et al., 2012; Liu et al., 2013; Park et al., 2013; Zhang et al., 2014; Li et al., 2015, 2017; Chen et al., 2016; Saboor et al., 2016; Gu et al., 2017a). Adopting the light with a wavelength at or close to the corresponding optical forbidden bandgap of the SMO, the sensing properties of SMO based sensors can be significantly enhanced at much lower operating temperature or even room temperature (Camagni et al., 1996; Fan et al., 2009; Prades et al., 2009; Lu et al., 2012; Wu et al., 2012; Liu et al., 2013; Park et al., 2013; Zhang et al., 2014; Li et al., 2015, 2017; Chen et al., 2016; Saboor et al., 2016; Gu et al., 2017a). The photogenerated electrons or holes can facilitate the chemical redox reactions between pre-adsorbed ionized oxygens and the targeted gas molecules thus inducing a sensor signal even at room temperature. Zhang made TiO_2 nanoparticles based chemiresistive gas sensor with the light illumination and working in the condition of 60°C (Zhang et al., 2014). However, by using the hollow structured TiO_2 nanotubes or microspheres, the selectivity and response speeds are improved significantly (Wu et al., 2012; Liu et al., 2013; Li et al., 2015; Chen et al., 2016). Chen et al. (2016) made a hollow ZnO based gas sensor and found a very promising to be used for a selective ethanol sensor working at 80°C with the UV activation. One more benefit of using light activation instead of DC-powered heaters may be that the light can be easily driven up by the random-mechanic vibration energy harvested by using triboelectric nanogenerators as demonstrated recently (Gu et al., 2017a). To facilitate the separation of photogenerated electron/hole pairs thus further improving the sensing performance under light activation, the formed heterojunctions between two or more different SMOs have been studied (Lu et al., 2012; Miller et al., 2014; Gu et al., 2017b; Walker et al., 2019). Lu et al. (2012) reported a NO_2 sensor using SnO_2 nanofibers decorated by ZnO under UV activation. The improved sensitivity was attributed to the formed heterojunctions facilitating the separation of the electron/hole pairs.

In this work, the porous SnO_2 nanofibers with ZnO heterojunctions have been examined for a gas sensor working at room temperatures under UV activation. Compared to its excellent sensitivity but poor selectivity to acetone operated under conventional heating method, the porous SnO_2 nanofiber/ZnO heterojunctions indicated a good sensitivity and selectivity to formaldehyde at room temperature under a UV (365 nm) LED illumination.

EXPERIMENTAL

Materials Preparation and Characterization

The SnO_2/ZnO heterojunction nanofibers were prepared following a two-step process (Mailhiot and Duke, 1986; Du et al., 2018). Firstly, the SnO_2 nanofibers were synthesized by the high-voltage electrospinning method. A certain amount of stannous chloride ($SnCl_2 \cdot 2H_2O$) was added to the ethanol solute and the solution was magnetically stirred for about 1 h until stannous chloride was completely dissolved. Subsequently, the polyvinylpyrrolidone (PVP'MW = 13,000,000) and IV'IV-dimethylformamide (DMF) were added into the mixed solution. The mixture was then stirred magnetically for 3 h at ambient temperature until PVP was completely dissolved to obtain a transparent viscous precursor ready for the followed electrospinning process. The precursor was then injected into

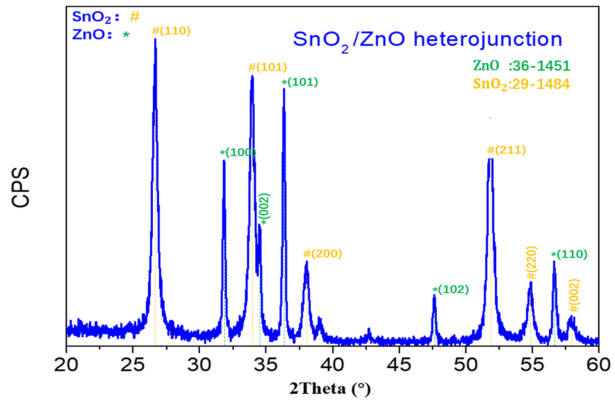

FIGURE 1 | XRD patterns of the SnO_2/ZnO composite heterojunction material.

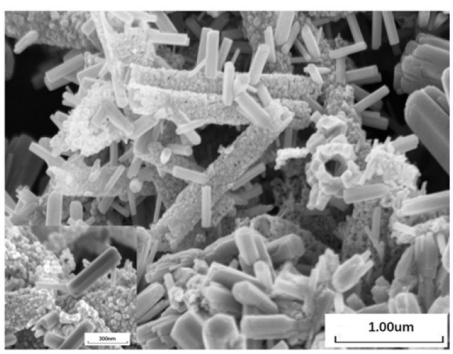

FIGURE 2 | SEM images of the SnO_2/ZnO composite heterojunction.

TABLE 1 | Element contents of SnO_2/ZnO composite heterojunctions.

Elements	wt%
O K	16.6
Zn K	18.9
Sn L	64.5

the electrospinning apparatus. A high-voltage at 20 kV was applied across the collecting plate and the nozzle with a distance of 13 cm in between. During the electrospinning process, the precursor was squeezed through the needle-like nozzle and the electro-spun nanofibers were collected on the collecting plate. Then, the collected white nanofibers were calcined at 600 °C for 2 h to obtain the $Sn0_2$ nanofiber framework. For a comparison, tin oxide nanoparticles were prepared by using the similar process with the replacement of PVP by PMMA in the electrospinning precursor.

Secondly, the SnO_2 nanofibers heterojuncted with the secondary phase of ZnO nanoparticles were prepared. A certain amount of SnO_2 nanofibers as obtained earlier was mixed with deionized water and the slurry was ground into a paste in an agate mortar. Then, the paste was spinning-coated onto a glass substrate and a drop of 0.05 mol/L zinc acetate in ethanol solution was evenly spread over the glass substrate. The substrate was baked in an oven at 200 °C for half an hour to grow the ZnO seeds on the SnO_2 nanofiber framework. Subsequently, the baked glass substrate was immersed into a solution of 0.04 mol/L zinc acetate in ethanol in a vessel and the whole set was heated in water bath at a constant temperature of 90 °C for 4 h to fabricate the final SnO_2/ZnO heterojunction product. After drying at room temperature, a white powdered $Sn0_2$/ZnO heterogeneous composite was obtained.

The powder X-ray diffraction patterns (XRD) of the samples were characterized by an X-ray diffractometer (XRD-6000, Shimadzu Corp.), utilizing the Cu-Ka radiation at 40 kV and 30 mA. The surface morphology of the heterojunction samples was characterized by the Scanning Electron Microscope (SEM: S-3000N, Hitachi, Japan). The X-ray photoelectron spectroscopy (XPS) was recorded by a Thermo ESCALAB 250 Xi X-ray photoelectron spectroscopy using an Al radiation excitation source operating at 150 W and a beam spot size of 500 μm while the binding energy was calibrated by C1s at 284.8 eV.

Sensor Fabrication and Electrical Measurements

The chemical resistance sensor was fabricated by depositing the SnO_2/ZnO composite heterojunctions on an alumina substrate preliminarily printed with the gold electrodes at a spacing distance around 200 μm.

During the sensing measurements, the LED light sources at three different wavelengths (365 nm, 395 nm, 405 nm) were placed, respectively, above the sensor to provide the activation energy to the sensor. Before the testing, the sensors were illuminated under the LED light for 10 min to reach a stable state of the resistance. The distance between LED light and the sensor is 1 cm and the sensors were operated at the room temperature (25°C). The gas sensing characteristics of the sensor was tested in a sealed chamber with an inner volume of 50 L. The relative humidity in the chamber is measured by a hydrometer. The different concentrations of the testing gases were achieved by evaporation of the corresponding liquids. The resistances of the sensors were measured for the sensor signals by the multimeter (Agilent 34410A) automatically controlled by a PC. The response of sensor (R_s) is defined by the relative change of the sensor resistance in air (R_a) and in test gas (R_s) according

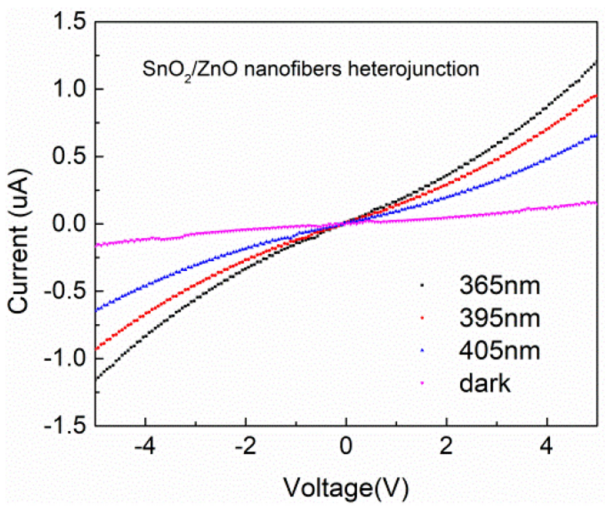

FIGURE 4 | I–V polarization curves of the SnO_2/ZnO composite heterojunction material under different light sources.

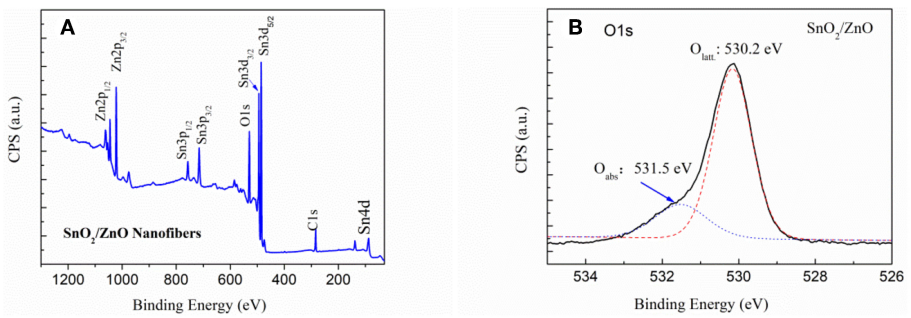

FIGURE 3 | XPS spectrum of the SnO_2/ZnO nanofiber heterojunctions: **(A)** overall survey and **(B)** local O1s region.

to below equation:

$$R_s = \frac{R_a}{R_g} \ (for\ reducing - type\ gas)$$

RESULTS AND DISCUSSION

Microstructure Characterization

Figure 1 shows the XRD pattern of the fabricated SnO_2/ZnO composite heterojunction material. It shows that the SnO_2/ZnO heterojunction has both a tetragonal rutile structure of SnO_2 and a hexagonal wurtzite structure of ZnO which are indexed according to JCPDS No.41-1445 and 36-1451, respectively. There is no other impure phase, indicating that there is no chemical reaction between SnO_2 nanofibers and ZnO nanoparticles formed on the nanofibers during the thermal treatments.

Figure 2 shows the SEM images of the SnO_2/ZnO composite heterojunction material. The SEM image indicate the SnO_2 nanofibers the porous microstructure. It is obvious that ellipsoid ZnO nanoparticles were grown on the nanofiber structure of SnO_2. The diameter of the SnO_2 nanofiber is about 300 nm. The diameter of the ZnO nanoparticles is about 30∼90 nm. **Table 1** lists the content of each element in the SnO_2/ZnO nanofiber. As shown in the table, the mass ratio of SnO_2 to ZnO is estimated to be approximately 7:2.

Figure 3 shows the XPS spectrum of the SnO_2/ZnO composite heterojunction. **Figure 3A** is the survey of the sample and indicated that there are eight characteristic peaks. The binding energy for the C_{1s} peak at 284.6 eV is used as a reference to calibrate the spectra. **Figure 3B** shows the local region of the O_{1s} in the SnO_2/ZnO composite heterojunction material. The binding energy of O_{1s} at 530.2 eV can be assigned to the lattice oxygen. The lattice oxygen did not participate in the sensing reaction. The O_{ads} is a kind of adsorbed, ionized oxygen usually in the form of O_2^- at low temperatures on the surface of the heterojunction material (Barsan and Weimar, 2001).

Photo-Electronic Characterization and Gas Sensing Performance

The I–V polarization curves of the SnO_2/ZnO composite heterojunction material under different light sources are shown in **Figure 4**. Under UV lights with a wavelength from 405 nm to 365 nm, the measured currents were significantly enhanced

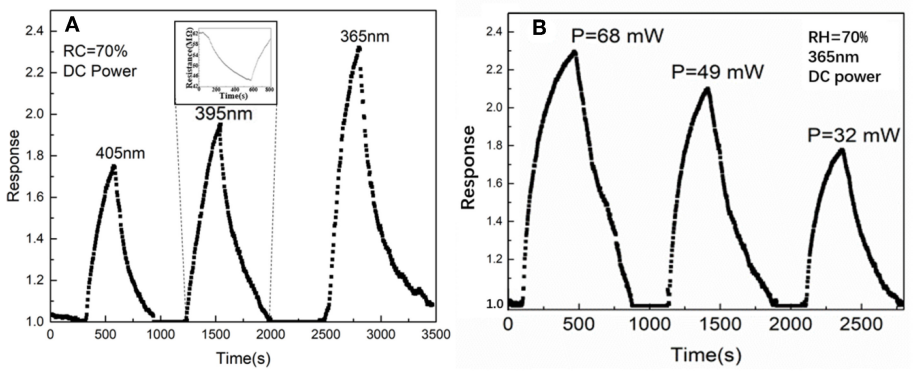

FIGURE 5 | The gas response of the SnO_2/ZnO heterojunction based sensor to three different UV LED lights in ambient: **(A)** Wavelength effect and **(B)** Power density effect.

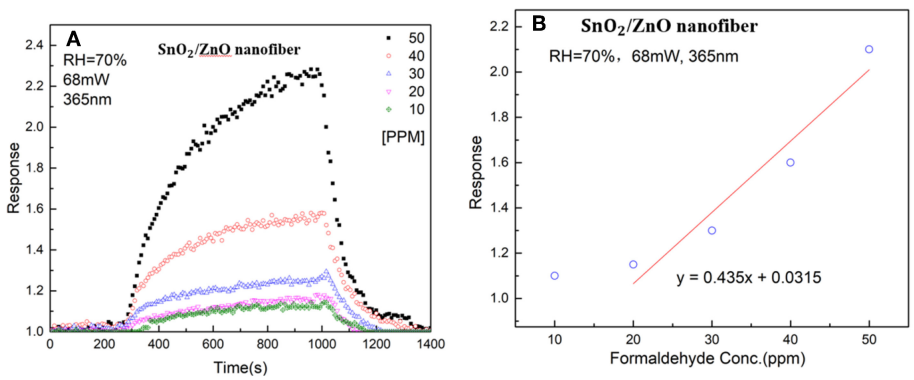

FIGURE 6 | (A) Response of the SnO_2/ZnO heterojunction based gas sensor to different concentrations of formaldehyde from 10 ppm to 50 ppm with the light illumination at a wavelength of 365 nm and the humidity of RH = 70% in ambient and **(B)** the correlation curve of the sensor response to formaldehyde vapor concentrations.

compared to the dark and increased as the wavelength became shorter. There is a slightly non-linear relationship between the measured currents and the applied bias when the applied voltages beyond the range of +4 V to −4 V indicating a non-Ohmic type connections. This is most likely due to the heterojunction formed by the SnO_2 and ZnO which formed the n-n diode junctions indicating slight rectifying properties.

The gas response of the SnO_2/ZnO composite heterojunctions under different wavelength and power density are shown in **Figure 5**. From **Figure 5A**, it can observe that with the shorter wavelength at 365 nm at the same power density, the sensor shows a highest response. This is due to the fact that both SnO_2 and ZnO have a wide-band gap which corresponds to optical wavelength around 360–370 nm depending upon the microstructure and the degree of defective density (Mailhiot and Duke, 1986). Further, **Figure 5B** shows the response of the sensor increased as the power density of the UV light at 365 nm increased. With the light illumination of 365 nm, the response of SnO_2/ZnO composite heterojunction based sensor rises from 40 to 70% with the power supply increased form 32 mW to 68 mW. However, the response and recovery speeds are sluggish which is mainly due to the slow adsorption and desorption of ionized oxygen during the "on" and "off" states of the sensor.

Figure 6A shows the response of the SnO_2/ZnO composite nanofiber heterojunctions based chemiresistive-type sensor to different concentrations of formaldehyde from 10 ppm to 50 ppm with the LED light illumination at the wavelength of 365 nm and at room temperature and the relative humidity of RH = 70% in ambient. It can be observed that with the formaldehyde induced into the testing chamber, the resistance of the sensor reduced and the resistance recover fully back with the formaldehyde vapor was removed from the chamber. It indicates that the SnO_2/ZnO

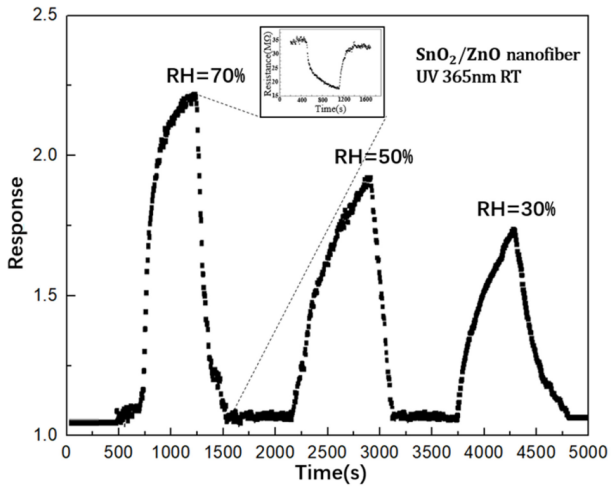

FIGURE 7 | The influence of humidity to the response of SnO_2 based sensor with the light illumination (365 nm) to the 50 ppm formaldehyde.

TABLE 2 | Comparison of the gas sensing properties of SnO_2 based heterojunctions.

Sensing material	Test gas	Irradiation/ T(°C)	Response/ C (ppm)	References
SnO2-ZnO composite film	Ethanol	300°C	4.69/200	Kim et al., 2007
SnO2-ZnO	methanol	350°C	8.5/10	Yan et al., 2015
SnO2-ZnO	o_2	UV/R.T.	2.25/250	Xiong et al., 2017
SnO2-ZnO	CO	UV/R.T.	0.12/250	Camagni et al., 1996
SnO2/ZnO	HCHO	UV/R.T.	2.3/50	This work

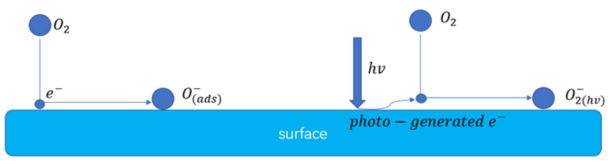

FIGURE 9 | Schematic illustration of possible enhanced gas sensing mechanism of the sensors under 365 nm light activation.

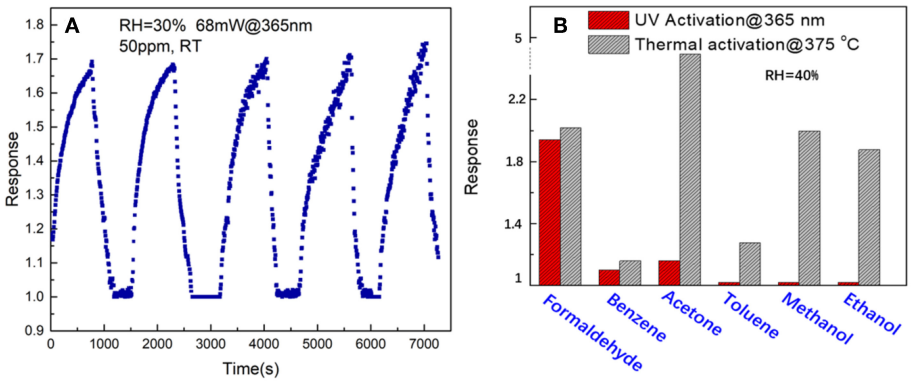

FIGURE 8 | (A) Signal repeatability and **(B)** comparison of the response of the SnO_2/ZnO heterojunction based sensor to formaldehyde with other several possible interference such as benzene, acetone, toluene, methanol and ethanol with 50 ppm each under the 365 nm light illumination and with the humidity of RH=40%.

heterojunction shows a typical n-type response behavior since the formaldehyde is regarded as a reducing-type gas and would consume the adsorbed ionized oxygen thus releasing the trapped electrons back to the sensing materials. As the concentrations of the formaldehyde increased from 10 ppm to 50 ppm, the sensor response increased from 10 to 70 %. **Figure 6B** shows the relationship between the sensor response and the formaldehyde concentrations indicates a non-linear feature. Moreover, as the concentrations of formaldehyde increased, the response and recovery times increased too. This may be because as the number of the testing gas molecules in the air increased, it consumed more time to react with the adsorbed ionized oxygen on the surface of the heterojunctions.

Figure 7 shows the influence of humidity to the response of SnO_2/ZnO composite heterojunction based formaldehyde sensor with the UV light activation (365 nm) to the 50 ppm formaldehyde at room temperature. It can observe that with the increase of the relative humidity in testing chamber from 30 to 70 %, the response of the sensor increased. This is contrary to the response of the most SMO based chemiresistive-type gas sensors when operated at the conventional heating model, during which the response would be significantly suppressed when the relative humidity increased. Here, it could be due to the assistance of the adsorbed H_2O molecule in the photocatalytic oxidation of formaldehyde by the pre-adsorbed ionized oxygen (Liu et al., 2013).

Figure 8A shows the repeatability of response curves of the SnO_2/ZnO composite heterojunction based sensor to 50 ppm formaldehyde under the 365 nm light illumination at 25°C with the relative humidity of 30%. The sensor shows an excellent signal repeatability and stable response at 25°C when periodically exposed to the formaldehyde vapor. **Figure 8B** shows the comparison of response of the SnO_2/ZnO nanofiber-shaped composite heterojunction based chemiresistive-type sensor to several possible interferents such as ammonia, benzene, acetone, toluene, methanol and ethanol with 50 ppm each under UV activation and conventional thermal activation at its optimum temperature of 375°C. It indicates that the nanofiber structure of SnO_2/ZnO composite heterojunction based sensor has a much better response to formaldehyde indicating a possible excellent selectivity under UV activation. However, the sensor shows highest response to acetone instead under thermal activation at 375 °C and also a poor selectivity. It indicates that UV activated SnO_2/ZnO nanofiber heterojunction based sensor could be an effective way to improve the selectivity of the sensor and lower down the operating temperature as well.

The gas properties of SnO_2 based heterojunctions based sensors developed in this work and the previously published data are compared in **Table 2**. It can be observed that SnO_2/ZnO under UV-light irradiation has a good gas-sensing performance to formaldehyde at room temperature.

Sensing Mechanism

At lower operating temperatures below 100°C, the major form of the adsorbed ionized oxygen is O_2^- by trapping the electrons at the surface of the sensing materials according to below possible reaction:

$$O_{2\,(air)} + e^-_{(cond.\ band)} \rightarrow 2O^-_{2(ads.)} \quad (1)$$

The reason for the induced change of the electrical resistance of the metal oxide based sensors when exposed to the targeted gases is attributed to the redox reactions between these adsorbed ionized oxygen and the targeted gases during which the trapped electrons by oxygen were released back to the sensing materials (Wu et al., 2012; Liu et al., 2013; Li et al., 2015; Chen et al., 2016). However, this sensing reaction process needs higher energy to be triggered at low temperatures.

Figure 9 shows the schematic illustration of the possible enhanced gas sensing mechanism of the sensors under 365 nm light activation. After introducing the UV light energy, the photo-generated electrons reacted with the oxygen in the air and generate $O^-_{2\,(hv)}$. When the SnO_2/ZnO composite heterojunction material was exposed to the formaldehyde, the formaldehyde molecules would react with the $O^-_{2\,(hv)}$ adsorbed on the surface according to below reaction:

$$HCHO + O^-_{2(hv)} \rightarrow H_2O + CO_2 + e^- \quad (2)$$

Then, the electrons were released, resulting to the decrease in the resistance of the sensor. However, since the ionized oxygen species with negative monovalence which usually has a lower

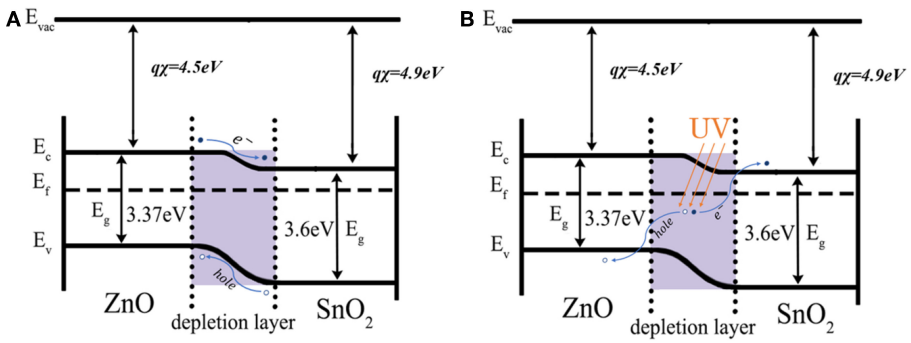

FIGURE 10 | Electron transfer between the formed SnO_2/ZnO nanofiber heterojunctions **(A)** in dark and **(B)** under UV.

photocatalytic properties to react to organic vapors, the reaction of O_2^- according to equation (2) would prefer to react with more active polar gases such as formaldehyde and reluctant to react with the slight inertia gases such as benzene, acetone, ethanol, methanol and toluene thus significantly improving the selectivity of the sensor (Wu et al., 2012; Liu et al., 2013; Li et al., 2015; Chen et al., 2016).

Figure 10 shows a comparison of the band diagrams of ZnO/SnO_2 heterojunction under UV light. With the formed heterojunctions between n-type SnO_2 and n-type ZnO, the separation of the photogenerated electron/hole pairs can thus be enhanced according to the illustrations shown in **Figure 10**. The electron affinity of tin dioxide and zinc oxide is 4.5 and 4.3 eV, respectively. The work functions of SnO_2 and ZnO are 4.9 and 4.45 eV, respectively. The forbidden band gaps of SnO_2 and ZnO are 3.6 and 3.37 eV, respectively. Therefore, electrons will transfer from the conduction band of ZnO to that of SnO_2 due to the former has a higher energy level of the conduction band when ZnO/SnO_2 heterojunctions were formed. With UV light activation, the photogenerated electrons would be extracted to the conduction band of SnO_2 and thus there would be more ionized O_2^- according to reaction (1). Consequently, the energy barrier of SnO_2/ZnO heterojunctions could reduce the recombination of photogenerated electron/hole pairs making the electrons and holes have a longer remaining lifetime in the sensing materials which thus enhanced the redox reaction according to equation (2) (Lu et al., 2012; Miller et al., 2014; Walker et al., 2019).

CONCLUSIONS

As an alternative method to activate the SMO based chemiresistive-type gas sensors, UV light has been employed to activate the gas sensing properties of the SnO_2/ZnO nanofiber heterojunction based chemical gas sensors at room temperature. The SnO_2/ZnO nanofiber heterojunctions based sensor shows a good sensitivity to different concentrations of formaldehyde and an excellent selectivity compared to several possible interferents such as ethanol, methanol, acetone, benzene, and toluene under UV at room temperature. The satisfied performance including the sensitivity and selectivity under UV at room temperature could be due to the UV-assisted redox reactions between the polar formaldehyde and the adsorbed, slight-weak oxidant of adsorbed ionized oxygen with monovalence. The formed heterojunctions between SnO_2/ZnO can enhance the effective separation of the photogenerated electron/hole pairs making them stay a longer lifetime in the sensing materials. This would further enhance the redox reactions and thus improve the sensitivity of the sensor.

DATA AVAILABILITY

The raw data supporting the conclusions of this manuscript will be made available by the authors, without undue reservation, to any qualified researcher.

AUTHOR CONTRIBUTIONS

JL and DG designed and conducted the study, contributed to the data analysis, and writing the manuscript. YY and HD contributed to data analysis. XL supervised the study and contributed to study design, data analysis and writing the manuscript. All authors provided feedback on the manuscript.

ACKNOWLEDGMENTS

XL wishes to thank the financial supports from the National Natural Science Foundation of China (61474012, 61611130065).

REFERENCES

Barsan, N., and Weimar, U. (2001). Conduction model of metal oxide gas sensors. *J. Electroceram.* 7, 143–167. doi: 10.1023/a:1014405811371

Camagni, P., Faglia, G., Galinetto, P., Perego, C., Samoggia, G., and Sberveglieri, G. (1996). Photosensitivity activation of SnO_2 thin film gas sensors at room temperature. *Sens. Actuators B Chem.* 31, 99–103. doi: 10.1016/0925-4005(96)80023-2

Chen, Y., Li, X., Li, X., Wang, J., and Tang, Z. (2016). UV activated hollow ZnO microspheres for selective ethanol sensors at low temperatures. *Sens. Actuators B Chem.* 232, 158–164. doi: 10.1016/j.snb.2016.03.138

Du, H., Li, X., Yao, P., Wang, J., Sun, Y., and Dong, L. (2018). Zinc oxide coated tin oxide nanofibers for improved selective acetone sensing. *Nanomaterials* 8:509. doi: 10.3390/nano8070509

Fan, S. W., Srivastava, A. K., and Dravid, V. P. (2009). UV-activated room-temperature gas sensing mechanism of polycrystalline ZnO. *Appl. Phys. Lett.* 95:142106. doi: 10.1063/1.3243458

Gu, D., Li, X., Wang, H., Li, M., Xi, Y., Chen, Y., et al. (2017a). Light enhanced VOCs sensing of WS $_2$, microflakes based chemiresistive sensors powered by triboelectronic nangenerators. *Sens. Actuators B Chem.* 256, 992–1000. doi: 10.1016/j.snb.2017.10.045

Gu, D., Li, X., Zhao, Y., and Wang, J. (2017b). Enhanced NO_2 sensing of SnO_2/SnS_2 heterojunction based sensor. *Sens. Actuators B Chem.* 244, 67–76. doi: 10.1016/j.snb.2016.12.125

Kim, K. W., Cho, P. S., Kim, S. J., Lee, J. H., Kang, C. Y., and Kim, J. S. (2007). The selective detection of C2H5OH using SnO2–ZnO thin film gas sensors prepared by combinatorial solution deposition. *Sens. Actuators B: Chem.* 123, 318–324. doi: 10.1016/j.snb.2006.08.028

Lee, J. H. (2009). Gas sensors using hierarchical and hollow oxide nanostructures: overview. *Sens. Actuators B Chem.* 140, 319–336. doi: 10.1016/j.snb.2009.04.026

Li, H. Y., Yoon, J. W., Lee, C. S., Lim, K., Yoon J. W., Lee, J. H, et al. (2017). Visible light assisted NO $_2$, sensing at room temperature by CdS nanoflake array. *Sens. Actuators B Chem.* 225, 2963–2970. doi: 10.1016/j.snb.2017.09.118

Li, X., Li, X., Wang, J., and Lin, S. (2015). Highly sensitive and selective room-temperature formaldehyde sensors using hollow TiO_2 microspheres. *Sens. Actuators B Chem.* 219, 158–163. doi: 10.1016/j.snb.2015.05.031

Liang, X., Kim, T. H., Yoon, J. W., Kwak, C. H., and Lee, J. H. (2015). Ultrasensitive and ultraselective detection of H_2S using electrospun CuO-loaded In_2O_3 nanofiber sensors assisted by pulse heating. *Sens. Actuators B Chem.* 209, 934–942. doi: 10.1016/j.snb.2014.11.130

Liu, L., Li, X., Dutta, P. K., and Wang, J. (2013). Room temperature impedance spectroscopy-based sensing of formaldehyde with porous TiO_2 under UV illumination. *Sens. Actuators B Chem.* 185, 1–9. doi: 10.1016/j.snb.2013.04.090

Lu, G., Xu, J., Sun, J., Yu, Y., Zhang, Y., and Liu, F. (2012). UV-enhanced room temperature NO_2 sensor using ZnO nanorods modified with SnO2 nanoparticles. *Sens. Actuators B Chem.* 162, 82–88. doi: 10.1016/j.snb.2011.12.039

Mailhiot, C., and Duke, C. B. (1986). Many-electron model of equilibrium metal-semiconductor contacts and semiconductor heterojunctions. *Phys. Rev. B*. 33, 1118–1133. doi: 10.1103/PhysRevB.33.1118

Miller, D. R., Akbar, S. A., and Morris, P. A. (2014). Nanoscale metal oxide-based heterojunctions for gas sensing: a review. *Sens. Actuators B Chem.* 204, 250–272. doi: 10.1016/j.snb.2014.07.074

Park, S., An, S., Mun, Y., and Lee, C. (2013). UV-enhanced NO_2 gas sensing properties of SnO_2-Core/ZnO-shell nanowires at room temperature. *ACS Appl. Mater. Interfaces* 5, 4285–4292. doi: 10.1021/am400500a

Prades, J. D., Jimenez-Diaz, R., Manzanares, M., Ramirez, F. H., Cirera, A., Rodriguez, A. R., et al. (2009). A model for the response towards oxidizing gases of photoactivated sensors based on individual SnO_2 nanowires. *Phy. Chem. Chem. Phys*. 11:10881. doi: 10.1039/b915646a

Saboor, F. H., Ueda, T., Kamada, K., Hyodo, T., Mortazavi, Y., Khodadadi, A. A., et al. (2016). Enhanced NO_2 gas sensing performance of bare and Pd-loaded SnO_2 thick film sensors under UV-light irradiation at room temperature. *Sens. Actuators B Chem*. 223, 429–439. doi: 10.1016/j.snb.2015.09.075

Seiyama, T., and Kagawa, S. (1966). Study on a detector for gaseous components using semiconductive thin films. *Analyt. Chem.* 38, 1069–1073. doi: 10.1021/ac60240a031

Shimizu, Y., and Egashira, M. (1999). Basic aspects and challenges of semiconductor gas sensors. *MRS Bull.* 24, 18–24. doi: 10.1557/S0883769400052465.

Tiemann, M. (2007). Porous metal oxides as gas sensors. *Chem. Eur. J.* 13, 8376–8388. doi: 10.1002/chem.200700927

Walker, J. M., Akbar, S. A., and Morris, P. A. (2019). Synergistic effects in gas sensing semiconducting oxide nano-heterostructures: a review. *Sens. Actuators B*. 286, 624–640. doi: 10.1016/j.snb.2019.01.049

Wood, R. W., and Coleman, J. B. (1995). Behavioral evaluation of the irritant properties of formaldehyde. *Tox. Appl. Pharmacol.* 130, 67–72. doi: 10.1006/taap.1995.1009

Wu, G., Zhang, J., Wang, X., Liao, J., Xia, H., Akbar, S. A., et al. (2012). Hierarchical structured TiO_2 nanotubes for formaldehyde sensing. *Ceram. Int.* 38, 6341–6347. doi: 10.1016/j.ceramint.2012.05.004

Xiong, Y., Lu, W., Ding, D., Zhu, L., Li, X., Ling, X., and Xue, Q. (2017). Enhanced room temperature oxygen sensing properties of laocl–sno2 hollow spheres by uv light illumination. *ACS Sens.* 2, 679–686. doi: 10.1021/acssensors.7b00129

Yamazoe, N. (2005). Toward innovations of gas sensor technology. *Sens. Actuators B Chem*. 108, 2–14. doi: 10.1016/j.snb.2004.12.075

Yan, S. H., Ma, S. Y., Li, W. Q., Xu, X. L., Cheng, L., Song, H. S., et al. (2015). Synthesis of SnO2–ZnO heterostructured nanofibers for enhanced ethanol gas-sensing performance. *Sens. Actuators B Chem.* 221, 88–95. doi: 10.1016/j.snb.2015.06.104

Zhang, S., Lei, T., Li, D., Zhang, G., and Xie, C. (2014). UV light activation of TiO_2 for sensing formaldehyde: how to be sensitive, recovering fast, and humidity less sensitive. *Sens. Actuators B: Chem.* 202, 964–970. doi: 10.1016/j.snb.2014.06.063

Conflict of Interest Statement: The authors declare that the research was conducted in the absence of any commercial or financial relationships that could be construed as a potential conflict of interest.

frontiers in Materials

ORIGINAL RESEARCH
published: 16 August 2019
doi: 10.3389/fmats.2019.00188

Silver Nanoparticle-Decorated Tin Oxide Thin Films: Synthesis, Characterization, and Hydrogen Gas Sensing

Amar K. Mohamedkhair[1,2], *Q. A. Drmosh*[2] *and Zain H. Yamani*[1,2]*

[1] *Physics Department, King Fahd University of Petroleum and Minerals, Dhahran, Saudi Arabia,* [2] *Center of Research Excellence in Nanotechnology, King Fahd University of Petroleum and Minerals, Dhahran, Saudi Arabia*

In this work, sputtered tin oxide films, decorated with silver nanoparticles were fabricated as hydrogen sensors. The fabricated thin films were characterized for their structural, compositional, morphological properties using various characterization techniques including X-ray photoelectron spectroscopy, UV-Vis absorption, X-ray diffraction, field emission scanning electron microscope, and atomic force microscopy. The morphological characterization confirmed the formation of nanoparticle-decorated SnO_2 thin films. X-ray photoelectron spectroscopy analysis established the presence of silver/silver oxide on SnO_2 thin films. The gas sensing properties of the fabricated sensors were investigated at different concentrations of hydrogen gas, over an operating temperature range of room temperature to 500°C. It was found that the prepared sensor can detect a low hydrogen concentration (50 ppm) at high operation temperature, while the higher concentration (starting from 600 ppm) can be detected even at room temperature. Furthermore, on the basis of the electronic interaction between the SnO_2 and the Ag nanoparticles, we propose a reaction model to explain the qualitative findings of the study.

Keywords: tin oxide, silver, silver oxide, thin film, gas sensor, hydrogen

OPEN ACCESS

Edited by:
Kalisadhan Mukherjee, Pandit Deendayal Petroleum University, India

Reviewed by:
Tarapada Sarkar, University of Maryland, College Park, United States
Subhasis Roy, University of Calcutta, India

***Correspondence:**
Zain H. Yamani
zhyamani@kfupm.edu.sa

Specialty section:
This article was submitted to Functional Ceramics, a section of the journal Frontiers in Materials

Received: *20 June 2019*
Accepted: *24 July 2019*
Published: *16 August 2019*

Citation:
Mohamedkhair AK, Drmosh QA and Yamani ZH (2019) Silver Nanoparticle-Decorated Tin Oxide Thin Films: Synthesis, Characterization, and Hydrogen Gas Sensing. Front. Mater. 6:188. doi: 10.3389/fmats.2019.00188

INTRODUCTION

Intense research is ongoing for green "future fuel" due to its extraordinary abilities including availability in the natural resources and zero CO_2 emission (Crabtree et al., 2004). Since hydrogen (H_2) has these characteristics, research is taking place in order to produce H_2-fueled engines, in order to reduce atmospheric pollution and harmful emissions (Crabtree et al., 2004; Pal and Agarwal, 2018; Tsujimura and Suzuki, 2019). In addition, H_2 is used in petrochemical processes, including the hydrocracking process (Lippke et al., 2018) for example.

H_2 is tasteless, colorless, and odorless. With a very low ignition energy of 0.02 mJ, it inflames easily in the air at volume concentrations ranging from 4 to 75%. Therefore, detecting H_2 by a proper sensor prevents the threat of fire and explosions. So far, several different types of H_2 sensors have been established such as optical fibers (Wu et al., 2018) and surface acoustic wave (D'amico et al., 1982). Metal oxide sensors (Moseley, 1997) have been widely studied as H_2 sensors due to their excellent qualities in terms of low cost, high sensitivity, fast response, and compact size. Furthermore, their non-stoichiometric nature allows them to absorb the ambient oxygen and

exchange electrons during the adsorption and desorption processes. However, these metal oxide gas sensors have some limitations such as their inability to detect extremely low concentrations of the target gas and their requirement to operate at high temperatures. This usually puts restrictions on their portability.

Currently, a lot of research focuses on improving the sensing features of the metal oxide gas sensors. Doping of the metal oxide sensors with noble metal nanoparticles is a powerful method that improves selectivity and sensitivity, even at low operation temperatures (Kohl, 1990; Ippolito et al., 2005). Among the various metal oxide sensors, tin oxide (SnO_2), which is an n-type semiconductor, is one of the most promising materials for gas sensing applications, and especially for H_2 detection. H_2 sensors based on SnO_2 nanowires, nanorods, and nanotubes have good sensitivity, but they are still unsuitable for commercial purposes due to limitations in their fabrication techniques (Van Duy et al., 2012). Indeed, for commercialization purposes, thin films are the most investigated gas sensor nanostructures due to their simplicity in configuration and scalability of fabrication. As sensitivity is one of the most important parameters in H_2 gas sensing, many efforts have been made to enhance the sensitivity of the SnO_2 thin-film sensors. The decoration of SnO_2 with noble metals leads to charge transfer between their two surfaces, hence modifying the Fermi level of the metal oxide and affecting the charge depletion layer. This leads to increasing the electrons in the metal oxide conduction band, which in turn increases the surface interaction between the sensor and the ambient oxygen, and hence enhancing the performance of the sensor.

Korotcenkov et al. (2007) reported that by doping SnO_2 with Pd, both response time and sensitivity to CO and H_2 increase. Kocemba and Rynkowski (2011), in addition, noticed that sputtered SnO_2 thin-film doping with Pt as a catalyst gives a high sensitivity to H_2 as a function of different operating temperatures. Chen et al. (2011) reported that the synthesis of SnO_2 and Ag_2O nanocomposites demonstrate an enhancement in their gas sensing properties. Wu et al. (2013) formed Ag/SnO_2 core shells and noticed an improvement in the sensor response to ethanol at room temperature.

For improved H_2 gas sensing properties, such as higher sensing and stability capabilities, we have developed an H_2 sensor using catalytic particles (a noble metal loading). In particular, we decorated the surface of sputtered SnO_2 thin films with Ag nanoparticles. More specifically, to maximize the catalytic effect of the sensor, the Ag nanoparticles were homogeneously decorated, covering the whole area of the surface of SnO_2 thin films through a new synthetic method. The details about H_2-gas sensing mechanism are discussed in the results section.

EXPERIMENTAL

Synthesis of Ag Nanoparticle-Decorated SnO_2 Thin Films

Three steps were used to prepare Ag nanoparticle-decorated SnO_2 thin films for fabricating H_2 sensors. Firstly, a target of 99.995% SnO_2 (purchased from ACI Alloys INC) was utilized to fabricate SnO_2 thin films using the RF sputtering technique (model NSC-4000, Nanomaster). Before deposition

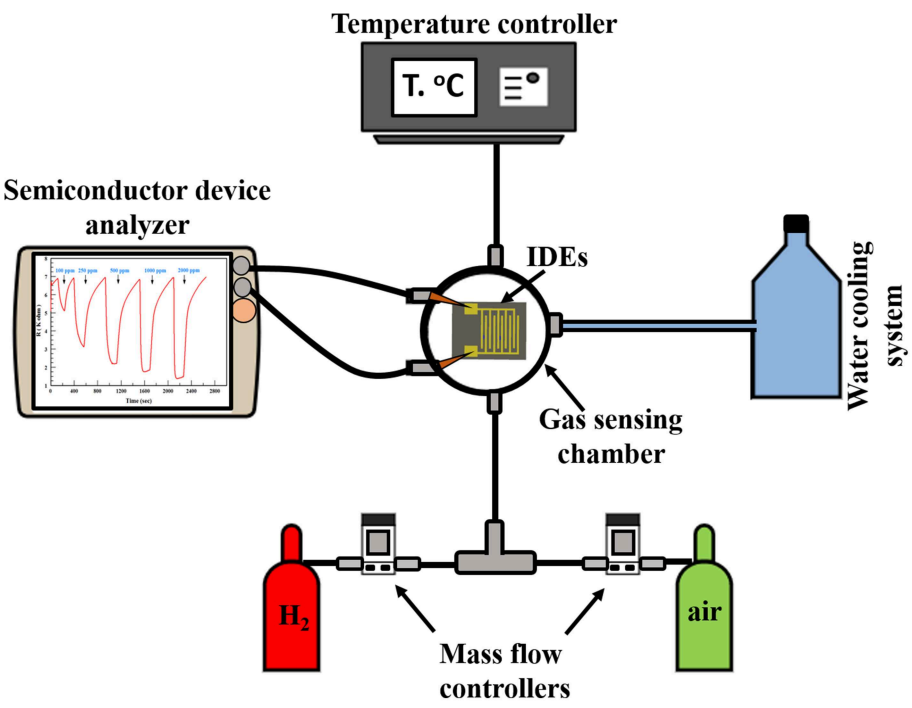

FIGURE 1 | Experimental setup used for sensing hydrogen.

of the thin films, the deposition chamber and targets were cleaned with acetone and isopropanol while the substrates were sonicated in ethanol for 30 min. For sputtering deposition, the base pressure and deposition pressure were adjusted at 6×10^{-6} and 4.8×10^{-3} torr, respectively. The SnO_2 thin films with 250 nm thickness were deposited at 60 standard cubic centimeters per minute (sccm) argon and 10 sccm oxygen gas flow rate using 100 W RF sputtering power for 120 min. The film was deposited on SiO_2 substrates with pre-interdigitized Au electrodes (IDEs) to be used as hydrogen gas sensor, and also deposited on glass substrate to study the structural, compositional, morphological, and optical characterization of the fabricated films. The IDEs have 22 electrodes that are 200 nm thick, with 250 μm interspacing distance, connected to two pads used for electrical measurements. Secondly, a metallic target of 99.995% Ag (purchased from Semiconductor wafer) was used

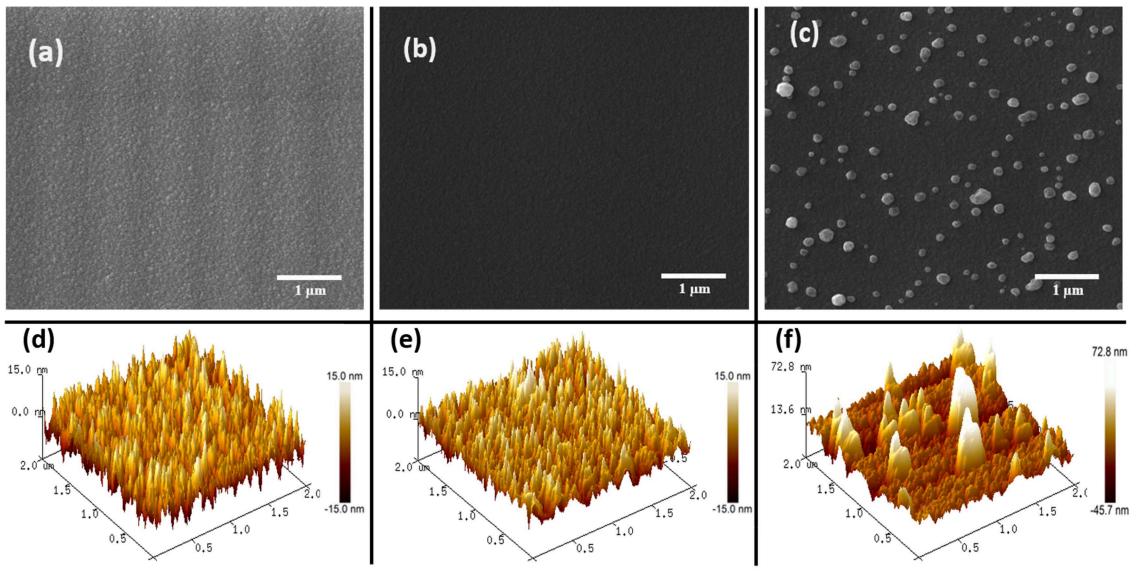

FIGURE 2 | (a–c) FESEM images of as-deposited SnO_2, annealed SnO_2, and AgNPs/SnO_2, respectively. **(d–f)** AFM images of as-deposited SnO_2, annealed SnO_2, and AgNPs/SnO_2, respectively.

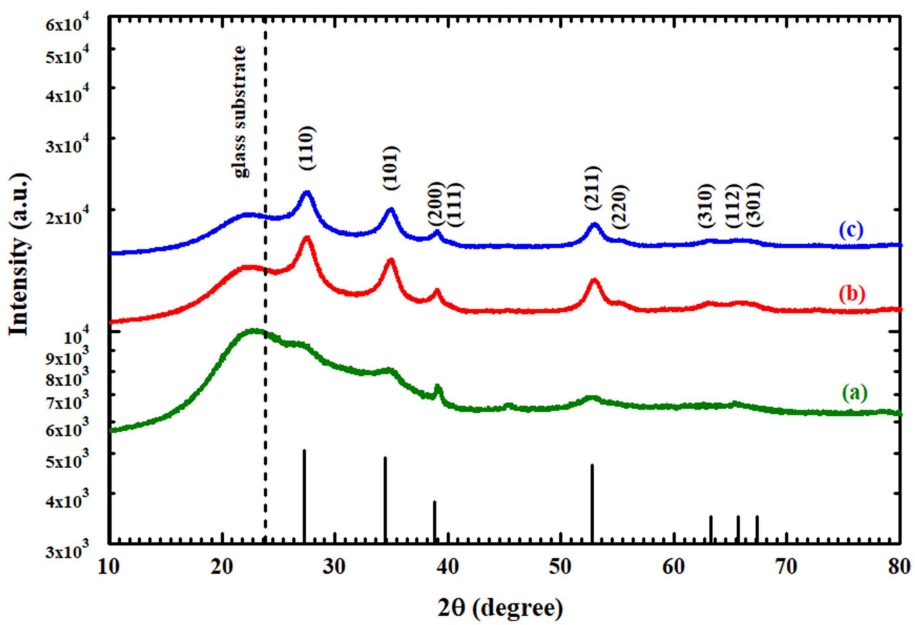

FIGURE 3 | XRD spectra of **(a)** as-deposited SnO_2, **(b)** annealed SnO_2, and **(c)** AgNPs/SnO_2.

to deposit a thin layer of Ag using 20 W DC sputtering power for 30 s. The Ar flow was kept at 70 sccm during the Ag layer deposition. Finally, the obtained thin films were heated at 600°C in a sealed tubular furnace (OTF-1200X from MTI corp.) with a temperature ramp rate of 20°C/min in a flowing argon atmosphere for 2 h to convert Ag layer into nanoparticles in the case of the Ag nanoparticle-decorated SnO_2 film and to enhance the crystallinity and stabilize the based SnO_2 deposited film for both pure SnO_2 film (termed as annealed SnO_2) and Ag nanoparticle-decorated SnO_2 film (termed as AgNPs/SnO_2). In addition to these two samples, one sample was left as-deposited (termed as as-deposited SnO_2) in order to study the effect of the annealing process.

Characterization

The synthesized thin films were characterized using different techniques. X-ray diffraction [Rigaku Miniflex 600 X-Ray Diffraction (XRD), with Cu K irradiation at $\lambda = 1.5406$ Å] was used to examine the crystalline phases, lattice parameter, and the crystalline size. X-ray photoelectron spectroscopy (Model: ESCALAB250Xi, XPS) was utilized to determine the chemical composition of the fabricated thin films. The structural morphology was investigated using a field-emission scanning electron microscope (FE-SEM; Tescan Lyra 3) and atomic force microscopy (AFM; Dimension Icon, Bruker). Optical transmittance and optical band gap measurements were carried out using double beam UV/Vis spectrophotometer (Jasco V-570) in the wavelength range of 200–1,400 nm.

Gas Sensing Measurements

The H_2 sensing measurements of the thin-film sensors were conducted by a flow-through technique. The measurement system consists of a gas sensing chamber (Linkam stage, Model HFS-600E-PB4, UK). It contains two metal needles as electrical connections between the IDE pads (i.e., the sensor) and the electrical measurement setup. In addition, the Linkam stage involves a heating unit that has the ability to reach up to 600°C. A mass flow controller (MFC, Horiba, USA) was utilized to control the gas injection into the testing chamber. The sensor resistance was measured through an Agilent B1500A Semiconductor Device Analyzer (SDA) using I/V-t measurements. Dry air, from a cylinder, was used as the background reference gas. H_2 gas cylinder (1% H_2-bal. N_2) was used as the test-gas source. The resistance across the IDE pads would change depending on the H_2 concentration changing inside the Linkam stage. The gas sensing system layout is shown in **Figure 1**.

RESULTS AND DISCUSSION

Structure, Morphology, and Composition Test

FE-SEM and AFM imaging techniques were used to investigate the morphological properties of the fabricated thin films. **Figures 2a,b** shows the FE-SEM micrograph of the as-deposited SnO_2 and the annealed SnO_2 thin films. Both micrographs show the uniformity of the SnO_2 thin film though there seems to be a slight difference in the roughness of SnO_2 surface before and after the annealing. **Figure 2c** displays the annealed AgNPs/SnO_2 films at 600°C. The Ag nanoparticles were nearly uniformly distributed over the SnO_2 film surface with different particle sizes (Drmosh et al., 2015).

Figures 2d,e are 2 μ m × 2 μm AFM topography images of the as-deposited SnO_2 and annealed SnO_2 thin films. As presented by SEM, the AFM images show a rough surface for the pristine film, and a more mild roughness for the film after annealing. This accentuates that annealing the SnO_2 thin film makes it denser and smoother. This is a result of the film obtaining sufficient energy from the annealing process enabling the atoms to rearrange their position, and hence become closer packed and crystalline (Shinde et al., 2005), as confirmed below by the XRD results. The AFM image of the AgNPs/SnO_2 film (**Figure 2f**) shows the growth of large, separated, and spaced Ag particles over the smooth SnO_2. The AgNPs size ranged approximately from 50 to 250 nm.

Figure 3 shows the XRD patterns of the pure SnO_2 thin film before and after the heat treatment and the annealed AgNPs/SnO_2. The wide peaks that appear at ~24°C correspond to the substrate (Chakraborty et al., 2010). All XRD peaks identify the standard crystal planes of tetragonal SnO_2 (Ansari

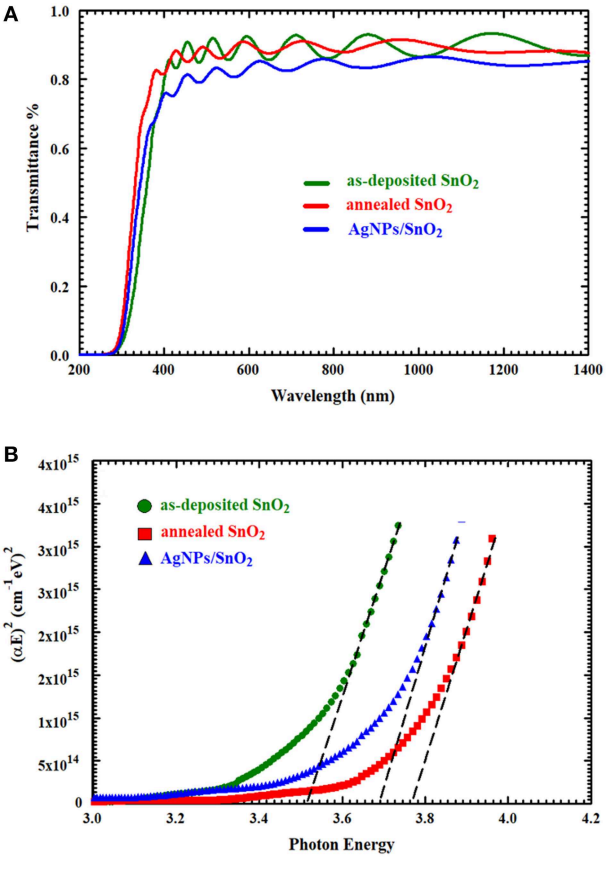

FIGURE 4 | (A) The UV–Vis transmittance spectra of as-deposited SnO_2, annealed SnO_2, and AgNPs/ SnO_2 films. **(B)** Optical band gap of as-deposited SnO_2, annealed SnO_2, and AgNPs/SnO_2 films.

et al., 1997). From **Figure 3a**, the observed low and wide peaks correspond to the diffractions peaks (110), (101), and (200) (Ansari et al., 1997). This confirms the amorphous nature of the as-deposited SnO_2. After heating the as-deposited SnO_2 to 600°C, it is observed that the peaks become sharper, as displayed in **Figure 3b**. This is attributed to the transformation of the SnO_2 from an amorphous to a polycrystalline structure. No diffraction peaks were found related to Ag nanoparticles as there is no change in the diffraction pattern between **Figures 3a,c**. This might be due to the random distribution and low concentration of Ag nanoparticles at the surface of the SnO_2 film (Yang et al., 2014). No impurity peaks or other phases were observed, confirming the purity of the prepared films.

UV-Vis spectra of the synthesized thin films were obtained within a wavelength range of 200–1,400 nm, as shown in **Figure 4A**. In the IR and visible region, the optical transmittance fluctuated due to the interference of light being sandwiched inside the thin film between the substrate and air (Cho, 2014). It can be observed that the transmittance of the AgNPs/SnO_2 slightly decreased below the pure and annealed SnO_2. Certainly, this is attributed to the existence of Ag nanoparticles on the SnO_2 surface (Dasgupta et al., 2010) which has considerable absorption to electromagnetic radiation. Tauc relation $(\alpha E)^2 = A\ (E - E_g)$ was used to calculate the optical band gap of these films by plotting the values of $(\alpha E)^2$ against E and extrapolating the linear portion of the curves, where E and E_g are the photon energy of incident light and optical band gap, respectively, A is a constant, and α is the absorption coefficient (Kumar et al., 1999). As can be seen from the extrapolation in **Figure 4B**, the optical band gap of the both annealed SnO_2 and AgNPs/SnO_2 increased in comparison with the as-deposited SnO_2 sample, and hence, the absorption edge was shifted to shorter wavelength as

TABLE 1 | Surface element composition of the as-deposited SnO_2, annealed SnO_2, and AgNPs/SnO_2.

Name	Sample	Peak binding energy (eV)	FWHM (eV)	Area ($\times 10^3$)	Atomic %
Sn3d	As-deposited SnO_2	483.9	2.37	85	3.4
		485.9	1.62	2425	96.6
	Annealed SnO_2	485.8	1.66	1508	100
	AgNPs/SnO_2	486.3	1.63	2303	100
O1s	As-deposited SnO_2	529.6	1.51	448	78.1
		530.4	1.92	126	21.9
	Annealed SnO_2	529.6	1.53	447	77.1
		530.4	2.03	133	22.9
	AgNPs/SnO_2	530.0	1.56	449	81.5
		530.9	2.01	102	18.5
Ag3d	AgNPs/SnO_2	367.4	1.06	62	44.4
		368.0	1.47	42766	55.6

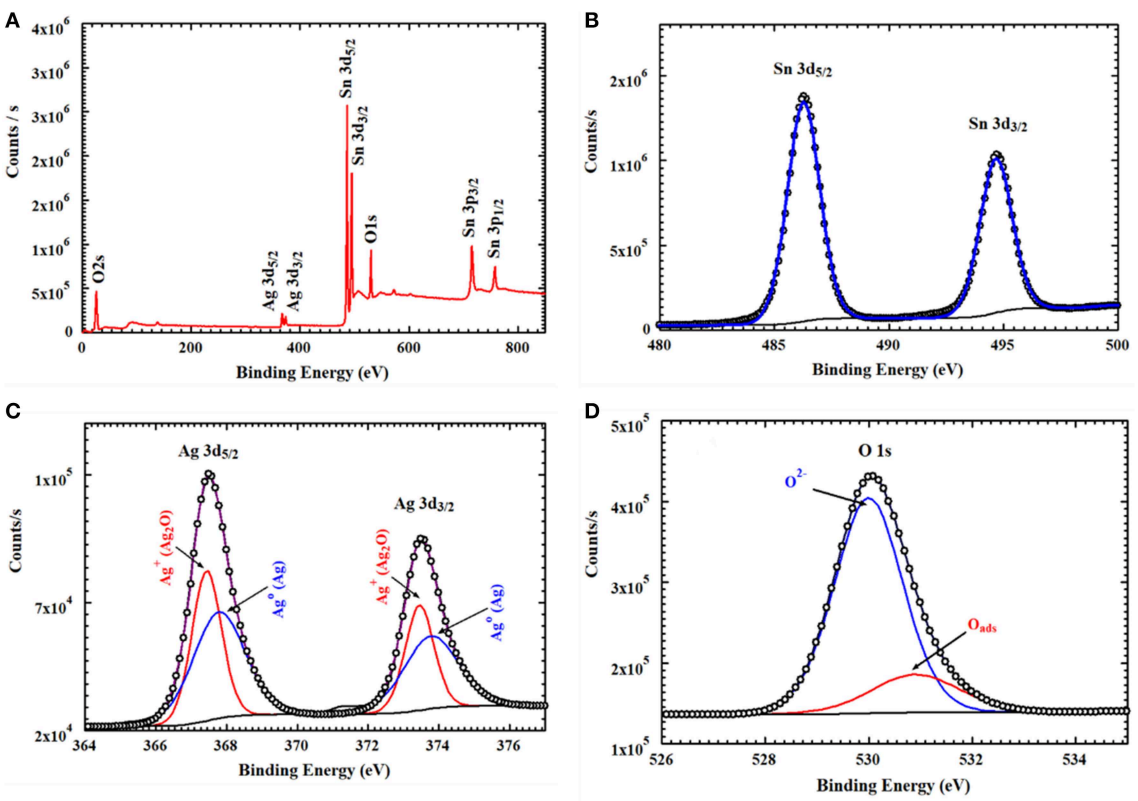

FIGURE 5 | XPS spectra of AgNPs/SnO_2 **(A)** survey spectrum, **(B)** XPS peaks of Sn3d, **(C)** XPS peaks of Ag 3d, and **(D)** XPS peaks of O1s.

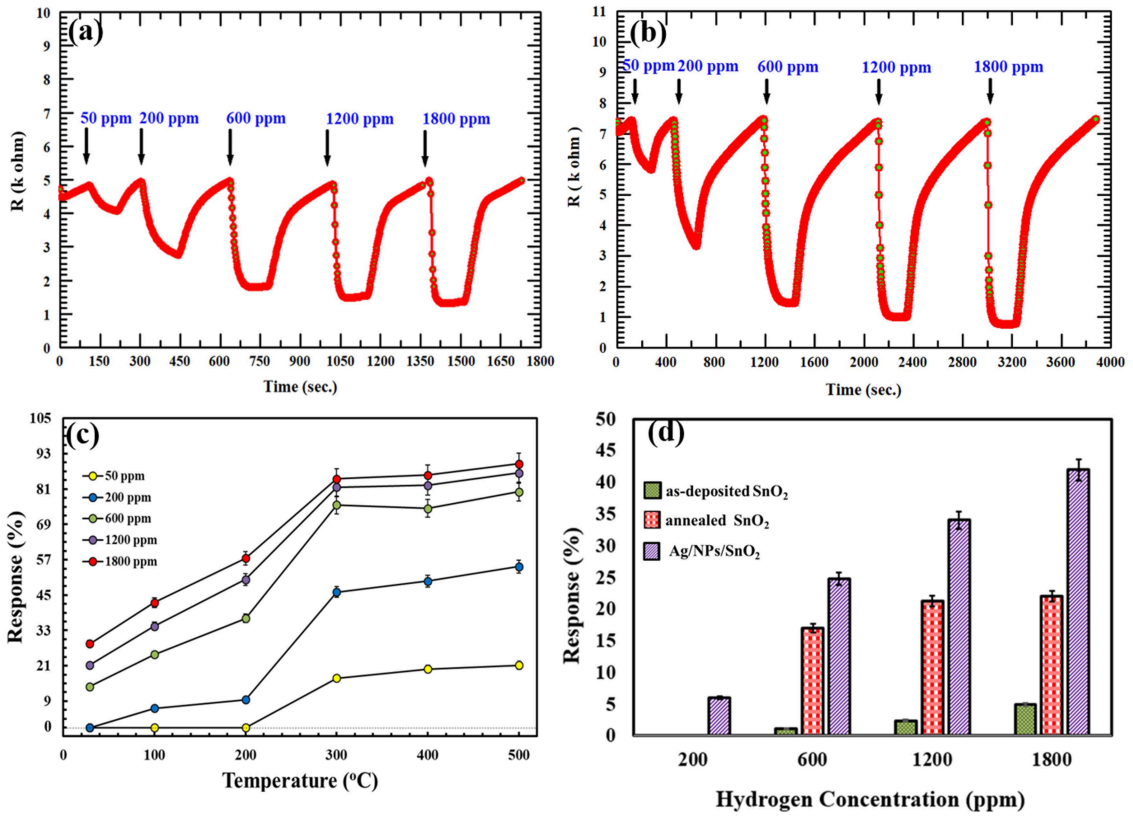

FIGURE 6 | (a,b) Dynamic responses of annealed SnO_2 and AgNPs/SnO_2 (respectively) gas sensor to different H_2 concentrations (50–1,800) ppm at 500°C. **(c)** Gas responses of AgNPs/SnO_2 sensor toward different H_2 concentrations (50–1,800) ppm as a function of operating temperature ranging from room temperature to 500°C. **(d)** A comparison between the as-deposited SnO_2, annealed SnO_2, and AgNPs/SnO_2 at different H_2 concentrations (200, 600, 1,200, and 1,800) at 100°C.

shown in **Figure 4A** (Reddy et al., 2013). As an effect of the annealing process, the Ag diffuses into the SnO_2 crystal. As a result, the band gap of the Ag/NPs/SnO_2 sample is smaller than the annealed SnO_2 (Hwang et al., 2011).

XPS analysis provided information about the thin film's composition. It also determined the oxidation states of the elements. From example, **Figure 5** relates to the annealed AgNPs/SnO_2 sample. The survey scan (**Figure 5A**) confirms the presence of the Sn 3d, O 1s, and the Ag 3d. The binding energy and atomic ratio of each element are demonstrated in **Table 1**. **Figure 5B** shows two peaks in the range from 483 to 489 eV and from 492 to 498 eV. These relate to the binding energies of the Sn $3d_{5/2}$ and Sn $3d_{3/2}$, respectively (Wang et al., 2005). **Figure 5C** shows the Ag $3d_{5/2}$ and Ag $3d_{3/2}$ located in the range of 365 to 370 eV and 372 to 376 eV, respectively. In each of the two peaks, two Ag oxidization states are identified; the Ag^0 peaks are centered at 367.8 and 373.8 eV, while the Ag^+ peaks are centered at 367.5 and 373.4 eV (Zielinska et al., 2010). The Ag^+ peak is due to the presence of the Ag_2O layer on top of Ag nanoparticles that are exposed to ambient oxygen (Matsushima et al., 1988). The O 1s spectrum is shown in **Figure 5D**. The convolution peak centered at 529.9 eV is ascribed to surface lattice oxygen O_2^-, while the O_{ads} peak, centered at 530.8 eV, is attributed to water species adsorbed on the surface of the film (Wang et al., 2016).

Gas Sensing Studies

The gas sensing performance of the AgNPs/SnO_2 thin film was tested toward H_2, and the results were compared with that of the annealed SnO_2. **Figures 6a,b** shows the response of annealed SnO_2 and AgNPs/SnO_2 for different H_2 concentrations (50–1,800 ppm) at 500°C operation temperature. The comparison of H_2 sensing performance of the two sensors reveals that addition of Ag nanoparticles to the SnO_2 thin film results in a remarkable enhancement in the sensitivity of the sensor. For example, the response of the SnO_2 decorated by Ag toward 50 ppm of H_2 is around 21% while that for pure SnO_2 is 14%. That is, Ag decoration improved the sensitivity by about 67%.

The synthesized Ag-decorated sensor was studied at wide range of operating temperatures starting from room temperature (RT = 29°C) and up to 500°C as shown in **Figure 6c**. For low concentrations (i.e., 50 and 200 ppm), the film showed no response at RT and only a small response at 100 and 200°C for 200 ppm. At higher concentrations (600, 1,200, and 1,800 ppm), the films gave an acceptable response at RT, with the response increasing by increasing the operating temperature to 500°C.

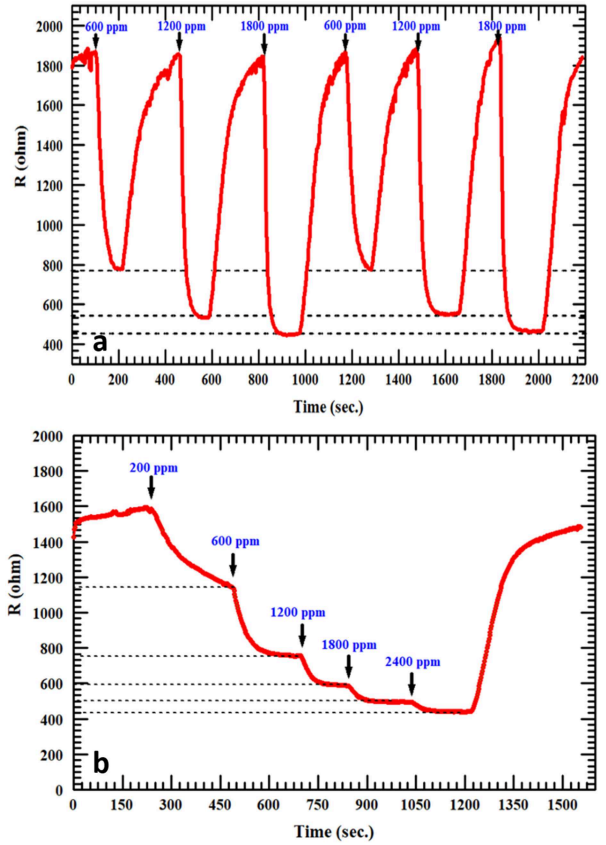

FIGURE 7 | (a) Repeatability test at 600, 1,200, and 1,800 ppm of H_2 for AgNPs/SnO_2. **(b)** Staircase behavior of AgNPs/SnO_2 sensor.

Figure 6d shows the comparison between the as-deposited SnO_2, annealed SnO_2, and AgNPs/SnO_2 sensors toward various H_2 concentrations (200–1,800 ppm) at low operation temperature (100°C). The annealed AgNPs/SnO_2 sensor exhibits higher response for all H_2 concentrations. For example, at 1,800 ppm, the response of as-deposited and annealed SnO_2 was ∼6 and ∼20%, respectively, while the response reached ∼42% from the AgNPs/SnO_2 sensor. On the other hand, at low concentration (200 ppm), both as-deposited and annealed SnO_2 had no response and yet AgNPs/SnO_2 gave an acceptable response of ∼7%, which confirms the value of using Ag to boost the sensitivity of the hydrogen sensor.

The reproducibility of measurements was tested in order to study the stability of the AgNPs/SnO_2 sensor, which is one of the vital properties for H_2 sensors. **Figure 7a** shows that two cycles of three different concentrations (600, 1,200, and 1,800 ppm) were used in this test. Clearly, the sensor has the ability to recover to the same initial response (600 ppm) after introducing different amounts of H_2 concentrations (1,200, 1,800 ppm), which confirms the stability of the fabricated sensor. The staircase behavior was also obtained, as shown in **Figure 7b**. The AgNPs/SnO_2 sensor shows excellent resistance descending mode from 200 to 2,400 ppm besides its ability to recover the initial resistance level, as it should for a stable sensor, when decreasing the concentration back to 200 ppm. **Table 2** compares the H_2 sensing properties of the fabricated AgNPs/SnO_2 sensor with the different sensors, operating in the dynamic mode, reported in the literature.

TABLE 2 | A comparison between the fabricated AgNPs/SnO_2 sensor with the different sensors reported in the literature.

Sensor	Optimum operation temperature	Response	H_2 concentration (ppm)	References
Co/SnO_2	175	47.2 [a]	1,000	Zhang et al., 2019
Polyaniline/SnO_2	30	42 [a]	6,000	Sonwane et al., 2019
SnO_2@rGO	80	1.58 [b]	1,000	Ren et al., 2018
SnO_2	150	5.5 [a]	1,000	Shen et al., 2015
SnO_2/Au-SiO_2	100	11.5 [b]	1,000	El-Maghraby et al., 2013
CNT/SnO_2	350	95 [c]	40,000	Majumdar et al., 2014
Pd-SnO_2/MoS_2	RT	8 [c]	1,000	Zhang et al., 2017
Pt-loaded SnO_2	200	10 [a]	1,000	Liewhiran et al., 2014
Ce doped SnO_2	200	80 [c]	500	Deivasegamani et al., 2017
Er-doped SnO_2	360	28[a]	100	Singh and Singh, 2019
AgNPs/SnO_2	300	80 [c]	600	This work

a: response $= \frac{R_a}{R_g}$, *b: response* $= \frac{R_a - R_g}{R_g} \times 100$, $c = \frac{R_a - R_g}{R_a} \times 100$.

Sensing Mechanism

SnO_2 was used as a gas sensor-based material that has the ability to sense reducing gases such as H_2. In the atmosphere, the surface of the SnO_2 film interacts with the oxygen molecules in the air. The adsorbed oxygen molecules form O^-, O^{-2}, and O_2^- moieties, resulting in the formation of depletion layers at the surface of the SnO_2 film (Chang, 1980). As a result, the SnO_2 becomes more resistive (due to lack of electrons in the film conduction band). **Figure 8A** describes the resulting band bending and the formation of the electron barrier at the SnO_2 film surface. In the presence of H_2, the H_2 molecules capture the oxygen moieties and release electrons back into the conduction band of the SnO_2 thin film, therefore decreasing its resistance. This process is described by the following equation:

$$H_2 + O^- \longrightarrow H_2O + e^-$$

The enhanced gas-sensing performances of the AgNPs/SnO_2 sensor can be explained by the electronic sensitization mechanism, which is based on the controlled carrier concentration (Yamazoe et al., 1983). The surface region of Ag nanoparticles contains two oxidation states Ag^0 and Ag^+ (Ag_2O), as confirmed by the XPS analysis. This mixture leads to the production of the redox couple Ag^+/Ag^0 (Matsushima et al., 1988). The couple has an electronic potential of 5.3 eV (Matsushima et al., 1988). When a contact is formed between Ag

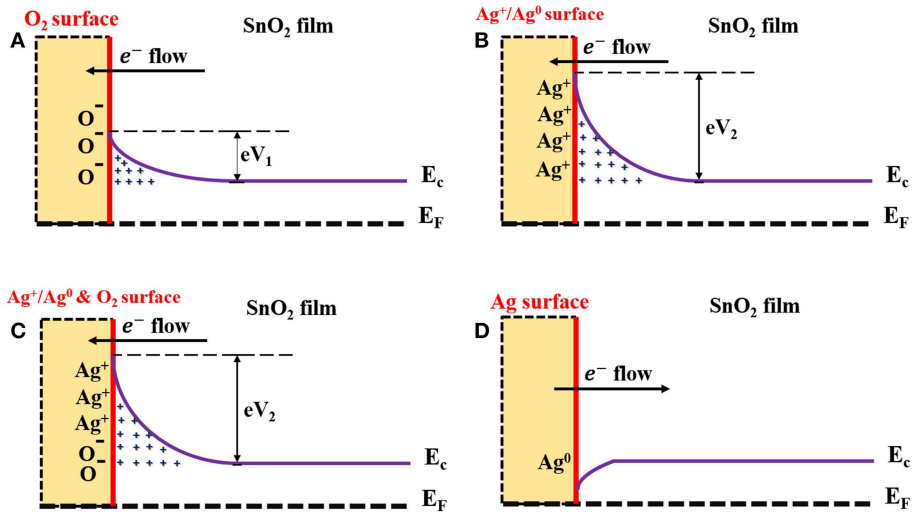

FIGURE 8 | Schematic diagram describes mechanism underlying enhanced H_2 sensing by AgNPs/SnO_2 nanocomposites. **(A)** Formation of the electrons barrier at the SnO_2 film surface. **(B)** Formation of the electrons barrier at the AgNPs/SnO_2 film surface. **(C)** Formation of the electrons barrier at the AgNPs/SnO_2 film surface in the ambient air. **(D)** Formation of the electrons barrier at the AgNPs/SnO_2 film surface after introducing H_2 gas.

NPs and n n-type semiconductor oxide whose electron affinity is <5.3 eV, the Fermi level of the n-type semiconductor is pinned to the Ag^+/Ag^0 potential. This leads to the increase of the electron depletion region and to a decrease of the semiconductor oxide conductivity. In our case, the electron affinity (Φ_s) of the SnO_2 is 4.60 eV (Li et al., 2016). Therefore, the Fermi level of the SnO_2 becomes aligned with the work function and electron affinity of Ag^0 and Ag^+, respectively. As a result of electron flows from the SnO_2 surface, the energy bands of the SnO_2 will bend downward to reach the equilibrium level with the energy of the Ag^+/Ag^0, and hence, the AgNPs/SnO_2 film will have a higher resistance than that of pure SnO_2 as shown in **Figure 8B**. The electron barrier at the surface of the SnO_2 film now depends on the energy of the barriers eV_1 and eV_2, which result from oxygen adsorption and Ag decoration, respectively, as in **Figure 8C**. Nevertheless, the significance conurbation would be from the larger energy eV_2. Now, when H_2 is introduced, and following the same mechanism mentioned above as a result of oxygen removal, the Ag_2O changes into metallic Ag, which has a work function of Φ_{Ag} 4.33 (Luth, 1993). Consequently, the energy bends upward to reach the level of the metallic Ag Fermi energy as a result of restoring electrons from Ag to SnO_2 surface as described in **Figure 8D**. Thus, the resistance of the SnO_2 film is more significantly decreased as an indication of H_2 presence.

CONCLUSION

Pristine and post-annealed SnO_2 thin films as well as silver-decorated SnO_2 thin films were fabricated using the DC/RF sputtering system. The structural, morphological, and compositional properties of the as-deposited SnO_2, annealed SnO_2, and AgNPs/SnO_2 were studied by various characterization techniques. The gas sensing properties of the silver-decorated tin oxide film were tested at different operating temperatures (RT to 500°C), and with varying H_2 concentration (50 to 1,800 ppm), in order to investigate the sensor sensitivity effect. It was found that the addition of the Ag nanoparticles has significantly increased the sensitivity by 67% compared with annealed SnO_2 at 500°C operation temperature. The observed improvement in H_2 sensing was explained according to an electronic sensitization mechanism.

DATA AVAILABILITY

All datasets generated for this study are included in the manuscript/supplementary files.

AUTHOR CONTRIBUTIONS

AM took the measurements, analyzed the data, contributed to the writing of the manuscript, synthesized the films, characterized the materials, and evaluated the sensors. QD designed the experiment, characterized the materials, evaluated the sensors, synthesized the films, and contributed to the writing of the manuscript. ZY designed the experiment, analyzed the data, and contributed to the editing of the manuscript.

ACKNOWLEDGMENTS

Center of Excellence in Nanotechnology (CENT) and the Physics department at King Fahd University of Petroleum and Minerals (KFUPM) are acknowledged for their support.

REFERENCES

Ansari, S. G., Boroojerdian, P., Sainkar, S. R., Karekar, R. N., Aiyer, R. C., and Kulkarni, S. K. (1997). Grain size effects on H_2 gas sensitivity of thick film resistor using SnO_2 nanoparticles. *Thin Solid Films* 295, 271–276. doi: 10.1016/S0040-6090(96)09152-3

Chakraborty, R., Dey, A., and Mukhopadhyay, A. K. (2010). Loading rate effect on nanohardness of soda-lime-silica glass. *Metall. Mater. Trans. A* 41, 1301–1312. doi: 10.1007/s11661-010-0176-8

Chang, S. C. (1980). Oxygen chemisorption on tin oxide: correlation between electrical conductivity and EPR measurements. *J. Vac. Sci. Technol.* 17, 366–369. doi: 10.1116/1.570389

Chen, X., Guo, Z., Xu, W. H., Yao, H. B., Li, M. Q., Liu, J. H., et al. (2011). Templating synthesis of SnO_2 nanotubes loaded with Ag_2O nanoparticles and their enhanced gas sensing properties. *Adv. Funct. Mater.* 21, 2049–2056. doi: 10.1002/adfm.201002701

Cho, S. (2014). Effect of growth temperature on structural, electrical, and optical properties of Gd-doped zinc oxide films. *Phys. Status Solidi A Appl. Res.* 211, 709–713. doi: 10.1002/pssa.201330345

Crabtree, G. W., Dresselhaus, M. S., and Buchanan, M. V. (2004). The hydrogen economy. *Phys. Today* 57, 39–44. doi: 10.1063/1.1878333

D'amico, A., Palma, A., and Verona, E. (1982). Surface acoustic wave hydrogen sensor. *Sens. Actuators* 3, 31–39. doi: 10.1016/0250-6874(82)80004-8

Dasgupta, N. P., Neubert, S., Lee, W., Trejo, O., Lee, J. R., and Prinz, F. B. (2010). Atomic layer deposition of Al-doped ZnO films: effect of grain orientation on conductivity. *Chem. Mater.* 22, 4769–4775. doi: 10.1021/cm101227h

Deivasegamani, R., Karunanidhi, G., Santhosh, C., Gopal, T., Neogi, A., Nivetha, R., et al. (2017). Chemoresistive sensor for hydrogen using thin films of tin dioxide doped with cerium and palladium. *Microchim. Acta* 184, 4765–4773. doi: 10.1007/s00604-017-2514-7

Drmosh, Q. A., Hossain, M. K., Alharbi, F. H., and Tabet, N. (2015). Morphological, structural and optical properties of silver treated zinc oxide thin film. *J. Mater. Sci-Mater. El.* 26, 139–148. doi: 10.1007/s10854-014-2375-3

El-Maghraby, E. M., Qurashi, A., and Yamazaki, T. (2013). Synthesis of SnO_2 nanowires their structural and H_2 gas sensing properties. *Ceram. Int.* 39, 8475–8480. doi: 10.1016/j.ceramint.2013.01.112

Hwang, I. S., Choi, J. K., Woo, H. S., Kim, S. J., Jung, S. Y., Seong, T. Y., et al. (2011). Facile control of C_2H_5OH sensing characteristics by decorating discrete Ag nanoclusters on SnO_2 nanowire networks. *ACS Appl. Mater. Interfaces* 3, 3140–3145. doi: 10.1021/am200647f

Ippolito, S. J., Kandasamy, S., Kalantar-Zadeh, K., and Wlodarski, W. (2005). Hydrogen sensing characteristics of WO_3 thin film conductometric sensors activated by Pt and Au catalysts. *Sens. Actuators B Chem.* 108, 154–158. doi: 10.1016/j.snb.2004.11.092

Kocemba, I., and Rynkowski, J. (2011). The influence of catalytic activity on the response of Pt/SnO_2 gas sensors to carbon monoxide and hydrogen. *Sens. Actuators B Chem.* 155, 659–666. doi: 10.1016/j.snb.2011.01.026

Kohl, D. (1990). The role of noble metals in the chemistry of solid-state gas sensors. *Sens. Actuators B Chem.* 1, 158–165. doi: 10.1016/0925-4005(90)80193-4

Korotcenkov, G., Blinov, I., Ivanov, M., and Stetter, J. R. (2007). Ozone sensors on the base of SnO_2 films deposited by spray pyrolysis. *Sens. Actuators B Chem.* 120, 679–686. doi: 10.1016/j.snb.2006.03.029

Kumar, V., Sharma, S. K., Sharma, T. P., and Singh, V. (1999). Band gap determination in thick films from reflectance measurements. *Opt. Mater.* 12, 115–119. doi: 10.1016/S0925-3467(98)00052-4

Li, H. H., He, Y., Jin, P. P., Cao, Y., Fan, M. H., Zou, X., et al. (2016). Highly selective detection of trace hydrogen against CO and CH_4 by Ag/Ag_2O–SnO_2 composite microstructures. *Sens. Actuators B Chem.* 228, 515–522. doi: 10.1016/j.snb.2016.01.078

Liewhiran, C., Tamaekong, N., Tuantranont, A., Wisitsoraat, A., and Phanichphant, S. (2014). The effect of Pt nanoparticles loading on H_2 sensing properties of flame-spray-made SnO_2 sensing films. *Mater. Chem. Phys.* 147, 661–672. doi: 10.1016/j.matchemphys.2014.06.005

Lippke, G. M. G., Singh, S., and Hoehn, R. K. (2018). *Staged Hydrotreating and Hydrocracking Process and Apparatus*. United States Patent Application No. US20180223198A1.

Luth, H. (1993). *Surfaces and Interfaces of Solids*. Berlin: Springer. doi: 10.1007/978-3-662-10159-9

Majumdar, S., Nag, P., and Devi, P. S. (2014). Enhanced performance of CNT/SnO_2 thick film gas sensors towards hydrogen. *Mater. Chem. Phys.* 147, 79–85. doi: 10.1016/j.matchemphys.2014.04.009

Matsushima, S., Teraoka, Y., Miura, N., and Yamazoe, N. (1988). Electronic interaction between metal additives and tin dioxide in tin dioxide-based gas sensors. *Jpn. J. Appl. Phys.* 27:1798. doi: 10.1143/JJAP.27.1798

Moseley, P. T. (1997). Solid state gas sensors. *Meas. Sci. Technol.* 8, 223–237. doi: 10.1088/0957-0233/8/3/003

Pal, A., and Agarwal, A. K. (2018). "Hydrogen for internal combustion engines," in *Prospects of Alternative Transportation Fuels* (Singapore: Springer), 39–54. doi: 10.1007/978-981-10-7518-6_4

Reddy, A. S., Figueiredo, N. M., and Cavaleiro, A. (2013). Nanocrystalline Au: Ag: SnO_2 films prepared by pulsed magnetron sputtering. *J. Phys. Chem. Solids* 74, 825–829. doi: 10.1016/j.jpcs.2013.01.023

Ren, H., Gu, C., Joo, S. W., Cui, J., Sun, Y., and Huang, J. (2018). Preparation of SnO_2 nanorods on reduced graphene oxide and sensing properties of as-grown nanocomposites towards hydrogen at low working temperature. *Mater. Express* 8, 263–271. doi: 10.1166/mex.2018.1428

Shen, Y., Wang, W., Fan, A., Wei, D., Liu, W., Han, C., et al. (2015). Highly sensitive hydrogen sensors based on SnO_2 nanomaterials with different morphologies. *Int. J. Hydrogen Energy* 40, 15773–15779. doi: 10.1016/j.ijhydene.2015.09.077

Shinde, V. R., Lokhande, C. D., Mane, R. S., and Han, S. H. (2005). Hydrophobic and textured ZnO films deposited by chemical bath deposition: annealing effect. *Appl. Surf. Sci.* 245, 407–413. doi: 10.1016/j.apsusc.2004.10.036

Singh, G., and Singh, R. C. (2019). Highly sensitive gas sensor based on Er-doped SnO_2 nanostructures and its temperature dependent selectivity towards hydrogen and ethanol. *Sens. Actuators B Chem.* 282, 373–383. doi: 10.1016/j.snb.2018.11.086

Sonwane, N. D., Maity, M. D., and Kondawar, S. B. (2019). Conducting polyaniline/SnO_2 nanocomposite for room temperature hydrogen gas sensing. *Mater. Today* 15, 447–453. doi: 10.1016/j.matpr.2019.04.106

Tsujimura, T., and Suzuki, Y. (2019). Development of a large-sized direct injection hydrogen engine for a stationary power generator. *Int. J. Hydrogen Energy* 44, 11355–11369. doi: 10.1016/j.ijhydene.2018.09.178

Van Duy, N., Hoa, N. D., and Van Hieu, N. (2012). Effective hydrogen gas nanosensor based on bead-like nanowires of platinum-decorated tin oxide. *Sens. Actuators B Chem.* 173, 211–217. doi: 10.1016/j.snb.2012.06.079

Wang, L., Li, J., Wang, Y., Yu, K., Tang, X., Zhang, Y., et al. (2016). Construction of 1D SnO_2-coated ZnO nanowire heterojunction for their improved n-butylamine sensing performances. *Sci. Rep.* 6:35079. doi: 10.1038/srep35079

Wang, Y., Ma, J., Ji, F., Yu, X., and Ma, H. (2005). Structural and photoluminescence characters of SnO_2: Sb films deposited by RF magnetron sputtering. *J. Lumin.* 114, 71–76. doi: 10.1016/j.jlumin.2004.12.003

Wu, B., Zhao, C., Xu, B., and Li, Y. (2018). Optical fiber hydrogen sensor with single Sagnac interferometer loop based on Vernier effect. *Sens. Actuators B Chem.* 255, 3011–3016. doi: 10.1016/j.snb.2017.09.124

Wu, R. J., Lin, D. J., Yu, M. R., Chen, M. H., and Lai, H. F. (2013). Ag@ SnO_2 core–shell material for use in fast-response ethanol sensor at room operating temperature. *Sens. Actuators B Chem.* 178, 185–191. doi: 10.1016/j.snb.2012.12.052

Yamazoe, N., Kurokawa, Y., and Seiyama, T. (1983). Effects of additives on semiconductor gas sensors. *Sens. Actuators* 4, 283–289. doi: 10.1016/0250-6874(83)85034-3

Yang, L., Yin, C., Zhang, Z., and Zhu, B. (2014). A study of hydrogen sensing properties and microstructure for highly dispersed Pd SnO_2 thin films with high response magnitude. *Appl. Surf. Sci.* 311, 74–82. doi: 10.1016/j.apsusc.2014.05.003

Zhang, D., Jiang, C., and Zhang, Y. (2017). Room temperature hydrogen gas sensor based on palladium decorated tin oxide/molybdenum disulfide

ternary hybrid via hydrothermal route. *Sens. Actuators B Chem.* 242, 15–24. doi: 10.1016/j.snb.2016.11.005

Zhang, Z., Yin, C., Yang, L., Jiang, J., and Guo, Y. (2019). Optimizing the gas sensing characteristics of Co-doped SnO_2 thin film based hydrogen sensor. *J. Alloys Compd.* 785, 819–825. doi: 10.1016/j.jallcom.2019.01.244

Zielinska, A., Kowalska, E., Sobczak, J. W., Łacka, I., Gazda, M., Ohtani, B., et al. (2010). Silver-doped TiO_2 prepared by microemulsion method: surface properties, bio-and photoactivity. *Sep. Purif. Technol.* 72, 309–318. doi: 10.1016/j.seppur.2010.03.002

Conflict of Interest Statement: The authors declare that the research was conducted in the absence of any commercial or financial relationships that could be construed as a potential conflict of interest.

frontiers in Materials

ORIGINAL RESEARCH
published: 20 August 2019
doi: 10.3389/fmats.2019.00197

Improvement of NO_2 Sensing Properties in Pd Functionalized Reduced Graphene Oxides by Electron-Beam Irradiation

Myung Sik Choi[1], Ali Mirzaei[2], Jae Hoon Bang[1], Wansik Oum[1], Sang Sub Kim[3] and Hyoun Woo Kim[1,4]**

[1] Division of Materials Science and Engineering, Hanyang University, Seoul, South Korea, [2] Department of Materials Science and Engineering, Shiraz University of Technology, Shiraz, Iran, [3] Department of Materials Science and Engineering, Inha University, Incheon, South Korea, [4] The Research Institute of Industrial Science, Hanyang University, Seoul, South Korea

Herein, we present the effect of electron-beam irradiation (EBI) on the gas-sensing properties of Pd-functionalized reduced graphene oxide (RGO). Scanning electron microscopy, transmission electron microscopy, and X-ray photoelectron spectroscopy were used to characterize the synthesized products. The samples were irradiated using electron beams at doses of 0 (Pd-RGO-0), 100 (Pd-RGO-100), and 500 kGy (Pd-RGO-500), and the NO2 gas-sensing properties were investigated. It was found that irradiation by electron beams has a critical effect on the gas-sensing properties of the samples, and the Pd-RGO-500 sensor showed the highest response to NO_2 gas. In particular, the response of the unirradiated sensor and the sensor irradiated at doses of 100 and 500 kGy to 10 ppm NO_2 were 1.027, 1.045, and 1.047, respectively. The response times of Pd-RGO-0, Pd-RGO-100, and Pd-RGO-500 to 10 ppm NO_2 gas were 389, 335, and 345 s, respectively. The corresponding recovery times for these sensors were 808, 766, and 816 s, respectively. The increased numbers of oxygen functional groups and high-energy defects were the main reasons for the increased gas response. This study will eventually lead to increased performance levels of RGO-based sensors that use EBI, as this technology can introduce changes into materials in a non-contact, clean, and powerful manner.

Keywords: reduced graphene oxide, electron-beam irradiation, Pd nanoparticles, gas sensor, NO_2 gas

OPEN ACCESS

Edited by:
Xiaogan Li,
Dalian University of Technology (DUT), China

Reviewed by:
Sen Liu,
Jilin University, China
Yuanjie Su,
University of Electronic Science and Technology of China, China

****Correspondence:***
Sang Sub Kim
sangsub@inha.ac.kr
Hyoun Woo Kim
hyounwoo@hanyang.ac.kr

Specialty section:
This article was submitted to Functional Ceramics, a section of the journal Frontiers in Materials

Received: *24 April 2019*
Accepted: *02 August 2019*
Published: *20 August 2019*

Citation:
Choi MS, Mirzaei A, Bang JH, Oum W, Kim SS and Kim HW (2019) Improvement of NO_2 Sensing Properties in Pd Functionalized Reduced Graphene Oxides by Electron-Beam Irradiation. Front. Mater. 6:197. doi: 10.3389/fmats.2019.00197

INTRODUCTION

Metal oxide gas sensors at present are among the most important sensing instruments for the detection of gases (Mirzaei et al., 2016; Kim et al., 2018) and humidity (Su et al., 2017). In spite of their remarkably high sensitivity, short response, and quick recovery times, they can exhibit poor stability and high sensing temperatures, thus limiting their wider use (Choi et al., 2014).

This has motivated researchers to develop alternative materials, especially those that may decrease the sensing temperature. Carbon-based materials are suitable candidates for gas sensors due to their large surface area, thermal stability, and extraordinary electrical conductivity (Uddin and Chung, 2014). Among the carbon materials developed thus far, graphene is a rising star with the abovementioned attributes, and it has been extensively investigated in different areas of science and technology (Banhart et al., 2010; Terrones et al., 2012). A converted form of graphene known as reduced graphene oxide

(RGO) has properties similar to those of pristine graphene, but a difference lies in the presence of certain oxygen-containing functional groups in RGO, even after a reduction process (Paredes et al., 2008). These oxygen-functional groups render RGO hydrophilic making soluble in water and many other solvents. This solubility allows RGO to be uniformly deposited onto any substrate (Craciun et al., 2013). Furthermore, chemical reduction for the synthesis of RGO is perceived to be a very economical and efficient approach, as it can produce RGO on a large scale from cost-effective natural graphite (Pham et al., 2011). Thus, due to such an inexpensive means of production and the availability of large quantities, RGOs are commercially available at reasonable prices, making them extremely attractive materials for sensing studies. For example, Du et al. (2019), reported the NH_3 sensing properties of RGO and proposed a model for its sensing behavior.

RGO sheets have a tendency to agglomerate through van der Waals forces between adjacent layers. As a result, this greatly increases the internal resistance and thus limits the broader application of this material. However, RGO-based composites are effective when used to prevent the re-stacking of RGOs to improve its properties (Lu et al., 2011).

The utilization of nanomaterials has explosively increased with a great amount of work reported (Jung et al., 2016; Karimipour and Molaei, 2016; Kiani et al., 2016; Kim J. et al., 2016; Kim T. U. et al., 2016); Lee et al., 2016; Meang et al., 2016; Tola et al., 2016; Truong and Park, 2016). Recently, nanocomposites based on RGO have been synthesized through the decoration of different NPs on graphene oxide (GO) or RGO, which have numerous applications in lithium ion batteries (Chen et al., 2015), surface-enhanced Raman spectroscopy (Huang et al., 2015), sensors (Bas, 2015), photo-catalysts

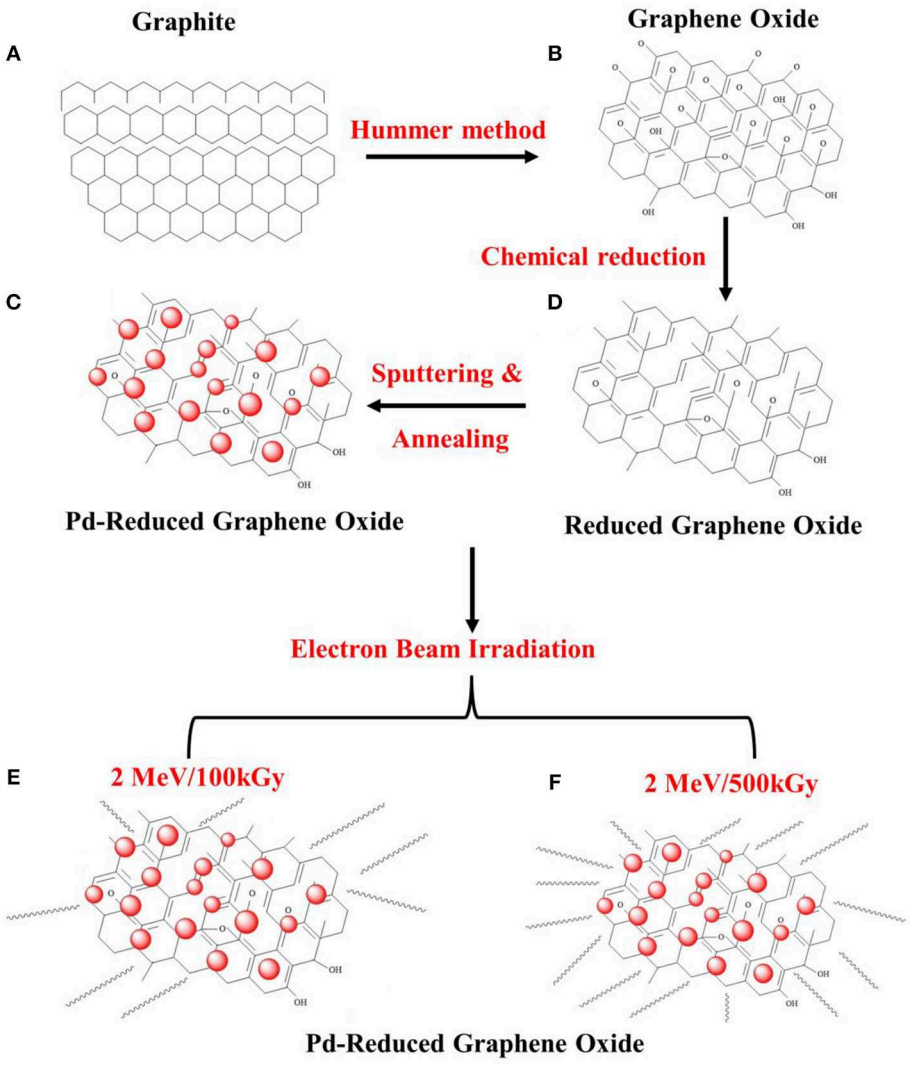

FIGURE 1 | Schematic illustration for the synthesis procedure in this study: **(A)** graphite, **(B)** graphene oxide, **(C)** RGO, **(D)** Pd-functionalized RGO, **(E)** 2 MeV/100 kGy irradiated Pd-functionalized RGO, and **(F)** 2 MeV/500 kGy irradiated Pd-functionalized RGO.

(Yan et al., 2014; Hareesh et al., 2016), and others. In the research on gas sensing, one advantage of nanoparticle decoration is that a noble metal can be used to enhance the gas responses of sensors by chemical and electrical sensitization (Lin and Hsu, 2013; Zhang et al., 2018). For example, Tran et al. (2014) synthesized RGO/Ag with enhanced NH_3 sensing properties relative to pristine RGO at room temperature. Also, Su et al. (2016) used RGO-polyethylene oxide film for detection of toluene at room temperature.

EBI has become extensively used in a variety of applications, such as the cleaning and sterilization of medical tools and the synthesis of different materials and nanocomposites (Hareesh et al., 2016). This is mainly due to the environmentally friendly characteristics and cost-effectiveness of this method. It has also been utilized for the synthesis and modification of carbon-based materials such as carbon nanotubes (Smith and Luzzi, 2001) and fullerenes (Krasheninnikov and Banhart, 2007). The modification of its properties principally results from the creation of defects by EBI, which can greatly affect the final properties of materials, such as the gas-sensing properties (Kwon et al., 2014).

Although there are some reports of the gas-sensing properties of noble-metal-loaded RGO sensors (Yu et al., 2013), to the best of our knowledge, reports about the effect of EBI on the sensing behavior of RGO-based sensors are rare. NO_2 is a highly toxic gas, and exposure causes lung irritation and decreased fixation of oxygen molecules on red blood corpuscles. Furthermore, it is one of the main causes of acid rain (Brunet et al., 2001). Moreover, with increasing industrialization, the release of NO_2 and its derivatives has significantly threatened human health and public security (Su et al., 2018). Thus, the development of gas sensors for the detection of NO_2 is extremely urgent. In this study, we investigate the effects of EBI on the NO_2 sensing behavior of Pd-functionalized RGO sensors. To do this, RGOs were prepared by the chemical reduction of GO and a Pd layer was subsequently deposited by a sputtering process. The final step was thermal annealing. The effects of EBI on the physical/chemical properties of RGOs were investigated and the NO_2 sensing properties of irradiated sensors were compared with those of unirradiated samples.

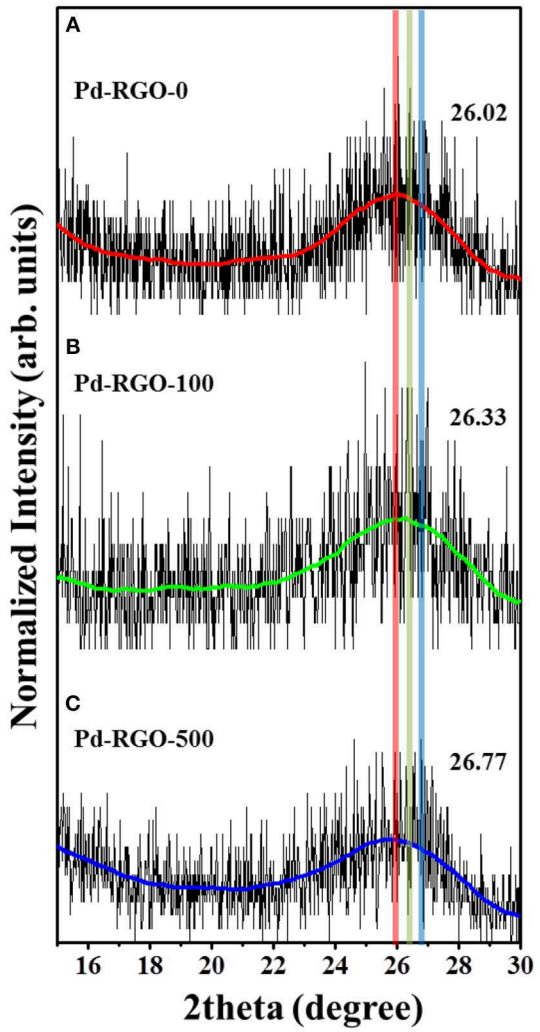

FIGURE 2 | XRD patterns of **(A)** Pd-RGO,-0 **(B)** Pd-RGO-100, and **(C)** Pd-RGO-500.

EXPERIMENTAL

Sample Preparation

Graphite was used as a starting material and GO was prepared by Hummer's method (Hummers and Offeman, 1958) with the same procedure in the previous report (Kwon et al., 2014). The oxidation process of 1 g of graphite was accomplished by stirring with 46 ml of H_2SO_4 and 12 g $KMnO_4$ in the presence of 12 g H_3PO_4, which acted as strong oxidizing agents. The purpose of this step was to increase the interlayer distance between the graphite packed layers to facilitate exfoliation and separation of graphene sheets in the final step. After repeating the washing and filtration several times, a very fine brown powder was allowed to dry in a vacuum oven. By adding hydrazine monohydrate and subsequently heating at 150°C in an oil bath, the exfoliated GO nanosheets were transformed to RGO. Re-dispersion in dimethylformamide (DMF) by sonication led to the formation of homogenous RGO suspension. Subsequently, by coating the RGO suspension on quartz substrates, the RGO films were prepared. Before annealing, they were heated at 250°C for 3 h to remove the moisture and annealing was conducted at 1100°C for 30 min. All heating and cooling processes were carried out with a gas flow of ($Ar + H_2$) at a rate of 100 sccm. The thickness of the RGO films were in the range of 100–300 nm.

To coat the Pd layer, a turbo sputter coater with a Pd target (Emitech K575X, Emitech Ltd., Ashford, Kent, UK) was used at room temperature. In the Ar plasma sputtering process, deposition time and DC sputter current were kept to 5 s and 65 mA, respectively. As a result, the Pd layer with a thickness of 3 nm was deposited on the RGOs. Following this, the samples were annealed at 700°C for 30 min, in the presence of Ar gas with flow rate of 2,000 sccm. This resulted in the creation of Pd NPs as isolated islands dispersed on the surface of RGO that are beneficial for gas sensing applications.

The Pd-functionalized RGO films were irradiated with an electron beam in air at room temperature in the absence of

a vacuum system. The ELV-8 electron accelerator (EBTech, Daejeon, Korea) was used to deliver an accelerating energy of 2 MeV with doses of 100 and 500 kGy, a beam current of 1 mA, and a pulse duration of 400 ps. Accordingly, un-irradiated Pd-functionalized RGO, Pd-functionalized RGO irradiated at 100 kGy and Pd-functionalized RGO irradiated at 500 kGy gas sensors, were coded as Pd-RGO-0, Pd-RGO-100, and Pd-RGO-500, respectively. **Figure 1** schematically shows the steps of the synthesis procedure in this study.

Characterization

Morphological features of the Pd-functionalized RGOs samples were examined using a scanning electron microscope (SEM, JEOL, JSM 5900 LV, Japan) and transmission electron microscopy

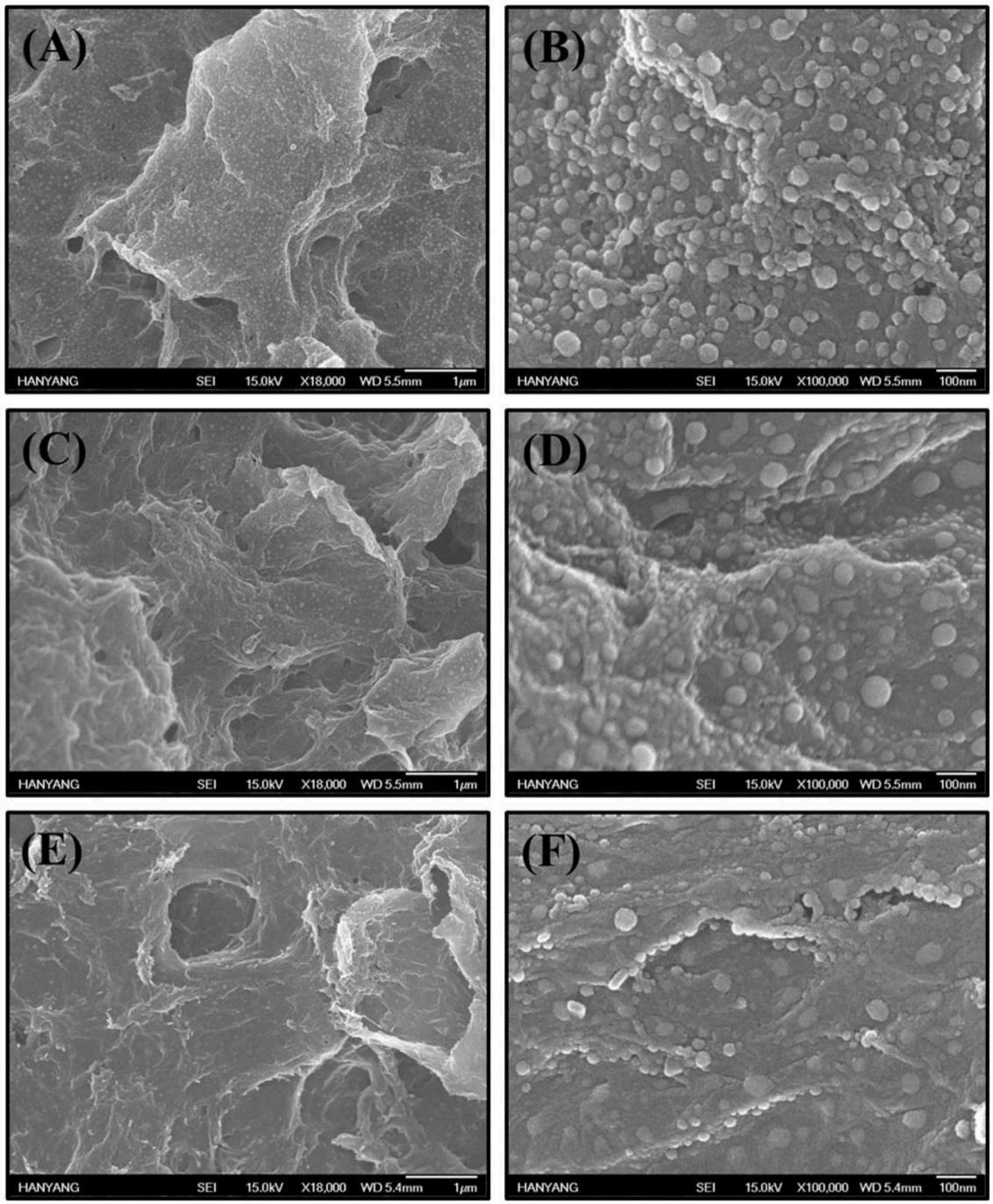

FIGURE 3 | (A,B) SEM images of Pd-RGO-0, **(C,D)** Pd-RGO-100, and **(E,F)** Pd-RGO-500.

(HR-TEM) with a TECNAI 20 microscope operated at 200 kV and coupled with an energy dispersive spectrometer (EDS). X-ray diffraction (XRD) patterns were recorded using Cu Kα (λ = 1.541 Å) radiation (Rigaku, Japan) to study structure and phase formation of samples in the Figures. X-ray photoelectron spectroscopy (XPS, VG Multilab ESCA 2000 system, UK) was employed to analyze the elemental compositions, by means of a monochromatized Al Kα x-ray source (hv = 1486.6 eV) at the Korean Basic Science Institute (KBSI). The binding energies obtained from the XPS analysis were corrected for specimen charging by referencing the C1s line to 284.5 eV. Raman scattering under an Ar-ion laser source (532 nm) was performed using a Horiba Jobin-Yvon LabRam HR Evolution system, equipped with a confocal microscope (100× microscope objective lens).

Gas Sensing Characterization

For sensing studies, Ni/Au double-layer electrodes were used in which Ni (∼200 nm thickness) and Au (∼50 nm thickness) were sequentially deposited via sputtering by an interdigital electrode mask. The sensor was placed in a horizontal-type tube furnace that was connected to an electrical measuring system (Keithley 2400) interfaced with a computer. The tube furnace was evacuated to 10^{-3} Torr by a rotary pump. The gas concentration was controlled by changing the mixing ratio of the target gas and dry air through mass flow controllers, with the total flow rate fixed at 100 sccm to avoid any possible variation in sensing properties. NO_2 concentration was adjusted to 10 ppm. During the recovery period, the system was purged at a flow rate of 100 sccm with ambient dry air. The sensing setup is similar to that used previously by our research group (Kwon et al., 2017). The change of resistance was measured in the presence of NO_2 at room temperature inside the chamber. The sensor response was defined as $R = R_a/R_g$. The response and recovery times were defined as the times taken for the resistance to change by 90% on exposure to the target gas (NO_2) and air, respectively.

RESULTS AND DISCUSSIONS

Structural, Morphological, and Chemical Analyses

XRD was performed to study the phase formation characteristics of the samples. **Figure 2** compares the positions of the (002) XRD peaks of all samples. For Pd-RGO-0, Pd-RGO-100, and Pd-RGO-500, the peak positions of the (002) plane are located at 26.02°, 26.33°, and 26.77°, respectively, which is in accordance with the (002) plane of graphite as a raw material (Yeung et al., 2008). It has been reported that the interplanar spacing is proportional to the degree of oxidation (Xu et al., 2011) and the compressive residual strain (Babitha et al., 2014). Due to the generation of oxygen-functional groups between the layers, the d-spacing of RGO can be increased and the presence of strain will result in a decrease in the interplanar spacing (Xu et al., 2011; Babitha et al., 2014). As observed here, the peak positions are shifted to higher angles after irradiation with an electron beam, resulting in a slight decrease in the lattice spacing. This decrease is in accordance with Bragg's law: $2d\sin\theta = n\lambda$, where d is the

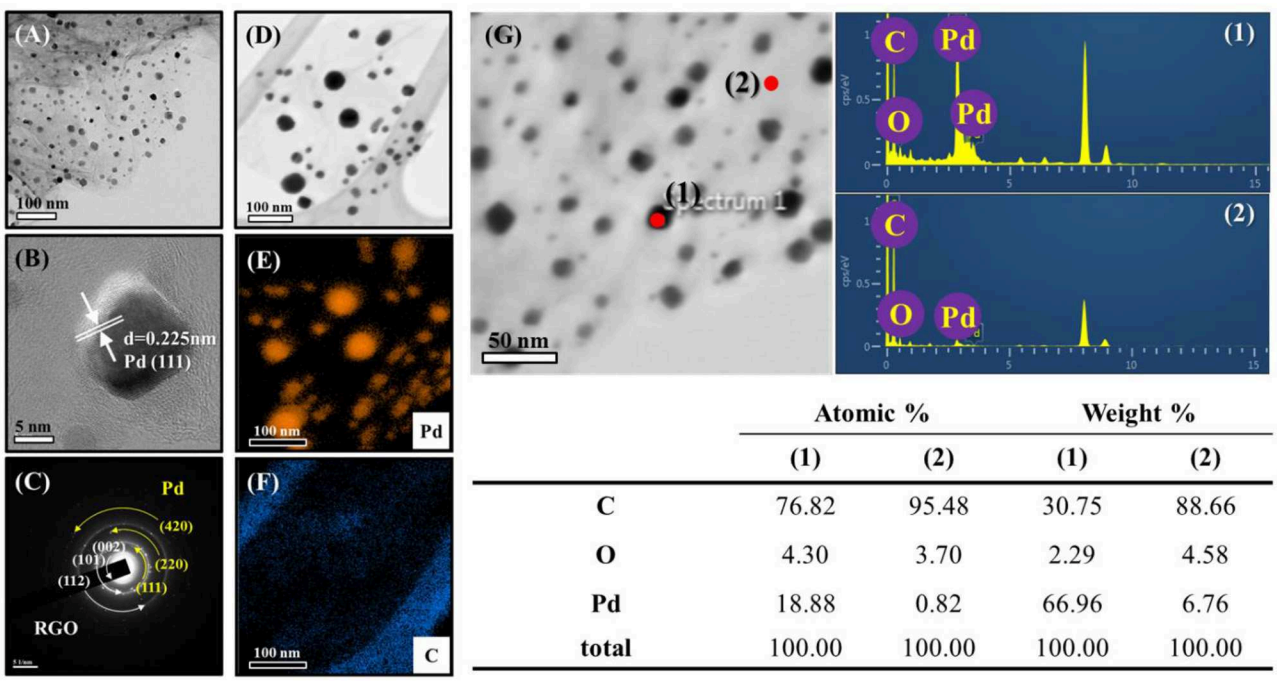

	Atomic %		Weight %	
	(1)	(2)	(1)	(2)
C	76.82	95.48	30.75	88.66
O	4.30	3.70	2.29	4.58
Pd	18.88	0.82	66.96	6.76
total	100.00	100.00	100.00	100.00

FIGURE 4 | (A) TEM images of Pd-RGO-0 and the corresponding **(B)** lattice-resolved-TEM image **(C)** SAED pattern. **(D)** TEM image for EDS analysis. EDS elemental mapping of **(E)** Pd and **(F)** C. **(G)** EDS analysis with the corresponding compositional Table.

interplanar spacing, θ is the angle of diffraction, and λ is the wavelength of the X-rays (0.1541 nm). The small decrease in the lattice spacing can be attributed to the compressive residual strain caused by electron irradiation. The electron irradiation creates ion vacancies, non-stoichiometry, and surface defects, which can introduce strain into the lattice (Babitha et al., 2014). Similarly Chen et al. investigated the structural changes in GO caused by an electron beam with an absorbed dose of 500 kGy, finding that the interlayer spacing of GO was decreased.

SEM images are presented in **Figure 3**, showing that Pd NPs are uniformly distributed on the RGO surfaces. **Figures 3A,B** show low- and high-magnification SEM images of Pd-RGO-0. The un-irradiated sample has a relatively smooth surface with the presence of Pd NPs. **Figures 3C–F** show SEM images of Pd-RGO-100 and Pd-RGO-500, respectively. After irradiation with an electron beam at a dose of 100 kGy, the surface appeared slightly rough. Under a high dosage of electron beams (500 kGy), the surfaces become rougher and more distorted. It was assumed that when RGO is irradiated by an electron beam at a high dose, its morphology changes.

The morphologies and structures of the samples were also subjected to a TEM analysis. **Figure 4A** shows a TEM image of Pd-RGO-100. Transparent RGO sheets functionalized by the fine dark NPs of Pd are easily observed in this image. The sizes of the Pd NPs ranged from 5 to 20 nm. **Figure 4B** shows an HRTEM image of the lattice fringe with a spacing of 0.225 nm, which is likely related to the (111) plane of Pd with a face-centered cubic structure. The selected-area electron diffraction (SAED) pattern of the sample is presented in **Figure 4C**, where the ring patterns of the (111), (220), and (420) planes of Pd and the (002), (101), and (112) planes of RGO are clearly observed, indicating the presence of both Pd and RGO. Elemental maps in **Figure 4D** are presented in **Figures 4E,F** for Pd and C, respectively, providing further evidence of the presence of

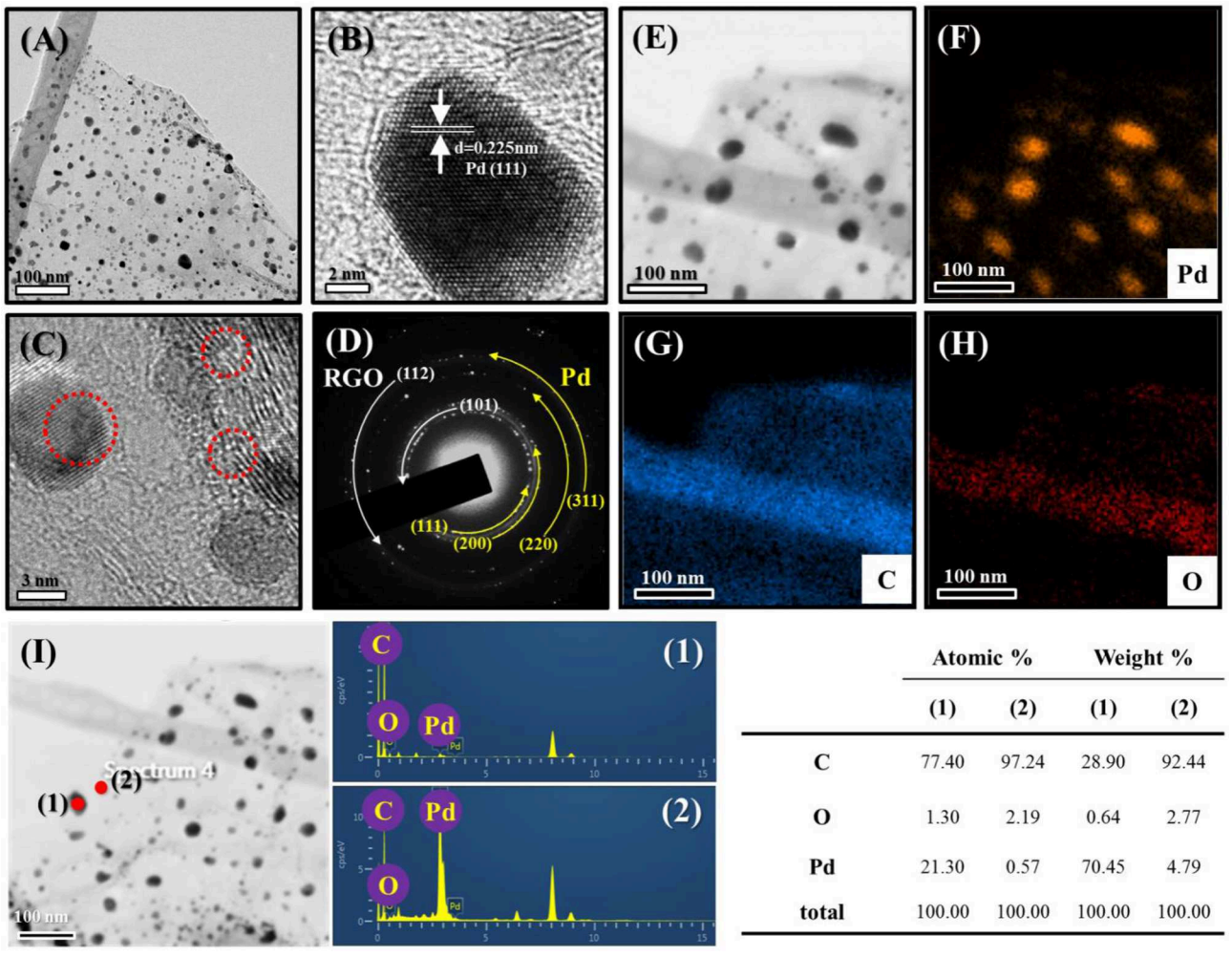

	Atomic %		Weight %	
	(1)	(2)	(1)	(2)
C	77.40	97.24	28.90	92.44
O	1.30	2.19	0.64	2.77
Pd	21.30	0.57	70.45	4.79
total	100.00	100.00	100.00	100.00

FIGURE 5 | (A) TEM images of Pd-RGO-500 and the corresponding **(B)** lattice-resolved-TEM image. **(C)** TEM image indicating defects in the sample. **(D)** SAED pattern. **(E)** TEM image for EDS analysis. EDS elemental mapping of **(F)** Pd, **(G)** C, and **(H)** O. **(I)** EDS analysis with the corresponding compositional Table.

fine and disperse Pd NPs in a matrix of carbon. According to the corresponding chemical analysis by EDS, the dark points correspond to Pd, whereas the transparent point is rich in carbon (**Figure 4G**). Furthermore, it can be seen that there are no other impurities in the sample, demonstrating the high purity of the starting materials and the appropriate synthesis procedure used. The Pd-RGO-500 underwent the same analysis. **Figures 5A,B** show TEM and HRTEM images of the samples, respectively, in which the presence of Pd NPs in a carbon matrix is evident. **Figure 5C** shows an HRTEM image, where the defects due to irradiation with high-energy electron beams are denoted by red circles in the image. If the kinetic energy transferred to the RGO is greater than a threshold value for bond-breaking, the carbon atoms will be displaced in a sub-picosecond time, generating a vacancy of displacement from their regular sites [37]. In the SAED pattern (**Figure 5D**), the rings correspond to the (111), (200), (220), and (311) planes of Pd and the (101) and (112) planes of carbon. The results of the EDS elemental mapping of the TEM image in **Figure 5E** are given in **Figures 5F–H** for Pd, C, and O, respectively. Some traces of oxygen were observed, likely due to atmospheric oxygen and the oxygen-functional groups of RGO. A precise chemical analysis of the sample is shown in **Figure 5I**, with elements of Pd, C and O apparent.

As a surface-sensitive technique, XPS can only detect elements at a depth of no more than 10 nm (Huo et al., 2014), and a large analysis area will result in the simultaneous analysis of elements in the sample. **Figures 6A–C** show the XPS survey spectra of Pd-RGO-0, Pd-RGO-100, and Pd-RGO-500, respectively. In the survey-scan XPS spectra, the peaks at approximately 285.5, 335.5 and 534.0 eV correspond to the C1s, Pd3d, and O1s core levels, respectively (Brun et al., 1999). The atomic percentage (at.%) of each element was calculated from the wide-scan spectra, and the results are summarized in **Figure 6**. In the Pd-RGO-0, the atomic concentration ratios of C, O, and Pd were calculated and found to be approximately 68.58, 25.84, and 5.58%, respectively. For, Pd-RGO-100, the atomic concentration ratios of C, O, and Pd were changed to 75.23, 20.60, and 4.17%, respectively, while for the Pd-RGO-500 sample, the corresponding ratios were 71.07, 26.08, and 2.85%, respectively. It appears that after irradiation at 100 kGy, some oxygen defects are created, which is in accordance with the results of Know et al. for GO (Kwon et al., 2016). Kang et al. also reported oxygen decreases after irradiation with electron beams in GO (Kang et al., 2015). In another study, Jin et al. reported a similar trend for RGO irradiated with electron beams (Jin et al., 2013). However, after irradiation with 500 kGy, numerous defective sites can be created, which eventually can adsorb some of the oxygen from the ambient environment. In other words, the RGO is partially oxidized after irradiation with a dose of 500

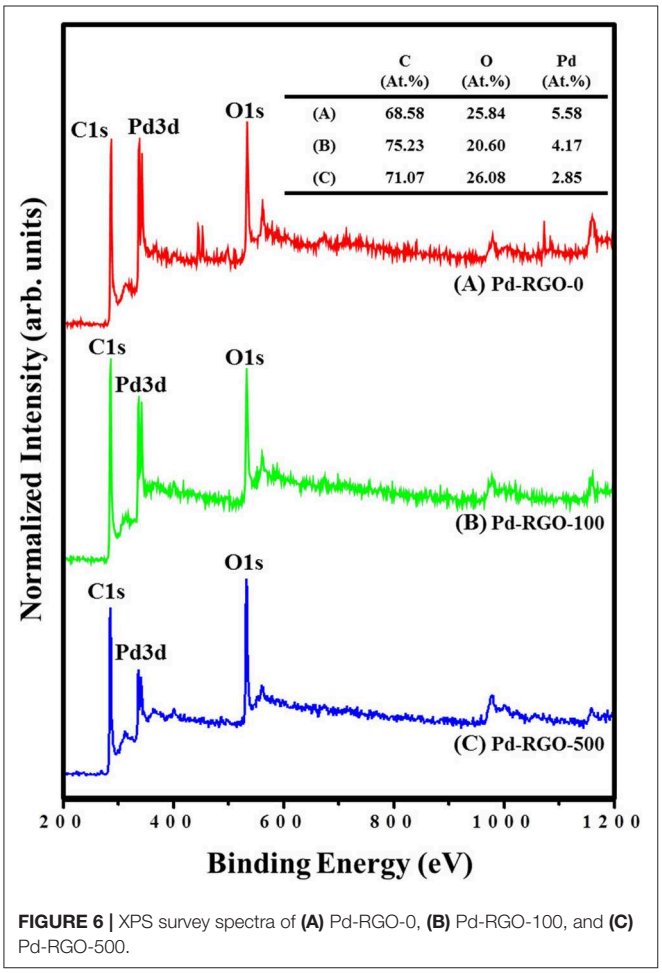

FIGURE 6 | XPS survey spectra of **(A)** Pd-RGO-0, **(B)** Pd-RGO-100, and **(C)** Pd-RGO-500.

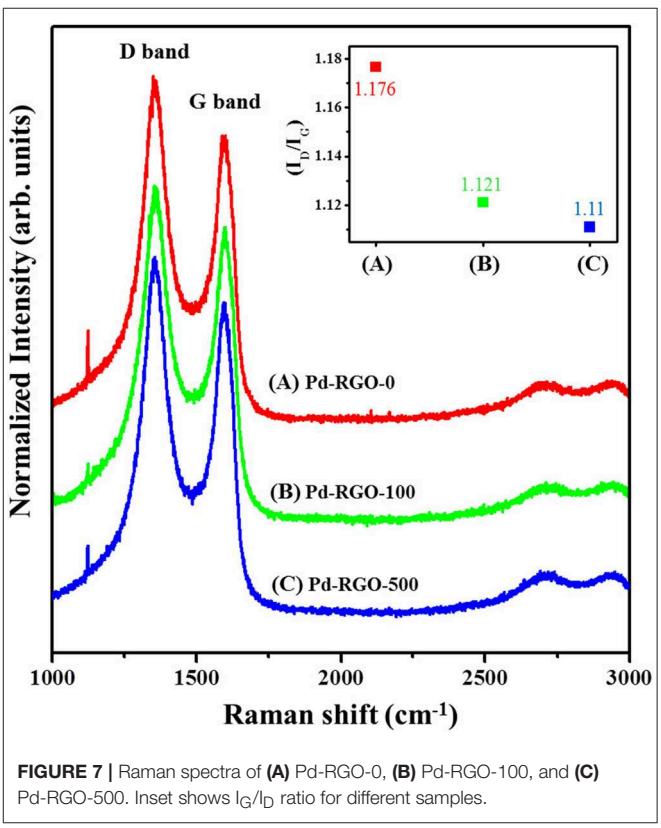

FIGURE 7 | Raman spectra of **(A)** Pd-RGO-0, **(B)** Pd-RGO-100, and **(C)** Pd-RGO-500. Inset shows I_G/I_D ratio for different samples.

kGy, which is the reason for the increased oxygen content in this sample.

The Raman spectra of the different gas sensors are shown in **Figure 7**. The two peaks around ∼1,350 and ∼1,580 cm^{-1} are present in all samples, known as the D peak and G peak, respectively. The G band corresponds to the E_{2g} mode, which exists for all sp^2 carbon systems. Unlike the G band, the D band is due to the presence of defects. The Tuinstra-Koenig relation, which is the ratio of the intensity of the D and G peaks (I_D/I_G), represents the disorder of the material. A greater ratio indicates more disorder of the RGO (Mirzaei et al., 2018).

The I_D/I_G values of Pd-RGO-0, Pd-RGO-100, and Pd-RGO-500 gas sensors were 1.176, 1.121, and 1.11, respectively. It can be assumed that during the reduction of graphite, many defects, including oxygen and carbon vacancies or the incomplete removal of epoxy/oxygenated functional groups, are generated in the RGO. During EBI, the removal of oxygen functional groups is accompanied by the creation of more oxygen defects. At the same time, the RGO is oxidized, which decreases the number of oxygen defects. The sample irradiated with the higher dose initially generated higher amounts of defects; subsequently in air, more oxygen species were adsorbed onto the active defects of RGO, thus decreasing the number of active defects for the sample irradiated at the higher dose.

Gas-Sensing Studies

The NO_2 gas-sensing properties of the RGO-based sensors were studied at room temperature. **Figures 8A–C** show the dynamic resistance changes of the gas sensors for 10 ppm of NO_2 gas. In all cases, the resistance was decreased after the introduction of

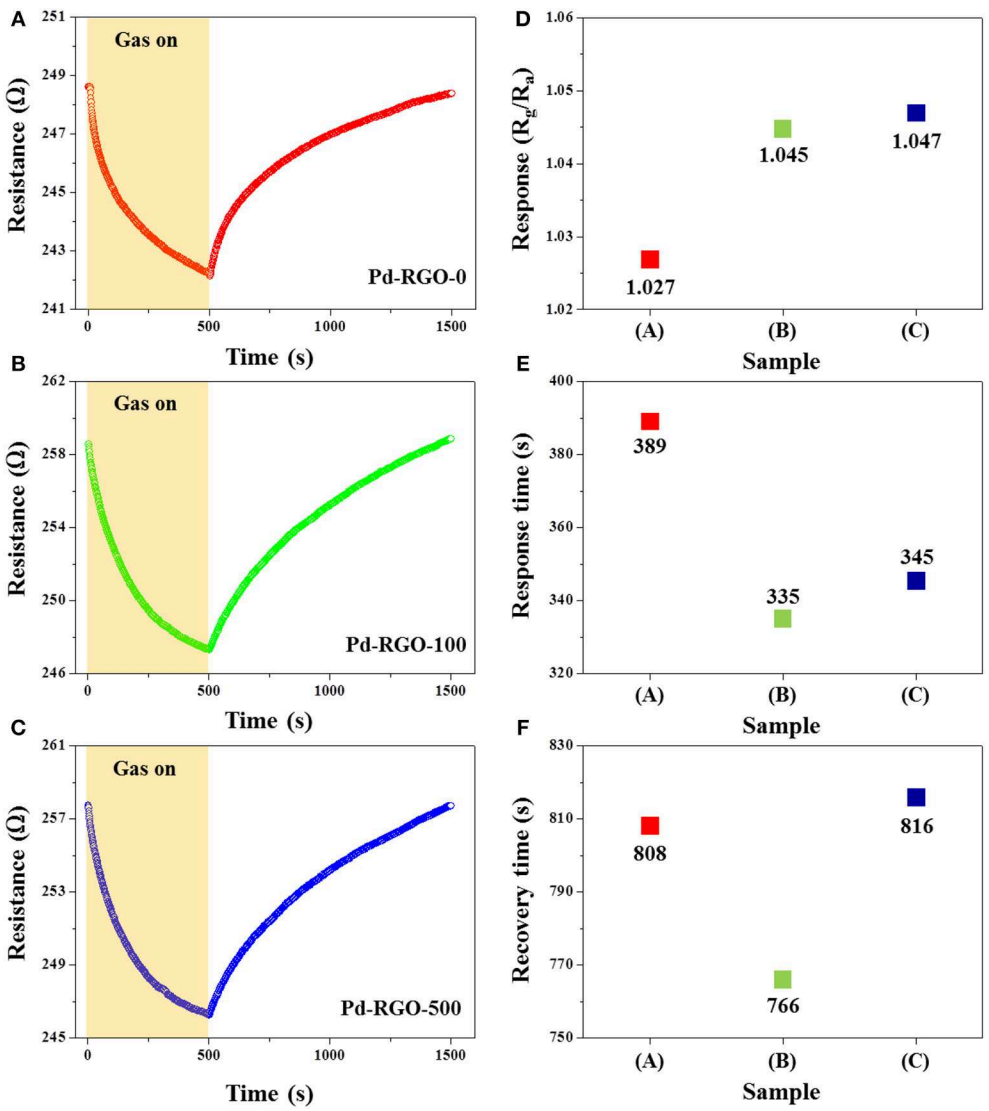

FIGURE 8 | Dynamic resistance curves of **(A)** the Pd-RGO-0 sensor, **(B)** Pd-RGO-100 sensor, and **(C)** Pd-RGO-500 sensor to 10 ppm NO_2 gas at room temperature. **(D)** Response of each gas sensor to 10 ppm NO_2 gas. **(E)** Response time and **(F)** recovery times of the gas sensors to 10 ppm NO_2 gas at room temperature.

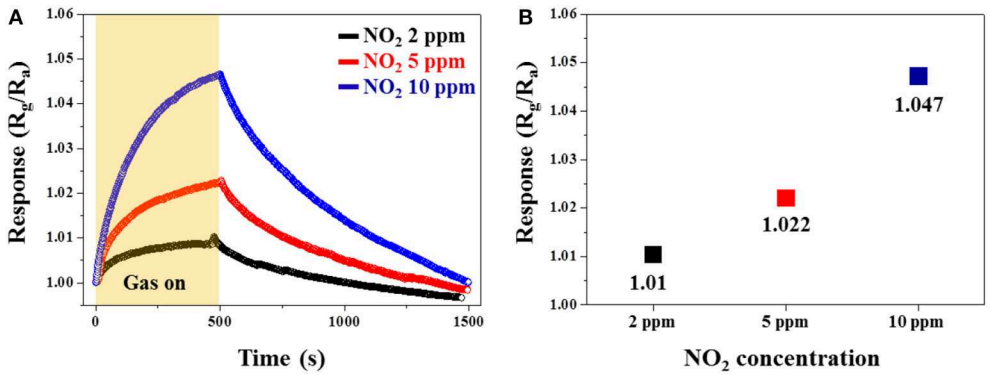

FIGURE 9 | (A) Dynamic responses of the Pd-RGO-500 gas sensor to 2, 5, and 10 ppm NO_2 gas at room temperature. **(B)** Response of the gas sensor versus the NO_2 gas concentration.

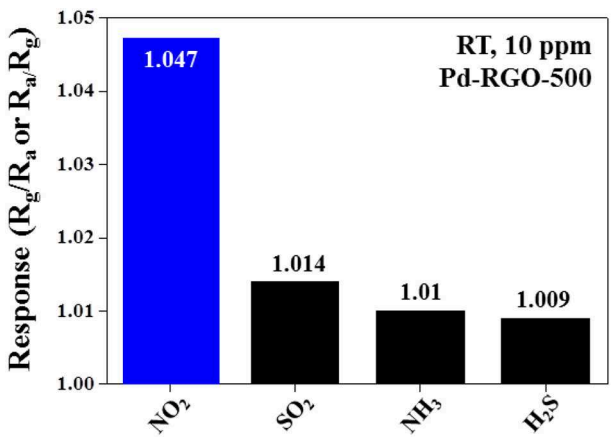

FIGURE 10 | Selectivity pattern of the Pd-RGO-500 gas sensor to 10 ppm of different gases at room temperature.

NO_2 gas, demonstrating the p-type behavior of the gas sensors. This result is in good agreement with the findings of a previous work (Wang et al., 2012). **Figure 8D** shows the response of all gas sensors to 10 ppm NO_2 gas, indicating that the responses of Pd-RGO-0, Pd-RGO-100, and Pd-RGO-500 sensors were 1.027, 1.045, and 1.047, respectively. It was clearly observed that the order of increase in the gas sensor responses is as follows: Pd-RGO-500 > Pd-RGO-100 > Pd-RGO-0. As shown in **Figures 8D,E**, the response times of Pd-RGO-0, Pd-RGO-100, and Pd-RGO-500 to 10 ppm NO_2 gas were 389, 335, and 345 s, respectively, and the corresponding recovery times for these sensors were 808, 766, and 816 s, respectively. It can be seen that the response time for the Pd-RGO-0 sensor is longer than that of the irradiated gas sensors. This is due to presence of more oxygen functional groups and the higher number of oxygen defects in the sensors irradiated with the electron beam. Thus, these materials act as favorable adsorption sites for gas molecules. Further, the Pd-RGO-500 sensor has a longer recovery time relative to that of the Pd-RGO-0 sensor. As 500 kGy of irradiation has high energy, the ratio of high-energy to low-energy binding sites is increased in the sensor irradiated at 500 kGy. Therefore, detachment of NO_2 molecules requires more time. Similarly, Yang et al. reported a slow desorption rate of NO_2 gas compared to the fast adsorption rate as a result of defective sites on the surface in pristine graphene (Yang et al., 2013). The longer response time may also be related to the more tortuous structure of the irradiated samples. With the assumption of a Knudsen flow for NO_2 diffusion, the diffusion coefficient of NO_2 gas can be determined by the following equation (Huang et al., 2010):

$$D_K = \frac{\varepsilon d}{3\tau}\left(\frac{8RT}{\pi M}\right)^{0.5}. \quad (1)$$

Here, D_K is the Knudsen diffusion coefficient in a porous medium, ε is dimensionless porosity, τ is the dimensionless tortuosity, d is the pore diameter, R is the gas constant, T is the temperature, and M is the molar mass. From the above equation, NO_2 diffusion is directly proportional to the porosity and pore diameter, whereas it is inversely proportional to the tortuosity of the sensor. As EBI can generate more complex channels and pores within the structure, more time is required for NO_2 molecules to be completely desorbed from the sensor.

Figure 9A shows the dynamic response curves of the Pd-RGO-500 gas sensor to 2, 5, and 10 ppm NO_2 gas. As shown in **Figure 9B**, the response of the gas sensor to 2, 5, and 10 ppm NO_2 gas is 1.01, 1.022, and 1.047, respectively. **Figure 10** shows the selectivity histogram of the Pd-RGO-500 gas sensor irradiated at a dose of 500 kGy. As observed, the response of the gas sensor to 10 ppm NO_2, SO_2, NH_3, and H_2S gases is 1.047, 1.014, 1.01, and 1.009, respectively.

When sensors are placed in an open air environment, oxygen molecules adsorb on their surfaces and trap the electrons from the conduction band of the sensing layer, leaving oxygen absorbents (O^{2-}) at room temperature (Choi et al., 2011). It is noteworthy that oxygen molecules can easily be adsorbed onto the oxygen vacancies of RGO.

$$O_2\,(\text{gas}) + e^- \rightarrow O^-_{2(\text{ads})} \quad (2)$$

At higher temperatures, other forms of oxygen ions, specifically O^- and O^{2-}, can exist (Xu et al., 2011); however, as our sensors work at room temperature, we do not consider these species of oxygen. When NO_2 gas is introduced into the gas chamber, it interacts with the RGO surface, acting as an oxidizing gas that traps electrons and is dissociated in the form of NO, thus leaving oxygen absorbents (O_2^-). This O_2^- anion then becomes an active site to absorb NO_2 molecules. Subsequently, NO can again be converted into NO_2 after reacting with half of an O_2 molecule (Yaqoob et al., 2015).

$$2NO_2\,(g) + e^- \rightarrow 2NO\,(g) + O_2^-(ads) \quad (3)$$

$$NO_2\,(g) + O_2^-\,(ads) + 2e^- \rightarrow NO\,(g) + O_2^-\,(ads) + 2O^-(\text{ads}) \quad (4)$$

$$NO_{(gas)} + 1/2O_2 \rightarrow NO_{2(gas)} \quad (5)$$

Chemical sensitization (CS) and the electronic effect are two important aspects of Pd-functionalization. In CS, NO_2 initially adsorbs onto the surfaces of Pd, dissociates, and then spills over onto the RGO (Kim et al., 2011). Moreover, due to the difference in the work functions of Pd [∼5.12 eV (Kim et al., 2017)] and RGO [∼4.75 eV (Abideen et al., 2015)], the electron transfer from RGO to Pd results in the formation of a hole-accumulation layer in RGO. After NO_2 adsorption and the capture of electrons, the thickness of the hole-accumulation layer in the RGO increases, leading to a decrease in the resistance and the appearance of a response in the sensor (Wang et al., 2015).

Several effects are associated with EBI. First, when the electrons strike the RGO surfaces, if they have enough kinetic energy they can generate surface defects. Second, electron beams can collide with oxygen molecules in the ambient environment and generate reactive and high-energy oxygen species. These reactive oxygen species combine with the RGO surfaces, generating oxygen-functional groups (Chung et al., 2013). Accordingly, it can be concluded that the changes in the sensing characteristics induced by EBI can be attributed to the modification of structural defects and oxygen-functional groups. The high-energy oxygen species may oxidize the graphene nanosheets.

After the EBI process was carried out at doses of 100 and 500 kGy, the NO_2 response was increased to 1.045 and 1.047, respectively. Therefore, the response was increased with EBI dose. In the case of the 100 kGy irradiated sensor, according to the XPS results, the amount of oxygen decreased and amount of carbon increased relative to that of the un-irradiated sensor. Therefore, enhanced gas response can be attributed to the higher amounts of oxygen vacancies or oxygen functional groups in this sensor, where more adsorption sites for the gas molecules exist. In the case of the Pd-RGO-500 sensor, XPS revealed that the oxygen content of RGO was increased due to EBI. Accordingly, the Pd-RGO-500 sensor generates numerous structural defects, as denoted in **Figure 5C** by the red circles. These sites can adsorb considerable amounts of oxygen-functional groups. For example, An et al. studied the adsorption of NO_2 on ZnO nanotubes. It was found that on a defect site, binding by NO_2 was nearly three times stronger compared to that on defect-free ZnO nanotubes (a binding energy of −0.98 eV compared to −0.30 eV). Therefore, a defective structure had a higher response level to NO_2 gas (An et al., 2008). The 500-kGy-irradiation-induced enhancement of sensing behavior is mainly related to the presence of oxygen-functional groups, which are preferential sites for the adsorption of NO_2 molecules. In addition, some non-oxygen defects such as carbon vacancies and 5-8-5 defects (Hashimoto et al., 2004) may be generated after irradiation via 500 kGy of energy with possible beneficial effects on the NO_2 response.

CONCLUSION

In summary, Pd-functionalized RGO gas sensors were synthesized by a reduction of GO by Hummer's method and the subsequent sputtering of a Pd thin layer followed by thermal treatment. The structural, morphological and NO_2 gas-sensing properties of the synthesized samples were studied after they were irradiated by a 2 MeV electron accelerator at doses of 100 and 500 kGy. The results of SEM/TEM and EDS analyses confirmed the existence of fine and dispersed Pd NPs on the surfaces of the RGO nanosheets. The highest response to NO_2 gas was observed in the Pd-RGO-500 sensor due to the presence of higher amounts of oxygen functional groups as well as higher energy defects. These results demonstrate the promotional effect of EBI, which is an eco-friendly, simple and cost-effective method to enhance the gas-sensing properties of Pd-functionalized RGO sensors, which could be applied to other sensing materials in the near future.

DATA AVAILABILITY

The raw data supporting the conclusions of this manuscript will be made available by the authors, without undue reservation, to any qualified researcher.

AUTHOR CONTRIBUTIONS

MC, JB, and WO carried out the experiments. AM prepared a draft of the manuscript. HK and SK supervised the experiments and finalized the manuscript.

FUNDING

This research was supported by Basic Science Research Program through the National Research Foundation of Korea (NRF) funded by the Ministry of Education (2016R1A6A1A03013422). This work was supported by the National Research Foundation of Korea (NRF) grant funded by the Korea government (MSIT) (2019R1A2C1006193).

REFERENCES

Abideen, Z. U., Katoch, A., Kim, J.-H., Kwon, Y. J., Kim, H. W., and Kim, S. S. (2015). Excellent gas detection of ZnO nanofibers by loading with reduced graphene oxide nanosheets. *Sens. Actuators B Chem*. 221, 1499–1507. doi: 10.1016/j.snb.2015.07.120

An, W., Wu, X., and Zeng, X. C. (2008). Adsorption of O_2, H_2, CO, NH_3, and NO_2 on ZnO nanotube: a density functional theory study. *J. Phys. Chem. C* 112, 5747–5755. doi: 10.1021/jp711105d

Babitha, K. K., Priyanka, K. P., Sreedevi, A., Ganesh, S., and Varghese, T. (2014). Effect of 8 MeV electron beam irradiation on the structural and optical properties of CeO_2 nanoparticles. *Mater. Charact*. 98, 222–227. doi: 10.1016/j.matchar.2014.11.004

Banhart, F., Kotakoski, J., and Krasheninnikov, A. V. (2010). Structural defects in graphene. *ACS Nano* 5, 26–41. doi: 10.1021/nn102598m

Bas, S. Z. (2015). Gold nanoparticle functionalized graphene oxide modified platinumelectrode for hydrogen peroxide and glucose sensing. *Mater. Lett*. 150, 20–23. doi: 10.1016/j.matlet.2015.02.130

Brun, M., Berthet, A., and Bertolini, J. C. (1999). XPS, AES and Auger parameter of Pd and PdO. *J. Electron Spectros. Relat. Phenomena* 104, 55–60. doi: 10.1016/S0368-2048(98)00312-0

Brunet, J., Talazac, L., Battut, V., Pauly, A., Blanc, J. P., Germain, J. P., et al. (2001). Evaluation of atmospheric pollution by two semiconductor gas sensors. *Thin Solid Films* 391, 308–313. doi: 10.1016/S0040-6090(01)01001-X

Chen, X., Huang, Y., Zhang, X., Li, C., Chen, J., and Wang, K. (2015). Graphene supported ZnO/CuO flowers composites as anode materials for lithium ion batteries. *Mater. Lett*. 152, 181–184. doi: 10.1016/j.matlet.2015.03.136.

Choi, S.-W., Jung, S.-H., and Kim, S.-S. (2011). Significant enhancement of the NO_2 sensing capability in networked SnO_2 nanowires by Au nanoparticles synthesized via γ-ray radiolysis. *J. Hazard. Mater*. 193, 243. doi: 10.1016/j.jhazmat.2011.07.053

Choi, S.-W., Katoch, A., Sun, G.-J., Kim, J.-H., Kim, S.-H., and Kim, S. S. (2014). Dual functional sensing mechanism in SnO_2-ZnO core–shell nanowires. *ACS Appl. Mater. Interfaces* 6, 8281–8287. doi: 10.1021/am501107c

Chung, M. G., Kim, D. H., Lee, H. M., Kim, T., Choi, J. H., Seo, D. K., et al. (2013). Highly sensitive NO_2 gas sensor based on ozone treated graphene. *Sens. Actuators B Chem*. 166-167, 172–176. doi: 10.1016/j.snb.2012.02.036

Craciun, M. F., Khrapach, I., Barnes, M. D., and Russo, S. (2013). Properties and applications of chemically functionalized graphene. *J. Phys. Condes. Matter* 25:423201. doi: 10.1088/0953-8984/25/42/423201

Du, H., Xie, G., Su, Y., Tai, H., Du, X., Yu, H., et al. (2019). A new model and its application for the dynamic response of RGO resistive gas sensor. *Sensors* 19:889. doi: 10.3390/s19040889

Hareesh, K., Joshi, R. P., Dahiwale, S. S., Bhoraskar, V. N., and Dhole, S. D. (2016). 6 MeV energy electron beam assisted synthesis of Ag–rGO nanocomposite and its photocatalytic activity. *Mater. Lett*. 164, 35–38. doi: 10.1016/j.matlet.2015.10.129

Hashimoto, A., Suenaga, K., Gloter, A., Urita, K., and Iijima, S. (2004). Direct evidence for atomic defects in graphene layers. *Nature* 430, 870–873. doi: 10.1038/nature02792

Huang, J., Wu, Y., Gu, C., Zhai, M., Yu, K., Yang, M., et al. (2010). Large-scale synthesis of flowerlike ZnO nanostructure by a simple chemical solution route and its gas-sensing property. *Sens. Actuators B Chem*. 146, 206–212. doi: 10.1016/j.snb.2010.02.052

Huang, Q., Wei, W., Yan, Q., Wu, C., and Zhu, X. (2015). A facile and green method for synthesis of rGO@SiO_2@FeOOH@Ag nanocomposite as efficient surface enhanced Raman scattering (SERS) platforms. *Mater. Lett*. 152, 203–206. doi: 10.1016/j.matlet.2015.03.117

Hummers, W. S., and Offeman, R. E. (1958). Preparation of graphitic oxide. *J. Am. Chem. Soc*. 80:1339. doi: 10.1021/ja01539a700

Huo, D., He, J., Li, H., Yu, H., Shi, T., Feng, Y., et al. (2014). Fabrication of Au@Ag core-shell NPs as enhanced CT contrast agents with broad antibacterial properties. *Colloids Surf. B Biointerfaces* 117, 29–35. doi: 10.1016/j.colsurfb.2014.02.008

Jin, E., He, J., Sheng, K., Zhang, Z., Shi, G., and Zheng, Q. (2013). Electron-irradiation-induced reinforcement of reduced graphene oxide papers. *Acta Mater*. 61, 6466–6473. doi: 10.1016/j.actamat.2013.07.025

Jung, D., Cho, S. G., Moon, T., and Sohn, H. (2016). Fabrication and characterization of porous silicon nanowires. *Electron. Mater. Lett*. 12, 17–23. doi: 10.1007/s13391-015-5409-y

Kang, M., Lee, D. H., Kang, Y.-M., and Jung, H. (2015). Electron beam irradiation dose dependent physico-chemical and electrochemical properties of reduced graphene oxide for supercapacitor. *Electrochim. Acta* 184, 427–435. doi: 10.1016/j.electacta.2015.10.053

Karimipour, M., and Molaei, M. (2016). Red florescent Ag_2S-CdS hybrid nanoparticles prepared by a one pot and rapid microwave method. *Electron. Mater. Lett*. 12, 205–210. doi: 10.1007/s13391-015-5278-4

Kiani, M. J., Akbari, E., Kooshkaki, F. R., and Zeinalinezhad, A. (2016). Analytical investigation of carrier concentration effect on one-dimensional graphene nanoscroll. *Electron. Mater. Lett*. 12, 219–223. doi: 10.1007/s13391-015-5352-y

Kim, H., Park, S., Jin, C., and Lee, C. (2011). Enhanced gas sensing properties of p-type TeO_2 nanorods functionalized with Pd. *Nano* 6, 455–460. doi: 10.1142/S1793292011002858

Kim, J., Oh, E., Yang, Y., and Yu, D. (2016). Bias dependent photocurrent characteristics of copper sulfide single nanowires. *J. Korean Phys. Soc*. 69, 202–206. doi: 10.3938/jkps.69.202

Kim, J.-H., Kim, H. W., and Kim, S. S. (2017). Ultra-sensitive benzene detection by a novel approach: core-shell nanowires combined with the Pd-functionalization. *Sens. Actuators B Chem*. 239, 578–585. doi: 10.1016/j.snb.2016.08.071

Kim, J. H., Lee, J. H., Mirzaei, A., Kim, H. W., and Kim, S. S. (2018). SnO_2 (n)-NiO (p) composite nanowebs: gas sensing properties and sensing mechanisms. *Sensors and Actuators B Chem.* 258, 204–214. doi: 10.1016/j.snb.2017.11.063

Kim, T. U., Gang, M. G., Kim, J. A., Moon, J. H., Kim, D. G., Kim, S. H., et al. (2016). The study of light waveguide effects on ZnO nanorod arrays. *Electron. Mater. Lett*. 12, 224–231. doi: 10.1007/s13391-015-5324-2

Krasheninnikov, A. V., and Banhart, F. (2007). Engineering of nanostructured carbon materials with electron or ion beams. *Nat. Mater*. 6, 723–733. doi: 10.1038/nmat1996

Kwon, S.-N., Jung, C.-H., and Na, S.-I. (2016). Electron-beam-induced reduced graphene oxide as an alternative hole-transporting interfacial layer for high-performance and reliable polymer solar cells. *Org. Electron*. 34, 67–74. doi: 10.1016/j.orgel.2016.04.008

Kwon, Y. J., Cho, H. Y., Na, H. G., Lee, B. C., Kim, S. S., and Kim, H. W. (2014). Improvement of gas sensing behavior in reduced graphene oxides by electron-beam irradiation. *Sens. Actuators B Chem*. 203, 143–149. doi: 10.1016/j.snb.2014.06.025

Kwon, Y. J., Na, H. G., Kang, S. Y., Choi, M. S., Bang, J.-H., Kim, T. W., et al. (2017). Attachment of Co_3O_4 layer to SnO_2 nanowires for enhanced gas sensing properties. *Sens. Actuators B Chem*. 239, 180–192. doi: 10.1016/j.snb.2016.07.177

Lee, H., Lee, C.-R., Ahn, H.-K., Kim, J. S., and Ryu, M.-R. (2016). Emission characteristics of shape-engineered InAs/InAlGaAs quantum dots subjected to thermal treatments. *J. Korean Phys. Soc*. 69, 85–90. doi: 10.3938/jkps.69.85

Lin, Y. K., and Hsu, Y. J. (2013). "Preparation of M@Cu_2O (M = Au, Ag, Pd) core-shell nanocrystals by a facile citrate-chelating approach," in *224th ECS Meeting*, San Francisco, CA: The Electrochemical Society.

Lu, X., Dou, H., Gao, B., Yuan, C., Yang, S., Hao, L., et al. (2011). A flexible graphene/multiwalled carbon nanotube film as a high performance electrode material for supercapacitors. *Electrochim. Acta* 56, 5115–5121. doi: 10.1016/j.electacta.2011.03.066

Meang, W. J., Seo, J., Ahn, Y., and Son, J. Y. (2016). Magnetic force microscopy of conducting nanodots in NiO thim films. *Electron. Mater. Lett*. 12, 251–254. doi: 10.1007/s13391-015-5260-1

Mirzaei, A., Kwon, Y. J., Wu, P., Kim, S. S., and Kim, H. W. (2018). Converting the conducting behavior of graphene oxides from n-type to p-type via electron-beam irradiation. *ACS Appl. Mater. Interfaces* 10, 7324–7333. doi: 10.1021/acsami.7b16458

Mirzaei, A., Park, S., Sun, G. J., Kheel, H., Lee, C., and Lee, S. (2016). Fe_2O_3/Co_3O_4 composite nanoparticle ethanol sensor. *J. Korean Phys. Soc*. 69, 373–380. doi: 10.3938/jkps.69.373

Paredes, J. I., Rodil, S. V., Alonso, A. M., and Tascon, J. M. D. (2008). Graphene oxide dispersions in organic solvents. *Langmuir* 24, 10560–10564. doi: 10.1021/la801744a

Pham, V. H., Cuong, T. V., Hur, S. H., Oh, E., Kim, E. J., Shin, E. W., et al. (2011). Chemical functionalization of graphene sheets by solvothermal reduction of a graphene oxide suspension in N-methyl-2-pyrrolidone. *J. Mater. Chem. A* 21:3371. doi: 10.1039/C0JM02790A

Smith, B. W., and Luzzi, D. E. (2001). Electron irradiation effects in single wall carbon nanotubes. *J. Appl. Phys.* 90:3509. doi: 10.1063/1.1383020

Su, Y., Xie, G., Chen, J., Du, H., Zhang, H., Yuan, Z., et al. (2016). Reduced graphene oxide–polyethylene oxide hybrid films for toluene sensing at room temperature. *RSC Adv.* 6, 97840–97847. doi: 10.1039/C6RA21077E

Su, Y., Xie, G., Tai, H., Li, S., Yang, B., Wang, S., et al. (2018). Self-powered room temperature NO_2 detection driven by triboelectric nanogenerator under UV illumination. *Nano Energy* 47, 316–324. doi: 10.1016/j.nanoen.2018.02.031

Su, Y., Xie, G., Wang, S., Tai, H., Zhang, Q., Du, H., et al. (2017). Novel high-performance self-powered humidity detection enabled by triboelectric effect. *Sens. Actuators B. Chem.* 251, 144–152. doi: 10.1016/j.snb.2017.04.039

Terrones, H., Lv, R., Terrones, M., and Dresselhaus, M. S. (2012). The role of defects and doping in 2D graphene sheets and 1D nanoribbons. *Rep. Prog. Phys.* 75:062501. doi: 10.1088/0034-4885/75/6/062501

Tola, P. S., Kim, D. J., Phan, T. L., Liu, C., and Lee, B. W. (2016). Magnetic properties and magnetocaloric effect of $LaMnO_3$ nanoparticles prepared by using the sol-gel method. *J. Korean Phys. Soc.* 69, 65–71. doi: 10.3938/jkps.69.65

Tran, Q. T., Hoa, H. T. M., Yoo, D. H., Cuong, T. V., Hur, S. H., and Chung, J. S. (2014). Reduced graphene oxide as an over-coating layer on silver nanostructures for detecting NH_3 gas at room temperature. *Sens. Actuators B Chem.* 194, 45–50. doi: 10.1016/j.snb.2013.12.062

Truong, N. T. N., and Park, C. (2016). Synthesis and characterization of tin disulfide nanocrystals for hybrid bulk hetero-junction solar cell applications. *Electron. Mater. Lett.* 12, 308–314. doi: 10.1007/s13391-015-5266-8

Uddin, A. S. M. I., and Chung, G. S. (2014). Synthesis of highly dispersed ZnO nanoparticles on graphene surface and their acetylene sensing properties. *Sens. Actuators B Chem.* 205, 338–344. doi: 10.1016/j.snb.2014.09.005

Wang, J., Kwak, Y., Lee, I.-Y., Maeng, S., and Kim, G.-H. (2012). Highly responsive hydrogen gas sensing by partially reduced graphite oxide thin films at room temperature. *Carbon* 50, 4061–4067. doi: 10.1016/j.carbon.2012.04.053

Wang, J., Rathi, S., Singh, B., Lee, I., Maeng, S., Joh, H.-I., et al. (2015). Dielectrophoretic assembly of Pt nanoparticle-reduced graphene oxide nanohybrid for highly-sensitive multiple gas sensor. *Sens. Actuators B Chem.* 220, 755–761. doi: 10.1016/j.snb.2015.05.133

Xu, Z., Chen, L., Li, J., Wang, R., Qian, X., Song, X., et al. (2011). Oxidation and disorder in few-layered graphene induced by the electron-beam irradiation. *Appl. Phys. Lett.* 98, 1183112. doi: 10.1063/1.3587798

Yan, W. M., Wei, Z., En, Z. D., An, L. S., Xing, M. W., Wei, T. Z., et al. (2014). CeO_2 hollow nanospheres decorated reduced graphene oxide composite for efficient photocatalytic dye-degradation. *Mater. Lett.* 137, 229–232. doi: 10.1016/j.matlet.2014.08.128

Yang, G., Lee, C., Kim, J., Ren, F., and Pearton, S. J. (2013). Flexible graphene-based chemical sensors on paper substrates. *Phys. Chem. Chem. Phys.* 15, 1798–1801. doi: 10.1039/c2cp43717a

Yaqoob, U., Phan, D.-T., Uddin, A. S. M. I., and Chung, G.-S. (2015). Highly flexible room temperature NO_2 sensor based on MWCNTs-WO_3 nanoparticles hybrid on a PET substrate. *Sens. Actuators B Chem.* 221, 760–768. doi: 10.1016/j.snb.2015.06.137

Yeung, C. S., Liu, L. V., and Wang, Y. A. (2008). Adsorption of small gas molecules onto Pt-doped single-walled carbon nanotubes. *J. Phys. Chem. C* 112, 7401–7411. doi: 10.1021/jp07 53981

Yu, H., Xu, P., Lee, D. W., and Li, X. (2013). Porous-layered stack of functionalized AuNP–rGO (gold nanoparticles–reduced graphene oxide) nanosheets as a sensing material for the micro-gravimetric detection of chemical vapor. *J. Mater. Chem. A* 1, 4444–4450. doi: 10.1039/c3ta01401k

Zhang, Q., Xie, G., Xu, M., Su, Y., Tai, H., Du, H., et al. (2018). Visible light-assisted room temperature gas sensing with ZnO-Ag heterostructure nanoparticles. *Sens. Actuators B. Chem.* 259, 269–281. doi: 10.1016/j.snb.2017. 12.052

Conflict of Interest Statement: The authors declare that the research was conducted in the absence of any commercial or financial relationships that could be construed as a potential conflict of interest.

frontiers in Materials

ORIGINAL RESEARCH
published: 20 August 2019
doi: 10.3389/fmats.2019.00195

Three-Dimensional Fe_3O_4@Reduced Graphene Oxide Heterojunctions for High-Performance Room-Temperature NO_2 Sensors

Cheng Zou[1], Jing Hu[2], Yanjie Su[1], Feng Shao[1], Zejun Tao[1], Tingting Huo[1], Zhihua Zhou[1], Nantao Hu[1], Zhi Yang[1], Eric Siu-Wai Kong[1] and Yafei Zhang[1]**

[1] Key Laboratory of Thin Film and Microfabrication (Ministry of Education), Department of Micro/Nano Electronics, School of Electronics, Information and Electrical Engineering, Shanghai Jiao Tong University, Shanghai, China, [2] School of Chemistry, Biology and Materials Engineering, Research Center for Nanophotonic and Nanoelectronic Materials, Suzhou University of Science and Technology, Suzhou, China

OPEN ACCESS

Edited by:
Xiaogan Li,
Dalian University of Technology (DUT), China

Reviewed by:
Qiuxia Feng,
Dalian Neusoft University of Information, China
Lili Wang,
Jilin University, China

***Correspondence:**
Yanjie Su
yanjiesu@sjtu.edu.cn
Yafei Zhang
yfzhang@sjtu.edu.cn

Specialty section:
This article was submitted to Functional Ceramics, a section of the journal Frontiers in Materials

Received: 24 May 2019
Accepted: 29 July 2019
Published: 20 August 2019

Citation:
Zou C, Hu J, Su Y, Shao F, Tao Z, Huo T, Zhou Z, Hu N, Yang Z, Kong ES-W and Zhang Y (2019) Three-Dimensional Fe_3O_4@Reduced Graphene Oxide Heterojunctions for High-Performance Room-Temperature NO_2 Sensors. Front. Mater. 6:195. doi: 10.3389/fmats.2019.00195

Metal oxide/reduced graphene oxide (RGO) heterojunctions have been widely used to fabricate room-temperature gas sensors due to large specific surface areas of RGO nanosheets and enhanced carrier separation efficiency at the interface. However, the sheet stacking of RGO nanosheets limits the full utilization of metal oxide/RGO heterojunctions. Herein, we demonstrate a high-performance room-temperature NO_2 gas sensor based on 3D Fe_3O_4@RGO p-n heterojunctions with a core-shell structure, which were synthesized by self-assembly method and further reduction. The effects of different Fe_3O_4/RGO ratios and the relative humidity on the sensing performances have been investigated. The experimental results suggest that the 3D Fe_3O_4@RGO sensor exhibits a good selectivity and high sensitivity of 183.1% for 50 ppm NO_2, which is about 8.17 times higher than that of the pure 2D RGO sensor. When exposed to 50 ppb of NO_2, the response value still reaches 17.8%. This enhanced sensing performance is mainly ascribed to the formed heterojunctions and the larger surface area of RGO nanosheets. This 2D to 3D heterostructure strategy provides a general route to fabricating ultrahigh-performance room-temperature RGO-based gas sensors.

Keywords: Fe_3O_4@RGO heterojuntions, NO_2 sensor, electrostatic self-assembly method, heterostructures, three-dimensional core-shell structure

INTRODUCTION

Toxic gases in the environment pose a severe threat to human health, which has drawn increasing attention in the past few years. Therefore, the detection of toxic gases has become increasingly important (Tyagi et al., 2017; Zhang et al., 2018; Wang et al., 2019a,b). Among common toxic gases, nitrogen dioxide (NO_2) is a corrosive common toxic gas with physiological irritants, which mainly derives from automobile exhaust (Wetchakun et al., 2011). NO_2 is an important factor of the formation of photochemical smog, and it also causes respiratory injury and lung damage to the human body (Kim et al., 2013).

So far, multiple sensors have been presented to monitor NO_2 gas (Patil et al., 2016), but the majority of them require operating at high temperatures, have poor sensitivity and contain harmful components. Hence, developing good-performance room-temperature gas sensors based on environmentally friendly materials to detect NO_2 is for both human health and environmental protection. Recently, reduced graphene oxide (RGO) has attracted increasing attention in the field of gas sensors due to its regulable functional groups, extremely large specific surface area and good room-temperature conductivity, and it has been used as sensitive materials to detect NO_2 at room temperature (Li et al., 2011; Huang et al., 2017a; Hu et al., 2017).

However, 2D RGO generally suffers from agglomeration and overlap during the reduction of GO (Compton and Nguyen, 2010), which may result in a poor sensing performance and long-term response/recovery time under ambient conditions. Recently, more attention has been paid to the 3D RGO (Huang et al., 2017b; Wu et al., 2017). Compared with the traditional 2D RGO, 3D RGO has larger surface areas, which can provide more active sites for adsorbing gas molecules and enhance the sensing performance (Wu et al., 2016).

One the other hand, the sensing performances of pure RGO nanosheets are still suppressed due to the recombination of charged carriers in the RGO channel (Hu et al., 2013; Lipatov et al., 2013). It has been proven that the formation of the heterostructures between RGO and metal oxide semiconductors can accelerate the charge separation at the interface and the transportation process, improving effectively the sensing performance (Zhang et al., 2014; Xia et al., 2016). Moreover, the combination of RGO with metal oxide semiconductors results in a synergistic effect on enhancing the sensing properties of the gas sensors. For example, Zhang et al. (2017) fabricated CuO/rGO isotype heterojunction by a layer-by-layer self-assembly method, which is competent in sub-ppb-level CO gas detection. Wan et al. (2015) synthesized hierarchical $In(OH)_3$ modified graphene p-n heterojunction *via* a microwave-assisted hydrothermal method, which showed enhanced NO_2 sensing performances and excellent selectivity. Song et al. (2016) prepared SnO_2/rGO nanocomposites by a one-step colloidal synthesis strategy and reported accelerative electron transfer across SnO_2/RGO interfaces, which contributed to ultrasensitive H_2S gas detection. Among these types of metal oxide/RGO heterojunctions, the 2D heterostructures not only limit the number of adsorption sites for gas molecules but also reduce the interface area between metal oxide and RGO nanosheets, limiting the maximization of the sensing performance.

In this work, a high-performance room-temperature NO_2 gas sensor has been demonstrated using unique 3D Fe_3O_4@RGO core-shell heterostructures, which were synthesized by a self-assembly method and further reduced by ascorbic acid. The effect of different Fe_3O_4/RGO ratios and the relative humidity on the sensing performances have been investigated. The experimental results show that the 3D Fe_3O_4@RGO sensor exhibits more prominent sensitivity and selectivity than that of pure RGO, which demonstrates tremendous potential for practical application.

EXPERIMENTAL

Preparation of Modified Fe_3O_4 Nanospheres

The Fe_3O_4 nanospheres were synthesized by a hydrothermal method, which has been reported elsewhere (Deng et al., 2005). The as-synthesized Fe_3O_4 nanospheres were collected and washed by ethanol and water, and then dried at room temperature for further modification. The modification was conducted by adding aminopropyltriethoxysilane (APTES) into the Fe_3O_4 suspension (Ebrahiminezhad et al., 2013). In a typical procedure, the as-obtained Fe_3O_4 nanospheres (100 mg) were dissolved in a mixed solution of 15 ml of distilled water and 15 ml of ethanol, followed by the addition of 1 ml of APTES. After stirring for 6 h at an oil bath temperature of 40°C, the as-obtained modified Fe_3O_4 nanospheres were precipitated magnetically and washed with water and ethanol iteratively to remove redundant APTES.

Preparation of 3D Fe_3O_4@GO Heterojunctions

Since GO itself is negatively charged and the APTES-modified Fe_3O_4 nanospheres are positively charged, the 3D Fe_3O_4@GO heterojunctions with core-shell structure were synthesized by an electrostatic self-assembly method. Firstly, the as-obtained APTES-modified Fe_3O_4 nanospheres were dispersed in ethanol (10 ml), followed by the addition of 3, 6, 10 and 30 ml of GO suspension (1 mg mL^{-1}), respectively. The mixture was stirred at room temperature for 12 h and the products were collected and washed with ethanol and water repeatedly for later use. The as-obtained products with different mass ratios were denoted as 3wt%-Fe_3O_4@GO, 6wt%-Fe_3O_4@GO, 10wt%-Fe_3O_4@GO, and 30wt%-Fe_3O_4@GO, respectively.

Fabrication of Fe_3O_4@RGO Sensors

Firstly, 2 μL of 3D Fe_3O_4@GO (10 mg/mL) with different mass ratios were dropped onto the interdigital electrodes to obtain a sensing layer, respectively. Afterwards, the electrodes were soaked in 20 mL of 2.5 mg/mL ascorbic acid, to which an appropriate amount of aqueous ammonia was added to make the solution pH≥7. The reduction reaction lasted 6 h in an oil bath at 60°C and was then washed with water and ethanol. The as-obtained devices were denoted as 3wt%-Fe_3O_4@RGO, 6wt%-Fe_3O_4@RGO, 10wt%-Fe_3O_4@RGO, and 30wt%-Fe_3O_4@RGO, respectively. For comparison, bare RGO without Fe_3O_4 was prepared by the same reduction process.

Characterization

The morphologies of samples were characterized by a transmission electron microscopy (TEM, Tecnai-G20 of FEI, USA) operating at 200 kV and a field-emission scanning electron microscope (SEM, Ultra 55 of Carl Zeiss, Germany) operating at 5 kV. X-ray diffraction (XRD) tests were used to

characterize the crystallographic structure of the as-synthesized samples at a diffraction angle ranging from 5 to 80° and a scan speed of 3°/min using Bruker D8 ADVANCE (Germany, Cu Kα, λ = 0.154184 nm) X-ray diffractometer. The thermal stability of the samples was measured by a thermogravimetric analyzer (Pyris 1, Perkin-Elmer, USA) under flowing air and with a heating rate of 5°C/min (from 50 to 800°C). Raman spectra were recorded using an inVia Reflex confocal Raman microscope (RENISHAW, England) with a laser wavelength of 633 nm. The X-ray photoelectron spectra (XPS) analysis was acquired using an Escalab 250Xi (Thermo Fisher Scientific) spectrometer with a monochromatic source (Al Kα). The specific surface area was determined by Brunauer-Emmett-Teller (BET) measurement (Micromeritics Tristar 3020, USA).

Gas Sensing Measurement

For the sensing measurement, the sensing device was fixed on a closed test chamber, followed by connection with a dynamic gas mixer system for signal collecting. A semiconductor parameter tester (Agilent 4156C) was used to monitor the sensing signal at a test voltage of 0.5 V. As reported in our previous work (Hu et al., 2017), a homemade gas mixer system was used to obtain different concentrations of NO_2 gas, which diluted NO_2 standard gas (5,000 ppm) with high-purity dry air. In addition, before testing or during the period of the recovery phase, high-purity dry air was also used for the balance of the adsorption-desorption on the sensing materials surface. Mass flow controllers (MFC, Beijing Qixing Co., Ltd, China) were used to adjust the flow ratio of gases. The NO_2 and the air gas mixtures were imported into the testing chamber at a rate of 0.1 L min^{-1} for sensing performance measurement. All the tests were performed at room temperature. The sensing response value (S) is valued by the electrical current change at a test voltage of 0.5 V, which is defined according to the following equation:

$$S\,(\%) = 100\% \times \frac{\Delta I}{I_a} = 100\% \times \frac{I_g - I_a}{I_a} \quad (1)$$

where I_a is the initial electrical current of the sensing device in air, and I_g is the electrical current of the sensing device in the gas mixtures of NO_2 and air. Response time and recovery time of the gas sensor are defined as the time which was required to achieve 90% of the total electrical current change.

RESULTS AND DISCUSSION

Microstructure Characterizations

The morphologies of the as-prepared materials were observed by SEM and TEM. **Figure 1a** shows the SEM image of Fe_3O_4 with a relatively uniform spherical structure. **Figures 1b–f** displays the morphologies of as-prepared Fe_3O_4@GO with different mass ratios. It can be clearly observed that GO is coated on the Fe_3O_4 nanospheres, indicating successful preparation of the 3D core-shell structure of GO by the electrostatic self-assembly method. As the mass ratio of GO in Fe_3O_4@GO increases, the coated GO becomes thicker and more numerous. However, when the GO mass ratio reaches as high as 30%, GO is stacked on the Fe_3O_4 nanospheres due to the excessive amount of GO, as exhibited in **Figure 1f**. Therefore, a suitable material mass ratio is beneficial to the formation of 3D core-shell structure of Fe_3O_4@GO. Among them, 10wt%-Fe_3O_4@GO exhibits a uniform coverage of GO on Fe_3O_4 nanospheres, as shown in **Figure 1d**. **Figure 1e** shows an enlarged view of the green region in **Figure 1d**, which demonstrates the uniformity of GO coating and the successful fabrication of 3D core-shell structures more intuitively.

Figure 2 shows the SEM and TEM images of 10wt%-Fe_3O_4@RGO heterojunctions. The morphology of the RGO wrapped on the Fe_3O_4 nanospheres was maintained after the reduction process by ascorbic acid, indicating that this reduction method did not destroy the 3D core-shell structures of Fe_3O_4@RGO, as shown in **Figure 2a** (SEM image). TEM images of Fe_3O_4@RGO are shown in **Figures 2b–d**. The RGO nanosheets cladded on the Fe_3O_4 nanospheres cannot be observed so expressly because of the lack of electron contrast. However, the RGO junctions between Fe_3O_4 nanospheres demonstrate the electrostatic self-assembly contact between RGO nanosheets and Fe_3O_4 nanospheres. An enlarged view of **Figure 2b** is displayed in **Figure 2c**, where it can be clearly seen that RGO nanosheets are tightly attached to the surface of the Fe_3O_4 nanospheres. The 0.48 nm lattice fringe spacing in **Figure 2d** (HRTEM image) corresponds to the (111) crystal planes of Fe_3O_4 (Lu et al., 2009a).

XRD patterns and TGA curves of the as-prepared Fe_3O_4@RGO heterojunctions are illustrated in **Figure 3** to confirm its crystallographic information and chemical composition. For XRD patterns in **Figure 3A**, the diffraction peaks of Fe_3O_4 are observed at 30.1, 35.4, 43.0, 57.0, and 62.6° which are assigned to the (220), (311), (400), (511), and (440) planes of Fe_3O_4 (JCPDS card 19-0629), respectively (Sun et al., 2009). The main XRD characteristic peaks for Fe_3O_4@GO and Fe_3O_4@RGO can be attributed to the inverse spinel structure of Fe_3O_4 (JCPDS card 19-0629). This is consistent with the results of TEM. However, the characteristic peaks of GO and RGO disappear in the patterns of the Fe_3O_4@GO and Fe_3O_4@RGO due to the relatively low contents.

TGA analysis was carried out to confirm the contents of RGO in the as-prepared Fe_3O_4@RGO heterojunctions, as exhibited in **Figure 3B**. For the Fe_3O_4 samples, the weight change can be segmented into three steps. The first stage of weight loss is occurring under 150°C, which is mainly ascribed to desorption of bond water on the surface of material. Subsequently, there is the formation of γ-Fe_2O_3 due to the oxidation process of Fe_3O_4 from 150 to 300°C, resulting in an increase in weight (Cao et al., 2008). Finally, the weight loss takes place again from 350–600°C, which can be ascribed to the phase conversion from γ-Fe_2O_3 to α-Fe_2O_3 (El Mendili et al., 2012). Notably, for the Fe_3O_4@RGO heterojunctions, the weight loss continues from about 300°C to about 450°C, which is attributed to the decomposition of RGO (Stankovich et al., 2007). Obviously, during the decomposition of RGO, there is more and more weight loss with the increase of the contents of RGO, indicating the successful preparation of different mass ratio of the Fe_3O_4@RGO. However, after the reduction process of GO, the weight of the RGO might be

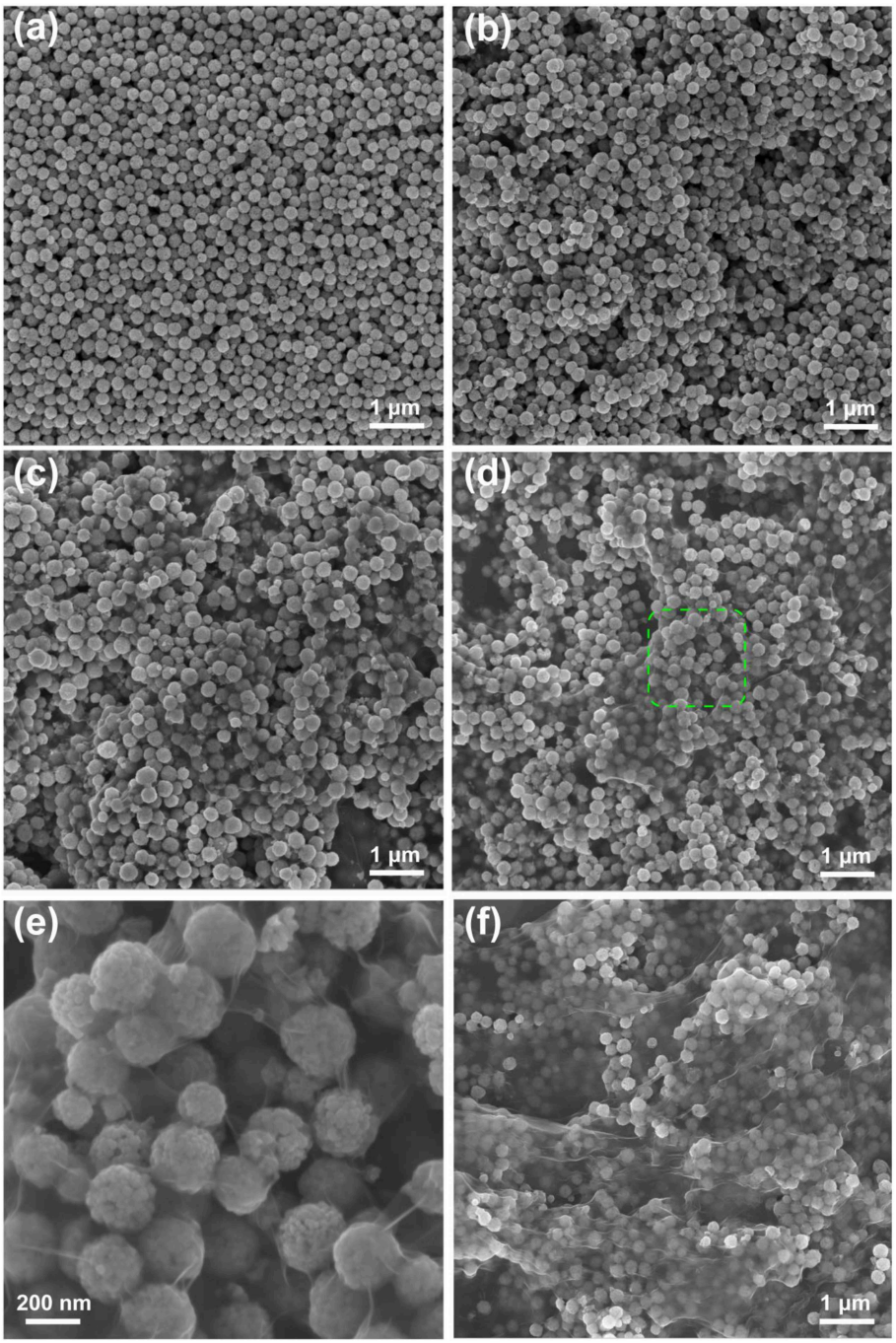

FIGURE 1 | The SEM images of **(a)** pure Fe_3O_4, **(b)** 3wt%-Fe_3O_4@GO, **(c)** 6wt%-Fe_3O_4@GO, **(d)** 10wt%-Fe_3O_4@GO, **(e)** enlarged view of 10wt%-Fe_3O_4@GO, **(f)** 30wt%-Fe_3O_4@GO.

changed, resulting in a change in the mass ratio. For instance, the mass ratio of RGO in the 10wt%-Fe_3O_4@RGO is ∼5.9% rather than 10%.

To characterize the surface areas of the as-prepared RGO and 10wt%-Fe_3O_4@RGO, nitrogen adsorption-desorption isotherm analysis was conducted (**Figure S1**). The BET surface area (34.5328 m^2/g) of 10wt%-Fe_3O_4@RGO is larger than that of the RGO (2.7045 m^2/g). The bare RGO has undergone heavy agglomeration in a large-scale preparation, resulting in its low BET surface area. In consideration of 10% content GO in Fe_3O_4@GO samples, the surface area is remarkably enhanced by forming 3D core-shell structures.

Raman spectra research was carried out to analyze graphene and its derivatives. **Figure 4A** shows the Raman spectra of

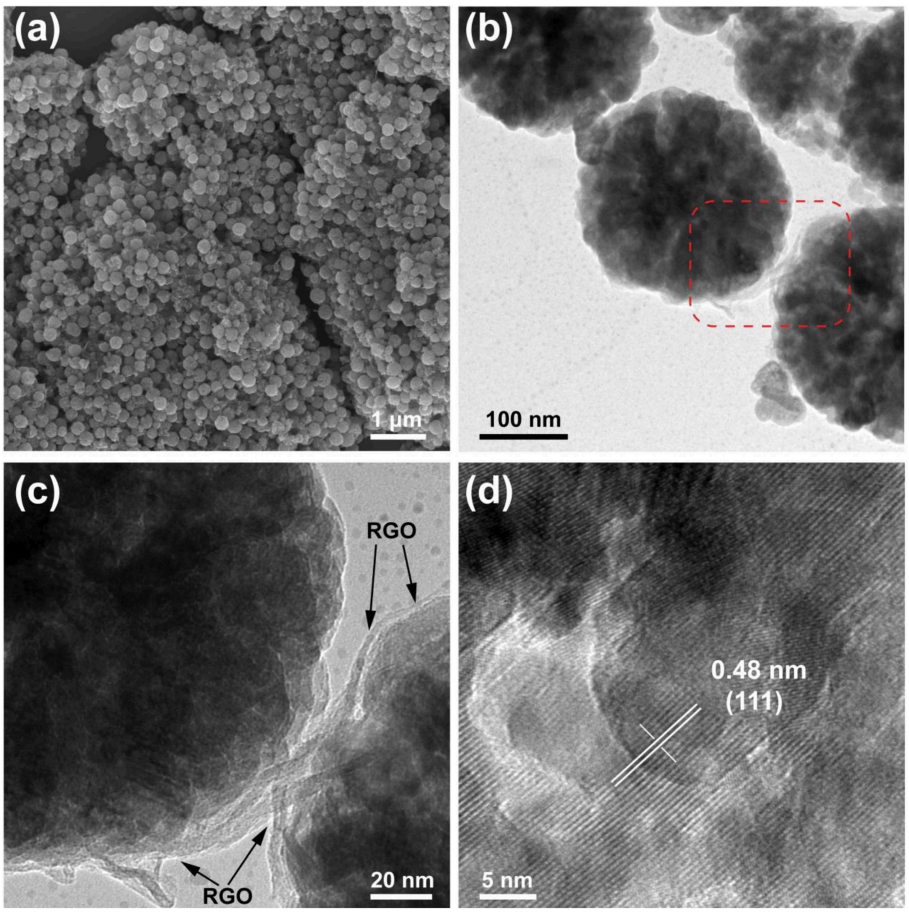

FIGURE 2 | The SEM images of **(a)** 10wt%-Fe_3O_4@RGO,typical TEM images of **(b)** 10wt%-Fe_3O_4@RGO, **(c)** enlarged view of 10wt%-Fe_3O_4@RGO and **(d)** HRTEM image of 10wt%-Fe_3O_4@RGO.

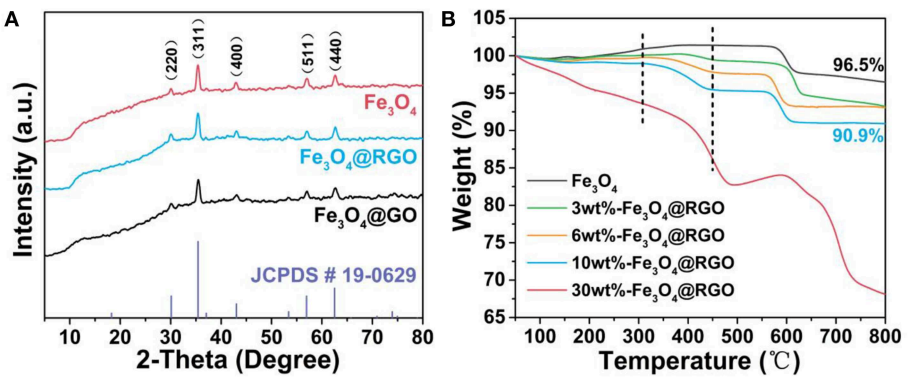

FIGURE 3 | (A) XRD patterns of pure Fe_3O_4, 10wt%-Fe_3O_4@GO and 10wt%-Fe_3O_4@RGO, and the standard patterns of Fe_3O_4 phase (JCPDS card 19-0629). **(B)** TGA curves of pure Fe_3O_4 and the different material mass ratio of the Fe_3O_4@RGO.

Fe_3O_4@GO, Fe_3O_4@RGO and RGO. The D and G peaks of graphene are clearly observed in all curves. The peaks at about 660 cm^{-1} of Fe_3O_4@GO and Fe_3O_4@RGO can be attributed to the A_{1g} mode of Fe_3O_4 (Sun et al., 2009). The appearance of the characteristic peaks of RGO and Fe_3O_4 indicates the successful modification of RGO on Fe_3O_4. The D band and G band of Fe_3O_4@RGO locate at 1324.9 cm^{-1} and 1595.9 cm^{-1}, respectively, while that of RGO locates at 1327.1 cm^{-1} and 1601.1

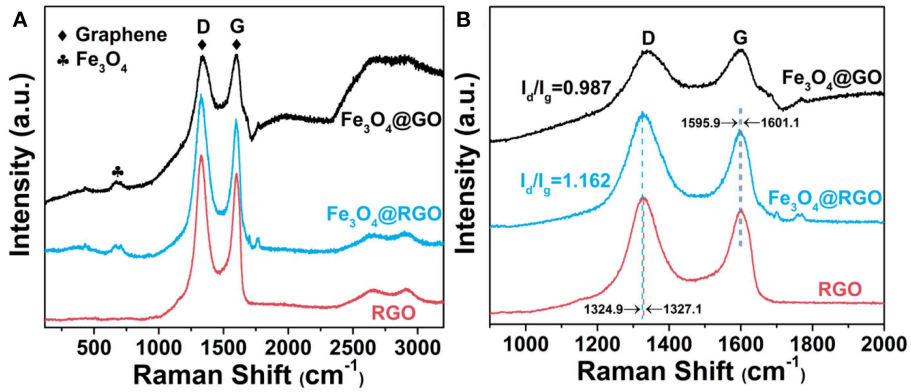

FIGURE 4 | (A) Raman spectra and **(B)** enlarged Raman spectra of RGO, 10wt%-Fe_3O_4@GO and 10wt%-Fe_3O_4@RGO.

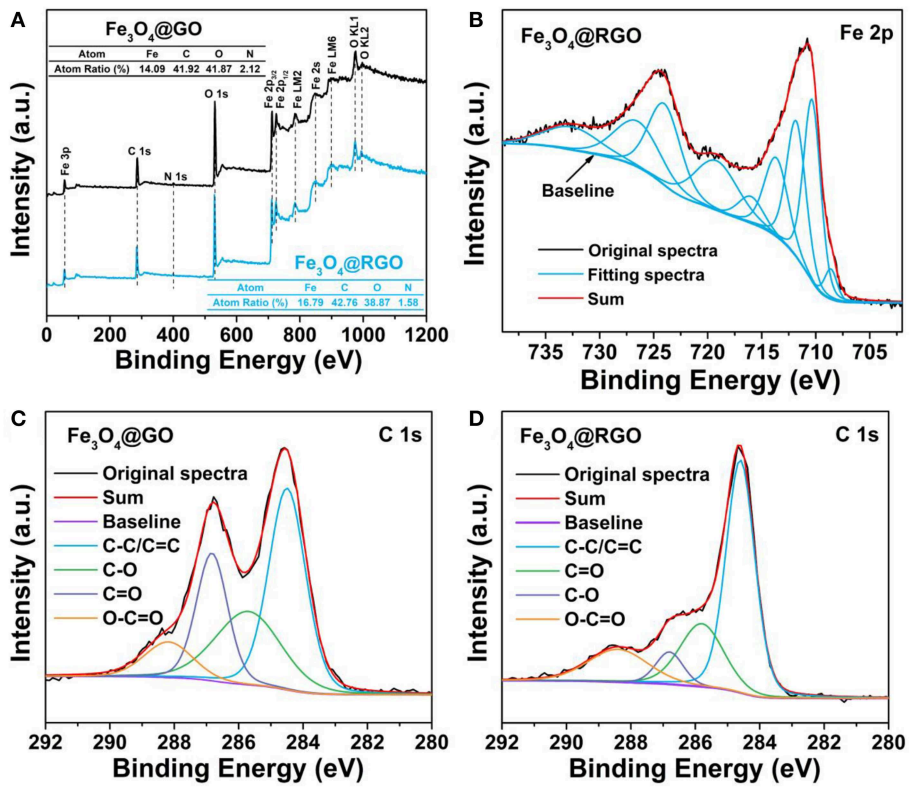

FIGURE 5 | (A) XPS survey spectra of 10wt%-Fe_3O_4@GO and 10wt%-Fe_3O_4@RGO. **(B)** High resolution XPS spectrum of Fe 2p of 10wt%-Fe_3O_4@RGO. C 1s deconvoluted spectra of **(C)** 10wt%-Fe_3O_4@GO and **(D)** 10wt%-Fe_3O_4@RGO.

cm^{-1}, respectively (Liu et al., 2017), as shown in **Figure 4B**. The downshift of several wavenumbers indicates electron transfer from Fe_3O_4 nanospheres to 3D RGO, as illustrated in the literature (Rao et al., 2014; Hu et al., 2018b). This also confirms the formation of heterostructures between RGO and Fe_3O_4 in Fe_3O_4@RGO. In addition, the I_D/I_G value of Fe_3O_4@RGO (1.162) is higher than that of Fe_3O_4@GO (0.987), implying a decrease in the average size of the sp^2 domain and an increase in domain numbers during the reduction process (Huang et al., 2017a). This in turn confirms the formation of Fe_3O_4@RGO by the reduction process of Fe_3O_4@GO.

The surface structure of Fe_3O_4@RGO heterojunctions was further investigated by XPS technique. As shown in **Figure 5A**, the survey spectra identify the presence of Fe, C, N, and O elements in the Fe_3O_4@GO and Fe_3O_4@RGO. The existence of N 1s can be ascribed to the residual APTES left on the

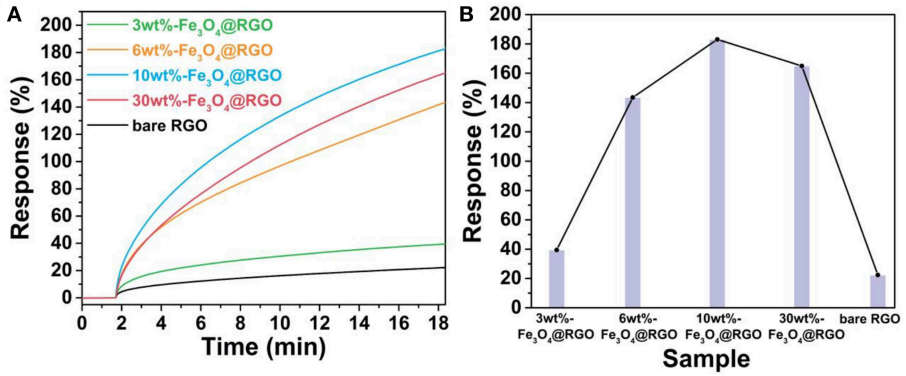

FIGURE 6 | (A) Response curves and **(B)** comparison of response values of RGO and the different material mass ratio of the Fe_3O_4@RGO toward 50 ppm NO_2.

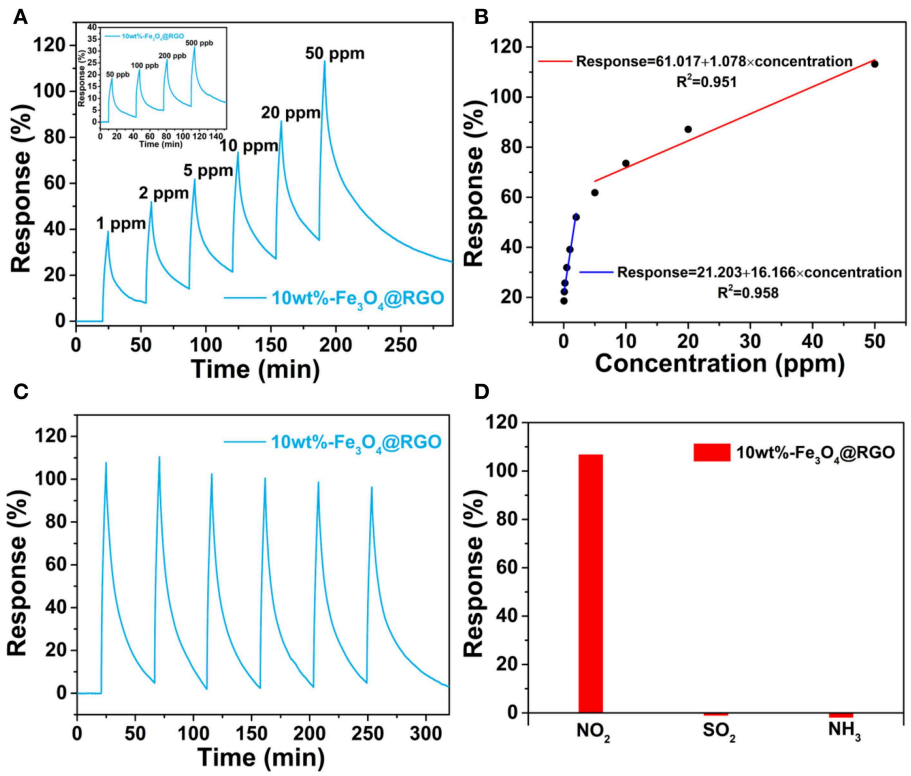

FIGURE 7 | (A) Dynamic curves of 10wt%-Fe_3O_4@RGO to different NO_2 concentrations. **(B)** Response variation of the 10wt%-Fe_3O_4@RGO sensor as a function of NO_2 concentration. **(C)** Six successive sensing cycles of 10wt%-Fe_3O_4@RGO to 50 ppm NO_2. **(D)** Selectivity of the as-fabricated sensor upon exposure to 50 ppm NO_2, SO_2 and NH_3 gas.

surface of Fe_3O_4 nanospheres. **Figure 5B** shows the Fe core level (Fe 2p) spectra of Fe_3O_4@RGO. The peaks at 708.6 eV and 716 eV correspond to the main peak and satellite peak of Fe^{2+} $2p_{3/2}$, respectively. The peaks at around 710.6 eV can be ascribed to the main peak of Fe^{3+} $2p_{3/2}$, while the peaks at around 724 eV are attributed to the main peak of Fe^{3+} $2p_{1/2}$. Additionally, the satellite peak of Fe^{3+} $2p_{3/2}$ appears at ~719 eV. All these results indicate the formation of Fe_3O_4 (Fujii et al., 1999). **Figures 5C,D** show the C 1s spectra of Fe_3O_4@GO and Fe_3O_4@RGO, these peaks can be grouped into four components: C-C/C=C (~284.6 eV), C-O (~285.8 eV), C=O (~286.8 eV), O-C=O (~288.4 eV) (Zhang et al., 2010; Zheng et al., 2018). It is apparent that the peak of the C=O tremendously decreases and that of C-C/C=C correspondingly increases after the reduction process, which indicates the successful reduction of the GO on the surface of Fe_3O_4 nanospheres.

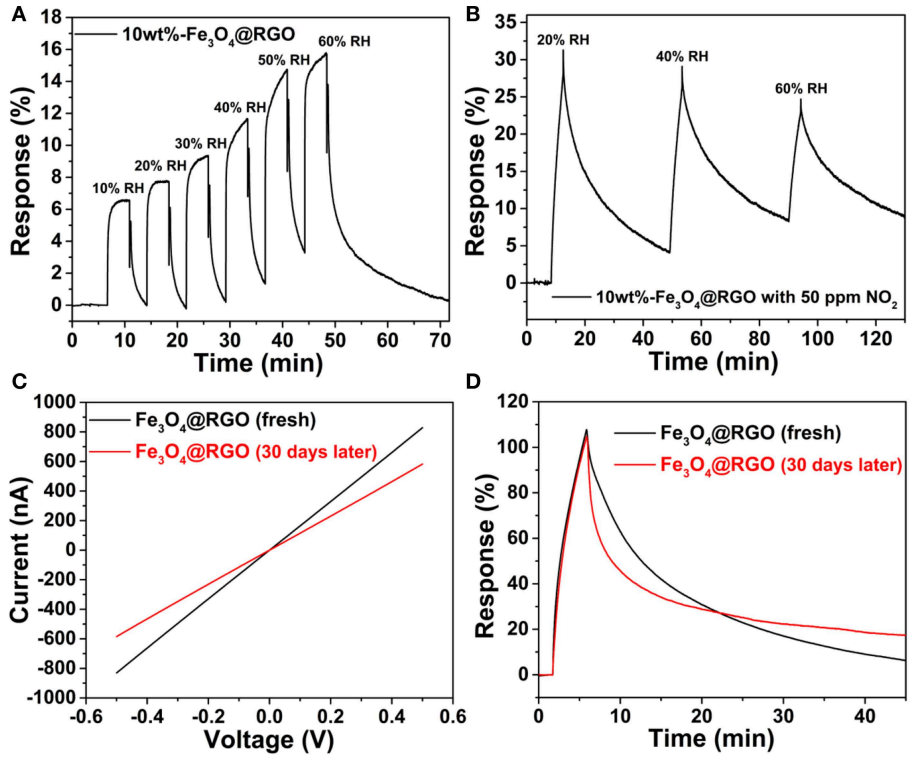

FIGURE 8 | (A) Dynamic curves of 10wt%-Fe_3O_4@RGO to different relative humidity. **(B)** Response curve for 10wt%-Fe_3O_4@RGO sensor at different relative humidity for 50 ppm NO_2. **(C)** I-V curves and **(D)** response-recovery curves toward 50 ppm NO_2 of the fresh 10wt%-Fe_3O_4@RGO sensor and the sensor after 30 days of storage.

Gas Sensing Properties

The sensing performance of the Fe_3O_4@RGO heterojunctions was firstly investigated by monitoring their response to NO_2 at room temperature. **Figure 6A** shows the single response curves of the devices toward 50 ppm NO_2, and **Figure S2** shows the resistance change of 10wt%-Fe_3O_4@RGO and pure RGO in this response process. When exposed to NO_2, the continuous increase of current means that the resistance of the devices continues to decrease, indicating that RGO and Fe_3O_4@RGO exhibit the p-type semiconductor properties (Lu et al., 2009b). The response value in 1000 s for bare RGO, 3wt%-Fe_3O_4@RGO, 6wt%-Fe_3O_4@RGO, 10wt%-Fe_3O_4@RGO, and 30wt%-Fe_3O_4@RGO toward 50 ppm NO_2 were 22.4, 39.5, 143.5, 183.1, and 165.1%, respectively. The greatly higher performance of Fe_3O_4@RGO heterojunctions than bare RGO could be ascribed to the optimized structures and the formed heterostructures. As shown in **Figure 6B**, the effect of the amount of RGO on the sensing performances was evaluated. As the amount of RGO increases, the response values increase initially and then decrease. 10wt%-Fe_3O_4@RGO possesses of the highest response value of 183.1%, which is 8.17 times higher than that of bare RGO. In consideration of the dramatic increases of the electrical current of the as-fabricated sensors in time of the initiatory detection period, an appropriate response time of 250 s was defined for the following tests.

Figure 7A shows the response-recovery curves of the 10wt%-Fe_3O_4@RGO upon successive exposure to NO_2 concentrations ranging from 50 to 500 ppb and from 1 to 50 ppm at room temperature, respectively. It can be seen that the as-fabricated sensor exhibits a prominent response behavior over a wide range of NO_2 concentrations. For example, the response value can still reach 17.8% when the as-fabricated sensor is exposed to 50 ppb of NO_2, which indicates that the 10wt%-Fe_3O_4@RGO sensor has an excellent detecting ability toward NO_2 with low concentration. It is interesting that the response value is linearly proportional to the concentration of NO_2 in two stages, with the first stage being in the range of lower than 2 ppm and the other stage being from 5 to 50 ppm (**Figure 7B**). It is attributed to partial saturation at higher NO_2 concentration, which causes the conductance response to diverge from linearity (Hu et al., 2017). The detection ability at lower concentration and the piecewise linear relationship between response values and NO_2 concentrations both imply that the 10wt%-Fe_3O_4@RGO sensor is beneficial for practical application.

To further evaluate the gas-sensing performance of 10wt%-Fe_3O_4@RGO heterojunctions, the curve of six sequential cycles of the as-fabricated sensor toward 50 ppm NO_2 are recorded in **Figure 7C**, demonstrating an excellent reproducibility and cycle stability. Besides high sensitivity and good stability, gas sensors require selectivity for practical applications. From **Figure 7D**,

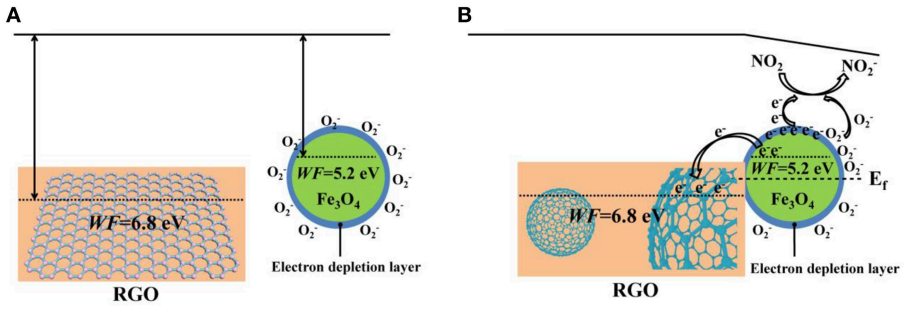

SCHEME 1 | (A) The schematic energy band structure of RGO and Fe_3O_4@RGO before forming the heterojunction state. **(B)** Schematic illustration of band bending, electron transfer process and NO_2-sensing mechanism of the Fe_3O_4@RGO after constructing the heterostructure.

it can be found that the 10wt%-Fe_3O_4@RGO sensor exhibits a prominent selectivity to NO_2 gas among NH_3, SO_2, and NO_2. When exposing the as-fabricated sensor to these gases with the same concentration (50 ppm) for 250 s, the 10wt%-Fe_3O_4@RGO sensor performs a 107% response to NO_2, which is ∼82 and ∼51 times as much as the response to SO_2 and NH_3, respectively.

As a crucial factor of sensor properties, the influence of relative humidity (RH) is very important. In this work, the sensor device was exposed to varying levels of humidity, and the influence of humidity on sensing properties was investigated. **Figure 8A** shows the response-recovery curves of the 10wt%-Fe_3O_4@RGO sensor with different RHs (from 10 to 60% RH) at room temperature. The results suggest that the as-fabricated sensor shows a fast response-recovery to humidity. However, the response value is still low even if the RH reached 60%. Since the NO_2 tests were carried out around 40% RH external environment, the as-fabricated sensor was repeatedly exposed to 40% RH. As shown in **Figure S3**, the 10wt%-Fe_3O_4@RGO sensor exhibited a stable response and fast recovery after six successive cycles, which indicates an excellent repeatability and cycle stability. Besides, rapid recovery means that the adsorbed water molecules can quickly desorb on the surface of the sensing materials. Hence, it can be concluded that humidity in the external environment has an acceptable impact on detecting NO_2. That will be favorable for practical tests and providing credible signals. In addition, the effects of different RHs on NO_2 detection (50 ppm) of the 10wt%-Fe_3O_4@RGO sensor at room temperature have also been studied, as shown in **Figure 8B**. The NO_2 detection performance of the 10wt%-Fe_3O_4@RGO sensor gets worse as the RHs increases from 20 to 60%, which can be attributed to the consumption of NO_2 molecules due to the reactions between NO_2 and water vapor in moist air (Hu et al., 2018a). As the humidity increases, the sensing film is covered by water molecules, which decreases the sensing performance.

Long-term stability is also an important parameter in gas sensing. For the purpose of evaluating the stability of the Fe_3O_4@RGO gas sensor, the sensing device had been stored under ambient conditions for 1 month for testing. The current-voltage (I-V) curves are shown in **Figure 8C**, which demonstrates that the resistance of the sensing device increased from 0.602 to 0.856 MΩ. The sensing test results toward 50 ppm NO_2 are shown in **Figure 8D**. It is noted that the response of the sensor did not decay after 1 month of storage. The only drawback is that the recovery capability became a little bit weaker, which may be ascribed to the effect of absorbed gas molecules in the air on the surface of the sensing material. In a word, the sensor based on Fe_3O_4@RGO exhibits an excellent stability.

Gas Sensing Mechanism

The enhancement of the NO_2 sensing performances in 3D Fe_3O_4@RGO can be interpreted by the following aspects. Firstly, a possible surface electron depletion layer mechanism is used to explain the sensing mechanism, as shown in **Scheme 1**. As we know, Fe_3O_4 is a typical n-type semiconductor (Ai et al., 2010). When exposed to air, oxygen molecules contact the surface of the Fe_3O_4 and capture electrons from the semiconductor, producing chemisorbed oxygen species (O^-, O_2^-) and causing a depletion layer on the surface of the Fe_3O_4 (Wagner et al., 2011; Hu et al., 2018b). Afterwards, when exposed to the oxidizing gases such as NO_2, NO_2 captures electrons from the surface electron depletion layer of the Fe_3O_4 and also reacts with O_2^- to form NO_2^-; the equations are as follows (Hu et al., 2017, 2018b):

$$O_2 + e^- \rightarrow O_2^- \quad (2)$$

$$O_2^- + e^- \rightarrow 2O^- \quad (3)$$

$$NO_2 + e^- \rightarrow NO_2^- \quad (4)$$

$$NO_2 + O_2^- + 2e^- \rightarrow NO_2^- + 2O^- \quad (5)$$

The process leads to a decrease in the number of electrons in the semiconductor (n-type), resulting in a decrease in electrical conductivity. On the contrary, for a p-type semiconductor such as RGO and the as-prepared Fe_3O_4@RGO, since their main carriers are holes rather than electrons, this process leads to an increase in electrical conductivity. When exposed to the reducing gas such as NH_3, the electron of the adsorbed electron-donated NH_3 is transferred to the p-type Fe_3O_4@RGO, which reduces the concentration of hole carriers, resulting in a decreased conductivity of the device (Huang et al., 2017b). The good selectivity for NO_2 gas can be interpreted as follows: As a small-sized polar molecule with lone pair electrons and

high affinity, NO_2 can undergo fierce electron exchange with Fe_3O_4@RGO (Shaik et al., 2016). Hence, it is very easy for NO_2 to capture electrons from p-type Fe_3O_4@RGO. This results in the formation of a large number of holes, which significantly changes the conductance of the device. Additionally, due to the presence of the Fe_3O_4@RGO heterojunctions, NO_2 can adsorb selectively and react easily with the generated oxygen species (Hu et al., 2017).

The gas-sensing response enhancement brought by the 3D Fe_3O_4@RGO core-shell structures can be attributed to the well-known p-n heterojunction effect. According to the previous report, RGO has a work function (WF) of 6.8 eV (Kumar et al., 2013), which contains only carboxyl groups and has an oxygen content of 20%. In this work, it can be seen from the results of XPS that the oxygen content in RGO is approximately 27.8%. The work function of Fe_3O_4 is about 5.2 eV (Fonin et al., 2005), which is lower than that of RGO. When Fe_3O_4 and RGO are in contact with each other, a p-n junction is formed at the interface of Fe_3O_4 and RGO, and electrons are transferred from Fe_3O_4 to RGO until the Fermi level (E_f) reaches equilibrium, forming a built-in electric field (space charge region). When the Fe_3O_4@RGO heterojunctions are exposed to electron-withdrawing NO_2, the electron concentration of Fe_3O_4 is lowered, and a large amount of holes are generated. These holes are rapidly transferred to RGO by the built-in electric field, which further enhances the electrical conductivity of the Fe_3O_4@RGO. It can be summarized that the formed heterojunctions promote the carrier transfer and further enhance the gas sensing properties (Miller et al., 2014; Song et al., 2016). Meanwhile, the high carrier mobility characteristics of RGO provide smooth and fast channels for carrier transport, which facilitates fast response of the sensor (Li et al., 2011; Feng et al., 2013).

In addition to the p-n junction, the 3D core-shell structure also plays a role in boosting the sensing properties of the Fe_3O_4@RGO heterojunctions. The 3D Fe_3O_4@RGO heterostructures prevent agglomeration during the reduction of RGO and can provide more adsorption sites than 2D RGO due to the larger surface area (Song et al., 2016; Huang et al., 2017a). The synergistic effect of Fe_3O_4 and RGO is also one of the reasons for promoting sensing performances. Therefore, these factors work together to have effects on the electrical properties at the interface of the 3D Fe_3O_4@RGO heterojunctions, dramatically improving the sensing performance.

CONCLUSION

Unique 3D Fe_3O_4@RGO core-shell heterostructures have been synthesized by self-assembly and further reduction, which can be used to fabricate high-performance room-temperature NO_2 gas sensors. We have investigated the effect of different Fe_3O_4/RGO ratios and relative humidity on the sensing performances. The sensor based on 3D Fe_3O_4@RGO p-n heterojunctions exhibits a high sensitivity of 183.1% for 50 ppm NO_2 at room temperature, which is about 8.17 times higher than that of the pure 2D RGO sensor. The as-formed heterojunctions and the larger surface area of RGO nanosheets with 3D structures are considered to play a key role in enhancing the sensing performance. We believe that this 2D to 3D core-shell heterostructures strategy enables us to enhance the sensing performance room-temperature RGO-based gas sensors.

DATA AVAILABILITY

All datasets generated for this study are included in the manuscript/**Supplementary Files**.

AUTHOR CONTRIBUTIONS

CZ and YS contributed to all the experimental work. JH and FS analyzed the data. EK and NH contributed to the synthesis of Fe_3O_4@GO. ZZ and ZT contributed to the synthesis of Fe_3O_4@RGO. TH and ZY contributed to the characterization of device performance. YS and YZ designed and directed the study. CZ and YS wrote the manuscript. All authors reviewed the paper.

FUNDING

This work was supported by National Natural Science Foundation of China (No. 51402190) and Shanghai Natural Science Foundation (No. 19ZR1426900). The authors also acknowledge the analysis support from the Center for Advanced Electronic Materials and Devices of Shanghai Jiao Tong University.

ACKNOWLEDGMENTS

We also acknowledge the analysis support from the Instrumental Analysis Center of Shanghai Jiao Tong University and the Center for Advanced Electronic Materials and Devices of Shanghai Jiao Tong University.

SUPPLEMENTARY MATERIAL

The Supplementary Material for this article can be found online at: https://www.frontiersin.org/articles/10.3389/fmats.2019.00195/full#supplementary-material

REFERENCES

Ai, Z., Deng, K., Wan, Q., Zhang, L., and Lee, S. (2010). Facile microwave-assisted synthesis and magnetic and gas sensing properties of Fe_3O_4 nanoroses. *J. Phy. Chem. C* 114, 6237–6242. doi: 10.1021/jp910514f

Cao, S.-W., Zhu, Y. J., Ma, M.-Y., Li, L., and Zhang, L. (2008). Hierarchically nanostructured magnetic hollow spheres of Fe_3O_4 and γ-Fe_2O_3: preparation and potential application in drug delivery. *J. Phy. Chem. C.* 112, 1851–1856. doi: 10.1021/jp077468+

Compton, O. C., and Nguyen, S. T. (2010). Graphene oxide, highly reduced graphene oxide, and graphene: versatile building blocks for carbon-based materials. *Small* 6, 711–723. doi: 10.1002/smll.200901934

Deng, H., Li, X., Peng, Q., Wang, X., Chen, J., and Li, Y. (2005). Monodisperse magnetic single-crystal ferrite microspheres. *Angew. Chem.* 117, 2842–2845. doi: 10.1002/ange.200462551

Ebrahiminezhad, A., Ghasemi, Y., Rasoul-Amini, S., Barar, J., and Davaran, S. (2013). Preparation of novel magnetic fluorescent nanoparticles using amino acids. *Coll. Surf. B Biointerf.* 102, 534–539. doi: 10.1016/j.colsurfb.2012.08.046

El Mendili, Y., Bardeau, J.-F., Randrianantoandro, N., Grasset, F., and Greneche, J.-M. (2012). Insights into the mechanism related to the phase transition from γ-Fe_2O_3 to α-Fe_2O_3 nanoparticles induced by thermal treatment and laser irradiation. *J. Phy. Chem. C* 116, 23785–23792. doi: 10.1021/jp308418x

Feng, H., Cheng, R., Zhao, X., Duan, X., and Li, J. (2013). A low-temperature method to produce highly reduced graphene oxide. *Nat. Commun.* 4:1539. doi: 10.1038/ncomms2848

Fonin, M., Pentcheva, R., Dedkov, Y. S., Sperlich, M., Vyalikh, D. V., Scheffler, M., et al. (2005). Surface electronic structure of the Fe_3O_4 (100): Evidence of a half-metal to metal transition. *Phys. Rev. B* 72:104436. doi: 10.1103/PhysRevB.72.104436

Fujii, T., de Groot, F. M. F., Sawatzky, G. A., Voogt, F. C., Hibma, T., and Okada, K. (1999). *In situ* XPS analysis of various iron oxide films grown by NO_2-assisted molecular-beam epitaxy, *Phy. Rev. B* 59, 3195–3202. doi: 10.1103/PhysRevB.59.3195

Hu, J., Zou, C., Su, Y., Li, M., Han, Y., Kong, E. S.-W., et al. (2018a). An ultrasensitive NO_2 gas sensor based on a hierarchical Cu_2O/CuO mesocrystal nanoflower. *J. Mater. Chem. A* 6, 17120–17131. doi: 10.1039/C8TA04404J

Hu, J., Zou, C., Su, Y., Li, M., Hu, N., Ni, H., et al. (2017). Enhanced NO_2 sensing performance of reduced graphene oxide by *in situ* anchoring carbon dots. *J. Mater. Chem. C* 5, 6862–6871. doi: 10.1039/C7TC01208J

Hu, J., Zou, C., Su, Y., Li, M., Ye, X., Cai, B., et al. (2018b). Light-assisted recovery for a highly-sensitive NO_2 sensor based on RGO-CeO_2 hybrids. *Sens Actuat. B Chem.* 270, 119–129. doi: 10.1016/j.snb.2018.05.027

Hu, N., Yang, Z., Wang, Y., Zhang, L., Wang, Y., Huang, X., et al. (2013). Ultrafast and sensitive room temperature NH_3 gas sensors based on chemically reduced graphene oxide, *Nanotechnology* 25:025502. doi: 10.1088/0957-4484/25/2/025502

Huang, D., Li, X., Wang, S., He, G., Jiang, W., Hu, J., et al. (2017a). Three-dimensional chemically reduced graphene oxide templated by silica spheres for ammonia sensing. *Sens. Actuat. B Chem.* 252, 956–964. doi: 10.1016/j.snb.2017.05.117

Huang, D., Yang, Z., Li, X., Zhang, L., Hu, J., Su, Y., et al. (2017b). Three-dimensional conductive networks based on stacked SiO_2@graphene frameworks for enhanced gas sensing, *Nanoscale* 9, 109–118. doi: 10.1039/C6NR06465E

Kim, K.-H., Jahan, S. A., and Kabir, E. (2013). A review on human health perspective of air pollution with respect to allergies and asthma. *Environ. Int.* 59, 41–52. doi: 10.1016/j.envint.2013.05.007

Kumar, P. V., Bernardi, M., and Grossman, J. C. (2013). The impact of functionalization on the stability, work function, and photoluminescence of reduced graphene oxide. *ACS Nano* 7, 1638–1645. doi: 10.1021/nn305507p

Li, W., Geng, X., Guo, Y., Rong, J., Gong, Y., Wu, L., et al. (2011). Reduced graphene oxide electrically contacted graphene sensor for highly sensitive nitric oxide detection. *ACS Nano*. 5, 6955–6961. doi: 10.1021/nn201433r

Lipatov, A., Varezhnikov, A., Wilson, P., Sysoev, V., Kolmakov, A., and Sinitskii, A. (2013). Highly selective gas sensor arrays based on thermally reduced graphene oxide. *Nanoscale* 5, 5426–5434. doi: 10.1039/c3nr00747b

Liu, J., Zhao, Y., Z., Li, X., Wang, C., Zeng, Y., Yue, G., et al. (2017). $CuCr_2O_4$@rGO nanocomposites as high-performance cathode catalyst for rechargeable lithium-oxygen batteries. *Nano-Micro Lett.* 10:22. doi: 10.1007/s40820-017-0175-z

Lu, G., Ocola, L. E., and Chen, J. (2009b). Gas detection using low-temperature reduced graphene oxide sheets. *Appl. Phys. Lett.* 94, 083111. doi: 10.1063/1.3086896

Lu, J., Jiao, X., Chen, D., and Li, W. (2009a). Solvothermal synthesis and characterization of Fe_3O_4 and γ-Fe_2O_3 nanoplates. *J. Phy. Chem. C* 113, 4012–4017. doi: 10.1021/jp810583e

Miller, D. R., Akbar, S. A., and Morris, P. A. (2014). Nanoscale metal oxide-based heterojunctions for gas sensing: a review. *Sens. Actuat. B Chem.* 204, 250–272. doi: 10.1016/j.snb.2014.07.074

Patil, V. L., Vanalakar, S. A., Kamble, A. S., Shendage, S. S., Kim, J. H., and Patil, P. S. (2016). Farming of maize-like zinc oxide via a modified SILAR technique as a selective and sensitive nitrogen dioxide gas sensor. *RSC Adv.* 6, 90916–90922. doi: 10.1039/C6RA06346B

Rao, R., Pierce, N., and Dasgupta, A. (2014). On the charge transfer between single-walled carbon nanotubes and graphene. *Appl. Phys. Lett.* 105:073115. doi: 10.1063/1.4893698

Shaik, M., Rao, V. K., Gupta, M., Murthy, K. S. R. C., and Jain, R. (2016). Chemiresistive gas sensor for the sensitive detection of nitrogen dioxide based on nitrogen doped graphene nanosheets. *RSC Adv.* 6, 1527–1534. doi: 10.1039/C5RA21184K

Song, Z., Wei, Z., Wang, B., Luo, Z., Xu, S., Zhang, W., et al. (2016). Sensitive room-temperature H_2S gas sensors employing SnO_2 quantum wire/reduced graphene oxide nanocomposites. *Chem. Mater.* 28, 1205–1212. doi: 10.1021/acs.chemmater.5b04850

Stankovich, S., Dikin, D. A., Piner, R. D., Kohlhaas, K. A., Kleinhammes, A., Jia, Y., et al. (2007). Synthesis of graphene-based nanosheets via chemical reduction of exfoliated graphite oxide. *Carbon* 45, 1558–1565. doi: 10.1016/j.carbon.2007.02.034

Sun, X., Zheng, C., Zhang, F., Yang, Y., Wu, G., Yu, A., et al. (2009). Size-controlled synthesis of magnetite (Fe_3O_4) nanoparticles coated with glucose and gluconic acid from a single Fe(III) precursor by a sucrose bifunctional hydrothermal method. *J. Phy. Chem. C.* 113, 16002–16008. doi: 10.1021/jp9038682

Tyagi, P., Sharma, A., Tomar, M., and Gupta, V. (2017). A comparative study of RGO-SnO_2 and MWCNT-SnO_2 nanocomposites based SO_2 gas sensors. *Sens. Actuators B Chem.* 248, 980–986. doi: 10.1016/j.snb.2017.02.147

Wagner, T., Hennemann, J., Kohl, C. D., and Tiemann, M. (2011). Photocatalytic ozone sensor based on mesoporous indium oxide: Influence of the relative humidity on the sensing performance. *Thin Solid Films* 520, 918–921. doi: 10.1016/j.tsf.2011.04.181

Wan, P., Yang, W., Wang, X., Hu, J., and Zhang, H. (2015). Reduced graphene oxide modified with hierarchical flower-like $In(OH)_3$ for NO_2 room-temperature sensing. *Sens. Actuat. B Chem.* 214, 36–42. doi: 10.1016/j.snb.2015.02.100

Wang, K., Li, J., Li, W., Wei, W., Zhang, H., and Wang, L. (2019b). Highly active Co-based catalyst in nanofiber matrix as advanced sensing layer for high selectivity of flexible sensing device. *Adv. Mater. Technol.* 4:1800521. doi: 10.1002/admt.201800521

Wang, L., Chen, S., Li, W., Wang, K., Lou, Z., and Shen, G. (2019a). Grain-boundary-induced drastic sensing performance enhancement of polycrystalline-microwire printed gas sensors. *Adv. Mater.* 31:1804583. doi: 10.1002/adma.201804583

Wetchakun, K., Samerjai, T., Tamaekong, N., Liewhiran, C., Siriwong, C., Kruefu, V., et al. (2011). Semiconducting metal oxides as sensors for environmentally hazardous gases. *Sens Actuat. B Chem.* 160, 580–591. doi: 10.1016/j.snb.2011.08.032

Wu, J., Tao, K., Guo, Y., Li, Z., Wang, X., Luo, Z., et al. (2017). A 3D chemically modified graphene hydrogel for fast, highly sensitive, and selective gas sensor. *Adv. Sci.* 4:1600319. doi: 10.1002/advs.201600319

Wu, J., Tao, K., Zhang, J., Guo, Y., Miao, J., and Norford, L. K. (2016). Chemically functionalized 3D graphene hydrogel for high performance gas sensing. *J. Mater. Chem. A*. 4, 8130–8140. doi: 10.1039/C6TA01426G

Xia, Y., Wang, J., Xu, J.-L., Li, X., Xie, D., Xiang, L., et al. (2016). Confined formation of ultrathin ZnO nanorods/reduced graphene oxide mesoporous nanocomposites for high-performance room-temperature NO_2 sensors. *ACS Appl. Mater. Inter.* 8, 35454–35463. doi: 10.1021/acsami.6b12501

Zhang, D., Jiang, C., Liu, J., and Cao, Y. (2017). Carbon monoxide gas sensing at room temperature using copper oxide-decorated graphene hybrid nanocomposite prepared by layer-by-layer self-assembly. *Sens. Actuat. B Chem.* 247, 875–882. doi: 10.1016/j.snb.2017.03.108

Zhang, H., Feng, J., Fei, T., Liu, S., and Zhang, T. (2014). SnO_2 nanoparticles-reduced graphene oxide nanocomposites for NO_2 sensing at low operating temperature. *Sens. Actuat. B Chem.* 190, 472–478. doi: 10.1016/j.snb.2013.08.067

Zhang, J., Yang, H., Shen, G., Cheng, P., Zhang, J., and Guo, S. (2010). Reduction of graphene oxide vial-ascorbic acid. *Chem. Commun.* 46, 1112–1114. doi: 10.1039/B917705A

Zhang, Z., Haq, M., Wen, Z., Ye, Z., and Zhu, L. (2018). Ultrasensitive ppb-level NO_2 gas sensor based on WO_3 hollow nanosphers doped with Fe. *Appl. Surf. Sci.* 434, 891–897. doi: 10.1016/j.apsusc.2017.10.074

Zheng, S., Zheng, L., Zhu, Z., Chen, J., Kang, J., Huang, Z., et al. (2018). MoS_2 nanosheets arrays rooted on hollow rGO spheres as bifunctional hydrogen evolution catalyst and supercapacitor electrode. *Nano-Micro Lett.* 10:62. doi: 10.1007/s40820-018-0215-3

Conflict of Interest Statement: The authors declare that the research was conducted in the absence of any commercial or financial relationships that could be construed as a potential conflict of interest.

frontiers in Materials

ORIGINAL RESEARCH
published: 13 September 2019
doi: 10.3389/fmats.2019.00220

Metal Decoration and Magnetic Field Effect on the Electrical Breakdown Voltage for ZnO Nanorods Gas Ionization Sensor

Chunming Liu[1,2†], Zhi Zheng[1,2†], Jiajun Chen[2], Haiqiao Su[2], Xia Xiang[1], Xiaotao Zu[1] and Weilie Zhou[2*]*

[1] School of Physics, University of Electronic Science and Technology of China, Chengdu, China, [2] Advanced Materials Research Institute, University of New Orleans, New Orleans, LA, United States

ZnO nanorod arrays with sharp tips were synthesized via chemical vapor deposition and utilized as the anode for gas ionization sensor. The effects of metal (Mn, $Ni_{81}Fe_{19}$, and Au) decoration and magnetic field on the electrical breakdown voltage were studied. Compared with the bare ZnO nanorod, metal decorated ZnO nanorod arrays in the magnetic field can effectively reduce the breakdown voltage for the air to 20 V. The possible mechanism is that metal decoration produces small size protuberance on the surface of ZnO nanorods and then enhances the electrical field near the tips. The magnetic field exerts action on the motion of the electron and therefore increases electron impact ionization efficiency and second electron emission efficiency.

Keywords: gas ionization sensor, ZnO, metal decoration, magnetic field effect, electrical breakdown voltage

OPEN ACCESS

Edited by:
Xiaogan Li,
Dalian University of Technology (DUT), China

Reviewed by:
Zhanying Zhang,
Henan Polytechnic University, China
Fengmin Liu,
Jilin University, China

***Correspondence:**
Xiaotao Zu
xtzu@uestc.edu.cn
Weilie Zhou
wzhou@uno.edu

†These authors have contributed equally to this work

Specialty section:
This article was submitted to Functional Ceramics, a section of the journal Frontiers in Materials

Received: *26 June 2019*
Accepted: *26 August 2019*
Published: *13 September 2019*

Citation:
Liu C, Zheng Z, Chen J, Su H, Xiang X, Zu X and Zhou W (2019) Metal Decoration and Magnetic Field Effect on the Electrical Breakdown Voltage for ZnO Nanorods Gas Ionization Sensor. Front. Mater. 6:220. doi: 10.3389/fmats.2019.00220

INTRODUCTION

Gas sensors have a significant impact in the areas of environmental emission control, public security, automotive application, workplace hazard monitoring, medical diagnosis (Zhang et al., 2001; Modi et al., 2003; Hou et al., 2006; Li et al., 2010, 2019a,b; Chen et al., 2011; Yao et al., 2012; Wang et al., 2015). Among different gas sensors, gas ionization sensors have shown great promise due to their high selectivity and sensitivity, giving that distinct gases have their unique electrical breakdown voltage (Zhang et al., 2001; Modi et al., 2003). However, traditional gas ionization sensor used in chromatography and mass spectrograph cannot be used on site because of the high-power consumption and risky operation high-voltage (Zhang et al., 2001; Modi et al., 2003; Hou et al., 2006). Thus, decreasing the operation voltage of gas ionization sensors is of great importance in practical applications. Due to high electric fields generated at sharp tips of nanotubes and nanorods electrode, new types of gas ionization sensor using nanomaterials as electrode has been developed (Zhang et al., 2001, 2013; Modi et al., 2003; Hou et al., 2006; Sadeghian and Kahrizi, 2007; Liao et al., 2008; Sadeghian, 2008; Azmoodeh et al., 2009; Baghgar et al., 2009; Huang et al., 2009; Min et al., 2011; Wang et al., 2011). The reported nanomaterials electrode includes various materials, such as carbon nanotubes (Zhang et al., 2001, 2013; Modi et al., 2003; Hou et al., 2006; Baghgar et al., 2009; Huang et al., 2009), ZnO nanorods (Liao et al., 2008; Min et al., 2011; Wang et al., 2011), gold nanorods (Sadeghian and Kahrizi, 2007; Sadeghian, 2008), and silver nanorods (Azmoodeh et al., 2009). With these nanomaterials used as the electrode, the gas electrical breakdown voltage (V_{EB}) is realized at a relatively low applied voltage, which is reduced several-folds in comparison to traditional plane electrodes

(Zhang et al., 2001; Modi et al., 2003; Hou et al., 2006; Sadeghian and Kahrizi, 2007; Liao et al., 2008; Sadeghian, 2008; Azmoodeh et al., 2009; Baghgar et al., 2009; Min et al., 2011; Wang et al., 2011). Moreover, this new type of gas ionization sensor was proved to be reversible and fast as there is no chemical absorption involved.

It was reported that field enhancement is related to the morphology of tips (Pan et al., 2010). Among plane, tapered, and abruptly sharpened tips, the abruptly sharpened tips have the highest electric field enhancement factor (Pan et al., 2010). As a widely studied material, the tip morphology of ZnO nanorods can be easily adjusted. In addition, it was confirmed that as an electrode material of gas ionization sensor, ZnO nanorods have better stability and anti-oxidation behavior than carbon nanotubes (Liao et al., 2008). However, the V_{EB} for ZnO nanorods electrode is much higher than that for carbon nanotubes electrode. For example, the V_{EB} of air for ZnO nanorods electrode is 188 V higher than that for carbon nanotube electrode (Liao et al., 2008). Although Pd capping and electrode separation narrowing were reported to decrease V_{EB} of gas (Wang et al., 2011), the V_{EB} of gas is still much higher than a safe voltage (the safe operation criteria voltage is below 36 V; Hou et al., 2006). For the ZnO nanorods electrode, the V_{EB} of air is as high as 335 V though the electrode separation is reduced to 25 μm (Liao et al., 2008). Even for the carbon nanotube electrode, the V_{EB} of air is still 208 V when the electrode separation is 25 μm (Liao et al., 2008). For the capacitance structured gas-gap device, further decreasing the separation of the electrode is very difficult (Hou et al., 2006). Sole Pd capping can only decrease the V_{EB} of air from 363 to 341 V (Wang et al., 2011). It is evidently seen that sole metal capping and electrode separation decreasing are not enough to reduce the V_{EB} below the safe operation criteria.

The magnetic field effect on the electrical breakdown of gases was widely studied (Haydon et al., 1971; Li and Uhm, 2004; Petraconi et al., 2004; Radjenović and Radjenović, 2006; Wais et al., 2011). An important factor is that both longitudinal (Petraconi et al., 2004) (parallel to the electrical field) and transverse (Li and Uhm, 2004; Radjenović and Radjenović, 2006; Wais et al., 2011) (perpendicular to electrical field) magnetic field are facilitating for gas electrical breakdown for the device with plane parallel electrodes with large separation distance (distance is about several centimeters). This behavior should be beneficial for decreasing V_{EB} for the device with the nanomaterial electrode since the electrical field direction near nanotips is not uniform. To the best of our knowledge, there is no report on the magnetic field effect on gas ionization for ZnO nanorods electrode. In this paper, we studied the metal decoration and magnetic field effect on the electrical breakdown voltage for ZnO nanorods gas ionization sensor. By combining the metal decoration and magnetic field effect, the V_{EB} of air can be well-reduced to 20 V, therefore provide a promising way to improve the performance for gas ionization sensors.

MATERIALS AND METHODS

ZnO nanorods fabrication process is similar to that reported by Xiao et al. (2008). The ZnO nanorods samples were fabricated using a conventional horizontal tube furnace with a quartz tube. The substrate is n-type Si wafers with a 300 nm thermal oxide SiO_2 layer. The crystal orientation of the Si wafer is (100). The size of the substrate is about $0.05 \times 0.8 \times 1.2$ cm^3. These substrates were first ultrasonically cleaned in ultrasonic with acetone, IPA, and distilled water and dried by nitrogen flow. After the substrate being carefully cleaned, about 30 nm thick gold film was sputter deposited using a Cressington 308R thin film coating system. The thickness of the film was monitored by a quartz oscillator equipped in the system. The base pressure of the sputter chamber is about 1×10^{-6} mbar, and the working pressure is about 0.02 mbar. Secondly, a drop coating process was used to deposit ZnO seeds layer on the gold film. Zinc acetate (Fisher scientific) ethanol solution of 0.015 M was prepared. About 20 μl of this solution was dropped on to the surface of the gold film. The substrate was then dried by nitrogen flow after waiting for about 30 s. This process was repeated for six cycles. Thirdly, Zn powder (Damon 5918J25) of about 0.5 grams was loaded on the center of an alumina boat and served as the source material. Substrates with gold film and seeds layer were put over the source material about 2–3 mm above and different distance to the center of the boat. Substrates were loaded with face down. The alumina boat that contained both the source material and the substrates was pushed to the center of the quartz tube, which was then pumped to a pressure of about 8 Torr with a mechanical pump. Argon gas was then introduced into the tube as a carrier gas with a flux of 50 standard cubic centimeters per minute (SCCM). The furnace temperature was subsequently increased from room temperature to 550°C within 50 min. During the heating up process, oxygen gas was introduced at a flux of 5 SCCM when the temperature of furnace reached 450°C. The temperature of the furnace was maintained at 550°C for 30 min. After that, the furnace temperature was decreased from 550 to 450°C within 40 min, and then the furnace was turned off and the substrates were allowed to cool down naturedly to room temperature. The morphology of the sample was measured with a Zeiss (LEO) 1530VP field emission scanning electron microscope (FESEM) and a JEOL 2010 transmission electron microscope (TEM). The composition analyses were conducted by the X-ray energy dispersive spectroscopy (EDS) equipped on the FESEM and TEM. For TEM observations, ZnO nanorods were scraped from the substrate by a blade and dispersed in ethanol using an ultra-sonicator. The ZnO nanorods dispersed in ethanol were introduced dropwise onto a Cu grid covered with carbon films. The crystal structure of the sample was characterized by Philips X'pert MPD X-ray diffraction (XRD). To fabricate the device, the Si/SiO_2 substrate with 30 nm gold films was fixed on a glass substrate and used as the cathode. The ZnO nanorod sample was biased as the anode. The separation between anode and cathode is kept constant as about 200 μm. The testing organic gases were obtained by putting 15 ml corresponding organic liquid into a flask with a volume of about 250 ml. The flask was then sealed with a rubber stopper and kept in room temperature for about 24 h. Then the rubber stopper was taken away and the ionization sensor was put into the atmosphere in the flask. The flask was sealed again with two leads from sensor outside the flask for the testing. The breakdown voltage of air was tested by putting the sensor in the open air condition. The volt-ampere (V-I) character of the device was measured by a Keithley 2400 source

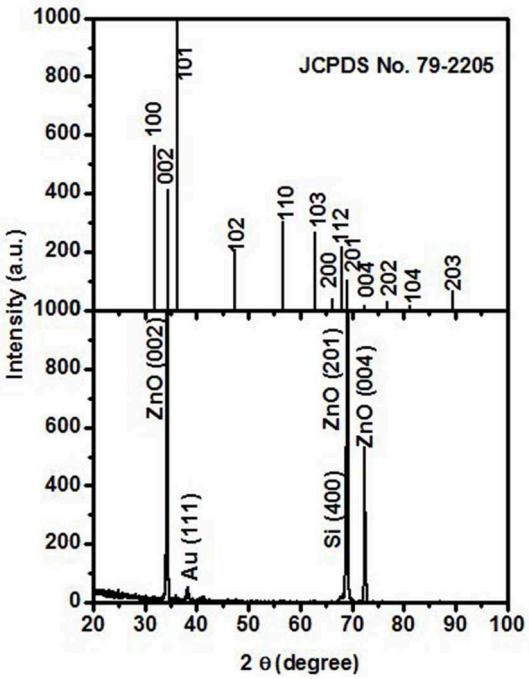

FIGURE 1 | XRD of ZnO nanorods sample. The up panel and the low panel are from JCPDS No. 79-2205 and ZnO nanorods sample, respectively.

meter. The metal decoration was deposited on the ZnO nanorods sample by sputter deposition using a Cressington 308R thin film coating system. The thickness of decoration was monitored by a quartz oscillator equipped in the system. The magnetic field was produced by a permanent magnet. The magnetic field was measured using Lakeshore 450 Gaussmeter.

RESULTS AND DISCUSSION

Figure 1 shows the XRD pattern of ZnO nanorods sample. The up panel of **Figure 1** is the XRD pattern of JCPDS No. 79-2205. The obtained ZnO nanorods sample has the hexagonal structure as confirmed by XRD measurement. The diffraction peaks located at 34.31 and 72.47° are indexed, respectively, as (002) and (004) of ZnO (JCPDS No. 79-2205). The lattice constant *c* is calculated to be about 0.522 nm. The peaks located at 69.04° may come from (004) of Si (JCPDS No. 75-0590) and (201) diffraction of ZnO. The peak at about 38.23° is indexed as (111) diffraction from gold (JCPDS No.04-0784).

The typical morphology of ZnO nanorods are shown in **Figure 2**. **Figures 2A,B** are the low and high magnified 30° tilt view of FESEM images, respectively. As shown in **Figure 2B**, the nanorod has a large base and abruptly sharp tips with a diameter of about 40 nm. The formation mechanism of the abruptly sharp tips of ZnO is not clear at present. It was reported that different tip shapes of ZnO nanorods can be controlled by the substrate direction relative to the gas flow during fabrication (Pan et al., 2005). The local oxygen concentration around the substrate also plays an important role in determining the tip shapes of ZnO nanorods (Pan et al., 2005). It was reported that ZnO nanorods with abruptly sharp tips have an advantage in electrical field enhancement (Pan et al., 2010). The sparse vertically aligned tips are useful to reduce the screening effect of the nearest neighbor tips (Pan et al., 2010). Taking into account the screening effect, the electrical field at the tip can be expressed as Filip et al. (2001):

$$E_{loc} = s\frac{V}{r} + (1-s)\frac{V}{d} \quad (1)$$

where V is the applied voltage between electrodes, d is the cathode to anode distance, r is the emitter tip's radius of curvature, and s is the factor in evaluating the degree of screening effect, which ranges from 0 (for extremely high-density tips arrays) to 1 (for a single tip). The higher is the density of tips, the greater the screening effect. The local field on every tip decreases quickly with the distance between the nearest neighbor tips decreasing (Nilsson et al., 2000). It is seen from Equation (1) that the electrical field has no dependence on the length of the nanorod. However, other literature reported that the electrical field at tips is also dependent on the length of nanorods (Wang et al., 2004). The common in literature is that the smaller the tip diameter, the higher the electrical field near the tip surface (Filip et al., 2001; Wang et al., 2004). This is one reason that small size metal decoration on the surface of nanotips would enhance the electrical field.

The obtained ZnO nanorods sample was biased as an anode electrode of the device. A typical scheme of the device is shown in **Figure 3**. A silica substrate with 30 nm gold film was used as a cathode. It was found that the ZnO nanorods electrode is able to ionize and distinguish acetone, IPA, and ethanol gas. **Figure 4** shows the I–V curves for these gases. As indicated in **Figure 4**, the current first increases linearly with the voltage increasing and then increases abruptly when the voltage is above a certain threshold. It was reported that the I–V curve of gas ionization sensor obeys the Ohmic law when the electrical field strength is less than the ionization threshold (Sadeghian, 2008). The current is determined by the movement of existing radiation-generated electron-ion pairs and proportional to electrical filed (Sadeghian, 2008). When the voltage is above the threshold, the current increase sharply because of the gas ionization is initiated (Sadeghian, 2008). The ionization energy of acetone, IPA, ethanol is 9.69, 10.12, and 10.62 eV, respectively (Huang et al., 2009). The V_{EB} is determined to be about 6.9, 17.8, and 19.3 V, respectively, which is distinct for different gases. It is seen that gas with higher ionization energy has a higher V_{EB}. This is reasonable as that V_{EB} is mainly determined by the ionization energy of gas (Sadeghian and Kahrizi, 2007). However, the device cannot make air electrical breakdown even though the applied voltage reaches 210 V. This may be due to the ionization energy of oxygen and nitrogen is higher than these organic gases. The ionization energy of oxygen and nitrogen is 12.06 and 15.58 eV, respectively.

In order to ionize gas with higher ionization energy, metal decoration, and magnetic field are used to ionize air as an example. **Figures 5A–C** show the TEM images for pure ZnO nanorods, 5 nm Mn and a 15 nm Mn decorated ZnO nanorods, respectively. The size of Mn particle is about 5 nm. As shown

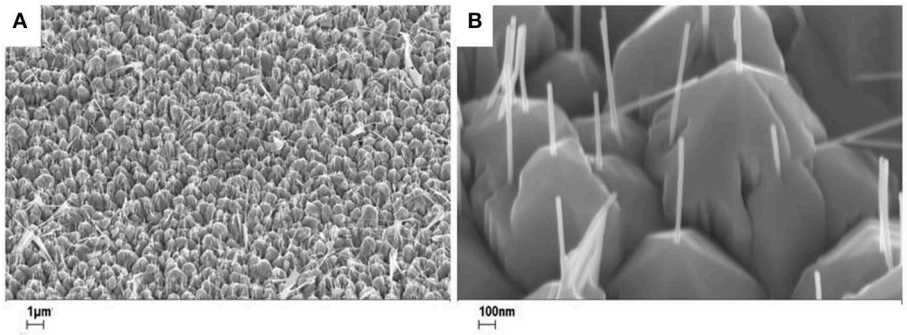

FIGURE 2 | FESEM of ZnO nanorods: lower magnified **(A)** and higher magnified **(B)** 30° tilt view.

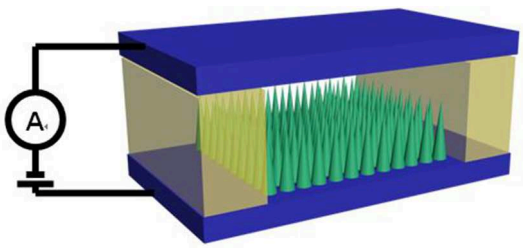

FIGURE 3 | The structural scheme of device. The ZnO nanorods were biased as anode.

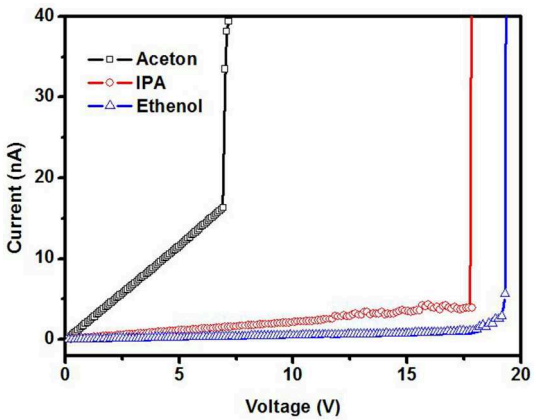

FIGURE 4 | The volt–ampere curves at different atmosphere.

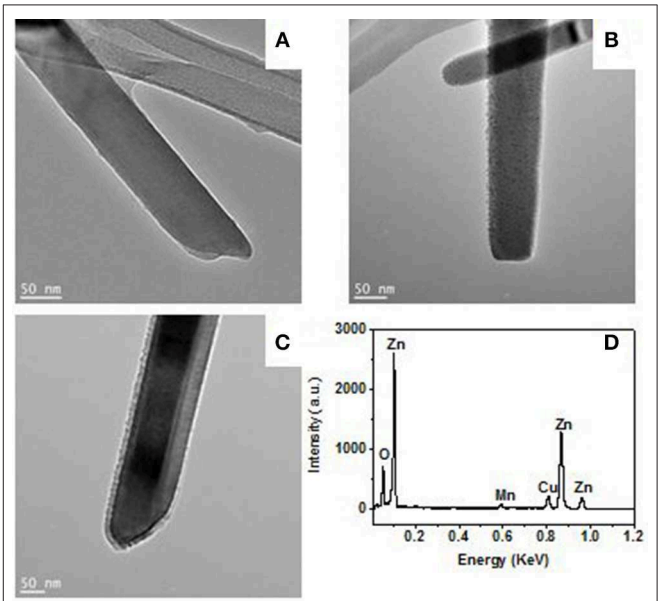

FIGURE 5 | TEM images for a pristine **(A)**, 5 nm Mn **(B)**, and 15 nm Mn **(C)** decorated ZnO nanorod. The EDX **(D)** is corresponding to 15 nm Mn decorated ZnO nanorod.

in the TEM images, the metal decoration produces some small size protuberances on the surface of nanorods. The EDS in **Figure 5D** is corresponding to that of the 15 nm Mn decorated ZnO nanorods sample. The signal peaks are corresponding to oxygen, zinc, manganese, and copper, respectively. The copper signal in EDS is from the copper grid.

Figure 6 shows the ionization I–V curves of air for a 5 nm Mn decorated ZnO nanorods electrode with and without magnetic field (6,000 Gs). Without a magnetic field, there is no electrical breakdown even though the applied voltage increases to 210 V. This means the breakdown voltage of air for 5 nm Mn decorated ZnO electrode is higher than 210 V. However, with the magnetic field, the breakdown was observed on the voltage of around 20 V. As shown in **Figure 6**, there is no obvious difference in the breakdown voltage between parallel or perpendicular magnetic field, thus in the later experiments, the magnetic field is applied perpendicular to the sample plane only. The breakdown voltage of air is about 20 V, which is small enough to be powered by portable batteries and safely handled. Compared to that of the bare ZnO, with Mn decoration and magnetic field working together, the breakdown voltage of air is decreased more than 10 times. **Figure 7** shows the ionization of air for various thickness Mn decorated ZnO nanorods under magnetic field. The breakdown voltage of air increases with the thickness of

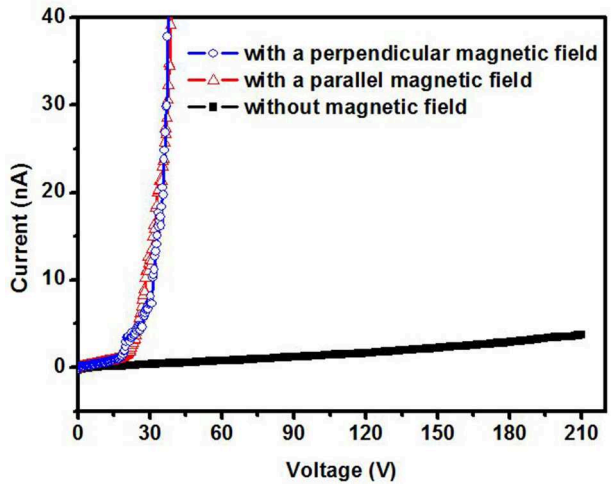

FIGURE 6 | Air ionization curve for a 5 nm Mn decorated ZnO nanorods electrode under parallel and perpendicular magnetic field.

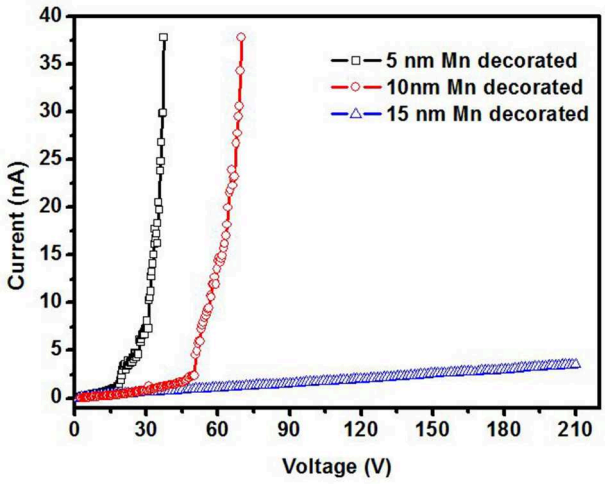

FIGURE 7 | Air ionization for ZnO nanorods electrode decorated with various Mn thickness under perpendicular magnetic field of 6,000 Gs.

decoration increasing. This may be due to that with thickness increasing, the protuberances diameter increases. **Figure 8** shows that 5 nm of Au, $Fe_{19}Ni_{81}$ decoration together with a magnetic field can also reduce the breakdown voltage of air. The difference among various metal decorations will be studied in the future. Here is to show that magnetic field combined with various metal decorations is effective to reduce V_{EB}. The role of metal decoration is to produce small size protuberances on the surface of nanorods and then creates a higher electric field at the surface of protuberances (Wang et al., 2011). Besides the change in surface roughness, the surface states created by decoration are also important in reducing the ionization voltage (Karaagac and Islam, 2014). The decoration may unintentionally introduce impurity into the semiconductor and create high density of surface states (Karaagac and Islam, 2014). However, the effect of sole metal decoration on the electrical field enhancement is not enough to decrease V_{EB} to a safe handle level. A magnetic field is helpful to decrease V_{EB}. The role played by the magnetic field on ionization will be discussed in the following.

In order to confirm that the gas ionization voltage is still the distinct character of gases when the electrode is decorated with metal and putting under a magnetic field, **Figure 9** shows the ionization of IPA and air for a 5 nm Mn decorated ZnO electrode under magnetic field. As shown in **Figure 9**, the breakdown voltage is distinct for IPA and air.

Electron impact ionization (EII) and field ionization (FI) processes were, respectively, proposed for nanomaterial configured as a cathode (Huang et al., 2009; Chivu and Kahrizi, 2013; Mahmood et al., 2013) and an anode (Longwitz et al., 2001; Huang et al., 2009). If the nanorod was biased as a cathode, electrons would be extracted form cathode and in turn be accelerated and impact with gas molecular. Then the gas molecular would be ionized by electron bombardment (Longwitz et al., 2001; Huang et al., 2009; Chivu and Kahrizi, 2013; Mahmood et al., 2013). If the nanorod was biased as an

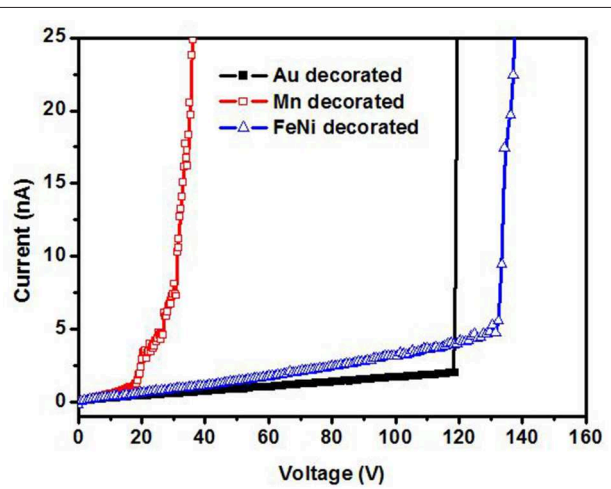

FIGURE 8 | Air ionization for various metal decorated ZnO nanorods under perpendicular magnetic field (6,000 Gs).

anode, gases would be ionized near the surface of nanotips by strong field extraction of the most loosely bound electrons from gas molecules (Longwitz et al., 2001). In our experiment, the ZnO nanorods were biased as an anode. In the absence of a magnetic field, the ionization of acetone, IPA, and ethanol should be FI. The ionization energy of these organic gases is low enough so that the electrical field is strong enough to extraction electron from these gases molecular and cause gases electrical breakdown. In the case of air, the ionization energy is high, and the electrical field is not strong enough so that no electrical breakdown happens in the applied voltage region. Although there is no gas electrical breakdown, there would be some electrons in the device space such as the cosmic radiation introduced electrons (Azmoodeh et al., 2009) and cathode emission electrons (Huang et al., 2009). Therefore, in

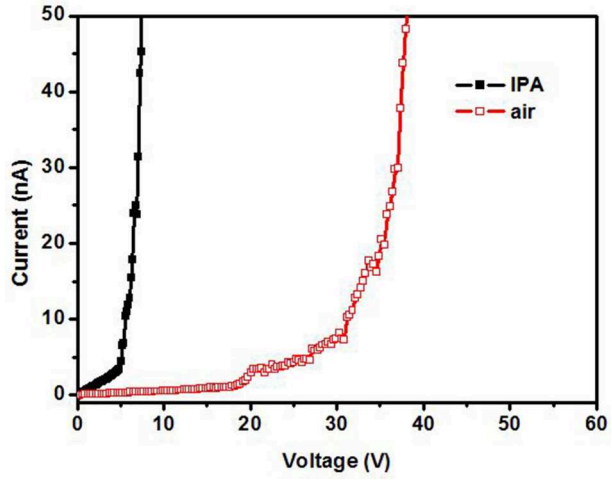

FIGURE 9 | Ionization in IPA and air for a 5 nm Mn decorated ZnO nanorods electrode under magnetic field.

the presence of a magnetic field, the efficiency of electron impact ionization and the second electron emission from cathode would be enhanced (Haydon et al., 1971; Li and Uhm, 2004; Petraconi et al., 2004; Radjenović and Radjenović, 2006; Wais et al., 2011). A transverse magnetic field can exert action on the motion of electrons, which makes the gyro-motion of electrons, reduces the mean free path of electrons and increases the number of collision and ionization coefficient (Li and Uhm, 2004). The effect of a longitudinal magnetic field on the motion of the electron is to reduce the lateral diffusion of electrons and effectively increases the collision frequency between electrons and the gas particles, thus increasing the ionization efficiency (Petraconi et al., 2004). Therefore, more and more free electrons and ions will be created if the process continues. When the number of free electrons increases exponentially, there will be the flow of a very large current that leads to the breakdown of gases. In a crossed magnetic and electric field, the breakdown voltage is expressed as Radjenović and Radjenović (2006):

$$V_{EB} = \frac{B_k^k pd\sqrt{1 + C\left(B^2/P^2\right)}}{\left[\ln A_k/\Gamma_k \ + \ln\left(pd\sqrt{1 + C\left(B^2/P^2\right)}\right)\right]^k} \qquad (2)$$

Where p is the gas pressure in units of Torr, k has been empirically determined to be one for the molecular gases and two for the atomic gases. A_k and B_k is the coefficients, for nitrogen $A_k = 12$ $cm^{-1}Torr^{-1}$ and $B_k = 342$ $Vcm^{-1}Torr^{-1}$. B is the magnetic flux density expressed in Gauss and C is a constant. Γ_k is related to the value of yield per ion γ as $\Gamma_k = \ln\left(1 + \frac{1}{\gamma}\right)$. It was confirmed that V_{EB} could be effectively decreased by the magnetic field (Radjenović and Radjenović, 2006). As seen from Equation (2), the breakdown voltage of gas is indeed dependent on the magnetic field B.

CONCLUSION

The gas ionization for ZnO nanorods electrode was explored. It was found that metal (Mn, $Fe_{19}Ni_{81}$, and Au) decoration together with a magnetic field can effectively reduce the electrical breakdown voltage of gases. The metal decoration introduces small size protuberances on the surface and thus increase the electric field enhancement. However, this enhancement is not enough to reduce the breakdown voltage of air to a safe voltage. The air electrical breakdown voltage as a function of metal decoration thickness and magnetic field direction was investigated. The magnetic field would increase the efficiency of ionization and second electron emission. Therefore, the electrical breakdown voltage of gases is reduced in the presence of metal decoration and magnetic field significantly.

DATA AVAILABILITY

All datasets generated for this study are included in the manuscript/supplementary files.

AUTHOR CONTRIBUTIONS

CL and ZZ conducted the experimental work together, as well contributed to the data analysis and manuscript preparation. JC and HS contributed to sensor measurements and data interpretation. XX and XZ contributed to the discussion of experimental results and manuscript preparation. WZ guided the entire experimental process and performed final revision for the manuscript.

FUNDING

The authors thank to the funding support from Louisiana Board of Regents Nos. LEQSF (2007-12)-ENH-PKSFI-PRS-04 and LESQSF (2011-13)-RD-B-08. ZZ, XX, and XZ thank the support of the National Natural Science Foundation of China (U1630126).

REFERENCES

Azmoodeh, N., Chivu, N., and Sadeghian, R. B. (2009). "A silver nanowire based gas ionization sensor Eurocon," in *IEEE EUROCON 2009* (St.-Petersburg), 1231.

Baghgar, M., Abdiand, Y., and Arzi, E. (2009). Fabrication of low pressure field ionization gas sensor using bent carbon nanotubes. *J. Phys. D Appl. Phys.* 42:135502. doi: 10.1088/0022-3727/42/13/135502

Chen, J., Wang, K., and Zhou, W. L. (2011). Vertically aligned ZnO nanorod arrays coated with SnO_2/noble metal nanoparticles for highly sensitive and selective gas detection. *IEEE Trans. Nanotech.* 10:968. doi: 10.1109/TNANO.2010.2091423

Chivu, N., and Kahrizi, M. (2013). Modeling and simulation of a miniaturized gas ionization sensor: detection of greenhouse gases. *Sens. Transducers* 153, 105–110.

Filip, V., Nicolaescu, D., Tanemura, M., and Okuyama, F. (2001). Modeling the electron field emission from carbon nanotube films. *Ultramicroscopy* 89, 39–49. doi: 10.1016/S0304-3991(01)00107-3

Haydon, S. C., Mcintosh, A. I., and Simpson, A. A. (1971). The effect of magnetic fields on electron energy distribution functions and derived collision frequencies. *J. Phys. D Appl. Phys*. 4:1257. doi: 10.1088/0022-3727/4/9/304

Hou, Z. Y., Xu, D., and Cai, B. (2006). Ionization gas sensing in a microelectrode system with carbon nanotubes. *Appl. Phys. Lett*. 89:213502. doi: 10.1063/1.2392994

Huang, J., Wang, J., Gu, C., Yu, K., Meng, F., and Liu, J. (2009). A novel highly sensitive gas ionization sensor for ammonia detection. *Sens. Actuat. A* 150, 218–223. doi: 10.1016/j.sna.2009.01.008

Karaagac, H., and Islam, M. S. (2014). Enhanced field ionization enabled by metal induced surface states on semiconductor nanotips. *Adv. Funct. Mater*. 24:2224. doi: 10.1002/adfm.201303308

Li, D. J., Tang, Y. L., Ao, D. Y., Xiang, X., Wang, S. Y., and Zu, X. T. (2019a). Ultra-highly sensitive and selective H_2S gas sensor based on CuO with sub-ppb detection limit. *Int. J. Hydrogen Energy* 44, 3985–3992. doi: 10.1016/j.ijhydene.2018.12.083

Li, D. J., Zu, X. T., Ao, D. Y., Tang, Q. B., Fu, Y. Q., Guo, Y. J., et al. (2019b). High humidity enhanced surface acoustic wave (SAW) H_2S sensors based on sol–gel CuO films. *Sens. Actuat. B Chem*. 294, 55–61. doi: 10.1016/j.snb.2019.04.010

Li, S. Z., and Uhm, H. S. (2004). Influence of magnetic field on the electrical breakdown characteristics in cylindrical diode. *Phys. Plasmas* 11:3443. doi: 10.1063/1.1737743

Li, Y., Xing, Q. F., Yan, Y., and Zhou, W. L. (2010). A large quantity synthesis of ZnO nanoneedles and their polarity determination. *J. Nanosci. Nanotech*. 10, 2023–2027. doi: 10.1166/jnn.2010.2129

Liao, L., Lu, H. B., Shuai, M., Li, J. C., Liu, Y. L., Liu, C., et al. (2008). A novel gas sensor based on field ionization from ZnO nanowires: moderate working voltage and high stability. *Nanotechnology* 19:175501. doi: 10.1088/0957-4484/19/17/175501

Longwitz, R., Lintel, H. V., Carr, R., Hollenstein, C., and Penaud, P. (2001). "Study of gas ionization schemes for micro devices," in *The 11th International Conference on Solid State Sensors and Actuators* (Munich).

Mahmood, S., Burhanudin, Z. A., and Salman, A. (2013). Field emission model of carbon nanotubes to simulate gas breakdown in ionization gas sensor. *J. Appl. Phys*. 113:023302. doi: 10.1063/1.4774073

Min, J., Liang, X., Wang, B., Wang, L., Zhao, Y., Shi, W., et al. (2011). The sensitivity and dynamic response of field ionization gas sensor based on ZnO nanorods. *J. Nanopart. Res*. 13:5171. doi: 10.1007/s11051-011-0500-2

Modi, A., Koratkar, N., Lass, E., Wei, B., and Ajayan, P. M. (2003). Miniaturized gas ionization sensors using carbon nanotubes. *Nature* 424, 171–174. doi: 10.1038/nature01777

Nilsson, L., Groening, O., Emmenegger, C., Kuettel, O., Schaller, E., Schlapbach, L., et al. (2000). Scanning field emission from patterned carbon nanotube films. *Appl. Phys. Lett*. 76:2071. doi: 10.1063/1.126258

Pan, N., Wang, X., Zhang, K., Hu, H., Xu, B., Li, F., and Hou, J. G. (2005). An approach to control the tip shapes and properties of ZnO nanorods. *Nanotechnology* 16, 1069–1072. doi: 10.1088/0957-4484/16/8/012

Pan, N., Xue, H., Yu, M., Cui, X., Wang, X., Hou, J. G., et al. (2010). Tip morphology dependent field emission from ZnO nanorod arrays. *Nanotechnology* 21:225707. doi: 10.1088/0957-4484/21/22/225707

Petraconi, G., Maciel, H. S., Pessoa, R. S., Murakami, G., Massi, M., Otani, C., et al. (2004). Longitudinal magnetic field effect on the electrical breakdown in low pressure gases. *Braz. J. Phys*. 34:1662. doi: 10.1590/S0103-97332004000800028

Radjenović, M. R., and Radjenović, B. (2006). The effect of magnetic field on the electrical breakdown characteristics. *J. Phys. D Appl. Phys*. 39, 3002–3009. doi: 10.1088/0022-3727/39/14/019

Sadeghian, R. B. (2008). A novel gas sensor based on tunneling field ionization on whisker covered gold nanowires. *IEEE Sens. J*. 8:161. doi: 10.1109/JSEN.2007.912788

Sadeghian, R. B., and Kahrizi, M. (2007). "A low voltage gas ionization sensor based on sparse gold nanorods," in *IEEE Sensors Conference* (Atlanta, GA).

Wais, S. I., Mohammed, R. Y., and Yousif, S. O. (2011). Influence of axial magnetic field on the electrical breakdown and secondary electron emission in plane parallel plasma discharge. *World Acad. Sci. Eng. Technol*. 56:1304. doi: 10.5281/zenodo.1333588

Wang, H., Zou, C., Tian, C., Zhou, L., Wang, Z., and Fu, D. (2011). A novel gas ionization sensor using Pd nanoparticle-capped ZnO. *Nanoscale Res. Lett*. 6:534. doi: 10.1186/1556-276X-6-534

Wang, S. Y., Ma, J. Y., Li, Z. J., Su, H. Q., Alkurd, N. R., Zhou, W. L., et al. (2015). Surface acoustic wave ammonia sensor based on ZnO/SiO composite film. *J. Hazard. Mater*. 285, 368–374. doi: 10.1016/j.jhazmat.2014.12.014

Wang, X. Q., Wang, M., He, P. M., Xu, Y. B., and Li, Z. H. (2004). Model calculation for the field enhacement factor of carbon nanotube. *J. Appl. Phys*. 96:6752. doi: 10.1063/1.1814439

Xiao, J., Zhang, X., and Zhang, G. (2008). Field emission from zinc oxide nanotowers the role of the top morphology. *Nanotechnology* 19:295706. doi: 10.1088/0957-4484/19/29/295706

Yao, K., Caruntu, D., Wozny, S., Huang, R., Ikuhara, Y. H., Cao, B. B., et al. (2012). Towards one key to one lock: catalyst modified indium oxide nanoparticle thin film sensor array for selective gas detection. *J. Mater. Chem*. 22, 7308–7313. doi: 10.1039/c2jm15179k

Zhang, Y., Li, S., Zhang, J. Y., Pan, Z., Min, D., Li, X., et al. (2013). High-performance gas sensors with temperature measurement. *Sci. Rep*. 3:1267. doi: 10.1038/srep01267

Zhang, Y., Liu, J., and Li, X. (2001). "Study of gas sensor with carbon nanotube film on the substrate of porous silicon," in *IVMC 2001. Proceedings of the 14th International Vacuum Microelectronics Conference* (Davis, CA).

Conflict of Interest Statement: The authors declare that the research was conducted in the absence of any commercial or financial relationships that could be construed as a potential conflict of interest.

frontiers in Materials

ORIGINAL RESEARCH
published: 24 September 2019
doi: 10.3389/fmats.2019.00231

Light-Activated Sub-ppm NO_2 Detection by Hybrid ZnO/QD Nanomaterials vs. Charge Localization in Core-Shell QD

Artem Chizhov[1], Roman Vasiliev[1,2], Marina Rumyantseva[1,3], Ivan Krylov[4], Konstantin Drozdov[4], Maria Batuk[5], Joke Hadermann[5], Artem Abakumov[5,6] and Alexander Gaskov[1,3]*

[1] Chemistry Department, Moscow State University, Moscow, Russia, [2] Department of Materials Science, Moscow State University, Moscow, Russia, [3] Institute of Chemistry, Saint Petersburg State University, Saint Petersburg, Russia, [4] Physics Department, Moscow State University, Moscow, Russia, [5] Electron Microscopy for Materials Science, University of Antwerp, Antwerp, Belgium, [6] Center for Electrochemical Energy Storage, Skolkovo Innovation Center, Moscow, Russia

New hybrid materials—photosensitized nanocomposites containing nanocrystal heterostructures with spatial charge separation, show high response for practically important sub-ppm level NO_2 detection at room temperature. Nanocomposites ZnO/CdSe, ZnO/(CdS@CdSe), and ZnO/(ZnSe@CdS) were obtained by the immobilization of nanocrystals—colloidal quantum dots (QDs), on the matrix of nanocrystalline ZnO. The formation of crystalline core-shell structure of QDs was confirmed by HAADF-STEM coupled with EELS mapping. Optical properties of photosensitizers have been investigated by optical absorption and luminescence spectroscopy combined with spectral dependences of photoconductivity, which proved different charge localization regimes. Photoelectrical and gas sensor properties of nanocomposites have been studied at room temperature under green light (λ_{max} = 535 nm) illumination in the presence of 0.12–2 ppm NO_2 in air. It has been demonstrated that sensitization with type II heterostructure ZnSe@CdS with staggered gap provides the rapid growth of effective photoresponse with the increase in the NO_2 concentration in air and the highest sensor sensitivity toward NO_2. We believe that the use of core-shell QDs with spatial charge separation opens new possibilities in the development of light-activated gas sensors working without thermal heating.

Keywords: room temperature semiconductor gas sensor, sub-ppm NO_2 detection, visible light activation, CdSe quantum dots, core/shell heterostructures, charge spatial localization

OPEN ACCESS

Edited by:
Qasem Ahmed Drmosh, King Fahd University of Petroleum and Minerals, Saudi Arabia

Reviewed by:
Teng Fei, Jilin University, China
Zhi Yang, Shanghai Jiao Tong University, China

****Correspondence:***
Marina Rumyantseva
roum@inorg.chem.msu.ru

Specialty section:
This article was submitted to Functional Ceramics, a section of the journal Frontiers in Materials

Received: *07 May 2019*
Accepted: *05 September 2019*
Published: *24 September 2019*

Citation:
Chizhov A, Vasiliev R, Rumyantseva M, Krylov I, Drozdov K, Batuk M, Hadermann J, Abakumov A and Gaskov A (2019) Light-Activated Sub-ppm NO_2 Detection by Hybrid ZnO/QD Nanomaterials vs. Charge Localization in Core-Shell QD. Front. Mater. 6:231. doi: 10.3389/fmats.2019.00231

INTRODUCTION

Semiconductor metal oxide gas sensors are promising for integration into mobile devices and information networks because of their extremely high sensitivity, stability and miniaturization capability. Their working principles are based on the chemisorption of molecules from the gas phase and chemical reactions on the surface of the semiconductor metal oxide, which lead to significant changes in the band structure in a narrow near-surface layer and the formation of energy barriers at the solid-gas interface (Bârsan and Weimar, 2001; Sun et al., 2015). This affects

the concentration and mobility of the charge carriers in the semiconductor, which generates a detectable electrical signal. Gas sensors based on semiconductor oxides can detect the main air pollutants at the corresponding threshold values, however, only at relatively high operating temperatures 150–350°C (Krivetskiy et al., 2013; Vorobyeva et al., 2013; Wang et al., 2018). This significantly increases the power consumption, which poses the main limitation for coupling gas sensors with portable and mobile devices.

To reduce the power consumption of metal oxide gas sensors, the effective strategies, mainly include surface modification, additive doping and light activation (Wang et al., 2017; Xu and Ho, 2017; Zhu and Zeng, 2017). Most of the publications dealing with the gas sensor properties of semiconductor materials under illumination discussed the effects observed under UV light (Saura, 1994; Mishra et al., 2004; Malagu et al., 2005; De Lacy Costello et al., 2008; Peng et al., 2008, 2009; Prades et al., 2009a,b; Carotta et al., 2011; Wang et al., 2011; Cui et al., 2013; Wagner et al., 2013; Klaus et al., 2015; Ilin et al., 2016; Nakate et al., 2016; Saboor et al., 2016; Trawka et al., 2016; Wongrat et al., 2016; Da Silva et al., 2017; Espid and Taghipour, 2017; Hsu et al., 2017; Hyodo et al., 2017; Wu et al., 2018). UV radiation with an energy exceeding the width of the band gap generates electron-hole pairs and thus increases conductivity. In polycrystalline semiconductors, photoexcitation can change the charge of surface states, which leads to a decrease in the height of intergranular barriers and affects the thickness of the depleted layer at the interface. This will change the tunneling probability of the charge carriers through the intergranular barriers. At the same time, the illumination changes the population of surface states by electrons and holes, which affects the concentration of active adsorption centers on the surface of the semiconductor.

Further reduction of the energy consumption of the sensor element is possible using photoactivation with visible light. However, for this it is necessary to shift the optical sensitivity of semiconductor oxides from the UV range to longer wavelengths. This can be achieved by creating the defects in the semiconductor matrix (Han et al., 2012, 2013; Varechkina et al., 2012; Geng et al., 2013; Zhang et al., 2017) or using the sensitizers that absorb light in the visible range (Peng et al., 2011; Vasiliev et al., 2013; Chizhov et al., 2014, 2016, 2018; Yang et al., 2014; Zhang et al., 2015; Geng et al., 2016a,b; Paolesse et al., 2017; Rumyantseva et al., 2018). In the latter case, the consistency between the energy levels of metal oxide and sensitizer, is the necessary condition ensuring the transfer possibility of photoexcited charge carriers from the sensitizer to the semiconductor matrix (Minami et al., 1998; Ivanov et al., 2007; Kim et al., 2009; Vasiliev et al., 2011; Mordvinova et al., 2014). $A^{II}B^{VI}$ and $A^{III}B^{V}$ semiconductor quantum dots (QDs) (Vasiliev et al., 2013; Chizhov et al., 2014, 2016, 2018; Yang et al., 2014; Geng et al., 2016a,b) and organic dyes (Peng et al., 2011; Zhang et al., 2015; Paolesse et al., 2017; Rumyantseva et al., 2018) are suitable visible light sensitizers for wide gap semiconductor metal oxides.

Thus, to achieve the improved sensor characteristics it is necessary to understand what processes are responsible for the formation of the sensor response in such hybrid systems under illumination. In this paper, the value of the sensor response was chosen as a characteristic to be optimized and the influence of the spatial separation of charge carriers in semiconductor core/shell nanoparticles (QDs) sensitizers on the sensor signal of hybrid materials based on ZnO/QDs was studied. The main problems with the use of semiconductor QDs as photosensitizers are the recombination of charge carriers inside the nanocrystals and the charge trapping by defects on their surfaces (Vasiliev et al., 2011). The use of core/shell nanoparticles opens new possibilities for increasing the efficiency of photosensitization. For example, the core of the nanoparticle can be covered by a shell of a semiconductor with a wider gap, i.e., type I heterostructures with the straddling gap arrangement such as CdS(shell)@CdSe(core) (Vasiliev et al., 2011). This increases the efficiency of charge transfer to the oxide matrix by passivation of the surface defects to reduce the capture of photoexcited charges (Drozdov et al., 2013). Type II heterostructures, such as ZnSe(shell)@CdS(core), have a staggered gap (Vasiliev et al., 2011). This results in a spatial separation of the photoexcited electron and hole in different regions of the nanoparticle. For CdS/ZnSe, for example, photoexcited electrons will be localized in CdS, which has a higher electron affinity. The spatial separation of the charge carriers reduces the probability of radiative recombination, leading to an increased lifetime of the photoexcited pair and thus promoting charge transfer between the nanoparticle and the oxide matrix. In addition, type II heterostructures have a smaller effective band gap than the constituent semiconductors forming the heterojunction, which allows a further shift of the absorption band to the longer wavelength region. However, these interesting features have so far been used in optical applications and in a few photocatalytic applications (O'Connor et al., 2012), but their possibilities as sensors have never been tested.

In the present work, we investigate photosensitized nanocomposites containing nanocrystalline heterostructures with spatial charge separation as materials for NO_2 sensors working at room temperature under photoactivation with visible light and show that such approach significantly improves the photoelectric and sensor properties of the semiconductor oxide.

MATERIALS AND METHODS

Materials

The semiconductor matrix—nanocrystalline zinc oxide—was obtained by the precipitation method (Vorobyeva et al., 2013). Zinc acetate $Zn(CH_3COO)_2$ solution was slowly added to a stirred solution of NH_4HCO_3 at 60°C. After aging for 1 h at room temperature, the white precipitate of zinc hydroxycarbonate $Zn_x(OH)_{2y}(CO_3)_{x-y}{\cdot}nH_2O$ was centrifuged, washed with deionized water to remove residual ions, dried in air at 50°C for 24 h, and finally annealed in air at 300°C for 24 h.

To prepare CdSe and CdS nanocrystals stabilized with oleic acid, a pre-synthesized anionic precursor tri-*n*-octylphosphine selenide (TOPSe) or tri-*n*-octylphosphine sulfide (TOPS) and a freshly prepared cationic precursor cadmium oleate were used (Vasiliev et al., 2013). To synthesize the anionic precursors 0.01 mole of ground selenium or sulfur were added to 10 ml of tri-*n*-octylphosphine $(C_8H_{17})_3P$ (TOP, 90% pure, Fluke). The reaction mixture was heated up to 100°C in an argon flow until

the chalcogen was completely dissolved. For the preparation of cadmium oleate, 7 ml of 1-octadecene (90% pure, Aldrich), 0.15 mmole of oleic acid $C_{17}H_{33}COOH$ (90% pure, Aldrich) and 0.5 mmole of cadmium acetate $Cd(CH_3COO)_2{}^*2H_2O$ (analytical grade, Aldrich) were added to a quartz flask of 15 ml and heated at 180°C for 1 h under the argon flow (15-20 ml/min). The temperature of the reaction mixture was then raised to 230°C and 0.5 ml of TOPSe (or TOPS) was rapidly injected. CdSe or CdS nanocrystals were grown for 35 s. Then the reaction was stopped by rapidly cooling the flask in a jar with cold water. To isolate CdSe or CdS nanocrystals, acetone and ethyl alcohol (96%) were added to the cooled reaction mixture. The precipitated nanocrystals were separated by centrifugation, dried at 50°C and redispersed in hexane. This procedure was repeated 3 times to remove unreacted precursors and the excess of stabilizer oleic acid.

To create the core-shell CdS@CdSe nanocrystals, the CdS shell was grown on the CdSe nuclei synthesized at 240°C for 300 s by slowly adding TOPS to a solution containing CdSe nanocrystals, oleic acid, and cadmium oleate. The temperature of the reaction mixture was maintained at 200°C, a 1 M TOPS solution in tri-*n*-octylphosphine was added dropwise with a rate of ∼ 0.3 ml/h. Under these conditions, a small supersaturation of the solution leads to a uniform growth of the shell. The core-shell CdS@CdSe nanocrystals were purified and redispersed in hexane as described above.

To obtain the core-shell ZnSe@CdS nanocrystals, the growth of the ZnSe shell on CdS nuclei was carried out in a similar manner. The cationic precursor of zinc oleate was prepared from zinc acetate $Zn(CH_3COO)_2{}^*2H_2O$ (analytical grade, Aldrich) by a procedure analogous to that used for the preparation of cadmium oleate. During the ZnSe shell growth, the temperature was maintained at 240°C. The aliquots were taken from the reaction mixture to investigate the evolution of optical absorption and luminescence spectra.

For gas sensor measurements nanocrystalline ZnO powder was mixed with a vehicle (α-terpineol in ethanol) and deposited in the form of thick films over functional substrates, provided with Pt contacts on the front side and a Pt-heater on the back-side. Thick films were dried at 30°C for 24 h and sintered at 300°C (using Pt-heater) for 10 h in air. The coatings produced in this way are formed by the agglomerated particles and have a porous structure. The films are continuous and uniform over the entire substrate. The estimated average film thickness is about 1 μm (Chizhov et al., 2016). To obtain QD/ZnO (QD = CdSe, CdS@CdSe, ZnSe@CdS) nanocomposites ZnO thick films deposited over functional substrates were immersed into hexane sol containing corresponding QDs (4^*10^{-4} M) for 24 h, washed with hexane and dried in air. As a result, the films acquired an orange color.

Methods

Phase composition was examined by X-ray powder diffraction (XRPD) with the Rigaku diffractometer [wavelength λ = 1.54059 Å ($Cu\ K_{\alpha 1}$ radiation)]. The crystallite size (d_{XRD}) was calculated from the broadening of the most intense XRPD peaks using the Scherrer equation. The specific surface area of ZnO powder was measured by nitrogen adsorption with the Chemisorb 2750 instrument (Micromeritics).

To prepare ZnO specimen for TEM analysis, the material was mixed with toluene using an ultrasonic bath. A few drops of the obtained suspension were deposited onto a Cu TEM grid covered with carbon. High angle annular dark field scanning transmission electron microscopy (HAADF-STEM) images were acquired using a FEI Osiris microscope operated at 200 kV. The TEM sample of the ZnSe@CdS nanocrystals was prepared by depositing drops of suspension of the nanoparticles in hexane onto holey carbon grids. HAADF-STEM images and electron energy loss (EELS) spectra were obtained with a Titan G^3 electron microscope operated at 120 kV equipped with a probe aberration corrector and GIF QUANTUM spectrometer.

The morphology and size of CdSe, CdS@CdSe, and ZnSe@CdS nanocrystals were investigated using transmission electron microscopy (TEM) performed with a LEO Omega 912AB microscope. The absorption spectra of the QDs in hexane sol in the wavelength range of 300–800 nm were recorded using Varian Cary 50 spectrometer.

Spectral dependence of the photoconductivity of QD/ZnO thick films was investigated in the range 430–700 nm with a step of 5 nm. To obtain illumination at a predetermined wavelength with a narrow spectral band, the radiation from a 100 W white light source was passed through a MDR-206 monochromator. The time of illumination at each wavelength was 20 s. The dark interval between consecutive measurements was 60 min. The conductivity of the samples was measured using a Keithley 6517 instrument. The photoconductivity was calculated as a conductance ratio:

$$\frac{\Delta\sigma}{\sigma_0} = \frac{\sigma(\lambda) - \sigma_0}{\sigma_0} \quad (1)$$

where $\sigma(\lambda)$ is film conductance under illumination with corresponding wavelength, σ_0–film conductance in dark conditions. The measurements were carried out in ambient air at room temperature.

The gas sensor measurements were carried out *in situ* in a 100 ml flow cell under conditions of a controlled gas flow of 100 ± 0.1 ml/min at room temperature (25 ± 2°C). Gas mixtures containing 0.12–2 ppm NO_2 in air were created by diluting the certified gas mixture (20.4 ± 0.9 ppm NO_2 in N_2) with dry synthetic air using Bronkhorst electronic gas flow controllers. The range of NO_2 concentrations is selected in accordance with the Recommendation from the Scientific Committee on Occupational Exposure Limits for Nitrogen Dioxide (2014) (8-h TWA is 0.5 ppm, STEL 15 min is 1 ppm) and the WHO guidelines (2010) for NO_2 in indoor air (1 h average is 0.1 ppm, annual average is 0.02 ppm). The DC conductivity measurements were carried out using a Keithley 6517A electrometer under conditions of periodic illumination with a green LED (20 mW/cm^2, the wavelength of the emitted light lies in the range 500–600 nm, λ_{max} = 535 nm). Flow through humidifier P-2 (Cellkraft AB) was used to adjust the humidity (RH_{25} = 0–40%) of gases passing through the sensor chamber.

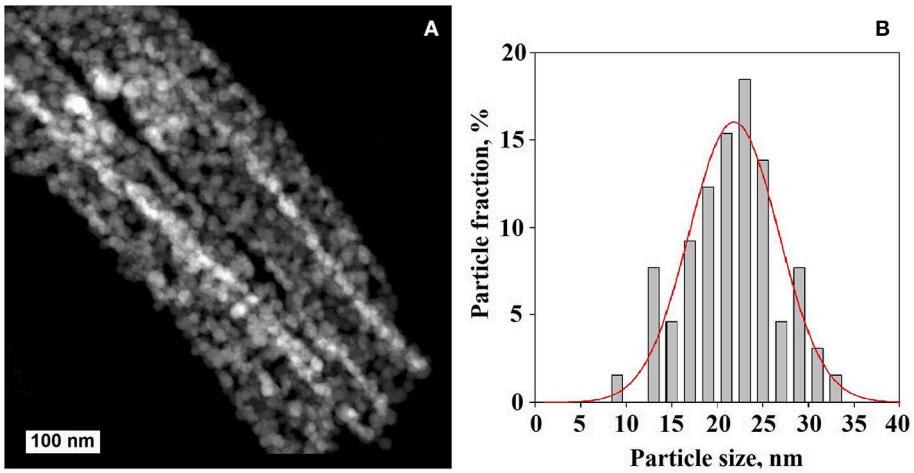

FIGURE 1 | HAADF-STEM image **(A)** and particle size distribution **(B)** of ZnO nanocrystalline matrix.

RESULTS AND DISCUSSION

X-ray powder diffraction data indicate that the annealing of zinc hydroxycarbonate results in the formation of ZnO with the wurtzite structure (**Supplementary Figure 1**). The average crystallite size, calculated from the broadening of the reflections using the Scherrer formula, is 15 ± 2 nm. The specific surface area was estimated from the low-temperature nitrogen adsorption data using the BET model to be 30 ± 5 m^2/g. According to the HAADF-STEM images (**Figure 1**), the material is composed of crystalline ZnO particles of random shape aggregated into agglomerates of mainly rod-shape form. The size of the ZnO particles varies from 8 to 33 nm with an average size of 21 ± 5 nm.

Synthesized CdSe nanocrystals have the crystalline structure of zinc-blende (**Supplementary Figure 2**). The crystallite size estimated by Scherrer formula is 3.0 ± 0.5 nm. Low magnification TEM images (**Figure 2**) show that CdSe nanocrystals obtained at 230°C for 35 s are nearly spherical and have a narrow size distribution of 2.8 ± 0.2 nm (**Figure 2**). The increase in synthesis temperature and duration leads to the growth of CdSe crystals up to 3.3 ± 0.1 nm. As a result of the formation of the CdS shell, the average size of nanocrystals increases to 4.2 ± 0.5 nm while maintaining a narrow size distribution (**Figure 2**). Thus, the shell thickness is about 0.5 nm, corresponding to $\sim$ 1 monolayer of CdS.

The absorption spectrum of the CdSe nanocrystals has the series of exciton transitions characteristic for spherical quantum dots with the distinct low-energy absorption maximum corresponding to the first exciton transition $1S_{h3/2}$–$1S_e$ at $\lambda =$ 536 nm (**Figure 3**). The increase in the particle size from 2.8 to 3.3 nm leads to a red shift of this absorption maximum by 40 nm, while maintaining a bandwidth due to narrow dispersion of sizes. The formation of CdS shell on the CdSe nuclei results in a further shift of the exciton maximum to the red region ($\lambda = 590$ nm) and retains a sharp exciton band confirming type I heterostructure formation. A small but distinct red shift corresponds to the delocalization of electron over the whole core–shell nanoparticle volume. At the same time, the hole remains localized in the CdSe core, which is supported by a strong increase in luminescence.

The average size of the synthesized CdS nanocrystals determined by TEM was 3.6 ± 0.8 nm. According to X-ray diffraction data, the synthesized CdS nanocrystals have a zinc blende structure (**Supplementary Figure 3**) and average size 4.0 $\pm$ 0.5 nm based on the broadening of the reflections. The buildup of the ZnSe shell on the surface of the CdS nuclei leads to an increase in the average particle size to 4.2 ± 1.2 nm accompanied by a substantial broadening of the particle size distribution (**Figure 2**). The ZnSe shell thickness thus does not exceed 1 nm, explaining why it is not detected by X-ray diffraction. The reflections of the CdS phase of the ZnSe@CdS heterostructures are shifted toward larger angles (**Supplementary Figure 3**). This corresponds to a decrease in the interplanar distances, and, consequently, of the unit cell parameter, which may be due to the compression of the CdS nucleus by the ZnSe shell with a smaller unit cell parameter.

The structure of ZnSe@CdS nanocrystals was investigated in detail by high resolution high angle annular dark field scanning transmission electron microscopy (HAADF-STEM) and electron energy loss spectroscopy (EELS). The sample consists of particles with a crystalline core and amorphous shell (**Figure 4**). The HAADF-STEM image of ZnSe@CdS nanocrystals (**Figure 4**) reveals the perfect crystal structure of the CdS core with a clear projection of the atomic columns. The corresponding Fast Fourier Transform (FFT) of the selected area (marked in a white square) can be indexed as the zinc-blende $F\bar{4}3m$ structure with a [001] zone axis.

The size of the crystalline core varies between 3 and 14 nm with the average value of 6 ± 2 nm. The thickness of the amorphous layer is of 1–2 nm. According to the STEM-EELS compositional mapping, the crystalline core of the particles contains Cd, whereas the amorphous layer around the core contains Zn (**Figure 4**).

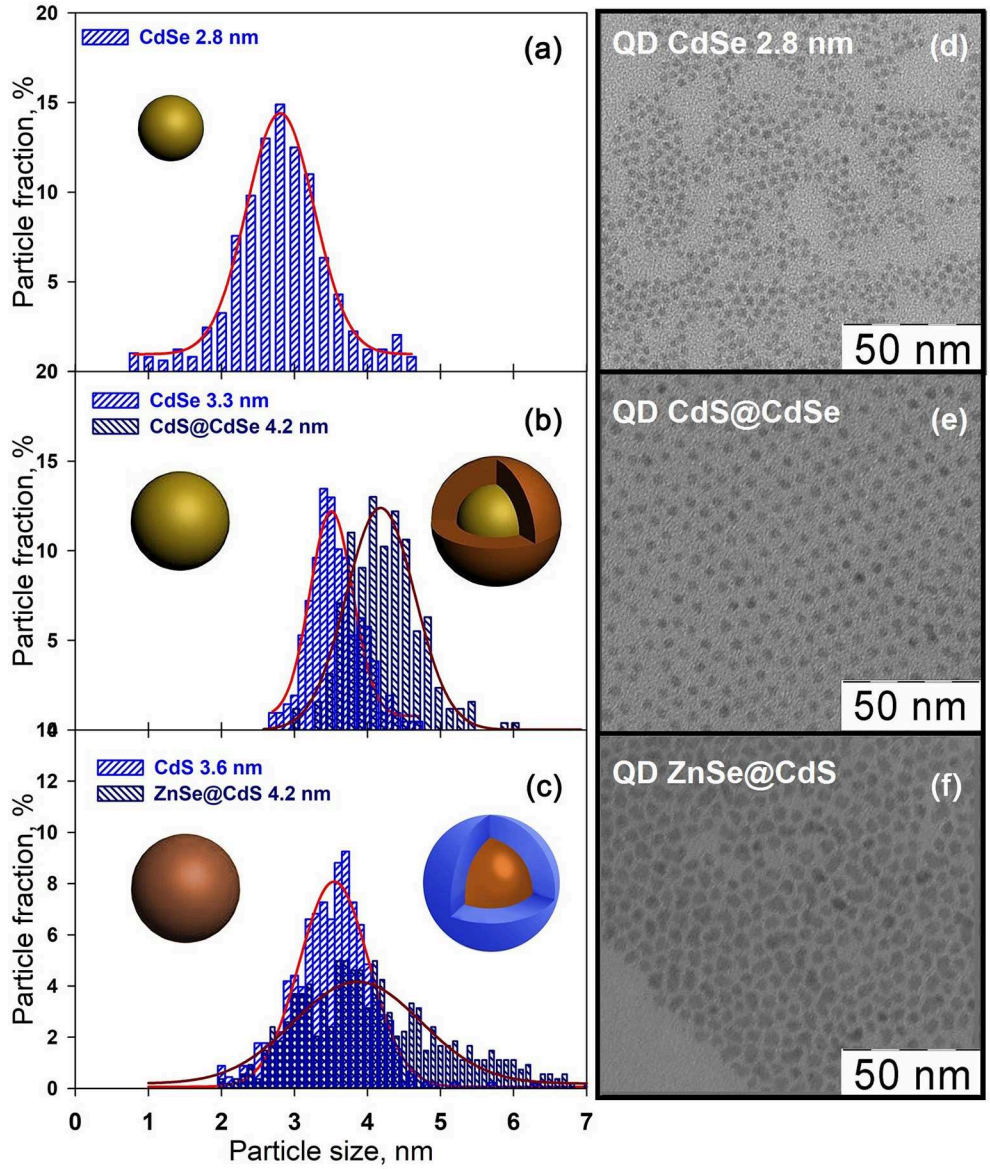

FIGURE 2 | Left panels: Particle size distribution of CdSe **(a)**, CdS@CdSe **(b)**, and ZnSe@CdS **(c)** nanocrystals. For CdS@CdSe and ZnSe@CdS heterostructures, the size distribution for the CdSe and CdS core is also presented. Right panels: Low magnification TEM images of CdSe **(d)**, CdS@CdSe **(e)**, and ZnSe@CdS **(f)** nanocrystals.

Analysis of the optical properties during the shell growth of ZnSe@CdS nanocrystals was used to verify type II heterostructure formation. The change in the absorption spectra of ZnSe@CdS nanocrystals is shown in **Figure 5A** as a function of the growth time (0–180 min) of the ZnSe shell on the surface of the CdS nuclei. The first exciton maximum in the 440–460 nm region is observed in the absorption spectrum of the CdS nanocrystals. With increasing ZnSe shell growth time, the band corresponding to an electronic transition in a heterostructure of type II with a spectral position of 550–620 nm can be distinguished in semilogarithmic coordinates (**Figure 5A**, inset). The profile of the spectra shows the appearance, growth of intensity and shift of this band to the red region. The form of the spectrum in the short-wavelength region remains practically unchanged. The inflection corresponding to the exciton absorption on the spectrum of the original CdS nuclei is conserved on the ZnSe@CdS nanocrystals spectra.

A narrow exciton band (520 nm, 2.38 eV) and a wide defect band in the long-wave region of the spectrum (550–700 nm) are present in the luminescence spectrum of the CdS nanocrystals (**Figure 5B**). As in the case of the absorption spectra, the change in the luminescence spectra with the growth time of the ZnSe shell proves that the system under investigation belongs to type II heterostructures. The appearance and growth of the intensity

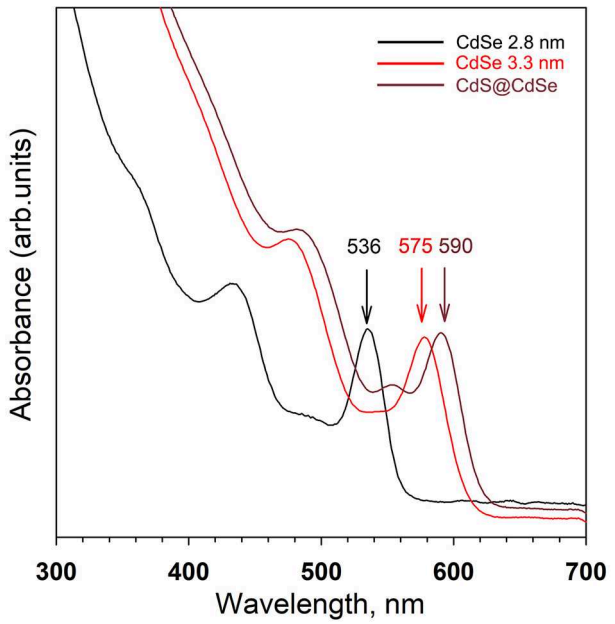

FIGURE 3 | Optical absorption spectra of CdSe and CdS@CdSe nanocrystals.

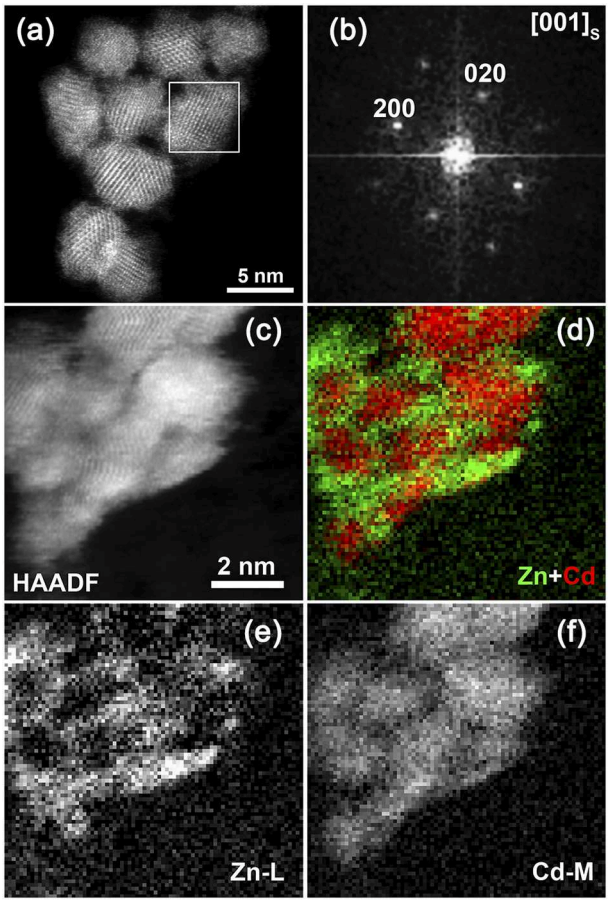

FIGURE 4 | (a,b) HAADF-STEM image of the ZnSe@CdS nanocrystals and Fourier transform of the selected area indexed in the zinc-blende structure; **(c–f)** HAADF-STEM image of the ZnSe@CdS nanocrystals, the maps of the Zn-L and Cd-M EELS signals and the color-coded mixed compositional map.

of the luminescence band in the long-wave region (600–625 nm) is observed in the luminescence spectra. The energy of this band is less than the band gap of the core material (E_g (CdS) = 2.42 eV, ∼ 512 nm) and the shell material (E_g (ZnSe) = 2.82 eV, ∼440 nm), confirming the formation of a type II heterostructure (Ivanov et al., 2007). Simultaneously, the luminescence band caused by the recombination of charge carriers on defects disappears practically completely, indicating the passivation of surface defects of CdS.

To determine the effect of nanocrystals of CdSe, CdS@CdSe, and ZnSe@CdS on ZnO electrical properties under visible light illumination, the spectral dependences of the photoconductivity of QD/ZnO (QD = CdSe, CdS@CdSe, ZnSe@CdS) nanocomposites were investigated (**Figure 6**). The photoconductivity of pure ZnO in these conditions is negligibly small (Chizhov et al., 2014, 2016). The appearance and maxima in the photoresponse curve of the nanocomposites matches well with the onset and the maxima in the absorption spectra of the QDs. For all ZnO/QD nanocomposites, there is an important increase in the photoconductivity in the visible range ($\lambda <$ 600 nm) under illumination with a photon energy of 2.06 eV which is much less than the ZnO band gap (3.3 eV). This indicates the transfer of electrons, photoexcited at quantum dots, to the conduction band of the semiconductor oxide.

Our previous studies of the photoconductivity and gas sensor properties of nanocrystalline ZnO sensitized with CdSe and InP quantum dots have shown that the periodic backlight mode is more convenient than the constant one (Chizhov et al., 2018). This periodic mode consists in alternation of short (2 min) light on/off periods that leads to the corresponding periodic change in photoconductivity. When the lighting cycle is repeated multiple times, the system comes to a stationary state, which can be characterized by the minimum sensor resistance R_λ, which is achieved under illumination, and the maximum sensor resistance R_{dark}, which is achieved in dark period.

When illuminated with a green LED (λ_{max} = 535 nm), a decrease in the resistance is observed for all nanocomposites (**Figure 7**, inset). When the light is turned off, the resistance of the nanocomposites increases. Such a change in the electrophysical characteristics of the nanocomposites is due to the simultaneous occurrence of a complex set of processes. When the nanocomposite is illuminated by radiation corresponding to the energy of the first exciton transition $1S_h$-$1S_e$, an electron-hole pair is generated in the quantum dot and the electron is excited to the corresponding energy level. The main mechanism for transfer of photoexcitation from quantum dots to metal oxide is the injection (transfer) of charge carriers. From the thermodynamic point of view, the possibility of injecting charge carriers is provided by lowering the free energy of the system because of this process. In the first approximation, one can assume that the condition for the injection of electrons from the quantum dot into the metal oxide is the position of the $1S_e$

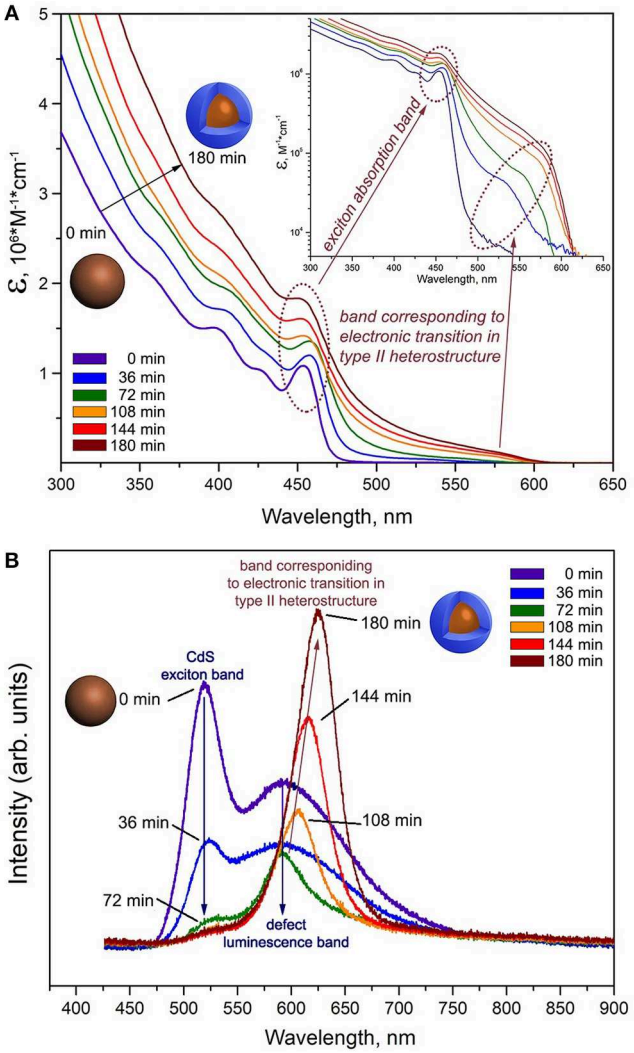

FIGURE 5 | (A) Evolution of optical absorption spectra of aliquots taken from the reaction mixture during the growth of the ZnSe shell on CdS nuclei in function of growth time (0–180 min). The data are presented in the form of spectral dependence of extinction coefficient ε. Inset: Absorption spectra in semilogarithmic coordinates. **(B)** Evolution of luminescence spectra of aliquots taken from the reaction mixture during the growth of the ZnSe shell on CdS nuclei in function of growth time (0–180 min).

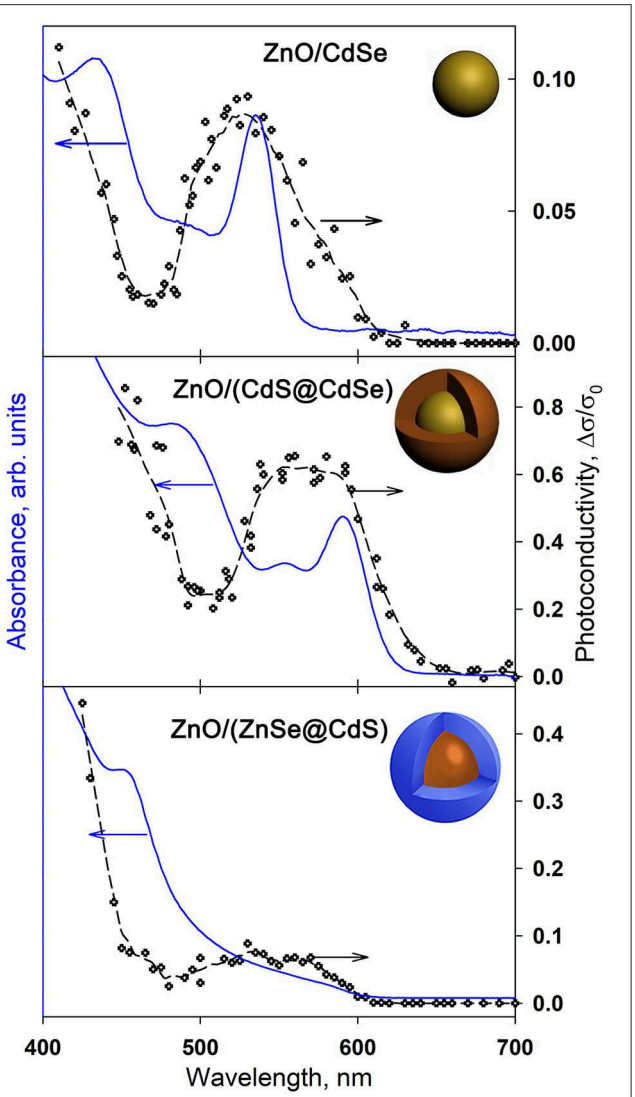

FIGURE 6 | Absorption spectra and spectral dependences of photoconductivity of ZnO/QDs nanocomposites.

level above the bottom of the conduction band (Chizhov et al., 2016). This case is observed in the sensitization of oxides such as In_2O_3, SnO_2, ZnO, with $A^{II}B^{VI}$, $A^{IV}B^{VI}$, $A^{III}B^{V}$ quantum dots etc. Electron transfer in the opposite direction—from metal oxide to photoexcited QD is possible if the position of the $1S_h$ level is below the bottom of the conduction band, which can also be regarded as the injection of holes from the photoexcited QD into the valence band of the metal oxide. This case is less common, and is observed, for example, with the sensitization of NiO with CdSe quantum dots (Zheng et al., 2014). Thus, the preferred direction of photoinduced electron transfer between the metal oxide and the quantum dot is determined by the mutual arrangement of their electronic levels.

Another process that causes a change in the electrophysical properties of a semiconductor under illumination is the photostimulated desorption of adsorbed molecules. It is known that the interaction of the atmospheric oxygen with the surface of *n*-type semiconductor oxides leads to the formation of molecular and atomic chemisorbed forms of oxygen. At temperatures below 200°C, the predominant form is molecular ion $O^-_{2(ads)}$:

$$O_{2(gas)} + e^- \leftrightarrow O^-_{2(ads)}, \quad (2)$$

where $O_{2(gas)}$ is an oxygen molecule in the gas phase. The localization of electrons on chemisorbed particles results in the formation of an electron depleted layer near the surface of the semiconductor oxide and in an increase in the resistance of the semiconductor under dark conditions. Under illumination, the photoexcited holes can be transferred from quantum dots to the

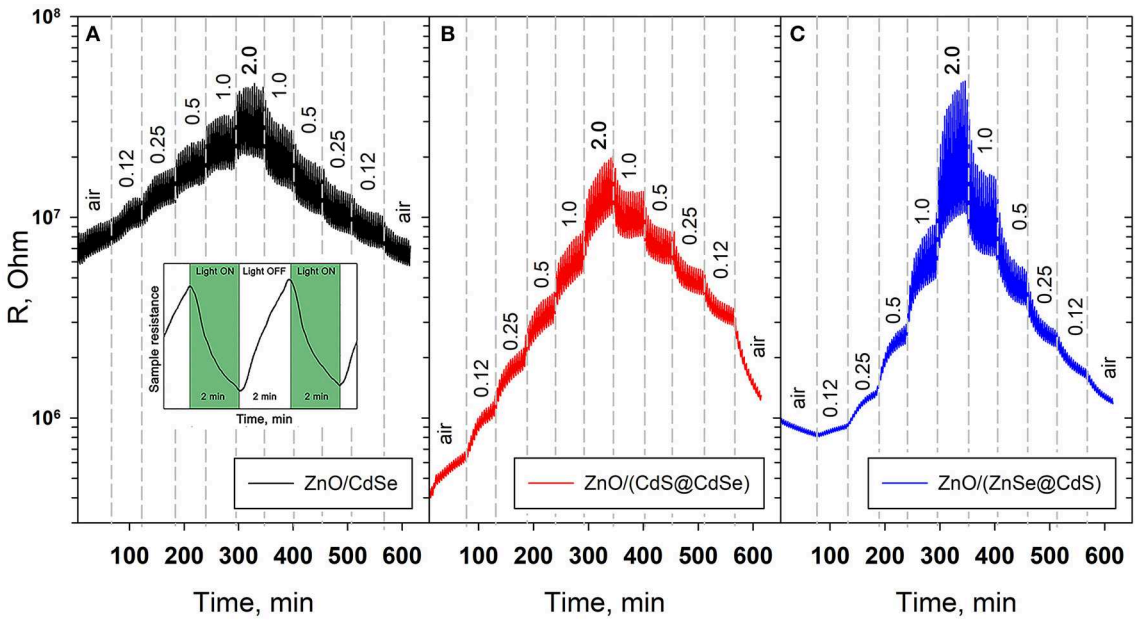

FIGURE 7 | Room temperature electrical resistance of **(A)** ZnO/CdSe, **(B)** ZnO/(CdS@CdSe), and **(C)** ZnO/(ZnSe@CdS) nanocomposites under periodic green light illumination (λ_{max} = 535 nm) depending on NO_2 content in the gas phase (in ppm). Inset: change of the sensing layer resistance under periodic LED illumination.

metal oxide by switching to local energy levels inside its forbidden zone (in other words, the electron is transferred from the local level of metal oxide to the quantum dot, resulting in the recovery of its electroneutrality). The holes transferred in this way can recombine with the electrons localized by chemisorbed oxygen on the surface of a semiconductor oxide:

$$O^-_{2(ads)} + h^+ \leftrightarrow O_{2(gas)}. \quad (3)$$

As a consequence, the oxygen molecule passes into a neutral physically adsorbed form, which can be removed back to the gas phase while the electron trapped by the oxygen returns to the semiconductor. So, the absorption of one photon actually leads to the transfer of two electrons into the conduction band of the metal oxide (Medved, 1961).

The sensor properties in NO_2 detection with periodic illumination were measured at room temperature for all nanocomposites. The concentration of NO_2 was changed stepwise, first increasing, then decreasing. The duration of each stage was 60 min, so 15 "dark–illumination" cycles were recorded for each NO_2 concentration.

As the concentration of NO_2 grows, both the resistances R_λ and R_{dark} increase (**Figure 7**). Using the example of SnO_2, the authors (Sergent et al., 2007) showed by Raman spectroscopy that the electrical conductivity of *n*-type semiconductor oxides in the presence of NO_2 correlates with the concentration of surface bidentate nitrite groups. So, based on the assumption that the chemisorption of NO_2 molecules proceeds with the capture of the conduction electron, and the chemisorbed NO_2 species are not dissociated, the following processes can be responsible for the formation of sensor response toward NO_2:

$$NO_{2(gas)} + e^- \leftrightarrow NO^-_{2(ads)} \quad (4)$$

$$NO_{2(gas)} + O^-_{2(ads)} \leftrightarrow NO^-_{2(ads)} + O_{2(gas)} \quad (5)$$

Due to the significant difference in the electron affinities E_{aff} of O_2 and NO_2 molecules (0.45 and 2.27 eV, respectively), the equilibrium (5) is shifted to the right, and chemisorbed NO_2 species should form deeper local levels in the forbidden zone of zinc oxide, on which the electrons localize. Therefore, even in the presence of excess of oxygen, the concentration of NO_2 in air becomes the controlling factor affecting the semiconductor conductivity.

Under green light illumination, when photoexcitation of the quantum dots occurs, the photoexcited electrons are injected from the QD into the oxide matrix, but photoexcited holes remain at the QD. Through interaction with local levels within the forbidden ZnO band, these photoexcited holes can also be injected into the oxide matrix, where they then recombine with the electrons localized in chemisorbed molecules of O_2 (Equation 3) and NO_2:

$$NO^-_{2(ads)} + h^+ \leftrightarrow NO_{2(gas)} \quad (6)$$

The result of this process is the release of an electron captured by chemisorbed molecules, the transition of molecules involved in the recombination into a physically adsorbed form, followed by their desorption, and the recovery of the quantum dot electrical neutrality. A schematic diagram of the interaction between ZnO matrix, QD and NO_2 molecules is shown in **Figure 8**.

The comparison of hybrid materials can be made based on a diagram reflecting the position of the energy bands and levels in the systems under investigation (**Figure 9**). The positions of ZnO valence (E_V) and conduction (E_C) bands were taken from Stevanović et al. (2014), and the positions of the $1S_h$ and $1S_e$ energy levels in CdSe quantum dots and CdS@CdSe and ZnSe@CdS heterostructures were calculated from optical absorption spectra. For this calculation we assumed that on decreasing size of the nanocrystals, the displacement of the edges of the valence and conduction bands is inversely proportional to the effective mass of electrons and holes in this material (Klimov, 2000; Vasiliev et al., 2011). In the model we propose, the most uncertain information is the energy of electrons localized in chemisorbed O_2 and NO_2 molecules. The literature states that the levels of electrons in O_2 molecules chemisorbed on the ZnO surface are 1.1–0.8 eV below the edge of the conduction band (Kiselev and Krylov, 2012). The information on the energy of trapped electrons in chemisorbed NO_2 molecules is not available. However, since for ZnO/CdSe nanocomposites the total recovery of conductivity to the base value occurs in experiments with NO_2 under constant illumination (Chizhov et al., 2014) it can be assumed that this is due to the complete NO_2 photodesorption. This is the case when the local levels of trapped electrons in the chemisorbed NO_2 molecules are close in energy with the $1S_h$ energy level in QDs. From the diagram in **Figure 9** one can see that in such case the assumed position of the electron levels in $NO^-_{2(ads)}$ can be in the range of 1.2–2.3 eV below the edge of the ZnO conduction band.

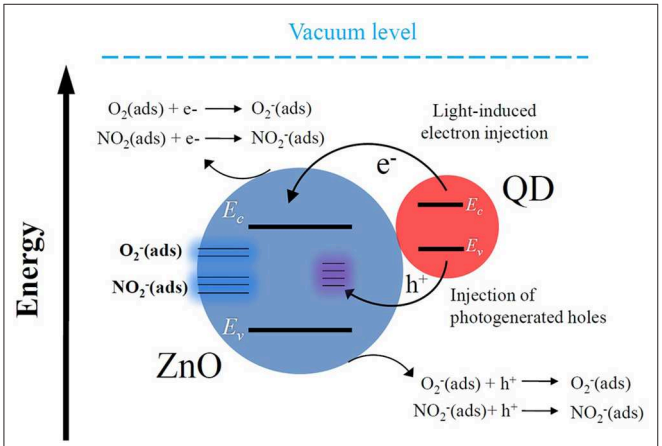

FIGURE 8 | A schematic diagram of the interaction between ZnO matrix, QD and NO_2 and O_2 molecules.

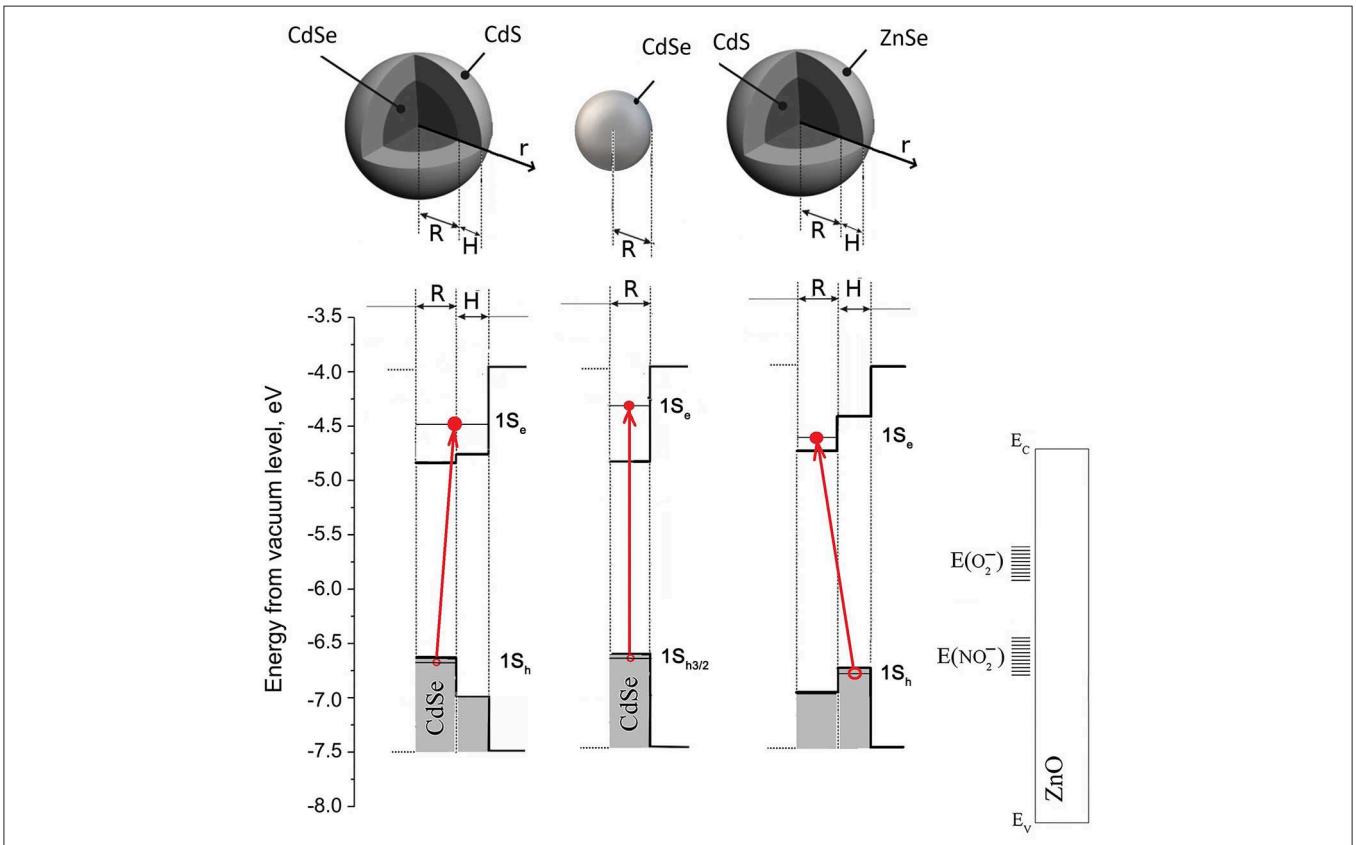

FIGURE 9 | Band diagram for ZnO/CdSe, ZnO/(CdS@CdSe), and ZnO/(ZnSe@CdS) systems. Band alignment for core-shell nanocrystals with core radius R and shell thickness H is shown. Band parameters are taken from O'Connor et al. (2012) and Yang et al. (2014). Electron-hole separation is shown by red arrows.

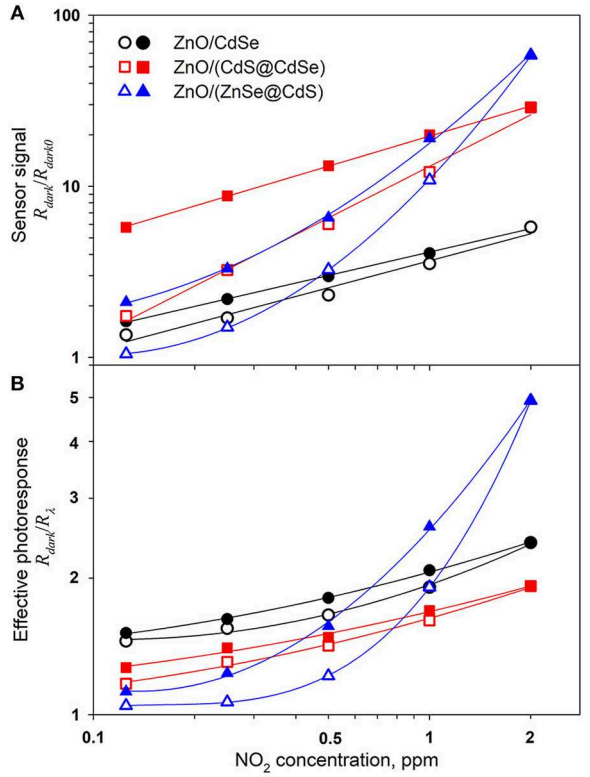

FIGURE 10 | Sensor signal $S = R_{dark}/R_{dark0}$ **(A)** and effective photoresponse $P_{eff} = R_{dark}/R_{\lambda}$ **(B)** of ZnO/CdSe, ZnO/(CdS@CdSe), and ZnO/(ZnSe@CdS) nanocomposites under periodic green light illumination ($\lambda_{max} = 535$ nm) with increasing (open symbols) and decreasing (filled symbols) NO_2 concentration in the gas phase.

When performing gas sensor measurements under periodic illumination conditions, the sensor signal may be calculated in different ways: (i) as the ratio of dark resistances $S = R_{dark}/R_{dark0}$, where R_{dark} is the dark resistance at given NO_2 concentration, R_{dark0} is the dark resistance in pure air; (ii) as the amplitude of effective photoresponse $P_{eff} = R_{dark}/R_{\lambda}$ at given NO_2 concentration. The change of these parameters with increasing and decreasing NO_2 concentration in air is presented in **Figure 10**. For nanocomposites ZnO/CdSe and ZnO/(CdS@CdSe) the concentration dependencies of the sensor signal are linear in double logarithmic coordinates (**Figure 10A**) that indicates their power-law nature, typical for the resistive type sensors (Yamazoe and Shimanoe, 2008):

$$S \propto p_{NO_2}^{m}. \tag{7}$$

Approximation of the experimental dependencies (with increasing NO_2 concentration) by the power function gives $m = 0.5$ and $m = 1$ for ZnO/CdSe and ZnO/(CdS@CdSe), respectively. For the latter system, perfect passivation of the CdSe core defect states eliminates side effects (Drozdov et al., 2013). This ensures the maximum concentration of electrons photogenerated at the quantum dot and transferred to the conduction band of the semiconductor during illumination, which can be then captured in dark conditions by the acceptor NO_2 molecules in accordance with the reaction (4). The concentration dependence of the sensor signal of nanocomposite ZnO/(ZnSe@CdS) is not linearized in double logarithmic coordinates. This dissimilarity may be caused by the fact that the shell growth on the core nanocrystal results in formation of heterostructures with different electron-hole spatial localization. In CdS@CdSe nanocrystals the photogenerated hole is localized strongly inside CdSe core, whereas the photoexcited electron is delocalized over whole core/shell nanocrystal. Oppositely, in ZnSe@CdS nanocrystals the electron is localized inside CdS core, whereas the hole is localized inside ZnSe shell.

As can be seen from the energy diagram (**Figure 9**), the formation of ZnSe@CdS type II heterostructure does not lead to a drastic change in the position of the $1S_h$ and $1S_e$ levels of a hole and an electron, respectively, as compared with a CdSe quantum dot and CdS@CdSe type I heterostructure. At the same time, the probability of the electron and hole transfer processes between the sensitizer and ZnO matrix is fundamentally different. The preferential spatial localization of a hole in the ZnSe shell (Ivanov et al., 2007) provides its more efficient transfer from the ZnSe@CdS sensitizer to the ZnO matrix. This leads to an increase in the probability of tunneling of electrons localized at the acceptor levels of chemisorbed NO_2 molecules to the $1S_h$ level at the sensitizer, promoting NO_2 desorption. In other words, in a quasi-equilibrium state under photoexcitation conditions, the larger efficiency of hole transfer from the ZnSe shell to localized levels in the ZnO forbidden band as compared with electron transfer from the CdS nucleus to the ZnO conduction band will lead to the partial negative charging of ZnSe@CdS nanocrystals. This, in turn, will lead to the discharge of the acceptor levels in the ZnO band gap, corresponding to the electrons trapped by chemisorbed NO_2 molecules.

Thus, in ZnSe@CdS nanocrystals, the shell plays a dual role. On the one hand, as in the case of type I heterostructure CdS@CdSe, the shell formation leads to the perfect passivation of CdS core defect states, ensuring the maximum concentration of photogenerated electrons transferred to the ZnO conduction band and then captured by the acceptor NO_2 molecules in dark interval of the measurement cycle. On the other hand, the localization of a hole in ZnSe shell ensures the efficient charge transfer from chemisorbed NO_2 molecules and their subsequent desorption in the light interval of the measurement cycle. The synergetic combination of these factors leads to a significant increase in the light activated sensor sensitivity to NO_2 in case of ZnO/ZnSe@CdS nanocomposites compared with ZnO/CdSe and ZnO/(CdS@CdSe) samples.

The validity of these arguments is confirmed by the character of the NO_2 concentration dependence of the effective photoresponse for different nanocomposites (**Figure 10B**). The hole localization in the CdSe core reduces the efficiency of its transfer to the ZnO matrix that leads to a decrease in the photoresponse of the ZnO/(CdS@CdSe) nanocomposite in comparison with ZnO/CdSe. On the contrary, the hole localization in the ZnSe shell promotes the transfer of electrons from acceptor levels in the ZnO forbidden zone. Consequently, the effective photoresponse of

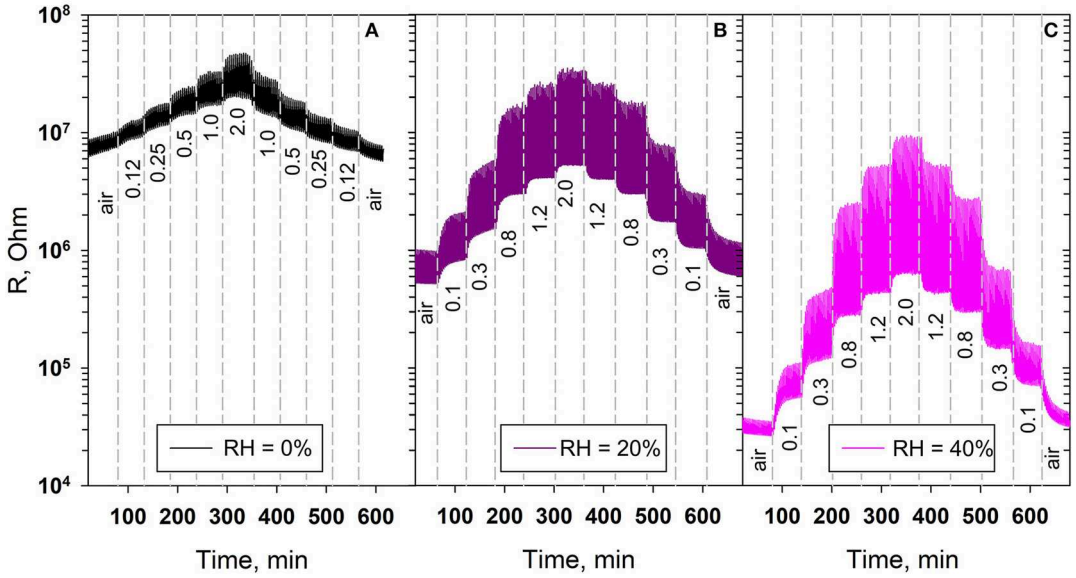

FIGURE 11 | Room temperature electrical resistance of ZnO/CdSe nanocomposites under periodic green light illumination (λ_{max} = 535 nm) depending on NO_2 content in the gas phase (in ppm) at **(A)** RH_{25} = 0%, **(B)** RH_{25} = 20%, **(C)** RH_{25} = 40%.

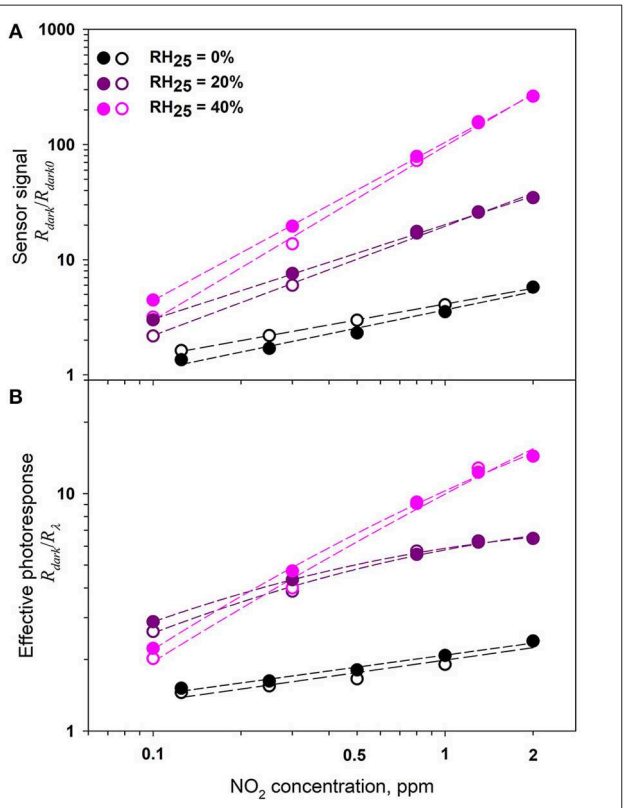

FIGURE 12 | Sensor signal $S = R_{dark}/R_{dark0}$ **(A)** and effective photoresponse $P_{eff} = R_{dark}/R_{\lambda}$ **(B)** of ZnO/CdSe nanocomposite under periodic green light illumination (λ_{max} = 535 nm) with increasing (open symbols) and decreasing (filled symbols) NO_2 concentration in the gas phase at different humidity.

ZnO/(ZnSe@CdS) nanocomposite grows rapidly with increasing NO_2 concentration in air.

At the same time, as one can note from **Figure 7**, the sensors containing CdS@CdSe and ZnSe@CdS core-shell nanoparticles exhibit significant signal drift. The reasons of this drift can be discussed as follows. Formation of the type I CdS(shell)@CdSe(core) heterostructure with a straddling gap arrangement leads to the perfect passivation of CdSe core defect states and to the localization of photogenerated holes inside the CdSe core. The first factor determines the increase in sensor sensitivity toward NO_2, while the latter one leads to the decrease in effective photoresponse at given NO_2 concentration, and increase in the time needed to recover the signal of ZnO/(CdS@CdSe) nanocomposites as compared with ZnO/CdS hybrid material. In ZnO/(ZnSe@CdS) hybrid material the hole localization in the shell of nanoparticle CdS@CdSe results in the increase of contribution from the capturing of photoexcited charges at surface traps. This changes the charge-injection processes at the nanocrystal-matrix interface. It may lead to long-lived charge accumulation and the increase of the relaxation time resulted in the change of steady-state conductivity.

The effect of humidity on the values of the sensor response and the effective photoresponse as a function of the NO_2 concentration was studied for ZnO/CdSe hybrid materials. **Figure 11** shows the change in room temperature electrical resistance of ZnO/CdSe nanocomposites under periodic green light illumination depending on NO_2 content in dry (RH_{25} = 0%) and humid (RH_{25} = 20% and RH_{25} = 40%) air. We have to note the following: with increasing humidity, (i) the resistance of ZnO/CdSe in pure air decreases, and (ii) the sensor response and the effective photoresponse of ZnO/CdSe increase. This may

be due to the adsorption of water vapor on the ZnO surface, which leads to an increase in the concentration of free charge carriers (electrons) in *n*-type semiconductor oxides (Bârsan and Weimar, 2001). In turn, this stimulates the adsorption of NO_2 by reaction (4), which leads to an increase in the sensor signal and an increase in the effective photoresponse (**Figure 12**). The low detection limit (LDL) values were calculated from the calibration curves as NO_2 concentration corresponding to the minimum measurable sensor signal $(R_{av} + 3\sigma)/R_{av}$, where R_{av} is the average dark resistance in pure air with given humidity, σ is the standard deviation of average dark resistance in pure air with given humidity. An increase in the air humidity is accompanied by a decrease in LDL from 58 ppb ($RH_{25} = 0\%$) to 49 ppb ($RH_{25} = 40\%$).

CONCLUSIONS

We investigated the photoconductivity and visible light activated room temperature NO_2 gas sensor properties of hybrid materials based on nanocrystalline ZnO sensitized with two types of core/shell nanoparticles with different localization of photoexcited electron-hole pair between the core and the shell. Formation of the type I CdS(shell)@CdSe(core) heterostructure with a straddling gap arrangement leads to the localization of photogenerated holes inside the CdSe core and to the perfect passivation of CdSe core defect states. These factors determine the increase of sensor sensitivity toward NO_2 and the decrease of effective photoresponse at given NO_2 concentration of ZnO/(CdS@CdSe) nanocomposites as compared with ZnO/CdS hybrid material. In type II ZnSe(shell)@CdS(core) heterostructures with staggered gap, the shell formation also provides the perfect passivation of CdS core defect states but in this case the photogenerated hole localization in the ZnSe shell ensures the efficient charge transfer from chemisorbed NO_2 molecules and their subsequent desorption under illumination. Compared with ZnO/CdSe and ZnO/(CdS@CdSe) samples, in case of ZnO/ZnSe@CdS nanocomposites the synergetic combination of these factors leads to a significant increase in the light activated sensor sensitivity to NO_2 and to the rapid growth of effective photoresponse with increasing NO_2 concentration in air.

Thus, the use of heterostructures with different spatial separation of photogenerated charges opens new possibilities in controlling the photoelectric and light activated gas sensor properties of hybrid nanomaterials based on wide gap semiconductor oxides with quantum dots of narrow-band semiconductors as photosensitizers.

DATA AVAILABILITY STATEMENT

All datasets generated for this study are included in the manuscript/**Supplementary Files**.

AUTHOR CONTRIBUTIONS

AC, RV, MR, and AG contributed conception and design of the study. AC and RV performed the synthesis of all the materials. RV effectuated the optical characterization of the materials. AC performed the sensor measurements. IK and KD conducted photoelectrical characterization of the materials. MB, JH, and AA effectuated HAADF-STEM and EELS analysis. MR and RV wrote the first draft of the manuscript. All authors contributed to manuscript revision, read, and approved the submitted version.

FUNDING

This work was financially supported by RFBR grant No. 16-53-76001 (RFBR – ERA.Net FONSENS 096) and in part by a grant from the St. Petersburg State University – Event 3-2018 (id: 26520408). AC acknowledges support from the RFBR grant No. 18-33-01004.

SUPPLEMENTARY MATERIAL

The Supplementary Material for this article can be found online at: https://www.frontiersin.org/articles/10.3389/fmats.2019.00231/full#supplementary-material

REFERENCES

Bârsan, N., and Weimar, U. (2001). Conduction model of metal oxide gas sensors. *J. Electroceram.* 7, 143–167. doi: 10.1023/A:1014405811371

Carotta, M. C., Cervi, A., Fioravanti, A., Gherardi, S., Giberti, A., Vendemiati, B., et al. (2011). A novel ozone detection at room temperature through UV-LED-assisted ZnO thick film sensors. *Thin Solid Films* 520, 939–946. doi: 10.1016/j.tsf.2011.04.173

Chizhov, A., Rumyantseva, M., Vasiliev, R., Filatova, D., Drozdov, K., Krylov, I., et al. (2016). Visible light activation of room temperature NO_2 gas sensors based on ZnO, SnO_2 and In_2O_3 sensitized with CdSe quantum dots. *Thin Solid Films* 618, 253–262. doi: 10.1016/j.tsf.2016.09.029

Chizhov, A. S., Mordvinova, N. E., Rumyantseva, M. N., Krylov, I. V., Drozdov, K. A., Li, X., et al. (2018). The effect of CdSe and InP quantum dots on the interaction of ZnO with NO_2 under visible light irradiation. *Russ. J. Inorg. Chem.* 63, 512–518. doi: 10.1134/S0036023618040071

Chizhov, A. S., Rumyantseva, M. N., Vasiliev, R. B., Filatova, D. G., Drozdov, K. A., Krylov, I. V., et al. (2014). Visible light activated room temperature gas sensors based on nanocrystalline ZnO sensitized with CdSe quantum dots. *Sens. Actuators B* 205, 305–312. doi: 10.1016/j.snb.2014.08.091

Cui, J., Wang, D., Xie, T., and Lin, Y. (2013). Study on photoelectric gas-sensing property and photogenerated carrier behavior of Ag–ZnO at the room temperature. *Sens. Actuators B* 186, 165–171. doi: 10.1016/j.snb.2013.05.088

Da Silva, L. F., M'Peko, J.-C., Catto, A. C., Bernardini, S., Mastelaro, V. R., Aguir, K., et al. (2017). UV-enhanced ozone gas sensing response of ZnO-SnO_2 heterojunctions at room temperature. *Sens. Actuators B* 240, 573–579. doi: 10.1016/j.snb.2016.08.158

De Lacy Costello, B. P. J., Ewen, R. J., Ratcliffe, N. M., and Richards, M. (2008). Highly sensitive room temperature sensors based on the UV-LED activation of zinc oxide nanoparticles. *Sens. Actuators B* 134, 945–952. doi: 10.1016/j.snb.2008.06.055

Drozdov, K. A., Kochnev, V. I., Dobrovolsky, A. A., Popelo, A. V., Rumyantseva, M. N., Gaskov, A. M., et al. (2013). Photoconductivity of structures based on the SnO_2 porous matrix coupled with core-shell CdSe/CdS quantum dots. *Appl. Phys. Lett.* 103:133115. doi: 10.1063/1.4823549

Espid, E., and Taghipour, F. (2017). UV-LED photo-activated chemical gas sensors: a review. *Crit. Rev. Solid State Mater. Sci.* 42, 416–432. doi: 10.1080/10408436.2016.1226161

Geng, Q., He, Z., Chen, X., Dai, W., and Wang, X. (2013). Gas sensing property of ZnO under visible light irradiation at room temperature. *Sens. Actuators B* 188, 293–297. doi: 10.1016/j.snb.2013.07.001

Geng, X., You, J., and Zhang, C. (2016a). Microstructure and sensing properties of CdS-ZnO_{1-x} coatings deposited by liquid plasma spray and treated with hydrogen peroxide solution for nitrogen dioxide detection at room temperature. *J. Alloys Compd.* 687, 286–293. doi: 10.1016/j.jallcom.2016.06.079

Geng, X., Zhang, C., and Debliquy, M. (2016b). Cadmium sulfide activated zinc oxide coatings deposited by liquid plasma spray for room temperature nitrogen dioxide detection under visible light illumination. *Ceram. Int.* 42, 4845–4852. doi: 10.1016/j.ceramint.2015.11.170

Han, L., Wang, D., Cui, J., Chen, L., Jiang, T., and Lin, Y. (2012). Study on formaldehyde gas-sensing of In_2O_3-sensitized ZnO nanoflowers under visible light irradiation at room temperature. *J. Mater. Chem.* 22, 1295–12920. doi: 10.1039/c2jm16105b

Han, L., Wang, D., Lu, Y., Jiang, T., Chen, L., Xie, T., et al. (2013). Influence of annealing temperature on the photoelectric gas sensing of Fe-doped ZnO under visible light irradiation. *Sens. Actuators B* 177, 34–40. doi: 10.1016/j.snb.2012.10.096

Hsu, C.-L., and Chang, L.-F., Hsueh, T.-J. (2017). Light-activated humidity and gas sensing by ZnO nanowires grown on LED at room temperature. *Sens. Actuators B* 249, 265–277. doi: 10.1016/j.snb.2017.04.083

Hyodo, T., Urata, K., Kamada, K., Ueda, T., and Shimizu, Y. (2017). Semiconductor-type SnO_2-based NO_2 sensors operated at room temperature under UV-light irradiation. *Sens. Actuators B* 253, 630–640. doi: 10.1016/j.snb.2017.06.155

Ilin, A., Martyshov, M., Forsh, E., Forsh, P., Rumyantseva, M., Abakumov, A., et al. (2016). UV effect on NO_2 sensing properties of nanocrystalline In_2O_3. *Sens. Actuators B* 231, 491–496. doi: 10.1016/j.snb.2016.03.051

Ivanov, S. A., Piryatinski, A., Nanda, J., Tretiak, S., Zavadil, K. R., Wallace, W. O., et al. (2007). Type-II core/shell CdS/ZnSe nanocrystals: synthesis, electronic structures, and spectroscopic properties. *J. Am. Chem. Soc.* 129, 11708–11719. doi: 10.1021/ja068351m

Kim, Y.-S., Hummer, K., and Kresse, G. (2009). Accurate band structures and effective masses for InP, InAs, and InSb using hybrid functionals. *Phys. Rev. B* 80:035203. doi: 10.1103/PhysRevB.80.035203

Kiselev, V. F., and Krylov, O. V. (2012). "Adsorption and catalysis on transition metals," in *Adsorption and Catalysis on Transition Metals and Their Oxides (Springer Series in Surface Sciences), Vol. 9*, eds G. Ertl, R. Gomer, and H. K. V. Lotsch (Berlin; Heidelberg: Springer; Springer Science + Business Media), 136–265.

Klaus, D., Klawinski, D., Amrehn, S., Tiemann, M., and Wagner, T. (2015). Light-activated resistive ozone sensing at room temperature utilizing nanoporous In_2O_3 particles: influence of particle size, *Sens. Actuators B* 217, 181–185. doi: 10.1016/j.snb.2014.09.021

Klimov, V. I. (2000). Optical nonlinearities and ultrafast carrier dynamics in semiconductor nanocrystals. *J. Phys. Chem. B* 104, 6112–6123. doi: 10.1021/jp9944132

Krivetskiy, V. V., Rumyantseva, M. N., and Gaskov, A. M. (2013). Chemical modification of nanocrystalline tin dioxide for selective gas sensors. *Russ. Chem. Rev.* 82, 917–941. doi: 10.1070/RC2013v082n10ABEH004366

Malagu, C., Carotta, M. C., Comini, E., Faglia, G., Giberti, A., Guidi, V., et al. (2005). Photo-induced unpinning of Fermi level in WO_3. *Sensors* 5, 594–603. doi: 10.3390/s5120594

Medved, D. (1961). Photoconductivity and chemisorption kinetics in sintered zinc oxide semiconductor. *J. Phys. Chem. Solids* 20, 255–267. doi: 10.1016/0022-3697(61)90012-9

Minami, T., Miyata, T., and Yamamoto, T. (1998). Work function of transparent conducting multicomponent oxide thin films prepared by magnetron sputtering. *Surf. Coat. Technol.* 108–109, 583–587. doi: 10.1016/S0257-8972(98)00592-1

Mishra, S., Ghanshyam, C., Ram, N., Bajpai, R. P., and Bedi, R. K. (2004). Detection mechanism of metal oxide gas sensor under UV radiation. *Sens. Actuators B* 97, 387–390. doi: 10.1016/j.snb.2003.09.017

Mordvinova, N. E., Vinokurov, A. A., Dorofeev, S. G., Kuznetsova, T. A., and Znamenkov, K. O. (2014). Phosphine synthetic route features and post synthetic treatment of InP quantum dots. *J. Alloys Compd.* 582, 43–49. doi: 10.1016/j.jallcom.2013.08.003

Nakate, U. T., Patil, P., Bulakhe, R. N., Lokhande, C. D., Kale, S. N., Naushad, M., et al. (2016). Sprayed zinc oxide films: ultra-violet light-induced reversible surface wettability and platinum-sensitization-assisted improved liquefied petroleum gas response. *J. Colloid Interface Sci.* 480, 109–117. doi: 10.1016/j.jcis.2016.07.010

O'Connor, T., Panov, M. S., Mereshchenko, A., Tarnovsky, A. N., Lorek, R., Perera, D., et al. (2012). The effect of the charge-separating interface on exciton dynamics in photocatalytic colloidal heteronanocrystals. *ACS Nano* 6, 8156–8165. doi: 10.1021/nn302810y

Paolesse, R., Nardis, S., Monti, D., Stefanelli, M., and Di Natale, C. (2017). Porphyrinoids for chemical sensor applications. *Chem. Rev.* 117, 2517–2583. doi: 10.1021/acs.chemrev.6b00361

Peng, L., Qin, P., Zeng, Q., Song, H., Lei, M., Mwangi, J. J. N., et al. (2011). Improvement of formaldehyde sensitivity of ZnO nanorods by modifying with $Ru(dcbpy)_2(NCS)_2$. *Sens. Actuators B* 160, 39–45. doi: 10.1016/j.snb.2011.07.008

Peng, L., Xie, T., Yang, M., Wang, P., Xu, D., Pang, S., et al. (2008). Light induced enhancing gas sensitivity of copper-doped zinc oxide at room temperature. *Sens. Actuators B* 131, 660–664. doi: 10.1016/j.snb.2007.12.060

Peng, L., Zhao, Q., Wang, D., Zhai, J., Wang, P., Pang, S., et al. (2009). Ultraviolet-assisted gas sensing: a potential formaldehyde detection approach at room temperature based on zinc oxide nanorods. *Sens. Actuators B* 136, 80–85. doi: 10.1016/j.snb.2008.10.057

Prades, J. D., Diaz, R. J., Hernandez-Ramirez, F., Barth, S., Cirera, A., Romano-Rodriguez, A., et al. (2009a). Equivalence between thermal and room temperature UV light modulated responses of gas sensors based on individual SnO_2 nanowires. *Sens. Actuators B* 140, 337–341. doi: 10.1016/j.snb.2009.04.070

Prades, J. D., Jimenez-Diaz, P., Manzanares, M., Hernandez-Ramirez, F., Cirera, A., Romano-Rodriguez, A., et al. (2009b). A model for the response towards oxidizing gases of photoactivated sensors based on individual SnO_2 nanowires. *Phys. Chem. Chem. Phys.* 11, 10881–10889. doi: 10.1039/b915646a

Rumyantseva, M., Nasriddinov, A., Vladimirova, S., Tokarev, S., Fedorova, O., Krylov, I., et al. (2018). Photosensitive organic-inorganic hybrid materials for room temperature gas sensor applications. *Nanomaterials* 8:671. doi: 10.3390/nano8090671

Saboor, F. H., Ueda, T., Kamada, K., Hyodo, T., Mortazavi, V., Khodadadi, A. A., et al. (2016). Enhanced NO_2 gas sensing performance of bare and Pd-loaded SnO_2 thick film sensors under UV-light irradiation at room temperature. *Sens. Actuators B* 223, 429–439. doi: 10.1016/j.snb.2015.09.075

Saura, J. (1994). Gas-sensing properties of SnO_2 pyrolytic films subjected to ultraviolet radiation. *Sens. Actuators B* 17, 211–214. doi: 10.1016/0925-4005(93)00874-X

Sergent, N., Epifani, M., Comini, E., Faglia, G., and Pagnier, T. (2007). Interactions of nanocrystalline tin oxide powder with NO_2: a Raman spectroscopic study. *Sens. Actuators B* 126, 1–5. doi: 10.1016/j.snb.2006.10.013

Stevanović, V., Lany, S., Ginley, D. S., Tumas, W., and Zunge, A. (2014). Assessing capability of semiconductors to split water using ionization potentials and electron affinities only. *Phys. Chem. Chem. Phys.* 16, 3706–3714. doi: 10.1039/c3cp54589j

Sun, Z., Huang, D., Yang, Z., Li, X., Hu, N., Yang, C., et al. (2015). ZnO nanowire-reduced graphene oxide hybrids based portable NH_3 gas sensing electron device. *IEEE Electron Device Lett.* 36, 1376–1379. doi: 10.1109/LED.2015.2496177

Trawka, M., Smulko, J., Hasse, L., Granqvist, C.-G., Annanouch, F. E., and Ionescu, R. (2016). Fluctuation enhanced gas sensing with WO_3-based nanoparticle gas sensors modulated by UV light at selected wavelengths. *Sens. Actuators B* 234, 453–461. doi: 10.1016/j.snb.2016.05.032

Varechkina, E. N., Rumyantseva, M. N., Vasiliev, R. B., Konstantinova, E. A., and Gaskov, A. M. (2012). UV-VIS photoconductivity of nanocrystalline tin oxide. *J. Nanoelectron. Optoelectron.* 7, 1–6. doi: 10.1166/jno.2012.1399

Vasiliev, R., Babynina, A., Maslova, O., Rumyantseva, M., Ryabova, L., Dobrovolsky, A., et al. (2013). Photoconductivity of nanocrystalline SnO_2

sensitized with colloidal CdSe quantum dots. *J. Mater. Chem.?* 1, 1005–1010. doi: 10.1039/C2TC00236A

Vasiliev, R. B., Dirin, D. N., and Gaskov, A. M. (2011). Semiconductor nanoparticles with spatial separation of charge carriers: synthesis and optical properties. *Russ. Chem. Rev.* 80, 1139–1158. doi: 10.1070/RC2011v080n12ABEH004240

Vorobyeva, N., Rumyantseva, M., Filatova, D., Konstantinova, E., Grishina, D., Abakumov, A., et al. (2013). Nanocrystalline ZnO(Ga): paramagnetic centers, surface acidity and gas sensor properties. *Sens. Actuators B* 182, 555–564. doi: 10.1016/j.snb.2013.03.068

Wagner, T., Kohl, C.-D., Malagù, C., Donato, N., Latino, M., Neri, G., et al. (2013). UV light-enhanced NO_2 sensing by mesoporous In_2O_3: interpretation of results by a new sensing model. *Sens. Actuators B* 187, 488–494. doi: 10.1016/j.snb.2013.02.025

Wang, C. Y., Becker, R. W., Passow, T., Pletsche, W., and Kohler, K., Cimalla, V., et al. (2011). Photon-stimulated sensor based on indium oxide nanoparticles I: wide-concentration-range ozone monitoring in air. *Sens. Actuators B* 152, 235–240. doi: 10.1016/j.snb.2010.12.014

Wang, T., Sun, Z., Huang, D., Yang, Z., Ji, Q., Hu, N., et al. (2017). Studies on NH_3 gas sensing by zinc oxide nanowire-reduced graphene oxide nanocomposites. *Sens. Actuators B* 252, 284–294. doi: 10.1016/j.snb.2017.05.162

Wang, T., Xu, S., Hu, N., Hu, J., Huang, D., Jiang, W., et al. (2018). Microwave preparation and remarkable ethanol sensing properties of ZnO particles with controlled morphologies in water-ethylene glycol binary solvent system. *Sens. Actuators B* 252, 1006–1014. doi: 10.1016/j.snb.2017.08.099

Wongrat, E., Chanlek, N., Chueaiarrom, C., Samransuksamer, B., Hongsith, N., and Choopun, S. (2016). Low temperature ethanol response enhancement of ZnO nanostructures sensor decorated with gold nanoparticles exposed to UV illumination. *Sens. Actuators A* 251, 188–197. doi: 10.1016/j.sna.2016.10.022

Wu, T., Wang, Z., Tian, M., Miao, J., Zhang, H., and Sun, J. (2018). UV excitation NO_2 gas sensor sensitized by ZnO quantum dots at room temperature. *Sens. Actuators B* 259, 526–531. doi: 10.1016/j.snb.2017.12.101

Xu, F., and Ho, H.-P. (2017). Light-activated metal oxide gas sensors: a review. *Micromachines* 8, 333. doi: 10.3390/mi8110333

Yamazoe, N., and Shimanoe, K. (2008). Theory of power laws for semiconductor gas sensors. *Sens. Actuators B* 128, 566–573. doi: 10.1016/j.snb.2007.07.036

Yang, Z., Guo, L., Zu, B., Guo, Y., Xu, T., and Dou, X. (2014). CdS/ZnO core/shell nanowire-built films for enhanced photodetecting and optoelectronic gas-sensing applications. *Adv. Opt. Mater.* 2, 738–745. doi: 10.1002/adom.201400086

Zhang, C., Geng, X., Li, J., Luo, Y., and Lu, P. (2017). Role of oxygen vacancy in tuning of optical, electrical and NO_2 sensing properties of ZnO_{1-x} coatings at room temperature. *Sens. Actuators B* 248, 886–893. doi: 10.1016/j.snb.2017.01.105

Zhang, C., Wang, J., Olivier, M.-G., and Debliquy, M. (2015). Room temperature nitrogen dioxide sensors based on N719-dye sensitized amorphous zinc oxide sensors performed under visible-light illumination. *Sens. Actuators B* 209, 69–77. doi: 10.1016/j.snb.2014.11.090

Zheng, K., Žídek, K., Abdellah, M., Zhang, W., Chábera, P., Lenngren, N., et al. (2014). Ultrafast charge transfer from CdSe quantum dots to p-type NiO: hole injection vs hole trapping. *J. Phys. Chem. C* 118, 18462–18471. doi: 10.1021/jp506963q

Zhu, L., and Zeng, W. (2017). Room-temperature gas sensing of ZnO-based gas sensor: a review. *Sens. Actuators A* 267, 242–261. doi: 10.1016/j.sna.2017.10.021

Conflict of Interest: The authors declare that the research was conducted in the absence of any commercial or financial relationships that could be construed as a potential conflict of interest.

frontiers in Materials

ORIGINAL RESEARCH
published: 04 October 2019
doi: 10.3389/fmats.2019.00250

Detection of Semi-volatile Plasticizers as a Signature of Early Electrical Fire

*Jia Han, Wenjia Chen, Aihua Yu and Jianxin Yi**

State Key Laboratory of Fire Science, Department of Safety Science and Engineering, University of Science and Technology of China, Hefei, China

Detection of characteristic species released from over-heated PVC cables may enable early warning of electrical fire. This work identified the major volatile species for over-heated PVC cables, and verified their potential as fire signatures with metal oxide gas sensors. Semi-volatile Dioctyl phthalate (DOP) and 2-Ethylhexanol (2-EH) were found to be ubiquitously present in the cable vapors as major species. Detection of these species and the vapors of overheated cables was accomplished with a metal oxide gas sensor. The response of the gas sensor to the cable vapors resulted mainly from DOP and 2-EH, demonstrating them as effective signature gases for over-heated PVC cables. A gas sensor based on SnO_2 nanofibers was prepared with greatly enhanced response to the signature gases. Large-scale simulation tests showed that the nanofiber gas sensor could effectively detect the cable overheating at an early stage.

Keywords: gas sensor, detection, electrical fire, plasticizer, semi-volatile

OPEN ACCESS

Edited by:
Xiaogan Li,
Dalian University of Technology (DUT), China

Reviewed by:
Azhar Ali Haidry,
Nanjing University of Aeronautics and Astronautics, China
Zhenyu Li,
Southwest Petroleum University, China

****Correspondence:***
Jianxin Yi
yjx@ustc.edu.cn

Specialty section:
This article was submitted to Functional Ceramics, a section of the journal Frontiers in Materials

Received: *21 May 2019*
Accepted: *19 September 2019*
Published: *04 October 2019*

Citation:
Han J, Chen W, Yu A and Yi J (2019) Detection of Semi-volatile Plasticizers as a Signature of Early Electrical Fire. Front. Mater. 6:250. doi: 10.3389/fmats.2019.00250

INTRODUCTION

Fire cause severe property damages and casualties in modern society. A key to successful fire prevention and controlling is the accurate detection of fire characteristics as early as possible. The fire characteristics can vary greatly for various types and at different stages of fires (Fonollosa et al., 2018). So far numerous fire detectors based on the detection of gas, smoke, temperature, flame, etc., have been developed (Han and Lee, 2009; Verstockt et al., 2010). Gases or chemical vapors due to pyrolysis or smoldering of the combustible materials are usually emitted before the other fire characteristics become evident, such as smoke and temperature change, and could thus be used as a signature of fire (Fonollosa et al., 2018; Vincent et al., 2019). For many conventional fires, CO has been recognized as the signature gas, which has led to successful application of CO gas sensors in commercial fire detectors. However, CO sensors are not suitable for detection of electrical fire at the early stage as little CO may be emitted then (Beneš et al., 2004; Li, 2014; Chen and Yi, 2019).

Electrical cables with insulation and/or sheath based on PVC (polyvinyl chloride) materials are currently widely used in residential and industrial applications. The PVC insulation/sheath starts to degrade significantly or ignite at a temperature above ~200–240°C, outgassing HCl, CO, CO_2, etc. (Beneš et al., 2004; Li, 2014; Courty and Garo, 2017; Wang et al., 2018; Chen and Yi, 2019). Typically the PVC used for cables contains a large amount of various additives in the polymeric PVC matrix, such as plasticizers, stabilizers, inorganic fillers, and antioxidants (Linde and Gedde, 2014). Plasticizers such as DOP are semi-volatile organic compounds (SVOC) with low saturation vapor pressures at normal cable operation temperatures (70–90°C). At higher temperatures where cable is overheated, release of these volatile species could become substantial due to the increased vapor

pressure and large abundance in the cable insulation (Li, 2014; Chen and Yi, 2019). In particular, they may accumulate in confined/closed spaces, such as cabinets for electric power distribution or control, electrical apparatuses, and appliances. Detection of the major species therein may allow warning of malfunctioned cables and early stage of fires.

Recent studies showed that metal oxide semiconductor (MOS) gas sensors could respond to the emitted vapors of overheated or pyrolyzed PVC cables (Zhao et al., 2014; Knoblauch et al., 2015; Lee et al., 2017; Chen and Yi, 2019). Unfortunately, the compositions of these vapors, which are rather complex and could vary greatly with the type, composition of the cable and heating conditions (temperature and duration), etc., have not yet been determined. So far, it is still uncertain what species are predominantly and ubiquitously present in the vapors for different cables, and their quantitative concentrations as a function of temperature. Moreover, the response characteristics of MOS sensors to these major species remain also unknown. Knowledge about these will not only enable identification of the signature gases for early detection of electrical fires, but also provide a vital guideline for the selection and development of gas sensors specifically targeting these gases.

In this study, vapor compositions for different overheated PVC cables were systematically examined. Semi-volatile plasticizers were assessed as the signature gases of early-stage PVC cable fires. A TGS 822 gas sensor was responsive to the signature gases, but the response values were rather low. Considering that semiconductor-typed gas sensors based on nanostructured SnO_2 are often effective for detection of VOCs (Srivastava, 2003; Upadhyay, 2013; Knoblauch et al., 2015; Kou et al., 2016; Jiang et al., 2017), we prepared a SnO_2 nanofiber gas sensor for detection of the plasticizers. The sensor showed significantly enhanced response to the signature gases, and could detect the hazard due to the cable overheating.

EXPERIMENTAL

Analysis of Vapor Composition

Nine different commercial PVC cables of various model types from several different domestic manufacturers listed in **Table 1** were studied in this work. Cables 1–8 are single-cored while cable 9 is two-cored. The maximum continuous operation temperature is 70°C for all the cables. The PVC insulation of the cables was stripped from the cables and cut into a length of 2 mm per piece. The samples were ultrasonically cleaned successively in water and ethanol, which procedures were repeated for several times.

To analyze the vapor composition, gas chromatography-mass spectrometry (GC-MS) was conducted on an Agilent 6890N/5973 system equipped with a headspace injector (G1888, Agilent). 0.5–2.0 g PVC insulation sample was hermetically sealed in a 20 ml headspace bottle and heated by the headspace injector. The temperature of the GC column (HP-5MS) was programmed as follows: held at 60°C for 1 min, and ramped to 220°C at 20°C/min, held for 1 min, and subsequently ramped to 280°C at 5°C/min, held for 4 min. Helium (99.999%) was used as the carrier gas of the GC.

Variation of vapor compositions with heating time and sample mass was examined. To attain reasonable experimental accuracy and high efficiency, the vapors obtained by heating 1 g sample for 30 min is used for the identification of GC-MS, which could allow the major components in the vapors to reach saturation (**Supplementary Figure 1**). In some experiments, in order to examine variation of the concentration of the major vapor components with the pre-heating time, the PVC samples were subjected to pre-heating for a certain period in open air prior to being sealed in the headspace bottles. Note that as a large tailing peak appeared at the beginning of the GC-MS spectra due to the ambient air contained in the headspace bottles, the GC-MS data acquisition began from the retention time of 3 min.

Dioctyl phthalate (purity >99.5%) and 2-Ethylhexanol (purity >99.6%) purchased from SIGMA-ALDRICH were used as standards for the GC-MS measurements and sensor tests. The concentration of DOP and 2-EH in the vapors released from the cable insulation was quantified by external standard calibration. To obtain the calibration plots (**Supplementary Figure 2**), 1 μl of the standard solutions containing various concentrations of DOP and 2-EH in ethanol was injected to the GC-MS.

Gas Sensor Preparation and Tests

Gas sensing measurements were conducted with a TGS-822 MOS gas sensor (Figaro, Japan) and home-made gas sensor based on SnO_2 nanofibers. The SnO_2 nanofibers were synthesized via electrospinning followed by calcination at 600°C for 3 h. Details of the materials preparation and characterization using X-ray diffraction (XRD), scanning electron microscope (SEM), transmission electron microscopy (TEM), and X-ray photoelectron spectroscopy (XPS) can be found in Yi et al. (2018). To prepare the gas sensor, the nanofibers were dispersed in ethanol, and the obtained paste was coated onto an alumina tube with two gold electrodes and platinum wires. The coated tube was then calcined at 400°C for 2 h. The width of the electrodes and the gap between them were around 1 mm. A Ni-Cr wire was inserted

TABLE 1 | Specification of the cables used in this study.

Cable no.	1	2	3	4	5	6	7	8	9
Company	**Yuandong**	**Yuandong**	**Delixi**	**Feidiao**	**Lvbao**	**Lvbao**	**Zhengtai**	**Xiongmao**	**Xiongmao**
Type	BV 2.5	BV 4.0	BV 2.5	BV 2.5	BV 2.5	BV 4.0	BV 4.0	BVR2.5	RVV 2*1
Sectional Area of conductor (mm^2)	2.5	4.0	2.5	2.5	2.5	4.0	4.0	2.5	1
Insulation thickness (mm)	0.8	0.8	0.8	0.8	0.8	0.8	0.8	0.8	0.6

Maximum continuous operation temperature of the cables is 70°C.

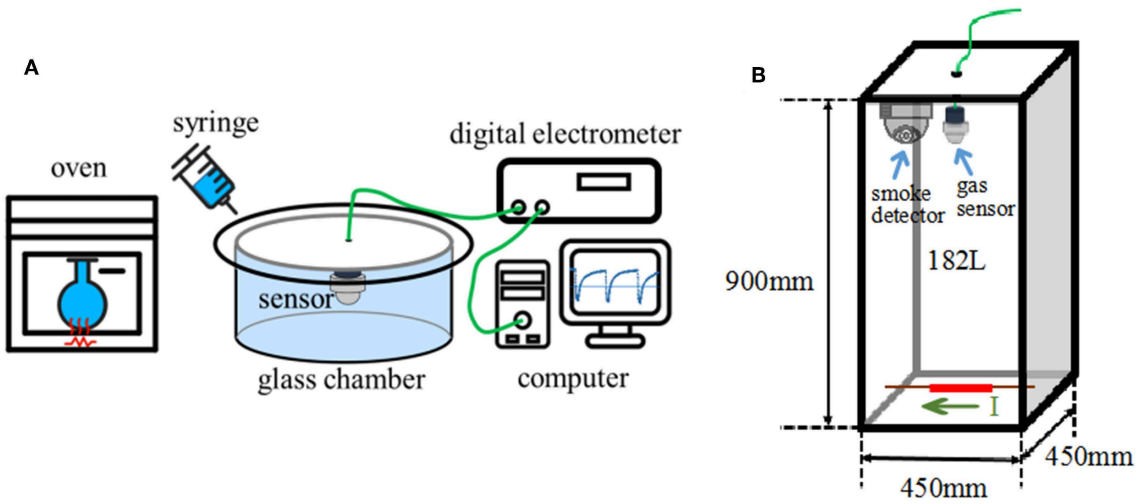

FIGURE 1 | Schematic diagrams of sensor tests. **(A)** Bench-scale test, **(B)** large-scale simulation test.

through the core of the alumina tube as the heater of the sensor.

Bench-scale gas sensing measurements were conducted in a 480 ml glass chamber to evaluate the response characteristics of the gas sensor using a static air testing method similar to that described in Li and Yi (2017) and Chen and Yi (2018). The gas sensor was first allowed to reach steady state in ambient air (**Figure 1A**). Sample vapors of desired concentration were injected with a syringe injector into the test chamber to result in changes in the sensor resistance. The sensor was removed from the glass chamber and exposed in ambient air to recover the resistance after the test. Vapors of DOP, 2-EH, and their mixtures were obtained by evaporating appropriate amounts of the respective liquids in a glass reagent bottle at 150–200°C. Vapors of cable insulation were obtained through a method similar to that used in the GC-MS measurements. Resistance of the sensor was measured by a digital electrometer (Agilent, 34972A). The sensor response is defined as $S = R_a/R_g$, where R_a and R_g are the resistance of the sensor in ambient air and target gas, respectively. Humidity of the ambient air was measured with a hygrometer, which varied in the range of 48–54% in this study.

Large scale sensor tests were also conducted in a 45 cm × 45 cm × 90 cm acrylic chamber of 182 L volume (**Figure 1B**), in order to simulate the actual scenario that cables become overheated under load in confined spaces. A piece of 11 cm long cable insulation (1.0 g) was placed at the bottom center of the chamber. A Ni/Cr heating wire running through the cable core was used to control the cable temperature by adjusting the electric current passing it. A thermocouple was tightly attached to heating wire to monitor the actual temperature. The cable insulation was heated from room temperature to and dwelled at a target temperature. The gas sensors were located at the upper center of the chamber to monitor the gas release. For comparison, a Honeywell photoelectric smoke detector (JTYJ-GD-01LM/BW) was also installed adjacent to the gas sensors.

RESULTS AND DISCUSSION

GC-MS analyses for 9 different cables under overheating conditions showed that the vapors released consisted of various organic compounds of high boiling points (**Figure 2** and **Table 2**). Although the compositions varied significantly with the type of cables and temperature, it can be distinctly seen that DOP and 2-EH, two widely used plasticizers, were present as common and most abundant species in all cable vapors. The quantified saturation concentrations of DOP and 2-EH in the vapors increased with increasing temperature (**Figure 3**). The evident release of DOP began since a cable temperature of 130°C with a saturated concentration of ∼10–30 ppm, which climbed to 550–2,000 ppm at 200°C. With regard to 2-EH, the concentration was higher for most cables, and evident release began for some cables already at a temperature as low as 70°C. The concentrations of both DOP and 2-EH can be maintained at these high values, even after the cable was subject to prolonged pre-heating in open air at 150°C for up to 12 h (**Supplementary Figure 3**), indicating that their release are sustainable under the given conditions. Note that significant presence of 2-EH under similar conditions was not detected by pyrolysis GC-MS or TG-IR measurements in previous reports (Li, 2014; Chen and Yi, 2019), which can be ascribed to the too low concentration of 2-EH therein. In those measurements only a small amount (up to several tens of mg) of PVC sample was used, and the carrier gases further diluted the vapors generated. In contrast, a much larger sample mass (1 g) was used and the 2-EH was enriched in the sealed headspace bottle in this work. The results obtained herein suggest that both DOP and 2-EH hold promise as candidates of a universal signature gas of early cable fires.

A fire signature must be able to be reliably detected for warning of fires. Currently, no commercial gas sensor that is known to be specifically sensitive to DOP and 2-EH is available. As a result, a TGS822 MOS gas sensor, which is designated for sensing VOC gases, was used to assess the

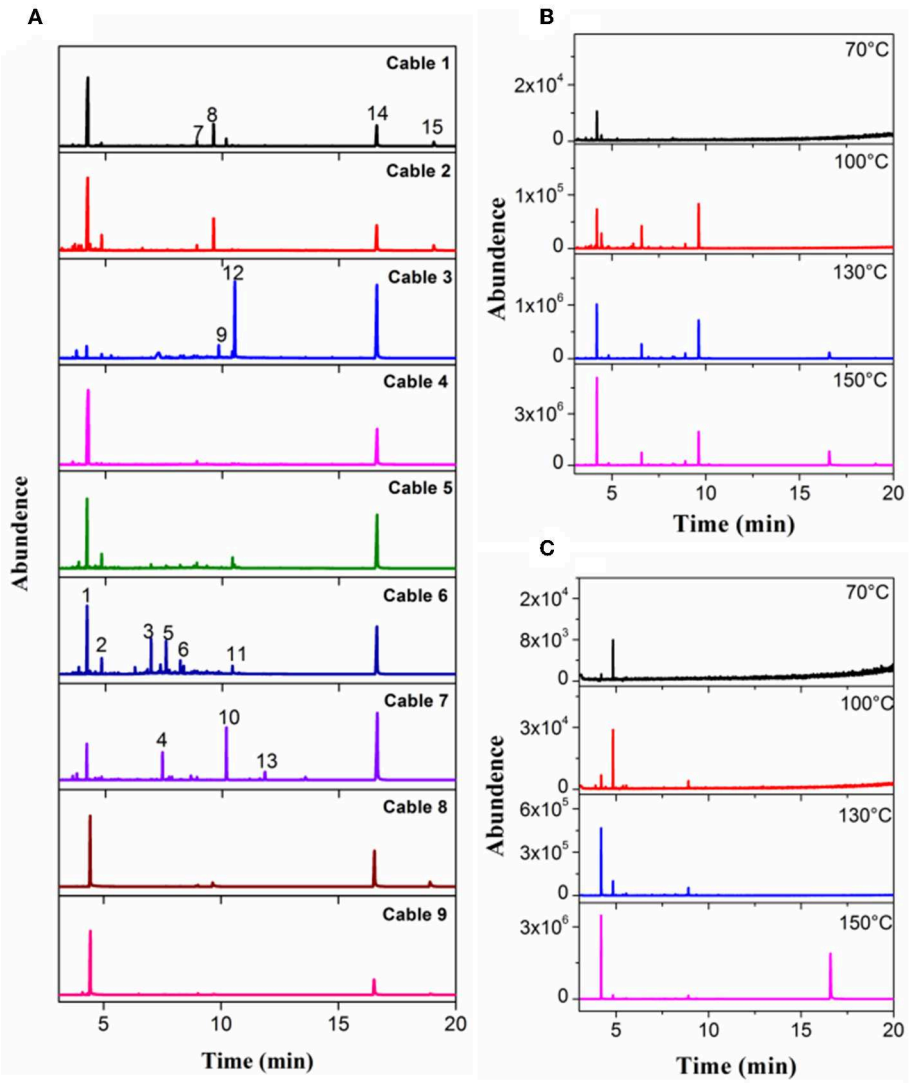

FIGURE 2 | Chromatograms measured with headspace GC-MS for **(A)** Cable 1–9 at 200°C, **(B)** Cable 1, and **(C)** Cable 4 at selected temperatures.

validity of using DOP and 2-EH as the signature gases of electrical fires. Bench-scale gas sensing measurements were performed in a 480 ml chamber. As shown in **Figure 4A**, the resistance of the TGS sensor decreased rapidly in the presence of DOP and 2-EH. When the signature gases were removed, the sensor resistance restored gradually back to the initial values. The resistance change, i.e., the sensor response, was found to vary greatly for DOP on the heating voltage and hence the temperature of the sensor. A typical volcano-shaped dependence was observed, with a maximum response of 8.6 for 100 ppm DOP at 4.1 V (**Figure 4B**). In contrast, the sensor response to 2-EH exhibited much weaker temperature dependence, and varied only slightly within 2.5–3.2. Based on these results, the heater voltage was set at 4.1 V for this sensor where optimized sensor performance can be achieved for both DOP and 2-EH in the following measurements.

Figure 5 compares the sensor response to the cable vapors with that to the simulated vapors. The simulated vapors were obtained by heating and vaporizing a mixture of DOP and 2-EH standards, wherein the concentration of DOP and 2-EH was kept, respectively, equal to that in the cable vapors according to **Figure 3**. The gas concentration in the sensor testing chamber was adjusted by varying the sampling volume of the vapors or the heating temperature of the cables/standards. As a representative, cable 1 and cable 4 were tested. It can be seen that for the cable vapors, the sensor response increased monotonically with either the sampling volume or heating temperature, i.e., with increase of the gas concentration. Furthermore, the sensor response for the cable vapors matched very closely with that for the simulated vapors in all cases. These results have two important implications. The first is that the response of the gas sensor to the cable vapors contributes

TABLE 2 | Compositions of cable 1–9 determined by the headspace GC-MS at a sample temperature of 200°C.

Peak no.	R.T.min	Species	Formula	M.W.	B.P./°C	C1	C2	C3	C4	C5	C6	C7	C8	C9
1	4.2	2-Ethyl hexanol	$C_8H_{18}O$	130	184	S*	S	M	VS	S	S	M	S	S
2	4.8	Tetrahydrodicyclopentadiene	$C_{10}H_{16}$	136	192	W*	M	W		M	M			
3	6.9	Tetradecane	$C_{14}H_{30}$	198	253						M			
4	7.4	Nonylcyclopropane	$C_{12}H_{24}$	168	208							M		
5	7.6	Pentadecane	$C_{15}H_{32}$	212	270						M			
6	7.7	Hexadecane	$C_{16}H_{34}$	226	287						M			
7	8.9	Tetradecanoic acid	$C_{14}H_{28}O_2$	228	319	M*	M							
8	9.6	Benzoic acid, 2-ethylhexyl ester	$C_{15}H_{22}O_3$	250	313	M	M						M	
9	9.8	Diisobutyl phthalate (DIBP)	$C_{16}H_{22}O_4$	278	295			M						
10	10.2	Methyl hexadecanoate	$C_{17}H_{34}O_2$	270	332	M						S		
11	10.4	Hexadecanoic acid	$C_{16}H_{32}O_2$	256	351					M	M			
12	10.5	Dibutyl phthalate (DBP)	$C_{16}H_{22}O_4$	278	337			S						
13	11.8	Methyl octadecanoate	$C_{19}H_{38}O_2$	298	355							M		
14	16.6	DOP	$C_{24}H_{38}O_4$	390	385	S	S	S	S	S	S	S	S	S
15	19.1	Dioctyl terephthalate (DOTP)	$C_{24}H_{38}O_4$	390	400	M	M						M	M

**VS, S, M, and W denote very strong, strong, medium, and weak, respectively. They correspond to an area of the chromatographic peak of $>10^9$, $10^8 \sim 10^9$, $10^7 \sim 10^8$, and $<10^7$, respectively.*

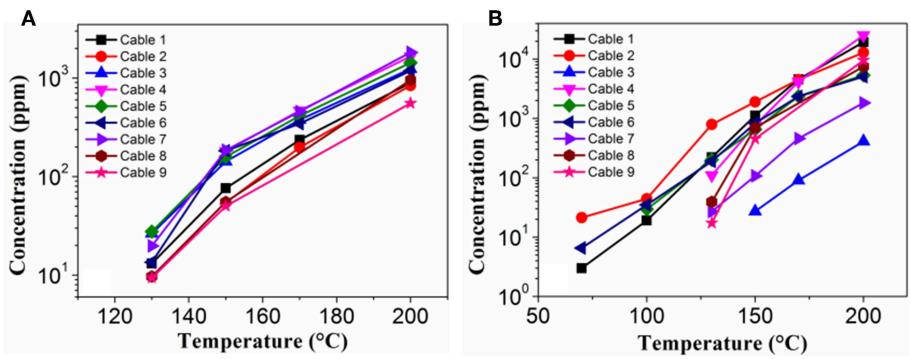

FIGURE 3 | Calibrated concentration of **(A)** DOP and **(B)** 2-EH at different cable temperatures.

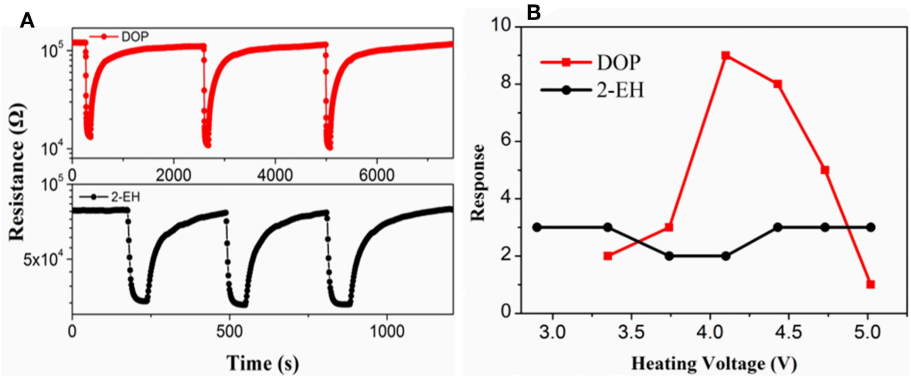

FIGURE 4 | (A) Response transients and **(B)** response values of the TGS-822 sensor to 100 ppm vapors of DOP and 2-EH standards.

primarily from that to DOP and 2-EH, since both DOP and 2-EH are dominant species in the cable vapors. Note that for cable 1, some additional compounds were present in the obtained vapors (**Table 2**), which did not seem to interfere significantly the sensor response. The second is that change of the cable temperature can be detected by monitoring the concentration variation of DOP and 2-EH with gas detectors. These results clearly demonstrate that early warning of electrical fires is feasible through detection of DOP and 2-EH with MOS gas sensors.

Although the TGS-822 sensor was able to respond to the signature gases, the response value was very limited especially for 2-EH (**Figure 4B**). High sensing response to the signature gases is crucial for reliable and timely detection of cable over-heating in practical large-scale scenarios and at low cable temperatures, where the concentrations of the gases will be very low. Improved performance could in principle be achieved by using gas sensors based on nanostructured materials (Kim et al., 2013). As a demonstration, a gas sensor based on electrospun SnO_2 nanofibers was prepared. The SnO_2 nanofibers exhibited a single-phase tetragonal rutile structure. They were found to be porous and hollow, assembled by particles of several tens of nanometers. The diameter was ~120 nm and the length varied typically in the range of 0.5–2 μm. More details about the phase composition, morphology, and chemical states of the nanofibers can be found in Yi et al. (2018). This work was instead focused on the gas sensing performance of the sensor based on these nanofibers. Similar to the TGS-822, the nanofiber sensor also exhibited resistance reduction when exposed to the reducing gases of DOP and 2-EH, suggesting n-type semiconductor mechanism. Following this mechanism, the reducing gas reacts with the oxygen anion adsorbed on the surface of the semiconductor, resulting in a decrease of the resistance (Haidry et al., 2018). As shown in **Figure 6**, the maximum response reached 41 and 26 for 100 ppm DOP and 2-EH, respectively, much larger than those for the TGS sensor (Yi et al., 2019). Note

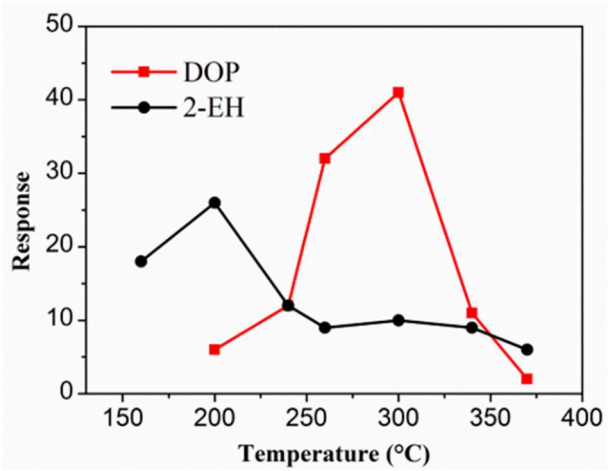

FIGURE 6 | Response of SnO_2 nanofiber sensor to 100 ppm vapors of DOP and 2-EH standards.

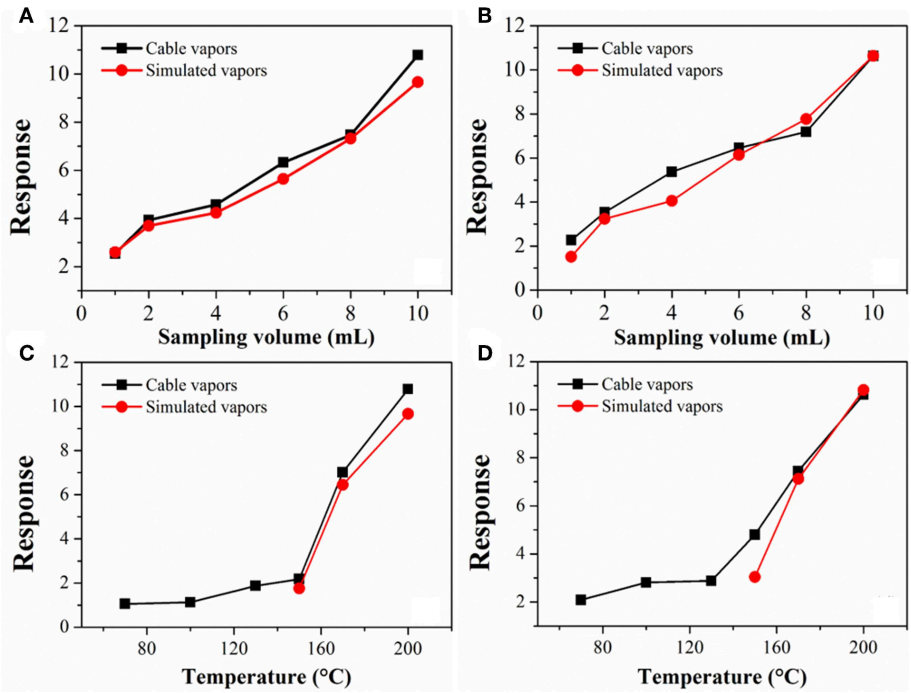

FIGURE 5 | Response variation of TGS-822 sensor with **(A,B)** the sampling volume and **(C,D)** temperature for vapors of **(A,C)** cable 1 and **(B,D)** cable 4. For comparison, data for simulated vapors consisting of only DOP and 2-EH standards are also presented.

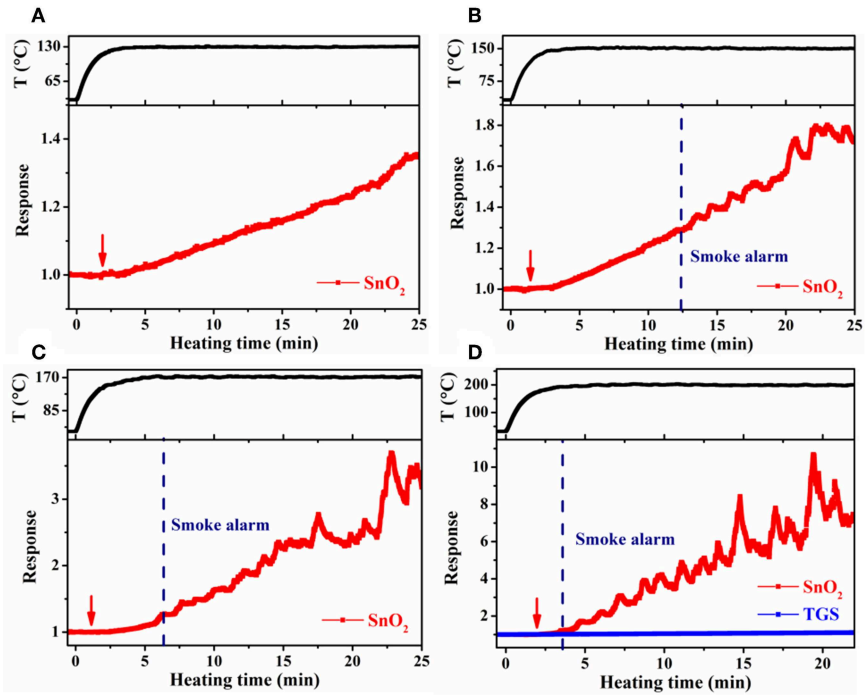

FIGURE 7 | Response of SnO_2 nanofiber sensor as a function of heating time at a cable temperature of **(A)** 130°C, **(B)** 150°C, **(C)** 170°C, and **(D)** 200°C during large-scale simulation tests for cable 1. Arrow indicate onset of sensor response.

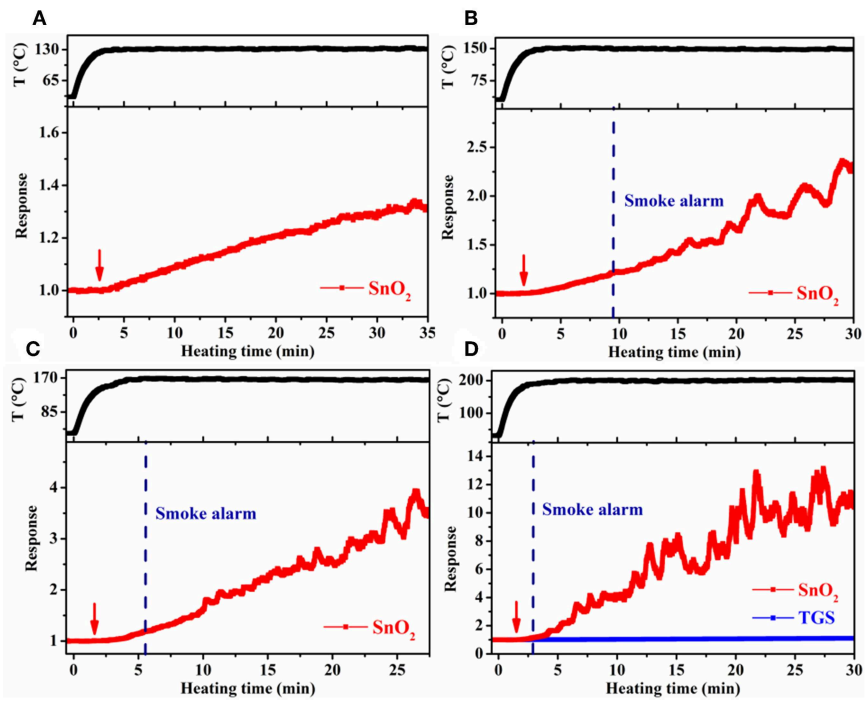

FIGURE 8 | Response of SnO_2 nanofiber sensor as a function of heating time at a cable temperature of **(A)** 130°C, **(B)** 150°C, **(C)** 170°C, and **(D)** 200°C during large-scale simulation tests for cable 4.

that the optimal temperature of SnO_2 nanofiber for sensing DOP (300°C) and 2-EH (200°C) was very different, thus the sensor temperature was set at 260°C as a compromise in the following tests. Note also that other experimental conditions, such as electrode structure and dimension, may also affect the sensor performance (Langer et al., 2015; Haidry et al., 2016, 2019; Sun et al., 2018; Fatima et al., 2019), which deserves further investigation.

Large-scale simulation sensor tests were performed in a 182 L acrylic chamber, wherein the temperature of the cable insulation was controlled through adjusting the electric current passing the heater in the cable core. In such a way, the conditions resembled the actual scenario that cables become overheated under load in confined spaces, such as power distribution cabinets and electrical appliances. To obtain higher target cable temperatures, a larger heating current had to be used. As a result, the heating time to reach 70°C (the maximum continuous working temperature of the PVC cables used) slightly decreased from 0.5 to 0.3 min, as the target cable temperature increased from 130° to 200°C. Despite this difference, it took ∼5 min in each case for the cable temperature to reach steady at the target temperature. Cable 1 and 4 were tested, and the results were presented in **Figures 7**, **8**. For the target temperature of 130°C (**Figure 7A**), response of the SnO_2 nanofiber gas sensor started distinctly at ∼3.3 min (referred to as gas alarm time hereafter), and the value continuously increased with time. The increase of response with time is consistent with the more pronounced emission of the signature gases at higher temperatures in **Figure 3**. In contrast to the gas sensor response, no alarm was triggered for the smoke detector. As the target temperature was raised, the gas alarm time slightly reduced to 3.0, 2.5, and 2.1 min (**Figures 7B–D**), for 150°, 170°, and 200°C, respectively. For these higher temperatures, the smoke alarm was triggered, but at a much later time than the gas alarm, i.e., at 12.4, 6.4, and 3.6 min, respectively. For the case of cable 4, similar phenomena were observed, where both the gas and smoke alarm time were slightly shorter (**Figure 8**). It is also important to note that during simulation tests, no significant response was observed for the TGS gas sensor (**Figures 7D**, **8D**), consistent with its low response to the signature gases. These results reveal that gas sensors of high response to the signature gases, DOP and 2-EH, may be able to effectively detect the overheating of PVC cables and thus enable early alarm of electrical fires.

CONCLUSIONS

The vapor compositions for nine different over-heated PVC cables were measured at various temperatures. Despite the varied compositions, two species of substantial abundance, DOP and 2-EH, were found ubiquitously present in the cable vapors. The concentration of both species in the vapors increased with temperature. Gas sensing measurements with a commercial TGS resistive gas sensor showed that these species can be effectively detected and could be used as fire signatures. A SnO_2 nanofiber gas sensor exhibited significantly enhanced response to the signature gases. The nanofiber sensor could detect the overheating of PVC cables and thus enable early alarm of electrical fires.

DATA AVAILABILITY STATEMENT

All datasets generated for this study are included in the manuscript/**Supplementary Files**.

AUTHOR CONTRIBUTIONS

JY designed the project. JH, WC, and AY conducted the experiments and analyzed the results. JY, JH, and WC wrote the manuscript.

FUNDING

This work was supported by the National Natural Science Foundation of China (grant No. 61871359) and fundamental research funds for the Central University (grant No. WK2320000044).

SUPPLEMENTARY MATERIAL

The Supplementary Material for this article can be found online at: https://www.frontiersin.org/articles/10.3389/fmats.2019.00250/full#supplementary-material

REFERENCES

Beneš, M., Milanov, N., Matuschek, G., Kettrup, A., Plaček, V., and Balek, V. (2004). Thermal degradation of PVC cable insulation studied by simultaneous TG-FTIR and TG-EGA methods. *J. Therm. Anal. Calorimetry* 78, 621–630. doi: 10.1023/B:JTAN.0000046123.59857.ad

Chen, D., and Yi, J. (2018). One-pot electrospinning and gas-sensing properties of $LaMnO_3$ perovskite/SnO_2 heterojunction nanofibers. *J. Nanoparticle Res.* 20:65. doi: 10.1007/s11051-018-4158-x

Chen, W., and Yi J. (2019). Identification and gas sensor testing of volatile signature gas for early detection of PVC cable fires. *Fire Safety Sci.* 28, 133–139. doi: 10.3969/j.issn.1004-5309.2019.02.04

Courty, L., and Garo, J. (2017). External heating of electrical cables and auto-ignition investigation. *J. Hazard. Mater.* 321, 528–536. doi: 10.1016/j.jhazmat.2016.09.042

Fatima, Q., Haidry, A. A., Yao, Z., He, Y., and Xie, L. (2019). The critical role of hydroxyl groups on water vapor sensing of Graphene oxide. *Nanoscale Adv.* 1, 1319–1330. doi: 10.1039/C8NA00135A

Fonollosa, J., Solórzano, A., and Marco, S. (2018). Chemical sensor systems and associated algorithms for fire detection: a review. *Sensors* 18:553. doi: 10.3390/s18020553

Haidry, A. A., Cetin, C., Kelm, K., and Saruhan, B. (2016). Sensing mechanism of low temperature NO_2 sensing with top–bottom electrode (TBE) geometry. *Sens. Actuat. B* 236, 874–884. doi: 10.1016/j.snb.2016.03.016

Haidry, A. A., Sun, L., Saruhan, B., Plecenik, A., Plecenik, T., Shen, H., et al. (2018). Cost-effective fabrication of polycrystalline TiO_2 with tunable n/p response for selective hydrogen monitoring. *Sens. Actuat. B* 274, 10–21. doi: 10.1016/j.snb.2018.07.082

Haidry, A. A., Xie, L., Li, Z., Dong, B., Quwareer, F., and Wang, Z. (2019). Sol-gel synthesis of TiO_2 with p-type response to hydrogen gas at elevated temperature. *Front. Mater.* 6:96. doi: 10.3389/fmats.2019.00096

Han, D., and Lee, B. (2009). Flame and smoke detection method for early real-time detection of a tunnel fire. *Fire Safety J.* 44, 951–961. doi: 10.1016/j.firesaf.2009.05.007

Jiang, Z., Yin, M., and Wang, C. (2017). Facile synthesis of Ca^{2+}/Au co-doped SnO_2 nanofibers and their application in acetone sensor. *Mater. Lett.* 194, 209–212. doi: 10.1016/j.matlet.2017.02.031

Kim, I.-D., Rothschild, A., and Tuller, H. L. (2013). Advances and new directions in gas-sensing devices. *Acta Mater.* 61, 974–1000. doi: 10.1016/j.actamat.2012.10.041

Knoblauch, J., Illyaskutty, N., and Kohler, H. (2015). Early detection of fires in electrical installations by thermally modulated SnO_2/additive-multi sensor arrays. *Sens. Actuat. B* 217, 36–40. doi: 10.1016/j.snb.2015.02.014

Kou, X., Wang, C., Ding, M., Feng, C., Li, X., Ma, J., et al. (2016). Synthesis of Co-doped SnO_2 nanofibers and their enhanced gas-sensing properties. *Sens. Actuat. B* 236, 425–432. doi: 10.1016/j.snb.2016.06.006

Langer, F., Perl, S., Höfling, S., and Kamp, M. (2015). p- to n-type conductivity transition in 1.0 eV GaInNAs solar cells controlled by the V/III ratio. *Appl. Phys. Lett.* 106, 277–292. doi: 10.1063/1.4909507

Lee, K., Shim, Y.-S., Song, Y., Han, S., Lee, Y.-S., and Kang, C.-Y. (2017). Highly sensitive sensors based on metal-oxide nanocolumns for fire detection. *Sensors* 17:303. doi: 10.3390/s17020303

Li, N. (2014). Study on new electrical fire monitoring technology for low-voltage distribution cabinet. *Build. Electricity* 33:4. doi: 10.3969/j.issn.1003-8493.2014.07.007

Li, Z., and Yi, J. (2017). Enhanced ethanol sensing of Ni-doped SnO_2 hollow spheres synthesized by a one-pot hydrothermal method. *Sens. Actuat. B* 243, 96–103. doi: 10.1016/j.snb.2016.11.136

Linde, E., and Gedde, U. W. (2014). Plasticizer migration from PVC cable insulation - The challenges of extrapolation methods. *Polymer Degradation Stability* 101, 24–31. doi: 10.1016/j.polymdegradstab.2014.01.021

Srivastava, A. (2003). Detection of volatile organic compounds (VOCs) using SnO_2 gas-sensor array and artificial neural network. *Sens. Actuat. B* 96, 24–37. doi: 10.1016/S0925-4005(03)00477-5

Sun, L., Haidry, A. A., Fatima, Q., Li, Z., and Yao, Z. (2018). Improving the humidity sensing below 30% RH of TiO_2 with GO modification. *Mater. Res. Bull.* 99, 124–131. doi: 10.1016/j.materresbull.2017.11.001

Upadhyay, S. B. (2013). Volatile organic compounds (VOCs) response characteristics of the hydrothermally synthesized SnO_2 nanocapsules. *Sens. Lett.* 11, 1–6. doi: 10.1166/sl.2013.3020

Verstockt, S., Vanoosthuyse, A., Hoecke, S. V., Lambert, P., and Walle, R. V. D. (2010). "Multi-sensor fire detection by fusing visual and non-visual flame features," in *International Conference on Image & Signal Processing* (Trois-Rivières, QC). doi: 10.1007/978-3-642-13681-8_39

Vincent, T. A., Xing, Y., Cole, M., and Gardner, J. W. (2019). Investigation of response of high-bandwidth MOX sensors to gas plumes for application on a mobile robot in hazardous environments. *Sens. Actuat. B* 279, 1–510. doi: 10.1016/j.snb.2018.08.125

Wang, L., Zhang, J., Zhang, B., Liu, M., Fan, M., and Li, Q. (2018). "Experimental investigations on combustion behaviors of live PVC cables," in *Materials Science Engineering Conference Series* (Shanghai). doi: 10.1088/1757-899X/322/3/032004

Yi, J., Chen, W., Han, J., and Chen, D. (2019). Sensitive and selective detection of plasticizer vapors with modified-SnO_2 hollow nanofibers for electrical fire warning. *Sens. Actuat. B* 287, 364–370. doi: 10.1016/j.snb.2019.02.025

Yi, J., Zhang, H., Zhang, Z., and Chen, D. (2018). Hierarchical porous hollow SnO_2 nanofiber sensing electrode for high performance potentiometric H_2 sensor. *Sens. Actuat. B* 268, 456–464. doi: 10.1016/j.snb.2018.04.086

Zhao, Y., Zhang, S., Zhang, G., Deng, X., and Xie, C. (2014). Highly sensitive porous metal oxide films for early detection of electrical fire: surface modification and high throughput screening. *Sens. Actuat. B* 191, 431–437. doi: 10.1016/j.snb.2013.09.111

Conflict of Interest: The authors declare that the research was conducted in the absence of any commercial or financial relationships that could be construed as a potential conflict of interest.

frontiers in Materials

ORIGINAL RESEARCH
published: 04 October 2019
doi: 10.3389/fmats.2019.00238

A Simple Flow Injection Sensing System for the Real-Time On-Line Determination of Chemical Oxygen Demand Based on 3D Au-NPs/TiO_2 Nanotube Arrays

Hewei Si[1,2], *Xidong Zhang*[1,2] *and Shiwei Lin*[1,2]*

[1] State Key Laboratory of Marine Resource Utilization in South China Sea, Hainan University, Haikou, China, [2] School of Materials Science and Engineering, Hainan University, Haikou, China

3D bare TiO_2 nanotube arrays loaded with Au nanoparticles (3D Au-NPs/TNTAs) were prepared to effectively enhance the photoelectrocatalytic properties. A simple flow injection sensing system was proposed for the real-time on-line determination of chemical oxygen demand using the 3D Au-NPs/TNTAs electrode. The proposed photoelectrochemical oxidative degradation principle of the sensing system was analyzed and validated by the representative organic compounds with known COD values at a potential bias 1.5 V under UV illumination. A practical detection limit of the sensing system is 0.18 mg/L and the linear range is 1.92–3,360 mg/L under the optimum conditions. In the experimental process, the sensing system exhibits long-term stability and good reproducibility.

Keywords: 3D Au-NPs/TNTAs, photoelectrocatalytic, chemical oxygen demand (COD), flow injection sensing, real-time on-line COD determination

OPEN ACCESS

Edited by:
Girish Kale,
University of Leeds, United Kingdom

Reviewed by:
Mukul Pradhan,
National Institute of Technology Meghalaya, India
Ramendra Sundar Dey,
Institute of Nano Science and Technology (INST), India

***Correspondence:**
Shiwei Lin
linsw@hainanu.edu.cn

Specialty section:
This article was submitted to Functional Ceramics, a section of the journal Frontiers in Materials

Received: *14 May 2019*
Accepted: *12 September 2019*
Published: *04 October 2019*

Citation:
Si H, Zhang X and Lin S (2019) A Simple Flow Injection Sensing System for the Real-Time On-Line Determination of Chemical Oxygen Demand Based on 3D Au-NPs/TiO_2 Nanotube Arrays. Front. Mater. 6:238. doi: 10.3389/fmats.2019.00238

INTRODUCTION

Chemical oxygen demand (COD) is the oxygen equivalent on degradation of the organic compounds, which is a significant parameter of water quality assessment (Kondo et al., 2014). Even though potassium dichromate oxidation method is widely used, many inherent shortcomings such as time-consuming (2–4 h) reflux process, highly toxic chemicals, corrosiveness and high cost (Ag_2SO_4) were existing (Allan Moore et al., 1949; Zhang J. et al., 2009; Zhang S. et al., 2009). Photocatalytic methods can effectively solve these problems, but the resulting electron hole pairs are easy to recombine. Currently, an environmentally friendly and rapid photoelectrochemical COD determination way was considered a more promising approach to surmount the recombination of electron-hole pairs further to improve the degradation efficiency (Qu et al., 2011; Li et al., 2012).

However, the photoelectrocatalytic COD determination method implies a relatively narrow working range and poor reproducibility with a stop-flow operation mode in the quartz cell. Also, the shortcomings of conventional photoelectrochemical method are as follows: one is the complex three-electrode structure, the other is that it's hard to improve sensitivity because of inadequate degradation efficiency of working electrode (Liao et al., 2016).

TiO_2 nanotube arrays (TNTAs) extending on the Ti foil have been used as sensing electrode to detect chemical oxygen demand (COD) in recent years, owning to its intrinsic nanotubular architecture and remarkable properties (Li et al., 2006; Grimes, 2007; Zheng et al., 2008). Ti foil could be entirely transformed into nanotubes but a few micrometers thickness of nanotubes are sufficient for performing efficient photocatalysis. In addition, it is easy to have scattering effects in the liquid (Paulose et al., 2007; Kar and Smith, 2009). It's wasteful for Ti foil since it has relatively much loss of photons (Zhuang et al., 2007; Beranek et al., 2009). However, three-dimensional (3D) TNTAs photoelectrode extending radically on a grid of titanium wires can avoid this wastage and because of absorbing the reflected and/or refracted light (Liao et al., 2012). Furthermore, the 3D TNTAs on Ti mesh possess larger surface area than TiO_2 nanotube arrays on the Ti foil which means higher photocatalytic activity. Nevertheless, TiO_2 nanotube arrays show shorter lifetime, poor stability, unsatisfactory photocatalytic activity in real application for COD analysis (Liang et al., 2019). Therefore, it is important to propose a new sensor further to improve the weakness of present TiO_2 sensing.

To tackle these problems, we propose a flow injection photoelectrocatalytic COD determination method by combining continuous flow injection thin-cell reactor mode and Au nanoparticles (Au-NPs) loaded on 3D TNTAs. The influence of annealing temperature and anodizing time on the as-prepared bare 3D TNTAs were studied. The as-prepared 3D TiO_2 nanotube arrays were characterized via material characterizations and photoelectrochemical testing, such as FE-SEM, EDS, XRD, photocurrent-density potential characteristics and chronoamperometry experiments, to investigate their morphology, elements, structure, and photoelectrocatalytic activities. A new COD determination analytical principle was proposed, which was experimentally validated with representative organic compounds. Because of the different adsorption position on the surface of TiO_2, glucose, glutamic acid and GGA (glucose: glutamic acid = 1:1) were chosen as the representative organic compounds (Zhang et al., 2006; Han et al., 2010; Liu et al., 2014). The analytical signal generation of the proposed sensing system was optimized on the important experimental parameters such as supporting electrolyte and applied potential bias.

EXPERIMENTAL SECTION

Preparation of 3D Au-NPs/TNTAs/Ti

The working electrode was prepared by following steps. Firstly, titanium mesh (>99% purity, 50 meshes) was sliced rectangle pieces of 30 × 70 mm, which were fixed by titanium wire. Above treated titanium meshes were dipped into the mixture solution (HF: HNO_3: H_2O=1:4:5 in v/v) about 30 s to polish, then treated with acetone, ethanol and ultrapure water by ultra-sonication in order. Subsequently, dried in air. Secondly, the treated titanium mesh was electrochemical anodization in ethylene glycol electrolyte solution (2 wt% H_2O and 0.3 wt% NH_4F) by two electrode configurations in different anodization time 10, 20, 30, and 60 min. With the rate of heating 2°C min^{-1}, the obtained samples were calcinated at 350, 450, 550, and 650°C for 3 h in muffle furnace, respectively. Among them, the electrode material with the best oxidation ability was selected as the as-prepared working electrode. Thirdly, to improve photocatalytic activity and stability of the as-prepared working electrode, Au nanoparticles were deposited on the bare 3D TNTAs by the photo-reduction method. The as-prepared working electrode was dipped into the electrolyte consisted of mixture ($HAuCl_4$ (0.1g/L): HCHO =100:1 in v/v) in the quartz cell under UV irradiation for 40 s. Then the electrode was washed with ethanol, deionized water and dried in the air, which then was used as the working electrode. As for the counter electrode, Pt nanoparticles were electrodeposited on the titanium mesh treated above at −0.3V for 3 min in the mixed solution (H_2PtCl_6 (0.2g/L): HCHO =100:1 in v/v) (Si et al., 2019).

Characterization

The morphologies and microstructure of the electrode material were studied by scanning electron microscopy (FE-SEM) equipped with an energy-dispersive spectrometer (EDS). Crystal phase of the working electrode was analyzed by X-ray diffraction (XRD, Bruker D8) with Cu Kα radiation. To choose a 3D TNTAs electrode material with best oxidation ability, linear sweep voltammetry (LSV) was performed in cube quartz reactor (50 × 50 × 50 mm) at room temperature using saturated Ag/AgCl (KCl) reference electrode, platinum foil counter electrode and the as-prepared 3D TiO_2 nanotube arrays working electrode in all the experiments.

Fabrication of Flow Injection Sensing System and Measurement of Their Photoelectrocatalytic Real-Time On-Line COD Sensing Properties

Au modified 3D TiO_2 Nanotube Arrays as sensing electrode was used for real-time on-line COD determination in our proposed thin-cell reactor which can be seen from our previous work (Si et al., 2019). The schematic diagram and digital image of the real-time on-line thin-cell reactor was shown in **Figure S1**. The application potential bias and the recording of response current signal were supplied by the electrochemical workstation (Zahner Zennium, Germany). A 5W UV lamp was used as the UV source in the experiment. A 0.2 mM Na_2SO_4 solution was as the supporting electrolyte in the photoelectrochemical measurements.

RESULTS AND DISCUSSION

Characterization of the Electrode Materials

The effect of preparation parameters of anodic time and calcination temperature on the saturated photocurrent density of the as-prepared electrodes was obtained in LSV under the UV illumination (Zhang J. et al., 2009). As shown in **Table S1**, the electrode with anodic oxidation for 10 min and calcination temperature at 450°C possess the highest saturated photocurrent density. Therefore, the electrode which is prepared at 60 V for anodic time 10 min and calcination temperature at 450°C for

3 h (No. 2 in **Table S1**) was selected as the as-prepared working electrode in our proposed flow injection sensing system.

Figure 1 shows the surface morphology of the working electrode material where highly-ordered TNTAs are distributed uniformly and aligned vertically on the Ti meshes (Liao et al., 2012). The average inner diameter of the 3D TNTAs is 65 nm with length of 3 um, as depicted in **Figures 1B,C**. **Figure 1D** displays Au-NPs loaded on the 3D TNTAs and the EDS spectrum further identify the presence of Au-NPs on the bare 3D TNTAs where the weight of Au is 0.48% (**Figure S2**). The XPS results show the coexistence of Ti, O and Au elements in the prepared nanocomposite, as shown in **Figure S3**. From the XPS spectra, Ti 2p1/2 and Ti 2p3/2 were obtained at 464 eV and 458 eV while O 1s was at 530 eV, which are all consistent with the literature reports (Luo et al., 2016; Siavash et al., 2017). Furthermore, the existence of Au in the nanocomposite is confirmed by the Au 4f7/2 and Au 4f5/2 peaks at 83 and 86.7 eV, respectively. The role of Au in the Au/TiO_2 composite enhances the electrical conductivity and raises the optical conductivity further to improve the photoelectrocatalytic properties (Rudra et al., 2018a,b).

Figure 2 shows the XRD patterns of the 3D TNTAs before, and after calcinated. The diffraction peaks attributed to the formation of anatase TiO_2 structure after annealing, which has higher photocatalytic activity (Zhang et al., 2016). There appears rutile when the annealing temperature reaches to 650°C. Furthermore, the photocurrent response of the samples annealed at different temperatures were measured in comparation to that of Au nanoparticles modified TiO_2 nanotube arrays, as depicted in **Figure S4**. Among them, the sample annealed at 450°C has the optimal photocurrent density. The obtained working electrode possess the higher photocurrent density compared to pure TiO_2 nanotube arrays, indicating the existence of Au nanoparticles can improve the sensing property.

The Photoelectrocatalytic Properties of the Sensing System

Figure 3 shows photocurrent response of the sensing system as a function of time at the repeated on/off cycles with applied

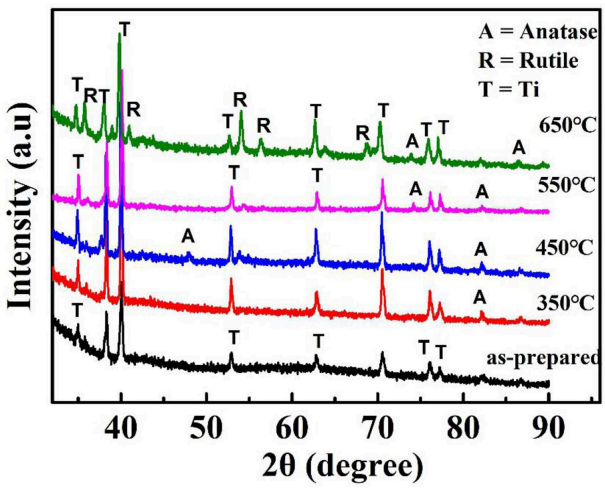

FIGURE 2 | XRD patterns of the reduced at 350, 450, 550, and 650°C, respectively and non-reduced as-prepared 3D TNTAs electrode.

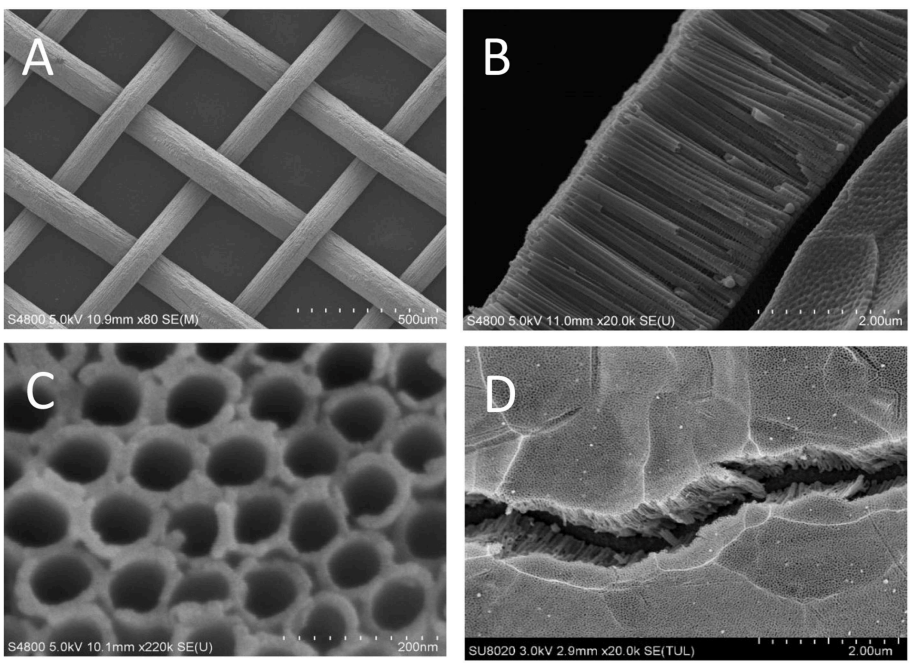

FIGURE 1 | SEM images: **(A)** Ti meshes, **(B)** side view and **(C)** top view of the bare 3D TNTAs, **(D)** Au-NPs on the bare 3D TNTAs.

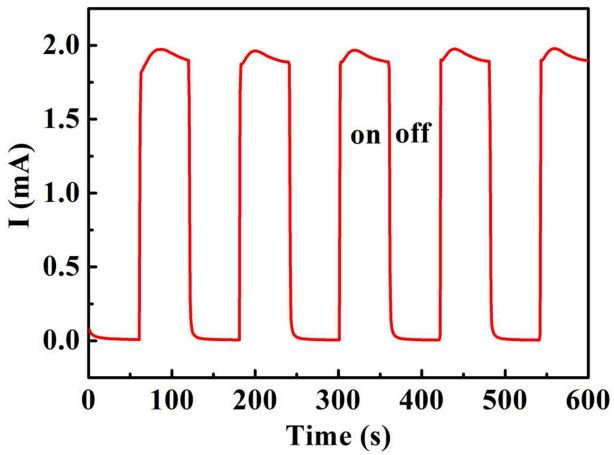

FIGURE 3 | Photocurrent responses of the sensing system as a function of time at the repeated on/off cycles with an applied potential 1.5 V under UV illumination. 0.2 mM Na_2SO_4 solution as the supporting electrolyte.

potential 1.5 V under UV illumination. The 0.2 mM Na_2SO_4 solution is as the supporting electrolyte. The photocurrent density of non-reduced bare 3D TNTAs was measured nearly to be 0 mA without UV light, but a significant increasing in current value was seen under UV illumination. The non-light current was measured to be low upon switch off the light, but the current quickly increased when turned on the UV light, indicating the sensing system responds quickly to UV source.

Figure 4 shows linear sweep voltammograms of the Au-NPs/3D TNTAs electrode in 0.2 mM Na_2SO_4 and 1 mM glucose in 0.2 mM Na_2SO_4 solution with and without UV irradiation, respectively, in order to investigate the response of oxidation current produced by degradation of organic compounds. As we can see from **Figure 4**, there was almost no response to oxidation current when glucose was added in the non-UV light (**Figure 4A**). However, a significant oxidation current appears when ultraviolet light was applied (**Figure 4B**).

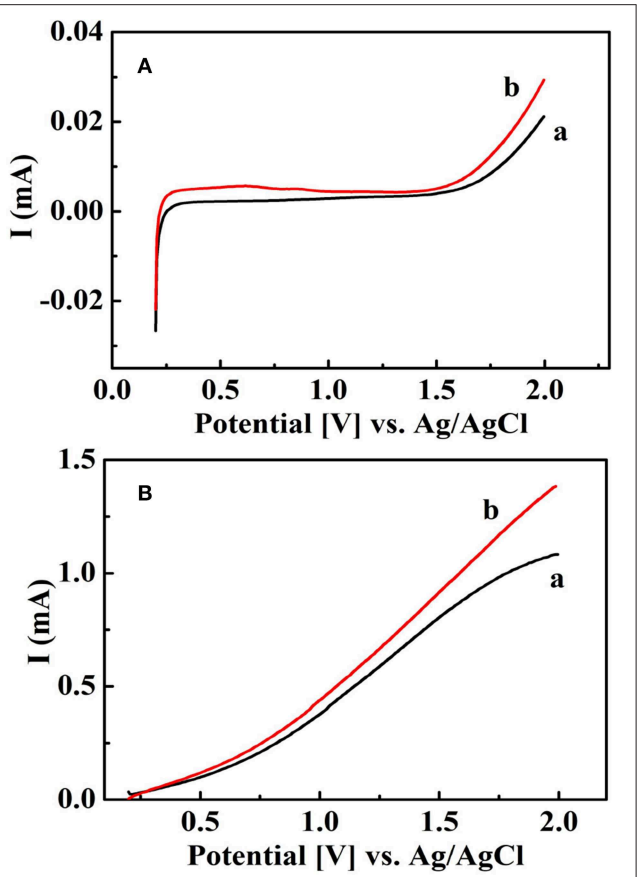

FIGURE 4 | Linear voltammograms of the sensing system: (a) 0.2 mM Na_2SO_4 and (b) 0.2 mM Na_2SO_4 containing glucose organic using 3D Au-NPs/TNTAs sensing electrode at the potential scan rate of 10 mVs^{-1} without **(A)** and with **(B)** UV illumination.

COD Sensing Mechanism

A new detection principle was proposed based on the postulate that the potential of the counter electrode

$$\varphi_{\text{counter}} = 0 \tag{1}$$

The analog circuit diagram of the proposed COD sensor is as follows **Figure 5**:

According to the "Closed Circuit Ohm Law," for the proposed COD sensor

$$E = \mathrm{v}_{reactor} + IR \tag{2}$$

Where E is the applied voltage; $\mathrm{v}_{\text{reactor}}$ is the voltage on the photoelectrochemical reactor; I is the current in the closed circuit; R is the resistance of the closed circuit except reactor.

When ultraviolet light irradiates the sensing electrode, photoholes possess strong oxidizing capacities which can mineralize organic compounds. Assuming that the organic compounds are stoichiometrically mineralized on surface of the sensing electrode, the potential of sensing electrode can be given by Nernst equation

$$\varphi_{\text{working}} = -2.30\frac{kT}{nq}\log C_m + A_1 \tag{3}$$

Where C_m, T, k, n, A are the molar concentration, temperature, Boltzmann constant, the electron transfer number of the individual organic compound and constant, respectively.

Therefore, the applied voltage on the reactor can be given as follows:

$$v_{reactor} = -2.30\frac{kT}{nq}\log C_m + A_1 \tag{4}$$

According to the relationship between molar concentration (C_{m}) and COD concentration [COD] = 8000 nC_m (Wang et al., 2013), then Equation (4) can be given by:

$$v_{reactor} = -2.30\frac{kT}{nq}\log[COD] + A_2 \tag{5}$$

Figure 6 shows the photocurrent-time profiles with the absence (i_{blank}) and existence (i_{total}) of organic compounds using the proposed sensing system. When the sensing electrode is illuminated with UV light, i_{blank} obtained in the supporting electrolyte mainly from the oxidation of water, while the observed photocurrent (i_{total}) in the sample organic solution originates from both the oxidation of water and the photoelectrocatalytic oxidation of organic compounds. As we know, i_{net} (net steady state current) originates from i_{total} via subtracting the i_{blank}, which is the step between the blank photocurrent and the total photocurrent in **Figure 6** (Chen et al., 2012).

$$I_{net} = i_{total} - i_{blank} \tag{6}$$

I_{net} can be transformed into the equivalent COD values according to Faraday's law.

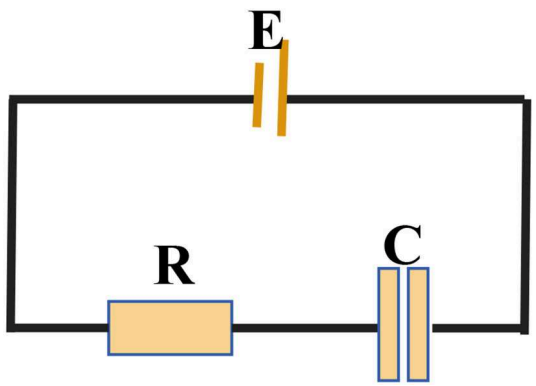

FIGURE 5 | Internal circuit diagram of the proposed real-time on-line sensing system.

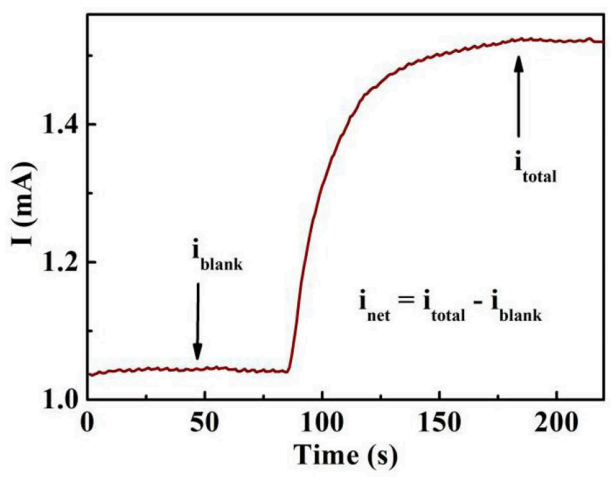

FIGURE 6 | Photocurrent response of a 0.2 mM Na_2SO_4 blank solution (i_{blank}) and the 0.2 mM Na_2SO_4 solution containing organic compounds (i_{total}). The step originates from the oxidation of the organic compounds.

According to Equations (2), (5), and (6), I_{net} can be given by:

$$I_{net} = \frac{2.30\frac{kT}{nq}\log[COD] - A_1 + v_{blank}}{R} \tag{7}$$

$$= \frac{2.30\frac{kT}{nq}\log[COD]}{R} + A \tag{8}$$

$$= \alpha \log[COD] + A \tag{9}$$

Where both α and A are constant. The I_{net} possess linear relationship with the logarithm of the COD value.

COD Sensing Properties

Photogenerated hole is a strong oxidant for degradation of organic compounds during the process of photocatalytic oxidation. The combination of photogenerated electrons and holes often limits the degradation efficiency. However, the addition of a bias voltage can transfer photogenerated electrons to the internal circuit, thereby improving the degradation efficiency (Zheng et al., 2008). In order to find the proper applied bias, the effect of applied bias on net current is studied under different bias conditions (Li et al., 2014), as shown in **Figure 7A**. The determined I_{net} values are lower than that the applied bias value is above 1 V, however, the obtained I_{net} values are not fluctuation when the applied voltages are between 1.0 and 1.5 V. In all the experiments, the applied bias 1.5 V was chosen as the proper voltage. In addition, the current signal is influenced by the large solution resistance due to the solution channel in the thin-layer reactor. The influence of supporting electrolyte concentration on the generated photocurrent is also studied. In **Figure 7B**, the current rises with the increase of conductive ions at a certain concentration range. The current reaches its saturation value at higher electrolyte concentration. Thus, 0.2 mM Na_2SO_4 was selected as the optimal supporting electrolyte concentration.

In order to validate the proposed COD analysis principle, some pure organic compounds such as glucose and sucrose and synthetic sample (GGA) were chosen as the representative organic compounds. Chronoamperometric experiments were performed via injecting various molar concentration organic compounds at a constant applied bias V = 1.5 V with UV light. When various concentration organic compounds were added, the rapidly raising photocurrent responses were obtained and then recorded by the electrochemical workstation (Zahner zennium, Germany). The relationship between I_{net} and molar concentration of individual organic compounds with equal COD values of each is presented in **Figure 8A**. In addition, the relationship between I_{net} and the equivalent theoretical COD values converted from the molar concentrations of organic compounds ($[COD] = 8000nC_m$) were deduced in **Figure 8B**. In the figure, I_{net} possess linear relationship with the logarithm of the organic compound concentrations studied in this paper. The plots display that the investigated organic compounds are fitted into a line $y = 0.000887\ \log(x) - 3.22\times10^{-4}$ (where y represents I_{net} obtained from organics oxidation, x represents the COD value of the organics) with $R^2 = 0.975$, indicating the proportional relationship between the I_{net} and the COD value

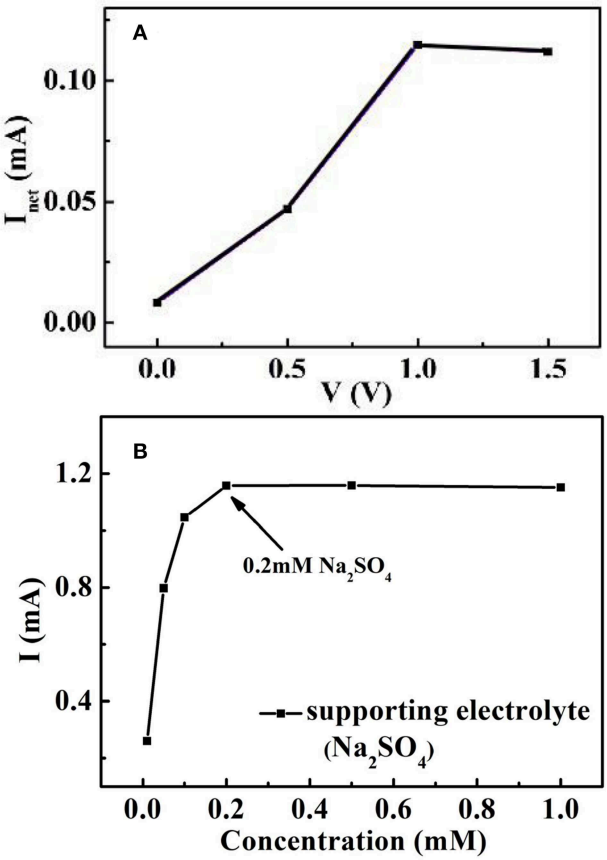

FIGURE 7 | Optimization of the real-time on-line sensing system: effect of **(A)** applied voltage and **(B)** supporting electrolyte concentration on photocurrent.

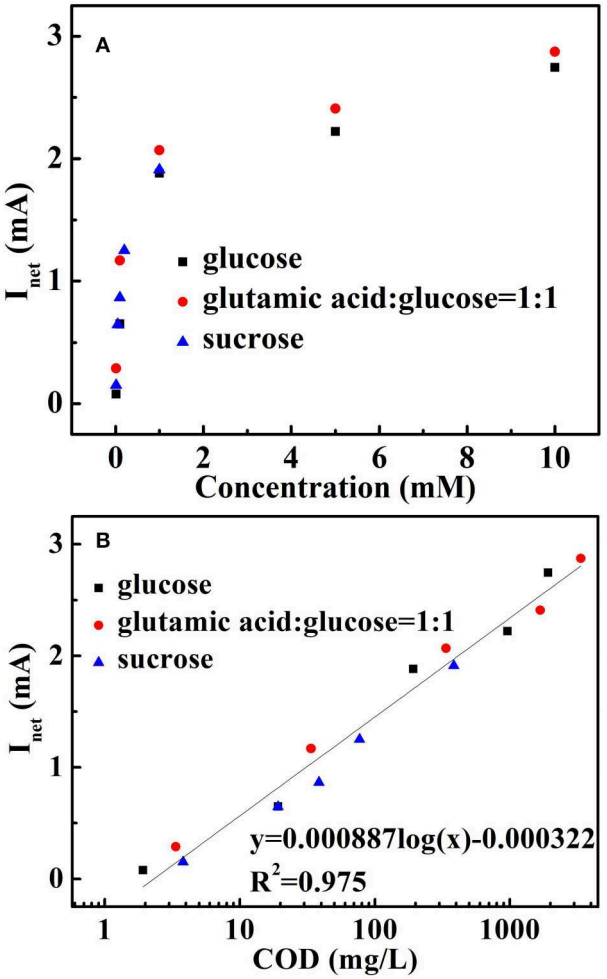

FIGURE 8 | Verification of analysis principle: **(A)** the correlation of I_{net} and molar concentrations of selected organic compounds; **(B)** the relationship between I_{net} and the theoretical COD values of the selected organic compounds.

for the 3D Au-NPs/TNTAs COD sensing system. Furthermore, a wide working linear range from 1.92 to 3,360 mg L^{-1} were obtained. The proposed COD sensing system also possess a detection limit of 0.18 mg L^{-1} COD (S/N=3).

Reproducibility and Operational Stability of the Proposed Sensing System

The reproducibility of the photoelectrochemical sensor was assessed by measuring the current signal at 19.2 mg/L COD (Yao et al., 2015). The relative standard deviation was 2.5% for 11 determinations, suggesting excellent reproducibility. To study the long-term stability about the proposed sensing system, response photocurrent to 0.1 mM glucose (theoretical COD value 19.2 mg/L) was measured during 10 days period. The RSD is 3.7%, showing good stability of the sensing system.

CONCLUSIONS

A real-time on-line sensing system combining with 3D Au-NPs/TNTAs sensing electrode and photoelectrochemical reactor is proposed toward the determination of COD, which is on account of the relationship between the COD values and the quantity captured charge applying the photoelelctrocatalytic method. In the photoelectrochemical experiments, the optimum conditions such as applied bias and supporting electrolyte were investigated. Glucose, sucrose and GGA were chosen as the representative organic compounds to validated the proposed sensing principle. The sensing photocurrent presents a linear relationship with the logarithm of COD values. The proposed sensing system shows a detection limit of 0.18 mg/L with the linear range from 1.96 to 3,360 mg/L.

DATA AVAILABILITY STATEMENT

All datasets generated for this study are included in the manuscript/**Supplementary Files**.

AUTHOR CONTRIBUTIONS

HS designed and conducted the experiments and analyzed the results. XZ prepared the bare 3D TNTAs nanotube arrays. SL revised, read, and approved the submitted version.

FUNDING

This work was supported by the National Natural Science Foundation of China (Grant No. 61764003), Major Science and Technology Planning Project of Hainan Province (ZDKJ201810).

SUPPLEMENTARY MATERIAL

The Supplementary Material for this article can be found online at: https://www.frontiersin.org/articles/10.3389/fmats.2019.00238/full#supplementary-material

REFERENCES

Allan Moore, W., Kroner, R. C., and Ruchhoft, C. C. (1949). Dichromate reflux method for determination of oxygen consumed. *Anal. Chem*. 21, 953–957. doi: 10.1021/ac60032a020

Beranek, R., Macak, J. M., Gärtner, M., Meyer, K., and Schmuki, P. (2009). Enhanced visible light photocurrent generation at surface-modified TiO_2 nanotubes. *Electrochim. Acta* 54, 2640–2646. doi: 10.1016/j.electacta.2008.10.063

Chen, H., Zhang, J., Chen, Q., Li, J., Li, D., Dong, C., et al. (2012). Assessment of a COD analytical method based on the photoelectrocatalysis of a TiO_2 nanotube array sensor. *Anal. Methods* 4:1790. doi: 10.1039/c2ay05940a

Grimes, C. A. (2007). Synthesis and application of highly ordered arrays of TiO_2 nanotubes. *J. Mater. Chem*. 17, 1451–1457. doi: 10.1039/b701168g

Han, Y., Zhang, S., Zhao, H., Wen, W., Zhang, H., Wang, H., et al. (2010). Photoelectrochemical characterization of a robust TiO_2/BDD Heterojunction electrode for sensing application in aqueous solutions. *Langmuir* 26, 6033–6040. doi: 10.1021/la903706e

Kar, A., and Smith, Y. R. (2009). Improved photocatalytic degradation of textile dye using titanium dioxide nanotubes formed over titanium wires. *Environ. Sci. Technol.* 43, 3260–3265. doi: 10.1021/es8031049

Kondo, T., Tamura, Y., Hoshino, M., Watanabe, T., Aikawa, T., Yuasa, M., et al. (2014). Direct determination of chemical oxygen demand by anodic decomposition of organic compounds at a diamond electrode. *Anal. Chem*. 86, 8066–8072. doi: 10.1021/ac500919k

Li, J., Zheng, L., Li, L., Shi, G., Xian, Y., and Jin, L. (2006). Photoelectro-synergistic catalysis at Ti/TiO_2/PbO_2 electrode and its application on determination of chemical oxygen demand. *Electroanalysis* 18, 2251–2256. doi: 10.1002/elan.200603644

Li, L., Zhang, S., Li, G., and Zhao, H. (2012). Determination of chemical oxygen demand of nitrogenous organic compounds in wastewater using synergetic photoelectrocatalytic oxidation effect at TiO_2 nanostructured electrode. *Anal. Chim. Acta* 754, 47–53. doi: 10.1016/j.aca.2012.10.008

Li, X., Bai, J., Liu, Q., Li, J., and Zhou, B. (2014). WO_3/W nanopores sensor for Chemical Oxygen Demand (COD) determination under visible light. *Sensors* 14, 10680–10690. doi: 10.3390/s140610680

Liang, L., Yin, J., Bao, J., Cong, L., Huang, W., Lin, H., et al. (2019). Preparation of Au nanoparticles modified TiO_2 nanotube array sensor and its application as chemical oxygen demand sensor. *Chin. Chem. Lett*. 30, 167–170. doi: 10.1016/j.cclet.2018.01.049

Liao, J., Lin, S., Zeng, M., and Yang, Y. (2016). A miniature photoelectrochemical sensor based on organic electrochemical transistor for sensitive determination of chemical oxygen demand in wastewaters. *Water Res*. 94, 296–304. doi: 10.1016/j.watres.2016.02.061

Liao, J., Lin, S., Zhang, L., Pan, N., Cao, X., and Li, J. (2012). Photocatalytic degradation of methyl orange using a TiO_2/Ti mesh electrode with 3D nanotube arrays. *ACS Appl. Mater. Interfaces* 4, 171–177. doi: 10.1021/am201220e

Liu, C., Zhao, H., Ma, Z., An, T., Lau, C., Zhao, L., et al. (2014). Novel environmental analytical system based on combined biodegradation and photoelectrocatalytic detection principles for rapid determination of organic pollutants in wastewaters. *Environ. Sci. Technol*. 48, 1762–8. doi: 10.1021/es4031358

Luo, J., Chen, J., Wang, H., and Liu, H. (2016). Ligand-exchange assisted preparation of plasmonic Au / TiO_2 nanotube arrays photoanodes for visible-light-driven photoelectrochemical water splitting. *J. Power Sources* 303, 287–293. doi: 10.1016/j.jpowsour.2015.11.016

Paulose, M., Prakasam, H. E., Varghese, O. K., Peng, L., Popat, K. C., Mor, G. K., et al. (2007). TiO_2 nanotube arrays of 1000 μm length by anodization of titanium foil: phenol red diffusion. *J. Phys. Chem. C* 111, 14992–14997. doi: 10.1021/jp075258r

Qu, X., Tian, M., Chen, S., Liao, B., and Chen, A. (2011). Determination of chemical oxygen demand based on novel photoelectro-bifunctional electrodes. *Electroanalysis* 23, 1267–1275. doi: 10.1002/elan.201000641

Rudra, S., Nayak, A. K., Chakraborty, R., Maji, P. K., and Pradhan, M. (2018a). Synthesis of Au-V_2O_5 composite nanowires through the shape transformation of a vanadium(iii) metal complex for high-performance solid-state supercapacitors. *Inorg. Chem. Front*. 5, 1836–1843. doi: 10.1039/C8QI00325D

Rudra, S., Nayak, A. K., Koley, S., Chakraborty, R., Maji, P. K., and Pradhan, M. (2018b). Redox-mediated shape transformation of Fe_3O_4 nanoflakes to chemically stable Au–Fe_2O_3 composite nanorods for a high-performance asymmetric solid-state supercapacitor device. *ACS Sustain. Chem. Eng.* 7, 724–733. doi: 10.1021/acssuschemeng.8b04300

Si, H., Pan, N., Zhang, X., Liao, J., Rumyantseva, M. N., Gaskov, A. M., et al. (2019). A real-time on-line photoelectrochemical sensor toward chemical oxygen demand determination based on field-effect transistor using an extended gate with 3D TiO_2 nanotube arrays. *Sens. Actuators B Chem*. 289, 106–113. doi: 10.1016/j.snb.2019.03.071

Siavash, R., Kia, G., Goh, L., Dolati, A., and Ghorbani, M. (2017). Applied catalysis B: environmental sunlight-driven photoelectrochemical sensor for direct determination of hexavalent chromium based on Au decorated rutile TiO_2 nanorods. *Appl. Catal. B Environ*. 201, 411–418. doi: 10.1016/j.apcatb.2016.08.026

Wang, C., Wu, J., Wang, P., Ao, Y., Hou, J., and Qian, J. (2013). Photoelectrocatalytic determination of chemical oxygen demand under visible light using Cu_2O-loaded TiO_2 nanotube arrays electrode. *Sens. Actua. B Chem*. 181, 1–8. doi: 10.1016/j.snb.2013.02.011

Yao, N., Liu, Z., Chen, Y., Zhou, Y., and Xie, B. (2015). A novel thermal sensor for the sensitive measurement of chemical oxygen demand. *Sensors* 15, 20501–20510. doi: 10.3390/s150820501

Zhang, J., Zhou, B., Zheng, Q., Li, J., Bai, J., Liu, Y., et al. (2009). Photoelectrocatalytic COD determination method using highly ordered TiO_2 nanotube array. *Water Res*. 43, 1986–1992. doi: 10.1016/j.watres.2009.01.035

Zhang, S., Jiang, D., and Zhao, H. (2006). Development of chemical oxygen demand on-line monitoring system based on a photoelectrochemical degradation principle. *Environ. Sci. Technol.* 40, 2363–2368. doi: 10.1021/es052018l

Zhang, S., Li, L., and Zhao, H. (2009). A portable photoelectrochemical probe for rapid determination of chemical oxygen demand in wastewaters. *Environ. Sci. Technol*. 43, 7810–7815. doi: 10.1021/es901320a

Zhang, Z., Chang, X., and Chen, A. (2016). Determination of chemical oxygen demand based on photoelectrocatalysis of nanoporous TiO_2 electrodes. *Sens. Actua. B Chem*. 223, 664–670. doi: 10.1016/j.snb.2015.10.001

Zheng, Q., Zhou, B., Bai, J., Li, L., Jin, Z., Zhang, J., et al. (2008). Self-organized TiO_2 nanotube array sensor for the determination of chemical oxygen demand. *Adv. Mater*. 20, 1044–1049. doi: 10.1002/adma.200701619

Zhuang, H. F., Lin, C. J., Lai, Y. K., Sun, L., and Li, J. (2007). Some critical structure factors of titanium oxide nanotube array in its photocatalytic activity. *Environ. Sci. Technol*. 41, 4735–4740. doi: 10.1021/es0702723

Conflict of Interest: The authors declare that the research was conducted in the absence of any commercial or financial relationships that could be construed as a potential conflict of interest.

frontiers in Materials

ORIGINAL RESEARCH
published: 07 November 2019
doi: 10.3389/fmats.2019.00277

Improved Gas Selectivity Based on Carbon Modified SnO_2 Nanowires

Matteo Tonezzer[1], Sandro C. Izidoro[2], João P. A. Moraes[2] and Le Thi Thanh Dang[3]*

[1] IMEM-CNR, Sede di Trento - FBK, Trento, Italy, [2] Institute of Technological Sciences (ICT), Advanced Campus at Itabira, Universidade Federal de Itajubá, Itabira, Brazil, [3] ITIMS, Hanoi University of Science and Technology, Hanoi, Vietnam

The analysis of ambient (home, office, outdoor) atmosphere in order to check the presence of dangerous gases is getting more and more important. Therefore, tiny sensors capable to distinguish the presence of specific pollutants is crucial. Herein, a resistive sensor based on a carbon modified tin oxide nanowires, able to classify different gases and estimate their concentration, is presented. The C-SnO_2 nanostructures are grown by chemical vapor deposition and then used as a conductometric sensor under a temperature gradient. The device works at lower temperatures than pure SnO_2, with a better response. Five outputs are collected and combined to form multidimensional data that are specific of each gas. Machine learning algorithms are applied to these multidimensional data in order to teach the system how to recognize different gases. The six tested gases (acetone, ammonia, CO, ethanol, hydrogen, and toluene) are perfectly classified by three models, demonstrating the goodness of the raw sensor response. The gas concentration can also be estimated, with an average error of 36% on the low concentration range 1–50 ppm, making the sensor suitable for detecting the exceedance of the danger thresholds.

Keywords: metal oxide, tin oxide, carbon, hybrid material, gas sensor, selectivity

OPEN ACCESS

Edited by:
Xiaogan Li,
Dalian University of Technology (DUT), China

Reviewed by:
Yangong Zheng,
Ningbo University, China
Haiying Du,
Dalian Nationalities University, China
Han Jin,
Ningbo University, China

****Correspondence:***
Matteo Tonezzer
matteo.tonezzer@cnr.it

Specialty section:
This article was submitted to Functional Ceramics, a section of the journal Frontiers in Materials

Received: *20 May 2019*
Accepted: *21 October 2019*
Published: *07 November 2019*

Citation:
Tonezzer M, Izidoro SC, Moraes JPA and Dang LTT (2019) Improved Gas Selectivity Based on Carbon Modified SnO_2 Nanowires. Front. Mater. 6:277. doi: 10.3389/fmats.2019.00277

INTRODUCTION

Increasing pollution is following the progressive urbanization of green areas. Respiratory diseases are increasing due to air contamination in urbanized areas (Jiang et al., 2016; Mo et al., 2018). Consequently, a large number of sensors able to monitor the air quality in workplaces, public places, and residential buildings is required. Such devices clearly need to be tiny, cheap and easy-to-use. A good option could be using metal oxide semiconductor gas sensors, due to their strong corrosion resistance, low cost, simple fabrication, and portability. The huge surface-to-volume ratio of nanostructures improves the sensing performance of metal oxides very much, consenting to detect a gas down to concentrations lower one part per million (ppm). Furthermore, metal oxides (MOs) are sensitive to a wide range of volatile compounds and gases, and this makes them useful for a variety of applications: medical diagnosis (Saidi et al., 2018), defense against terrorist threats (Konstantynovski et al., 2018), agriculture (Sabir et al., 2014), and food and beverages quality (Miller et al., 2014). Finally, adjusting the size and shape of MO nanostructures permits to tune their sensing parameters, owed to their structure-dependent properties (Tonezzer and Iannotta, 2014). Unfortunately, these materials show two weak points: high working temperature and poor selectivity. In order to reduce the MO sensor working temperature, many groups are focusing on decorating it with catalyst. Typical catalysts for SnO_2 gas sensors are noble metals such as Pt, Ag, Au, and Pd that increase the sensors response at the same temperature (Iftekhar Uddin et al., 2015; Zhou et al., 2018). This method is effective, but its high cost limits its application.

Selectivity, on the other hand, can be achieved combining a set of these sensors in an electronic nose (Hines et al., 1999; Lee et al., 2002; Tai et al., 2004; Gulbag and Temurtas, 2006; Wolfrum et al., 2006; Cho et al., 2008, 2012; Marco and Gutiérrez-Galvez, 2012; Zhao et al., 2016; Chen et al., 2017; Jiang et al., 2017; Moon et al., 2018; Zhang and Gao, 2019), which however is more cumbersome, complex and expensive. Herein we overcome these problems using carbon modified tin oxide nanowires (Kim et al., 2011, Koo et al., 2017, Wang et al., 2019) and operating them in a temperature gradient. This approach should contain costs much lower than those of an electronic nose, using several different materials.

The idea (a virtual sensor array induced by a thermal gradient) is indeed in between the simple MO resistive sensor and the electronic nose, summarizing the best properties of both (Tonezzer et al., 2018, 2019). Good results can be achieved also with a single nanostructure (Tonezzer, 2019), but that setup is harder to obtain and difficult to replicate for practical purpose out of the laboratory. Using carbon modified SnO_2 nanowires as an active material, we could decrease the working temperature range down to 150–270°C. Combining five responses, the nanosensor is able to perfectly classify the six target gases (acetone, ammonia, CO, ethanol, hydrogen, and toluene). It also estimates the gas concentration of each gas with a good average error (36%). This performance is not as good as that of electronic noses but comes from one tiny single material nanosensor that can be easily integrated into distributed networks, mobiles, and wearable electronics.

MATERIALS AND METHODS

Synthesis of Nanowires

The tin oxide-carbon nanostructures were grown by chemical vapor deposition (CVD) in a horizontal quartz tube positioned inside a Lindberg Blue M furnace. The tin oxide evaporation source (an alumina boat filled with SnO powder) was put at the center of the furnace, where the temperature has its maximum. A Si/SiO_2 substrate, deposited with a very thin film of gold catalyst (3–5 nm) was placed at 1 cm from the alumina source.

The quartz tube was pumped down to 80 Pa, and purged with high purity (99.999%) argon. The pump-purge step was cycled three times, and then the tube was pumped down to its limit pressure. The temperature was raised from 25 to 800°C at a rate of 25°C per min. After 5 min at 800°C, an oxygen flow of 0.5 standard cubic centimeters (sccm) was inserted into the tube. After 20 min, 1 sccm of acetylene was added to the process for 10 min, and then the equipment was switched off and cooled down naturally.

Material Characterization

The film grown by CVD was investigated by X-ray diffraction (XRD) using a Philips Xpert Pro working with CuKα radiation at 40 kV. The morphology of the nanostructures was studied by secondary electron microscopy (SEM) with a Hitachi S-4800. Transmission electron microscopy (TEM) was accomplished with a JEM-100CX operated at 90 kV.

Fabrication of the Sensor

Small drops of silver paste were dropped on the nanostructured film in order to get electrical contacts. The resistive sensor is then measured with two micromanipulators in order to measure the resistance of the C-SnO_2 nanostructures as the surrounding atmosphere changes.

Gas Sensors Measurements

The resistive gas sensor was measured in a home-built system. The apparatus includes measuring chamber, sensor holder with integrated heater, four micromanipulators, mass flow controllers connected to high purity gas bottles, and Keithley 2410 multimeter connected to a data acquisition system (LabView, National Instruments).

First, the device was kept at 500°C in N_2 for 3 h while biased at 1 V in order to improve its base resistance and the stability of the nanostructures. This treatment reduces the drift of the sensor response during the measurements (Tischner et al., 2008). A good linear relation of the I-V curves was found, proving a good ohmic contact between the nanostructures and the silver paste. The device was operated under a continuous voltage of 1 V in the temperature range of 150–270°C. At different times, six different gases (acetone, ammonia, CO, ethanol, hydrogen, and toluene) were inserted into the measuring chamber, adjusting their concentration through mass flow controllers. The concentration values were the same for all the gases: 1, 5, 10, 20, and 50 parts per million (ppm). The total gas flow (target gas + dry air) was kept constant at 400 sccm. Along this paper, the sensor response S is defined as $S = R_{gas}/R_{air}$, where R_{gas} and R_{air} are the resistance of the sensor in presence of the target gas or in dry air, respectively. This choice was made because all the target gases were reducing. Selectivity to a target gas A toward any interfering gas B is traditionally defined as the ratio of the sensor response to gas A to the response to gas B (Kalantar-zadeh, 2013). The selectivity of the sensor is defined as the ratio of its best response to its second-best response.

Machine Learning Algorithms

Each measurement set (the five response values at 150, 180, 210, 240, and 270°C) relative to a gas and its concentration, is used as a five-dimensional point, fed to classifiers and then to the support vector regressor that estimates gas concentration. Train and test datasets were composed by 10 and 5 points for each gas, respectively. The classifiers use the label "gas" given together with the measurements in the train set and return a "gas" label for the new measures in the test set, classifying the new points. After the classification, the dataset was split in sub-datasets, each relative to a classified gas, and fed to a support vector regressor with linear kernel using R software. The regressor gave an estimate gas concentration that was compared with the true value in order to calculate its RMS relative error as $RMSE = \sqrt{\frac{\sum_{i=1}^{N}\left(\frac{E_i - C_i}{C_i}\right)^2}{N}}$, where N is the number of data in the sub-dataset and C_i and E_i are the gas concentration and gas estimate, respectively.

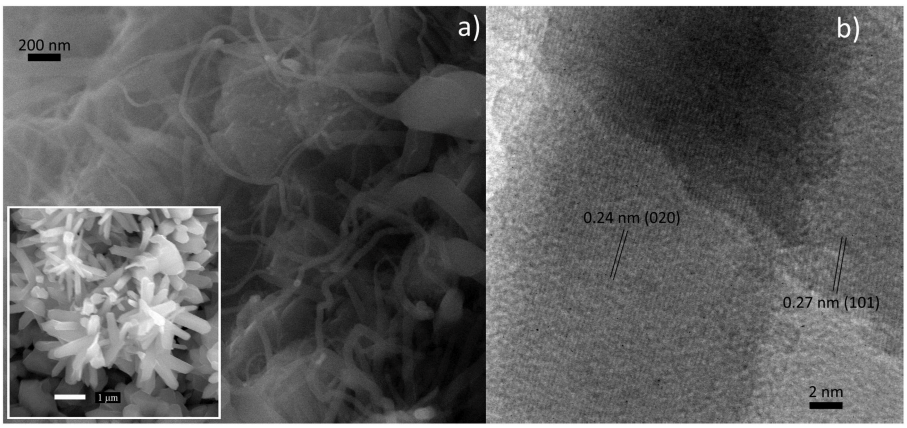

FIGURE 1 | (a) SEM image of the sensor: nanorods and nanowires with different diameters. Inset: The SnO_2 nanorods grown without carbon modification. **(b)** HR-TEM image of two nanowires from the same sample of **(a)**.

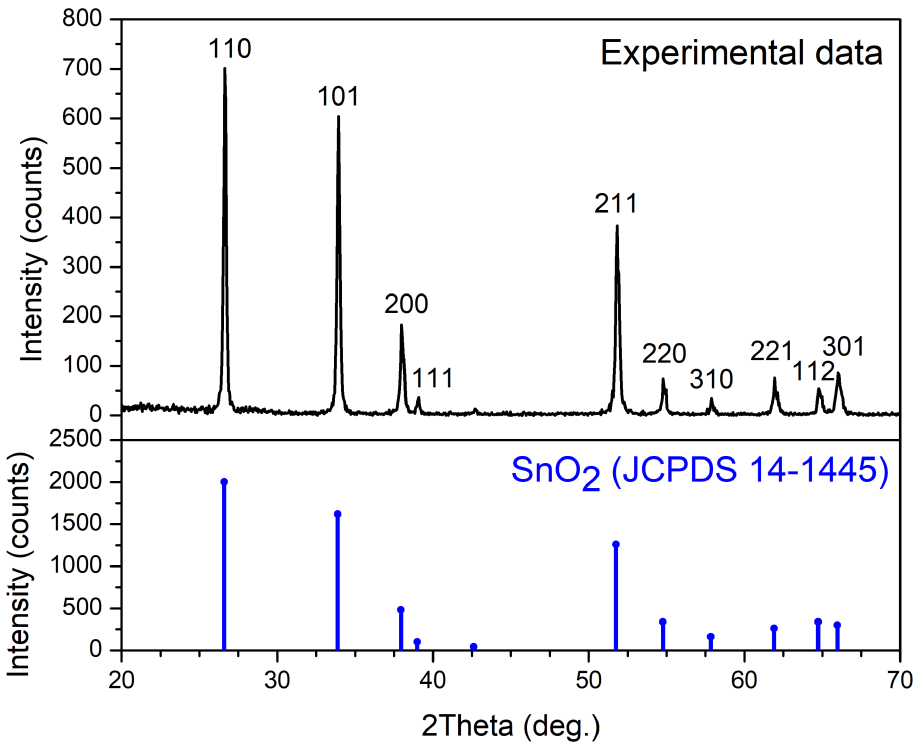

FIGURE 2 | XRD spectra. **Top**: spectrum of SnO_2:C nanowires; **Bottom** (blue online): reference spectrum of tin oxide (JCPDS 14-1445).

RESULTS AND DISCUSSION

Nanowires Characterization

The morphology of the C-SnO_2 nanowires has been investigated through secondary electron microscopy. A typical SEM image of the nanostructures is given in **Figure 1a**. As can be seen, there are worm-like structures with different size: nanorods with diameters around 150–200 nm and thinner nanowires with diameters down to 20–40 nm. This is different from the case of pure SnO_2 nanowires, shown in the inset of **Figure 1a**, which are similar for the large nanowires (diameters around 150–300 nm), but lack completely the smallest worm-like nanowires. We hypothesize that the different shape of the small nanostructures may derive from the mismatch between the SnO_2 crystal lattices due to the presence of carbon. The effect of crystalline defects is more intense for thinner nanowires, which are therefore more tortuous. **Figure 1b** shows a high-resolution TEM image of two nanowires from the same sample. It can be seen that the nanostructures are smooth and monocrystalline. Two interplanar spacings are visible in

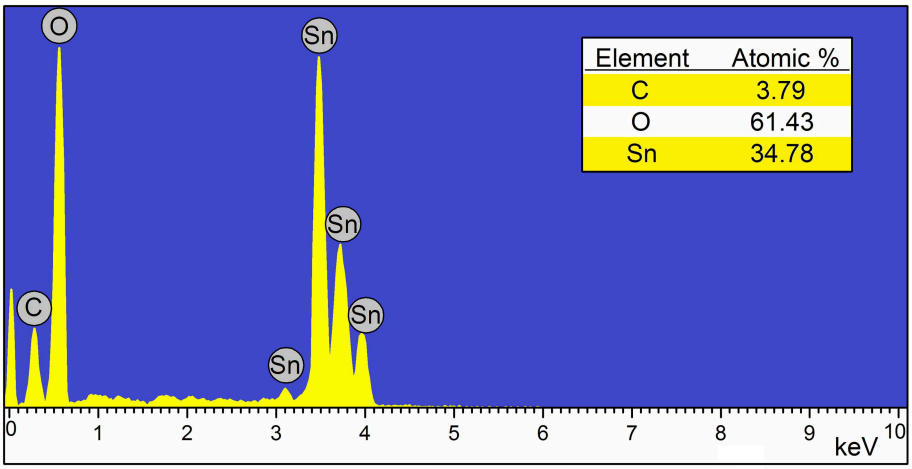

FIGURE 3 | Energy dispersive X-ray spectrometry (EDS) spectrum of the nanomaterial, evidencing the presence of only three elements: tin, oxygen, and carbon.

Figure 1b: one of 0.24 nm which corresponds to the (020) planes, and one of 0.27, corresponding to the (101) planes of the tin dioxide.

The structure of the nanostructures was investigated by XRD, and the results are shown in **Figure 2**.

All the diffraction peaks in **Figure 2** could be indexed to the tetragonal phase of tin oxide, with lattice parameters of a = b = 4.742 Å and c = 3.186 Å, which is well in agreement with the reference (JCPDS no. 14-1445). No other peaks are present, confirming that the carbon does not crystallize in nanoparticles, nor amasses in amorphous phase.

Unfortunately, TEM and XRD don't show any trace of carbon. Up to now, we can only hypothesize its presence due to the morphology of the nanowires. For this reason, we have performed compositional characterization, and the EDS spectrum is shown in **Figure 3**.

As can be seen, the presence of carbon is confirmed by energy dispersive X-ray spectrometry. It's percentage is a bit lower than 4%, while the stoichiometry of SnO_2 is a bit low in oxygen, probably due to the surface defects.

Response and Traditional Selectivity

Since the basis of our system is a resistive sensor, the first step is obviously to collect a dynamic resistance from it. From this output, the sensor response can be calculated, as defined in section Gas Sensors Measurements. This is a one-dimensional signal, and therefore intrinsically non-selective. All the target gases (acetone, ammonia, carbon monoxide, ethanol, hydrogen, and toluene) were tested at the same concentrations (1, 5, 10, 20, and 50 ppm) in order to facilitate the comparison. The response to various gases has been calculated and compared, showing that the nanosensor is not specific for any gas. The average selectivity of the C-SnO_2 sensors (averaged on the different concentrations) is 1.47, 1.30, 1.44, 1.82, and 1.18 at increasing working temperatures. At all the temperatures, the highest responses are found for acetone and ethanol, while the other gases who lower response values. It is obvious that, with the traditional definition, the present sensor is poorly selective, only for two gases. The selectivity as a function of the working temperature is reported in **Figure 4**. The bar color reflects the gas toward which the device is selective at that temperature (blue is acetone, cyan is ethanol).

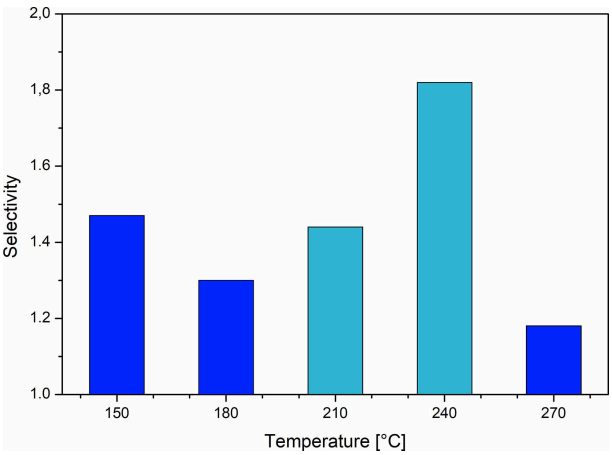

FIGURE 4 | Selectivity as a function of the sensor working temperature. At 150, 180, and 270°C the sensor is selective to acetone, while at 210 and 240°C it is selective to ethanol.

Exploiting different working temperatures, we could get a sensor that is selective to two different gases (Tonezzer et al., 2016), but here the selectivity is too low and does not provide a real discrimination among test gases. Therefore, we use machine learning techniques in order to give the system a way to distinguish the gases by itself.

From Dynamic Resistance to Thermal Response: the Basis for the System Working

The smart sensor working method is summarized in **Figure 5** using acetone as an example. The first step is the dynamic

resistance of the C-SnO_2 nanowires, measured at the various temperatures. As can be seen in the upper plots, the device resistance decreases abruptly when acetone is injected into the system and returns to the initial value when the gas is replaced with air.

This means that the carbon addition does not change the conduction behavior of SnO_2 materials, which is an n-type semiconductor, very sensitive to its surroundings (Tsuda et al., 2000). When the sensor is taken out of the furnace and exposed to air, oxygen is adsorbed on its surface in the form of O^- and O^{2-}, draining electrons from the nanowires and decreasing the conductivity. This is its basic state. When the molecules of a reducing gas like acetone, are flowed onto the sensor's nanomaterial, they react with the adsorbed oxygen on the surface, releasing electrons back to the nanowires. This increases the electrons density and decreases the sensor resistance.

As the acetone example in the top part of **Figure 5** shows, both response and recovery arise very sharply and then reduce their slope while the system reaches its saturation. When the acetone injection ends and is replaced by air again, the resistance recuperates its original value with negligible drift. This behavior is valid for all tested gases.

The sensor responses calculated from the transient resistance at each temperature, are plotted as a function of the working temperature, as show in the bottom-left part of **Figure 5**. As can be seen in that plot, the segmented line relative to each gas is different. We should stress that the segmented lines move upwards with increasing gas concentration, but always maintaining their shape. The five values forming each segmented line are then used as a five-dimensional point, which is used by the classifiers and by support vector regressor in order to discriminate which gas is present, and its concentration.

Visual Classification With UMAP

A first step, using the 5D points just obtained, is the classification of each measurement, in order to understand to which target gas it belongs. Machine learning models can be divided into tree-based models, linear models, neural networks, non-parametric models and ensembles. Models in the same category tend to perform similarly for the same task. The choice of a model still is heavily based on trial and error, and, for that reason, models of each of those classes were chosen. When working in classification tasks it is important to select a features space that represents the data, which were accomplished by the sensor data, which is high dimensional. To better inspect the algorithm and to use only relevant features it is common to introduce a dimensionality reduction technique and project the data onto a plane (the screen or the paper). In our case, we shrink the 5D space down to 2D using Uniform Manifold Approximation and Projection for dimension reduction (UMAP) (McInnes et al., 2018). Dimension reduction is indeed important because it allows both visualizing and pre-processing data for machine learning. UMAP is a very novel and powerful technique, very quick and strong. It finds a projection that closely approximates the conditions of the

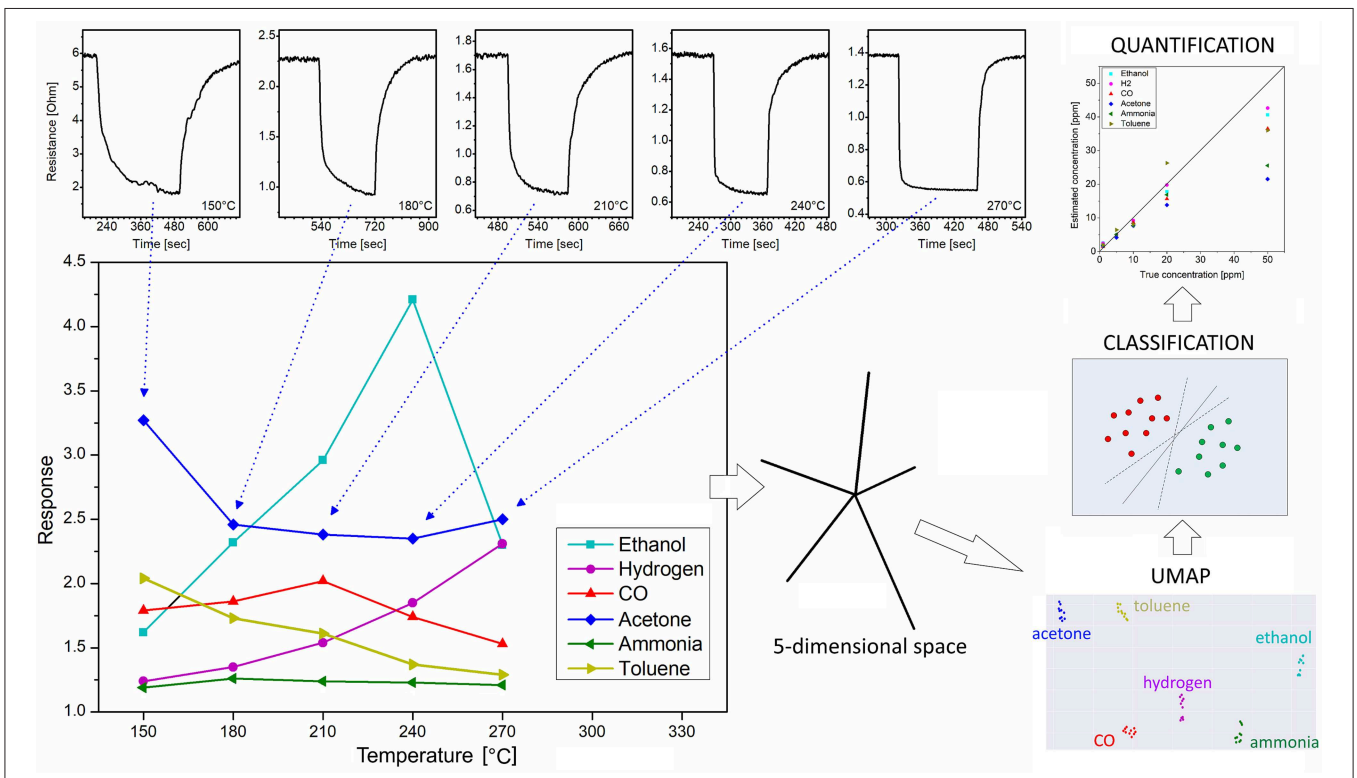

FIGURE 5 | Procedure to obtain the smart sensing: the dynamic response at the five temperatures is used to obtain a segmented line (the blue segmented line in the bottom-left plot of this example); this segmented line is used as a 5D point for both visualization (UMAP) and classification and regression (SVM).

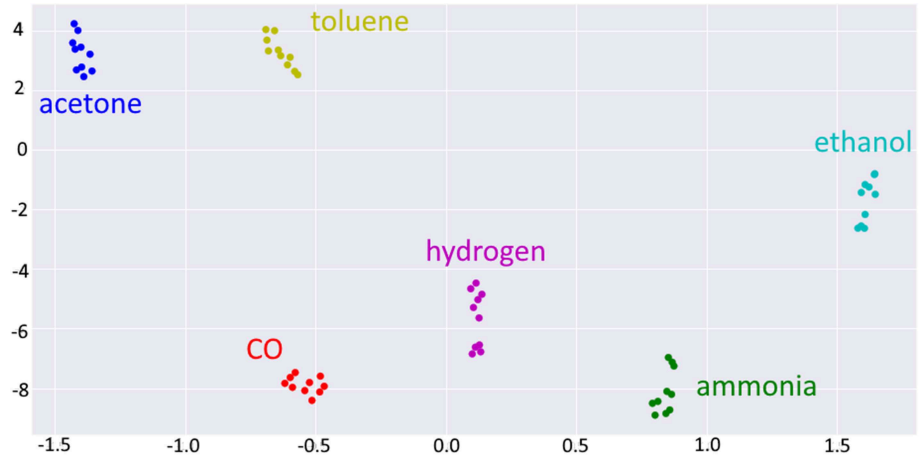

FIGURE 6 | Two-dimensional projection obtained with UMAP from the original 5D raw data points. Colors represent gases: Acetone (blue), Ammonia (green), CO (red), Ethanol (cyan), Hydrogen (purple), and Toluene (yellow).

original space, trying to preserve the global and local structures and to keep interpretability of data. The UMAP projection can be seen in **Figure 6**.

It is clear from **Figure 6** that the points belonging to different gases are well-separated and distinguishable. Unfortunately, this is not enough: dimension-reduction techniques only allow better visualization, but are not classification techniques. In other words, the eyes and the brain of the reader allow him to classify the different gases in **Figure 6**, but the sensor still doesn't know anything. For this reason, we have implemented several classification methods in order to test the classification performance of our system.

Classification With Different Methods

After the UMAP reduction, in order to better evaluate the performance our system, we have used seven different methods to classify the response data: Random Forest, SVM, Ada Boost, Bagging (KNN), Extra Trees, Decision Trees, and MLP (see **Supplementary Material**). We must here underline that, in order to avoid overfitting (due to the small number of data), the Stratified K-fold method was used to validate the data. This method consists of splitting the data into k random splits while keeping each class in the split proportional to its true proportion in the whole dataset. The model is trained with k−1 splits and validated on the missing split. The process is repeated k times until all data are used for validation.

To train an ensemble of classifiers there are two methods that stand out, the process of bagging and boosting. Bagging consists of training each classifier with a random sample from the data, and train each model independently. Boosting consists in training the models sequentially. Each model is trained to try to minimize the errors from the previous models and it does so by training the following model with a sample of the data that has a greater percentage of the class that was misclassified by the previous models.

Support vector machines (SVM) are supervised learning models that work by drawing a hyperplane in the features space of the data to maximize the separation of classes. Support vector machines are very popular when dealing with small datasets and should be one of the first models to be considered when dealing with linearly separable data (Haykin, 2009).

Multilayer perceptrons (MLP) are neural networks composed by an input layer followed by sequential hidden layers before the output layer. MLPs are universal function approximators dealing very well with non-linear data and have been very promising in the deep learning community (Haykin, 2009).

Decision Trees build a binary decision tree where each node tests a feature splitting the data into two paths. A classification is made by a path from the root node to the leaf node. Tree-based models had a lot of popularity before the advent of deep learning and still one of the best performant models in machine learning competitions. The models Random Forest, AdaBoost, and Extra trees are ensembles derived from the Decision Tree and were also tested as those variants are more widely used and avoid overfitting to the data (Sheppard, 2017).

Random forests work by creating several decision trees each of which are trained with a random subset of the data by the boosting algorithm. The classification is done by taking the mode of the classes produced by each tree. The AdaBoost works similarly to the random forest but it restricts the decision trees by only allowing shallow trees and trains the model by the boosting algorithm. Extra trees are also similar to the random forest but, when training a random forest the trees try to find for each node the best possible split for the binary tree. Extra trees pick a value a random and use it to build the split, this leads to more diversified trees (Sheppard, 2017).

The K-nearest neighbors algorithm (KNN) is a type of non-parametric model which classifies the data by looking at the k closest points on the feature space and classifying it according to the mode of their classes. KNN is a very common algorithm, especially when dealing with small datasets (Duda et al., 2003).

All methods used were set with the default parameters from the library sklearn (Pedregosa et al., 2011). **Table 1** shows the main parameters used in each method.

TABLE 1 | Models used to classify response data, their accuracy, and hyperparameters.

Model	Accuracy [%]	Hyperparameters
Random Forest	97	Number of estimators: 10 Criterion: Gini index
SVM	98	Penalty: L2 Loss: Squared hinge
Ada Boost	70	Number of estimators: 50 Algorithm: SAMME.R
Bagging (KNN)	100	Number of estimators: 10 Max samples: 1.0 Max features: 1.0 Bootstrap: False
Extra trees	100	Number of estimators: 10 Criterion: Gini index Bootstrap: False
Decision trees	97	Criterion: Gini index
MLP	100	Hidden layers sizes: 100 Activation: relu Solver: adam

The performance of the seven methods is evaluated through their accuracy, reported in **Table 1**.

As can be seen from **Table 1**, all the methods (but Ada Boost) behave well on the response data, giving an accuracy from 97 to 100%. This means that the sensor based on SnO_2:C nanomaterial gives very good raw output, suitable to distinguish different gases. A wise choice of the classification method allows us to rely on a perfect classification.

Quantitative Prediction

As can **Figure 5** shows, the points related to the various gases are in well-separated and distinct clouds. This is just a first step because a gas sensor is expected to evaluate also the concentration of that gas, even at low concentrations like in our case (few parts per million). For this reason, we used a least squares support vector machine (Shao et al., 2018) in order to estimate each gas concentration. To do this, we have split the data sets into smaller sets, one for each gas (we can do this because the classification was perfect). Each train sub-dataset was used to train the regressor, while the test sub-dataset was used to check the performance of our sensor toward that specific gas. The sensor estimates are then compared to the real concentration for that measurement. The average percentage error is calculated on each sub-dataset in order to evaluate the performance of the system for that target gas. These values are given in **Table 2**.

The average percentage errors shown in **Table 2** are quite homogeneous, with CO having the lowest value. Even if these values look high, we must underline that being percentage errors, they estimate the order of magnitude of the concentration very well. We must also highlight that the measured concentrations are quite low (1 ppm at minimum), well-below the exposure limits. Therefore, this error combined with the perfect classification obtained in the previous step is more than adequate to warn users of a possible danger due to the presence of gas. In order to better understand the source of the error, we analyzed the error as a function of the actual gas concentration, as shown in **Figure 7**.

TABLE 2 | Average percentage error of the nanosensor to different gases.

Gas	Average % error
Acetone	38.7
Ammonia	36.5
CO	24.3
Ethanol	41.8
Hydrogen	33.5
Toluene	40.9

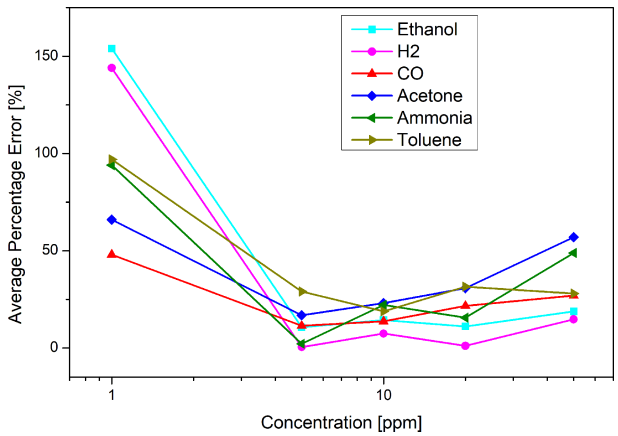

FIGURE 7 | Percentage error as a function of the gas concentration. It is clear that all gases follow a similar trend, with higher error at the extremities of the concentration range.

Since **Figure 7** shows a percentage error, one could expect a more or less constant value, but this is not the case. As can be seen, the error is minimal within the range, and greater at the ends. This effect is probably because the system has been trained on the 1–50 ppm range, and therefore loses accuracy toward the ends of this range. Furthermore, we can see that the error is not symmetrical, but is higher at lower concentrations. We must consider that 1 ppm is a rather low concentration, close to the limit of detection of the sensor itself, and this certainly negatively influences its error.

We want to point out that this is a transversal method that works regardless of the measured gases, and therefore can be applied in many different contexts.

CONCLUSIONS

Carbon modified SnO_2 nanowires were used as active material for a resistive gas sensor. Measuring the response at 5 different working temperatures (150–270°C) and using machine learning techniques, the system was able to distinguish all the tested gases

(acetone, ammonia, carbon monoxide, ethanol, hydrogen, and toluene) with a perfect classification (100%). The nanosensor is also able to estimate the gas concentration with a good average error (24–41%, depending on the gas) at low concentrations (1–50 ppm), proving to be useful to detect dangerous concentrations of different gases.

DATA AVAILABILITY STATEMENT

The datasets generated for this study are available on request to the corresponding author.

AUTHOR CONTRIBUTIONS

All authors listed have made a substantial, direct and intellectual contribution to the work, and approved it for publication.

SUPPLEMENTARY MATERIAL

The Supplementary Material for this article can be found online at: https://www.frontiersin.org/articles/10.3389/fmats.2019.00277/full#supplementary-material

REFERENCES

Chen, Z., Zheng, Y., Chen, K., Li, H., and Jian, J. (2017). Concentration estimator of mixed VOC gases using sensor array with neural networks and decision tree learning. *IEEE Sensors J.* 17, 1884–1892. doi: 10.1109/JSEN.2017.2653400

Cho, J., Li, X., Gu, Z., and Kurup, P. U. (2012). Recognition of explosive precursor using nanowire sensor array and decision tree learning. *IEEE Sensors J.* 12, 2384–2391. doi: 10.1109/JSEN.2011.2182042

Cho, J. H., Kim, Y. W., Na, K. J., and Jeon, G. J. (2008). Wireless electronic nose system for real-time quantitative analysis of gas mixtures using micro-gas sensor array and neuro-fuzzy network. *Sensor Actuat. B-Chem.* 134, 104–111. doi: 10.1016/j.snb.2008.04.019

Duda, R. O., Hart, P. E., and Stork, D. G. (2003). *Pattern Classification, 2nd Edn.* New York, NY: John Wiley and Sons, Inc.

Gulbag, A., and Temurtas, F. (2006). A study on quantitative classification of binary gas mixture using neural networks and adaptive neuro-fuzzy inference systems. *Sensor Actuat. B-Chem.* 115, 252–262. doi: 10.1016/j.snb.2005.09.009

Haykin, S. O. (2009). *Neural Networks and Learning Machines, 3rd Edn.* Upper Saddle River, NJ: Pearson Education.

Hines, E. L., Llobet, E., and Gardner, J. W. (1999). Electronic noses: a review of signal processing techniques. *IEE Proc. Circ. Devices Sust.* 146, 297–310. doi: 10.1049/ip-cds:19990670

Iftekhar Uddin, A. S. M., Phan, D.-T., and Chung, G.-S. (2015). Low temperature acetylene gas sensor based on Ag nanoparticles-loaded ZnO-reduced graphene oxide hybrid. *Sensor Actuat. B-Chem.* 207, 362–369. doi: 10.1016/j.snb.2014.10.091

Jiang, S., Wang, J., Wang, Y., and Cheng, S. (2017). A novel framework for analyzing MOS E-nose data based on voting theory: application to evaluate the internal quality of Chinese pecans. *Sensor Actuat. B-Chem.* 242, 511–521. doi: 10.1016/j.snb.2016.11.074

Jiang, X.-Q., Mei, X.-D., and Feng, D. (2016). Air pollution and chronic airway diseases: what should people know and do? *J. Thorac. Dis.* 8, E31–E40. doi: 10.3978/j.issn.2072-1439.2015.11.50

Kalantar-zadeh, K. (2013). *Sensors: An Introductory Course*. New York, NY: Springer Science+Business Media.

Kim, H.-R., Haensch, A., Kim, I.-D., Barsan, N., Weimar, U., and Lee, J.-H. (2011). The role of NiO doping in reducing the impact of humidity on the performance of SnO_2-based gas sensors: synthesis strategies, and phenomenological and spectroscopic studies. *Adv. Funct. Mater.* 21, 4456–4463. doi: 10.1002/adfm.201101154

Konstantynovski, K., Njio, G., Börner, F., Lepcha, A., Fischer, T., Holl, G., et al. (2018). Bulk detection of explosives and development of customized metal oxide semiconductor gas sensors for the identification of energetic materials. *Sensor Actuat. B-Chem.* 258, 1252–1266. doi: 10.1016/j.snb.2017.11.116

Koo, W.-T., Jang, J.-S., Choi, S.-J., Cho, H.-J., and Kim, I.-D. (2017). Metal-organic framework template catalysts: dual sensitization of PdO-ZnO composite on hollow SnO_2 nanotubes for selective acetone sensors. *ACS Appl. Mater. Interfaces* 9, 18069–18077. doi: 10.1021/acsami.7b04657

Lee, D.-K., Lee, D.-D., Ban, S.-W., Lee, M., and Kim, Y. T. (2002). SnO_2 gas sensing array for combustible and explosive gas leakage recognition. *IEEE Sensors J.* 2, 140–149. doi: 10.1109/JSEN.2002.800685

Marco, S., and Gutiérrez-Galvez, A. (2012). Signal and data processing for machine olfaction and chemical sensing: a review. *IEEE Sensors J.* 12, 3189–3214. doi: 10.1109/JSEN.2012.2192920

McInnes, L., Healy, J., and Melville, J. (2018). UMAP: uniform manifold approximation and projection for dimension reduction. *ArXiv e-prints* 1802.03426. doi: 10.21105/joss.00861

Miller, D. R., Akbar, S. A., and Morris, P. A. (2014). Nanoscale metal oxide-based heterojunctions for gas sensing: a review. *Sensor Actuat. B-Chem.* 204, 250–272. doi: 10.1016/j.snb.2014.07.074

Mo, Z., Fu, Q., Zhang, L., Lyu, D., Mao, G., Wu, L., et al. (2018). Acute effects of air pollution on respiratory disease mortalities and outpatients in Southeastern China. *Sci. Rep.* 8:3461. doi: 10.1038/s41598-018-19939-1

Moon, H. G., Jung, Y., Han, S. D., Shim, Y.-S., Jung, W.-S., Lee, T., et al. (2018). All villi-like metal oxide nanostructures-based chemiresistive electronic nose for an exhaled breath analyzer. *Sensor Actuat. B-Chem.* 257, 295–302. doi: 10.1016/j.snb.2017.10.153

Pedregosa, F., Varoquaux, G., Gramfort, A., Michel, V., Thirion, A., Grisel, O., et al. (2011). Scikit-learn: machine learning in python. *arXiv:1201.0490.*

Sabir, S., Arshad, M., and Chaudhari, S. K. (2014). Zinc oxide nanoparticles for revolutionizing agriculture: synthesis and applications. *Sci. World J.* 2014:925494. doi: 10.1155/2014/925494

Saidi, T., Palmowski, D., Babicz-Kiewlicz, S., Welearegay, T. G., Bari, N. E., Ionescu, R., et al. (2018). Exhaled breath gas sensing using pristine and functionalized WO3 nanowire sensors enhanced by UV-light irradiation. *Sensor Actuat. B-Chem.* 273, 1719–1729. doi: 10.1016/j.snb.2018.07.098

Shao, Y.-H., Li, C.-N., Liu, M.-Z., Wang, S., and Deng, N.-Y. (2018). Sparse Lq-norm least squares support vector machine with feature selection. *Pattern Recogn.* 78, 167–181. doi: 10.1016/j.patcog.2018.01.016

Sheppard, C. (2017). *Tree-Based Machine Learning Algorithms: Decision Trees, Random Forests, and Boosting*. CreateSpace Independent Publishing Platform.

Tai, H., Xie, G., and Jiang, Y. (2004). "An artificial olfactory system based on gas sensor array and back-propagation neural network" in *Advances in Neural Networs*, eds F. L. Yin, J. Wang, and C. Guo (Berlin: Springer), 892–897.

Tischner, A., Maier, T., Stepper, C., and Köck, A. (2008). Ultrathin SnO_2 gas sensors fabricated by spray pyrolysis for the detection of humidity and carbon monoxide. *Sensor Actuat. B-Chem.* 134, 796–802. doi: 10.1016/j.snb.2008.06.032

Tonezzer, M. (2019). Selective gas sensor based on one single SnO_2 nanowire. *Sensor Actuat. B-Chem.* 288, 53–59. doi: 10.1016/j.snb.2019.02.096

Tonezzer, M., and Iannotta, S. (2014). H_2 sensing properties of two-dimensional zinc oxide nanostructures. *Talanta* 122, 201–208. doi: 10.1016/j.talanta.2014.01.051

Tonezzer, M., Kim, J.-H., Lee, J.-H., Iannotta, S., and Kim, S. S. (2019). Predictive gas sensor based on thermal fingerprints from Pt-SnO_2 nanowires. *Sensor Actuat. B-Chem.* 281, 670–678. doi: 10.1016/j.snb.2018.10.102

Tonezzer, M., Le, D. T. T., and Huy, T. Q., Iannotta, S. (2016). Dual-selective hydrogen and ethanol sensor for steam reforming systems. *Sensor Actuat. B-Chem.* 236, 1011–1019. doi: 10.1016/j.snb.2016.04.150

Tonezzer, M., Le, D. T. T., Iannotta, S., and Hieu, N. V. (2018). Selective discrimination of hazardous gases using one single metal oxide resistive sensor. *Sensor Actuat. B-Chem.* 277, 121–128. doi: 10.1016/j.snb.2018.08.103

Tsuda, N., Nasu, K., Fujimori, A., and Siratori, K. (2000). *Electronic Conduction in Oxides, 2nd Edn*. Berlin: Springer-Verlag.

Wang, L., Fu, H., Jin, Q., Jin, H., Haick, H., Wang, S., et al. (2019). Directly transforming SnS_2 nanosheets to hierarchical SnO_2 nanotubes: Towards sensitive and selective sensing of acetone at relatively low operating temperatures. *Sensor Actuat. B-Chem.* 292, 148–155. doi: 10.1016/j.snb.2019.04.127

Wolfrum, E. J., Meglen, R. M., Peterson, D., and Sluiter, J. (2006). Metal oxide sensor array for the detection, differentiation, and quantification of volatile organic compounds at sub-parts-per-million concentration levels. *Sensor Actuat. B-Chem.* 115, 322–329. doi: 10.1016/j.snb.2005.09.026

Zhang, B., and Gao, P.-X. (2019). Metal oxide nanoarrays for chemical sensing: a review of fabrication methods, sensing modes, and their inter-correlations. *Front. Mater.* 60:55. doi: 10.3389/fmats.2019.00055

Zhao, L., Li, X., Wang, J., Yao, P., and Akbar, S. A. (2016). Detection of formaldehyde in mixed VOCs gases using sensor array with neural networks. *IEEE Sensors J.* 15, 6081–6086. doi: 10.1109/JSEN.2016.2574460

Zhou, Q., Xu, L., Umar, A., Chen, W., and Kumar, R. (2018). Pt nanoparticles decorated SnO_2 nanoneedles for efficient CO gas sensing applications. *Sensor Actuat. B-Chem.* 256, 656–664. doi: 10.1016/j.snb.2017.09.206

Conflict of Interest: The authors declare that the research was conducted in the absence of any commercial or financial relationships that could be construed as a potential conflict of interest.

frontiers in Materials

ORIGINAL RESEARCH
published: 08 November 2019
doi: 10.3389/fmats.2019.00254

Flame Spray Synthesis of $VOPO_4$ Polymorphs

Gagan Jodhani[1,2], *Fateh Mikaeili*[1] *and Pelagia Irene Gouma*[1,2]*

[1] *Department of Materials Science and Engineering, The Ohio State University, Columbus, OH, United States,* [2] *Department of Materials Science and Engineering, Stonybrook University, Stonybrook, NY, United States*

$VOPO_4$ is a polymorphic compound that exhibits excellent catalytic and electronic properties. Here, formation of different $VOPO_4$ polymorphs using two different organic compounds as precursors is investigated for the first time using flame spray pyrolysis as an alternative method to hydrothermal synthesis of $VOPO_4$, the only method currently known for its synthesis. Ammonium-based salts of vanadium and phosphorous dissolved in aqueous solution were used as precursors for the process. The products from the flame spray pyrolysis process were found to be hollow and amorphous particles in the range of 2–10 μm with shell thicknesses between 200 and 300 nm. Upon calcination and oxidation, the size of spherical particles grew in diameter and crystallization proceeded. However, the surface of calcined particles showed it was composed of smaller grains in the size range of 0.5–1 μm. Finally, the size dependence stability of different polymorphs of $VOPO_4$ is discussed as well as the effect of the different precursors used to stabilize alpha-II and Beta $VOPO_4$ polymorphs.

Keywords: VOPO4, sensors, flame spray pyrolysis, FSP, batteries, li ion batteries, vanadium phosphate

OPEN ACCESS

Edited by:
Xiaogan Li,
Dalian University of Technology (DUT), China

Reviewed by:
Huang Bao Yu,
Dalian University of Technology (DUT), China
Tridib Kumar Sinha,
Gyeongsang National University, South Korea

***Correspondence:**
Pelagia Irene Gouma
gouma.2@osu.edu

Specialty section:
This article was submitted to Functional Ceramics, a section of the journal Frontiers in Materials

Received: *28 June 2019*
Accepted: *25 September 2019*
Published: *08 November 2019*

Citation:
Jodhani G, Mikaeili F and Gouma PI (2019) Flame Spray Synthesis of $VOPO_4$ Polymorphs. Front. Mater. 6:254. doi: 10.3389/fmats.2019.00254

INTRODUCTION

Vanadium phosphates ($VOPO_4$) have gained some noted interest from researchers as functional oxide materials due to their outstanding catalytic and electronic properties. Among their various applications, they have been studied as catalysts for hydrocarbons (Albonetti et al., 1996; Guliants et al., 1996; Coulston et al., 1997; Conte et al., 2006), where the +5 valence state of vanadium is important in the extraction of hydrogen atoms from alkanes (Hutchings et al., 1998). Apart from their applications in catalysis, vanadium phosphates also find applications as electrode materials in lithium-ion batteries (Gaubicher et al., 1999; Kerr et al., 2000; Whittingham et al., 2005) and sodium-ion batteries (He et al., 2016a,b), pseudo capacitors (Wu et al., 2013; Lee et al., 2015), and sensors (Li et al., 2011; Khan et al., 2016). The variety of applications of $VOPO_4$ can be related to the various polymorphs exhibited by the compound.

There are seven reported polymorphs for $VOPO_4$. Among these polymorphs, four exhibit tetragonal structure (α_1, α_2, δ, and ω), two exhibit orthorhombic structure (β and γ) and one monoclinic structure (ε) (Dupré et al., 2004). Among these polymorphs, β-$VOPO_4$ has the lowest energy configuration. However, these polymorphs have been synthesized using various routes; furthermore, due to close relation in the structures of all the polymorphs and their low energy difference, obtaining a single phase is almost impossible (Dupré et al., 2004). The various techniques applied for synthesis of $VOPO_4$ compounds are solvothermal synthesis (Rownaghi et al., 2009; Allen et al., 2011), solid state interactions (Bartley et al., 2001; Sydorchuk et al., 2010), and electrochemical synthesis (Song et al., 2005). However, all these methods either result in big particle size or are commercially unfeasible due to their lengthy processing times.

In this paper, we investigate the Flame Spray Pyrolysis (FSP)-based synthesis of $VOPO_4$ powders. FSP is the process in which a liquid precursor is readily combusted and possesses a high enthalpy reaction, as to sustain the flame. FSP precursors generally consist of high-enthalpy solvents mixed with organometallics (Strobel and Pratsinis, 2007). As such, when the precursor droplets enter the flame zone, the organic solvents are evaporated and can proceed through a particle formation process. However, in cases where the enthalpy of the solution is insufficient, the solute may not sublimate or may partially sublimate and form particles that do not have characteristics of FSP particles (Wang and Huang, 2016). FSP is arguably the more popular flame aerosol technique. This can be attributed to the gas-particle conversion that typically results in finer particles coupled with the homogenous mixing of gaseous elements compared to that of liquid elements (Teoh et al., 2010). Since in an ideal FSP experiment, the particles immediately vaporize, Brownian motion in the gas phase is the dominant factor that determines their final morphology (Ulrich, 1971). The methodology used to produce particles in a laboratory-based FSP setup can be transferred to a foundry for the bulk synthesis of the material. Aeroxide P25 Titania, from Evonik industries, provides evidence for the scalable oxide synthesis via flame aerosol technique. Apart from the commercial aspect, the advantage of flame spray synthesis lies in ease of fabrication, elimination for the use of expensive raw materials, uniform size distribution, and high purity products. Flame-synthesized particles have small particle sizes and high surface area: volume ratios, which is desirable for catalysis and electrochemical processes.

For this study, aqueous solutions with two different organic components as precursors for FSP process are used. The obtained powders are then characterized using XRD, TGA-DTA, SEM, TEM with SAED, and FTIR for their crystallographic phases, morphologies, chemical compositions, and thermal stability.

EXPERIMENTAL METHODS

FSP $VOPO_4$ Using Aqueous Solution With Sucrose

Precursor solution was prepared using ammonium vanadate (1.17 g) and ammonium dihydrogen phosphate (1.15 g). The salts were mixed in 100 ml deionized water, bringing the concentration of the solution to 0.1 M. 1.5 g of sucrose was added to the solution as an organic component. The addition of the organic component was to produce a self-sustaining flame during the FSP process. The solution was stirred at 600 RPM and maintained at 60°C using a heated magnetic stirrer until a homogenous mixture was obtained. The solution was aged for a day and then fed into the FSP system (Tethis NPS 10). For the FSP process, the flame was generated using methane and oxygen, 1.5 slm methane and 3.0 slm oxygen were used, 5 slm oxygen was used as dispersion gas and the solution feed rate was 5 ml. The particles were collected on a glass fiber filter. The powders were calcined at 500°C for 8 h.

FSP $VOPO_4$ Using Aqueous Solution With DMF

Precursor solution was prepared with the same amount of ammonium vanadate and ammonium dihydrogen phosphate. The salts were mixed in 80 ml deionized water. The stirring and heating of the precursor was performed the same as mentioned earlier. A total of 20 ml of DMF, which was used as the organic compound of this solution, was added to make it 0.1 M, which is the same concentration of the other precursor made with sucrose; then, it was fed into the FSP system. The FSP process was done with the same parameters as mentioned in the previous part.

Material Characterization

The powders were characterized using Scanning Electron Microscopy (SEM, LEO 1550), Transmission Electron Microscopy (TEM, JEOL 1400) and selected area electron diffraction was carried out on both as synthesized and calcined samples. Thermogravimetric analysis (TGA, Perkin Elmer Diamond) was conducted on the as-synthesized samples. The particles, both as-synthesized and calcined, were also characterized using XRD (Rigaku Miniflex II) and FTIR (Thermo Scientific Nicolet 6700).

RESULTS

X-Ray Characterization

Figure 1 shows the XRD characterization of FSP-synthesized powders. The as-synthesized particles were relatively amorphous showing significant broad peaks; some extent of crystallinity was obtained. The powders synthesized using a sucrose-based solution, matched with JCPDS 36-0054 for Ammonium Vanadyl Hydrogen phosphate hydrate ($NH_4VOVO_2(HPO_4)_2.1.5H_2O$) and are denoted by the letter A in **Figure 1a**. **Figure 1a** also shows the pattern for powders synthesized using a DMF based solution. The pattern showed a mixed system and matched with JCPDS 36-0054 for Ammonium Vanadyl Hydrogen phosphate hydrate(denoted by A) and JCPDS 34-1247 for tetragonal $VOPO_4$ system(L→ R denoted by α, 200, and 301 planes). The tetragonal $VOPO_4$ system was identified to be α_{II}-$VOPO_4$ based on the lattice parameters (Ling et al., 2014).

Figure 1b shows the XRD characterization of calcined FSP synthesized powders. Both the powders resulted in mixed phases. In the case of calcined powders synthesized with sucrose-based solutions, the peaks from the XRD pattern were found to be orthorhombic β-$VOPO_4$ (JCPDS 71-0859) and tetragonal α_{II}-$VOPO_4$ (JCPDS 34-1247). The peaks for β-$VOPO_4$ are denoted by β(L→ R: 011, 002, 201, 221, 031, 400, and 040 planes) and the peaks for α_{II}-$VOPO_4$ are denoted by α(L→ R: 101, 200, 220, and 132 planes). For calcined powders synthesized with DMF-based solutions, the peaks from XRD pattern were found to be tetragonal δ-$VOPO_4$ (JCPDS 47-0951) and tetragonal α_{II}-$VOPO_4$ (JCPDS 34-1247). The peaks for δ-$VOPO_4$ are denoted by δ(L→ R: 002, 111, 012, 022, 031, 214, and 106 planes) and the peaks for peaks for α_{II}-$VOPO_4$ are denoted by α(L→ R: 101, 111, 200, 220, 112, 301, 311, and 420 planes).

The relative phase content was calculated using peak intensity ratios for all the samples. Quantitative analysis for crystallite size

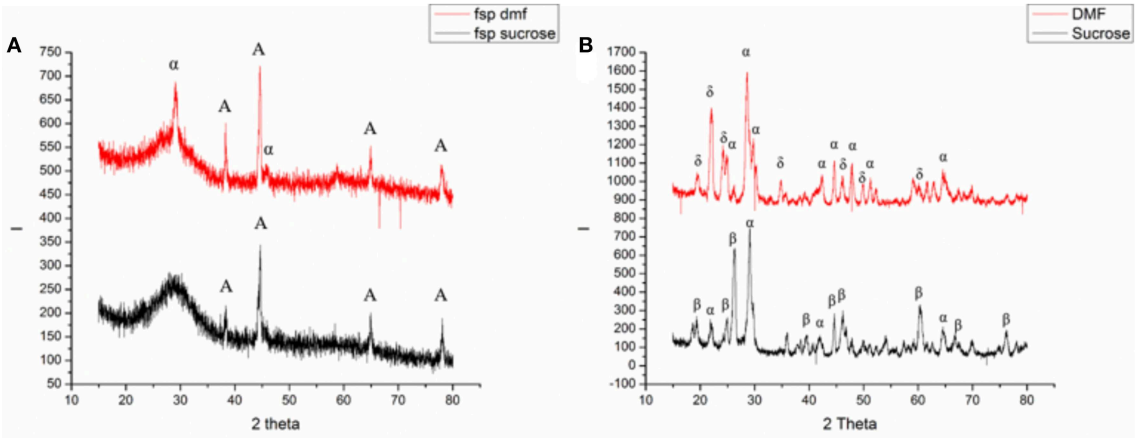

FIGURE 1 | Results of XRD analysis of **(A)** as-synthesized and **(B)** calcined powders [A: Ammonium Vanadyl Hydrogen phosphate hydrate ($NH_4VOVO_2(HPO_4)_2.1.5H_2O$], α: α-$VOPO_4$, β: β- $VOPO_4$, δ: δ- $VOPO_4$).

TABLE 1 | Phase content and crystallite sizes for FSP $VOPO_4$.

Sample	Polymorph	% phase	Crystallite size (nm)
Suc- calcined	β-$VOPO_4$	45.7	26.3
	α_{II}-$VOPO_4$	54.3	24.6
DMF- calcined	δ-$VOPO_4$	42.43	24.3
	α_{II}-$VOPO_4$	57.57	21.7

determination was conducted using Scherrer's formula. **Table 1** lists the phase content and their crystallite sizes.

Thermal Analysis

TGA-DTA was conducted on as-synthesized samples in the range of RT-550°C under oxygen atmosphere. **Figure 2** shows the plot for (a) powders synthesized using sucrose-based solution and (b) powders synthesized using DMF-based solution.

Powders synthesized using sucrose-based solution show a decrease in weight with increase in temperature. The weight loss can be associated with the release of ammonia and water by decomposition of NH_4VOVO_2 $(HPO_4)_2.1.5H_2O$ and formation of $VOPO_4$ structures. The DTA signals show two exothermic changes at 260 and 540°C; these changes can be associated with formation of β-$VOPO_4$ and α_{II}-$VOPO_4$.

Powders synthesized using DMF-based solution also show a decrease in weight with increase in temperature. Similar to the sucrose-based solutions, the weight loss can be associated with the release of ammonia and water by decomposition of $NH_4VOVO_2(HPO_4)_2.1.5H_2O$ and formation of $VOPO_4$ structures. The weight drop stops at 420°C and a slight spike in weight is noticed in the range of 420–550°C. The DTA signals show an exothermic change at 420°C. Since the as-synthesized particles were a mixture of vanadyl hydrogen phosphate hydrate & α_{II}-$VOPO_4$, which resulted in formation α_{II}-$VOPO_4$ and δ-$VOPO_4$, the exothermic reaction at 420°C can be associated with the formation of δ-$VOPO_4$.

Fourier Transform Infrared Spectroscopy

FTIR was conducted on all the samples in the range of 500–4,000 cm^{-1}. The signal received below 500 was erroneous due to significant noise; it was therefore omitted from the results. **Figure 3** shows the FTIR spectra for (a) powders obtained from sucrose-based solution (as-synthesized and calcined) and (b) powders obtained from DMF-based solution (as-synthesized and calcined).

For the as-synthesized particles from the sucrose-based solution, the peaks were obtained at 569, 1,040, 1,424, 1,654, and a broad peak in 3,200 cm^{-1}. The peak at 1,424 cm^{-1} and the broad peak at 3,200 cm^{-1} correspond to the N-H bending vibrations (Socrates, 2004). The peak at 1,654 cm^{-1} indicated presence of water. The strong peak at 1,040 cm^{-1} belongs to P-O (Jiao et al., 1998) vibrations and the peak at 569 cm^{-1} can be associated with V-O-V rotational vibrations (Xue et al., 2010). Upon calcination, the FTIR spectra for the calcined powders revealed peaks at 559, 673, 903, 949, shoulder at 1,080, 1,614, and a broad peak at 3,344 cm^{-1}. The broad peak at 3,344 cm^{-1} and the peak at 1,614 cm^{-1} correspond to N-H bending vibrations (Socrates, 2004) and signify the presence of undecomposed ammonia. The V-O-V rotational vibrations observed at 559 cm^{-1} were observed at 569 cm^{-1} in the calcined sample. Similarly, the peak for P-O vibrations observed at 1,040 cm^{-1} was observed at 1,080 cm^{-1}. New peaks were observed at 673, 903, and 949 cm^{-1}. The peak at 673 can be associated with metaphosphate (Socrates, 2004). The peaks in 903 and 949 cm^{-1} region belong to the V=O vibrations (Anumula et al., 2013). The different peak position signifies a shift in the V=O bonds, the shift can be associated with the presence of two phases.

For the as-synthesized particles from the DMF-based solution, the peaks were obtained at 566, 676, 879, 941, 1,064, 1,426, and 1,644 with a broad peak at 3,200 cm^{-1}. The peak at 1,426 cm^{-1} and the broad peak at 3,200 cm^{-1} correspond to N-H bending vibrations as was the as-synthesized particles from sucrose solution. Similarly, the peak at 1,644 cm^{-1} indicated inclusion of water. The peak at 1,040 cm^{-1} belongs to P-O

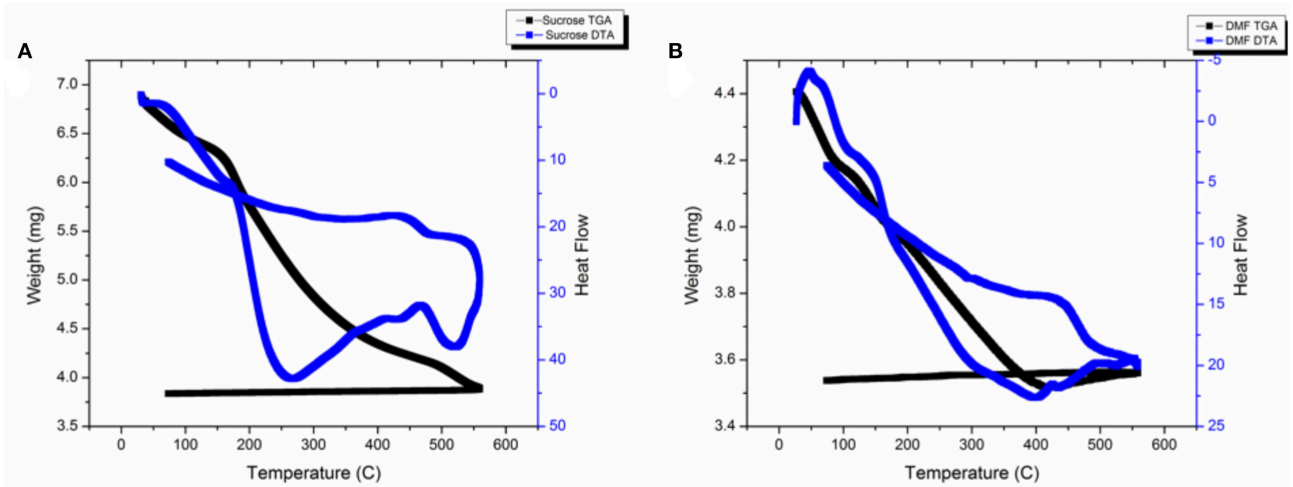

FIGURE 2 | TGA-DTA analysis for **(A)** FSP powders with sucrose **(B)** FSP powders with DMF.

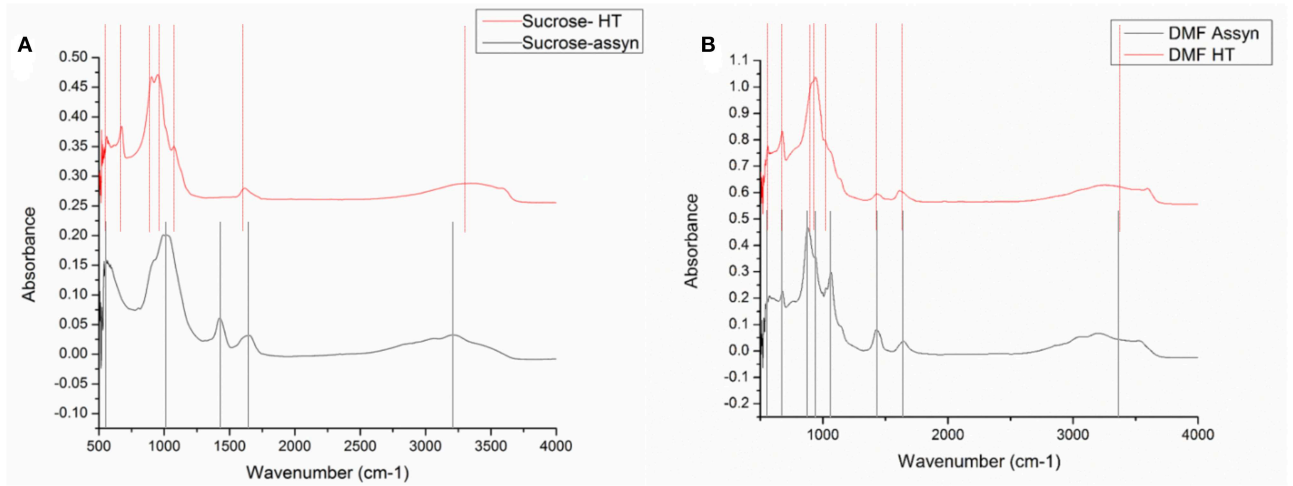

FIGURE 3 | FTIR images for **(A)** as-synthesized and calcined VOPO4 samples synthesized with DMF based precursor **(B)** as- synthesized and calcined VOPO4 samples synthesized with sucrose-based precursor.

vibrations, the peak at 941 belongs to V=O vibrations and the peak at 566 cm^{-1} can be associated with V-O-V rotational vibrations. The peak observed at 873 cm^{-1} corresponds to orthovanadates (Socrates, 2004). Upon calcination, the FTIR spectra for the calcined powders revealed peaks at 560, 674, 939, shoulder at 1,020, 1,428, and 1,612 with a broad peak at 3,254 $cm^{-}1$. The broad peak at 3,254 cm^{-1} and the peak at 1,612 cm^{-1} correspond to N-H bending vibrations (Socrates, 2004) and signify slight presence of undecomposed ammonia. The V-O-V rotational vibrations observed at 566 cm^{-1} were observed at 560 cm^{-1} in the calcined sample. Similarly, the peak for P-O vibrations observed at 1,040 cm^{-1} was observed at 1,020 cm^{-1}, the peak for V=O vibrations observed at 941 cm^{-1} shifted to 939 cm^{-1}, the metaphosphate peak shifted from 676 cm^{-1} to 674 cm^{-1}. A slight shift in peak positions and absence of new peaks indicate that no major change occurred in the structure upon heat treatment.

Scanning Electron Microscopy

The as-synthesized particles and heat-treated samples were characterized by SEM and the particle morphology was analyzed. **Figure 4** shows the SEM images for as-synthesized particles and **Figure 5** compares the SEM images of the heat-treated samples.

As-Synthesized Samples

For the particles synthesized using sucrose-based precursor (**Figures 4a–c**), the particle morphology was in the form of a sphere. Two different sizes of particles were obtained and the large spheres were hollow and in the size range

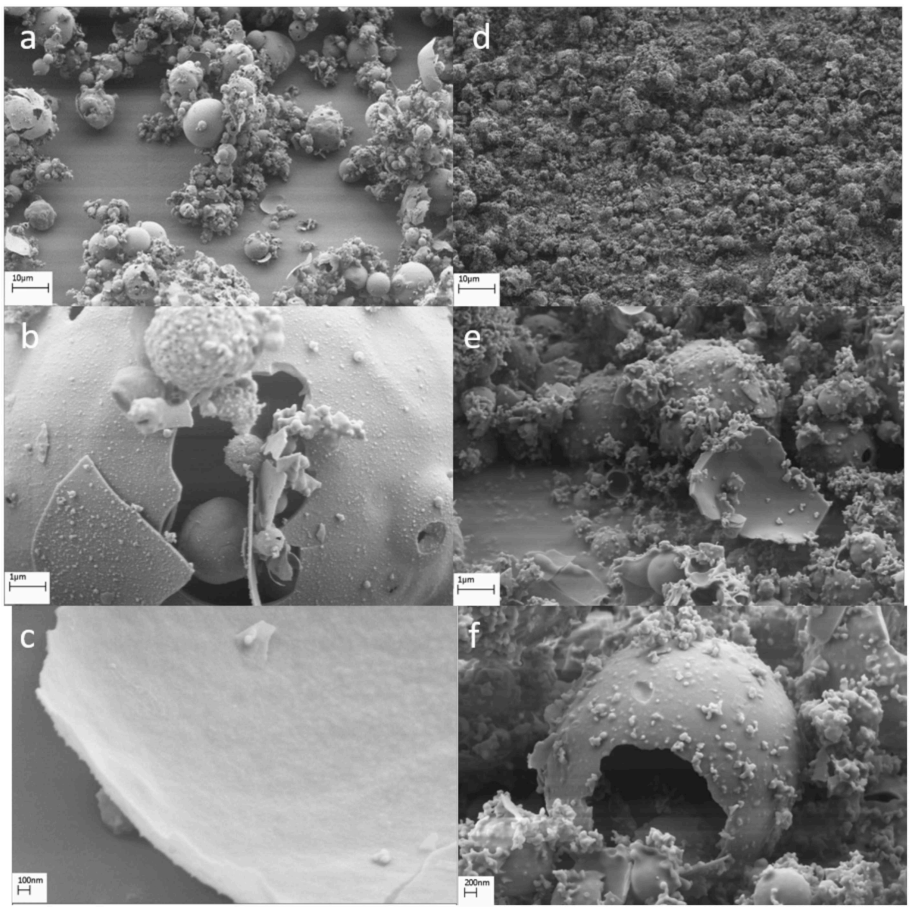

FIGURE 4 | Scanning electron microscopy images for as-synthesized particles from **(a–c)** sucrose-based solutions and **(d–f)** DMF-based solutions.

of 2–10 μm. From high-resolution imaging (**Figure 4c**), the thickness of these was found to be in the range of 100–150 nm. The smaller spheres were solid and in the size range of 200–300 nm. For the particles synthesized using DMF-based precursor (**Figures 4d–f**), the particles were found to be spheres. Similar to the as-synthesized particles from sucrose-based solutions, two different size ranges were noticed. The large spheres were found to be 2–5 μm with a thickness of 50–80 nm. Smaller sized particles were obtained in the range of 50–200 nm.

Calcined Samples

SThe calcined particles were characterized by SEM, and the effect of heat-treatment on particle morphology was analyzed. The particle morphology obtained for calcined particles from sucrose solution (**Figures 5a–c**) was similar to that of as-synthesized samples. The surface of hollow particles was analyzed using a higher resolution and revealed formation of smaller grains on the surface as opposed to an eggshell type of structure for as-synthesized particles. High-resolution imaging (**Figure 5c**) revealed the grain sizes to be in the order of 80–150 nm. The particle morphology obtained for calcined particles from DMF solution (**Figures 5d–f**) was similar to that of as-synthesized samples. However, the grains observed on the surface were found to represent a lamellar structure (**Figure 5f**).

Transmission Electron Microscopy

As-Synthesized Particles

Transmission electron microscopy with selected area electron diffraction was conducted on all samples. The TEM imaging of as-synthesized particles from sucrose-based solution showed thick spherical particles (**Figures 6a,b**). The particles over 1 μm were hollow. SAED pattern did result in any rings (**Figure 6c**), indicating the particles were amorphous, which was already observed in the XRD pattern of the as-synthesized samples. In case of as-synthesized particles from DMF-based solution, solid spheres in the range of 100–200 nm were noticed. No micron-sized particles were found; however, thin walled shell structures were seen indicating disintegration of hollow spheres that were noticed in SEM. SAED pattern on solid spheres resulted in rings that matched with JCPDS 34-1247 α_{II}-$VOPO_4$ (**Figure 6f**; 111 and 220 planes).

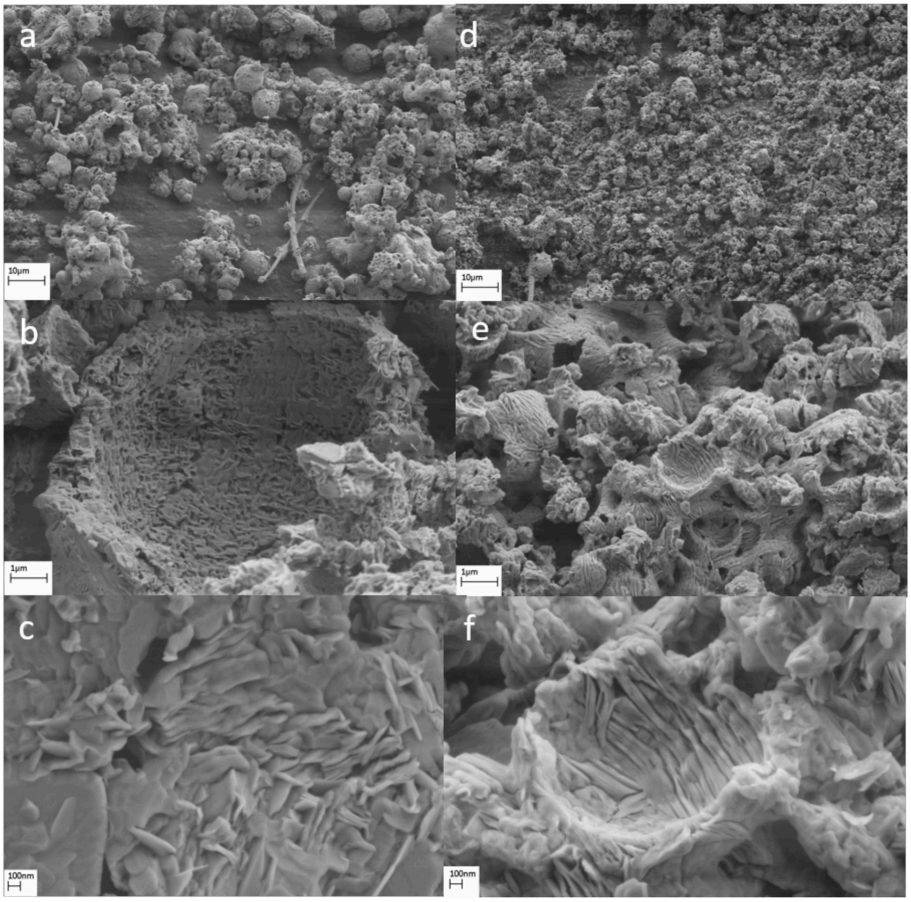

FIGURE 5 | Scanning electron microscopy images for calcined particles from **(a–c)** sucrose based solutions **(d–f)** DMF based solutions.

Calcined Particles

The TEM imaging of calcined particles from sucrose-based solution showed thin spherical disk-like particles (**Figures 7a,b**). The particle sizes for these disks were in the range of 40–300 nm. The SAED pattern on the disks resulted in rings that matched with JCPDS 34-1247 α_{II}-$VOPO_4$ (**Figure 7c**; 200 and 112 planes). No rings were found representing β-$VOPO_4$; however, the imaging showed growth of lathes on the edges of the disks which might be associated with β-$VOPO_4$. In case of calcined particles from DMF-based solution, the morphology was in the form of rectangular nanosheets. The size of these sheets was in the range of 50–500 nm in length. The particle sizes for these disks were in the range of 40–300 nm. SAED pattern on the disks resulted in rings that matched with JCPDS 34-1247 α_{II}-$VOPO_4$ (**Figures 6**, **7f**; 200 and 112 planes).

DISCUSSION

The resultant powders from flame spray pyrolysis (the as-synthesized samples) contained a large amount of $NH_4VOVO_2(HPO_4)_2.1.5H_2O$. The formation of the compound can be attributed to the reaction between ammonium vanadate and ammonium dihydrogen phosphate in aqueous medium. Also, significant difference between the particle sizes could be observed in the as synthesized samples of the two samples with different precursors. As mentioned in the introduction and the experimental sections of the manuscript, the organic components in the FSP precursor are used to produce self-sustaining flame during the FSP process. In the FSP process, the sustainability of the flame is very critical and small changes would lead to drastic changes in particles sizes, morphologies, etc. The particles formed from sucrose-based solutions were in the micron range and hollow, which is usually inconsistent with the results of FSP processing method since the precursor goes through atomization. The formation of such large particles was a result of precursors with low enthalpies coupled with high melting/decomposition points (Teoh et al., 2010). Moreover, due to the usage of an aqueous solution, the temperature of the flame is significantly reduced for complete atomization of particles. However, as it was observed in the SEM results the addition of sucrose helped forming partial submicron sized particles, which is the size range for FSP samples (Purwanto et al., 2011). The formation of organometallics also led to atomization of the precursor and formation of α_{II}-$VOPO_4$.

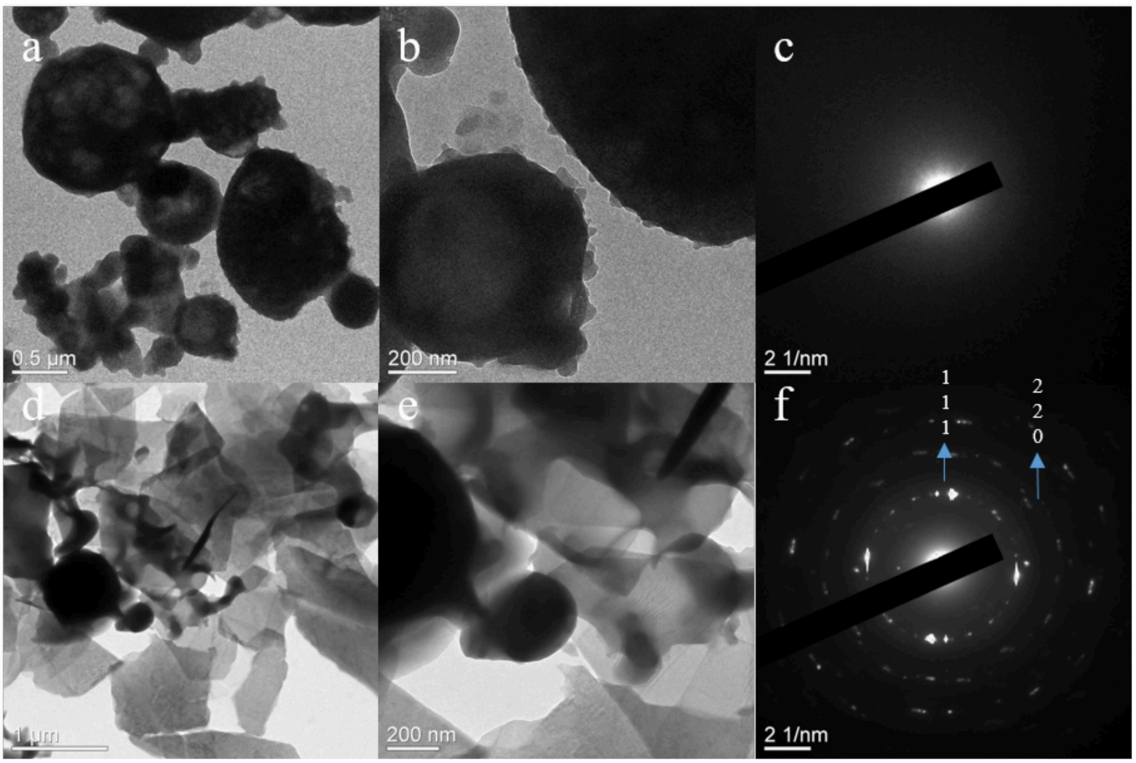

FIGURE 6 | TEM images and corresponding SAED pattern for as-synthesized particles from **(a–c)** sucrose-based solutions and **(d–f)** DMF-based solutions.

Upon calcination of as-synthesized products, the resultant powders were a mixture of α_{II}-$VOPO_4$ & β-$VOPO_4$ and α_{II}-$VOPO_4$ and δ-VOPO4 in the samples synthesized with the sucrose-based precursors and DMF-based precursors, respectively. According to the DFT calculations, the β-$VOPO_4$ is the most stable configuration for $VOPO_4$ (Ling et al., 2014; Sun and Du, 2017). However, based on the same findings, there is only a small difference in energy between $VOPO_4$ polymorphs, which suggests that temperature has little effect on phase transformation in $VOPO_4$. However, it was reported that a slight change in synthesis conditions could lead to the formation of different polymorphs (Dupré et al., 2004). The primary difference in $VOPO_4$ structures occur in the form of V-O bond length, which in turn leads to different crystal structures and polymorphs.

The mixed polymorphs obtained here can be associated with the precursor, where the formation of $NH_4VOVO_2(HPO_4)_2.1.5H_2O$ leads to multiple polymorphs. The precursor salt contains two valence states for VO in the form of $V(IV)O^{2-}$ and $V(V)O_2^-$. The vanadium oxide with +5 valence state exhibits an orthovanadate structure. Based on the results obtained, the orthovanadate structure exhibits similar V-O bond length to α_{II}-$VOPO_4$. Hence, formation of α_{II}-$VOPO_4$ was observed in all the samples. The formation of β and δ polymorphs are a result of the transformation of the +4-valence state VO^{2-} into a +5-valence state in an oxidative atmosphere. The oxidation leads to formation of V-O bond, the length of which determines the formation of either β or δ polymorphs. The oxidation was noticed during the TGA analysis of particles synthesized with the DMF precursor, where a slight increase in weight was observed at 420°C.

In case of powders synthesized using sucrose solution, the VO^{2-} transforms into the most stable state and thereby leads to the formation of β-$VOPO_4$. The synthesis of the δ polymorph has been reported earlier from the thermal oxidation of a +4 valency vanadium hydrogen phosphate compound (Girgsdies et al., 2009). The compound was held at 400°C for 7 days for successful transformation into δ polymorphs. In this study, the lower particle size led to faster transformations.

CONCLUSION

We have successfully demonstrated the formation of different $VOPO_4$ polymorphs with the FSP process. The precursor based on sucrose favors the formation of α_{II}-$VOPO_4$. Furthermore, the reason behind the formation of the secondary phases was addressed due to oxidation of lower valence state vanadium compound in the precursor. Moreover, it was discovered that particle size plays an important role in forming a polymorph upon oxidation of lower valence state compound; smaller particle size favors formation of δ polymorph, whereas large particle sizes tend to form β polymorph. Based on these results, other precursor compounds can be investigated toward formation of other polymorphs for $VOPO_4$.

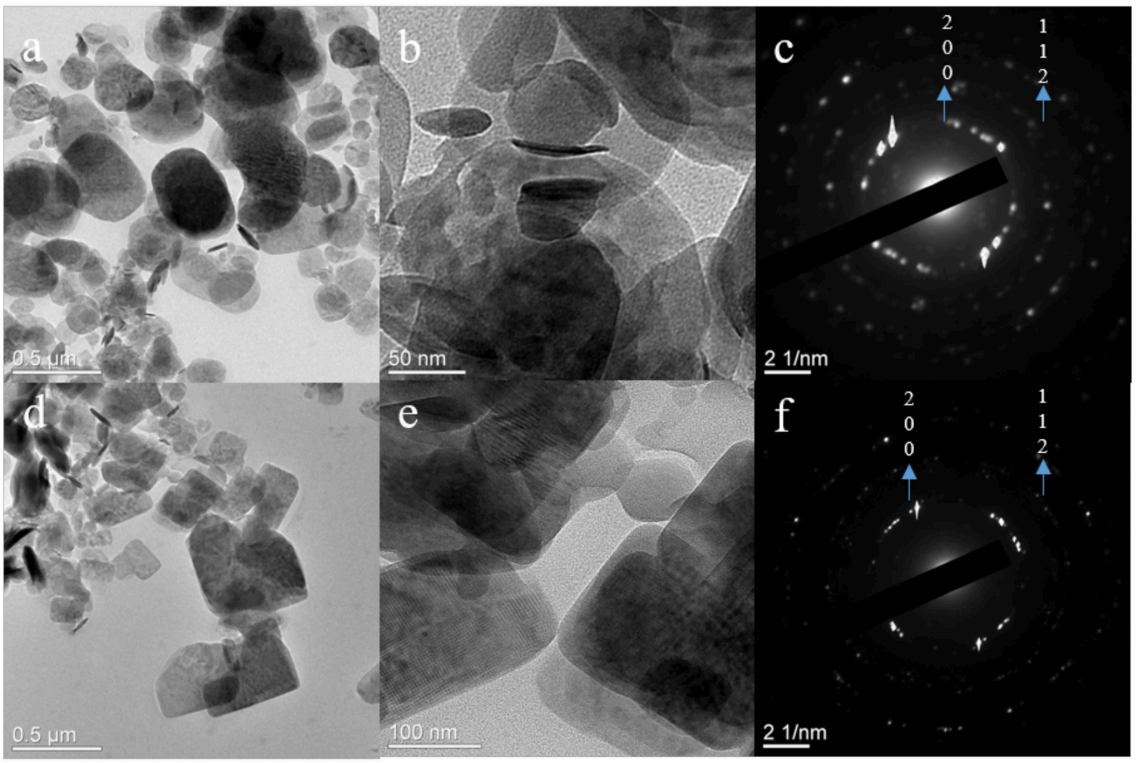

FIGURE 7 | TEM images and corresponding SAED pattern for calcined particles from **(a–c)** sucrose-based solutions and **(d–f)** DMF-based solutions.

DATA AVAILABILITY STATEMENT

All datasets generated for this study are included in the article/supplementary material.

AUTHOR CONTRIBUTIONS

GJ conducted the experiments and wrote the manuscript. FM proofread the manuscript and helped with the analysis of the data. Conceptualization, project administration, and funding acquisition was done by PG.

FUNDING

This project was sponsored by National Science Foundation DMR # 1724455.

REFERENCES

Albonetti, S., Cavani, F., Trifirò, F., and Venturoli, P. (1996). A comparison of the reactivity of "nonequilibrated" and "equilibrated" V-P-O catalysts: structural evolution, surface characterization, and reactivity in the selective oxidation of n-butane and n-pentane. *J. Catal.* 160, 52–64. doi: 10.1006/jcat.1996.0123

Allen, C. J., Jia, Q. Y., Chinnasamy, C. N., Mukerjee, S., and Abraham, K. M. (2011). Synthesis, structure and electrochemistry of lithium vanadium phosphate cathode materials. *J. Electrochem. Soc.* 158, A1250–A1259. doi: 10.1149/2.003112jes

Anumula, R., Nookaraju, M., Selvaraj, K., Reddy, I. A. K., and Narayanan, V. (2013). A novel vanadium n-propylamino phosphate catalyst: synthesis, characterization and applications. *Mater. Res.* 16, 181–189. doi: 10.1590/S1516-14392012005000161

Bartley, J. K., Kiely, C. J., Wells, R. P. K., and Hutchings, G. J. (2001). Vanadium(V) phosphate prepared using solvent-free method. *Catal. Lett.* 72, 99–105. doi: 10.1023/A:1009085127038

Conte, M., Budroni, G., Bartley, J. K., Taylor, S. H., Carley, A. F., Schmidt, A., et al. (2006). Chemically induced fast solid-state transitions of omega-VOPO4 in vanadium phosphate catalysts. *Science* 313, 1270–1273. doi: 10.1126/science.1130493

Coulston, G. W., Bare, S. R., Kung, H., Birkeland, K., Bethke, G. K., Harlow, R., et al. (1997). The kinetic significance of V5+ in n-butane oxidation catalyzed by vanadium phosphates. *Science* 275, 191–193. doi: 10.1126/science.275.5297.191

Dupré, N., Wallez, G., Gaubicher, J., and Quarton, M. (2004). Phase transition induced by lithium insertion in αI- and αII-VOPO4. *J. Solid State Chem.* 177, 2896–2902. doi: 10.1016/j.jssc.2004.04.006

Gaubicher, J., Le Mercier, T., Chabre, Y., Angenault, J., and Quarton, M. (1999). Li/beta-VOPO4: a new 4 V system for lithium batteries. *J. Electrochem. Soc.* 146, 4375–4379.

Girgsdies, F., Schneider, M., Brückner, A., Ressler, T., and Schlögl, R. (2009). The crystal structure of δ-VOPO4 and its relationship to ω-VOPO4. *Solid State Sci.* 11, 1258–1264. doi: 10.1016/j.solidstatesciences.2009.03.017

Guliants, V. V., Benziger, J. B., Sundaresan, S., Wachs, I. E., Jehng, J.-M., Roberts, J. E., et al. (1996). The effect of the phase composition of model VPO catalysts for partial oxidation of n-butane. *Catal. Today* 28, 275–295. doi: 10.1016/S0920-5861(96)00043-0

He, G., Huq, A., Kan, W. H., and Manthiram, A. (2016a). beta-NaVOPO4 obtained by a low-temperature synthesis process: a new 3.3 V cathode for sodium-ion batteries. *Chem. Mater.* 28, 1503–1512. doi: 10.1021/acs.chemmater.5b04992

He, G., Kan, W. H., and Manthiram, A. (2016b). A 3.4 V layered VOPO4 cathode for Na-Ion batteries. *Chem. Mater.* 28, 682–688. doi: 10.1021/acs.chemmater.5b04605

Hutchings, G. J., Kiely, C. J., Sananes-Schulz, M. T., Burrows, A., and Volta, J. C. (1998). Comments on the nature of the active site of vanadium phosphate catalysts for butane oxidation. *Catal. Today* 40, 273–286. doi: 10.1016/S0920-5861(98)00015-7

Jiao, X., Chen, D., Pang, W., Xu, R., and Yue, Y. (1998). Solvothermal synthesis and characterization of silica-pillared titanium phosphate. *J. Mater. Chem.* 8, 2831–2834. doi: 10.1039/a802838i

Kerr, T. A., Gaubicher, J., and Nazar, L. F. (2000). Highly reversible Li insertion at 4 V in epsilon-VOPO4/alpha-LiVOPO4 cathodes. *Electrochem. Solid State Lett.* 3, 460–462. doi: 10.1149/1.1391179

Khan, A., Khan, A. A. P., Rahman, M. M., and Asiri, A. M. (2016). High performance polyaniline/vanadyl phosphate (PANI-VOPO4) nano composite sheets prepared by exfoliation/intercalation method for sensing applications. *Eur. Poly. J.* 75, 388–398. doi: 10.1016/j.eurpolymj.2016.01.003

Lee, K. H., Lee, Y. W., Lee, S. W., Ha, J. S., Lee, S. S., and Son, J. G. (2015). Ice-templated Self-assembly of VOPO4-graphene nanocomposites for vertically porous 3D supercapacitor electrodes. *Sci. Rep.* 5:13696. doi: 10.1038/srep13696

Li, G. C., Li, Y. M., Li, Y., Peng, H. R., and Chen, K. Z. (2011). Polyaniline nanorings and flat hollow capsules synthesized by in situ sacrificial oxidative templates. *Macromolecules* 44, 9319–9323. doi: 10.1021/ma2014854

Ling, C., Zhang, R., and Mizuno, F. (2014). Phase stability and its impact on the electrochemical performance of VOPO4 and LiVOPO4. *J. Mater. Chem. A* 2, 12330–12339. doi: 10.1039/C4TA01708K

Purwanto, A., Wang, W. N., and Okuyama, K. (2011). "Flame spray pyrolysis," in *Handbook of Atomization and Sprays*, ed N. Ashgriz (Boston, MA: Springer)

Rownaghi, A., Taufiq-Yap, Y. H., and Rezaei, F. (2009). Solvothermal synthesis of vanadium phosphate catalysts for n-butane oxidation. *Chem. Eng. J.* 155, 514–522. doi: 10.1016/j.cej.2009.07.055

Socrates, G. (2004). *Infrared and Raman Characteristic Group Frequencies: Tables and Charts*. John Wiley & Sons.

Song, Y., Zavalij, P. Y., and Whittingham, M. S. (2005). ε-VOPO4: electrochemical synthesis and enhanced cathode behavior. *J. Electrochem. Soc.* 152, A721–A728. doi: 10.1149/1.1862265

Strobel, R., and Pratsinis, S. E. (2007). Flame aerosol synthesis of smart nanostructured materials. *J. Mater. Chem.* 17, 4743–4756. doi: 10.1039/b711652g

Sun, W., and Du, J. (2017). Structural stability, electronic and thermodynamic properties of VOPO4 polymorphs from DFT+U calculations. *Comput. Mater. Sci.* 126, 326–335. doi: 10.1016/j.commatsci.2016.09.046

Sydorchuk, V., Khalameida, S., Zazhigalov, V., Skubiszewska-Zieba, J., and Leboda, R. (2010). Solid-state interactions of vanadium and phosphorus oxides in the closed systems. *J. Thermal Anal. Calorimetry* 100, 11–17. doi: 10.1007/s10973-010-0696-x

Teoh, W. Y., Amal, R., and Mädler, L. (2010). Flame spray pyrolysis: an enabling technology for nanoparticles design and fabrication. *Nanoscale* 2, 1324–1347. doi: 10.1039/c0nr00017e

Ulrich, G. D. (1971). Theory of particle formation and growth in oxide synthesis flames. *Combust. Sci. Technol.* 4, 47–57. doi: 10.1080/00102207108952471

Wang, S. H., and Huang, Y. (2016). Flame aerosol synthesis of WO3/CeO2 from aqueous solution: two distinct pathways and structure design. *Chem. Eng. Sci.* 152, 436–442. doi: 10.1016/j.ces.2016.06.045

Whittingham, M. S., Song, Y. N., Lutta, S., Zavalij, P. Y., and Chernova, N. A. (2005). Some transition metal (oxy)phosphates and vanadium oxides for lithium batteries. *J. Mater. Chem.* 15, 3362–3379. doi: 10.1039/b501961c

Wu, C., Lu, X., Peng, L., Xu, K., Peng, X., Huang, J., et al. (2013). Two-dimensional vanadyl phosphate ultrathin nanosheets for high energy density and flexible pseudocapacitors. *Nat. Commun.* 4:2431. doi: 10.1038/ncomms3431

Xue, M., Chen, H., Zhang, H., Auroux, A., and Shen, J. (2010). Preparation and characterization of V-Ag-O catalysts for the selective oxidation of toluene. *Appl. Catal. A Gen.* 379, 7–14. doi: 10.1016/j.apcata.2010.02.023

Conflict of Interest: The authors declare that the research was conducted in the absence of any commercial or financial relationships that could be construed as a potential conflict of interest.

frontiers in Materials

ORIGINAL RESEARCH
published: 13 November 2019
doi: 10.3389/fmats.2019.00285

Ethanol Sensing Properties of Nanocrystalline α-MoO_3

*Sucheta Sau, Sonam Chakraborty, Tanushri Das and Mrinal Pal**

Council of Scientific and Industrial Research-Central Glass and Ceramic Research Institute, Kolkata, India

Ethanol sensors with effective and selective sensitivity are extensively used by traffic police to detect drunken drivers, in wine industries for controlling the fermentation process, food package testing, different medical applications etc. Orthorhombic phase pure α – MoO_3 nanoparticles were synthesized via facile sol-gel technique to ethanol sensor. It was observed that the gas sensing response of the sample toward 100 ppm of ethanol vapor is 59% at 350 °C. The response and the recovery time of the gas sensor toward 100 ppm ethanol vapor are found to be 34 s and 70 s, respectively. The main obstacle for a gas sensor to be an excellent breath analyser is to remain insensitive toward the main interfering agent of exhaling human breath i.e. moisture. Prepared sensor is highly selective and shows almost no response toward saturated moisture.

Keywords: α – MoO_3, nanoparticles, sol-gel, ethanol vapor, sensitivity

OPEN ACCESS

Edited by:
Sheikh A. Akbar,
The Ohio State University,
United States

Reviewed by:
Tridib Kumar Sinha,
Gyeongsang National University,
South Korea
Mukul Pradhan,
National Institute of Technology
Meghalaya, India

****Correspondence:***
Mrinal Pal
palm@cgcri.res.in

Specialty section:
This article was submitted to Functional Ceramics, a section of the journal Frontiers in Materials

Received: *01 July 2019*
Accepted: *23 October 2019*
Published: *13 November 2019*

Citation:
Sau S, Chakraborty S, Das T and Pal M (2019) Ethanol Sensing Properties of Nanocrystalline α-MoO_3. Front. Mater. 6:285. doi: 10.3389/fmats.2019.00285

INTRODUCTION

Nowadays due to the increase in environmental pollution and health hazards there is an increase in the demand for efficient chemical sensors to monitor environment (Wang et al., 2011a; Chao et al., 2012; Yang et al., 2013). Also, sensors are now considered as promising candidate for human exhale breath analysis to monitoring diseases. Acetone, alcohol, ammonia and so on, are some of the volatile organic compounds (VOCs) present in our breath (Guo et al., 2014; Xua et al., 2013; Tomer and Duhan, 2016). So, based on their elevated concentration in breath lots of diseases can be diagnosed which is very important to monitor human health (Endre et al., 2011; Reyes-Reyes et al., 2015; Brannelly et al., 2016). Among these VOCs ethanol is one of the widely studied pollutants. Accurate ppm level ethanol detection is quite difficult. Detection of ethanol vapor is very important for traffic police to detect drunken drivers, to control the fermentation process, etc. However, detection of a single target analyte amidst 1000 other volatiles (some of which could be cross-interfering) remains a challenge for the researchers. GC-MS, ion spectrometry etc. are traditional gas analysis tools. However, they are costly sophisticated and requires skilled manpower for operation. Need of the hour is metal oxide semiconductor based gas sensor which can be use as a breath analyzer.

Metal oxide semiconducting nanoparticles are considered to be the most efficient and promising material for gas sensors due to the presence of higher oxygen vacancies and surface area (Philip et al., 2006; Brezesinski et al., 2010; Greiner et al., 2013). There are many materials that are known to detect ethanol in ppm-ppb level. An n-type semiconducting pure orthorhombic molybdenum trioxide (MoO_3) nanoparticle delineate lots of astonishing applications e.g., catalysis, energy storage, gas sensors etc (Chen et al., 2000; Rahmani et al., 2010; Sui et al., 2015; Yan et al., 2015). MoO_3 stands out as it regards to ease of synthesis, excellent sensitivity, selectivity, and

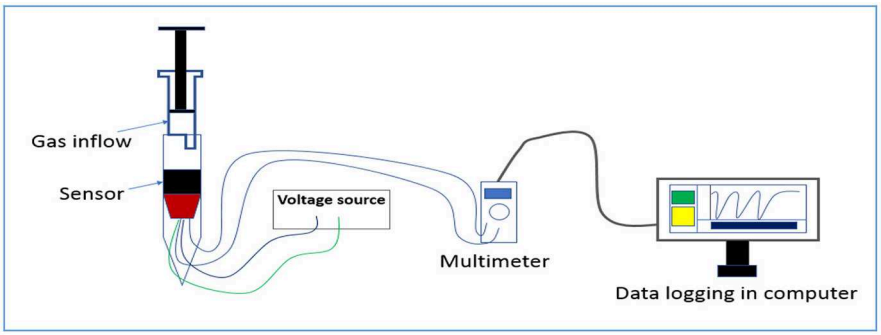

FIGURE 1 | Schematic of gas sensing measurement.

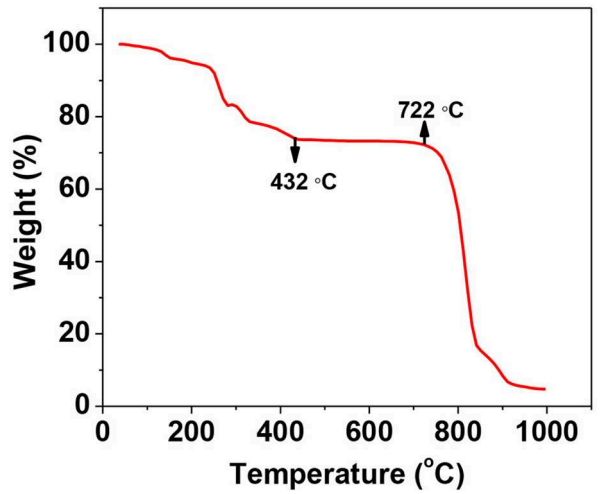

FIGURE 2 | TGA analysis of as prepared MoO_3 gel from room temperature to 1,000°C.

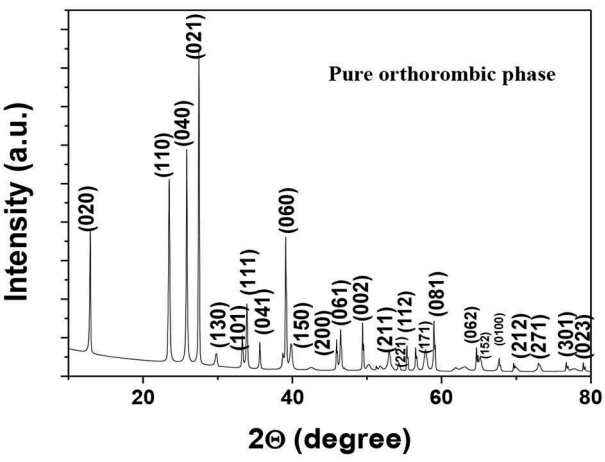

FIGURE 3 | X-ray diffraction pattern of α-MoO_3 calcined at 500°C.

excellent anti-aging properties. Work by Zadeh et al. delineates that Zn doped MoO_3 shows only 20% sensitivity toward 100 ppm of ethanol (Mousavi-Zadeh and Rahman, 2018). Another work by Mandal et al. demonstrates excellent ethanol sensitivity of MoO_3 nanobelts and nanofibres synthesized via hydrothermal route (Mandal et al., 2019). There are some literature which proves that MoO_3 nanoparticles are very good sensing elements (Sun et al., 2017; Yang et al., 2017).

In the present work nanocrystalline phase pure α-MoO_3 has been prepared using a facile sol-gel route. The phase purity and morphology of the sample were confirmed by analyzing it using different sophisticated tools namely thermogravimetric analysis (TGA), X-ray diffraction analysis (XRD), Fourier Transform Infrared Spectroscopy (FTIR), Ultraviolet-vis (UV-vis) spectroscopy, and field emission scanning electron microscopy (FESEM), transmission electron microscopy (TEM). The sufficiently good sensitivity of pristine MoO_3 toward ethanol is reported here.

EXPERIMENTAL

Material Preparation

α- MoO_3 nanoparticles have been prepared by using facile sol-gel route (Ganguly and George, 2007). At first 6.17 gm of ammonium heptamolybdate (NH4)6Mo7O24·4H2O, Merck) was added in 200 ml of distilled water and stirred it for 15 min to dissolve the precursor completely. Then 1.05 gm of citric acid monohydrate $(HOC(COOH)(CH_2COOH)_2 \cdot H_2O$, Sigma aldrich) was added to the above solution. The above solution was stirred until the acid gets dissolved. After this the solution was kept over a hot plate at 60°C and stirrer continuously. Then requisite amount of ammonium hydroxide (NH_3OH, Merck) was drop wise added to the above solution with constant stirring to keep the solution pH between 7 and 8. After that we left the solution on the hot plate until a thick gel is formed. Then the gel was kept in a furnace overnight at 120°C for drying. At last we calcined the material at 500°C for 4 h and collected the powdered sample for further use. It is to be noted here that the pH of the solution implies a lot of effect on the morphology of the product. There are some articles on the synthesis of α-MoO_3 nanostructures which describes the pH dependency of the sample on its morphology. Li et al. in his works very clearly showed the pH dependent growth of different morphology preparation of α-MoO_3 nanoparticles (Chao et al., 2012). Again Parwiz et al. delineates that how size

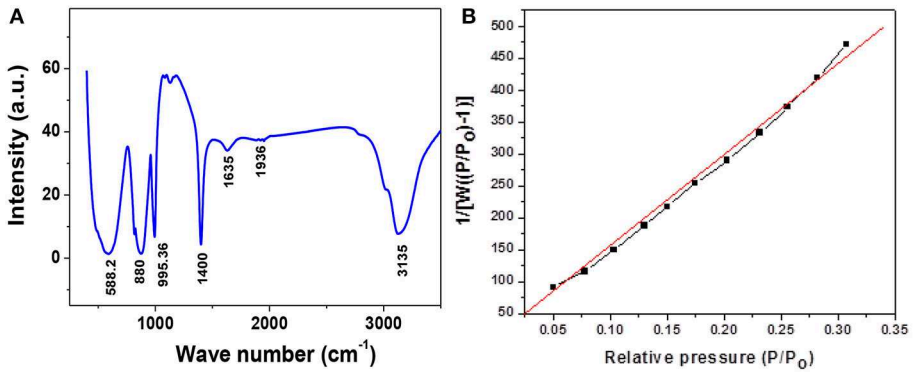

FIGURE 4 | (A) FTIR analysis of phase pure α-MoO_3 nanoparticles, **(B)** BET surface area plot.

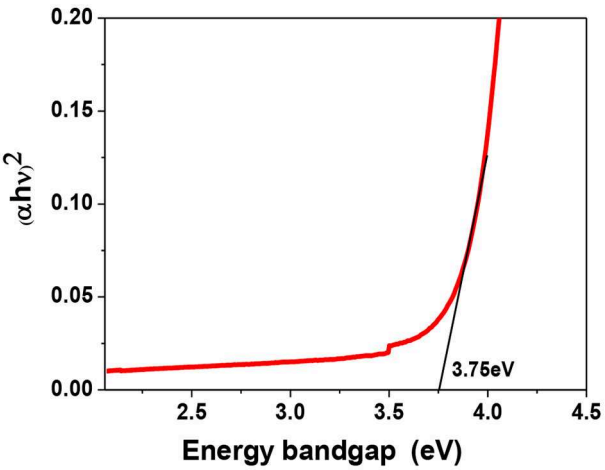

FIGURE 5 | Tauc plot of α-MoO_3 nanoparticles calcined at 500°C.

of the particles can be controlled on changing the pH of the solution (Yang et al., 2013).

Characterization

Using a NETZSCH 449C the thermogravitic analyser (TGA) of MoO_3 was performed from 25° to 1,000°C with a heating rate of 10°C/min. The XRD analysis of the sample was carried out using X'Pert pro MPD XRD (PANalytical) diffractometer fitted with Cu Kα radiation. Band gap of the sample was estimated from light absorption ability plot using a UV-Vis spectrometer (CECIL Aquarius 7200). FTIR absorption spectra of the samples were studied using a Nicolet 380 FTIR spectrometer. A Carl Zeiss Supra 35 VP FESEM was used to conduct the morphological study in detail. The microstructural characterization study was undertaken using a Tecnai G2 30ST (FEI) transmission electron microscope (TEM). Current voltage (I-V) measurement was performed using a Agilent B2901A precision source meter at different temperature. For sensitivity study with different VoCs at various concentration a computer interfaced Agilent U1253A multimeter was used. A schematic (**Figure 1**) for gas sensing study has been provided for better understanding.

RESULTS AND DISCUSSION

Structural and Morphological Analysis

TGA analysis of the as-prepared gel in the temperature range from room temperature to 1,000°C was as shown in **Figure 2**. It shows that the material at first shows 5% weight loss up to 100°C which can be ascribed to loss of water present in the sample. Then there is 30% cumulative weight loss up to 432°C and 80% cumulative weight loss between 722° and 910°C. These weight losses are due to combustion of citric acid and volatilisation of the material itself, respectively.

The X-ray diffraction pattern of α-MoO_3 calcined at 500 °C was shown in **Figure 3**. All the prominent peaks matched well with standard data (JCPDS card no. 35-0609) which confirms the formation of orthorhombic phase pure $\alpha - MoO_3$. The graph shows no extra peaks from any other impurity phase.

Figure 4A shows the FTIR pattern of pure phase $\alpha - MoO_3$ nanoparticles calcined at 500°C. Three strong vibrations peaks were detected at 588, 880 and 995 cm^{-1}, associated, respectively, with the stretching mode of oxygen linked with three metal atoms, the stretching mode of oxygen in Mo–O–Mo units, and the Mo=O stretching mode of a layered orthorhombic α-MoO_3 phase (Chiang and Yeh, 2013). The wavenumbers at 1,400, 1,635, 1,936, and 3,135 cm^{-1} are due to different stretching, vibration and bending modes of surface adsorbed water molecules, respectively. BET surface area of $\alpha - MoO_3$ nanoparticles calcined at 500°C is as shown in **Figure 4B**. The surface area calculated from the graph of the sample comes to be 2.360 m^2/g. Presence of various bonds indicates the growth of desire phase.

UV-Vis absorption study was carried out to get the information of energy ban structure. **Figure 5** delineates the Tauc plot of $\alpha - MoO_3$ nanoparticles for determining the energy bandgap. The energy bandgap of bulk MoO_3 is around 3.02 eV and the estimated bandgap of this sample comes to be around 3.75 eV. As compared to the bandgap of bulk MoO_3 there

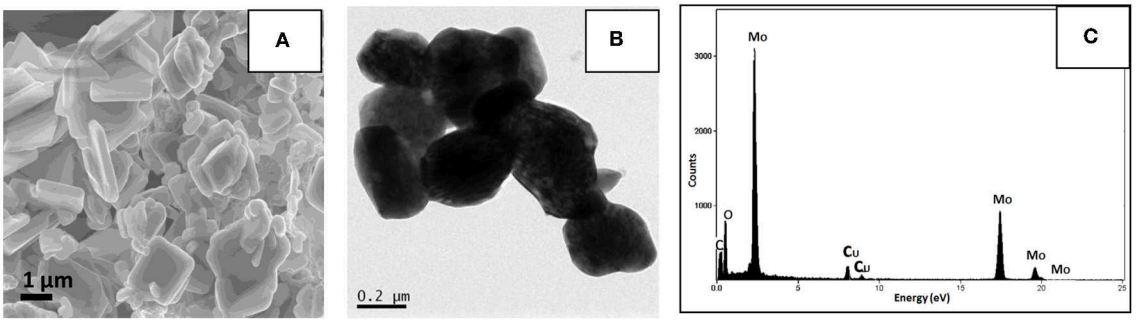

FIGURE 6 | α-MoO_3 nanoparticles calcined at 500°C **(A)** FESEM image, **(B)** TEM image, **(C)** EDAX analysis.

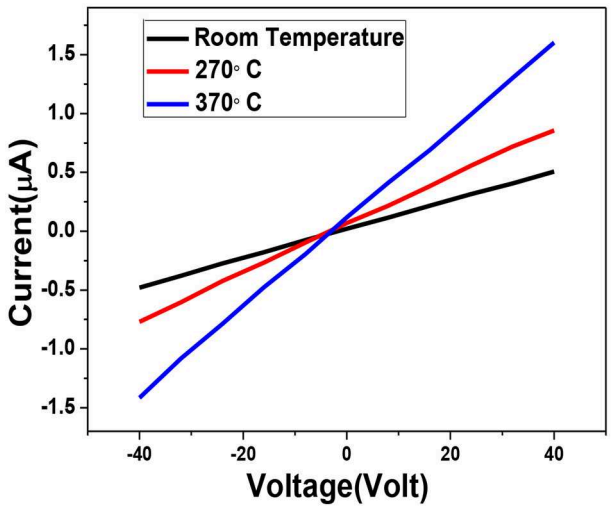

FIGURE 7 | IV-measurements of α-MoO_3 nanoparticles at room temperature, 270°C and 370°C.

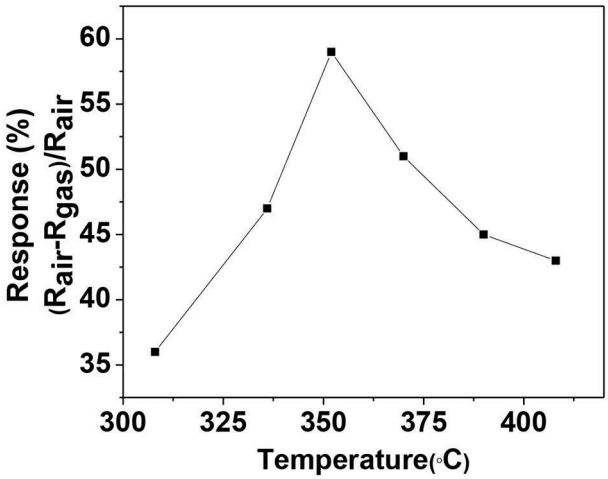

FIGURE 8 | Temperature vs. response (%) plot for α-MoO_3 nanoparticles for 100 ppm ethanol.

is a blue shift in this sample due to the decrease in particle size (Patil et al., 2011).

FESEM micrograph of the synthesized $\alpha - MoO_3$ nanoparticles is shown in **Figure 6A**. It was found that the particles tried to form a thin plate-like structures. Also they are agglomerated in nature. This plate-like structure will be more effective to interact with the gas analyte. The TEM image in **Figure 6B** is similar to the FESEM image which shows that the sample is not completely spherical but plate-like structure. The EDAX image (**Figure 6C**) in the above figure confirms the absence of any other elements other than Mo and O. Since the sample was mounted on a carbon-coated copper grid so C and Cu peaks were visible in the graph.

Electrical and Gas Sensing Study

Since the prepared sensors are chemiresistive in nature; we have investigated the electrical transport behavior before its gas sensing study. Current-voltage (I-V) study of the sensor at ambient as well as different higher temperature is displayed in **Figure 7**. IV-characteristic measurement is very important to check the semiconductor-metal contact of the sensor element. I-V curve demonstrate good linear behavior at higher temperature which implies that the contact will remain the good if the sensor is operated at this temperature range. We have observed an ohmic behavior in the voltage range from −40 V to +40 V up to temperature around 370°C. Furthermore, no asymmetry is observed between direct and reverse regimes. The material exhibits semiconducting nature as the resistance of the material decreases with increasing temperature.

For gas sensing study the prepared sample was ground thoroughly and mixed well with iso-propyl alcohol used as a binder. Then this paste was coated on the hollow aluminum tube which is electrode at with the gold paste at the two ends and connected to platinum wires of 0.1 mm diameter.

nichrome wire was inserted in the tube for heating the sensor element. Now the substrate was welded to stainless steel pins attached to a polymeric sensor head. The sensor head is covered with 200 µm mesh polymer net to protect the sensor from dust and other external particles (Chakraborty and Pal, 2017, 2019). Prepared sensor module was inserted in an indigenously built set up for sensing measurement. **Figure 8** shows the response

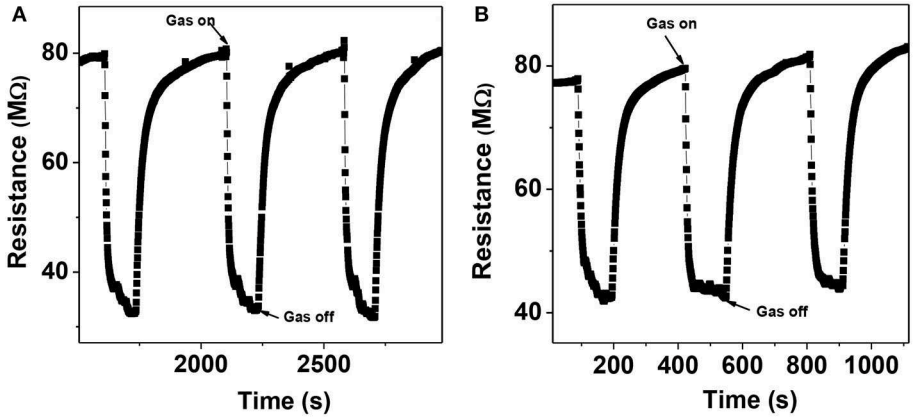

FIGURE 9 | Dynamic response curve of α-MoO_3 nanoparticles toward, **(A)** 100 ppm of ethanol, **(B)** 50 ppm of ethanol, at 350°C.

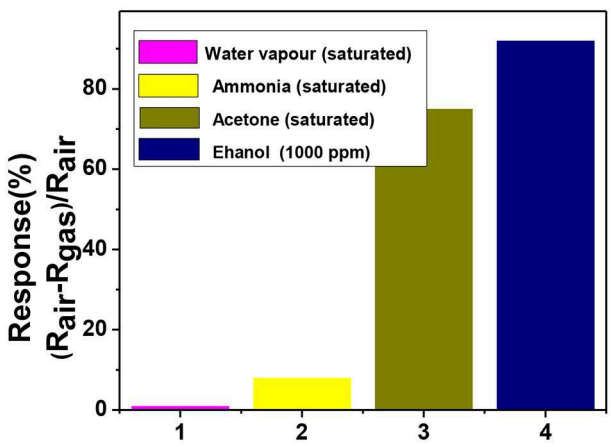

FIGURE 10 | Selectivity checks of α-MoO_3 nanoparticles at operating temperature (350°C).

(%) of the sensor with the increasing operational temperature from 310° to 410°C toward 100 ppm of ethanol vapor. The operating temperature of the material for ethanol sensing comes out to be 350°C at which it shows maximum sensitivity. The response (%) at first increases with the increasing temperature then reaches saturation and then again starts to decrease. This behavior is normal for metal-oxide based sensors (Chakraborty and Pal, 2019).

The dynamic response curve shows the reproducibility of the sensor, which is completely reversible and very much required for sensing application. **Figures 9A,B** gives the resistance vs. time plot for 100 and 50 ppm ethanol, respectively. The response percentage of the sensor was calculated using the relation (1),

$$S(\%) = (R_{air} - R_{gas})/R_{air} \quad (1)$$

It was observed that the sensors delineated a good response of 59% toward 100 ppm of ethanol at 350°C. The response time and recovery time of the sensor are calculated to be 34 and 70 s, respectively. The base resistance of the sample remains almost constant throughout the whole process.

Selectivity is another important property of gas sensors. **Figure 10** shows the selectivity of the sensing elements toward saturated ethanol and other VOCs like acetone and ammonia. The sensing performance was checked in the presence of moisture as it is an important interfering agent while considering for breathalyzer. The selectivity curve demonstrates that this sensor is very much selective toward ethanol vapor. The sensitivity of a particular material depends on its surface area, topology, morphology, defect states, and operating temperature. Though the material remains same if we change the operating temperature, morphology then the selectivity of the sample may change. The operating temperature plays a vital role in selecting gas analyte because the activation energy to break the gas analyte over the sensing material is different for different gas. The operating temperature for ammonia detection is higher around 400° to 450°C.

Gas Sensing Mechanism

MoO_3 is an n-type metal oxide semiconductor with lots of lattice oxygen vacancies. Since gas sensing depends on the surface adsorbed oxygen molecules so here surface oxygen vacancies (interstitial oxygen and oxygen vacancies) play the main role. There is a coexistence of interstitial oxygen and oxygen vacancies for a surface defective MoO_3 (Mandal et al., 2019). On the interaction of these oxygen defects with the ethanol, there is a release of free electrons in the conduction band. This oxygen vacancy activates the –CO and OH bond of ethanol and dehydrogenation takes place (Mandal et al., 2019). This will, in turn, increase the free electron concentration in the conduction band and hence the resistance will decrease.

CONCLUSION

We have successfully grown pure α-MoO_3 nanoparticles using the facile sol-gel technique. It was observed that the orthorhombic phase of MoO_3 shows a good response toward ethanol vapor in compared to acetone and ammonia. The gas sensors based on MoO_3 manifest proficient response of 59% toward 100 ppm of ethanol vapor with fast response (34s) and recovery time (70 s) at the operating temperature 350°C. It also shows insensitivity toward moisture which is very important if used as breath analyzer.

DATA AVAILABILITY STATEMENT

The datasets generated for this study are available on request to the corresponding author.

AUTHOR CONTRIBUTIONS

All authors listed have made a substantial, direct and intellectual contribution to the work, and approved it for publication.

ACKNOWLEDGMENTS

Authors are thankful to DST-INSPIRE for providing fellowship and also to Material Characterization division of CSIR-CGCRI, Kolkata for rendering their support toward XRD, TEM/SEM measurements. Authors acknowledge Sagnik Das, Sk. Md. Mursalin, Md. Jalaluddin Mondal, and Raju Manna for their help in making the sensor module and helping in measurement. The authors are also thankful to DST-CSIR Sensor Hub (GAP 0332) for providing the facilities to conduct our experiments. TD acknowledges the project sponsored by DST-Nanomission (GAP 0368) for financial support.

REFERENCES

Brannelly, N. T., Hamilton-Shield, J. P., and Killard, A. J. (2016). The measurement of ammonia in human breath and its potential in clinical diagnostics. *Crit. Rev. Anal. Chem*. 46, 490–501. doi: 10.1080/10408347.2016.1153949

Brezesinski, T., Wang, J., Tolbert, S. H., and Dunn, B. (2010). Ordered mesoporous α-MoO_3 with iso-oriented nanocrystalline walls for thin-film pseudocapacitors. *Nat. Mater*. 9, 146–151. doi: 10.1038/nmat2612

Chakraborty, S., and Pal, M. (2017). Improved sensitivity of CdS nanoparticles by virtue of calcium doping: promising candidate for monitoring alcohol in exhale human breath. *Mater. Des*. 126, 18–28. doi: 10.1016/j.matdes.2017.04.032

Chakraborty, S., and Pal, M. (2019). Highly selective and stable acetone sensor based on chemically prepared bismuth ferrite nanoparticles. *J. Alloys Compd*. 787, 1204–1211. doi: 10.1016/j.jallcom.2019.02.153

Chao, J. F., Xu, X., Huang, H. T., Liu, Z., Liang, B., Wang, X. F., et al. (2012). Porous SnO_2 nanoflowers derived from tin sulfide precursors as high performance gas sensor. *Cryst. Eng. Comm*. 14, 6654–6658. doi: 10.1039/c2ce25089f

Chen, K., Xie, S., Bell, A. T., and Iglesia, E. (2000). Alkali effects on molybdenum oxide catalystsfor the oxidative dehydrogenation of propane. *J. Catal.* 195, 244–252. doi: 10.1006/jcat.2000.3025

Chiang, T. H., and Yeh, H. C. (2013). The synthesis of α-MoO_3 by Ethylene Glycol. *Materials.* 6, 4609–4625. doi: 10.3390/ma6104609

Endre, Z. H., Pickering, J. W., Storer, M. K., Hu, W. P., Moorhead, K. T., Allardyce, R., et al. (2011). Breath ammonia and trimethylamine allow real-time monitoring of haemodialysis efficacy. *Physiol. Meas*. 32, 115–130. doi: 10.1088/0967-3334/32/1/008

Ganguly, A., and George, R. (2007). Synthesis, characterization and gas sensitivity of MoO_3 nanoparticles. *Bull. Mater. Sci*. 30, 183–185. doi: 10.1007/s12034-007-0033-6

Greiner, M. T., Chai, L., Helander, M. G., Tang, W. M., and Lu, Z. H. (2013). Metal/Metal-oxide in-terfaces: how metal contacts affect the work function and band structure of MoO3. *Adv. Funct. Mater.* 23, 215–226. doi: 10.1002/adfm.201200993

Guo, J., Zhang, J., Zhu, M., Ju, D., Xu H., and Cao, B. (2014) High-performance gas sensor based on ZnO nanowires functionalized by Au nanoparticles. *Sens. Actuators B.* 199, 339-345. doi: 10.1016/j.snb.2014.04.010

Mandal, B., Aaryashree, D., Htay, M., and Mukherjee, M. T. (2019). Architecture tailoring of MoO_3 nanostructures for superior ethanol sensing performance. *Mater. Res. Bull*. 109, 281–290. doi: 10.1016/j.materresbull.2018.09.041

Mousavi-Zadeh, S. H., and Rahman, M. B. (2018). Synthesis and ethanol sensing characteristics of nanostructured MoO_3:Zn thin films. *Surf. Rev. Lett*. 25, 1850046–1850056. doi: 10.1142/S0218625X18500464

Patil, S. B., Mane, S. R., Patil, V. R., Kharade, R. R., and Bhosale, P. N. (2011). Chemosynthesis and characterization of electrochromic vanadium doped molybdenum oxide thin films. *Arch. Appl. Sci. Res*. 3, 481–491.

Philip, J., Punnoose, A., Kim, B. I., Reddy, K. M., Layne, S., Holmes, J. O., et al. (2006). Carrier-controlled ferromagnetism intransparent oxide semiconductors. *Nat. Mater*. 5 298–304. doi: 10.1038/nmat1613

Rahmani, M. B., Keshmiri, S. H., Yu, J., Sadek, A. Z., Al-Mashat, L., Moafi, A., et al. (2010). Gas sensing properties of thermally eva-porated lamellar MoO3, Sens. *Actuat. Chem*. 145, 13–19. doi: 10.1016/j.snb.2009.11.007

Reyes-Reyes, A., Horsten, R. C., Urbach, H. P., and Bhattacharya, N. (2015). Study of the exhaled acetone in type 1 diabetes using quantum cascade laser spectroscopy. *Anal. Chem*. 87, 507–512. doi: 10.1021/ac504235e

Sui, L., Song, X., Cheng, X., Zhang, X., Xu, Y., Gao, S., et al. (2015). An ultraselective and ultrasensitive TEA sensor based on α-MoO_3 hierarchical nanostructures and the sensing mechanism. *Cryst. Eng. Comm*. 17, 6493–6503. doi: 10.1039/C5CE00693G

Sun, Y., Chen, L., Wang, Y., Zhao, Z., Li, P., Zhang, W., Hu, J., et al. (2017). Synthesis of MoO_3/WO_3composite nanostructures for highly sensitive ethanol and acetone detection. *J. Mater. Sci*. 52, 1561–1572. doi: 10.1007/s10853-016-0450-2

Tomer, V. K., and Duhan, S. (2016). Ordered mesoporous Ag-doped TiO2/SnO2 nanocomposite based highly sensitive and selective VOC sensors. *J. Mater. Chem.* 4, 1033–1043. doi: 10.1039/C5TA08336B

Wang, L. L., Fei, T., Lou, Z., and Zhang, T. (2011a). Three-dimensional hierarchical flowerlike -Fe_2O_3 nanostructures: synthesis and ethanol-sensing properties. *ACS Appl. Mater. Interfaces* 3, 4689–4694. doi: 10.1021/am201112z

Xua, Q. H., Xua, D. M., Guana, M. Y., Guoa, Y., Qi, Q., and Li, G. D. (2013). ZnO/Al2O3/CeO2 composite with enhanced gas sensing performance. *Sens. Actuators* 177, 1134 -1141. doi: 10.1016/j.snb.2012.12.029

Yan, H., Song, P., Zhang, S., Yang, Z., and Wang, Q. (2015). Facile fabrication and enhanced gassensing properties of hierarchical MoO_3 nanostructures. *RSC Adv.* 5, 72728–72735. doi: 10.1039/C5RA13036K

Yang, L., Lin, H. Y., Zhang, Z. S., Cheng, L., Ye, S. Y., and Shao, M. W. (2013). Gas sensing of tellurium-modified silicon nanowires to ammonia and propylamine. *Sens. Actuator.* 177 260–264. doi: 10.1016/j.snb.2012.10.136

Yang, S., Liu, Y., Chen, T., Jin, W., Yang, T., Cao, M., et al. (2017). Zn doped MoO3 nanobelts and the enhanced gas sensing properties to ethanol. *Appl. Surf. Sci*. 393, 377–384. doi: 10.1016/j.apsusc.2016.10.021

Conflict of Interest: The authors declare that the research was conducted in the absence of any commercial or financial relationships that could be construed as a potential conflict of interest.

Advantages of publishing in Frontiers

OPEN ACCESS
Articles are free to read for greatest visibility and readership

FAST PUBLICATION
Around 90 days from submission to decision

HIGH QUALITY PEER-REVIEW
Rigorous, collaborative, and constructive peer-review

TRANSPARENT PEER-REVIEW
Editors and reviewers acknowledged by name on published articles

Frontiers
Avenue du Tribunal-Fédéral 34
1005 Lausanne | Switzerland

Visit us: www.frontiersin.org
Contact us: info@frontiersin.org | +41 21 510 17 00

REPRODUCIBILITY OF RESEARCH
Support open data and methods to enhance research reproducibility

DIGITAL PUBLISHING
Articles designed for optimal readership across devices

FOLLOW US
@frontiersin

IMPACT METRICS
Advanced article metrics track visibility across digital media

EXTENSIVE PROMOTION
Marketing and promotion of impactful research

LOOP RESEARCH NETWORK
Our network increases your article's readership